AD-A219 957

UNITED STATES AIR FORCE
SUMMER FACULTY RESEARCH PROGRAM
1989
PROGRAM TECHNICAL REPORT
UNIVERSAL ENERGY SYSTEMS, INC.
VOLUME II of IV

Program Director, UES
Rodney C. Darrah

Program Administrator, UES
Susan K. Espy

Program Manager, AFOSR
Lt. Col. Claude Cavender

Submitted to

Air Force Office of Scientific Research

Bolling Air Force Base

Washington, DC

December 1989

ECURITY CLASSIFICATION OF THIS PAGE

REPORT DOCUMENTATION PAGE

REPORT SECURITY CLASSIFICATION: UNCLASSIFIED	1b. RESTRICTIVE MARKINGS
2a. SECURITY CLASSIFICATION AUTHORITY	3. DISTRIBUTION/AVAILABILITY OF REPORT: APPROVED FOR PUBLIC RELEASE; Distribution Unlimited
2b. DECLASSIFICATION/DOWNGRADING SCHEDULE	
4. PERFORMING ORGANIZATION REPORT NUMBER(S)	5. MONITORING ORGANIZATION REPORT NUMBER(S): AFOSR-TR-90-0367
6a. NAME OF PERFORMING ORGANIZATION: Universal Energy Systems, INc; 6b. OFFICE SYMBOL (If applicable)	7a. NAME OF MONITORING ORGANIZATION: AFOSR/XOT
6c. ADDRESS (City, State and ZIP Code): 4401 Dayton-Xenia Road, Dayton, OH 45432	7b. ADDRESS (City, State and ZIP Code): Building 410, Bolling AFB, DC 20332
8a. NAME OF FUNDING/SPONSORING ORGANIZATION: AFOSR; 8b. OFFICE SYMBOL (If applicable): XOT	9. PROCUREMENT INSTRUMENT IDENTIFICATION NUMBER: F49620-85-C-0013
8c. ADDRESS (City, State and ZIP Code): Building 410, Bolling AFB, DC 20332	10. SOURCE OF FUNDING NOS.

PROGRAM ELEMENT NO.	PROJECT NO.	TASK NO.	WORK UNIT NO.
61102F	3396	D5	

11. TITLE (Include Security Classification): USAF Summer Faculty Research Program - Management Report - Vol 2of4

12. PERSONAL AUTHOR(S): Rodney C. Darrah, Susan K. Espy

TYPE OF REPORT	13b. TIME COVERED	14. DATE OF REPORT (Yr., Mo., Day)	15. PAGE COUNT
Annual	FROM _____ TO _____	Dec 89	

16. SUPPLEMENTARY NOTATION

17. COSATI CODES			18. SUBJECT TERMS (Continue on reverse if necessary and identify by block number)
FIELD	GROUP	SUB. GR.	

19. ABSTRACT (Continue on reverse if necessary and identify by block number)

See Attached

20. DISTRIBUTION/AVAILABILITY OF ABSTRACT: LASSIFIED/UNLIMITED XX ☐ SAME AS RPT. ☐ DTIC USERS ☐	21. ABSTRACT SECURITY CLASSIFICATION: UNCLASSIFIED

22a. NAME OF RESPONSIBLE INDIVIDUAL	22b. TELEPHONE NUMBER (Include Area Code)	22c. OFFICE SYMBOL
Lt Col Claude Cavender	202-767-4970	XOT

PREFACE

The United States Air Force Summer Faculty Resarch Program (USAF-SFRP) is designed to introduce university, college, and technical institute faculty members to Air Force research. This is accomplished by the faculty members being selected on a nationally advertised competitive basis for a ten-week assignment during the summer intersession period to perform research at Air Force laboratories/centers. Each assignment is in a subject area and at an Air Force facility mutually agreed upon by the faculty members and the Air Force. In addition to compensation, travel and cost of living allowances are also paid. The USAF-SFRP is sponsored by the Air Force Office of Scientific Research, Air Force Systems Command, United States Air Force, and is conducted by Universal Energy Systems, Inc.

The specific objectives of the 1989 USAF-SFRP are:

(1) To provide a productive means for U.S. faculty members to participate in research at Air Force Laboratories/Centers;

(2) To stimulate continuing professional association among the faculty and their professional peers in the Air Force;

(3) To further the research objectives of the United States Air Force;

(4) To enhance the research productivity and capabilities of the faculty especially as these relate to Air Force technical interests.

During the summer of 1989, 168-faculty members participated. These researchers were assigned to 23 USAF laboratories/centers across the country. This four volume document is a compilation of the final reports written by the assigned faculty members about their summer research efforts.

TABLE OF CONTENTS

PREFACE

The United States Air Force Summer Faculty Resarch Program (USAF-SFRP) is designed to introduce university, college, and technical institute faculty members to Air Force research. This is accomplished by the faculty members being selected on a nationally advertised competitive basis for a ten-week assignment during the summer intersession period to perform research at Air Force laboratories/centers. Each assignment is in a subject area and at an Air Force facility mutually agreed upon by the faculty members and the Air Force. In addition to compensation, travel and cost of living allowances are also paid. The USAF-SFRP is sponsored by the Air Force Office of Scientific Research, Air Force Systems Command, United States Air Force, and is conducted by Universal Energy Systems, Inc.

The specific objectives of the 1989 USAF-SFRP are:

(1) To provide a productive means for U.S. faculty members to participate in research at Air Force Laboratories/Centers;

(2) To stimulate continuing professional association among the faculty and their professional peers in the Air Force;

(3) To further the research objectives of the United States Air Force;

(4) To enhance the research productivity and capabilities of the faculty especially as these relate to Air Force technical interests.

During the summer of 1989, 168-faculty members participated. These researchers were assigned to 23 USAF laboratories/centers across the country. This four volume document is a compilation of the final reports written by the assigned faculty members about their summer research efforts.

LIST OF 1989 PARTICIPANTS

NAME/ADDRESS	DEGREE, SPECIALTY, LABORATORY ASSIGNED
Thomas Abraham Instructor Saint Paul's College Sci. & Math. Dept. Lawrenceville, VA 23868 804\848-3111	Degree: MS Specialty: Mathematics Assigned: School of Aerospace Medicine
Charles Alajajian Assistant Prof. West Virginia University PO Box 6101 Morgantown, WV 26506 304\293-6371	Degree: PhD Specialty: Electrical Eng. Assigned: Rome Air Development Center
Barbara Alvin Associate Prof. Eastern Washington Univ. Math Dept. #32 Cheney, WA 99004 509\359-2203	Degree: PhD Specialty: Biostatistics Assigned: Occupational & Environmental Health Laboratory
Jon Anderson Assistant Prof. Texas Tech. University PO Box 4200 Lubbock, TX 79409 806\742-3538	Degree: PhD Specialty: Civil Engineering Assigned: Engineering & Services Center
Peter Armendarez Professor Brescia College 7th at Frederica Owensboro, KY 42301 502\686-4285	Degree: PhD Specialty: Physical Chemistry Assigned: Armament Laboratory
Pradip Bakshi Professor Boston College Physics Dept. Chestnut Hill, MA 02167 617\552-3585	Degree: PhD Specialty: Theoretical Physics Assigned: Geophysics Laboratory

NAME/ADDRESS	DEGREE, SPECIALTY, LABORATORY ASSIGNED
William Bannister Professor Lowell, University of Dept. of Chemistry Lowell, MA 01854 508\452-5000	Degree: PhD Specialty: Organic Chemistry Assigned: Engineering & Services Center
Beryl Barber Assistant Prof. Oregon Institute of Tech. 3201 Campus Dr. Klamath Falls, OR 97601 503\882-3899	Degree: MS Specialty: Electronic Engineering Assigned: Electronic Systems Division
Brian Beecken Assistant Prof. Bethel College 3900 Bethel Dr. St. Paul, MN 55112 612\638-6334	Degree: PhD Specialty: Physics Assigned: Arnold Engineering Development Center
Christopher Bell Assistant Prof. Illinois State Univ. 133 Stevenson Normal, IL 61761 309\438-8338	Degree: PhD Specialty: Psychology Assigned: Human Resources Laboratory: Manpower & Personnel Div.
Kevin Bennett Assistant Prof. Wright State University 309 Oelman Hall Dayton, OH 45435 513\873-2444	Degree: PhD Specialty: Applied Psychology Assigned: Human Resources Laboratory: Logistics & Human Factors
Emerson Besch Professor Florida, University of Box J-144 JHMHSC Gainesville, FL 32610 904\392-1841	Degree: PhD Specialty: Animal Physiology Assigned: Engineering & Services Center

NAME/ADDRESS	DEGREE, SPECIALTY, LABORATORY ASSIGNED
Robert Blystone Professor Trinity University 715 Stadium Dr. San Antonio, TX 78284 512\736-7231	Degree: PhD Specialty: Zoology Assigned: School of Aerospace Medicine
Karren Brito Research Chem. Dayton, University of 300 College Park Dayton, OH 45469 513\229-3118	Degree: PhD Specialty: Chemistry Assigned: Materials Laboratory
Lee Britt Instructor Grambling State University Dept. of Physics Grambling, LA 71245 318\274-2575	Degree: MS Specialty: Physics Assigned: Arnold Engineering Development Center
Joseph Brown Professor Mississippi State Univ. PO Brawer ME Mississippi State, MS 39762 601\325-7310	Degree: PhD Specialty: Mechanical Engineering Assigned: Armament Laboratory
Roger Bunting Professor Illinois State University Dept. of Chemistry Normal, IL 61761 309\438-7661	Degree: PhD Specialty: Inorganic Chemistry Assigned: Armament Laboratory
Larry Byrd Assistant Prof. Arkansas State University PO Box 1080 State University, AR 72467 501\972-2088	Degree: PhD Specialty: Mechanical Engineering Assigned: Flight Dynamics Laboratory

NAME/ADDRESS	DEGREE, SPECIALTY, LABORATORY ASSIGNED
Anthony Carlisle Assistant Prof. Huntingdon College 1500 E. Fairview Ave. Montgomery, AL 36194 205\265-0511	Degree: MS Specialty: Computer Science Assigned: Engineering & Services Center
Carolyn Caudle-Alexander Assistant Prof. Tennessee State University 3500 John A. Merritt Blvd. Nashville, TN 37209 615\320-3115	Degree: PhD Specialty: Microbiology Assigned: School of Aerospace Medicine
James Chambers Associate Prof. Texas-San Antonio, Univ. Brain Research Lab. of Biochemistry San Antonio, TX 78285 512\691-5477	Degree: PhD Specialty: Biochemistry Assigned: School of Aerospace Medicine
Satish Chandra Assistant Prof. Kansas State Univ. Dept. of Elec. and Comp. Eng. Manhattan, KS 66506 913\532-5600	Degree: PhD Specialty: Electrical Engineering Assigned: Armament Laboratory
Chi Chen Professor Southeastern Mass. Univ. Dept. of Elect. & Comp. Eng. North Dartmouth, MA 02747 508\999-8475	Degree: PhD Specialty: Electrical Engineering Assigned: Geophysics Laboratory
David Choate Assistant Prof. Transylvania University Dept. of Mathematics Lexington, KY 40508 606\233-8237	Degree: PhD Specialty: Mathematics Assigned: Avionics Laboratory

NAME/ADDRESS	DEGREE, SPECIALTY, LABORATORY ASSIGNED
Ajit Choudhury Associate Prof. Howard University Dept. of Electrical Eng. Washington, DC 20059 202\636-6593	Degree: PhD Specialty: Electrical Engineering Assigned: Electronic Systems Division
Derald Chriss Assistant Prof. Southern University PO Box 10572 Baton Rouge, LA 70813 504\771-3990	Degree: MS Specialty: Chemistry Assigned: Engineering & Services Center
Donald Chung Associate Prof. San Jose State Univ. Dept. of Mat. Eng. San Jose, CA 95192 408\924-3873	Degree: PhD Specialty: Material Science Assigned: Materials Laboratory
Mingking Chyu Assistant Prof. Carnegie Mellon University Dept. of Mechanical Eng. Pittsburgh, PA 15213 412\268-3658	Degree: PhD Specialty: Mechanical Engineering Assigned: Aero Propulsion Laboratory
David Cicci Assistant Prof. Auburn University 162 Wilmore Laboratories Auburn, AL 36849 205\826-4874	Degree: PhD Specialty: Aerospace Engineering Assigned: Armament Laboratory
Brian Circelli Assistant Prof. Mississippi, Univ. of Dept. of Chemical Eng. University, MS 38677 601\232-5347	Degree: PhD Specialty: Chemical Engineering Assigned: Arnold Engineering Development Ctr.

NAME/ADDRESS	DEGREE, SPECIALTY, LABORATORY ASSIGNED
Jerry Clark Assistant Prof. Wright State Univ. Dept. of Physics Dayton, OH 45435 513\873-2954	Degree: PhD Specialty: Physics Assigned: Aero Propulsion Laboratory
Stephen Cobb Assistant Prof. Murray State University Dept. of Physics Murray, KY 42071 502\762-6186	Degree: PhD Specialty: Physics Assigned: Arnold Engineering Development Ctr.
Kathryn Cochran Assistant Prof. Northern Colorado, University Div. of Res., Eval., & Devel. Greeley, CO 80639 303\351-2807	Degree: PhD Specialty: Educational Psychology Assigned: Human Resources Laboratory: Manpower & Personnel Division
R. H. Cofer Professor Florida Institute 150 W. University Blvd. Melbourne, FL 32901 407\984-5689	Degree: PhD Specialty: Electrical Eng. Assigned: Avionics Laboratory
George Coleman Instructor Elizabeth City St. University Dept. of Mathematics Elizabeth City, NC 27909 919\335-3487	Degree: MS Specialty: Applied Mathematics Assigned: Armament Laboratory
Kenneth Cornelius Assistant Prof. Wright State Univ. Dept. of Mechanical Eng. Dayton, OH 45435 513\873-3682	Degree: PhD Specialty: Fluid Mechanics Assigned: Flight Dynamics Laboratory

NAME/ADDRESS	DEGREE, SPECIALTY, LABORATORY ASSIGNED
Mark Cornwall Assistant Prof. Northern Arizona Univ. POB 15105 Flagstaff, AZ 86011 602\523-1606	Degree: PhD Specialty: Human Performance Assigned: School of Aerospace Medicine
Larry Crum Professor Wright State University Dept. of Comp. Sci. & Eng. Dayton, OH 45435 513\259-1342	Degree: PhD Specialty: Electrical Engineering Assigned: Avionics Laboratory
Kenneth Currie Assistant Prof. Kansas State Univ. 228 Durland Hall Manhattan, KS 66506 913\532-5606	Degree: PhD Specialty: Industrial Engineering Assigned: Materials Laboratory
Phanindramohan Das Professor Texas A&M University Dept. of Meteorology College Station, TX 77843 409\845-0633	Degree: PhD Specialty: *Geophysical Science* Assigned: Geophysics Laboratory
Vito DelVecchio Chairman Scranton, University of Biology Dept. Scranton, PA 18510 717\961-6117	Degree: PhD Specialty: Biochemical Engineering Assigned: School of Aerospace Medicine
Avery Demond Assistant Prof. Massachusetts, University of Dept. of Civil Eng. Amherst, MA 01003 413\545-0685	Degree: PhD Specialty: Civil Engineering Assigned: Engineering & Services Center

NAME/ADDRESS	DEGREE, SPECIALTY, LABORATORY ASSIGNED
Walter Drost-Hansen Professor Miami, University of Dept. of Chemistry Coral Gables, FL 33124 305\284-5842	Degree: PhD Specialty: Physical Chemical Assigned: Wilford Hall Medical Center
Thomas Dwyer Professor Illinois, University of 104 South Mathews Ave. Urbana, IL 61801 217\244-0720	Degree: PhD Specialty: Mathematics Assigned: Weapons Laboratory
Wayne Eckerle Associate Prof. Clarkson University MIE Dept. Clarkson University, NY 13676 315\268-2203	Degree: PhD Specialty: Fluid Mechanics Assigned: Aero Propulsion Laboratory
Dennis Farrell Associate Prof. Cincinnati, University of Mail Location 103 Cincinnati, OH 45210 513\556-6558	Degree: MS Specialty: Electrical Engineering Assigned: Flight Dynamics Laboratory
William Filippone Associate Prof. Arizona, University of Group X6, MS B226 Los Alamos, NM 87545 505\665-2307	Degree: PhD Specialty: Nuclear Engineering Assigned: Weapons Laboratory
John Francis Professor Oklahoma, University of 865 Asp, Room 210 Norman, OK 73019 405\325-5011	Degree: PhD Specialty: Mechanical Engineering Assigned: Arnold Engineering Development Ctr.

NAME/ADDRESS	DEGREE, SPECIALTY, LABORATORY ASSIGNED
Frank Gerner Assistant Prof. Cincinnati, University of 756 Baldwin Hall Mail Loc. #72 Cincinnati, OH 45221 513\566-2646	Degree: PhD Specialty: Mechanical Engineering Assigned: Aero Propulsion Laboratory
Robert Granger Professor US Naval Academy Dept. of Mechanical Engineering Annapolis, MD 21402 301\267-3186	Degree: PhD Specialty: Mechanical Engineering Assigned: Frank J. Seiler Research Lab.
William Grissom Assistant Prof. Morehouse College 830 Westview Dr. SW Atlanta, GA 30314 404\681-2800	Degree: MS Specialty: Mechanical Eng. Assigned: Weapons Laboratory
Ian Grosse Assistant Prof. Massachusetts, University of ELAB 213 Amherst, MA 01003 413\545-1350	Degree: PhD Specialty: Mechanical Eng. Assigned: Rome Air Development Center
John Hadjilogiou Professor Florida Instit.Tech. 150 West University Blvd. Melbourne, FL 32901 407\768-8000	Degree: PhD Specialty: Electrical Eng. Assigned: Rome Air Development Center
Ernest Hallford Assistant Prof. Moorhead State Univ. Dept. of Psychology Moorhead, MN 56560 218\236-4077	Degree: PhD Specialty: Psychology Assigned: Aerospace Medical Research Lab.

NAME/ADDRESS	DEGREE, SPECIALTY, LABORATORY ASSIGNED
Orlando Hankins Assistant Prof. North Carolina State Univ. NCSU Box 7909 Raleigh, NC 27695 919\737-3292	Degree: PhD Specialty: Nuclear Eng. Assigned: Arnold Engineering Development Center
Patrick Hannon Associate Prof. Northern Arizona University Box 6012 Flagstaff, AZ 86011 602\523-4331	Degree: PhD Specialty: Exercise Science Assigned: School of Aerospace Medicine
Cynthia Hardy Associate Prof. Jackson State Univ. 1400 Lynch St. Jackson, MS 39217 601\968-2371	Degree: PhD Specialty: Education Psychology Assigned: School of Aerospace Medicine
Kirk Hatfield Assistant Prof. Florida, University of 346 Weil Hall Gainesville, FL 32611 904\392-0956	Degree: PhD Specialty: Civil Engineering Assigned: Engineering & Services Center
Kim Hayes Assistant Prof. Michigan, University of Dept. of Civil Engineering Ann Arbor, MI 48109 313\763-9661	Degree: PhD Specialty: Environmental Eng. Assigned: Engineering & Services Center
Henry Helmken Professor Florida Atlantic University PO Box 3091 Boca Raton, FL 33431 407\367-3452	Degree: PhD Specialty: Physics Assigned: Rome Air Development Center

NAME/ADDRESS	DEGREE, SPECIALTY, LABORATORY ASSIGNED
Peter Henriksen Associate Prof. Akron, University Dept. of Physics Akron, OH 44325 216\375-6054	Degree: PhD Specialty: Physics Assigned: Materials Laboratory
Lloyd Hillman Assistant Prof. Cornell University 215 Phillips Hall Ithaca, NY 14853 607\255-8212	Degree: PhD Specialty: Optical Engineering Assigned: Frank J. Seiler Research Lab.
Jeffrey Himm Assistant Prof. North Dakota State University Dept. of Physics Fargo, ND 58105 701\237-7048	Degree: PhD Specialty: Physics Assigned: School of Aerospace Medicine
Stuart Hirshfield Associate Prof. Hamilton College Dept. of Math. & Comp. Sci. Clinton, NY 13323 315\859-4136	Degree: PhD Specialty: Computer Science Assigned: Rome Air Development Center
Harry Hogan Assistant Prof. Texas A&M University Eng./Physics Bldg. College Station, TX 77843 409\845-1538	Degree: PhD Specialty: Mechanical Eng. Assigned: Weapons Laboratory
Gwendolyn Howze Associate Prof. Texas Southern Univ. 3100 Cleburne Houston, TX 77004 713\527-7095	Degree: PhD Specialty: Molecular Biology Assigned: School of Aerospace Medicine

NAME/ADDRESS	DEGREE, SPECIALTY, LABORATORY ASSIGNED
Carl Ingling Associate Prof. Ohio State Univ. 1314 Kinnear Rd. Columbus, OH 43212 614\292-6424	Degree: PhD Specialty: Psychology Assigned: Aerospace Medical Research Lab.
Alan Kafka Associate Prof. Boston College Weston Observatory Weston, MA 02193 617\899-0950	Degree: PhD Specialty: Geophysics Assigned: Geophysics Laboratory
Mohammad Karim Associate Prof. Dayton, University of 300 College Park Dayton, OH 45469 513\229-3611	Degree: PhD Specialty: Electrical Eng. Assigned: Avionics Laboratory
John Kenney Assistant Prof. Eastern New Mexico University Station #33 Portales, NM 88130 505\562-2152	Degree: PhD Specialty: Physical Chemistry Assigned: Astronautics Laboratory
M. Kenney Instructor Eastern New Mexico University Station #33 Portales, NM 88130 505\562-2152	Degree: MS Specialty: Physical Chemistry Assigned: Astronautics Laboratory
Charles Kincaid Lecturer Florida, University of 477 Little Hall Gainesville, FL 32611 904\392-1941	Degree: MS Specialty: Statistics Assigned: Aerospace Medical Research Lab.

NAME/ADDRESS	DEGREE, SPECIALTY, LABORATORY ASSIGNED
Lynn Kirms Assistant Prof. Southern Oregon St. College Chemistry Dept. Ashland, OR 97520 503\482-6471	Degree: PhD Specialty: Organic Chemistry Assigned: Astronautics Laboratory
Mark Kirms Assistant Prof. Southern Oregon St. College Dept. of Chemistry Ashland, OR 97520 503\482-6471	Degree: PhD Specialty: Organic Chemistry Assigned: Astronautics Laboratory
Michael Klein Professor Worcester Poly Inst 100 Institute Rd. Worcester, MA 01609 508\831-5527	Degree: PhD Specialty: Physics Assigned: Rome Air Development Center
Faysal Kolkailah Professor California Polytec. Dept. of Aero. Eng. San Luis Obispo, CA 93407 805\786-2393	Degree: PhD Specialty: Mechanical Eng. Assigned: Astronautics Laboratory
William Kuriger Professor Oklahoma, University of EECS Dept. Norman, OK 73019 405\325-4721	Degree: PhD Specialty: Electrical Eng. Assigned: Rome Air Development Center
Thomas Lalk Associate Prof. Texas A&M Univ. Dept. of Mechanical Eng. College Station, TX 77843 409\845-4734	Degree: PhD Specialty: Mechanical Eng. Assigned: Aero Propulsion Laboratory

NAME/ADDRESS	DEGREE, SPECIALTY, LABORATORY ASSIGNED
John Lanning Associate Prof. Colorado-Denver, University Box 144, 1200 Larimer St. Denver, CO 80204 303\556-2557	Degree: PhD Specialty: Analytical Chemistry Assigned: Frank J. Seiler Research Lab.
Jay Lee Assistant Prof. Syracuse University Link Hall Syracuse, NY 13244 315\443-4395	Degree: PhD Specialty: Electrical Engineering Assigned: Rome Air Development Center
Lang-Wah Lee Professor Wisconsin-Plattevil. Dept. of Mechanical Eng. Platteville, WI 53818 608\342-1534	Degree: PhD Specialty: Mechanical Eng. Assigned: Arnold Engineering Development Center
Tze San Lee Assistant Prof. Western Illinois University Dept. of Mathematics Macomb, IL 61455 309\298-1485	Degree: PhD Specialty: Applied Mathematics Assigned: School of Aerospace Medicine
Baruch Lieber Assistant Prof. New York, State Univ. of Dept. of Mech. & Aero. Eng. Buffalo, NY 14260 716\636-2391	Degree: PhD Specialty: Aerospace Engineering Assigned: Aero Propulsion Laboratory
Charles Lishawa Assistant Prof. Utica College Burstone Rd. Utica, NY 13502 315\792-3139	Degree: PhD Specialty: Physical Chemistry Assigned: Geophysics Laboratory

NAME/ADDRESS	DEGREE, SPECIALTY, LABORATORY ASSIGNED
Dar-Biau Liu Professor California State University Dept. of Comp. Sci. and Eng. Long Beach, CA 90840 213\985-1594	Degree: PhD Specialty: Applied Math Assigned: Avionics Laboratory
Thomas Lockwood Associate Prof. Wright State Univ. 3640 Col. Glenn Hwy. Dayton, OH 45435 513\873-3060	Degree: PhD Specialty: Toxicology Assigned: Aerospace Medical Research Lab.
Harold Longbotham Assistant Prof. Texas-San Antonio, University 7000 Loop 1604 NW San Antonio, TX 78285 512\691-5518	Degree: PhD Specialty: Electrical Eng. Assigned: School of Aerospace Medicine
Lewis Lutton Associate Prof. Mercyhurst College Glenwood Hills Erie, PA 16546 814\825-0372	Degree: PhD Specialty: Envir. Physiology Assigned: Aerospace Medical Research Lab.
Ethel Matin Professor Long Island Univ. CW Post Campus/LIU Brookville, NY 11548 516\299-2063	Degree: PhD Specialty: Exper. Psychology Assigned: Aerospace Medical Research Lab.
Stewart Maurer Associate Prof. New York Inst. Tech. 1855 Bway New York, NY 10023 212\399-9698	Degree: PhD Specialty: Electrical Eng. Assigned: Occupational and Environmental Health Laboratory

NAME/ADDRESS	DEGREE, SPECIALTY, LABORATORY ASSIGNED
Amy Miller Assistant Prof. Oklahoma, Univ. of 620 Parrington Oval Norman, OK 73019 405\325-4836	Degree: PhD Specialty: Chemistry Assigned: Geophysics Laboratory
Thomas Miller Professor Oklahoma, Univ. of Dept. of Physics & Astronomy Norman, OK 73019 405\325-3961	Degree: PhD Specialty: Physics Assigned: Geophysics Laboratory
Deborah Mitta Assistant Prof. Texas A&M Univ. Dept. of Industrial Eng. College Station, TX 77843 409\845-3299	Degree: PhD Specialty: Industrial Eng. Assigned: Human Resources Laboratory: Logistics & Human Factors
Augustus Morris Assistant Prof. Central State Univ. Dept. of Manufacturing Eng. Wilberforce, OH 45384 513\376-6435	Degree: PhD Specialty: Biomedical Engineering Assigned: Flight Dynamics Laboratory
Rex Moyer Professor Trinity Univ. 715 Stadium Dr. San Antonio, TX 78284 512\736-7242	Degree: PhD Specialty: Microbiology Assigned: School of Aerospace Medicine
Sundaram Natarajan Associate Prof. Tennessee Tech Univ. Box 5004 Cookeville, TN 38505 615\372-3450	Degree: PhD Specialty: Electrical Eng. Assigned: Electronic Systems Division

NAME/ADDRESS	DEGREE, SPECIALTY, LABORATORY ASSIGNED
Henry Nebel Associate Prof. Alfred University Physics Dept. Alfred, NY 14802 607\871-2208	Degree: PhD Specialty: Physics Assigned: Geophysics Laboratory
Joseph Newkirk Assistant Prof. Missouri-Rolla, University 282 McNutt Hall Rolla, MO 65401 314\341-4725	Degree: PhD Specialty: Materials Science Assigned: Materials Laboratory
Duc Nguyen Assistant Prof. Old Dominion Univ. Civil Eng. Dept. Norfolk, VA 23529 804\683-3761	Degree: PhD Specialty: Civil Engineering Assigned: Weapons Laboratory
James Noyes Associate Prof. Wittenberg Univ. Box 720 Springfield, OH 45501 513\327-7858	Degree: PhD Specialty: Computer Science Assigned: Avionics Laboratory
Hugh Nutley Professor Seattle Pacific University 3307 3rd Ave. W. Seattle, WA 98119 206\281-2954	Degree: PhD Specialty: Physics Assigned: Geophysics Laboratory
Robert O'Connell Associate Prof. Missouri, Univ. of ECE Dept. Columbia, MO 65211 314\882-8373	Degree: PhD Specialty: Electrical Eng. Assigned: Rome Air Development Center

NAME/ADDRESS	DEGREE, SPECIALTY, LABORATORY ASSIGNED
Bipin Pai Associate Prof. Purdue Univ. Dept. of Eng. Hammond, IN 46323 219\989-2694	Degree: PhD Specialty: Mechanical Eng. Assigned: Astronautics Laboratory
Harvey Paige Associate Prof. Alfred University PO Box 546 Alfred, NY 14802 607\871-2201	Degree: PhD Specialty: Inorganic Chem. Assigned: Materials Laboratory
Arnold Polak Professor Cincinnati, University of M.L. #70 Cincinnati, OH 45221 513\556-3550	Degree: PhD Specialty: Aerospace Eng. Assigned: Flight Dynamics Laboratory
Randy Pollack Assistant Prof. Wright State Univ. Computer Sci. Dept. Dayton, OH 45435 513\873-2491	Degree: PhD Specialty: Anthropology Assigned: Aerospace Medical Research Lab.
Raymond Quock Professor Univ. of Illinois at Rockford 604 N. 16th St. Milwaukee, WI 53233 414\224-7251	Degree: PhD Specialty: Pharmacology Assigned: School of Aerospace Medicine
Vittal Rao Professor Missouri-Rolla, University Dept. of Electrical Eng. Rolla, MO 65401 314\341-4508	Degree: PhD Specialty: Control Systems Assigned: Astronautics Laboratory

NAME/ADDRESS	DEGREE, SPECIALTY, LABORATORY ASSIGNED
Craig Rasmussen Assistant Prof. Utah State Univ. CASS UMC 4405 Logan, UT 84322 801\750-2967	Degree: PhD Specialty: Physics Assigned: Geophysics Laboratory
Michael Resch Assistant Prof. Nebraska-Lincoln, University of 212 Bancroft Hall Lincoln, NE 68588 402\472-2354	Degree: PhD Specialty: Materials Science Assigned: Materials Laboratory
Richard Robertson Professor California State Univ. 3801 W. Temple Ave. Pomona, CA 91768 714\869-3488	Degree: MS Specialty: Mathematics Assigned: Astronautics Laboratory
Larry Roe Assistant Prof. Virginia Poly Institute Dept. of Mech. Eng. Blacksburg, VA 24061 703\231-7295	Degree: PhD Specialty: Mechanical Eng. Assigned: Aero Propulsion Laboratory
Deborah Ross Assistant Prof. Indiana-Purdue, University of 2101 Coliseum Blvd. East Fort Wayne, IN 46805 219\481-6313	Degree: PhD Specialty: Microbiology Assigned: Engineering & Services Center
Duane Sanders Assistant Prof Texas A&M Univ. Dept. of Civil Eng. College Station, TX 77843 409\845-9566	Degree: PhD Specialty: Civil Engineering Assigned: Weapons Laboratory

NAME/ADDRESS	DEGREE, SPECIALTY, LABORATORY ASSIGNED
John Sanders Assistant Prof. Northwestern State University Fournet Hall Natchitoches, LA 71497 318\357-5501	Degree: PhD Specialty: Chemistry Assigned: Frank J. Seiler Research Lab.
Paul Scheie Professor Texas Lutheran Coll 1000 West Court Seguin, TX 78155 512\379-4161	Degree: PhD Specialty: Biophysics Assigned: School of Aerospace Medicine
William Schulz Professor Eastern Kentucky University Moore 337 Richmond, KY 40475 606\622-1463	Degree: PhD Specialty: Analytical Chemistry Assigned: Aero Propulsion Laboratory
Ronald Seaman Associate Prof. Louisiana Tech University PO Box 3185 Ruston, LA 71272 318\257-4562	Degree: PhD Specialty: Biomedical Eng. Assigned: School of Aerospace Medicine
Sally Sedelow Professor Arkansas-Little Rock, Univ. 33rd and University Little Rock, AR 72204 501\569-8130	Degree: PhD Specialty: Computer Science Assigned: Rome Air Development Center
Nisar Shaikh Assistant Prof. Nebraska-Lincoln, University 212 Bancroft Hall Lincoln, NE 68588 402\472-6692	Degree: PhD Specialty: Applied Math. Assigned: Flight Dynamics Laboratory

NAME/ADDRESS	DEGREE, SPECIALTY, LABORATORY ASSIGNED
Clay Sharts Professor San Diego State University Dept. of Chemistry San Diego, CA 92182 619\594-5576	Degree: PhD Specialty: Chemistry Assigned: Frank J. Seiler Research Lab.
Edmund Shearer Professor Fort Hays State University 600 Park St. Hays, KS 67601 913\628-4506	Degree: PhD Specialty: Chemistry Assigned: Occupational and Environmental Health Laboratory
James Sherwood Assistant Prof. New Hampshire, University of Kingsbury Hall Durham, NH 03824 603\862-2624	Degree: PhD Specialty: Aero. Mechanics Assigned: Materials Laboratory
Robert Shock Associate Wright State Univ. Dept. of CEG and CS Dayton, OH 45435 513\259-8402	Degree: PhD Specialty: Mathematics Assigned: Avionics Laboratory
Hugh Siefken Chairman Greenville College Dept. of Physics Greenville, IL 62246 618\664-4081	Degree: PhD Specialty: Nuclear Physics Assigned: Weapons Laboratory
John Silvestro Assistant Prof. Clemson Univ. Riggs Hall Clemson, SC 29634 803\656-5921	Degree: PhD Specialty: Electrical Eng. Assigned: Weapons Laboratory

NAME/ADDRESS	DEGREE, SPECIALTY, LABORATORY ASSIGNED
Miles Simpson Associate Prof. North Carolina Cent. Univ. Dept. of Sociology Durham, NC 27707 919\560-6420	Degree: PhD Specialty: Sociology Assigned: Human Resources Laboratory: Manpower and Personnel Division
Boghos Sivazlian Professor Florida, Univ. of 303 Weil Hall Gainesville, FL 32611 904\392-1464	Degree: PhD Specialty: Operations Research Assigned: Armament Laboratory
William Smith Associate Prof. Pittsburgh, Univ. of 526 C.L. Pittsburgh, PA 15260 412\624-6559	Degree: PhD Specialty: Linguistics Assigned: Human Resources Laboratory: Training Systems
Michael Stanisic Assistant Prof. Notre Dame, University of Dept. of Aero/Mech Eng. Notre Dame, IN 46556 219\239-7897	Degree: PhD Specialty: Robotics Assigned: Aerospace Medical Research Lab.
Stanley Stephenson Associate Prof. Southwest Texas State University CIS/ADS Dept. San Marcos, TX 78666 512\245-2291	Degree: PhD Specialty: Psychology Assigned: Human Resources Laboratory: Training Systems
Chun Fu Su Assistant Prof. Mississippi State University Dept. of Physics Mississippi State, MS 39762 601\325-2931	Degree: PhD Specialty: Physics Assigned: Arnold Engineering Development Center

NAME/ADDRESS	DEGREE, SPECIALTY, LABORATORY ASSIGNED	
Khaja Subhani Associate Prof. Lawrence Tech. Univ. 21000 West Ten Mile Southfield, MI 48075 313\356-0200	Degree: Specialty: Assigned:	PhD Electrical Eng. Rome Air Development Center
Larry Swanson Assistant Prof. Denver, Univ. of 2390 S. York St. Denver, CO 80208 303\871-3816	Degree: Specialty: Assigned:	PhD Mechanical Eng. Astronautics Laboratory
Michael Sydor Professor Minnesota-Duluth, University of Dept. of Physics Duluth, MN 55812 218\726-7205	Degree: Specialty: Assigned:	PhD Physics Materials Laboratory
Joseph Szucs Associate Prof. Texas A&M Univ. GACD PO Box 1675 Galveston, TX 77553 409\740-4463	Degree: Specialty: Assigned:	PhD Functional Analytics Aerospace Medical Research Lab.
Chi-Ming Tang Associate Prof New York, State Univ. of Dept. of Math Geneseo, NY 14454 716\245-5386	Degree: Specialty: Assigned:	PhD Mathematics Aerospace Medical Research Lab.
Richard Tankin Professor Northwestern Univ. Mechanical Eng. Dept. Evanston, IL 60201 312\491-3532	Degree: Specialty: Assigned:	PhD Mechanical Eng. Aero Propulsion Laboratory

NAME/ADDRESS	DEGREE, SPECIALTY, LABORATORY ASSIGNED
Teresa Taylor Assistant Prof. Missouri-Columbia, University of 600 West Mechanic Independence, MO 64050 816\276-1285	Degree: PhD Specialty: Civil Eng. Assigned: Engineering & Services Center
Ebo Tei Professor Arkansas-Pine Bluff, Univ. of Social & Behavioral Sci. Pine Bluff, AR 71601 501\541-6787	Degree: PhD Specialty: Psychology Assigned: Aerospace Medical Research Lab.
Roger Thompson Assistant Prof. Pennsylvania St. University 233 Hammond Bldg. University Park, PA 16802 814\863-0968	Degree: PhD Specialty: Eng. Mechanics Assigned: Astronautics Laboratory
Richard Tipping Professor Alabama, University Dept. of Physics Tuscaloosa, AL 35487 205\348-3799	Degree: PhD Specialty: Physics Assigned: Arnold Engineering Development Ctr.
Phillip Tomporowski Assistant Prof. Alabama, University of Box 870348 Tuscaloosa, AL 35487 205\348-1936	Degree: PhD Specialty: Psychology Assigned: Human Resources Laboratory: Operations Training Division
Ram Tripathi Professor Texas-San Antonio, Univ. of Dept. of Mathematics San Antonio, TX 78285 512\691-5549	Degree: PhD Specialty: Statistics Assigned: School of Aerospace Medicine

NAME/ADDRESS	DEGREE, SPECIALTY, LABORATORY ASSIGNED
Steven Trogdon Associate Prof. Minnesota-Duluth, University of 108 Heller Hall Duluth, MN 55812 218\726-6173	Degree: PhD Specialty: Mechanics Assigned: Armament Laboratory
Timothy Troutt Associate Prof. Washington State University of Mech. & Mat. Eng. Dept. Pullman, WA 99164 509\335-4375	Degree: PhD Specialty: Mechanical Eng. Assigned: Frank J. Seiler Research Lab.
Donald Ucci Associate Prof. Illinois Inst.Tech. 3300 S. Federal St. Chicago, IL 60616 312\567-3405	Degree: PhD Specialty: Electrical Eng. Assigned: Rome Air Development Center
George Veyera Assistant Prof. Rhode Island, University of Dept. of Civil Eng. Kingston, RI 02881 401\792-2692	Degree: PhD Specialty: Civil Eng. Assigned: Engineering & Services Center
Hung Vu Assistant Prof. California State University Mech. Eng. Dept. Long Beach, CA 90840 213\985-1524	Degree: PhD Specialty: Applied Mechanics Assigned: Frank J. Seiler Research Lab.
Bonnie Walker Assistant Prof. Central State Univ. Psychology Dept. Wilberforce, OH 45384 513\376-6516	Degree: PhD Specialty: Experimental Psychology Assigned: Aerospace Medical Research Lab.

NAME/ADDRESS	DEGREE, SPECIALTY, LABORATORY ASSIGNED
William Wallace Professor Rensselaer Poly. Inst CII Room 5117 Troy, NY 12180 518\276-6452	Degree: PhD Specialty: Management Science Assigned: Rome Air Development Center
Ji Wang Professor San Jose State Univ. S. 7 St. San Jose, CA 95192 408\924-4299	Degree: PhD Specialty: Mechanical Eng. Assigned: Astronautics Laboratory
Phillip Wapner Associate Prof. Southern Illinois University Dept. of Mech. Eng. Carbondale, IL 62901 618\453-7021	Degree: PhD Specialty: Chemical Eng. Assigned: Astronautics Laboratory
Robert Wheasler Professor Wyoming, Univ. of Box 3295 University Station Laramie, WY 82071 307\766-5126	Degree: PhD Specialty: Engineering Assigned: Aero Propulsion Laboratory
D. Wilkes Assistant Prof. Vanderbilt Univ. Box 1649 Station B Nashville, TN 37235 615\343-6016	Degree: PhD Specialty: Electrical Eng. Assigned: Arnold Engineering Development Center
Robert Willis Associate Prof. Mercer University 1400 Coleman Ave. Macon, GA 31207 912\744-2704	Degree: PhD Specialty: Physics Assigned: Geophysics Laboratory

NAME/ADDRESS	DEGREE, SPECIALTY, LABORATORY ASSIGNED
John Wills Professor Indiana Univ. Physics Dept. Bloomington, IN 47405 812\855-1479	Degree: PhD Specialty: Physics Assigned: Geophysics Laboratory
David Woehr Assistant Prof. Texas A&M Univ. Dept. of Psychology College Station, TX 77843 409\845-2097	Degree: PhD Specialty: Industrial Psychology Assigned: Human Resources Laboratory: Manpower and Personnel Division
Michael Wolfe Assistant Prof. West Virginia Univ. PO Box 6025 Morgantown, WV 26506 304\293-4495	Degree: PhD Specialty: Management Science Assigned: Human Resources Laboratory: Logistics & Human Factors
William Wolfe Associate Prof. Ohio State Univ. 470 Hitchcock Hall Columbus, OH 43210 614\292-0790	Degree: PhD Specialty: Engineering Assigned: Flight Dynamics Laboratory
James Wolper Assistant Prof. Hamilton College Dept. of Math. & Comp. Sci. Clinton, NY 13323 315\859-4417	Degree: PhD Specialty: Mathematics Assigned: Rome Air Development Center
Asad Yousuf Assistant Prof. Savannah State College PO Box 20089 Savannah, GA 31404 912\356-2154	Degree: MS Specialty: Electrical Eng. Assigned: Armament Laboratory

NAME/ADDRESS	DEGREE, SPECIALTY, LABORATORY ASSIGNED
Juin Yu Professor West Virginia Tech. Mechanical Eng. Dept. Montgomery, WV 25136 304\442-3248	Degree: PhD Specialty: Mechanical Engineering Assigned: Flight Dynamics Laboratory
Gregory Zagursky Assistant Prof. Morris College Div. General Studies Sumter, SC 29150 803\775-9371	Degree: MS Specialty: Biology Assigned: Occupational and Environmental Health Laboratory
Lawrence Zavodney Assistant Prof. Ohio State Univ. 209 Boyd Lab. Columbus, OH 43210 614\292-2209	Degree: PhD Specialty: Mechanical Eng. Assigned: Flight Dynamics Laboratory
Yehoshua Zeevi Professor Harvard Univ. Applied Sciences Cambridge, MA 02138 617\495-2850	Degree: PhD Specialty: Electrical Eng. Assigned: Human Resources Laboratory: Operations Training Division
Robert Zerwekh Assistant Prof. Northern Illinois University Dept. of Comp. Sci. DeKalb, IL 60115 815\753-6949	Degree: PhD Specialty: Philosophy Assigned: Human Resources Laboratory: Training Systems
Henry Zmuda Assistant Prof. Stevens Inst Tech Dept. of Electrical Eng. Hoboken, NJ 07030 201\420-5507	Degree: PhD Specialty: Electrical Eng. Assigned: Rome Air Development Center

PARTICIPANT LABORATORY ASSIGNMENT

C. PARTICIPANT LABORATORY ASSIGNMENT (Page 1)

1989 USAF/UES SUMMER FACULTY RESEARCH PROGRAM

AERO PROPULSION LABORATORY (WRDC/APL)
(Wright-Patterson Air Force Base)

1. Mingking Chyu
2. Jerry Clark
3. Wayne Eckerle
4. Frank Gerner
5. Thomas Lalk
6. Baruch Lieber
7. Larry Roe
8. William Schulz
9. Richard Tankin
10. Robert Wheasler

ARMAMENT LABORATORY (ATL)
(Eglin Air Force Base)

1. Peter Armandarez
2. Joseph Brown
3. Roger Bunting
4. Satish Chandra
5. David Cicci
6. George Coleman
7. Boghos Sivazlian
8. Steven Trogdon
9. Asad Yousuf

HARRY G. ARMSTRONG AEROSPACE MEDICAL RESEARCH LABORATORY (AAMRL)
(Wright-Patterson AFB)

1. Ernest Hallford
2. Carl Ingling
3. Charles Kincaid
4. Thomas Lockwood
5. Lewis Lutton
6. Ethel Matin
7. Randy Pollack
8. Michael Stanisic
9. Joseph Szucs
10. Chi-Ming Tang
11. Ebo Tei
12. Bonnie Walker

ARNOLD ENGINEERING DEVELOPMENT CENTER (AEDC)
(Arnold Air Force Base)

1. Brian Beecken
2. Lee Britt
3. Brian Circelli
4. Stephen Cobb
5. John Francis
6. Orlando Hankins
7. Lang-Wah Lee
8. Chun Fu Su
9. Richard Tipping
10. D. Mitchell Wilkes

ASTRONAUTICS LABORATORY (AL)
Edwards Air Force Base)

1. John Kenney
2. M. Inga Kenney
3. Lynn Kirms
4. Mark Kirms
5. Faysal Kolkailah
6. Bipin Pai
7. Vittal Rao
8. Richard Robertson
9. Larry Swanson
10. Roger Thompson
11. Ji Wang
12. Phillip Wapner

AVIONICS LABORATORY (WRDC/AL)
(Wright-Patterson Air Force Base)

1. David Choate
2. R. H. Cofer
3. Larry Crum
4. Mohammad Karim
5. Dar-Biau Liu
6. James Noyes
7. Robert Shock

C. PARTICIPANT LABORATORY ASSIGNMENT (Page 2)

ELECTRONIC SYSTEMS DIVISION (ESD)
(Hanscom Air Force Base)

1. Beryl Barber
2. Ajit Choudhury
3. S. Natarajan

ENGINEERING AND SERVICES CENTER (ESC)
(Tyndall Air Force Base)

1. Jon Anderson
2. William Bannister
3. Emerson Besch
4. Anthony Carlisle
5. Derald Chriss
6. Avery Demond
7. Kirk Hatfield
8. Kim Hayes
9. Deborah Ross
10. Teresa Taylor
11. George Veyera

FLIGHT DYNAMICS LABORATORY (WRDC/FDL)
(Wright-Patterson Air Force Base)

1. Larry Byrd
2. Kenneth Cornelius
3. Dennis Farrell
4. Augustus Morris
5. Arnold Polak
6. Nisar Shaikh
7. William Wolfe
8. Juin Yu
9. Lawrence Zavodney

FRANK J. SEILER RESEARCH LABORATORY (FJSRL)
(USAF Academy)

1. R. Granger
2. L. Hillman
3. John Lanning
4. John Sanders
5. Clay Sharts
6. Timothy Troutt
7. Hung Vu

GEOPHYSICS LABORATORY (AFGL)
(Hanscom Air Force Base)

1. Pradhip Bakshi
2. Chi Chen
3. P. Das
4. Alan Kafka
5. Charles Lishawa
6. Amy Miller
7. Thomas Miller
8. Henry Nebel
9. Hugh Nutley
10. Craig Rasmussen
11. Robert Willis
12. John Wills

HUMAN RESOURCES LABORATORY (HRL)
(Brooks, Williams, and Wright-Patterson Air Force Bases)

1. Christopher Bell
2. Kevin Bennett
3. Kathryn Cochran
4. Deborah Mitta
5. Miles Simpson
6. William Smith
7. Stanley Stephensen
8. P. Tomporowski
9. David Woehr
10. Michael Wolfe
11. Yehoshua Zeevi
12. Robert Zerwekh

C. PARTICIPANT LABORATORY ASSIGNMENT (Page 3)

MATERIALS LABORATORY (ML)
(Wright-Patterson Air Force Base)

1. Karren Brito
2. Donald Chung
3. Kenneth Currie
4. Peter Henrisken
5. Joseph Newkirk
6. Harvey Paige
7. Michael Resch
8. James Sherwood
9. Michael Sydor

OCCUPATIONAL AND ENVIRONMENTAL HEALTH LABORATORY (OEHL)
(Brooks Air Force Base)

1. Barbara Alvin
2. Stewart Maurer
3. Edmund Shearer
4. Gregory Zagursky

ROME AIR DEVELOPMENT CENTER (RADC)
(Griffiss Air Force Base)

1. Charles Alajajian
2. Ian Grosse
3. John Hadjilogiou
4. Henry Helmken
5. Stuart Hirshfield
6. Michael Klein
7. William Kuriger
8. Jay Lee
9. Robert O'Connell
10. Sally Sedelow
11. Khaja Subhani
12. Donald Ucci
13. William Wallace
14. James Wolper
15. Henry Zmuda

SCHOOL OF AEROSPACE MEDICINE (SAM)
(Brooks Air Force Base)

1. Thomas Abraham
2. Robert Blystone
3. Carolyn Caudle-Alexander
4. James Chambers
5. Mark Cornwall
6. Vito DelVecchio
7. Patrick Hannon
8. Cynthia Hardy
9. Jeffrey Himm
10. Gwendolyn Howze
11. Tze San Lee
12. Harold Longbotham
13. Rex Moyer
14. Raymond Quock
15. Paul Scheie
16. Ronald Seaman
17. Ram Tripathi

WEAPONS LABORATORY (WL)
(Kirtland Air Force Base)

1. Thomas Dwyer
2. William Filippone
3. William Grissom
4. Harry Hogan
5. Duc Nguyen
6. Duane Sanders
7. Hugh Siekfen
8. John Silvestro

WILFORD HALL MEDICAL CENTER (WHMC)
(Lackland Air Force Base)

1. Walter Drost-Hansen

RESEARCH REPORTS

RESEARCH REPORTS

1989 SUMMER FACULTY RESEARCH PROGRAM

Arnold Engineering Development Center (continued)

13	Laser-Induced Fluorescence of Iodine and Sodium for Application in Resonant Doppler Velocimetry of Hypersonic Flows	Dr. Stephen Cobb
14	Thermal Analysis of Bodies Subjected to Aerodynamic Heating	Dr. John Francis
15	Diagnostics for Determination of Arc Plasma Parameters of the AEDC HEAT H1 Arc Heater	Dr. Orlando Hankins
16	The Design of Jet Mixers for an Arc Heater: An Experimental Approach	Dr. Lang-Wah Lee
17	Laser Induced Fluorescence (LIF) of Nitric Oxide (NO)	Dr. Chun Fu Su
18	Spectroscopic Monitoring of Exhaust Gases	Dr. Richard Tipping
19	Distributed and Parallel Image and Signal Processing	Dr. D. Wilkes

Astronautics Laboratory

20	Magnetic Perturbations of the Structural Characteristics, Photophysical Properties and Photochemical Behavior of Cryogenic Noble Gas-Alkali Metal Matrices	Dr. John W. Kenney
21	I_{sp} Enhancement Via Adsorption/ Absorption of Small Energetic Molecules on Solid Propellants	Dr. M. Inga Kenney
22	Studies Toward the Synthesis of Pentanitrobishomocubane	Dr. Lynn M. Kirms
23	The Preparation of Poly(imide Siloxane) Polymers: Oxygen Resistant Space Polymers	Prof. Mark Kirms
24	Numerical Presentation of Stress Analysis, Design and Fracture Mechanics for Composite Materials and Structures	Dr. Faysal Kolkailah
25	Fracture Behavior of a Composite Solid Rocket Propellant	Dr. Bipin Pai
26	Robust Control of a L Experimental Grid Using Reduced Order Models	Dr. Vittal Rao

Astronautics Laboratory (continued)

27	A Neural Network Approach to the Adaptive Control of Large Space Structures	Dr. Richard Robertson
28	Cryogenic Heat Pipes	Dr. Larry Swanson
29	Design and Development of a Flexible Multi-Body Dynamics Experiment	Dr. Roger Thompson
30	Synthesis of Active Space Structure Vibration Control Systems for an Astrex Test Article	Dr. Ji Wang
31	Dynamic Mechanical Response of Carbon/ Carbon Composites by Vibrating Reed Measurements	Dr. Phillip Wapner

Electronics Systems Division

32	Carrier Free Radar	Dr. Beryl Barber
33	Detection Performance for Over Resolved Targets with Varying Energy Level in Cells	Dr. Ajit Choudhury
34	Analysis of Testability Concepts and its Application to RSIP	Dr. S. Natarajan

Engineering and Services Center

35	Proposed Innovative Semi-Hard Aircraft Shelter	Dr. Jon Anderson
36	JP-8 Ignitability	Dr. William Bannister
37	Effect of Jet Aircraft Noise on Domestic Goats	Dr. Emerson Besch
38	An Algorithmic System for Subjective Comparisons	Dr. Anthony Carlisle
39	The Study of Alkali-Enhanced Cements and Concretes	Dr. Derald Chriss
40	Prediction of the Capillary Pressure-Saturation Relationships for Aquifiers Contaminated with Jet Fuels	Dr. Avery Demond
41	Contaminant Flux Reduction Through In Situ Solubility Modification	Dr. Kirk Hatfield

Geophysics Laboratory (continued)

56	Estimating Characteristics of Chemical Explosions in New England and Eastern Kazakhstan Using Local and Regional Seismic Data	Dr. Alan Kafka
57	A Study of the Water Vapor Cation-Neutral Reactions	Dr. Randal Lishawa
58	Acidities of Iron Hydride and Various Transition-Metal Compounds; Reactions of Iron and Iron Carbonyl Anions	Dr. Amy Miller
59	Acidities of Iron Hydride and Various Transition-Metal Compounds; Reactions of Iron and Iron Carbonyl Anions (Same Report as Dr. Amy Miller)	Dr. Thomas Miller
60	CO2(4.3μm) Vibrational Temperatures and Limb Radiances Under Sunlit Conditions in the 50-120 KM Altitude Range	Dr. Henry Nebel
61	Estimating Solar Flare Proton Fluences From 1850 with Tritium Data	Dr. Hugh Nutley
62	Electric Fields in the Middle-and Low-Latitude Ionosphere and Plasmasphere	Dr. Craig Rasmussen
63	Review and Assessment of Carbon Dioxide Pressure Broadening Data	Dr. Robert Willis
64	Non-Uniform Clouds	Dr. John Wills

Rome Air Development Center

65	Design Considerations in the Implementation of ACT Programmable Transversal Filters	Dr. Charles Alajajian
66	Automating Finite Element Reliability Assessment of Microelectronic Components	Dr. Ian Grosse
67	Design for Testability: From Components to Systems	Dr. John Hadjilogiou
68	Development of a High Resolution Research Facility	Dr. Henry Helmken
69	Iterative V&V: A Model for Verification and Validation in the Rapid Prototyping Life Cycle	Dr. Stuart Hirshfield

Rome Air Development Center (continued)

70	Capable Neural Networks for Applications in Data Analysis (1988 Participant)	Dr. Oleg Jakubowicz
71	A Study of Interacting Tunneling Units with Possible Application to High Temperature Superconductors	Dr. Michael Klein
72	Design of a Practical Binary Phase-Only Optical Correlator	Dr. William Kuriger
73	A Computer for Temporal Frequency Spectrum of Vegetation Clutter Return	Dr. Jay Lee
74	Material Effects in Photoconductive Frozen Wave Generators	Dr. Robert O'Connell
75	Parallel Processing for Associative Semantic Space Analysis	Dr. Sally Sedelow
76	Characterization of an Optical Switch	Dr. Khaja Subhani
77	Study of a Communication Receiver for Spread Spectrum Signals	Dr. Donald Ucci
78	Tactical Command and Control: A Group Problem Solving and Decision Making Process	Dr. William Wallace
79	Neural Networks for Invariant Pattern Recognition: A Survey of the State of the Art	Dr. James Wolper
80	Optical Beamforming for Phased Array Antennas	Dr. Henry Zmuda

Weapons Laboratory

81	An Experimental Protocol for Line-of-Sight Slewing, Optical Alignment and AFT Body Station Keeping Control Emulation	Dr. Thomas Dwyer
82	Linking the Twodant S_N Code and the MCNP Monte Carlo Code	Dr. William Filippone
83	Simulation of a Spray Reactor for Generating Excited Oxygen	Dr. William Grissom
84	Modeling the Response of Pressurized Composite Cylinders to Laser Damage	Dr. Harry Hogan

Weapons Laboratory (continued)

85	Parallel and Vector Processing for Nonlinear Finite Element Analysis ** To be published at Weapons Lab as Technical Memorandum **	Dr. Duc Nguyen
86	Scattering of Elastic Waves in a Random Inhomogeneous Soil Media	Dr. Duane Sanders
87	A Possible New Source of Negative Hydrogen Ions	Dr. Hugh Siefken
88	The Effect of a Maverick Missile on a Test Antenna at Spacings Less than $2D^2/\lambda$	Dr. John Silvestro

Volume III
(Wright Research Development Center)
Aero Propulsion Laboratory

89	Preliminary Report on Measurements of Turbulent Transport in a Rib Roughened Channel	Dr. Mingking Chyu
90	Experimental Study of Electronic Excitation of Xenon by Electron Impact	Dr. Jerry Clark
91	No Report Submitted	Dr. Wayne Eckerle
92	Flow Limitations in Micro Heat Pipes	Dr. Frank Gerner
93	Conceptual Design of an In-House Facility for Endothermic Fuels Research (Report is not publishable at this time)	Dr. Thomas Lalk
94	Large-Scale Motion and Coherent Structures in Axisymmetric Swirling Flow of a Dump Combustor	Dr. Baruch Lieber
95	Stability Modification and Flowfield Evaluation of a Ramjet Combustor Model	Dr. Larry Roe
96	Oxidative Thermal Degradation Studies of a Surrogate JP-8 with a Modified Thermal Precipitation Apparatus	Dr. William Schulz
97	Measurements of Droplet Velocity and Size Distributions in Sprays	Dr. Richard Tankin
98	Aircraft Engine Compressor and Fan Rework Practices	Dr. Robert Wheasler

Avionics Laboratory

99	A Theoretical Resolution of Multiple Frequencies	Dr. David Choate
100	Ladar Target Detection and Recognition	Dr. R. H. Cofer
101	Toolbox for Image Processing using Distributed Computing	Dr. Larry Crum
102	Analytical Model of a Unique E-O Beam Scanner	Dr. Mohammad Karim
103	Dynamic Task Scheduling for the "ADA Distributed System Evaluation Testbed (ADSET)"	Dr. Dar-Biau Liu
104	Ada Compiler Efficiency Evaluation	Dr. James Noyes
105	Towards a Course-Grained Test Suite for VHDL Validation	Dr. Robert Shock

Flight Dynamics Laboratory

106	Parametric Study of Combined Boiling and Partial Dryout in Liquid Metal Heat Pipe Wicks	Dr. Larry Byrd
107	3-D Analysis of Laser Measurements of Vortex Bursting on Chined Forebody Fighter Configuration	Dr. Kenneth Cornelius
108	Robust Design Using Internal Model Control	Dr. Dennis Farrell
109	Neural Networks and their Role in Visual Object Recognition	Dr. Augustus Morris
110	A Study of Surface Roughness Effects in Hypersonic Flow	Dr. Arnold Polak
111	Life Prediction of Aircraft Transparencies by Accelerated Crazing Tests	Dr. Nisar Shaikh
112	Strain Distribution in Composite Coupons in Tension	Dr. William Wolfe
113	Characteristics of an Osmotically Driven Thermal Transfer Cycle	Dr. Juin Yu
114	The Influence of Viscoelastically Damped Members on the Dynamic Response of Flexible Elastic Structures	Dr. Lawrence Zavodney

Harry G. Armstrong Medical Research Laboratory (continued)

128	Heart Rate and Other Cardiovascular Parameters as Measures of Mental Effort	Dr. Lewis Lutton
129	Breakdown of Total Information Processing Time into During-Display and Post-Display Components for Serial and Spatially Distributed Visual Presentations	Dr. Ethel Matin
130	An Investigation Into Techniques for Landmark Identification on 3-D Images of Human Subjects (Not publishable at this time)	Dr. Randy Pollack
131	Kinematic Mappings Between the EXOS Handmaster Exoskeleton[1] and the Utah/MIT Dexterous Robot Hand	Dr. Michael Stanisic
132	Harness Belt Task	Dr. Joseph Szucs
133	Articulated Total Body (ATB) View Program with Harness-Belt Implementation	Dr. Chi-Ming Tang
134	Insights into Human Factors in Aviation with Emphasis on Non-Canonical Flow Fields	Dr. Ebo Tei
135	Effects of Data Error on Problem-Solving Heuristics	Dr. Bonnie Walker

Human Resources Laboratory

136	Software Development to Support Data Collection and Analysis of Cognitive Task Analysis Studies	Dr. Christopher Bell
137	Computer-based Training for Complex, Dynamic Tasks	Dr. Kevin Bennett
138	Working Memory and Cognitive Structure	Dr. Kathryn Cochran
139	Investigation of Color Appearance within Low Light Levels (1988 Participant)	Dr. Douglas Mandra
140	Fisheye Representation of Information: IMIS User Interface	Dr. Deborah Mitta
141	The Validation of the Occupational Learning Difficulty (OLD) Index as a Predictor of Retrainee Performance	Dr. Miles Simpson

Human Resources Laboratory

142	Assessment of Intelligent Tutoring Systems	Dr. William Smith
143	The Role of the Instructor in Computer Based Training (CBT)	Dr. Stanley Stephenson
144	Evaluation of Air-Intercept Performance: Observer Reliability Issues	Dr. Phillip Tomporowski
145	Career Progression in Air Force Enlisted Personnel: An Examination of Two Alternate Criterion Measures	Dr. David Woehr
146	Development of the "City of Quality (Coq)" Group Decision Support System	Dr. Michael Wolfe
147	Variable Resolution Imagery for Flight Simulators	Dr. Yehoshua Zeevi
148	Neurocomputing the Student Model in an Intelligent Tutoring System	Dr. Robert Zerwekh

Occupational and Environmental Health Laboratory

149	Statistical Analyses of Data Pertaining to Ground Water Contamination and Laboratory Quality Control	Dr. Barbara Alvin
150	Design of an Automated Radiofrequency Radiation Measurement System (ARRMS)	Dr. Stewart Maurer
151	Construction and Use of an Identification Manual for Identifying Fibrous Material by Scanning Electron Microscopy with Attached X-Ray Analyzer	Dr. Edmund Shearer
152	Biological Analysis of Three Ponds at Peterson AFB, Colorado Springs, CO	Dr. Gregory Zagursky

School of Aerospace Medicine

153	Convergence Properties of the Occurrence/Exposure Rate	Mr. Thomas Abraham
154	Transmission Electron Microscopy of Mouse Macrophase RAW 264.7 Cells treated with Lipopolysaccharide, 3-Amino Tryosine, and RFR	Dr. Robert Blystone
155	Effects of Microwave Radiation on Cultured Cells	Dr. Carolyn Caudle-Alexander

School of Aerospace Medicine (continued)

156	The Effects of Three Reputed Carboxyesterase Inhibitors Upon Rat Serum Esterase Activity Using Paranitrophenyl and Naphthyl Esters as Substrates	Dr. James Chambers
157	Anti-G Suit Inflation Influence on Lower Extremity Muscle Performance during Sustained +G_z Acceleration	Dr. Mark Cornwall
158	PCR Analysis and in situ Detection of Ureaplasma urealyticum and Mycoplasma hominis	Dr. Vito DelVecchio
159	The Influence of Broad Spectrum Illumination on Circadian Neuroendocrine Responses and Performance	Dr. Patrick Hannon
160	The relationship between locus of control, performance on cognitive tasks, and affective states after the consumption of antihistamines in hi- and low-workload conditions among aircrew personnel	Dr. Cynthia Ford Hardy
161	Aspects of the Diffusion of Inert Gases in Biological Systems	Dr. Jeffrey Himm
162	Studies of Interactions Between Microwaves, Melanin and Melanocytes	Dr. Gwendolyn Howze
163	Two-Phase Regression Model with Application	Dr. Tze-San Lee
164	System and Signal Analysis of VEP Data and Joystick Error Analysis	Dr. Harold Longbotham
165	Higher Plant Hormones Effect Upon Chlamydomonas Phototaxis	Dr. Rex Moyer
166	Influence of Radio Frequency Radiation on Psychotropic Drug Effects	Dr. Raymond Quock
167	Porous Glass as Bed Material in a Pressure Swing Adsorption Unit Used for Air Purification	Dr. Paul Scheie
168	Models for RFR Biological Effects	Dr. Ronald Seaman

School of Aerospace Medicine (continued)

169	An Investigation of Dioxin Half-Life Heterogeneity in Humans Based on Two Measurements per Subject	Dr. Ram Tripathi

Wilford Hall Medical Center

170	Temperature Effects on Erythrocyte Sedimentation Rates in Whole Blood and on Erythrocyte and Platelet Volumes	Dr. Walter Drost-Hansen

1989 USAF-UES SUMMER FACULTY RESEARCH PROGRAM/

GRADUATE STUDENT RESEARCH PROGRAM

Sponsored by the

AIR FORCE OFFICE OF SCIENTIFIC RESEARCH

Conducted by the

Universal Energy Systems, Inc.

FINAL REPORT

THE VIBRATION OF THIN LEADING EDGES

Prepared by:	Robert A. Granger, Ph.D.
Academic Rank:	Professor
Department and	Mechanical Engineering
University	U.S. Naval Academy
Research Location:	FJSRL/NH
	U.S. Air Force Academy
	Colorado Springs, CO 80840-6528
USAF Researcher:	Major Robert F. Reilman, Jr.
Date:	21 August 1989
Contract No.	F49620-88-C-0053

The Vibration of Thin Leading Edges

by

Robert A. Granger

ABSTRACT

Leading edge vibrations occur in a wide variety of applications, e.g., rotary dynamics, turbomachinery, and unsteady aeroelasticity. The physics of leading edge vibrations is not clearly defined, so four separate and distinct theoretical investigations were made into leading edge vibrations of thin bodies, each investigation based on a different physical model which in turn is governed by a distinct phenomenon. The first theoretical solution was based on the possibility that flow induced vibrations is an aeroelastic instability problem, similar to one-degree-of-freedom flutter, like leading edge buzz. An analysis was conducted using Lagrange's equation of motion and revealed the unlikelihood the phenomenon is a flutter problem. The second theoretical solution was based on Lamb's formulation that the phenomenon is a highly nonlinear response. The nonlinear equation was solved in closed analytical form using Poincare's method of expanding solutions. The third theoretical model was based on the supposition that the vibrations are caused by the unsteady behavior of the stagnation point. The fourth theoretical model represented vortex shedding past a vibrating leading edge. Preliminary experimental results indicate the fourth model may correctly predict the behavior.

Acknowledgements

Appreciation is extended to the Air Force Systems Command and the Air Force Office of Scientific Research for sponsorship of this research. Acknowledgement is made to Universal Energy Systems for providing the administrative means whereby this research task could be successfully conducted.

A number of personnel at the U.S. Air Force Academy's Frank J. Seiler Research Laboratory deserve mention. Appreciation is given to Bobby Hatfield and Martin Holbrook for their technical support in the Aero Lab., to Inez Johnson for her skill in typing, and to Major Robert Reilman who made it all possible by providing every means to have me pursue this project. As Director of the Lasers and Aero Mechanics Division of the FJSRL, Major Reilman provided the leadership and counsel that maintained the highest level of research environment I've encountered.

I. INTRODUCTION:

The importance of flow induced vibrations of thin leading edges can be illustrated by citing one example. Ground testing of the space shuttle's main engine in late 1985 revealed excessive high strains in a high pressure line converging liquid oxygen (LOX) to the main injector. The LOX inlet tee acts as a mainfold, branching this incoming flow into three directions through the use of flow splitter vanes. The high strains coupled with the thinness of the vanes resulted in excessive vibrations identified as leading edge vibrations. These vibrations can lead to structural failure resulting in the catastrophic loss of the space craft*.

The USAF is particularly concerned about flow induced vibrations as it directly effects the performance of jet engines, notably fan jets, and helicopter rotary blades. The problem is circumvented by stiffening the rotary element or thickening the leading edge. For those cases where these alterations are not feasible, it is significant to be able to predict frequencies, amplitudes and stability envelopes.

As former Principal Engineer of the Boeing Co. and the Senior Staff Scientist of the Martin Co. in charge of aeroelastic research, the problem of flow induced vibrations is particularly challenging. Interesting, it was a

*See Design of Spacecraft, by R.A. Granger, Naval Academy Press, 1988

problem I failed to address in my test[+] due to the problem being single degree–of–freedom and therefore outside of what is commonly recognized as classical flutter. The problem is challenging due to a lack of understanding of the physical mechanism of the phenomenon: a problem to be rectified, hopefully, in the near future[x].

The Frank J. Seiler Research Laboratory was the obvious research laboratory to conduct the investigation as they are recognized internationally as contributors to unsteady aerodynamics. In fact, all workshops in unsteady separated flow have been held at the FJSRL. They also possess some of the finest research equipment in the world.

II. OBJECTIVES OF THE RESEARCH EFFORT:

The research objective of the flow induced vibration of thin leading edges is a theoretical investigation of four possible physical mechanisms that could initiate vibrations of thin bodies. The phenomenon is generally believed to be an aeroelastic instability of elastic bodies, but whether it is flutter or galloping vibrations, it is not known.

The goals of the investigation are to mathematically model the physical phenomenon as i) one–dimensional flutter, ii) a highly nonlinear instability,

+The Unified Method of Aeroelasticity, by R.A. Granger, to be published in 1990.

x1989 R.I.P. to AFOSR, submitted by R. A. Granger, 15 August 1989

iii) an unsteady stagnation point problem, and iv) flow induced vibrations with shed vortices. Frequency and amplitude analyses of each model will be made (if possible) and compared.

As the study progressed, I became increasingly more inquisitive which theoretical model might be the correct one, so an elementary experimental investigation was made using a simplistic model and very limited velocity range.

Research in this project will be resumed hopefully at the United States Naval Academy during June 1990, when I return from Yale University after a six month sabbatical as Visiting Professor. A RIP has been submitted for sponsorship of an AFOSR Mini Grant. While as a Summer Research Fellow at the FJSRL, a paper has been proposed for presentation at the International Symposium on Nonsteady Fluid Dynamics, 4–7 June 1990 in Toronto, Ontario, Canada. Papers are planned for presentation at the Pan American Congress on Applied Mechanics, at Vina Del Mar, Chile, January 1991, and the 9th International Conference on Experimental Mechanics at Copenhagen, Denmark, 20–24 August 1990. A paper either to the AIAA journal or ZAMP is also being planned.

III. THEORETICAL INVESTIGATION:

a. The one–dimensional flutter model. Classical flutter results from the coupling of two modes of vibration (e.g. bending and torsion). The nonclassical type of flutter is very difficult to analyze on a purely theoretical basis as it may involve flow separation, stall conditions, and various types of

time lag effects between the flow pattern and the motion. In this type of flutter, only a single degree–of–freedom of the structure may be prominently involved. We considered a wedge–shaped wing of very small thickness compared to the span such that it could be modeled as a flat plate. Lagrange's equation of motion for our physical model resulted in the simple equation

$$\frac{I_\alpha}{\pi\rho b^4}\left[\left[\frac{\omega_\alpha}{\omega}\right]^2 - 1\right] = \mathcal{R}e\left[M_\alpha - \left[a + \frac{1}{2}\right]\left[L_\alpha + M_h\right] + \left[a + \frac{1}{2}\right]^2 L_h\right] \quad \ldots (1)$$

and

$$\mathcal{I}m\left[M_\alpha - \left[a + \frac{1}{2}\right]\left[L_\alpha + M_h\right] + \left[a + \frac{1}{2}\right]^2 L_h\right] = 0 \quad \ldots(2)$$

where the notation is exactly that used in B.A.H., Ref. 1. Note, the unsteady aerodynamic forces and moments are functions of the Strouhal number k, and are evaluated in Ref. 1, with the result that Eq. (2) becomes

$$-\frac{1}{k} + \left[a + \frac{1}{2}\right]\left[-\frac{1}{k} - \frac{2F}{k} - \frac{2G}{k^2}\right] + \left[a + \frac{1}{2}\right]^2\left[-\frac{2F}{k}\right] = 0 \quad \ldots(3)$$

where

$$F(k) + i\,G\,k) = C(k) \qquad \ldots(4)$$

where C(k) is the well–known Theodorsen function. Thus, for a given elastic axis, one can solve Eq. (3) for the Strouhal number k, and knowing k, one can solve for the frequency ω in Eq. (1). To solve for the frequency in Eq. (1), one must know the structural properties of the wing in order to evaluate the torsional frequency ω_α.

b. The only instance of flutter was for the case where the elastic axis was on or near the leading edge, approximately 7/8 chord. Even for this special case, the flutter frequency was approximately the torsional frequency of the structure, which appears too prohibitive.

a. The highly nonlinear instability model. If both the energy input by the flow and the energy expended by the damping increase linearly with amplitude, then the amplitude of vibration will grow without limit once the stability boundary has been crossed. In real structures, the energy input by the flow has a finite limit because the fluid forces on the structure are limited. Thus, the amplitude of unstable galloping can only grow until it is limited by nonlinearities in the fluid force on the structure or nonlinearities in the structure itself. In this theoretical model, the effect of the nonlinear aerodynamic forces on a linear structure is calculated to determine the galloping response. To represent the unsteady aerodynamic moment in Lagrange's equation of motion, we use a cubic approximation. Thus, the governing equation is

$$I_\alpha \ddot{\alpha} + k_\alpha \alpha = Q_\alpha \qquad \ldots(5)$$

where

$$Q_{\alpha} = K_1 \, (f\alpha_H = \frac{\alpha^3_H}{8} \qquad ...(6)$$

where

$$\alpha_H = \alpha_0 + \alpha - \ell\dot{\alpha} \qquad ...(7)$$

where ℓ is a dimensionless moment arm, f is the length of the leading edge flap, α_0 is the initial angle–of–attack of the wing, α is the torsional deflection, and K, is the aerodynamic moment. After considerable transformations and algebraic manipulations, Eq. (5) can be expressed in the form as

$$\ddot{y} + y = A_1 \left\{ \left[B_1 y - C_1 y^2 - y^3 \right] \right.$$

$$\left. - A_2 \left[B_1 y - 2\, C_1 y - 3y^2 \right] \dot{y} \right\} \qquad ...(8)$$

Equations of the type Eq. (8) have been studied by the so–called Poincare* method of expanding solutions of y in powers of A_1.

A first and second order solution was obtained after a very lengthy analysis.

b. A fascinating result was obtained in closed analytical form:

*See Ref. 2

$$\alpha = \bar{\alpha} + \frac{\frac{2}{3}\sqrt{3}\,[8f - 3(\alpha_0 + \bar{\alpha})^2]}{\sqrt{1 + \frac{k_\alpha}{\Gamma_\alpha}\ell^2\,\bar{\omega}^2}} \cos\left[\bar{\omega}\sqrt{\frac{k_\alpha}{\Gamma_\alpha}}\,t + o\right] \quad ...(9)$$

where the barred terms are for equilibrium (i.e., the static solution) and o is the phase angle. Not only is Eq. (9) remarkable as being the solution of Eq. (5) but its form is identical to a CFD solution from a vortex shedding pressure, Ref. 3. In Eq. (9) the static solution for $\bar{\omega}$ is

$$\bar{\omega} = \left[1 + \left[\frac{\sigma}{2\pi}\right]\mu^2\right]^{-1} \quad ...(10)$$

where

$$\mu = \frac{K_1}{8k_\alpha} \quad ...(11)$$

$$\sigma = \pi K^2\left[\frac{9}{128}K^2 + \ell^2\left[\frac{k_\alpha}{\Gamma_\alpha}\right]\left\{\frac{63}{128}K^2 + 6K(\alpha_0 + \bar{\alpha})\right.\right.$$

$$\left.\left. - 9(\alpha_0 + \bar{\alpha})^2\right\} + 3\left[\alpha_0 + \bar{\alpha}\right]^2\right] \quad ...(12)$$

and

$$K = \frac{2}{3}\sqrt{3}\left[8f - 3\left[\alpha_0 + \bar{\alpha}\right]^2\right] \quad ...(13)$$

The beautiful part of the solution given by Eq. (9) is that the torsional response of a wide class of structures can now be analyzed. The sad part is

that we have no experimental data to which we can make comparisons. We do have, however, the confidence factor that Eq. (9) is identical in form to a result obtained in Ref. 3.

a. The unsteady stagnation point model. Consider the unsteady behavior of the stagnation point near a blunt leading edge. In the immediate vicinity of a rounded leading edge, the boundary layer is very thin and a first approximation to the flow may be obtained by neglecting viscosity. If the acoustic wavelength is large compared to any length dimension of the leading edge, compressibility may also be neglected. With these approximations, the flow is best represented by potential flow. Since the aft portion of the body is not important in the analysis, just the leading edge, we shall concern ourselves with the flow about an elliptical cylinder. The technique that was used for this physical model was to obtain a solution of the flow about a circular cylinder and map that solution onto an elliptical cylinder. The method is described in the text by Granger, Ref. 4. We let the circular cylinder experience uniform flow plus a downwash. We map this potential solution for an elliptical cylinder using coordinate transformations. We find the velocity field, and solve for the elliptical coordinates. We determine the maximum value of the vertical elliptical coordinate which is the maximum variation of the stagnation point.

b. The maximum variation of the stagnation point was found to be

$$(\eta)_{max} = (a - b^2/a)\ (W/U)/\left[1 + (W/U)^2\right]^{1/2} \qquad ...(14)$$

where

$$a = \frac{\xi \sin \theta + \eta \cos \theta}{\sin \theta \cos \theta} \qquad ...(15)$$

$$\Delta = \frac{\xi \sin \theta - \eta \cos \theta}{\sin \theta \cos \theta} \qquad ...(16)$$

Typical values of U = 20 m/s, W = 2 x 10^{-3} m/s, and $(a - b^2/a)$ = 6 mm yields $(\eta)_{max}$ = 6 x 10^{-4} mm, which shows the motion of the stagnation point is extremely small, i.e., less than 0.01% of the thickness of the elliptical nose of the body. Thus, the unsteady stagnation point model is an unlikely model of leading edge vibration.

a. <u>The flow induced vibrations with shed vortices model</u>. This model differs from the first two models in that the aerodynamic part is different. The aerodynamic moment for this model is due to the moment from the apparent mass, plus a moment due to the unsteady aerodynamic lift and a moment due to an additional lift from the vortex shedding. For a thin body having a leading edge flapping at an axis located at a distance ba from the mid chord of length b, the moment M' due to the apparent mass is

$$M' = \pi \rho b^4 \left[\left[a - \frac{1}{2}\right] \frac{U}{b} \dot{\alpha} - \left[a^2 + \frac{1}{8}\right] \ddot{\alpha}\right] \qquad ...(17)$$

the moment M_α due to lift is

$$M_\alpha = \pi \rho b^2 \left[2a + 1\right] U^2 C(k) \left[\alpha - \frac{b}{U} \left[a - \frac{1}{2}\right] \dot{\alpha}\right] \qquad ...(18)$$

and the moment M_1 due to vortex shedding is

$$M_1 = 0.2\ \rho\ U^2\ \frac{XD}{S}\ e^{\ i\omega t} \qquad ...(19)$$

where S is the Strouhal number defined as $D\omega_\alpha/U$. Substituting Eqs. (17) – (19) into Lagrange's equation of motion, identifying the frequency ω as having a real and imaginary part and partitioning the resultant equation into real and imaginary parts, one finds the torsional displacement α as

$$\alpha = \bar{\alpha} e^{i\omega t} \qquad ...(20)$$

where

$$\bar{\alpha} = \frac{0.2\ \rho\ U^2\ XD/S}{A_1 + A_2 + A_3} \qquad ...(21)$$

$$A_1 = \left\{ \frac{\pi\ \rho\ b^4\ (2a + 1)\ (U/b)^2\ G(k)}{c - \pi\ \rho\ b^3\ U\ \left[(a - 1/2) + (2a + 1)\ (a - 1/2)\ F(k)\right]} \right\}^2 \cdot$$

$$\left[I_\alpha + \pi\ \rho\ b^4\ (a^2 + 1/8)\right] \qquad ...(22)$$

$$A_2 = \frac{\left[-\pi\ \rho\ b^4\ (2a + 1)\ (U/b)^2\ G(k)\right]\left[-\pi\ \rho\ b^3 U\ (2a + 1)\ (a - 1/2)\ G(k)\right]}{c - \pi\ \rho\ b^3\ U\ \left[(a - 1/2) + (2a + 1)\ (a - 1/2)\ F(k)\right]} \qquad ...(23)$$

and

$$A_3 = k_\alpha - \pi \rho b^4 (2a + 1) (U/b)^2 F(k) \qquad ...(24)$$

The expression for the frequency ω is quite complicated. However, if we consider the structural damping c as negligibly small, then

$$\omega = - (U/b) \left[\frac{2a + 1}{a - 1/2}\right] \frac{G(k)}{[1 + (2a + 1) F(k)]_{c = 0}} \qquad ...(25)$$

b. Of all four models, this model appears the most feasible. The key lies in determining the axis of torsional displacement a and the correct value of the structural damping. Figure 1 shows the dependency of the frequency on structural damping and location of the elastic axis. Note that if we can keep the structural damping $c < \pi\rho b^3 U[(a - 1/2) + (2a + 1)(a - 1/2) F(k)]$, our frequency is "controllable." Also note the importance of "a" in both the magnitude of the frequency and damping.

Selecting a torsional displacement about the 3c/4, (a = 1/2), Figure 2 shows the amplitude $\bar{\alpha}$ of a thin wing vibrating versus the reduced frequency 1/k. Note that the minimum amplitude occurs when k ~ 0.25.

A stability analysis was performed to determine the conditions necessary for a stable or unstable response. Figure 3 is a stability plot of the torsional displacement α versus its velocity $\dot{\alpha}$. Here we see the elastic force is considerably larger than the damping force and therefore the trajectories in the phase plane are either inwardly or outwardly winding spirals from a

singular point called a focal point. All the trajectories cut the $\dot{\alpha}$ axis at right angles. The stationary point is either stable or unstable, depending upon whether the trajectory approaches it or leaves it. In the stable case, a small perturbation from the focal point results in a damped motion restoring the wing to the focal point. In the unstable case, see Figure 4, a small perturbation results in an oscillation with amplitude increasing until a limit cycle is reached. This is self–excited motion which was observed in the preliminary experiment. The limit cycle is represented by the closed curve in the phase plane of Figure 4.

It is unfortunate this final report must be confined to an abbreviated size as so much information resulted from this study that could not be presented herein. A description of the exploratory experiment and all the measured results cannot be shown in this report except for one figure. (Reference 5 is recommended reading for a brief description on some of the results.) Figure 5 is a plot of frequency versus velocity for a specific model. The experimental measurements are compared against theoretical calculations. The water tunnel had an extremely small range of velocity. The results are quite good considering the vast fluctuations that existed in the flow meter and that inclusion of structural damping would vastly improve the comparison. This and other results strongly conclude that the fourth theoretical model is the math model to use in the analysis.

IV. RECOMMENDATIONS:

a. The results of developing four different theories to explain vibrations of thin leading edges have resulted in the preparation of three technical

presentations at different symposiums and probably two technical papers that will be submitted to international scientific refereed journals. For certain specific physical models, we now have the capability to predict frequencies, amplitudes and stability criteria.

b. Though theoretical models now exist, we still do not know precisely what the physical model should be. We can postulate what it could be, but it is vital now to determine exactly what the physics of the phenomenon is. We also need experimental data to make comparisons against theory in order to lend credence to the theory. Hence an extensive experimental program has been written (see Ref. 5) that will accomplish this.

REFERENCES

1. Bisplinghoff, R. L., H. Ashley, and R. L. Halfman, Aeroelasticity, Addison-Wesley Publ. Co., 1955.

2. Minorsky, N., Nonlinear Oscillations, Princeton, N.J., D. Van Nostrand, 1962.

3. O'Connor, G. M. and J. Jones, "Flow Induced Vibrations of the SSME LOX Inlet Tee Vanes," 24th Joint Propulsion Conference, paper AIAA-88-3132, Boston, MA, 11-13 July 1988.

4. Granger, R. A., Fluid Mechanics, New York, N.Y., Holt, Rinehart and Winston Book Co., 1985.

5. Granger, R. A., "An Experimental Investigation of Flow Induced Vibrations of Thin Leading Edges," Mini Grant Proposal, submitted to AFOSR, 15 August 1989.

Figure 1. Frequency Versus Structural Damping and E.A. Location

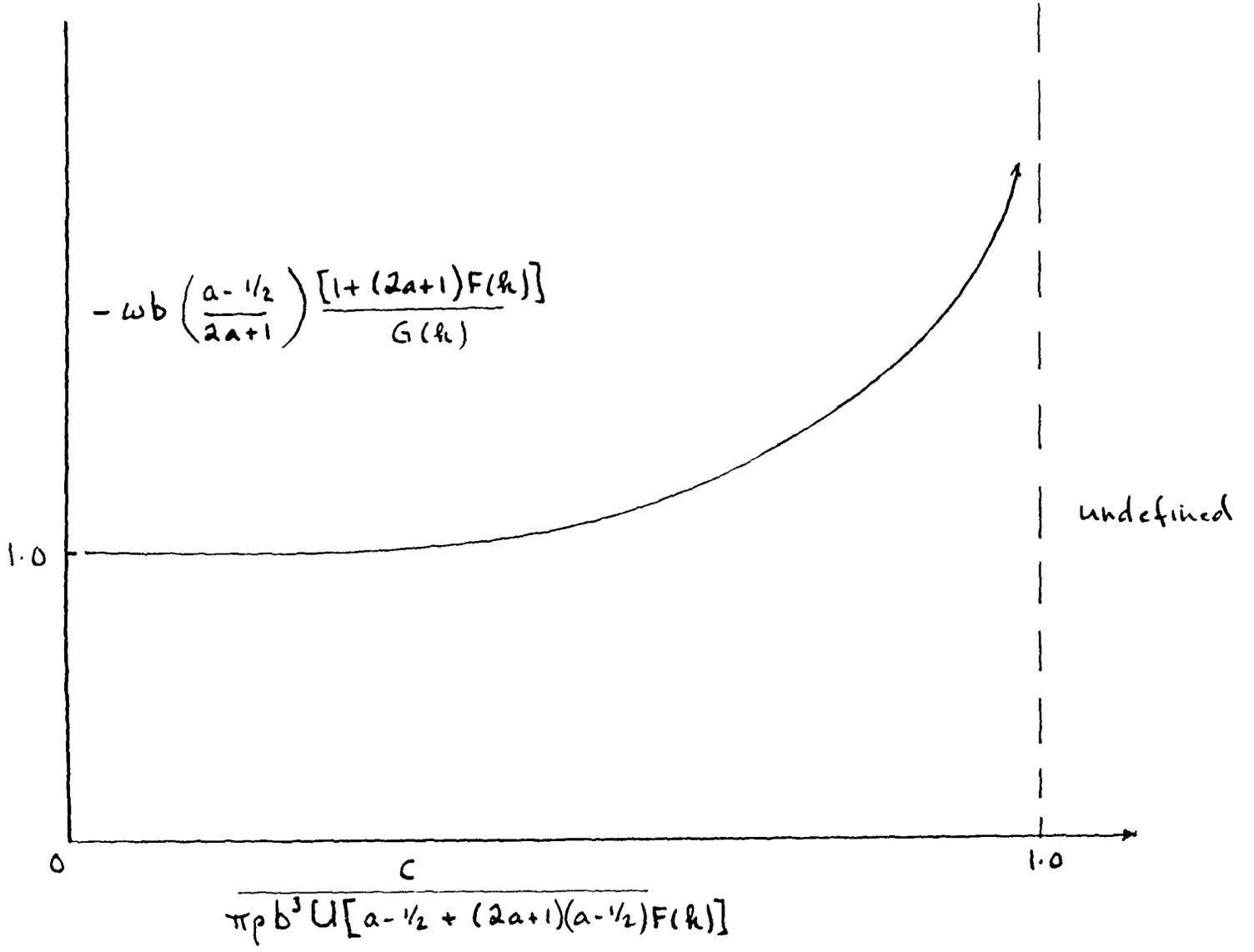

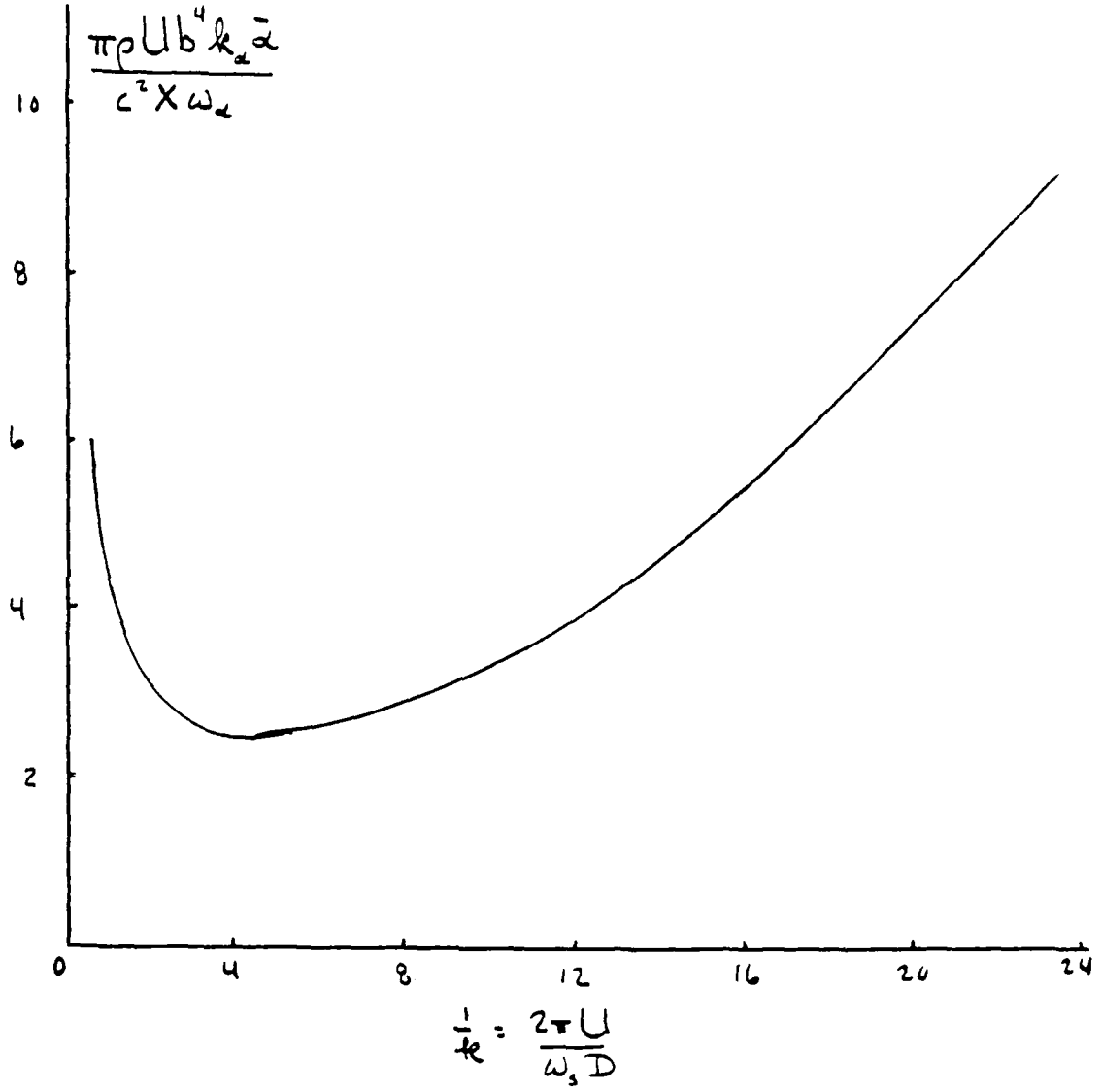

Figure 2. Amplitude of Thin Wings Vibrating Due to Apparent Mass, Unsteady Aerodynamics and Shed Vortices Versus Reduced Frequency for Torsional Mode about 3/4 Chord.

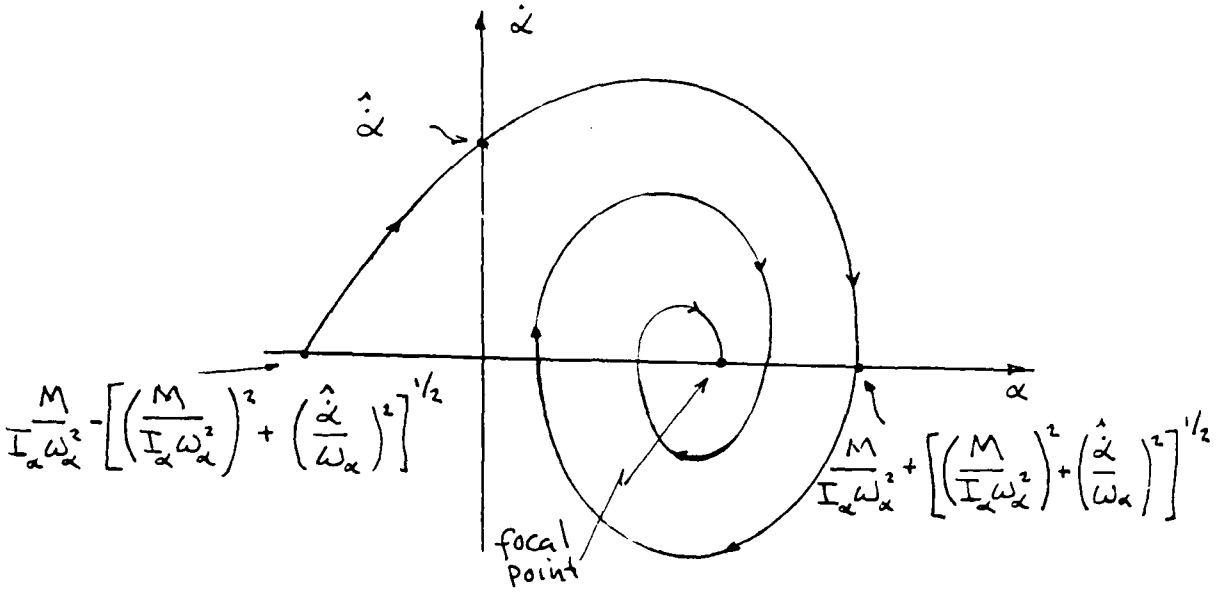

Figure 3. Phase Plane of Governing Equations Showing Stability Due to Small Perturbations: A Stable Response. (M = Sum of External Moments.)

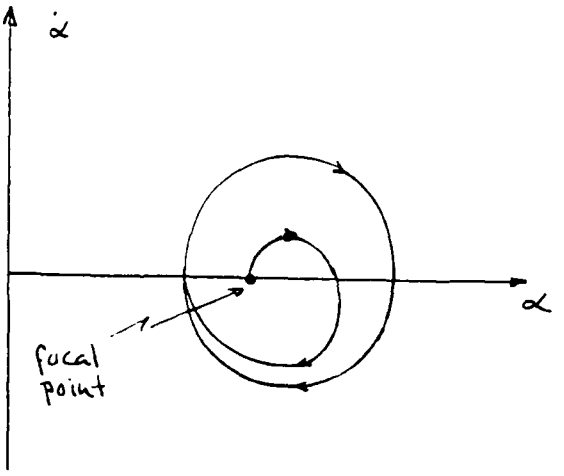

Figure 4. Phase Plane of Governing Equations Showing an Unstable Case Due to Small Perturbations with Limit Cycle.

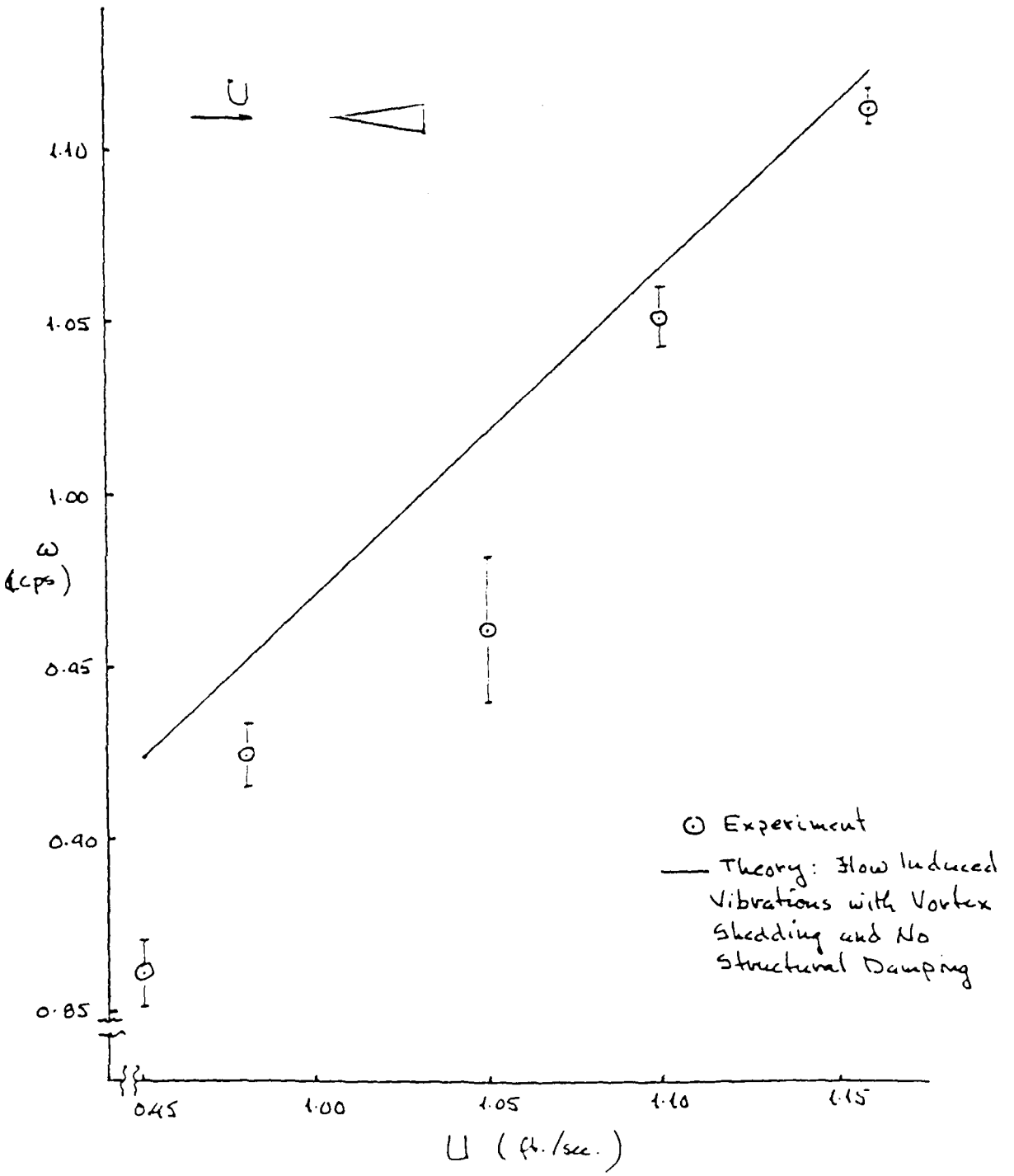

Figure 5. Comparison of Experimental Measured Frequency with Flow Induced Vibration with Vortex Shedding Theoretical Model Frequency for the Case of No Damping.

1989 USAF-UES SUMMER FACULTY RESEARCH PROGRAM/

GRADUATE STUDENT RESEARCH PROGRAM

Sponsored by the

AIR FORCE OFFICE OF SCIENTIFIC RESEARCH

Conducted by the

Universal Energy Systems, Inc.

FINAL REPORT

SECOND HARMONIC GENERATION IN OPTICAL FIBERS

Prepared by:	Lloyd W. Hillman, Ph.D.
Academic Rank:	Assistant Professor
Department and	Department of Physics
University	University of Alabama in Huntsville
And by:	Stephen McClain, Graduate Student
	Mojdeh Anderson, Graduate Student
Department and	School of Electrical Engineering
University	Cornell University
Research Location:	Frank J. Seiler Research Laboratory
	USAF Academy, CO 80840
USAF Researcher:	Maj Jim Rotgé
Date:	15 Oct. 89
Contract No:	F49620-88-C-0053

SECOND HARMONIC GENERATION IN OPTICAL FIBERS

by

Lloyd W. Hillman, Stephen McClain, and Mojdeh Anderson

ABSTRACT

Second Harmonic Generation (SHG) is the partial conversion of light at one frequency (the fundamental) to light at twice that frequency (the second harmonic). Although unexpected, highly efficient (>5%) SHG occurs in Ge-P doped silica-core optical fibers. Österberg and Margulis first demonstrated SHG at 532 nm using 1064 nm light from a mode-locked *Q*-switched Nd:YAG laser. Our goal was to investigate SHG in optical fibers starting with visible light at 514 nm and generating near uv-light at 257 nm. We report our failure to observe such conversion and on our subsequent investigation on the generation of sub-harmonic light.

ACKNOWLEDGMENTS

We wish thank to that the Air Force Systems Command and the Air Force Office of Scientific Research for the opportunity to contribute to their research efforts. Overall we would like to thank the hospitality extended by the whole staff at the Frank J. Seiler Research Laboratory at the U.S. Air Force Academy in Colorado Springs. In particular we acknowledge the support and discussions with Maj Jim Rotgé, Col Richard Cook, Maj Andy Motes, Dr. Ulf Österberg, and Maj Robert Reilman and the technical support we received from Duane Dunlap. Finally our sincerest blessings go out to Leah Kelly, who continually guided us to the best spots in Colorado Springs.

I. INTRODUCTION

For years the Frank J. Seiler Research Laboratory of the US Air Force has actively and successfully pursued basic research in modern optics. One particularly interesting program currently underway is the study of second harmonic generation in optical fibers. Ulf Österberg, one of the discoverers of the effect, has performed several critical and fruitful experiments at the lab, working in collaboration with many on the lab's research staff.

We (Lloyd W. Hillman, Mojdeh Anderson, and Stephen McClain) have a broad range of experience in modern optics including laser dynamics, integrated optics, optical recording, atomic spectroscopy and other topics. Our diverse backgrounds enable us to approach research problems with fresh viewpoints and novel approaches, and in this spirit we were very pleased to be able to join the Summer Faculty Research Program and the Graduate Student Research Program at the Frank J. Seiler Research Laboratory for the summer of 1989.

II. RESEARCH GOALS AND OBJECTIVES

Second Harmonic Generation (SHG) is the partial conversion of light at one frequency (the fundamental) to light at twice that frequency (the second harmonic). Al-

though there are thousands of different types of lasers in existence, there are still gaps in the optical spectrum that laser systems do not cover. Therefore, the use of SHG for creating coherent light at twice the frequency of another laser is one way to extend the range. SHG works by exploiting the non-linear optical characteristics of certain crystals. These crystals are delicate, difficult to grow, and normally very expensive--an alternative medium would be welcome.

Österberg and Margulis demonstrated that an ordinary glass optical fiber serves well as an alternative. This may seem theoretically improbable since glass, possessing approximate inversion symmetry, has vanishing $\chi^{(2)}$ and therefore should not support SHG. Even if generated, the second harmonic should not be phase matched, so no appreciable intensity should accumulate. The experimental evidence that optical fibers do support phase matched SHG is dramatic and undeniable.

Until now, most observations of the phenomenon have used a YAG laser, converting 1.064 μm light into 532 nm light. Our principal goal this summer was to investigate whether the same SHG process occurs in fibers illuminated instead with a mode-locked Argon laser at 514 nm. The theory of SHG in optical fibers is not yet understood. One of the most plausible explanations is that the second-order nonlinearity arises from some microscopic aspect of the

glass structure, such as induced defect centers associated with the Ge dopant. Such defects have a broad, but rather weak, absorption resonance line at 257 nm. If this resonance is responsible for the SHG from 1.064 μm light into 532 nm, then more nearly resonant light may lead to a resonant enhancement of the SHG process. Successful conversion to light near 257 nm light would provide a very useful coherent UV source and with immediate applications. At present, the only SHG crystal that works into the near-uv is β-BaB_2O_4. At present, the primary manufacture of this crystal is in China, which limits its availability and makes it very expensive. It seems most preposterous--replacing a crystal costing thousands of dollars with a few cents worth of optical fiber!

Theoretically, we characterize a material that can generate second harmonic light by a parameter called the second-order electric susceptibility, or $\chi^{(2)}$. Not only can a material with a non-zero $\chi^{(2)}$ generate second harmonic light, but it may also work in reverse. The material may create sub-harmonic light, or light whose frequency is one-half the fundamental. To our knowledge, this subharmonic generation process has never been experimentally or theoretically investigated in optical fibers. For our second task, we looked for this subharmonic light at 1028 nm produced by illumination of a fiber by 514 nm light from an Argon laser.

Our final goal is to begin theoretical investigations of the phenomenon. We studied most of proposed theories and found none totally satisfactory. This this summer, we initiated work on a simple model that traces the roots of the SHG to both defects in the fiber and the geometry of the fiber. In this model we find that under the geometric constraints of the fiber second harmonic light is generated although $\chi^{(2)}$ for the bulk material is zero.

III. APPROACH AND RESULTS

A. Introduction

The basic setup for our experiments is very simple. First, we installed a mode-locker into an Argon laser to create short, high power pulses of light at 514 nm. We then couple the output of this laser into the fiber. This involves carefully aligning and focusing of the beam onto the core of the fiber and matching the fiber's numerical aperture or *NA*. After traversing the length of the fiber (20 - 50 cm), the emerging light is collected and sent through a spectrometer and detected. For UV detection we used an CCD array detector coupled to an Optical Multi-channel Analyzer (OMA). For IR detection we used a cooled germanium photodetector.

B. Mode-locking the Argon laser

For the laser source we used a Spectra Physics model 2030 argon ion laser. This laser emits about 5 watts of cw power at 514 nm. To gain higher instantaneous power, we installed a Spectra Physics mode-locker. This creates a train of pulses at 82 MHz. To optimize the output and to obtain the shortest pulses, you must adjust and control the temperature of the mode locker, the rf-frequency of mode-locker, and the cavity length. The shortest pulses we obtained were roughly 200 ps long with the laser running at an average power of 600 mW. This gives a peak power of 35 W. Specifications on the mode-locker and laser say that the laser can produce pulses less than 100 ps long, but with weeks of tweaking we were never able to get close to this. Using a fast photodetector (response time <65 ps) we could measured the pulses and display their shape on a sampling oscilloscope.

C. Fiber preparation and alignment

For fibers, we used samples from two different, but similar, spools of fibers. Both fibers contained germanium and phosphorous and yielded SHG when illuminated with 1.064 μm light from a Nd:YAG laser. The core of each fiber was about 8 μm. We tried various interaction lengths ranging between 20 and 50 cm.

In addition, for some experiments, we used a previously prepared fibers; one that was illuminated all day by a Nd:YAG laser and produced second harmonic light of the Nd:YAG laser at 532 nm. When mounting this fiber in our setup, we were careful to illuminate the fiber with the same polarization as used in the preparation process. (The YAG laser is horizontally polarized; the argon laser is vertically polarized.)

To assure optimum, uniform coupling, we carefully prepared the ends of the fibers before mounting the fibers in the experiment. We stripped the protective plastic coating by either burning the jacket off or by soaking the fiber in Stripeze. We obtained high-quality cleaves by using a fiber cleaving tool. With a microscope, we could assess the cleave quality. The fibers were held by special jigs designed by Ulf Österberg which fit snugly into precisely adjustable Klinger mounts.

A microscope objective focused the light onto the tip of the fiber. Coupling efficiency (amount of light before the objective divided by amount of light after the fiber) was typically 30% to 70%.

When too much power was focused onto the fiber, the tip melted, destroying the coupling. The maximum average power we could couple in before melting the tip was between 600-900 mW.

We aligned the input beam so as to closely as possible couple only into the LP_{01} mode. This mode has a nearly circular Gaussian intensity distribution. As is found necessary for SHG at 1.064 μm, the system was left to "prepare" undisturbed for many hours (10-30 hours).

D. UV Detection

A lens focused light output from the fiber onto the input slit of the spectrometer. We verified that the lens passed > 90% of UV light by using a mercury lamp, which has a spectral line at 253 nm, only 4 nm from our signal. We also used the mercury lamp to verify the calibration of the spectrometer and the expected location of the 257 nm signal we sought. Setting the spectrometer to 257 nm, then the second-harmonic signal there would appear as a spike on the OMA screen.

We discovered that the noise limits of the OMA detection system could easily detect stray scattered light inside the spectrometer from the argon laser. The scattering of this green light inside the spectrometer required us to use many noise reduction techniques. First we inserted baffles into spectrometer. This proved moderately effective. Then we placed a uv-bandpass filter in front of the spectrometer's slit. This filter blocked out greater than 99% of the green while still passing 15% of the 257 nm mercury light.

Finally, we put the OMA system to work. Using the storage and operation capabilities of the OMA, we could subtract out the green laser background signal. First, we take a background scan with no input signal. This gives the inherent leakage current noise in the CCD array. We subtract this data from each subsequent data scan. We then take a scan with the laser on and store it. Next we insert a WG345 filter (blocking 257 nm, passing 514 nm) before the spectrometer and take a scan. Since this filter blocks a small amount of green, we normalize its average to that of the previous scan. Finally, we subtract this normalized no-UV scan from our UV scan. We detected no signal at 257 nm. Analyzing the detection capabilities,we conclude that with 25 W peak green (@ 514 nm) power, there is second harmonic conversion no greater than 500 nW peak UV (@ 257 nm) power (9 nW average UV power.) The conversion efficiency is less than 2×10^{-8}.

E. IR Detection

The CCD does not respond to infrared light at 1.028μm, the sub-harmonic of 514 nm. We therefore found a germanium detector. To reduce noise we used this in conjunction with a lock-in amplifier. Before entering the spectrometer (which we reconfigured as a monochrometer) the beam from the fiber is sent through an optical chopper. For the reference signal, we sent another beam from a HeNe laser

through the chopper. The germanium detector, cooled with liquid nitrogen, is very sensitive in the IR, but still detects a small amount in the visible, so we used filters to block the green. Insertion of RG590 and RG645 filters passed over 98% of 1028 nm light while blocking essentially all of the green. With the spectrometer set at 1028 nm we saw no signal above noise. (Spectrometer wavelength was calibrated by taking out the filters. The green light diffracted in second order by the grating appears exactly where the IR light diffracted in first order would be.) We conclude that with 35 W peak green power, there is subharmonic conversion no greater than 3 μW peak IR power (50 nW average IR power). The conversion efficiency is less than 8×10^{-8}.

F. Theory

As noted earlier, previous attempts to explain the SHG in optical fibers have been incomplete. Most of these theories concentrate on material properties of the fibers--the action of color centers or other defects in the doped fibers to produce an intrinsic $\chi^{(2)}$ or some combination of higher order nonlinear processes to produce an effective $\chi^{(2)}$. In addition, the theory needs to explain phase-matching that synergetically appears.

We are not specialists in nonlinear materials, so we take a different approach. We think that the circular ge-

ometry of the fiber plays a role more important than others have recognized. Preliminary results from a simple model show that it is possible to create second harmonic light of the correct polarization from the motion of charges associated with defects at the cylindrical core-cladding interface. We illustrate the geometry in the Fig. 1.

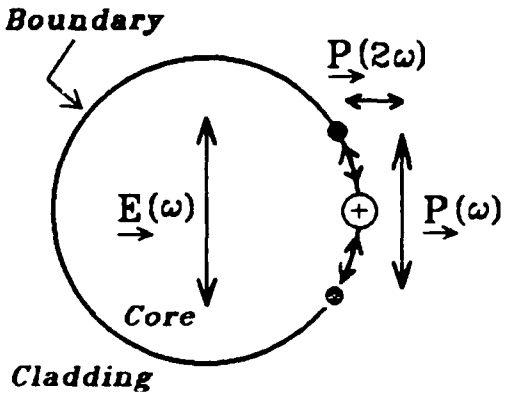

Fig. 1. Geometry for second harmonic generation in an optical fiber. The electric field induces periodic charge motion about the defect site. If the charge motion is confined to the boundary, then for each periodic cycle up in down at frequency ω, the charge moves back and forth at twice this frequency generating a second harmonic field.

We base our model on the simple idea that defect sites, similar to color centers, are formed in the fiber.

The dopants Ge and P may encourage these defect formations. We also note that in the fibers investigated the concentration of the dopants is highest at the interface between the core and cladding. Logically, the interface is also the point of highest stress, since it is the boundary of two dissimilar materials. The attractive potential of the charge will be different in the two materials. For simplicity, we therefore model this asymmetry in the attractive potential by confining the charge's motion to the boundary. As the electric field forces the charge to oscillate up and down at the fundamental frequency ω, it will move back and forth at twice this frequency or 2ω. The charge therefore radiates a new field at 2ω. Furthermore, we see that it is the geometry of the fiber that gives rise to the generation of the second harmonic. Outside of this simple picture, we did not have time to pursue this model very deeply this summer.

IV. RECOMMENDATIONS

It is not possible in ten weeks to perform investigations as thoroughly as one would like. We feel we have completed some good preliminary projects, but we have several recommendations for further research.

One major problem we had was lack of available peak power. Our peak power was typically 4 - 20 W, while that

of the YAG laser is many kW. Because the generation of the second harmonic scales as the square of the intensity, it may have been futile for us to try with such low peak powers. There are several ways to get more Argon power into the fiber. First, our mode-locker did not seem to meet specifications. A factor of two or three would be achieved if it did. Possibly our mode-locker was defective. Also, easier and more time-stable adjustments to the pulses could be made with the addition of a mode-locker temperature stabilizer, available from Spectra-Physics.

Another idea is to switch from the argon laser to another laser in the visible. The conventionally doubled YAG at 532 nm could be used. Also, dye lasers could be used over a broad wavelength range. The advantage of these other lasers is that much shorter pulses are achievable with them so that higher peak powers may be employed.

Different types of fibers could also be tried. We used fibers that were good for SHG in the infrared, but none of them was single mode in the visible.

Our detection apparatus could also be refined. More appropriate filters would give us at least an order of magnitude better sensitivity in the UV, but we didn't have time to locate and order them. Also, our IR detection apparatus suffered from noise. A more sophisticated low-noise circuit would improved our sensitivity there.

On the theoretical side, our work has just begun. We hope to extend our work to demonstrate how important the geometry of the fiber is in producing the second harmonic light.

REFERENCES

Mizrahi, V., U. Österberg, J.E. Sipe, and G.I. Stegeman, "Test of a model of efficient second-harmonic generation in optical fibers," *Optics Letters* **13**, 279-281 (1988).

Österberg, U. and W. Margulis, "Experimental studies on efficient frequency doubling in glass optical fibers," *Optics Letters* **11**, 57-59 (1987).

Österberg, U. and W. Margulis, "Second-harmonic generation in optical glass fibers," *J. Opt. Soc. Am. B* **5**, 312-315 (1988).

Terhune, R.W. and D.A. Weinberger, "Second-harmonic generation in fibers," *J. Opt. Soc. Am. B* **4**, 661-674 (1987).

Tsai, T.E., M.A. Saifi, E.J.Friebele, D.L. Griscom, and U. Österberg, "Correlation of defect centers with second-harmonic generation in Ge-doped and Ge-P-doped silica-core single-mode fibers," *Optics Letters* **14**, 1023-1025 (1989).

1989 USAF-UES SUMMER FACULTY RESEARCH PROGRAM

GRADUATE STUDENT RESEARCH PROGRAM

Sponsored by the

AIR FORCE OFFICE OF SCIENTIFIC RESEARCH

Conducted by the

Universal Energy Systems, Inc.

Final Report

EVALUATION OF COLD FUSION IN MOLTEN SALT SYSTEMS

Prepared by:	John A. Lanning, Ph.D.
Academic Rank:	Associate Professor Associate Dean
Department and University:	Department of Chemistry University of Colorado at Denver
Research Location:	Frank J. Seiler Research Laboratory USAF Academy, Colorado 80840
USAF Researcher:	John S. Wilkes, Ph.D.
Date:	18 September 1989
Contract No:	F49620-88-C-0053

EVALUATION OF COLD FUSION IN MOLTEN SALT SYSTEMS

by

John A. Lanning

ABSTRACT

The phenomenon of cold fusion was investigated in a neutral molten salt produced from the reaction of 1-methyl-3-ethylimidazolium chloride (MEIC) and deuterium chloride (DCl). The resulting molten salt, $MEI^{+}DCl_{2}^{-}$, provides the source of D^{+} ions which were reduced at a palladium cathode under constant current bulk electrolysis conditions. Although D^{+} ions from the $MEI^{+}DCl_{2}^{-}$ molten salt melt can be readily reduced at a palladium cathode, the phenomenon of cold fusion was not observed. The major restriction to cold fusion in a $MEI^{+}DCl_{2}^{-}$ melt appears to be limited current densities imposed by nonselective electrolysis of the D^{+} ions. Fundamental electrochemical and physical properties of the $MEI^{+}DCl_{2}^{-}$ melt were also examined during the research project.

I. INTRODUCTION:

Controlling nuclear fusion for an energy source has been a scientific priority for many years. The high temperatures necessary to overcome nuclear repulsion and the difficulty of containing a high temperature plasma are complicating high temperature fusion research. The recent announcements (Ref 1,2) that fusion may be possible using inexpensive electrochemical techniques at room temperature conditions has attracted a great deal of curiosity and controversy within the scientific community.

The Frank J. Seiler Research Laboratory at the U.S. Air Force Academy conducts fundamental electrochemical research in molten salt systems. One class of room temperature molten salt investigated at the Seiler laboratory is made from 1-methyl-3-ethylimidazolium chloride (MEIC) and aluminum chloride ($AlCl_3$). These chloroaluminate, room temperature molten salts exhibit low vapor pressure, high ionic conductivity, molten conditions over an extended temperature range, and a large electrochemical voltage window for studying battery systems. A neutral molten salt melt, one with neither an excess of MEIC Lewis base nor $AlCl_3$ Lewis acid, exhibits the largest voltage window.

The use of a molten salt electrolyte to study cold fusion has several possible advantages (Ref 3). The synthesis of $MEI^+DCl_2^-$ for use as a molten electrolyte and a source of deuterium should not be difficult. The codeposition of metals during the electrochemical reduction of deuterium appears to be important for cold fusion (Ref 2) and the large electrochemical voltage window in molten salts could make the metal codeposition study easier than in an aqueous system. Furthermore, the large electrochemical

window in molten salts may allow the use of a ^{6}Li cathode for extended ^{6}Li + ^{2}D cold fusion research.

Since my graduate research in electroanalytical chemistry, I have maintained electrochemistry research interests on the in situ electrochemical measurement of ground water parameters and, more recently, on the bromoaluminate analogs to chloroaluminate molten salt systems. One of my graduate students, Jeffrey Boon, conducted his master's thesis project on bromoaluminate molten salts at the Frank J. Seiler Research Laboratory.

II. OBJECTIVES OF THE RESEARCH EFFORT:

The original objectives of the 1989 Summer Research Faculty Research Program (SFRP) were two fold: (1) to complete the investigation of fundamental electrochemical parameters in bromoaluminate molten salt systems and (2) to conduct preliminary research on the applications of room temperature chloroaluminate molten salt systems to cold fusion energy production. Due to the short 10-week nature of the SFRP, only the cold fusion objective was attempted.

The objectives for the electrochemical investigation of cold fusion in a molten salt system were as follows:

1. synthesize the $MEI^{+}DCl_{2}^{-}$ molten salt
2. determine the physical and electrochemical properties of the $MEI^{+}DCl_{2}^{-}$ molten salt system
3. evaluate the feasibility of electrochemical cold fusion in the $MEI^{+}DCl_{2}^{-}$ molten salt melt

While learning to make room temperature chloroaluminate molten salt melts, an additional objective was added based on an anomalous reduction peak in neutral or slightly acidic chloroaluminate melts.

4. identify the source of the anomalous reduction peak at -1.8 volts in MEIC/$AlCl_3$ melts

III. RESULTS AND DISCUSSION:

Experimental

Most electrochemical experiments used an EG&G Princeton Applied Research Model 273 Potentiostat/Galvanostat utilizing PAR m270 software and interfaced to a Zenith Model 248 computer through an IEEE-488 bus. Bulk electrolysis experiments used a Princeton Applied Research Model 371 Potentiostat/Galvanostat operated in a constant current mode. Thermal analysis studies were carried out on a Perkin-Elmer DSC 7 Differential Scanning Calorimeter. Except where noted, all experiments were performed in a Vacuum Atmospheres Company glove box maintained under a highly purified helium atmosphere.

The reference electrode used for all potentiostatic experiments was an Al(III)/Al couple maintained in a 0.60 MEIC/$AlCl_3$ molten salt. Working electrodes consisted of metal rods or wires sealed in Teflon or glass and polished to a mirror surface. The working electrode surface was wet with melt and polished on a Kimwipe surface prior to each cyclic voltammetry experiment.

MEIC and $AlCl_3$ were prepared by Seiler personnel using procedures developed at the Seiler laboratory. Reagent grade HCl gas was donated by the University of Colorado at Denver. DCl gas from MSC Isotopes was 99.5 atom percent D. All other chemicals used were reagent grade.

Anomalous Reduction Peak in Chloroaluminate Melts

The MEIC/$AlCl_3$ chloroaluminate melts used in several research projects at the Frank J. Seiler Research Laboratory have occasionally shown an anomalous reduction peak at -1.6 to -1.8 volts. Over the course of this project, several efforts were initiated to identify the anomalous peak.

Figure 1 shows the anomalous reduction peak at -1.7 volts in a slightly acidic MEIC/$AlCl_3$ melt. Figure 2 shows the absence of the anomalous reduction peak in the same melt which has been made slightly basic.

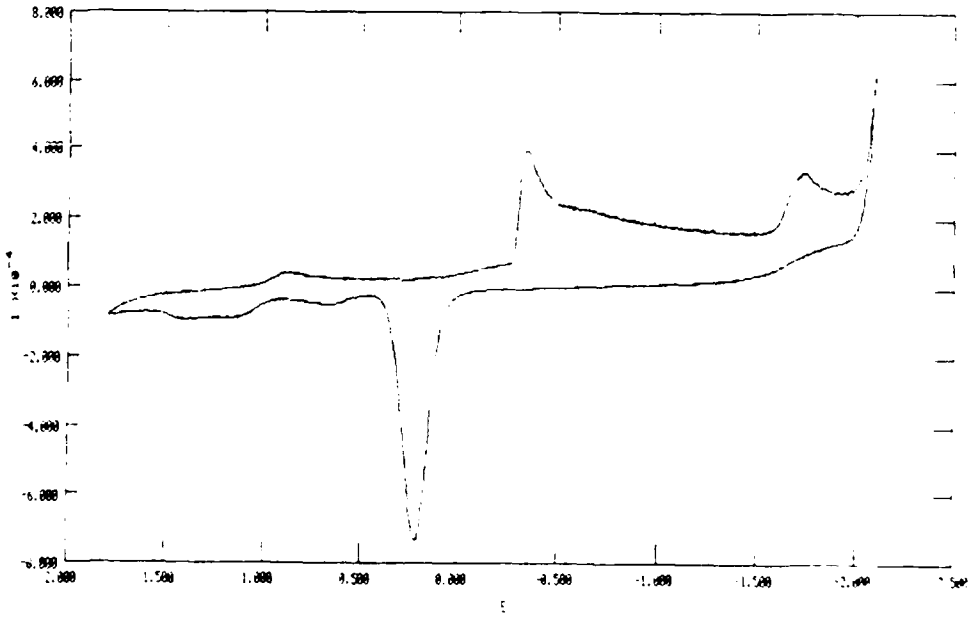

Figure 1 cyclic voltammogram of slightly acidic MEIC/$AlCl_3$ molten salt using Pt working electrode

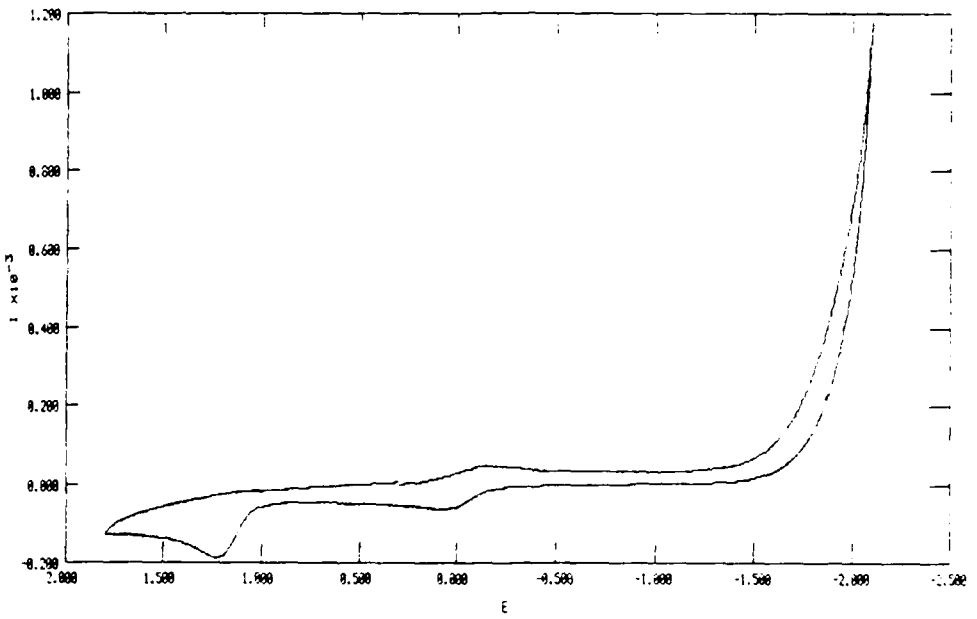

Figure 2 cyclic voltammogram of slightly basic MEIC/$AlCl_3$ molten salt using Pt working electrode

The following results were obtained on this anomalous reduction peak:

1. peak potentials varied between -1.6 and -1.8 volts
2. peak did not always exhibit diffusion-controlled shape
3. peak appearance occurred only in acidic or neutral choloro-aluminate melts
4. peak is only observed using a clean, polished electrode surface
5. peak is not water or other protonic impurity
6. buffering slightly acidic chloroaluminate melts to neutrality with NaCl did not alter the peak potential or current
7. peak currents were not increased by increasing the acidic nature of the chloroaluminate melt
8. melts prepared using highly purified $AlCl_3$ and MEIC still exhibited the anomalous peak

Although I was unable to unambiguously identify the source of the anomalous reduction peak in the chloroaluminate melts, these observations suggest an impurity in either the MEIC or $AlCl_3$. The impurity is not water or protonic in nature as the peak is readily observed on glassy carbon electrodes. Since repeated crystallizations of MEIC and double zone refining of the $AlCl_3$ did not eliminate the anomalous peak, the purification procedures currently used may not totally remove the impurity.

Synthesis of 1-Methyl-3-Ethylimidazolium Deuterium Dichloride

The synthesis of 1-methyl-3-ethylimidazolium deuterium dichloride, $MEI^+DCl_2^-$, is a modification of that by Zawodzinski and Osteryoung (Ref 4). The procedure is also used to synthesize the hydrogen analog, $MEI^+HCl_2^-$.

High purity MEIC is added to a 100 mL Schlenkware flask in the glove box. The flask is fitted with a glass rod and Teflon stopcock for delivering DCl or HCl gas. The remainder of the synthesis is carried out in a ventilation hood. Water is removed from DCl by passing the gas through a dry ice/acetone low-temperature bath at -77 ^oC (Ref 5). DCl is liquified on the sides of the Schlenkware flask by keeping the flask in a methanol/liquid nitrogen low-temperature bath at -98 ^oC (Ref 5). After a small quantity of DCl is liquified in the Schlenkware flask, the DCl gas flow is stopped, the flask allowed to warm to room temperature and the resulting molten salt melt is mixed by swirling the flask contents. This procedure of freezing and thawing is repeated two to three times until the MEIC is dissolved and a sufficient mass of DCl has been added to the molten salt melt. Excess DCl gas is removed by vacuum until gas evolution ceases. The resulting $MEI^+DCl_2^-$ melt is transferred to the glove box.

The synthesis outlined above is straight forward. The dry ice/ethanol bath used by Zawodzinski and Osteryoung has a temperature of -72 ^{o}C and should not be cold enough to liquify DCl which has a boiling point of -81.6 ^{o}C.

Physical and Electrochemical Properties of $MEI^{+}DCl_2^{-}$

The synthesis procedure above produces a $MEI^{+}DCl_2^{-}$ molten salt melt which is clear and virtually colorless. The melting point of the $MEI^{+}DCl_2^{-}$ molten salt melt is below -80 ^{o}C, the lower limit of the thermal analysis instrumentation. The specific heat was 0.411 cal g^{-1} $^{o}K^{-1}$ which is similar to that of other molten salt systems based on MEIC. The viscosity was not measured but appears to be comparable to the $MEIC/AlCl_3$ molten salt melts.

After the synthesis of $MEI^{+}DCl_2^{-}$ melts, the mass of the melt was monitored outside and then inside the glove box. The melt mass showed a slow decline, presumably from the loss of DCl. This suggests that the deuterated melt may possibly exist as the equilibrium:

$$MEI^{+}DCl_2^{-} \quad <----> \quad MEIC + DCl(g)$$

Given the small loss of DCl from the deuterated melts, the exact composition of the melt remains unknown. It is presumed that after synthesis, DCl in excess of a 1:1 neutral melt is removed by vacuum and the resulting neutral melt is stable for a short period of time.

In terms of electrochemical properties, $MEI^{+}DCl_2^{-}$ and $MEI^{+}HCl_2^{-}$ are virtually identical and only the $MEI^{+}DCl_2^{-}$ data will be presented.

The electrochemical properties of the $MEI^+DCl_2^-$ system are shown in Figure 3. The neutral melt, neither an excess of MEIC nor DCl, shows two quasireversible electrochemical couples. At -.24 volts is the reduction of D^+ and at +1.24 volts is the oxidation of Cl^-. Both the D^+/D_2 and $Cl_2(Cl_3^-)/Cl^-$ couples are electrochemically quasireversible.

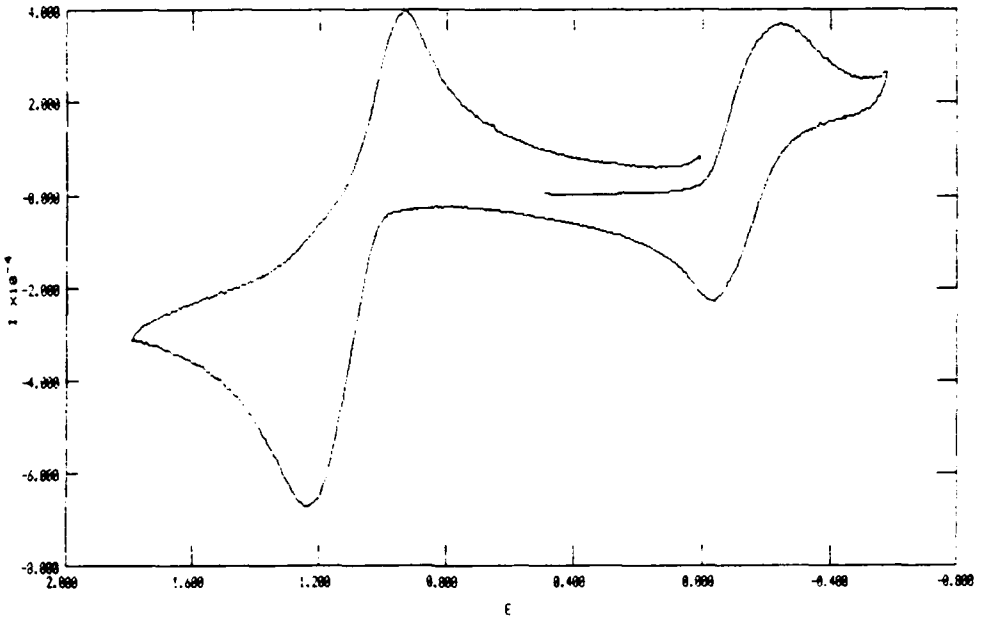

Figure 3 cyclic voltammogram of dilute $MEI^+DCl_2^-$ in neutral, unbuffered $MEIC/AlCl_3$, on Pt

The electrochemical behavior of a neutral $MEI^+DCl_2^-$ molten salt melt is radically different than the neutral $MEI^+AlCl_4^-$ analog. In a neutral melt, the predominant chloride species should be DCl_2^- and $AlCl_4^-$, respectively. $AlCl_4^-$ is electrochemically inactive which allows a neutral chloroaluminate melt to have such a large voltage window. DCl_2^- is clearly electrochemically active. DCl_2^- provides a source of D^+ for the cold fusion experiments, but severely reduces the voltage window available in a $MEI^+DCl_2^-$ neutral melt.

This significant behavior difference between neutral $MEI^+DCl_2^-$ and $MEI^+AlCl_4^-$ melts is due to bonding differences in the $AlCl_4^-$ and DCl_2^- species. $AlCl_4^-$ is

easily drawn by a simple Lewis dot structure which suggests a strong covalent bonded system. DCl_2^- is not easily represented by a Lewis dot structure and gas phase experiments indicate that XHX^- systems are linear with strong hydrogen bonding (Ref 6). Assuming a similar hydrogen bonded structure in the molten salt melts, the weaker hydrogen bonding explains the availability of D^+ and Cl^- to the molten salt melt.

The electrochemical behavior of a neutral $MEI^+DCl_2^-$ molten salt melt on a palladium electrode is shown in Figure 4. Although the reduction of D^+ and oxidation of Cl^- are clearly evident, the electrochemistry is much less reversible than with a platinum electrode. The electrochemistry of the deuterated molten salt melts using palladium was also less reproducible than with platinum. It is possible that clean electrode surface conditions were harder to reproduce on palladium. Nevertheless, there were considerable electrochemical differences for the deuterated melts between palladium and platinum.

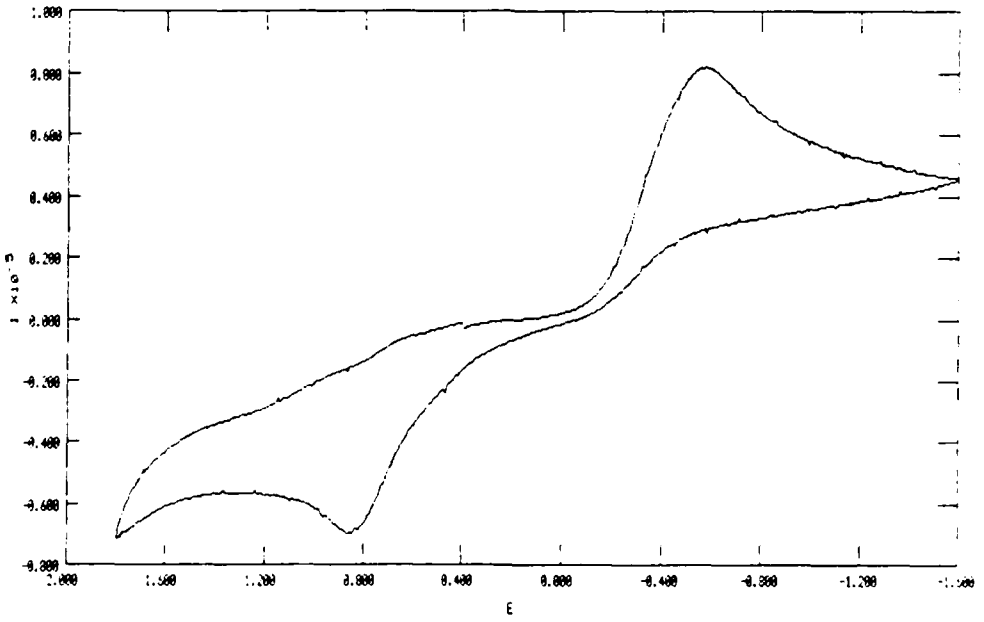

Figure 4 cyclic voltammogram of dilute $MEI^+DCl_2^-$ in neutral, unbuffered $MEIC/AlCl_3$, on Pd

The electrochemical properties of a pure, neutral $MEI^+DCl_2^-$ melt are shown in Figure 5. In a pure $MEI^+DCl_2^-$ melt, the reduction of D^+ and oxidation of Cl^- are poorly defined and much more irreversible than in a dilute system. Furthermore, the electrochemical voltage window of the melt is now defined by the D^+ reduction and Cl^- oxidation. The currents from the reduction of D^+ and the oxidation of Cl^- are not sharp as is typically encountered with melt limit reactions. It should also be noted that at higher current densities, the reduction of D^+ is poorly defined with large amounts of noise. This electrochemical noise is possibly from the evolution of $D_2(g)$ from the platinum electrode surface.

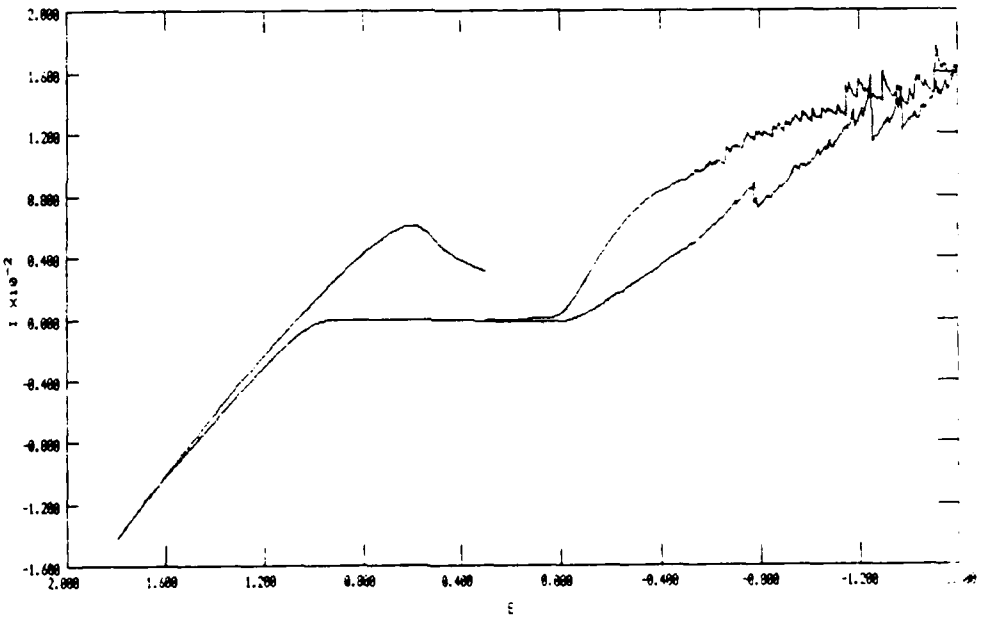

Figure 5 cyclic voltammogram of pure, neutral $MEI^+DCl_2^-$ melt, on Pt

Chronopotentiometry was used to study the behavior of the $MEI^+DCl_2^-$ melt under bulk electrolysis conditions. At currents of 5-25 mA cm^{-2} to a platinum cathode, the chronopotentiograms indicate slightly increasing operating cell potentials. However, at applied currents in excess 100 mA cm^{-2}, there was a large increase in operating cell potential and the PAR

273 potentiostat was unable to supply the required potential. These chronopotentiometry experiments are consistent with cyclic voltammetry of the pure, neutral MEI^+DCl^- melts (Figure 5) and suggest that at high current densities, not only is D^+ reduced at the cathode, but the organic portion of the melt is also being reduced.

Electrochemical Cold Fusion Studies of $MEI^+DCl_2^-$

A Teflon and glass cell was constructed to perform the bulk electrolysis under constant current conditions outside the glove box. The cathode compartment was separated from the anode compartment by a fine porosity glass frit to minimize anode electrolysis product(s) contamination of the cathode compartment. The cathode compartment uses a palladium wire electrode of 1 mm diameter which is pressure fit into Teflon plugs in order that the surface area of the cathode can be varied. The cathode compartment contains a thermocouple port to monitor the temperature rise expected if cold fusion conditions are attained. The anode compartment was designed to accept either a platinum or aluminum electrode. Both compartments were continually flushed with nitrogen to minimize water or oxygen contamination of the molten salt melt.

The use of a palladium cathode is suggested by the current literature on cold fusion. Although other electrode materials, such as titanium, absorb D_2 and have been used in cold fusion experiments (Ref 2), the majority of research has been performed using palladium. Pretreatment of the palladium cathode is essential to attaining cold fusion, and a vacuum degassing of the palladium electrode at 850 ^{o}C for 24 hours was carried out (Ref 7) immediately prior to electrolysis.

Two possible anode materials were considered. An aluminum anode in a basic chloroaluminate melt will result in the oxidation of aluminum in the presence of chloride to form tetrachloroaluminate, $AlCl_4^-$. Electrochemically, an aluminum anode is possible; however, large amounts of aluminum will be consumed over a long electrolysis experiment. A platinum anode results in the oxidation of chloride rather than oxidation of the metal anode.

An electrolysis cell consisting of a degassed palladium cathode in a pure, neutral $MEI^+DCl_2^-$ melt and a platinum anode in a 0.33 basic $MEIC/AlCl_3$ melt should result in the following cell reactions:

Anode: $2Cl^- \text{----} > Cl_2 + 2e^-$

$Cl_2 + Cl^- \text{----} > Cl_3^-$

Cathode: $2DCl_2^- + 2e^- \text{----} > D_2(g) + 4Cl^-$

Overall: $2DCl_2^- \text{----} > D_2(g) + Cl_3^- + Cl^-$

In terms of ionic migration, MEI^+ will migrate from the anode to cathode compartment while Cl^- will migrate in the opposite direction.

Bulk electrolysis of a fresh, neutral $MEI^+DCl_2^-$ melt under conditions thought suitable for the attainment of cold fusion was carried out at the end of the project. At low current densities, < 30 mA cm^{-2}, the electrolysis cell behaved exactly as predicted by earlier experiments. Gaseous D_2 was rapidly evolved from the palladium cathode and a yellow coloration from Cl_3^- was produced in the anode compartment. During almost four hours of electrolysis at these low current densities, there was no increase in cathode compartment temperature and thus no experimental evidence of cold fusion.

The chemical literature suggests that cold fusion is best attained at higher current densities, > 100 mA cm^{-2} (Ref 1,7). After four hours at relatively low current densities, the current density was increased to 40 mA cm^{-2}. Immediately, the electrolysis conditions changed. The cathode compartment started turning a dark color suggesting that the organic portion of the deuterated melt was undergoing reduction. Furthermore, a reddish brown film appeared on the palladium cathode and gaseous evolution of D_2 from the cathode was noticeably reduced.

Based on earlier electrochemical investigation using cyclic voltammetry and chronopotentiometry, I am confident that at higher current densities the bulk electrolysis results in a nonselective reduction at the palladium electrode. Instead of reducing only D^+, the organic matrix of the deuterated melt is also undergoing reduction. Nonselective electrode reactions are always a possibility when using constant current electrolysis.

The cold fusion experiments of Pons and Fleischman (Ref 1) use D_2O as the source of D^+. In the aqueous system of Pons and Fleischman, the bulk electrolysis is carried out at the solvent voltage limit. Essentially, there is nothing easier in the system to reduce than D_2O. However, in the $MEI^+DCl_2^-$ molten salt system, not only is DCl_2^- reduced (desired reaction) but so is the organic matrix of the melt (undesired reaction). This nonselective reduction in the $MEI^+DCl_2^-$ melt at higher current densities is a serious restriction to the study of cold fusion in molten salt systems.

IV. RECOMMENDATIONS:

Based on the results of the research outlined above and previous research from the chemical literature, I can make two broad recommendations.

Recommendation 1

The nonselective nature of constant current electrolysis coupled with the fact that both DCl_2^- and the organic melt matrix are reduced at high current densities imply that cold fusion will be very difficult, if not impossible, to attain in a $MEI^+DCl_2^-$ molten salt.

I do not recommend extensive further investigation of cold fusion in the $MEI^+DCl_2^-$ system. However, brief research into the feasibility of cold fusion in $MEI^+DCl_2^-$ molten salts could include:

a. sustained, low current density electrolysis

b. other cathode electrode materials, such as titanium

Recommendation 2

The $MEI^+DCl_2^-$ molten salt has some physical and electrochemical properties which suggest further investigation is warranted. This melt is molten at extremely low temperatures, is soluble in tetrachloroaluminate molten salts, and provides a source of protons.

It would be beneficial to continue the study of physical and electrochemical properties of the $MEI^+DCl_2^-$ melts. Specifically, I recommend further investigation in the following areas:

c. stability of DCl in the $MEI^+DCl_2^-$ melts

d. electrochemical differences between DCl_2^- and $AlCl_4^-$ in neutral melts

e. verification of physical properties including melting point, viscosity, and specific heat

Since $MEI^+DCl_2^-$ and $MEI^+HCl_2^-$ behaved so similarly in this project, it should be acceptable to use the hydrogen based system which is much less expensive.

ACKNOWLEDGEMENTS

I would like to acknowledge and thank the Air Force Systems Command, the Air Force Office of Scientific Research, and the Frank J. Seiler Research Laboratory for financial support and technical assistance during this summer research program.

In particular I wish to thank Dr. John S. Wilkes for his personal support and encouragement which were so necessary for the project. I would also like to recognize the following Frank J. Seiler personnel who assisted me greatly during the project:

Mr. Jeffrey Boon - technical assistance and patience towards his former research director

Ms. Maureen Parrish - MEIC and $AlCl_3$ preparation

Mr. Fred Kibler - several glass blowing projects

Mr. Robert Hatfield - machining of Teflon cell components

CPT Jack Stuff - thermal analysis of deuterated melts

I will hasten to add that one of the more enjoyable aspects of the SFRP program at the Frank J. Seiler Research Laboratory was the opportunity to discuss research results and problems with Seiler colleagues who are knowledgeable electrochemists and scientists. In that regard I thank Dr. Joe Maloy of Seaton Hall University, and Mr. Bradley Combs and Dr. Robert Carper of Wichita State University. Finally, I thank fellow SFRP participant Dr. John Sanders of Northwest Louisiana State University for our shared frustrations with PAR instrumentation and his assistance in understanding molten salt systems.

REFERENCES

1. Martin Fleischmann and Stanley Pons, "Electrochemically Induced Nuclear Fusion of Deuterium," J. Electroanal. Chem., 1989, 261, 301.

2. S.E. Jones, E.P. Palmer, J.B. Czirr, D.L. Decker, G.L. Jensen, J.M. Thorne and S.E. Taylor, "Observation of Cold Nuclear Fusion in Condensed Matter," Nature, 1989, 338, 737.

3. "A Study of Cold Nuclear Fusion Reactions in the Aluminum Chloride/ 1-Methyl-3-Ethylimidazolium Chloride Molten Salt System," Unpublished White Paper, Frank J. Seiler Research Laboratory, 1989.

4. Thomas A. Zawodzinski, Jr. and R.A. Osteryoung, "1-Methyl-3-ethylimidazolium Hydrogen Dichloride: Synthesis and Applications to the Study of Protons in Ambient-Temperature Chloroaluminate Ionic Liquids," Inorg. Chem., 1988, 27, 4383.

5. "The Chemist's Companion," Edited by A.J. Gordon and R.A. Ford, Wiley-Interscience, New York NY, 1972, p. 451.

6. G. Caldwell and P. Kebarle, "The Hydrogen Bond Energies of the Bihalide Ions XHX^- and YHX^-," Can. J. Chem., 1985, 63, 1399.

7. A. J. Appleby, S. Srinivasan, Y.J. Kim, O. J. Murphy and C. R. Martin, "Evidence for Excess Heat Generation Rates During Electrolysis of D_2O in LiOD Using a Palladium Cathode - A Microcalorimetric Study," Workshop on Cold Fusion Phenomena, Santa Fe NM, 23 May 1989.

1989 USAF-UES SUMMER FACULTY RESEARCH PROGRAM

GRADUATE STUDENT RESEARCH PROGRAM

Sponsored by the

AIR FORCE OFFICE OF SCIENTIFIC RESEARCH

Conducted by the

Universal Energy Systems, Inc.

FINAL REPORT

HIGH CHARGE DENSITY BATTERIES EMPLOYING IONIC LIQUID ELECTROLYTES

Prepared by:	John R. Sanders, Ph. D.
Academic rank:	Assistant Professor
Department and University:	Department of Mathematical and Physical Sciences Northwestern State University
Research Location:	Frank J. Seiler Research Laboratory United States Air Force Academy, CO
USAF Researcher:	Maj. Larry Vaughn

Date:	01 Oct 89
Contract No:	F49620-88-C-0053

High Charge Density Batteries Employing Ionic Liquid Electrolytes

by

John R. Sanders

ABSTRACT

The feasibility of constructing a high charge density battery employing a buffered chloroaluminate ionic liquid electrolyte was investigated. The electrochemical behavior of selected first and second row transition metals was observed in buffered melt to determine if those metals were viable candidates for use as battery cathodes. Copper and silver exhibited acceptable characteristics. A simple battery cell with a sodium anode was constructed and the charge/discharge behaviors of cells employing both a copper and a silver cathode were outlined. In addition, the physical characteristics of the electrode materials were observed during and following electrolysis by elemental X-ray analysis and scanning electron microscopy.

Acknowledgements

I wish to thank the Air Force Systems Command and the Air Force Office of Scientific Research for sponsorship of this research. I especially wish to thank the staff of the Frank J. Seiler Research Laboratory, United States Air Force Academy, CO, for the opportunity to work in such a stimulating and professional facility. Universal Energy Systems must be thanked for their assistance and patience.

I especially wish to thank Dr. John Wilkes for his suggestions and insightful comments and Maj. Larry Vaughn for all the help, guidance, and friendship that he unselfishly offered during my visit to Colorado.

I. INTRODUCTION

The use of ionic liquids, ambient or subambient melting salts, as electrolytes in batteries has been studied for some time. Batteries employing these materials should exhibit a large charge capacity, low weight, and an extended temperature range where the battery electrolyte is liquid. These characteristics are particularly sought for both aircraft and aerospace applications. Until recently, problems involving changes in the electrolyte composition, irreversible electrochemical decomposition of the organic cation, and the chemical reactivity of the salts with some potential electrode materials have limited the use of these salts as battery electrolytes. A technique for buffering the ionic liquids (melts) against changes in composition has recently been discovered. Employing a buffered melt as a battery electrolyte appears to limit composition changes and the electrolytic decomposition of the cation. This discovery has spurred a renewed interest in the development of high charge density batteries employing ionic liquid electrolytes.

The Chemistry Directorate of the Frank J. Seiler Research Laboratory at the United States Air Force Academy is the primary center for basic research involving ionic liquids. This facility is studying the use of low melting ionic materials in batteries and the development of more advan-

tageous systems. Current studies are underway describing the buffered melts' characteristics and on the behavior of certain materials in both the buffered and non-buffered melt systems.

My research interests are in the areas of the synthesis and characterization of ionic liquids and their application to power systems. I developed and conducted the initial physical properties studies of the 1-methyl-3-ethyl-imidazolium bromide - aluminum bromide melt system and participated in studies which described the processes of ionic transport and ion association in both the 1-methyl-3-ethylimidazolium bromide - aluminum bromide melt and the analogous chloride melt system. I have also participated in a study of the use of ionic liquids as electrolytes in thermally regenerative electrochemical systems.

II. OBJECTIVES OF THE RESEARCH EFFORT

Charge density calculations indicate that several Group I and Group II metals can be combined with selected first and second period transition metals to yield battery cells with high charge density. Ionic liquid electrolytes should provide both a wide electrochemical window and a large operating temperature range for these cells. No previous study has employed the buffered haloaluminate melt systems. The use of a buffered melt as an electrolyte should allow manufacture of a battery cell with the desirable high charge capacity and low weight.

The initial objective assigned to me in this study was to determine the electrochemical and physical characteristics of potential electrode materials in the buffered melt using cyclic voltammetry, chronocoulometry, and chronopotentiometry. This set of procedures will indicate whether an electrode material undergoes a redox process within the electrochemical window of the electrolyte, forms an acceptably conductive surface layer during electrolysis, and whether the process is electrochemically reversible.

These studies should also indicate if any attendant chemical reactions are present. The physical characteristics of the electrode materials and surface layer were to also be observed. Solubility in the melt and adhesion of any layer

to the bulk electrode are especially important. Scanning electron microscopy was to be used to aid in this portion of the study. Initial studies are to be made of copper, silver, and iron as cathode materials and sodium as the anode material. (Sodium was selected as the anode electrode material since NaCl is the only material which has been demonstrated to serve as an effective buffering agent for the melts.)

After these initial studies it was decided to construct a test cell employing first a copper cathode and later a silver cathode. This cell was to serve as a model for studying the electrochemical behavior of the redox couples and the physical characteristics of the cell necessary for optimum performance.

III. ELECTROCHEMICAL STUDIES OF POTENTIAL CATHODE MATERIALS

A. Energy Density Calculations

The energy density (ED) of an electrochemical cell is the free energy per unit mass of electrode material the cell can theoretically produce.

$$ED = \frac{-\Delta G^{\circ}}{M} \qquad (1)$$

where ΔG° is:

$$\Delta G^{o} = -nFE. \qquad (2)$$

M and E are, respectively, the atomic weight of the electrode materials and the cell potential of the electrode couple. Energy density calculations indicate that several alkali and alkaline earth metals can be combined with transition metals to produce cells with high energy density. these calculations indicate that a Li/Cu cell would have the largest energy density. However, LiCl is reported as soluble in basic ($X_{AlCl_3} < 0.5$) melts which would defeat the buffering system. Cells employing Na, K, and Ca as anode materials vs. Cu or Ag cathodes all appear to exhibit acceptably high energy densities. Copper and silver were initially studied for cathode materials because of their availability, relatively low cost, lack of toxicity, and the considerable body of data available describing their characteristics and behavior in melt systems. Sodium was selected for the anode since NaCl is employed as the buffering agent in current studies.

B. Preparation of Materials

Buffered melts were produced by the weighed addition of soluble chloride salts to pre-purified and deprotonated acidic ($X_{AlCl_3} > 0.5$) melts. Melts in the composition range $0.52 < X_{AlCl_3} < 0.60$ were titrated with purified NaCl until cyclic voltammetry showed the Al peak characteristic

of acidic melts was gone. An additional quantity of the NaCl was then added to the melt to serve as a reservoir for buffering capacity. Buffered melts of different capacity were made to determine if the excess of undissolved buffering salt affected the electrochemical behavior of the electrode materials.

Copper, silver, and iron microelectrodes were prepared by cleaning wires of each metal in nitric acid, drying, and sealing the wires under vacuum in glass. Each electrode was polished to a mirror finish with emery cloth and alumina powder, then inspected under magnification for surface flaws. The electrodes were regularly refinished to maintain consistent surface quality. Between scans of each electrochemical experiment the electrodes were buffed with Kim-Wipe to remove deposits. A 4.0 mm diameter tungsten counter electrode was prepared in the same manner.

C. Electrochemical Behavior of Selected Cathode Materials

Copper, silver, and iron were investigated in the buffered melts by cyclic voltammetry. The electrochemical behavior of each metal was observed across the entire electrochemical window of the melt while the scan rate was varied between 1 mV/s and 1000 mV/s. Each electrode response was also observed to varying the limits and the initial direction of the potential scans.

During an initial cathodic scan, there was no significant current generated at any of the electrodes. When the potential was scanned anodically, a strong deposition peak was observed, corresponding to the reaction:

$$M^0 - ne^- \text{-----} > M^{n+} + nCl^- \text{-----} > MCl_n$$

For each metal this deposition peak exhibited a very sharp termination, indicative of the formation of a passivation layer. Scanning anodic of the passivation potential yielded a small, steady current until the melt limit was reached. Reversing the potential scan yielded a complex cathodic process for all three of the metals studied.

For single cycle scans a solitary, broad stripping peak was observed. When the electrodes were cycled through multiple (up to 10) scans, the deposition peak remained relatively constant while the stripping peak underwent a series of changes. The single peak observed in the first cycle decreased in magnitude with repeated scans and two new peaks cathodic of this process appeared. With repeated scans the initial stripping peak decreased until a reproducible value was obtained while the two new peaks increased in magnitude, reaching a constant value concurrent with the initial stripping peak. This type of electrode behavior had not been previously observed in acidic or neutral melts.

The electrochemical behavior of iron was both unusual and erratic. Due to the irreproducibility, further study of iron as a potential electrode material was postponed until a better understanding of the redox processes occurring in the melt could be obtained.

The anodic deposition layer formed on silver was significantly less adherent than that formed on copper. Gentle buffing of the silver electrode removed the deposit while vigorous polishing was required to remove the deposit from the copper electrode. Based on these preliminary results, copper was chosen for more extensive study as the cathode material for a battery cell.

Double potential step chronoamperometry was conducted at the copper electrode to examine the characteristics of the developed currents. The potential was sequentially stepped from open circuit in a series of experiments through a range of potentials, initially cathodic of the start of the deposition peak. In each successive scan the initial potential was stepped more anodic until the melt limit was reached. Following the anodic potential step of each experiment, the potential was stepped cathodically to a value that would assure complete reduction of the deposition layer.

Anodic and cathodic charge for each chronoamperometric cycle was determined by integration of the currents. It was observed that potential steps up to the passivation potential yielded smooth charge curves who's magnitudes were a function of the potential step. Exceeding the passivation potential yielded irregular charge curves characteristic of the formation of a passivation layer. Comparison of the anodic and cathodic charges for each step shows that the electrochemical processes under observation were reversible.

IV. PRELIMINARY BATTERY CELL STUDIES

A simple battery cell was constructed employing a sodium anode and a copper foil cathode. Sodium was melted into a 25 mL beaker, then compressed and polished to provide a smooth surface. A platinum wire, imbedded in the molten sodium and insulated from the electrolyte with a glass tube, was used as a current collector. Copper foil was cleaned in nitric acid, dried, and an approximately 2 cm^2 disc was cut to use as the cathode. Our first cell used a 4mm high glass ring as a separator. Subsequent cells employed layers of woven glass fabric to maintain electrode separation. A quantity of sodium chloride was placed in the cell to serve as a buffering reservoir and to supply the chloride ion necessary for formation of the deposition layer on the cathode during the charge cycle.

Each cell constructed was charged at constant current until a preselected potential was reached. This was to prevent electrochemical decomposition of the electrolyte. Following the charge cycle the cell was discharged at constant current. Consecutive charge/discharge cycles were run on several cells. Open circuit potential was monitored on each cell constructed following completion of the charge/discharge experiments.

Preliminary tests of the cells showed that a layer identified by X-ray analysis as a copper chloride species formed on the copper electrode during the charge cycle. The cells did not, however, deposit a significant portion of the available chloride ion, as determined by the excess buffering capacity of the electrolyte. The cells tested exhibited less than 50% recovery during discharge. Repeated charge/discharge cycles rapidly generated a dead cell. It was also noted that a black surface layer appeared on the sodium electrode and the electrolyte discolored near the sodium in a manner characteristic of electrochemical reduction of the organic cation.

Despite the lack of adherence of the deposition layer on the silver microelectrode, it was decided to determine if a silver cathode would produce a cell with desirable operational characteristics. An electrode was manufactured by

coiling a silver wire into a disc. The cell was assembled as described above with a glass fabric separator. Charge/discharge cycles on this cell yielded results similar to the copper/sodium cells. X-ray analysis indicated a silver chloride species was deposited on the coil during charge. Similar analysis also detected silver metal in the glass fabric following a series of charge/discharge cycles, indicating that the cathode surface layer had migrated into the separator.

Our preliminary investigation of these materials indicated that construction of an electrochemical cell capable of high charge density employing the buffered chloroaluminate ionic liquid as the electrolyte may be feasible. Several problems were encountered during the course of the limited investigation conducted which were not solved. The sodium metal electrode appears to react with the electrolyte. Some process inhibits the discharge cycle, with one of the electrode surfaces appearing to completely passivate after a few cycles. Additionally, the electrochemical behavior of the materials selected for study in buffered melt must be clarified.

V. RECOMMENDATIONS

The results obtained in this study prompt several recommendations for further investigation.

1. The electrochemical behavior of the first and second row transition metals in buffered melts needs further study. It would be especially valuable to study the behavior of the chloride salts of these metals to determine what role each different species has in forming the deposition layer.
2. From energy density calculations several alkali and alkaline earth metals appear to be promising candidates for anode materials. However, nothing is known about the ability of their chloride salts to act as buffering agents in the chloroaluminate ionic liquids. It should be determined to what extent these salts, especially potassium chloride, magnesium chloride, and calcium chloride can act as buffering agent in these melts.
3. Additional cell designs for the battery should be investigated to determine what effect different placement of the battery materials could have on the cell's performance.

1989 USASF-UES SUMMER FACULTY RESEARCH PROGRAM

Sponsored by the
AIR FORCE OFFICE OF SCIENTIFIC RESEARCH
Conducted by the
Universal Energy Systems, Inc.
FINAL REPORT

A CONVENIENT PREPARATION OF NITRONIUM TRIFLATE AND ITS USE FOR NITRATION

Prepared by:	Clay M. Sharts, Ph.D.
Academic Rank:	Professor
Department and	Chemistry
University	San Diego State University
	San Diego, CA 92182-0328
Research Location:	USAF FJSRL/NC (AFSC)
	United States Air Force Academy
	Colorado Springs, CO 80840-6528
USAF Researcher:	Major Scott A. Shackelford, USAF
Date:	September 20, 1989
Contract No:	F49620-88-C-0053

A CONVENIENT PREPARATION OF NITRONIUM TRIFLATE AND ITS USE FOR NITRATION

by

Clay M. Sharts

ABSTRACT

The reaction of anhydrous lithium or ammonium nitrate with trifluoromethanesulfonic anhydride (triflic anhydride) catalyzed by nitromethane at 60-70° was found to be the best and most convenient method for preparing nitronium trifluoromethylsulfonate (nitronium triflate). Nitronium triflate could also be prepared in refluxing anhydrous dichloromethane in the absence of nitromethane catalyst, albeit, in lower yield. Nitronium triflate in anhydrous dichloromethane was found to be a useful and convenient nitrating agent for substituting a nitro group for a hydrogen atom bonded to a nitrogen or carbon atom. For example, 2-pyrrolidone dissolved in dichloromethane was converted at room temperature to N-nitro-2-pyrrolidone in 30% yield. In a preliminary study with an aromatic compound, bromobenzene was converted in 70% yield into para-bromonitrobenzene. No ortho-bromonitrobenzene was found when the sample was analyzed by gc/mass spectroscopy. This result is viewed with caution until it has been repeated and the gc/ms analysis confirmed by other methods.

ACKNOWLEDGEMENTS

I wish to thank the Air Force Systems Command and the Air Force Office of Scientific Research for sponsoring this research and the Universial Energy Systems for the prompt and timely logistical support provided.

I really appreciated the environment of the F. J. Seiler Laboratory and the helpfulness of the civilian and military personnel associated with the Chemistry Section. I want to thank all associated with the lab for providing a pleasant and safe work place. I especially want to thank Major Scott Shackelford for his careful planning for my summer at Seiler and his ready and available assistance in support of my research requirements and Mr. Lloyd Pflug who provided gc/mass and nmr spectra on a prompt turnaround basis. My wife Jean also deserves special thanks for her support which freed me to concentrate on research.

Finally, thanks to the helpful and friendly people of Colorado Springs who make the city a wonderful place to live. Jean fell in love with Colorado Springs and says that we will return. It was a productive and enjoyable summer for both of us (Jean wrote four research papers.) Maybe the altitude got to both of us. Super summer!

I. INTRODUCTION: Although explosives are the major way for inflicting damage on the enemy during war, the military has continued to rely on explosives developed prior to or during World War II. In an authoritative review, chemists from the Explosives Technology Group at the Los Alamos National Laboratory have reviewed explosives development since World War II and pointed out just how limited the development of new explosives has been [1]. Although the military is the major consumer of explosives in wartime, none of the services has changed significantly the explosives used in ordnance from old standbys: TNT, HMX, RDX, PETN. Not until the U. S. Navy nearly lost a carrier was there a high-level push for insensitive safer explosives (the IHEP program). In spite of short term sporadic efforts by individual armed services, the only consistent major push for more powerful but less sensitive (read safer) explosives has been in the nuclear energy program. The introduction to ref. 1 provides an accurate concise statement of history and problems in explosive development.

Ubiquitous to explosives is the nitro group. Nearly all explosives contain nitro groups bonded to carbon or nitrogen. Classically, nitration reactions are carried out in strongly acidic conditions. Under typical nitration conditions many potential compounds for nitration to explosives undergo rearrangement or decomposition. For synthesis of a new generation of nitro-based explosives, a new method of nitration is very desirable. A reagent is needed which will nitrate in non-aqueous solvents at temperatures as low or lower than room temperature. Such reagents are available. They are various nitronium salts: for example, nitronium tetrafluoroborate, nitronium trifluoroacetate, and nitronium trifluoromethylsulfonate (nitronium triflate). A series of papers by Olah, Kuhn and Flood [2], [3], [4] describe fluorination by nitronium fluoroborate. Suri and Chapman [5] have nitrated nitrogen heterocycles at zero degrees in nitromethane using nitronium trifluoroacetate derived from ammonium nitrate and trifluoroacetic anhydride. Coon, Blucher and Hill [6] have reported nitration of aromatic compounds by nitronium triflate in the temperature range -110° up to room temperature. Their source of nitronium triflate was anhydrous nitric acid and trifluoromethanesul-

fonic acid (triflic acid), conditions which are very strong and inconvenient to achieve in the laboratory.

On the basis of reported reactions, we decided that the work of Suri and Chapman [6] provided the most promise; however, we decided that substitution of triflic anhydride for trifluoroacetic anhydride would give us the more powerful nitronium triflate under possibly very mild conditions. In the nitration reactions of Suri and Chapman the trifluoroacetic acid formed during nitration limited the yield of product to a maximum of 50%. We believed that the triflic acid coproduct formed during nitration by nitronium triflate could be selectively removed by sodium sulfate during reaction and give a chance to approach 100% yield. We set our goal as nitration of organic compounds in low-boiling organic solvents by nitronium triflate formed from a nitrate salt and triflic anhydride. We particularly wanted to use dichloromethane as solvent and specifically wanted to avoid the use of nitromethane (bp 101^{o}) if possible in order to simplify workup of the reactions and to avoid the hazards involved in working with large amounts of toxic and flammable nitromethane.

A second part of the problem of designing new insensitive explosives is understanding how explosives degrade, decompose, deflagrate, and detonate. Shackelford and coworkers [7] have pioneered the use of deuterium isotope effects for study of the decomposition of explosives. The role of hydrogen atom transfer is key for many decompositions. It is desirable to be able to replace key hydrogen atoms in various structures by fluorine atoms. Also, substitution of fluorine for hydrogen can lead to compounds which are potentially more energetic. Xenon difluoride is a convenient fluorinating reagent which has not been fully investigated. Another goal of this research was to replace selected hydrogen atoms on nitrogen or carbon by fluorine atoms.

Five model compounds drawn in Chart A were selected for preliminary nitration and fluorination studies. The expected nitration products of the five model compounds are also drawn in Chart A. These five nitro

Proposed Nitration Products

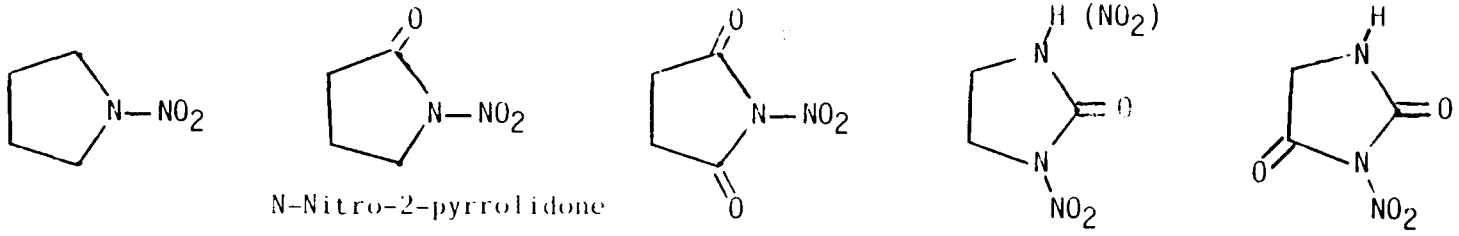

N-Nitro-2-pyrrolidone

Nitrogen Heterocyclic Compounds Proposed for Reaction

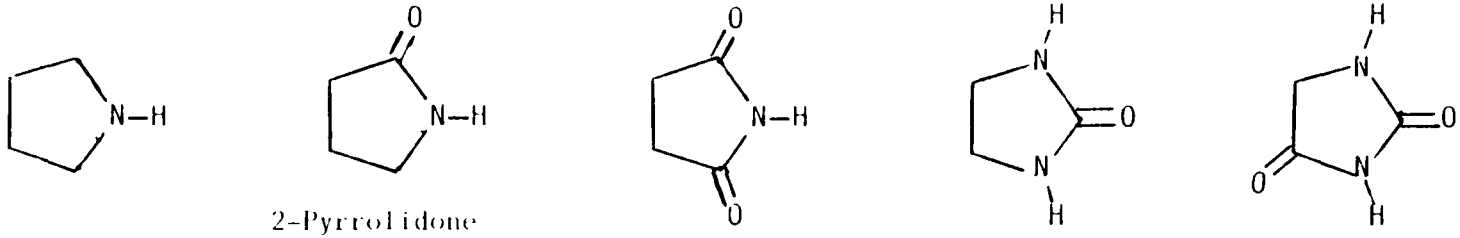

2-Pyrrolidone

Proposed Fluorination Products

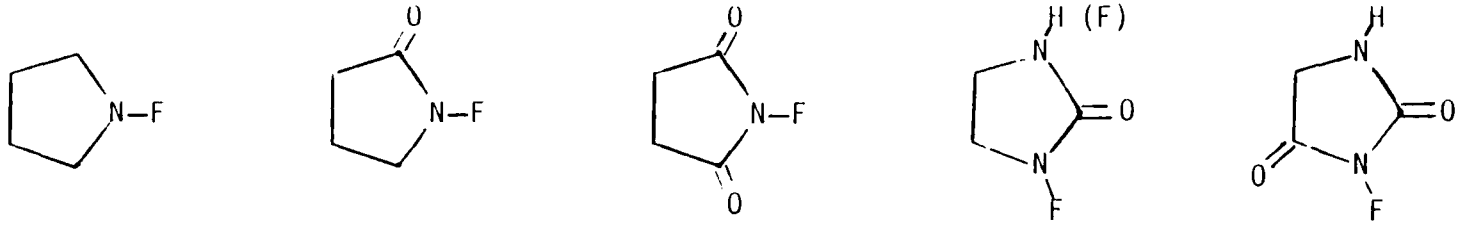

CHART A. Nitrogen heterocylic compounds for nitration and fluorination (center row) and the expected nitration products (top row) and fluorination products (bottom row). The center row products are named from left to right: pyrrolidine, 2-pyrrolidone, succinimide, 2-imidizolidone, and uracil.

compounds are not expected to be explosives but contain structural features that are desirable in a new class of explosives. If the nitro groups of the nitrated products in Chart A are replaced by fluorine atoms, the proposed products of xenon difluoride fluorination result.

II. NITRATION OF 2-PYRROLIDONE BY AMMONIUM NITRATE AND TRIFLIC ANHYDRIDE

Nitration of 2-pyrrolidone by nitronium triflate formed from ammonium nitrate and triflic anhydride occurred in several experiments to form up to a 30% yield of N-nitro-2-pyrrolidone.

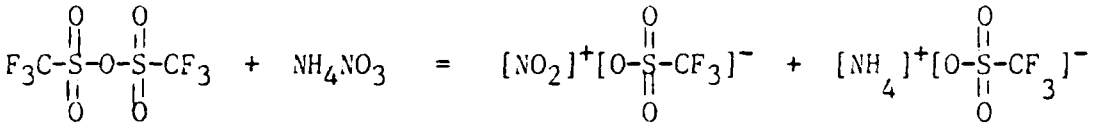

triflic anhydride nitronium triflate ammonium triflate

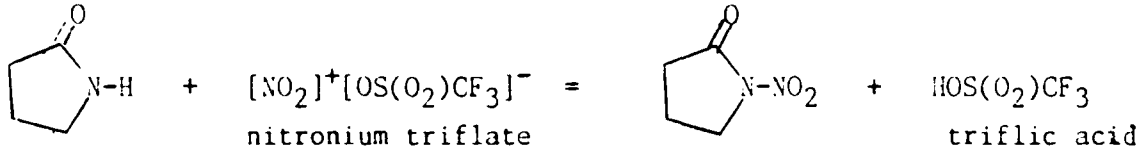

2-pyrrolidone nitronium triflate N-nitro-2-pyrrolidone triflic acid

On other occasions the same procedure failed to form nitronium triflate intermediate and gave a mixture of products from reaction of triflic anhydride and 2-pyrrolidone. The inconsistent results obtained led to the conclusion that in many attempted nitrations of 2-pyrrolidone, nitronium triflate had not been formed. Incomplete reaction or no reaction had occurred between ammonium nitrate and triflic anhydride. Unreacted triflic anhydride remained which reacted with 2-pyrrolidone when 2-pyrrolidone was added. The gas chromatography/mass spectra were consistent with structures expected from reaction of triflic anhydride and 2-pyrrolidone. Structures for these products will be determined in future research.

Ammonium nitrate used in the experiments was dried in an oven at 90-100° and pulverized as finely as possible by a mortar and pestle to give powdered ammonium nitrate. No ball mill was available. It was clear from experimental results that the rate of reaction of ammonium nitrate with triflic anhydride was slow in refluxing dichloromethane. Changing the

solvent to sulfolane did not improve the formation of nitronium triflate. Attempted reactions in sulfolane did not give the desired product. One successful preparation of N-nitro-2-pyrrolidone is described next.

N-nitro-2-pyrrolidone. To a dry 2-necked 100-ml round-bottomed flask fitted with a reflux condenser and a compensating dropping funnel, were added 1.20 g (15.0 mmol) anhydrous ammonium nitrate, 40.0 ml dry dichloromethane and 4.23 g (15 mmol) triflic anhydride. The mixture was stirred and heated at reflux under a nitrogen atmosphere for 66 hours. The amount of solid in the flask increased and solid was distributed on the walls of the flask rather than on the bottom as was observed initially. Brown vapors were apparent in the flask and condenser. An excess of 2-pyrrolidone (1.70 g, 20 mmol) dissolved in 10 ml dichloromethane was added dropwise over a 40-minute period. After 30 minutes, 50 ml of water were added and layers separated. The dichloromethane layer was washed with three 25-ml portions of 5% sodium bicarbonate solution, two 25-ml portions of water, and two 25-ml portions of saturated NaCl solution. The dichloromethane solution was dried over 2.0 g Na_2SO_4. After filtration dichloromethane was distilled (bp 33-34 °, 590 torr). Residual dichloromethane was removed under reduced pressure (16mm, water aspirator). An orange residue (0.42 g) remained which was analyzed by gc/mass spectroscopy.

COMPOSITION OF CRUDE RESIDUE

GC/MC #	% Sample	BP,100%	m/z MAX		Possible Compound Identity
1-15-A1	4.36%	42	86		Dihydro-2(3H)-furanone
1-15-A2	0.32%	46	90		?
1-15-A3	0.36%	46	104	???	4-Hydroxybutanoic acid
1-15-A4	0.13%	46	90		?
1-15-A5	0.62%	28	217	?	N-Trifonyl-2-pyrrolidone
1-15-A6	92.60%	56	130		N-Nitro-2-pyrrolidone
1-15-A7	1.61%	151	153	???	O-Trifonyl-2-pyrrolidone

An analytical sample of N-nitro-2-pyrrolidone (mp 55.5-56.0°) was prepared by recrystallizing sample 1-15-A6 (mp 52-54°) from diethyl ether.

For this sample a parent peak of 130 (fw = 130) was observed. A copy of the gc/mass spectrum is shown in Figure 1 on a separate page. The 1-hydrogen and 13-carbon nuclear magnetic (nmr) spectra were observed in deuterobenzene and deuterochloroform. The spectra in deuterobenzene agreed with spectra for N-nitro-2-pyrrolidone reported earlier [5]. The spectra in deuterochloroform are shown in Figure 2 and differ only in the chemical shifts from the spectra in deuterobenzene. The second crop of crystals from the recrystallization of 1-15-A6 was colored bright yellow and melted slightly lower (mp 54.5-55.5°) than the first crop which was off-white in color. Analysis of the second crop by gc/mass spectra showed 99% N-nitro-2-pyrrolidone and 1% N-nitroso-2-pyrrolidone.

III. NITRATION OF 2-PYRROLIDONE BY LITHIUM NITRATE AND TRIFLIC ANHYDRIDE

The nonrepeatable results which were observed when ammonium nitrate was used to form nitronium triflate led to a literature search to find some other nitrate salt that might have better solubility in dichloromethane and thereby be better in forming nitronium triflate. A study by Harner, Sydnor and Gilreath [8] showed that lithium nitrate and calcium nitrate had much greater solubility in anhydrous methanol than other alkali or alkaline-earth metallic nitrate salts.

SOLUBILITIES OF GROUP I AND II SALTS IN ANHYDROUS METHANOL

Grams salt/100 grams anhydrous methanol

	Fluoride (1.36)	Chloride (1.81)	Bromide (1.95)	Iodide (2.16)	Nitrate	Carbonate	Sulfate
Lithium (0.60)	0.0176	20.98	34.29	...	**42.95**	0.0555	0.1261
Sodium (0.95)	0.0231	1.401	16.09	62.51	2.936	0.3109	0.0113
Potassium (1.33)	2.286	0.5335	2.080	17.07	0.380	6.165	0.0005
Calcium (0.99)	0.0145	23.26	55.83	67.37	**127.13**	0.0012	0.0046
Strontium (1.13)	0.0142	18.05	...	...	1.061	0.0014	0.0074
Barium (1.35)	0.0044	1.379	...	...	0.048	0.0064	0.0063

(Ionic radii in Angstroms are given in parentheses.)

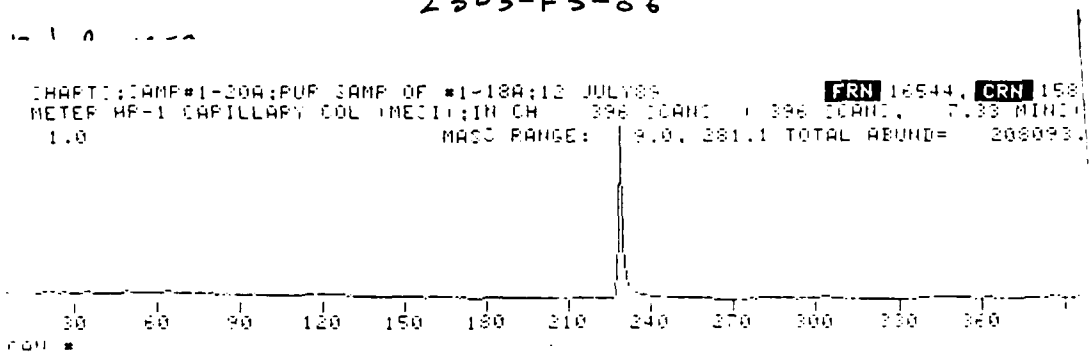

mp = 55½-56.0°C

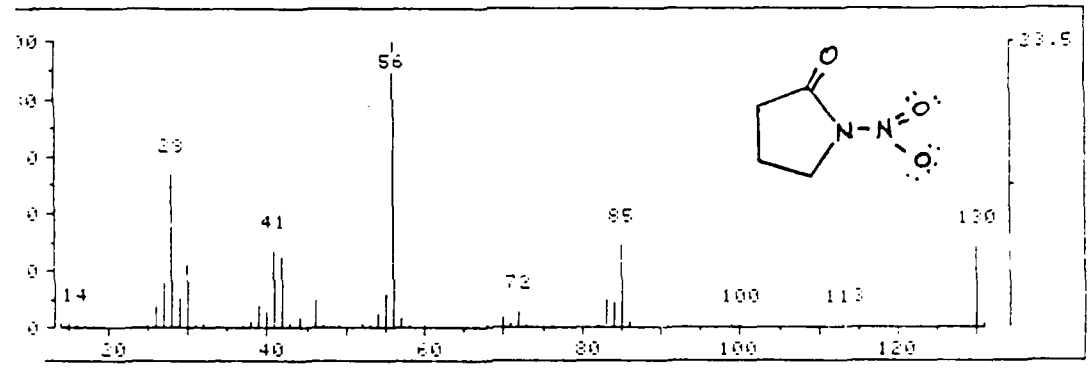

AGED SPECTRUM: FRN 16544, 48 PEAKS

M/Z	REL ABUND	M/Z	REL ABUND	M/Z	REL ABUND	M/Z	REL ABUND
14	1.5	38	1.5	51	.7	72	6.0
15	1.5	37	1.3	52	3.0	73	1.0
16	.7	38	2.2	53	1.0	82	1.0
17	.4	39	7.7	54	4.4	83	4.8
18	.9	40	5.9	55	12.1	84	9.3
25	.9	41	27.0	56	100.0	[illegible]	39.1
[illegible]	[illegible]	[illegible]	[illegible]	[illegible]	[illegible]	[illegible]	[illegible]

Figure 1. Gas Chromatography and Mass Spectra of N-Nitro-2-pyrrolidone

Figure 2. NMR Spectra of N-Nitro-2-pyrrolidone in Deuterochloroform

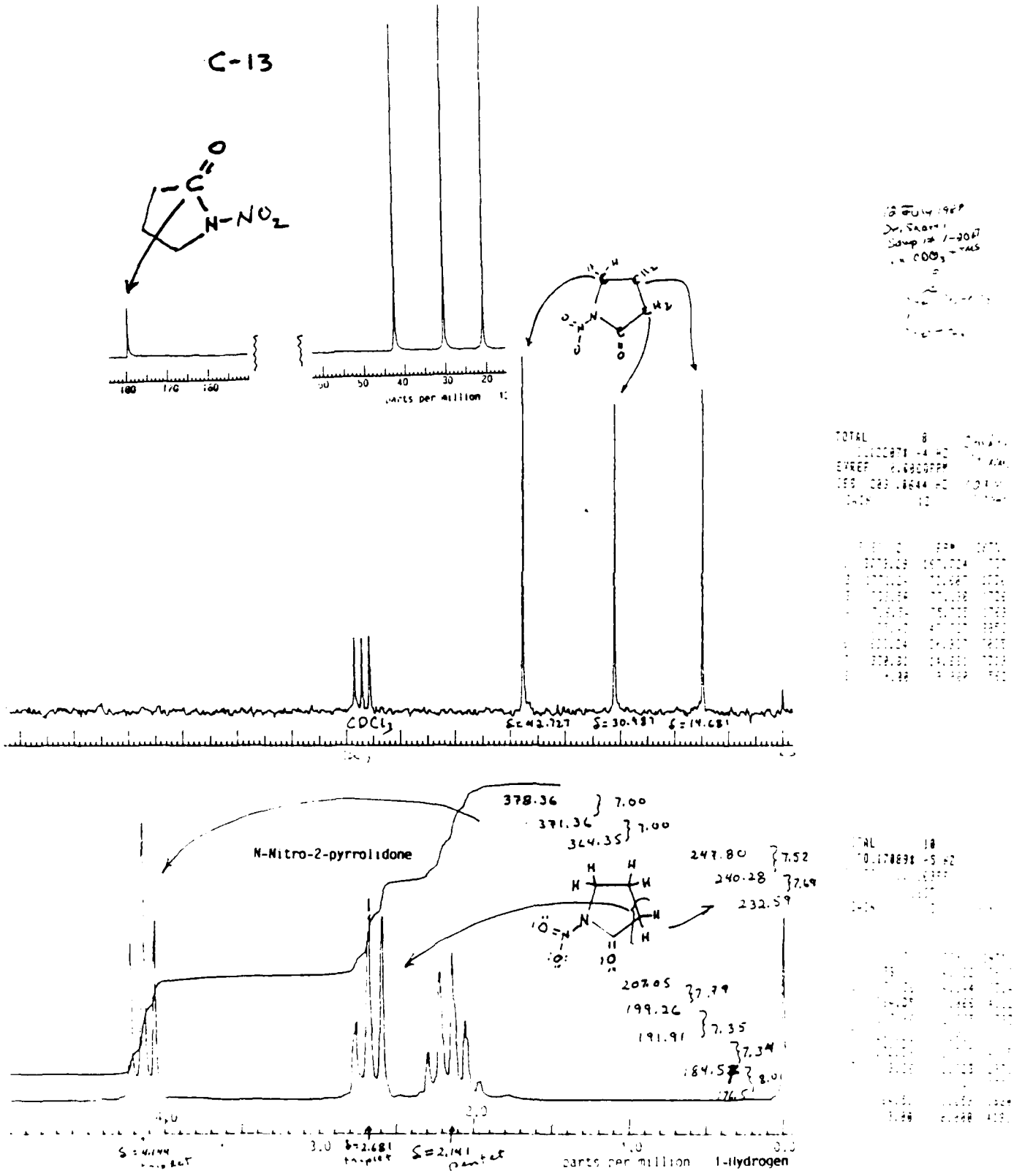

In another study lithium salts were found to be very soluble in a variety of organic solvents [9] with a linear dependence found between the logarithm of mole fraction solubility and the reciprocal of the dielectric constant. No studies were found that directly compared ammonium salts with lithium salts. However, a study of salt solubilities in sulfolane [10] indicates that ammonium salts have solubilities comparable with sodium salts. On the basis of limited references it was concluded that lithium nitrate and calcium nitrate salts are much more soluble in organic solvents than ammonium nitrate, and that the reaction of these nitrates with triflic anhydride should be investigated as a source of nitronium triflate. Lithium nitrate forms a monohydrate which decomposes at 55°. In contrast the trihydrate of calcium nitrate decomposes at 180°. Although it might be suspected anhydrous calcium nitrate might react more readily with triflic anhydride than anhydrous lithium nitrate, the experimental ease of making anhydrous lithium nitrate made lithium nitrate the nitrate salt of choice for further investigation for forming nitronium triflate.

N-nitro-2-pyrrolidone. Anhydrous lithium nitrate was prepared from lithium nitrate monohydrate by azeotropically distilling water from a mixture of excess carbon tetrachloride and $LiNO_3 \cdot H_2O$. Lithium nitrate was separated by filtration and stored in an oven at $90\text{-}100^{\circ}$. Glassware was flame dried and stored overnight in an oven at $90\text{-}100^{\circ}$. The center neck of a 125-ml 3-necked flask was fitted with a compensating dropping funnel on top of a reflux condensor and a magnetic stirring bar. A gas inlet tube and stopper were fitted to the other necks. The system was flame dried under a stream of nitrogen and maintained under nitrogen atmosphere with a slightly positive pressure above atmospheric pressure. Hot anhydrous lithium nitrate (2.75 g, 40 mmol) and triflic anhydride (5.64 g, 20 mmole) were added and the reaction vessel heated at 70° overnight. Initially two phases were clearly evident: solid $LiNO_3$ in liquid triflic anhydride (TfOTf). After overnight heating no liquid layer was seen; the solid appeared damp. Clearly nitronium triflate solid (NO_2OTf) formed.

$$Tf\text{-}O\text{-}Tf\ (liquid) + LiNO_3\ (solid) = LiOTf\ (solid) + NO_2OTf\ (solid)$$

The following morning the heating bath was removed and the flask permitted to cool to room temperature before 50 ml of dry dichloromethane and 5.68 g (40 mmol) anhydrous sodium sulfate were added. The mixture was heated to gentle reflux (33-34°, 590 torr) and a solution of 1.70 g (20 mmole) 2-pyrrolidine in 10 ml dichloromethane added over a 40-minute period. After two days at gentle reflux the reaction was cooled and solids removed by filtration. The continued reaction sequence is:

$$NO_2OTf + \text{2-pyrrolidone} = HOTf + \text{N-nitro-2-pyrrolidone}$$
$$HOTf + LiNO_3 = HNO_3 + LiOTf$$
$$HNO_3 + Na_2SO_4 = NaNO_3 + NaHSO_4$$

The methylene chloride layer was washed as follows: three times with 25 ml water, three times with 5% aq NaHCO3 solution, and two times with 25 ml saturated NaCl solution. After drying over 2.0 g Na_2SO_4, methylene chloride was distilled and residual dichloromethylene chloride removed at reduced pressure. When seeded with a crystal of N-nitro-2-pyrrolidone, the 0.80 g (6.2 mmole, 31%) of residual yellow oil crystallized. The gc/mass spectra identified the solid product as N-nitro-2-pyrrolidone.

Reactions of lithium nitrate with triflic anhydride to form nitronium triflate were not consistent. However, results were less variable and more consistent than results had been with ammonium nitrate. In separate reactions it was observed that both ammonium nitrate and lithium nitrate reacted rapidly and completely in nitromethane to form nitronium triflate. With 50 ml of nitromethane solvent, 20 mmole of either salt reacted in two hours with 20 ml of triflic anhydride to give clear solutions. This suggested that nitromethane be tried as a catalyst for the reaction. The postulate was that nitromethane forms a 1:1 complex with either $LiNO_3$ or NH_4NO_3 which may be represented in two dimensions:

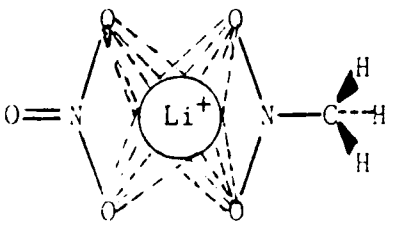

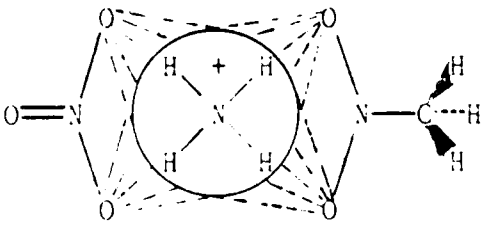

IV. NITROMETHANE CATALYZED FORMATION OF NITRONIUM TRIFLATE FOR NITRATION

One reaction was carried out similarly to the reactions described in the paragraphs N-2-nitropyrrolidone of sections II and III of this report except that a catalytic amount of nitromethane was present. Mixing 2.75 g (40.0 mmol) lithium nitrate, 5.64 g (20 mmol) triflic anhydride, and 1.02 grams (16.1 mmol) nitromethane gave a two-phase mixture. After four hours at room temperature with occasional stirring, only a solid phase existed which appeared to be wetted by liquid. Dichloromethane solvent was now added along with sodium sulfate for neutralizing nitric acid formed during the nitration reaction. A solution of 1.70 g (20 mmol) pyrrolidine in dichloromethane was added dropwise to the solid which was cooled at ice-bath temperature. After twenty minutes 50 ml of water was added followed by solid potassium carbonate sufficient in amount to give a basic solution, pH>10. Following the usual workup procedure, 0.50 grams (20%) of N-nitro-2-pyrrolidone was obtained. The low yield is attributed to incomplete reaction of 2-pyrrolidone in the short time period at zero degrees. This reaction was conducted on the last day of laboratory work of the summer period. A similar reaction using ammonium nitrate as the source of the nitronium ion was carried out by Major Shackelford and gave a yield of 27%. His reaction was carried out to confirm the catalytic effect of nitromethane. Confirmation was needed to allow this report to have an additional example of the catalytic effect of nitromethane.

V. NITRONIUM TRIFLATE REACTION WITH BROMOBENZENE IN DICHLOROMETHANE

Throughout the studies made and presented in this report, there was always a question as to whether nitronium triflate was formed in a given reaction. There was not a convenient way to determine how much nitronium triflate was formed before a reaction with another reagent was carried out. Only after the fact that nitromethane could be used as a catalyst for reaction of triflic anhydride with either lithium nitrate or ammonium nitrate to form nitronium triflate, did we know that we had significant results upon which future research could be firmly based. As a final experiment to confirm that we really had a room temperature

nitrating agent for use in dichloromethane, the decision was made to nitrate bromobenzene. The choice was made for one major reason. The expected mononitration products of bromobenzene are both solids: o-bromonitrobenzene (mp = 41-42°) and para-bromonitrobenzene (mp = 125-126°). Further, the para isomer can be isolated from the mixture by crystallization and the ortho isomer can then be obtained by column chromatography. The normal ratio of ortho/para isomer is 38:62. Another reason for choosing bromobenzene for nitration was that samples of pure ortho, meta, and para bromonitrobenzene isomers were available in the lab for standards. The following experiment was carried out on the final day of lab work for the summer research period.

para-Bromonitrobenzene. The reaction apparatus and procedures used were similar to those used earlier for preparation of n-nitro-2-pyrrolidone. Anhydrous lithium nitrate (1.415 g, 20.52 mmol), triflic anhydride (5.59 g, 19.82 mmol), and nitromethane (0.107 g, 1.75 mmol) were added to the reaction flask and heated at 65±5° overnight. The following morning some liquid remained. An additional 1.415 g of anhydrous lithium nitrate (20.52 mmol) and 1.02 g (16.72 mmol) nitromethane was added. Almost immediately some brown fumes were visible which were probably due to adventitious water. After 1 hour at 70° no liquid phase was observable. (I AM GUESSING THAT A 1:1 RATIO OF NITROMETHANE TO STOICHIOMETRIC LITHIUM NITRATE IS NEEDED. THE RATIO USED IN THIS EXPERIMENT WAS 18.5:20.0. THE USE OF LESS THAN STOICHIOMETRIC NITROMETHANE WAS DELIBERATE. THIS MAY HAVE LIMITED THE YIELD OF PRODUCT.) The reaction system was purged by nitrogen gas at 70°. Transluscent crystals sublimed into the condensor during the passage of nitrogen. Similar crystals were observed earlier and are believed to have been nitronium triflate. A crystal was removed and added to acetone. A vigorous reaction occurred with evolution of brown fumes. These crystals are believed to have been nitronium triflate. Sublimation may be a method for isolating nitronium triflate as pure solid crystals. Dry dichloromethane (50.0 ml) was added to the reaction flask and the flask heated to maintain a gentle reflux of solvent. A solution of 3.14 g (20.0 mmole) of bromobenzene in 15 ml of

dichloromethane was added over a 35-minute period and the reaction mixture heated 2.5 hours under reflux. The solution was cooled and solids removed by filtration. The methylene chloride solution was washed with water or aqueous solutions as follows: three times with 25 ml water, three times with 25 ml 5% $NaHCO_3$, four times with 25 ml 5% NaOH, twice with 5% $NaHCO_3$, two times with 25 ml water, and two times with saturated NaCl. The dichloromethane solution was dried over 2.0 g of Na_2SO_4 and distilled. Residual dichloromethane was removed at reduced pressure. A solid formed as the last of the dichloromethane was removed that amounted to 2.14 gram (53.0%). Since the starting material bromobenzene is a liquid and the products are solids, it was immediately apparent that the nitration reaction was a success.

Analysis of Nitration Products of Bromobenzene. The product was submitted for gc/mass spectral analysis on the day of departure from the Seiler Laboratory. Subsequently it was reported to me by Major Shackelford that the sample analyzed as follows in mole-fraction percent: 54% para-bromonitrobenzene, 37.4% bromobenzene starting material, and 8.6% 2,4-dinitrobromobenzene. This result is remarkable because of what was not present. There was NO ORTHO-BROMONITROBENZENE, a result that is exceedingly difficult to accept on the basis of over a century of results for nitration of bromobenzene. The accepted course of reaction ALWAYS gives both ortho and para isomers. A second analysis with a larger amount of the same sample and greater sensitivity gave the following remarkable analysis:

35.45% bromobenzene (starting material = s.m.)	2.96% para-dibromobenzene (probable impurity in s.m.)
51.2 % para-bromonitrobenzene (major product)	0.22% ortho-dibromobenzene (probable impurity in s.m.)
8.19% 2,4-dinitrobromobenzene (minor product)	0.56% nitrodibromobenze (prob. nitr. prod. of s.m.)

0.00% NO ortho-bromonitrobenzene formed contrary to conventional wisdom

Obviously this reaction needs to be repeated and the results duplicated.

Nitration of Bromobenzene with Ammonium Nitrate and Triflic Anhydride

The nitration of bromobenzene was carried out by Major Shackelford using

triflic anhyride and ammonium nitrate (rather than lithium nitrate). He ran the reaction on half the scale of the preceding reaction: 11.0 mmol ammonium nitrate, 9.96 mmol triflic anhydride, 9.96 mmol nitromethane. He formed the nitronium triflate at 59-61° over a 15-hour period. He used dichloromethane as a reaction solvent and reacted 10.0 mmol bromobenzene in a period of 2.0 hours. Analysis of his product showed two substances: the product para-nitrobromobenzene (76%), and the starting material bromobenzene (24%). Presumably there were impurities below the detection level. His crude yield was 1.74 grams. This gives a mixture of 1.39 g para-bromonitrobenzene and .35 grams of bromobenzene for the isolated product. Since .35 grams of bromobenzene were recovered the actual amount of starting material is only 1.24 g (8.21 mmol). Suitable corrections give an 83% yield of p-bromonitrobenzene based on bromobenzene. Since the more expensive reagent is triflic anhydride, a more realistic yield is 68% based on triflic anhydride. For a one time reaction this is an excellent result.

VI. SIGNIFICANT FINDINGS AND CONCLUSIONS. A new and convenient synthesis for the nitrating intermediate nitronium triflate, $(NO_2^+)(OSO_2CF_3^-)$, has been developed. This intermediate may be used for nitration in the unreactive solvent dichloromethane, a convenient low-boiling solvent which is readily separated from starting materials and products. The key to reproducable reactions is the use of nitromethane as a catalyst for direct reaction between lithium or ammonium nitrate and trifluoromethanesulfonic anhydride (triflic anhydride), $CF_3S(O_2)OS(O_2)CF_3$. The use of anhydrous sodium sulfate as a base to neutralize anhydrous nitric acid and trifluoromethanesulfonic acid may be very important in increasing the yield of nitration products. Nitronium triflate has given both N-nitration and C-nitration in the very limited studies carried out. The unexpected finding that no ortho-nitrobenzene formed in the nitration of bromobenzene needs confirmation before it can be accepted as real. The finding is contrary to all conventional wisdom concerning aromatic substitution.

VII. RECOMMENDATIONS BASED ON SIGNIFICANT FINDINGS AND CONCLUSIONS

The new method for nitration is probably patentable and should be exploited as soon as possible as a synthetic tool for nitrating relatively sensitive nitrogen heterocyclic compounds. Major Shackelford will use nitronium triflate for addition-elimination/substitutions with alkenes. I plan to apply for a mini grant to continue substitution studies on nitrogen heterocycles as shown in Chart A. If funded, I hope to have undergraduate and graduate students pursue the nitration of aromatic compounds to determine the scope of reaction and confirm the unexpected selectivity in the nitration. Since I begin a sabbatical leave in January 1990, I can use a mini grant optimally to obtain student assistance in research. Regardless of the mini grant, I believe there was a significant discovery this summer which should be exploited immediately. A patent should be filed as soon as sufficient examples of the use of nitronium triflate are obtained.

VIII. REFERENCES: References are presented on the two pages which immediately follow.

REFERENCES

1. Michael D. Coburn, Betty W. Harris, Klen-Yin Lee, Mary M. Stinecipher, and Helen H. Hayden; "Explosives Synthesis at Los Alamos"; I&EC PRODUCT RESEARCH & DEVELOPMENT, 1986, 25, 68-72. Chem. Abstr., 1986, 104, 112304z.

2. Stephen J. Kuhn and George A. Olah; "Aromatic Substitution. VII. Friedel-Crafts Type Nitration of Aromatics"; J. Am. Chem. Soc., 1962, 83, 4564-4571. Chem. Abstr., 1962, 56, 8607g.

3. George A. Olah, Stephen J. Kuhn, and Sylvia H. Flood; "Aromatic Substitution. VIII. Mechanism of the Nitronium Tetrafluoroborate Nitration of Alkylbenzenes in Tetramethylene Sulfone Solution. Remarks on Certain Aspects of Electrophilic Aromatic Sustitution"; J. Am. Chem. Soc., 1962, 83, 4571-80. Chem. Abstr., 1962, 56, 8607f.

4. Stephen J. Kuhn and George A. Olah; "Aromatic Substitution. IX. "Nitronium Tetrafluoroborate Nitration of Halobenzenes in Tetramethylene Sulfone Solution"; J. Am. Chem. Soc., 1962, 83, 4581-4585. Chem. Abstr., 1962, 56, 8607h.

5. S. C. Suri and R. D. Chapman; "A Convenient Method for N-Nitration Using Ammonium Nitrate/Trifluoroacetic Anhydride". SYNTHESIS, 1988, 473-476. Chem. Abstr., 1989, 110, 192709x.

6. Clifford L. Coon, William G. Blucher, and Marion E. Hill; "Aromatic Nitration with Nitric Acid and Trifluoromethanesulfonic Acid; J. Org. Chem., 1973, 38, 4243-4248. Chem. Abstr., 1974, 80, 14671h.

7. (a) S. A. Shackelford, J. W. Beckmann and J. S. Wilkes; "Deuterium Isotope Effects in the Thermochemical Decomposition of Liquid 2,4,6-Trinitro toluene: Application to Mechanistic Studies Using Isothermal Difential Scanning Calorimetry Analysis"; J. Org. Chem., 1977, 42, 4201-4206. Chem. Abstr., 1978, 88, 6022x.

7. (b) S. A. Shackelford, M. B. Coolidge, B. B. Goshgarian, B. A. Loving, R. N. Rogers, J. L. Janney, and M. H. Ebinger; "Deuterium Isotope Effects in Condensed-Phase Thermochemical Decomposition Reactions of Octahydro-1,3,5,7-tetrazocine; J. Phys. Chem., **1985**, **89**, 3118-3126. Chem. Abstr., **1985**, **103**, 36985j

8. R. E. Harner, J. B. Sydnor, and E. S. Gilreath; "Solubilities of anhydrous Ionic Substances in Absolute Methanol"; J. Chem. Eng. Data., **1963**, **8**, 411-412. Chem. Abstr., **1963**, **59**, 8178g.

9. B. S. Krumgal'z, V. A. Smirnova, Yu. I. Gerkzhberg; "Solubility of Lithium Salts in Acetone and Methyl Ethyl Ketone in the -50 to +50° Range"; Zh. Prikl. Khim. (Leningrad), **1973**, **46**, 237-239. Chem. Abstr., **1973**, **68**, 102560k.

10. P. Srivastava, Mohd. M. Husain, and Ram Gopal; "Solubilities of Inorganic Salts and Tetraalkylammonium Iodides in Sulfolane at Several Temperatures"; J. Chem. Eng. Data., **1985**, **30**, 144-145. Chem. Abstr., **1985**, **102**, 155665u.

1989 USAF-UES SUMMER FACULTY RESEARCH PROGRAM/
GRADUATE STUDENT RESEARCH PROGRAM

Sponsored by the

AIR FORCE OFFICE OF SCIENTIFIC RESEARCH

Conducted by the

Universal Energy Systems, Inc.

FINAL REPORT

AN INVESTIGATION OF DYNAMIC STALL VORTEX CHARACTERISTICS

Prepared by:	J.A. Albertson and T.R. Troutt
Department and University:	Department of Mechanical and Materials Engineering Washington State University
Research Location:	Frank J. Seiler Research Laboratory Aerospace Mechanics Division United States Air Force Academy, CO
USAF Researcher:	Major Robert F. Reilman, Jr.
Date:	September 29, 1989
Contract Number:	F49620-88-C-0053

AN INVESTIGATION OF DYNAMIC STALL VORTEX CHARACTERISTICS

by

Julie A. Albertson and T.R. Troutt

ABSTRACT

This research investigation concentrated on expanding knowledge of the unsteady aerodynamics produced by pitching airfoils in uniform flows. The specific experimental situation focused on three distinct areas. A laser–Doppler–velocimetry system was assembled and aligned for use in a water tunnel. Preliminary verification tests show promise for accurate future velocity measurements. A separate flow visualization study involved a two–dimensional NACA 0015 airfoil pitched at constant rates through angles of attack from 0–50 degrees. The experimental results included 35 mm still and video camera flow visualization using dye. These tests showed it was possible to entrain dye within the center of the dynamic stall vortex if it was injected through the airfoil surface. This is a necessary step for any future image analysis or laser–Doppler–anemometry experiments on pitching airfoils in wind tunnels. The use of different colored dye injected at various airfoil locations also helped to clarify the mechanisms leading to dynamic stall, and shows great promise as a future flow visualization technique. A third part of the project involved a preliminary literature review of active control methods. It was determined that acoustic forcing, spanwise blowing, and an external oscillatory flap should yield the most effective control of dynamic stall flows.

I. INTRODUCTION

My previous related research interests have been in the areas of turbulent free shear flows and reattaching separated flows, with special emphasis on development of suitable flow visualization techniques and analysis procedures. The focal point of my efforts has been the improved understanding of the rate of quasi–deterministic flow structures in the development of these flows through data acquisition and analysis. Such studies were the subject of my Masters research.[1]

The unsteady aerodynamics research pursued under this summer's research program is a natural extension of the work done previously by myself and Dr T. Troutt as well as others at the Frank J. Seiler Research Laboratory. Previous work under the UES/USAF Graduate Student Research Program has concentrated on developing a greater understanding of the dynamic stall vortex phenomenon and the mechanisms that drive it. In the past, work has concentrated on obtaining pressure measurements and flow visualization of airfoils pitching at constant rates, and subsequent analysis of such measurements. The current research focuses on the development of an accurate means by which to measure velocity levels within the unsteady separated region created by the pitching airfoil, namely LDV, and the determination of the optimum means by which to actively control the flow.

The motivation behind this work involves the interest of the US Air Force in developing improved understanding of the aerodynamics produced by unsteady maneuvering of high performance aircraft. By obtaining vorticity levels within the dynamic stall vortex, existing numerical methods can be verified and perfected for future use. Subsequent development of active forcing techniques could lead to significant improvements in aircraft agility.

II. OBJECTIVES OF THE RESEARCH EFFORT

The primary goal of this research program was to improve understanding of dynamic stall phenomena associated with airfoils undergoing constant pitch rates. This goal was pursued primarily through flow visualization in the Department of Aeronautics water tunnel. A secondary goal of this program was to determine the most advantageous means of actively controlling the dynamic stall vortex development in order to enhance aerodynamic performance.

One goal which was proposed in the original objectives statement was to obtain vorticity measurements within the separated region created by a pitching

airfoil. Because of some difficulties in locating the laser–Doppler–velocimetry (LDV) components required and in obtaining the necessary accessories, the system was only aligned by the end of the project period and had not been verified. It is hoped at this time that additional experiments employing the LDV system in the water tunnel and the Seiler Laboratory's wind tunnel facility could be performed at a later time with the support of the Research Initiation Program grant associated with the USAF–UES Summer Faculty Research Program. A grant application concerning this work and further studies on vortex control has been submitted.

III. APPROACH

1. EXPERIMENTAL PROCEDURES

FLOW VISUALIZATION

All flow visualization experiments were performed in the Department of Aeronautics closed circuit water tunnel at the Air Force Academy. The water tunnel has a 0.38m x 0.51m test section, and all tests were run at a speed of 0.15 m/s, corresponding to a chord Reynolds number of 16,700. A NACA 0015 airfoil with a 10 cm chord and a 30 cm span was pitched at constant rates from 0° to 50°. The nondimensional pitch rate, α^+, ($\alpha^+ = \frac{\dot{\alpha} c}{U_\infty}$, where $\dot{\alpha}$ = actual pitch rates, c = chord length, and U_∞ = free stream velocity) was varied between 0.04 and 0.2. Flow visualization was accomplished by injecting six different color dyes through the airfoil into the upper surface separated region. Locations of the dye ports are shown in Figure 1. A Nikon FE–2 with diffuse lighting was used to obtain 35 mm still shots of the flow containing the dye. In addition, real–time video tape of the flow was used to analyze overall flow motion.

LASER–DOPPLER–VELOCIMETRY

A laser Doppler–velocimetry (LDV) system using backscatter was aligned for future use in the water tunnel. The system used is a TSI two–color LDV which uses the blue (488 nm) and green (514.5 nm) wavelengths of a five watt argon–ion laser beam to obtain velocity profiles, within a given flow. For simplicity, only the blue wavelength was originally used. Beginning with only a one–component system allowed the researchers to become familiar with the LDV process and to more easily

inspect a system which had not been used for several years. The optical assembly was set up in a modular fashion and is shown in Figure 2.

2. RESULTS

LASER–DOPPLER–VELOCIMETRY

A single–component LDV system was aligned for future use in the water tunnel. Although the TSI, Inc. system used had the capability of measuring two components simultaneously, it was decided to establish only a one–component system until the researchers became familiar with the method and until all necessary materials for the two–component system were located. The LDV system used the dual–beam backscatter technique shown in Figure 3. Monochromatic laser light is divided into two parallel beams of equal power, which are focused with a transmitting lens to cross at a predetermined point in the flow, known as the probe volume. Particles passing through the probe volume scatter light back through the transmitting/collecting lens onto a photomultiplier tube. The photomultiplier transmits an output current proportional to the scattered intensity to a given processing system.

The relationship between the intensities received by the photomultiplier and the velocity component of the particle passing through the probe volume is based on the Doppler shift. A simplified interpretation for the dual–beam system used in this case can be obtained from interference fringe pattern analysis. When the two laser beams intersect, they form a constructive and destructive interference pattern which results in a set of parallel fringes contained within the ellipsoidal probe volume as shown in Figure 4. The fringes are perpendicular to the plane of the two beams, and their spacing can be determined from the equation[2]

$$\delta = \frac{\lambda}{2 \sin \frac{\Theta}{2}} \tag{1}$$

where δ = fringe spacing, λ = laser light wavelength, and Θ = included angle between the two beams. Preliminary calculations made on the aligned LDV system show an accuracy of 1.01% between calculated and measured values.[3]

When a particle moves through the probe volume, its scattered light depends on fringe spacing and transit time. The velocity component perpendicular to the fringes is the distance per time,

$$\vec{V} \cdot \vec{n} = \frac{\delta}{\tau} = \left[\frac{\lambda}{2\sin\frac{\Theta}{2}}\right]\frac{1}{\tau} \tag{2}$$

where $\vec{V}$ = particle velocity vector, $\vec{n}$ = unit vector perpendicular to fringes, τ = particle transit time between two fringes. The frequency of the scattered intensity oscillations can then be expressed as,

$$f = \frac{2\sin\frac{\Theta}{2}\,(\vec{V} \cdot \vec{n})}{\lambda} \tag{3}$$

where $f = \frac{1}{\tau}$. This is the same frequency as that obtained from the Doppler principle.[2] Preliminary observations through the photomultiplier eyepiece were made of the laminar flow in the water tunnel. Although the alignment is not completely satisfactory, general indications are that viable measurements will be possible in the near future.

Seiler Research Laboratory and Department of Aeronautics personnel will continue fine–tuning the LDV alignment and will install the electronic equipment necessary for velocity measurements. Current plans are for first testing the system on the laminar flow alone within the water tunnel, and then on a stationary flat plate installed in the water tunnel. A traverse has been ordered to allow accurate measurements over a given volume.

ACTIVE CONTROL METHODS – LITERATURE SURVEY

A preliminary literature survey was conducted to determine possible active forcing methods for dynamic stall vortex control. Considering the available amount of data regarding the behavior and effects of the dynamic stall vortex, a next logical step is to evaluate possible means of modifying the development of the unsteady separation region created by a pitching airfoil and subsequently the vortex itself. Previous research has shown that the maximum lift on a constantly pitched airfoil occurs immediately prior to rapid growth of the dynamic stall vortex.[4] It is thus natural to assume that preventing growth of the vortex might maintain this maximum lift for extended attack angles and thus enlarge the flight envelope for the airfoil. The first step in this process is to identify possible active control methods and determine their potential for use in unsteady flow.

Research has been conducted concerning the active forcing of flows over static airfoils. Zaman, Bar–Sever, and Mangalam[5] and Huang, Maestrello, and

Bryant[6] utilized acoustic methods to modify flows over static airfoils. Zaman, Bar–Sever, and Mangalam excited the flow from beneath the airfoil and were able to eliminate laminar separation and the pre–stall periodic shedding of large–scale vortices at low Reynolds numbers. However, tests showed that tunnel resonance also played a part in flow modification. Since tunnel resonance will not occur in actual flight applications, this matter must be evaluated thoroughly before acoustic forcing is considered as a viable means of flow control. Using a slightly different approach, Huang, Maestrello, and Bryant drastically reduced the separation region by introducing sound through a gap in the leading edge of a symmetric airfoil. Increases in lift and reduction in drag were also evident as a result of the acoustic forcing.

The use of an oscillating flap to modify static flows has also been a focus of past research. Nagib, Reisenthal, and Koga showed that periodic oscillations of a flap placed inside the separated zone behind wedges and rearward facing steps drastically altered the flow.[7] Substantial reductions in reattachment length and thus pressure recovery point occurred in both flows. Katz, Nishri, and Wygnanski found that installing an apex flap on a static airfoil and oscillating it in a two–dimensional. harmonic fashion caused the flow over a stalled airfoil to reattach itself.[8] In a separate study, a vibrating ribbon placed upstream of the anticipated static stall separation point delayed stall, increased the maximum lift of the airfoil, and extended the angle at which the flow remained attached.[9]

Surface roughness is a means of forcing which has received attention, but because of problems with increased drag has not shown significant benefits for use on airfoil performance enhancement.[10] Although in some cases it has been shown to delay stall, it has also increased airfoil drag.[11] Spanwise blowing, on the other hand, has shown promise as a control method. Seginer and Salomon found that spanwise blowing over a 60–degree delta wing increased maximum lift and the lift–curve slope, resulting in a significantly increased usable flight envelope.[12] Nelson, Koga, and Eaton used pulsed blowing and suction to reduce the pressure peak of the vortex generated by a two–dimensional oscillating flap.[13]

These successful attempts to modify static airfoil and dynamic flap flow fields lead to the strong possibility that unsteady dynamic stall flows can also be modified by some means of active forcing. To date, the most successful methods

have been acoustic forcing, spanwise blowing, and oscillatory flap control. Significant problems with tunnel resonance need to be worked out in regards to acoustic forcing, but it is believed that all three of these methods have promise and should be evaluated in dynamic stall flows.

FLOW VISUALIZATION

Dynamic stall vortex characteristics were studied further by injecting dye through a NACA 0015 airfoil pitched at constant rates in a water tunnel. The purpose of this part of the project was not to necessarily obtain new information concerning dynamic stall phenomena, but rather to explore the feasibility of the surface dye injection techniques and determine future possible experiments. In addition, the method of surface injection was evaluated as a mechanism to inject a flow visualization medium within the center of the dynamic stall vortex itself.

A series of photographs for the $\alpha^+ = 0.2$ case is shown in Figure 5. For this case, six different colors were injected through the upper airfoil surface in the following order: red, leading edge; yellow, 1/16c; green, 1/8 c; pink, 1/4c; brown, 1/2c; and blue, trailing edge. In Figure 5a, the separation point can be detected at approximately 3/4 chord with organized trailing edge vortices evident. In this case the red (leading edge) dye remains on the outer edge of the separation region. The pulsating pattern of the red dye is due to a pressure problem and has been corrected. Figures 5b and 5c show the separation point moving towards the leading edge and the trailing edge vortices becoming less organized as the angle of attack increases. In Figure 5d, the separation point has not yet reached the leading edge, but the separated region near the airfoil trailing edge appears very turbulent. In Figure 5e, the separation point has reached the leading edge, causing the separation region to grow in size and turbulence level, as evidenced by the mixing occurring between the colors. Figure 5f shows a great deal of mixing occurring in the leading edge region, which appears divided from the remainder of the separation region. This highly turbulent region can clearly be defined as the so–called dynamic stall vortex in Figures 5g and 5h, and has detached from the airfoil completely in Figure 5i. Close observation of Figure 5g also clearly shows the vortex center is completely covered with dye, which leads to the conclusion that surface smoke or particle

injection would prove a feasible method of entraining a medium within the vortex for velocity studies.

A second series of photographs for the $\alpha^+=0.2$ case is shown in Figure 6. To improve picture clarity, only three dye colors were injected in this case: red, leading edge; green, 1/8c; and blue, trailing edge. In Figure 6a, the separation point can be identified moving upstream along the airfoil surface, shown in color photos by a clear stream of blue dye (trailing edge) moving upstream. This process continues in Figures 6b and 6c, with the separated region near the trailing edge increasing in width. The use of only three colors is beneficial at this point due to the entrainment of only blue dye within the separated region itself and red and green dye (leading edge and 1/8c on the edge of the separation region. Mixing near the trailing edge of Figure 6d indicates an increased turbulence level, and by Figure 6e and subsequently 6f, the entire upper surface of the airfoil has separated. The dark region near the leading edge of the airfoil in Figure 6f also indicates a great deal of mixing between the leading edge and 1/8c dyes. In effect, very little of the red dye and virtually none of the green dye can be discerned near the trailing edge of the airfoil. In Figure 6g, this "highly mixed" region has clearly become the dynamic stall vortex. A concentration of green dye (1/8c) near the leading edge indicates a region of low velocities. In Figure 6h, the dynamic stall vortex has grown to cover approximately 2/3c, and by Figure 6i has detached from the airfoil surface. The high concentrations of green dye in the last two photographs indicate a region of low velocities that is progressing slowly towards the airfoil trailing edge.

The process of injecting dye through the airfoil surface has shown great promise for future use in studying dynamic stall phenomena. Although numerous experiments involving smoke visualization have yielded viable data, the use of multiple colors offers yet one more avenue for information. By injecting different colors from varied locations along the airfoil, a greater understanding of the mechanisms leading to separation and subsequent dynamic stall can be obtained. Coordinating such flow visualization with future LDV measurements should also prove enlightening.

3. CONCLUSIONS

The following conclusions were obtained from this study of dynamic stall phenomena and possible future experimental techniques:

1. The Frank J. Seiler Research Laboratory's laser–Doppler–velocimetry system will be a viable tool in obtaining future water tunnel velocity measurements.
2. A flow visualization medium can be entrained within the entire dynamic stall vortex if injected through the surface of the airfoil. This will prove useful for future laser–Doppler–anemometry and image analysis studies in wind tunnels.
3. The use of varied colors injected through different airfoil surface locations help discern the mechanisms which lead to dynamic stall.
4. A preliminary literature review has determined that acoustic forcing, spanwise blowing, and an external oscillatory flap hold the most promise for application to dynamic stall active control.

IV RECOMMENDATIONS

This study has shown important insights into three areas related to the study of dynamic stall phenomena. Specific recommendations in regards to each of these areas are as follows:

1. LASER–DOPPLER–VELOCIMETRY (LDV)

Initial results have shown that the Frank J. Seiler Research Laboratory's LDV system is operational. Current plans are to verify it first in the laminar flow alone within the water tunnel and then on a stationary flat plate installed in the water tunnel. It is recommended that once the system has been completely verified, velocity measurements be taken first in the separated region of a static airfoil and then int he separation region and dynamic stall vortex of a pitching airfoil. This will offer not only valuable information on the unsteady flow fields, but will also assist in developing a similar laser–Doppler–anemometry system for wind tunnel studies.

2. ACTIVE CONTROL METHODS – LITERATURE SURVEY

A preliminary literature review has determined that acoustic forcing, spanwise blowing, and external oscillatory flaps afford the best possibilities for dynamic stall vortex control. It is recommended that the literature study be

continued to investigate any possible drawbacks for control methods. Experiments need to be designed for constantly pitching airfoils in the wind tunnel to determine the optimum means of control, the optimum frequencies at which to force the flow, and the extent to which dynamic stall flows can be beneficially modified.

3. FLOW VISUALIZATION

The process of injecting dye through a NACA 0015 airfoil pitched at constant rates in a water tunnel proved a viable means of entraining a flow visualization medium into the center of the dynamic stall vortex. It is recommended not only to continue studies using varied colors in the water tunnel, but also to apply the procedure to wind tunnel experiments. This method can be used to inject smoke or particles within the vortex for possible image analysis or laser–Doppler–anemometry measurements. In addition, it should be possible to utilize fluorescing media in conjunction with a laser light sheet as an alternate flow visualization method.

REFERENCES

1. Albertson, Julie, Flow Visualization Techniques for Controlled Separated Flows, Master's Thesis, Washington State University, Pullman WA, 1987.
2. Durst, Melling and Whitelaw, Principles and Practice of Laser–Dopler–Anemometry, London England, Academic Press, Inc., 1976.
3. Private communication with Dr B. Terry Beck.
4. Albertson, J., Troutt, T., and Kedzie, C., "Unsteady Aerodynamic Forces at Low Airfoil Pitching Rates," AIAA Paper 88–2579, June 1988.
5. Aaman, K.B.M.Q., Bar–Sever, A., and Mangalam, S., "Effects of Acoustic Excitation on the Flow Over a Low–Re Airfoil," J. Fluid Mech., Vol. 182, 1987, pp 127–148.
6. Huang, L., Maestrello, T., and Bryant, T., "Separation Control Over an Airfoil at High Angles of Attack by Sound Emanating From the Surface," AIAA Paper 87–1261, June 1987.
7. Nagib, H., Reisenthel, P., and Koga, D., "On the Dynamical Scaling of Forced Unsteady Separated Flows," AIAA Paper 85–0553, March 1985.
8. Katz, Y., Nishri, B., and Wygnanski, I., "The Delay of Turbulent Boundary Layer Separation by Oscillatory Active Control," AIAA Paper 89–0975, March 1989.
9. Neuburger, D., and Wygnanski, I., "The Use of a Vibrating Ribbon to Delay Separation on Two–Dimensional Airfoils: Some Preliminary Observations," Workshop II on Unsteady Separated Flow, FJSRL–TR–88–0004, Sep 1988.
10. Collins, F., "Boundary–Layer Control on Wings Using Sound and Leading Edge Serrations," AIAA J., Vol. 19, No. 2, Feb 1981, pp 129–130.
11. Mueller, T., and Butill, S., "Experimental Studies of Separation on a Two–Dimensional Airfoil at Low Reynolds Numbers," AIAA J., Vol. 20, No. 4, April 1982, pp 457–463.
12. Seginer, A., and Salomon, M., "Performance Augmentation of a 60–Degree Delta Aircraft Configuration by Spanwise Blowing," J. Aircraft, Vol. 23, No. 11, Nov 1986, pp 801–807.
13. Nelson, C., Koga, D., and Eaton, J., "Control of the Unsteady Separated Flow Behind an Oscillating, Two–Dimensional Flap," AIAA Paper 89–1027, March 1989.

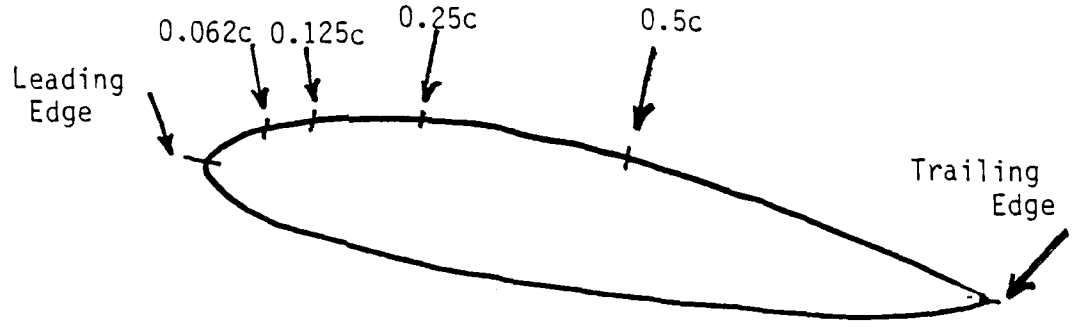

Figure 1. Dye Port Locations.

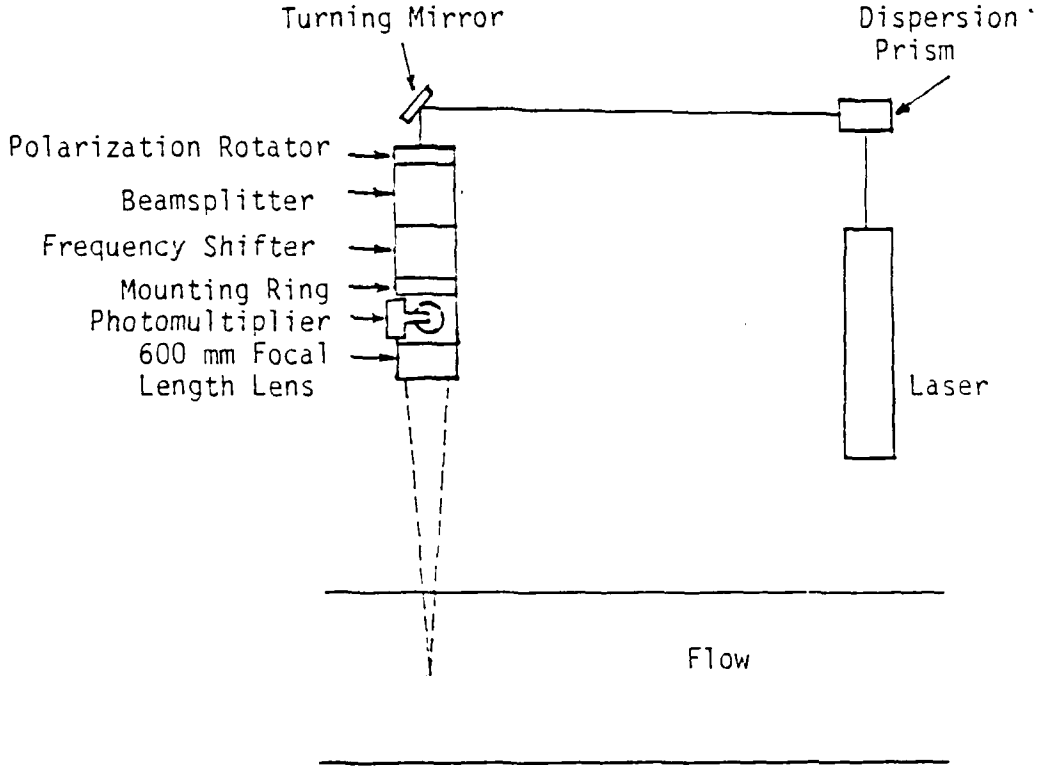

Figure 2. LDV Optical Schematic

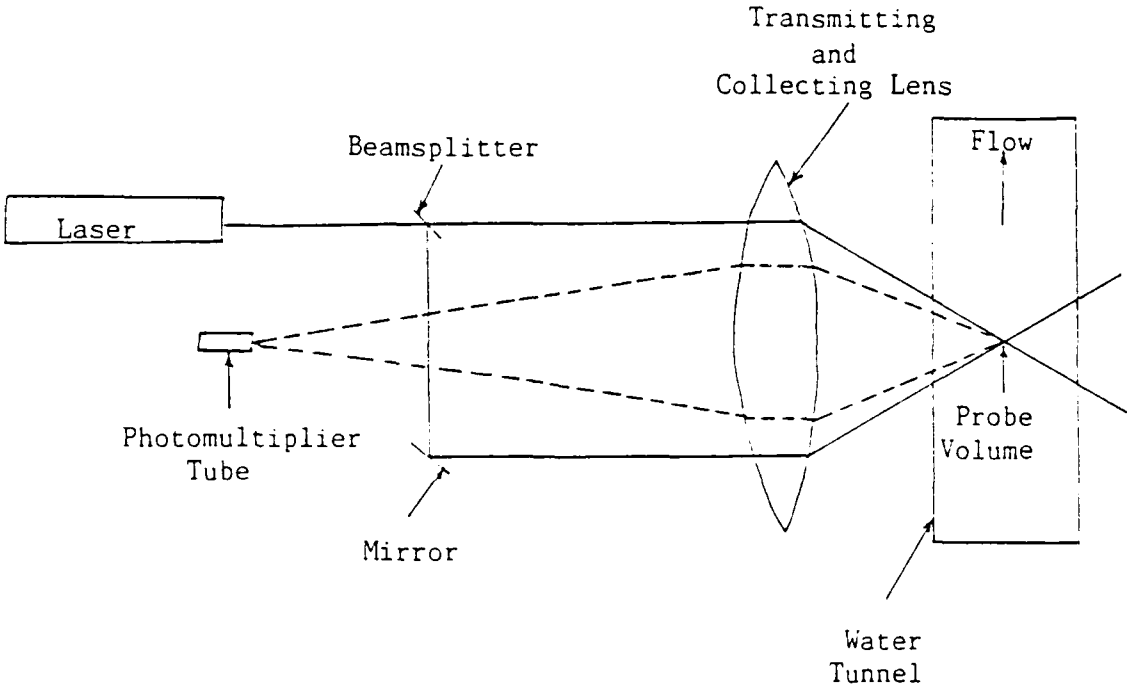

Figure 3. Principles of Laser-Doppler-Velocimetry System

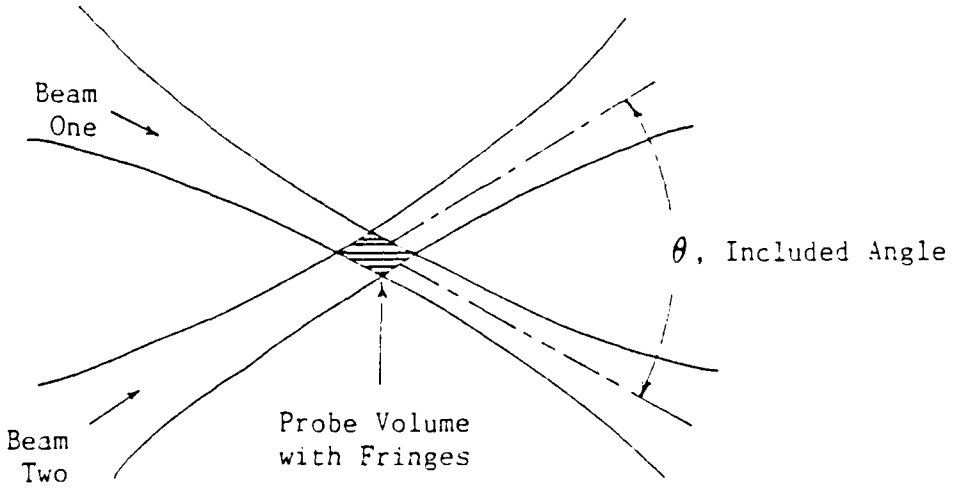

Figure 4. Fringe Pattern

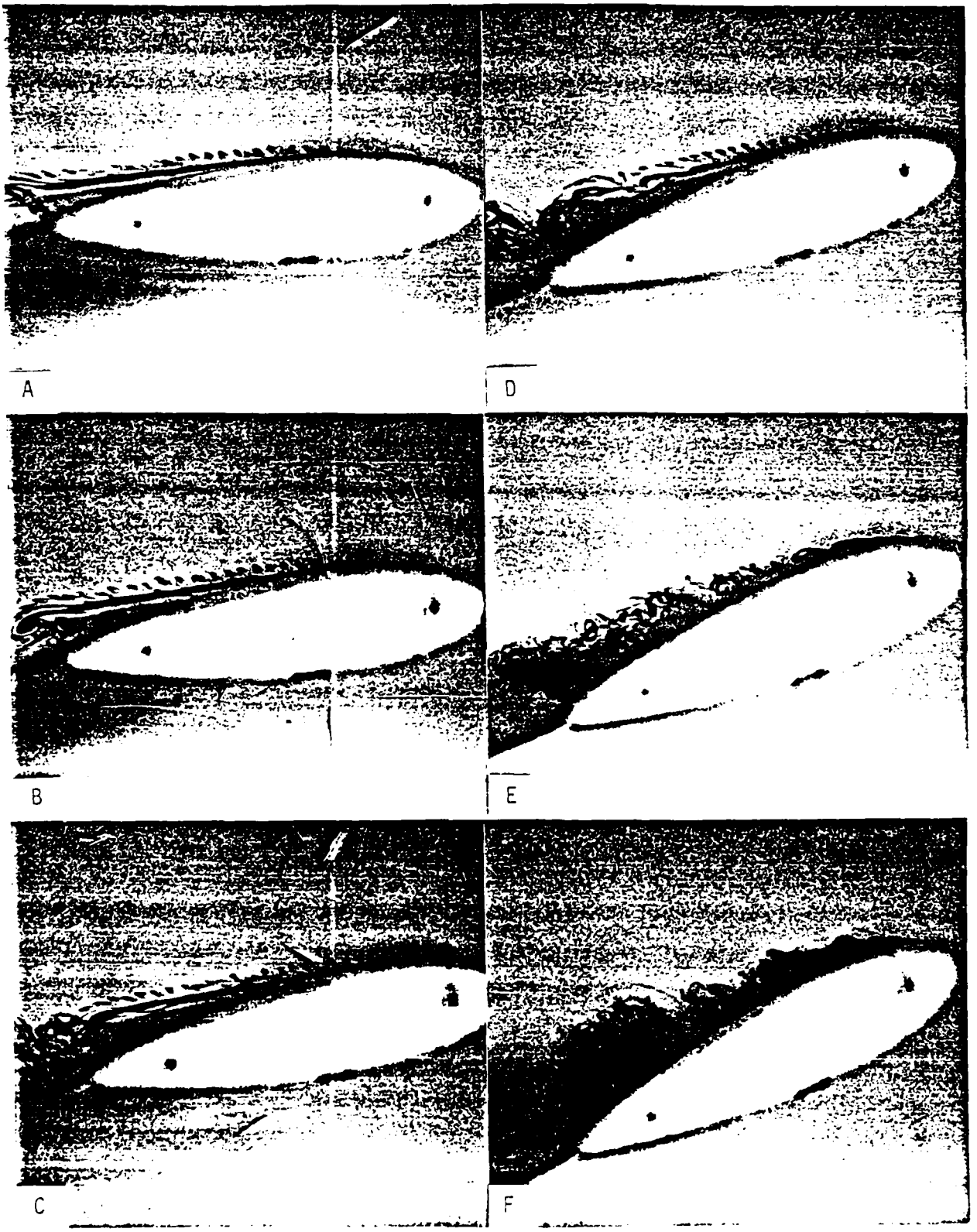
A
D
B
E
C
F

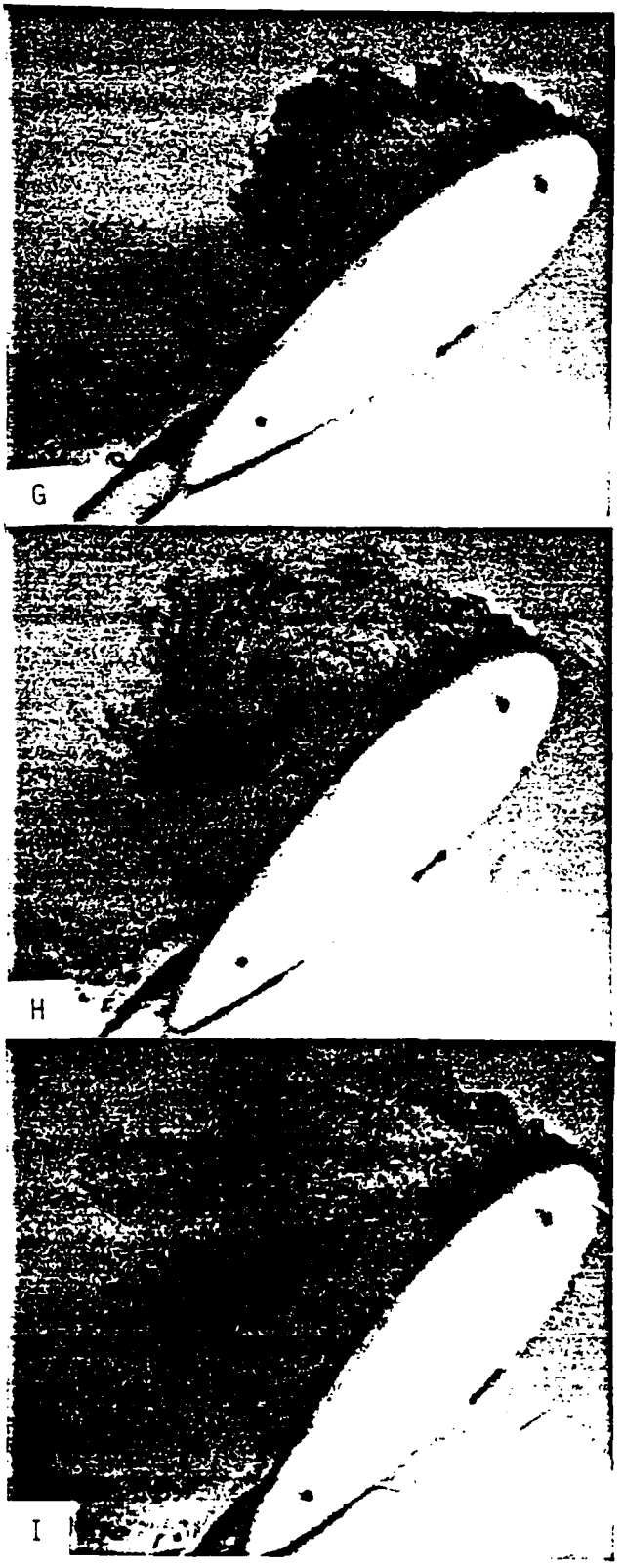

Figure 5. $\alpha^+ = 0.20$, Six Color - Flow Visualization

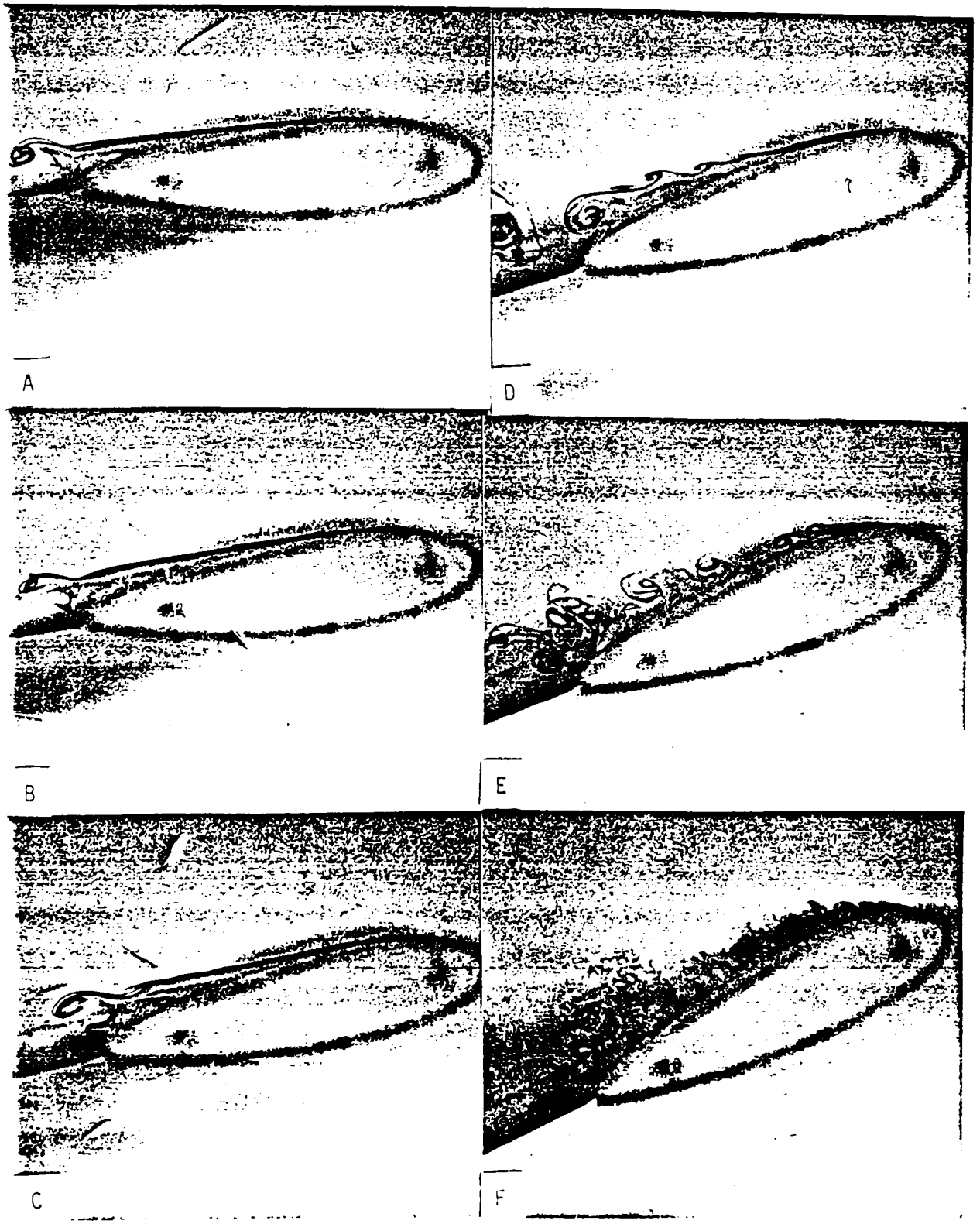
A
D
B
E
C
F

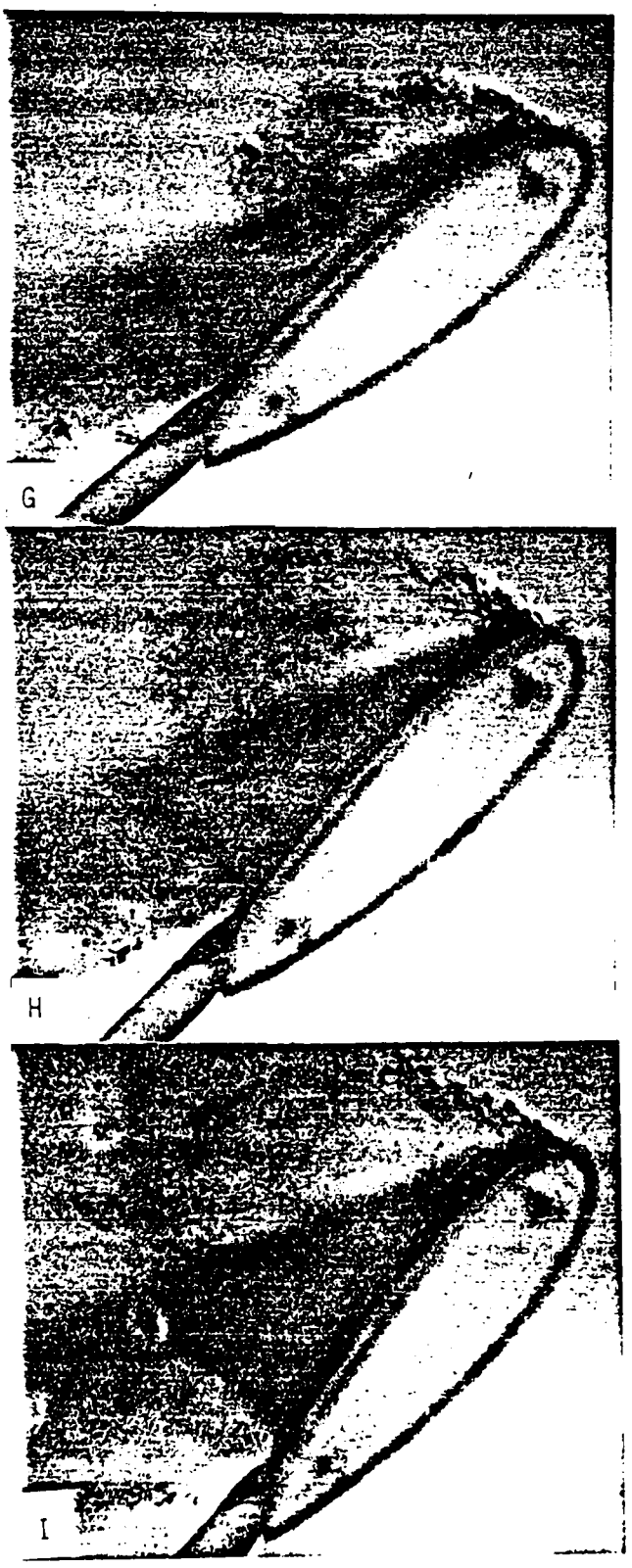

Figure 6. α^+ = 0.20, Three Color - Flow Visualization

1989 USAF-UES SUMMER FACULTY RESEARCH PROGRAM

GRADUATE STUDENT RESEARCH PROGRAM

Sponsored by the

AIR FORCE OFFICE OF SCIENTIFIC RESEARCH

Conducted by the

Universal Energy Systems, Inc.

FINAL REPORT

MODELING OF A STRUCTURE-ACTUATOR SYSTEM WITH STRUCTURE-BORNE REACTION-MASS ACTUATORS AND OPTIMAL DESIGN OF PASSIVE VIBRATION ABSORBERS

Prepared by:	Hung V. Vu, PhD, Assistant Professor
	Hao Q. Pham, Graduate Student
Department and	Mechanical Engineering
University:	California State University, Long Beach CA 90840
Research Location:	Frank J. Seiler Research Laboratory
	United States Air Force Academy CO 80840-6528
USAF Researchers:	Major John P. Duke
	Dr William L. Hallauer, Jr.
	Captain Jeff Turcotte
	Captain Steven G. Webb

Date:	15 August 1989
Contract No.:	F49620-88-C-0053

Modeling of a Structure-Actuator System with Structure-Borne Reaction-Mass Actuators and Optimal Design of Passive Vibration Absorbers

Prof. Hung Vu and Hao Pham, Graduate student

ABSTRACT

A structure–control system, which possesses dynamic characteristics of large space structure (LSS), was built. The system consists of a beam structure whose first two natural frequencies in bending and torsional modes are low (near 5 Hz) and two structure–borne reaction mass actuators (RMA). The system is modeled and analyzed using finite–element method (FEM) and NASTRAN. Optimal design of passive vibration absorber (PVA) is developed with the aid of $MATRIX_x$. The optimal PVA is designed by applying, with appropriate modifications, the classical formulas of optimal tuning and damping[1,2,3] with the absorber tuned to the lowest structure resonance.

I. INTRODUCTION:

Control of structural vibrations is essential in designing large space structures (LSS). In this area of research, structure–actuator interactions are actively pursued. When an actuator is attached to a structure, the dynamics of the system is a combination of both dynamics of structure and actuator because the actuator has its own dynamics. Many different types of actuators have been investigated in the literature, but only structure–borne reaction–mass actuators are considered in this work.

Passive vibration absorbers, which are actuators in the passive mode, can be used to reduce vibrations effectively if these devices are designed properly. The optimal design of an absorber attached to a single–DOF structure is a well known result.[1,2,3] However, designing one passive absorber that will, in some sense, optimally damp the vibrations of a multi–DOF system has not been adequately developed.

The first author has been teaching and conducting research in both areas of structural dynamics and controls, and the second author is currently working on his master's degree. His thesis is in the area of passive and active vibration controls and structure–actuator interactions.

II. OBJECTIVES OF THE RESEARCH EFFORT:

Our assignment as participants in the 1989 Summer Research Program for Faculty and Graduate Students was to model the structure–absorber system which was built at the Frank J. Seiler Research Laboratory at the United States Air Force Academy and to design an optimal passive vibration absorber for the system.

III. APPROACH:

Finite–element model of the structure assembly under consideration is first obtained then reduced–order model is used for designing an optimal passive vibration absorber (PVA).

The following are the primary software used to aid in the analysis and design: (a) MSC/NASTRAN for structure dynamics and (b) $MATRIX_x$ for system dynamics.

IV.

A. FINITE ELEMENT MODELING:

The purposed structural system places numerous constraints on the design, which should be simple and have the same characteristics as a LSS such as coupled flexural–torsional structural modes, low frequencies, and light damping. The first two resonances of the system can be closely spaced or well separated, and they must be isolated to higher frequencies.

A test structural system was built to meet the above requirements. The system consists of a structure and two horizontally movable reaction mass actuators (RMAs) shown in Fig. 1. The reaction mass is the movable part of the RMA and it can be free or locked (Fig. 2). The RAM can be moved in or out in the x direction to couple or decouple the first two natural frequencies. Due to the limitation of the operating range of the RMAs, the lowest natural frequency of the structure must be above 1 hz.

The finite element model of the system is obtained using MSC/NASTRAN. Ten grid points are specified and nine flexible "bar elements" are used for the structure (Fig. 3). The structure is clamped to the ceiling so the model has $6(10–2) = 48$ degrees of freedom. The two RMAs with the reaction masses locked are modeled as two rigid bars connected to the horizontal beam of the structure (Fig. 3). The two rigid bars do not add any DOF to the structure.

The natural frequencies of the system, with the reaction masses locked, are determined analytically and experimentally, and the comparison is shown in Table 1.

We also need to model the structural system when the reaction masses are free. The properties of the RMA are given by (1). The predicted and measured natural frequencies of the system, with the free reaction masses, are obtained, then compared in Table 2. The predicted values are expected to be lower than the measured values. When the reaction mass is free to move, it acts as a mass absorber connected to the system by a spring and damper. This spring is considered as a "very soft" spring and is neglected in the model. Therefore, the model is "less stiff" and has low predicted natural frequencies. If the values of this mass and spring can be found and included in the model, the predicted natural frequencies of the system will increase and have a better agreement with the measured natural frequencies.

$$\begin{bmatrix} m & & & & & \\ & m & & & & \\ & & m-m_R & & & \\ & & & I_{xx} & I_{xy} & I_{xz} \\ & & & & I_{yy} & I_{yz} \\ & Sym & & & & I_{zz} \end{bmatrix} \qquad (1)$$

where m = mass of RMA

m_R = mass of the reaction mass

I_{ij} = mass moments of inertia of RMA

The high-order finite element model is unnecessarily large for designing an optimal passive vibration absorber so it is reduced to a low-order model. An exact reduced-order model technique[6] is used to reduce the structure model from 48 DOF to 4 DOF (Fig. 4) such that the accuracy of the natural frequencies and mode shapes are

preserved. The reduced–order mass and stiffness matrices are given by

$$\underline{m} = (\Phi_R^r)^{-1}\,\Phi_R^{-1} \tag{2}$$

$$\underline{k} = (\Phi_R^T)^{-1}\,[\ \omega_R^2\ ]\,\Phi_R^{-1} \tag{3}$$

where Φ_R and ω_R^2 are the reduced–order modal matrix and eigenvalues, respectively.

B. OPTIMAL DESIGN OF A PASSIVE VIBRATION ABSORBER

For a structure with well separated resonances, if the primary concern is suppressing a local resonance, the absorber must be tuned to the resonance under consideration. But if the global structure resonances must be suppressed the absorber should be tuned to the lowest structural mode, since the absorber is not only effective in suppressing the resonance to which it is tuned but it also damps out the resonances at higher frequencies.[4]

A passive vibration control system of a simple two–DOF structure and an absorber is considered in Ref. 5 where the absorber is tuned to the lowest structural mode and the damping is adjusted to obtain an optimal result in some sense. But, neither a simple set of formulas nor a procedure for obtaining optimal tuning and damping is provided.

1) PROBLEM STATEMENT: It is desirable to develop a method for finding the optimal tuning and damping for a vibration absorber to be used on a multi–DOF structure. Hence, this paper extends the design of an optimal absorber for a single–DOF structure to that of a multi–DOF structure. Specifically, the following questions will be addressed: (a) What are the formulas for optimal tuning and damping? and (b) What happens when the structure resonances are relatively closely spaced?

2) BACKGROUND: SINGLE–DOF STRUCTURES

The optimal design of a vibration absorber attached to a single–DOF structure (Fig. 5) is given by the following formulas:[4]

$$f_{opt} = \frac{1}{1+\mu} \quad \text{optimal tuning} \tag{4}$$

$$\zeta_{opt} = \left[\frac{3\mu}{8(1+\mu)^3}\right]^{1/2} \quad \text{optimal damping} \tag{5}$$

where

$$\mu = \frac{m}{M} \quad \text{absorber/structure mass ratio} \tag{6}$$

$$f = \frac{\omega_a}{\omega_n} = \frac{\sqrt{k/m}}{\sqrt{K/M}} \quad \text{absorber/structure natural frequency ratio} \tag{7}$$

$$\zeta = \frac{c}{2m\omega_n} \quad \text{damping ratio} \tag{8}$$

It will be seen in the following that these formulas can be applied to the design of optimal tuning and damping of an absorber for use on multi–DOF structures if proper modifications are taken.

3) MULTI–DOF STRUCTURES

The procedure of designing an optimal absorber, which is attached to a multi–DOF structure, involves two steps:

a) "Coarse tuning" or sub–optimal solution

b) "Fine tuning" or optimal solution

COARSE TUNING:

If the absorber is tuned to the first structure resonance, the sub–optimal tuning and damping are given by modifications of Eqs. (4,5)

$$f_{subopt} = \frac{1}{1+\mu} \quad \text{sub–optimal tuning} \tag{9}$$

$$\zeta_{subopt} = \left[\frac{3\mu}{8(1+\mu)^3}\right]^{1/2} \quad \text{sub–optimal damping} \tag{10}$$

where the parameters are redefined as follows

$$\mu = \frac{m}{M_1} \quad \text{absorber mass/1st structure modal mass ratio} \tag{11}$$

$$f = \frac{\omega_a}{\omega_1} = \frac{\sqrt{k/m}}{\omega_1} \quad \text{absorber/1st structure natural frequency ratio} \tag{12}$$

$$\zeta = \frac{c}{2m\omega_1} \quad \text{damping ratio} \tag{13}$$

Note that the modal mass must be normalized in a special way such that the component of the structure eigenvector, which corresponds to the DOF of the structure where the absorber is attached, must be unity.

After coarse tuning, if further improvement in the frequency response results is desired, then fine tuning may be used.

FINE TUNING:

With fine tuning, the optimal design of the vibration absorber for a multi-DOF structure is, finally, given by

$$f_{opt} = k_f \frac{1}{1+\mu} \quad \text{optimal tuning} \tag{14}$$

$$\zeta_{opt} = k_\zeta \left[\frac{3\mu}{8(1+\mu)^3}\right]^{1/2} \quad \text{optimal damping} \tag{15}$$

where k_f and k_ζ are correction factors which may be obtained by trial-and-error using computer simulation. Note that if these correction factors turn out to be close to unity, then fine tuning is really unnecessary for global optimum.

4) CASE STUDY:

Consider an experimental set-up (Fig. 1) which is under development for studying the structure-control interaction technology of large space structures (LSS) at the Frank J. Seiler Research Laboratory at the United States Air Force Academy (USAFA). Fig. 6 is a simplified model of the experimental structure with only one reaction-mass actuator in the set-up.

The actuator in the "passive mode" is a passive vibration absorber. The structure-absorber system is first modeled with a 49-DOF finite element representation, and then is reduced to 5-DOF model (Fig. 6) using a model reduction technique[6] for analysis and design of an optimal vibration absorber. NASTRAN and MATRIX$_x$ are used for these studies. The first two structure resonances, which are relatively closely spaced, are determined both analytically and experimentally.

The frequency response plots of this system are shown in Fig. 7 (with coarse tuning) and Fig. 8 (with fine tuning, $k_f = .85$, $k_\zeta = 2$). It is a remarkable result that all the system resonances are significantly reduced with this optimal solution (Fig. 9).

V. RECOMMENDATIONS:

As a suggestion for the follow–on basic research, consider a fundamental structure control system of a cantilever beam and a reaction mass actuator. The following topics are proposed to be investigated.

- a better model of the structure–actuator system
- stability, sensitivity, and performance of active vibration control
- robust control

Note that the method presented in this report should be utilized just to obtain optimal parameters for passive vibration absorbers, which is the actuator in the system. Then, other aspects of control studies should be followed. After having a better understanding of this proposed fundamental system, the results can then be applied to the complex structure control systems.

ACKNOWLEDGEMENTS

We wish to express our appreciation to the Air Force Office of Scientific Research and Universal Energy Systems, Inc., for sponsoring and administrating this research program, respectively.

We also greatly appreciate the people who provided us with support and a friendly working environment. In this regard, special thanks are due to Dr William Hallauer, Lt Col William G. Thorpe, Major Robert F. Reilman, Jr., Major John P. Duke, Captain Jeff Turcotte, Captain Steven G. Webb, Mr James Smith, Ms Leah Kelly, and SSgt Angela Berry. We thank, again, Captain Turcotte for his constructive comments.

REFERENCES

1. Den Hartog, J.P., Mechanical Vibrations. New York: McGraw–Hill Book Co., 1956.
2. Ormondroyd, J. and J.P. Den Hartog, "The Theory of the Dynamic Vibration Absorber," Trans. ASME, 50, A9, 1928.
3. Brock, J.E., "A Note on the Damped Vibration Absorber," Journal of Applied Mechanics, 13(4), A–284, 1946.
4. Snowdon, J.C., Vibration and Shock in Damped Mechanical Systems. New York: John Wiley & Sons, Inc., 1968.
5. Miller, D.W., and E.F. Crawley, "Theoretical and Experimental Investigation of Space–Realizable Inertial Actuation for Passive and Active Structural Control," Journal of Guidance, Vol. 11, No. 5, Sep–Oct 1988, pp. 449–458.
6. Hallauer, W. and S. Lamberson, "Experimental Active Vibration Damping of a Plane Truss Using Hybrid Actuation," 30th AIAA/ASME/ASCE/AHS/ASC Structures, Structural Dynamics and Material Conference, Mobile AL, 3–5 Apr 89.

TABLE 1
Comparison between predicted and measured natural frequencies
when the reaction masses are locked

Natural Frequencies	Predicted, Hz	Measured, Hz	% Error
f_1	4.19	4.24	−1.19
f_2	5.09	5.04	+0.98

TABLE 2
Comparison between predicted and measured natural frequencies
when the reaction masses are free

Natural Frequencies	Predicted, Hz	Measured, Hz	% Error
f_1	3.59	3.94	−9.75
f_2	7.10	7.23	−1.83

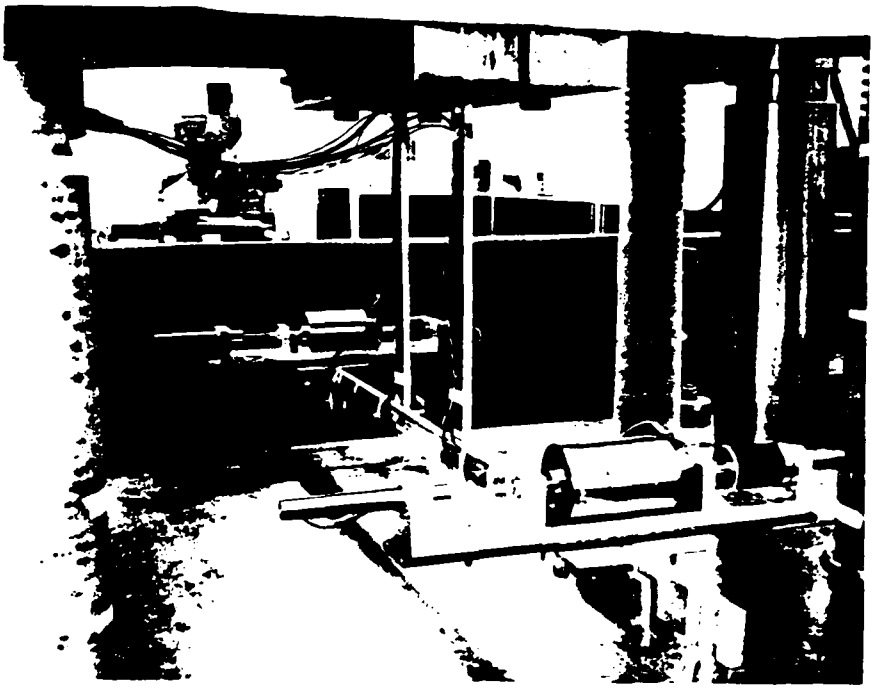

(a)

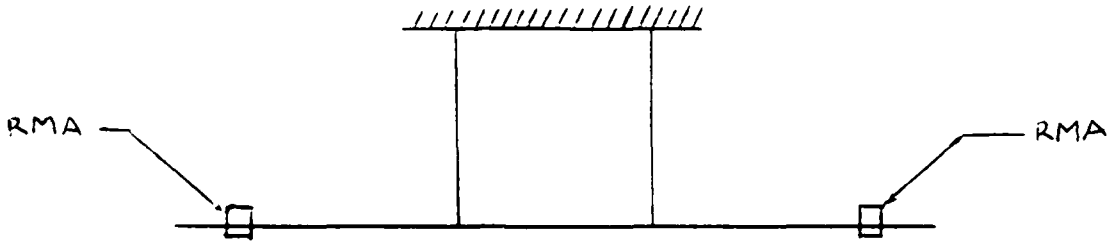

(b)

Figure 1. The system of a structure and two identical reaction-mass actuators (RMAs)
(a) Photograph
(b) Schematic

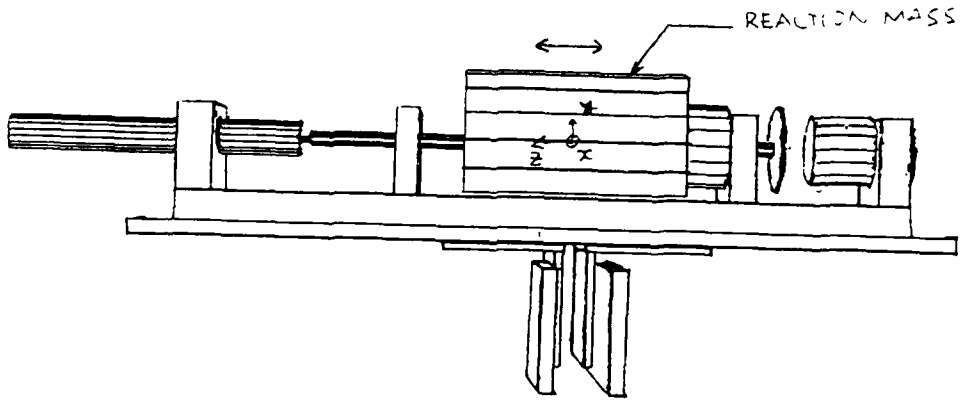

Figure 2. Reaction mass actuator (RMA)

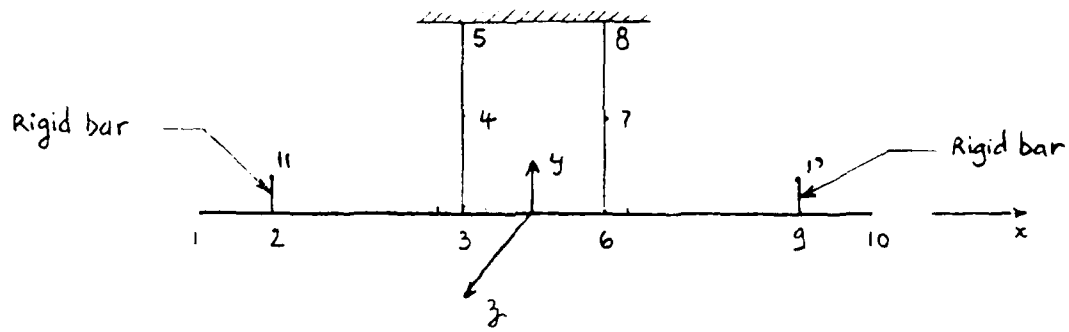

Figure 3. Finite element model

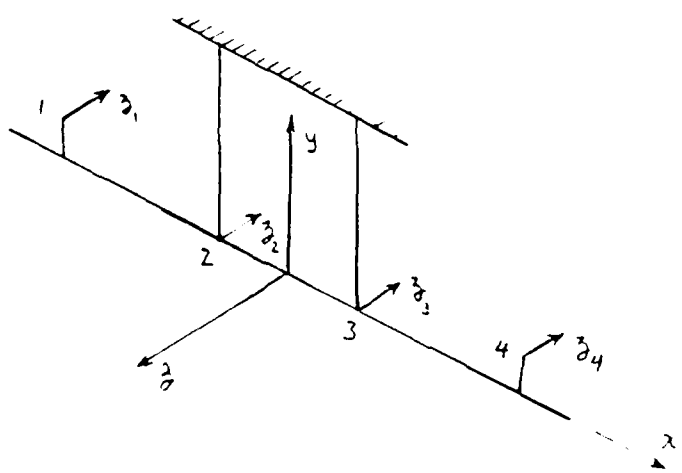

Figure 4. Reduced-order model

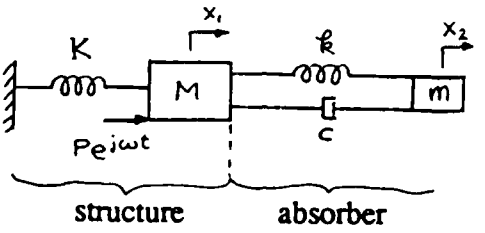

Figure 5. A single-DOF structure and an absorber

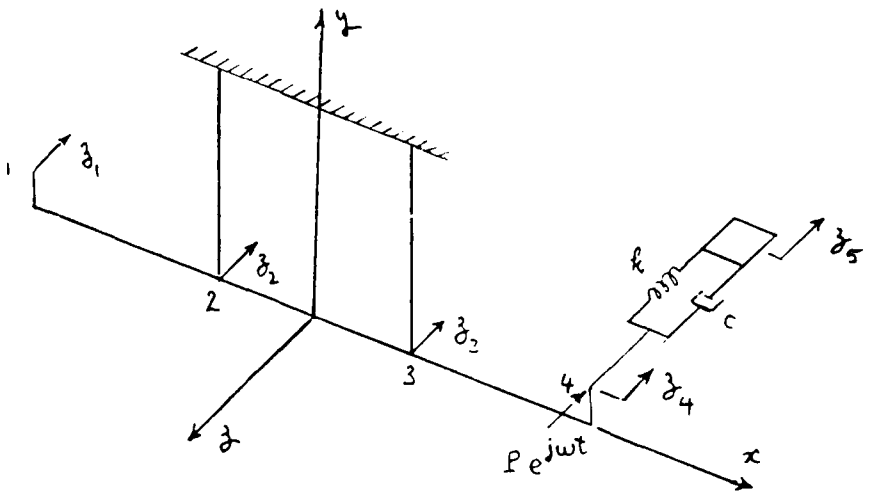

Figure 6. A simple model of the set-up with one reaction-mass actuator

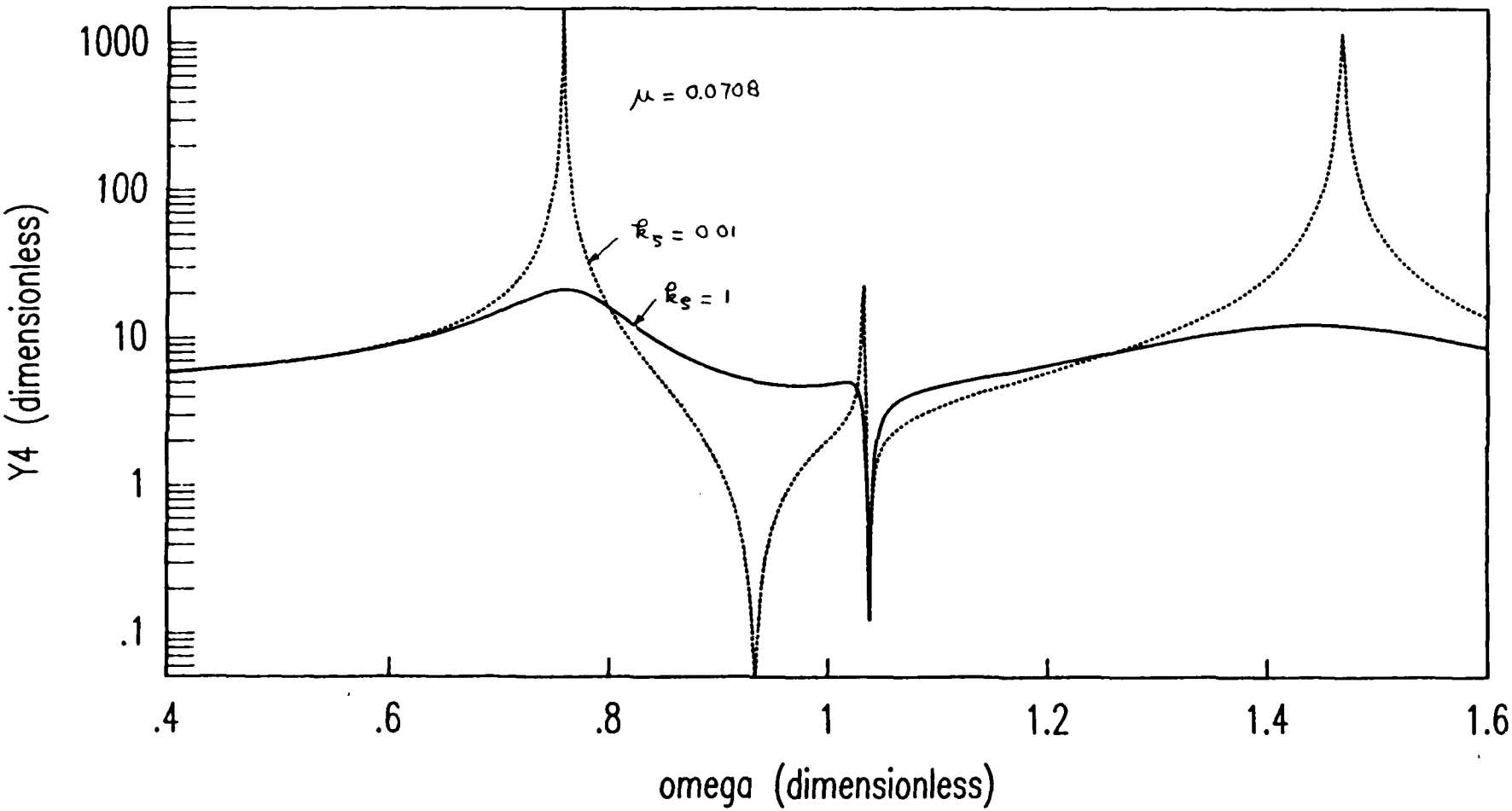

Fig. 7. System with coarse tuning.

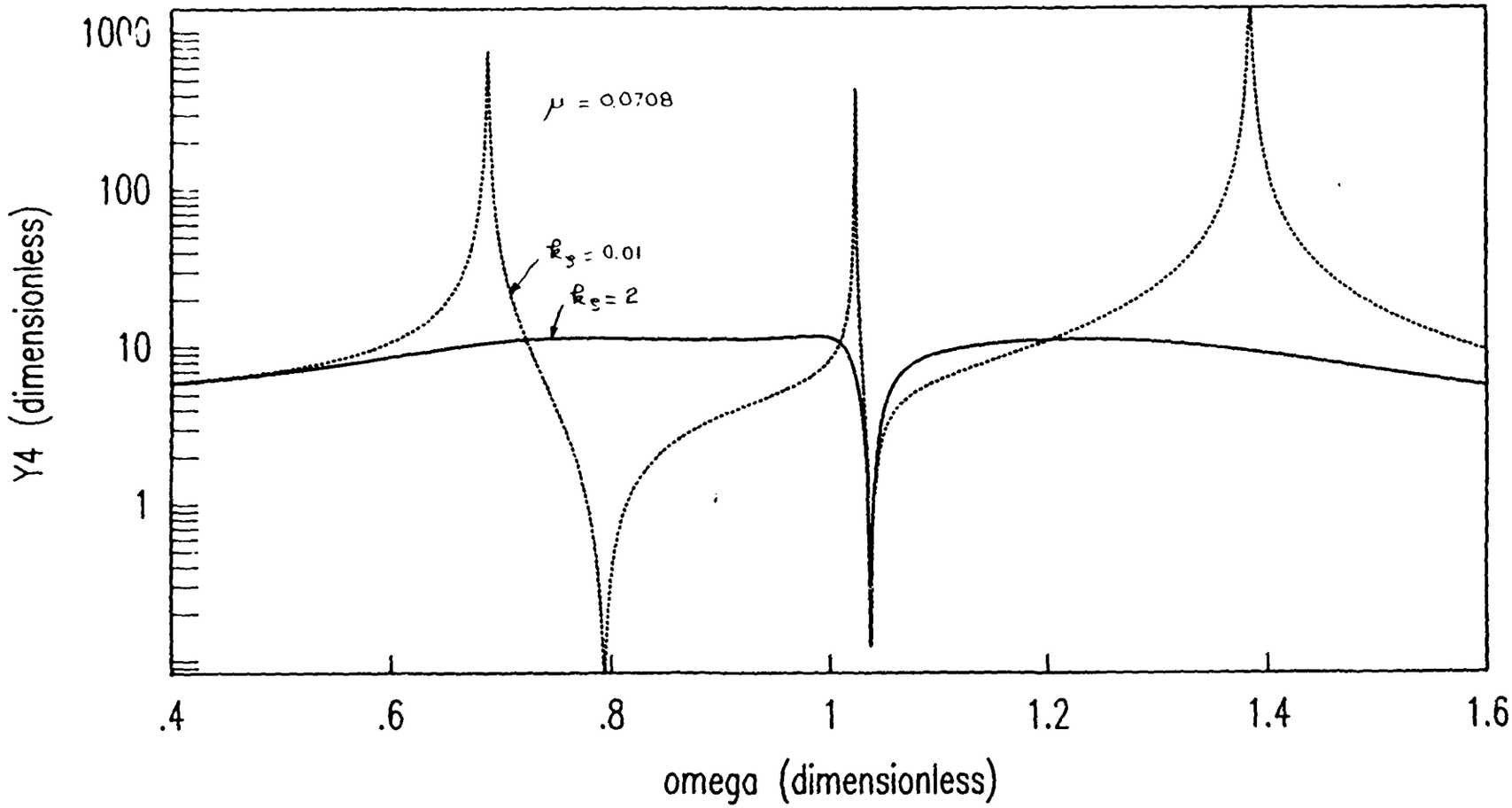

Fig. 8. System with fine tuning, $k_f = .85$, $k_s = 2$.

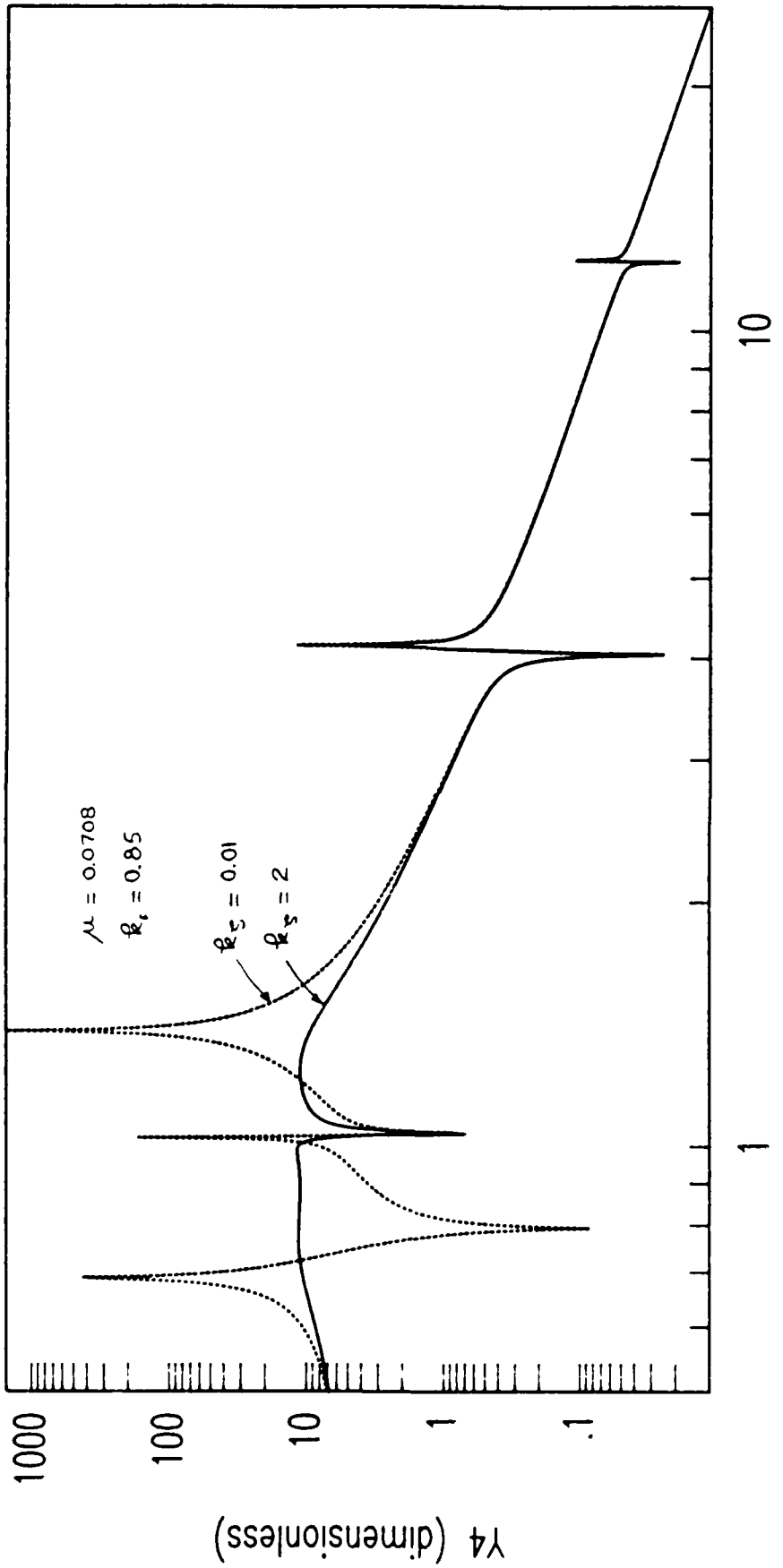

Fig. 9. System with fine tuning and all resonances.

```
id simple, MODES
sol 3
Time 30
cend
echo=unsort
Title= JFSRL finite element model
spc=1
disp=all
METHOD=10
subcase 1
MODES=5
begin bulk
baror                                                                   1.0
spc1            1  123456        6        9
pbar            1         1  0.5774  7.06-3  0.1093  0.0237
rbar            2         2       3  123456
rbar           20        10      11  123456
mat1            1  10.0+6  3.80+6            0.098
param      wtmass .002588
param      grdpnt       0
param    coupmass       1
param      newseq      -1

param     autospc     yes
param      spcgen       1
eigr            10     inv      3.     100.       5
              mass
conm2           10       4              0.100
conm2           11       7              0.100
conm2           12       2              9.803     0.0  1.4913 -0.1418
         102.274     0.0   93.586       0.0  -0.769  19.265
conm2           13      10              5.898     0.0  0.8496 -0.1053
          89.321     0.0   87.320       0.0  -0.699  10.221
conm2           14      11              3.905     0.0     0.0      0.
          5.8442     0.0   5.8442       0.0     0.0   3.016
$cmass2         77 -3.9050       11         3
$cmass2         78  3.9050       13         3
$celas2         99   8.406       11         3       13        3
grid            1           -25.0
grid            2           -18.0
grid            3           -18.0     2.50
grid            4            -4.0
grid            5            -4.0      7.5
grid            6            -4.0     15.0
grid            7             4.0

grid            8             4.0      7.5
grid            9             4.0     15.0
grid           10            18.0
grid           11            18.0     2.50
grid           12            25.0
$grid          13            18.0     2.50     1.00
cbar            1        1        1        2
cbar            3        1        2        4
cbar            4        1        4        5
cbar            5        1        5        6
cbar            6        1        4        7
cbar            7        1        7        8
cbar            8        1        8        9
cbar            9        1        7       10
cbar           21        1       10       12
enddata
```

1989 USAF-UES SUMMER FACULTY RESEARCH PROGRAM/

GRADUATE STUDENT RESEARCH PROGRAM

Sponsored by the

AIR FORCE OFFICE OF SCIENTIFIC RESEARCH

Conducted by the

Universal Energy Systems, Inc.

FINAL REPORT

Impulse Approximation Formalism for Atom Molecule Collisions: Exact Theory and Limitations

Prepared by:	Pradip Bakshi, Ph.D.
Academic Rank:	Professor
Department and University:	Physics Department, Boston College
Research Location:	AFGL/OPB Hanscom AFB Bedford, MA 01730
USAF Researcher:	Ramesh Sharma, Ph.D.
Date:	20 September 1989
Contract No.:	F49620-88-C-0053

Impulse Approximation Formalism for Atom Molecule Collisions: Exact Theory and Limitations

by

Pradip M. Bakshi

ABSTRACT

An exact formulation of the Impulse Approach (IA) to atom-diatomic molecule collisions has been developed. Inadequacy of the Peaking Approximation, especially for high energy loss or small angle scattering has been established. Validity of IA has been investigated through general principles such as time reversal invariance and semi-detailed balancing. While these symmetry requirements are satisfied for large scattering angles, substantial violations occur for smaller angles, lower energies and lower projectile masses. The neglect in IA of multiple collision terms may be responsible for these departures from symmetry requirements. Various extensions and suggestions for further work are discussed.

ACKNOWLEDGEMENTS

I wish to thank the Air Force Office of Scientific Research for sponsorship of this research. Universal Energy Systems, Inc. has been very helpful in all administrative matters of this program.

This has been a very rewarding and productive summer. I am much indebted to Dr. Ramesh Sharma at AFGL for providing a very hospitable and stimulating environment, and for his active participation in this program. I also wish to thank Joe Sindoni for his help in the substantial numerical computations of this program.

I. INTRODUCTION:

Quantum mechanical Impulse Approximation(IA) has been employed in the literature [Bogan(1974); Eckelt, Korsch and Philipp (1974); Beard and Micha (1981)] to study the collisions between fast atomic projectiles and target diatomic molecules. The central idea of IA is to treat the three body (atom-diatomic molecule) process as a pair of two-body (atom-atom) collisions with the third atom remaining a spectator. It was recently suggested by Sharma (1988) at AFGL that IA may also be relevant for collisions of low energy particles with target molecules having large internal energy. Such an extension of the formalism may eventually prove helpful in explaining the R-branch band-heads observed in vibration-rotation band emission from high-altitude atmospheric and flow tube laboratory experiments, which are of interest at AFGL.

An effort along these lines was initiated during the last summer program and continued through the academic year. A general formalism for IA was developed to obtain the state to state differential cross sections, (Sharma, Bakshi and Sindoni, 1989a). Specific results for excitation from the ground state were compared with the corresponding Peaking Approximation results, and this demonstrated the gross inadequacy of the latter approach for small angle scattering. Considerable further work, however, remained to be done. The past success of this program and its momentum were relevant in its continuation through the present summer program.

II. OBJECTIVES OF THE RESEARCH EFFORT:

The preliminary objectives of this program were: (1) to test the present IA formalism to check whether it satisfies general principles such as detailed balancing and the optical theorem connection; (2) to trace what is responsible if the general requirements in (1) are not met, and if possible, to improve the formulation to remedy this. Also, (3) some work was to continue on comparisons with Peaking Approximation results in order to prepare a detailed paper.

During the course of our work it was realized that the semi detailed balance (sdb) condition was violated significantly in the near forward directions. Our IA formalism up to this point was based on a convenient (and valid) simplification obtained by choosing the direction of momentum transfer along the quantization axis. Cross sections averaged over the initial and final azimuthal quantum numbers m and m' are independent of the choice of the direction of the momentum transfer. Individual $m \to m'$ processes, however, do depend on the relative orientations of the momentum transfer $\vec{q}$, and the incident momentum $\vec{P}_3$. In order to fully understand where the symmetry considerations fail in IA, it became necessary to develop the general amplitude, without any specialization of the directions of $\vec{q}$ and $\vec{P}_3$. This, then, became an important additional objective. It was recognized that a precise understanding of the dependence of the general amplitude on the directions of $\vec{q}$ and $\vec{P}_3$ would facilitate the inclusion of multiple collision terms in IA.

Considerable progress was made on these objectives during the

summer program. Various symmetry considerations, and the development of the general scattering amplitude in IA, are described in section III. It was shown that the time reversal invariance and the semi detailed balance condition are violated for smaller angles. A paper based on this material was written during the summer and has already been submitted for publication (Sharma, Bakshi and Sindoni, 1989b). New results on the comparison of the exact IA and the Peaking Approximation formulations are given in section IV. A paper based on this material, and also including formal details not given earlier is under preparation (Sharma, Bakshi and Sindoni, 1989c)

Finally the recommendations for follow-up research are described in section V.

III. SYMMETRIES OF IA AMPLITUDES:

The basic formalism of IA has been described in Sharma, Bakshi and Sindoni (SBS), 1989a, and earlier references mentioned in that paper. Our contribution was to show that the IA amplitude can be evaluated exactly, without any approximations. As a matter of convenience, the momentum transfer was taken to be parallel to the quantization axis in evaluating the amplitude and the differential cross section. The more general expression, without any special choice of directions, is given by Eq. (5), SBS (1989a). By using a standard angular momentum algebraic identity, it can be simplified to

$$\langle \phi'_3 | T^{(s)} | \phi_3 \rangle = \sum_J C(jJj'; m, m'-m)\, F_{Jm''}(s), \qquad (1)$$

where $m'' = m'-m$, and

$$F_{Jm''}(s) = \sum_{\beta\lambda LM} (\pm i)^{\beta}\, i^{j-\lambda}\, [\hat{j}\hat{L}\hat{\beta}/\hat{j}']^{1/2}\, Y^{*}_{\beta,m''-M}(\hat{q})$$

$$N^{(s)}_{LM\lambda\beta}(\vec{q}, \vec{P}_3)\; C(jL\lambda;00)\; C(\lambda\beta j;00)$$

$$W(jLj'\beta;\lambda J)\; [\hat{\lambda}\hat{J}]^{1/2}\; C(L\beta J;\, M,\, m''-M). \qquad (2)$$

In this form it separates the geometrical effects, depending on both m and m' through the Clebsch-Gordan coefficient, and the dynamical effects which depend only on their difference m". This representation allows us to explore the general transformation properties and symmetries of the IA amplitudes.

The expected symmetry relationships between these amplitudes for different physical scenarios were tested by explicit evaluation, using Eq. (1). The main results were as follows:

(1) Time reversal (TR) symmetry requires that the scattering amplitudes $A(i, \vec{p} \to f, \vec{p}')$ satisfy

$$A(i, \vec{p} \to f, \vec{p}') = A(Rf, -\vec{p}' \to Ri, -\vec{p}), \qquad (3)$$

where $|i\rangle = |njm\rangle$ represents the initial molecular state and $\vec{p}$ the projectile atom momentum, $|f\rangle = |n'j'm'\rangle$ and $\vec{p}'$ the corresponding final state labels, R is the time reversal operator, and the state $R|i\rangle$ differs from $|i\rangle$ by a phase factor and the sign of m. By evaluating the two expressions in Eq. (3), we found that TR is not satisfied for moderate and small scattering angles θ.

(2) Space inversion (SI) symmetry requires

$$A(i, \vec{p} \to f, \vec{p}') = A(i, -\vec{p} \to f, -\vec{p}'). \qquad (4)$$

This was accurately satisfied for all cases.

(3) Combining TR and SI, and summing over m and m' leads to the semidetailed balance (sdb) condition (SBS, 1989b). Since SI is exactly satisfied, one can examine the violation of TR through the more convenient sdb relation, which is independent of the choice of direction of the momentum transfer. The sbd relation was quantitatively tested as a function of scattering angle θ by evaluating the ratio of the forward and normalized reverse cross sections. The systems studied included $Li^+ - N_2$ and $H - N_2$, for various relative kinetic energies (E = 1,4 and 10 eV). We find that TR and sdb are violated for moderate and small θ. The violation increases as θ decreases, exceeding factors of 2 for small enough angles. For a given angle, the agreement improves at higher relative kinetic energies and for the smaller projectile mass. These results have been reported in detail in SBS (1989b).

(4) The more stringent detailed balancing (db) condition requires

$$|A(i,\vec{p} \to f,\vec{p}')| = |A(f,\vec{p}' \to i,\vec{p})|. \qquad (5)$$

One can derive this from TR and SI if the symmetry

$$A(m \to m') = A(-m \to -m') \qquad (6)$$

were satisfied. This relation was tested for the IA amplitudes and was found to be (approximately) well satisfied. Unlike SI, however, it was not an exact relation, and violations up to 2 to 5% could be found for some m and m' for moderate scattering angles. Thus db is not an exact symmetry for IA, and even if somehow the time reversal were satisfied, violation of Eq. (6) would prevent satisfaction of the detailed balance condition.

All of the symmetry violations disappear at large scattering angles. This is also the domain where the multiple collision terms, ignored in IA, are truly negligible. This suggests that one should include the higher collision terms for the smaller angles, where they might be quite significant, and could conceivably improve or eliminate the symmetry breaking. This is a major follow-up problem worth pursuing. It should also be noted that the general expression, Eq. (2), and its transformation properties under rotations will prove useful in developing the formalism for the inclusion of higher collision terms.

IV. COMPARISON OF EXACT IA AND PEAKING APPROXIMATION RESULTS:

We have already shown the inadequacy of the Peaking Approximation (PA) results for differential as well as total cross sections, SBS (1989a). Those studies emphasized the processes ($v=0$, $j=0 \rightarrow v=0, 1, 2$; any j'). It was found that in these excitation processes, PA gave a significant overstatement of the cross sections, especially for small angles. We have now considered the deexcitation processes as well, and in most of these, PA leads to an understatement of the cross sections. Together, these features lead to a severe breaking of the sdb condition in PA. Thus PA should not be relied upon in assessing these cross sections. The precise ratios of IA to PA results, and also the sdb violation in PA, are being described in detail in SBS (1989c).

The PA results are easier to calculate and take much less time than IA (exact) calculations. Also, the PA and exact cross sections as a function of angle θ track each other fairly well over the full range with the ratio generally a smooth and slowly varing function. We have

analyzed this ratio ρ as a function of θ for various relative kinetic energies E_{rel} (SBS, 1989c). We find that for a given E_{rel} the ratio is a function of the energy loss ε irrespective of how the energy loss is distributed between the vibrational and rotational energy transfers, $\rho = \rho\ (\theta, \varepsilon, E_{rel})$, indicating a "universality." Furthermore, we find that for different E_{rel}, the same ratios are obtained for the same fractional energy losses (ε/E_{rel}), i.e. $\rho = \rho(\theta, \varepsilon/E_{rel})$, indicating a second "universality." These relations make it possible to predict the exact IA cross sections for a variety of situations from the corresponding, simpler PA results, once the universal $\rho(\theta, \varepsilon/E_{rel})$ curves have been determined. Such curves have been plotted and the task of obtaining the exact IA cross sections has been thus simplified for a broad range of processes and physical parameters. Further work is in progress in determining how far these universality relations extend. This is also an important practical area for future work.

V. RECOMMENDATIONS:

Considerable progress was made during this summer program in understanding the advantages of the IA exact results over the PA, and also in recognizing some of the limitations of the existing IA theory through symmetry considerations. It is clear that IA has some limitations in the small scattering angle domain and further efforts should be directed towards eliminating these shortcomings. Then IA would be effectively applicable to all processes. Our specific recommendations for future work are as follows:

1) Including the multiple collision terms. This requires summation over all possible intermediate states, which in turn requires

t-matrix elements for an arbitrary orientation of the momentum transfer. Our Eq. (1) can be utilized to show that the general structure of the two-collision term involves the same C factor, multiplied by a "convolution" of two F factors. Some preliminary work was done on this problem and further effort along those lines should be continued.

2) After including the higher collision terms in IA, one should recheck the optical theorem connection between the total cross section and the forward scattering amplitude. It is not satisfied at the present level of description, and probably indicates the same IA inadequacy at smaller angles. The optical theorem check will provide an independent assessment of whether including higher collision terms has eliminated the present difficulties of the IA formalism.

3) So far only the hard core potential has been studied in the IA formulation. The IA formalism is quite general, it is the difficulty of obtaining t-matrix elements for other potentials that has prevented their use. A systematic program should be developed to consider softer potentials. This might improve agreement with experiments, since the hard core is not necessarily a very good approximation to actual potentials.

4) Finally, the extended formalism should be applied to various recent experimental results on atom-molecule collisions such as Magill et al. (1988), Stewart et al. (1988), Chawla et al. (1988), and also to the high-altitude atmospheric studies at AFGL mentioned in the Introduction.

REFERENCES

Beard, L.H. and D.A. Micha, J. Chem. Phys. 74, 6700, (1981).

Bogan, A., Phys. Rev. A 9, 1230, (1974).

Chawla, G., G. McBane and P. Houston, J. Chem. Phys. 88, 5481, (1988).

Eckelt, P., H.J. Korsch and V. Philipp, J. Phys. B. 7, 1649, (1974).

Magill, P., B. Stewart, N. Smith and D. Pritchard, Phys. Rev. Letters, 60, 1943, (1988).

Sharma, R.D., AFGL Report, AFGL-88-TR-0110, (1988).

Sharma, R.D., P.M. Bakshi and J.M. Sindoni, Phys. Rev. A 40, 1692, (1989a).

Sharma, R.D., P.M. Bakshi and J.M. Sindoni, "On the Validity of the Impulse Approach to Collisions," submitted to Phys. Rev. Letters (1989b).

Sharma, R.D., P.M. Bakshi "Impulse Approach to Atom Molecule Collisions" paper under preparation (1989c).

Stewart B., P. Magill, T. Scott, J. Derouard and D. Pritchard, Phys. Rev. Letters, 60, 282, (1988).

1989 USAF-UES SUMMER FACULTY RESEARCH PROGRAM

GRADUATE STUDENT RESEARCH PROGRAM

Sponsored by the

AIR FORCE OFFICE OF SCIENTIFIC RESEARCH

Conducted by the

Universal Energy Systems, Inc.

FINAL REPORT

A Statistical Analysis of the Geomagnetic Indices, 1932-1989

Prepared by: Chi Hau Chen, Ph.D

Academic Rank: *Professor*

Department and University: Electrical and Computer Engineering, Southeastern Massachusetts University

Research Location: AFGL/LIS
Hanscom AFB MA 01731

USAF Researcher: Paul F. Fougere, Ph.D

Date: 27 October 89

Contract No: F49620-88-C-0053

A Statistical Analysis of the Geomagnetic Indices, 1932-1989

by

Chi Hau Chen

ABSTRACT

Geomagnetic indices K_p and a_p have been used for many years in statistical studies correlating magnetic activity with other phenomena occurring on the sun, in the interplanetary medium and in the magnetosphere. An excellent statistical analysis of these indices was made by earlier AFGL researchers for the years 1932-1971. The present study incorporates the data since 1971 in the statistical analysis. Although there have been little change in statistical parameters, the overall trend has been a slight increase in the geomagnetic activity in recent years. By using the modern spectral analysis techniques, the power spectra of the yearly K_p, the sunspot numbers and the solar flux numbers are calculated to determine the major periodicities. The spectral analysis also allows us to correlate the geomagnetic indices with sunspot numbers and the solar flux.

Acknowledgements

I wish to thank the Air Force Systems Command and the Air Force Office of Scientific Research for sponsorship of this research. Universal Energy Systems must be mentioned for their concern and help to me in all administrative and directional aspects of this program.

My experience at the Air Force Geophysics Laboratory was truly rewarding and enriching. My special thanks go to Dr. Paul F. Fougere for his continued encouragement and support. In fact he introduced me at the 1979 USAF Summer Faculty Research Program the nonlinear maximum entropy spectral analysis technique which is still used in the present study. The help of Drs. W. K. Vickery and Jurgen Buchau with their valuable suggestions and comments is greatly appreciated.

I. INTRODUCTION:

Geomagnetic indices K_p and a_p have been used for many years in statistical studies correlating magnetic activity with other phenomena occurring on the sun, in the interplanetary medium and in the magnetosphers. An excellent statistical analysis of the geomagnetic indices K_p and a_p has been provided by Cage and Zawalick (1972) for 1932 to 1971 and by Pazich (1976) for 1932 to 1972. With the large amount of additional data available since 1971, it is necessary to update now the statistical analysis and to use the more recently developed spectral analysis techniques to gain further insights about the geomagnetic indices.

The Ionospheric Effects Branch of the Ionospheric Physics Division of the Geophysics Laboratory has a need to update a number of information on the geomagnetic indices in the Handbook of Geophysics and the Space Environment. Also there is a need to estimate the conditional probabilities associated with various magnetic activity levels. My research interests have been in the statistical and spectral analysis of geophysical signals using modern signal processing techniques. My work on high resolution spectral analysis in the last ten years has been particularly useful to the present assignment.

An important conclusion from the analysis incorporating the data from 1972 to 1989 is that there are only slight changes in the statistical parameters of the geomagnetic indices since 1972 as compared to the parameter values of 1932 to 1971. The overall trend has been a slight increase in the geomagnetic activity in recent years.

II. OBJECTIVES OF THE RESEARCH EFFORT:

The primary objective is to update the statistical analysis of the geomagnetic indices particularly K_p, by including the data from 1972 to 1989 in the analysis. The desired information includes the relative frequency of occurrence for the indices, the probability of occurrence of different magnetic activity levels, conditional frequency distribution of K_p given the value of K_p in previous time interval, etc.

The secondary objective is the spectral analysis of the geomagnetic indices. The results from spectral analysis can be correlated with that of statistical analysis to provide us further insights of the geomagnetic and solar activities.

Most of the objectives have been met in this assignment. However a more in-depth study is much recommended and it requires a much more extensive effort funded from the 1989-90 Research Initiation Program.

III. ANALYSIS OF THE K_p INDICES

Table 1 lists the frequency of occurrence of K_p indices for 1972 to 1989, with K_p taking the integer values of 0 to 9. It is interesting that all years seem to have some geomagnetic activity up to $K_p = 8$, with a notable exception of 1977 and 1987 when $K_p = 7$. This table should be used in conjunction with Table 2 of Cage and Zawalick (1972). Figure 1 shows the relative frequency of occurrence of K_p values for the years 1932-1989 in solid line and 1932-1971 in dashed line. The slight shift of the curve to the right for 1932-1989 indicates an increased geomagnetic activity since 1971, though the two curves are very similar. The dip in the curve at $K_p = 2-$ is less evident. Some statistical parameters are listed as follows. The K_p takes on 28 possible values while the average values can have different decimal numbers.

Years	Mean	Mode	Median
1932-1971	$K_p = 2.25$	4/3	11/6
1932-1989	2.31	4/3	2

Table 2 lists the frequencies of K_p indices (cumulative), 1932 to 1971 and 1932-1989, with K_p taking only the integer values 0 to 9. If we define the magnetic activity level according to K_p, the probability of occurrence of each activity level can be listed as follows.

K_p values	Magnetic activity level	Probability
0, 1	quiet	0.3364
2	unsettled	0.2542
3	active	0.2087
4	minor storm	0.1201
5, 6, 7, 8, 9	major storm	0.0806

The conditional probability distribution of all K_p indices that occurred in the 3-hour interval following that of given value of K_p, for 1932-1989, is shown in Table 3. It is noted that K_p occur mostly in the same way as

Table 1 Frequency of Occurrence of K_p Indices for 1972 to 1989

K_p	1972	1973	1974	1975	1976	1977	1978	1979	1980	1981	1982	1983	1984	1985	1986	1987	1988	1989	SUM
0	290	164	114	192	201	214	194	146	218	121	77	111	89	165	188	212	175	41	2912
1	812	627	395	667	763	840	649	607	877	558	376	431	420	719	844	877	727	326	11515
2	824	677	634	781	860	844	746	848	844	862	635	718	756	831	901	880	905	457	14003
3	598	651	784	650	594	598	642	759	612	724	782	774	765	682	552	549	657	435	11808
4	254	457	595	411	365	278	386	359	265	385	594	543	529	323	270	280	322	259	6875
5	96	247	291	171	106	96	177	136	79	165	290	248	257	135	117	99	88	145	2943
6	18	75	86	41	20	38	78	41	27	71	105	67	80	49	28	21	36	65	946
7	23	16	16	6	10	12	34	19	5	24	42	20	27	14	11	2	16	13	310
8	11	6	4	1	9	0	14	5	1	10	15	8	5	2	5	0	2	7	105
9	2	0	1	0	0	0	0	0	0	0	4	0	0	0	4	0	0	4	15
																		Total:	51432

Note: For 1989, we have only 219 days in the data base as of Sept. 19, 1989.

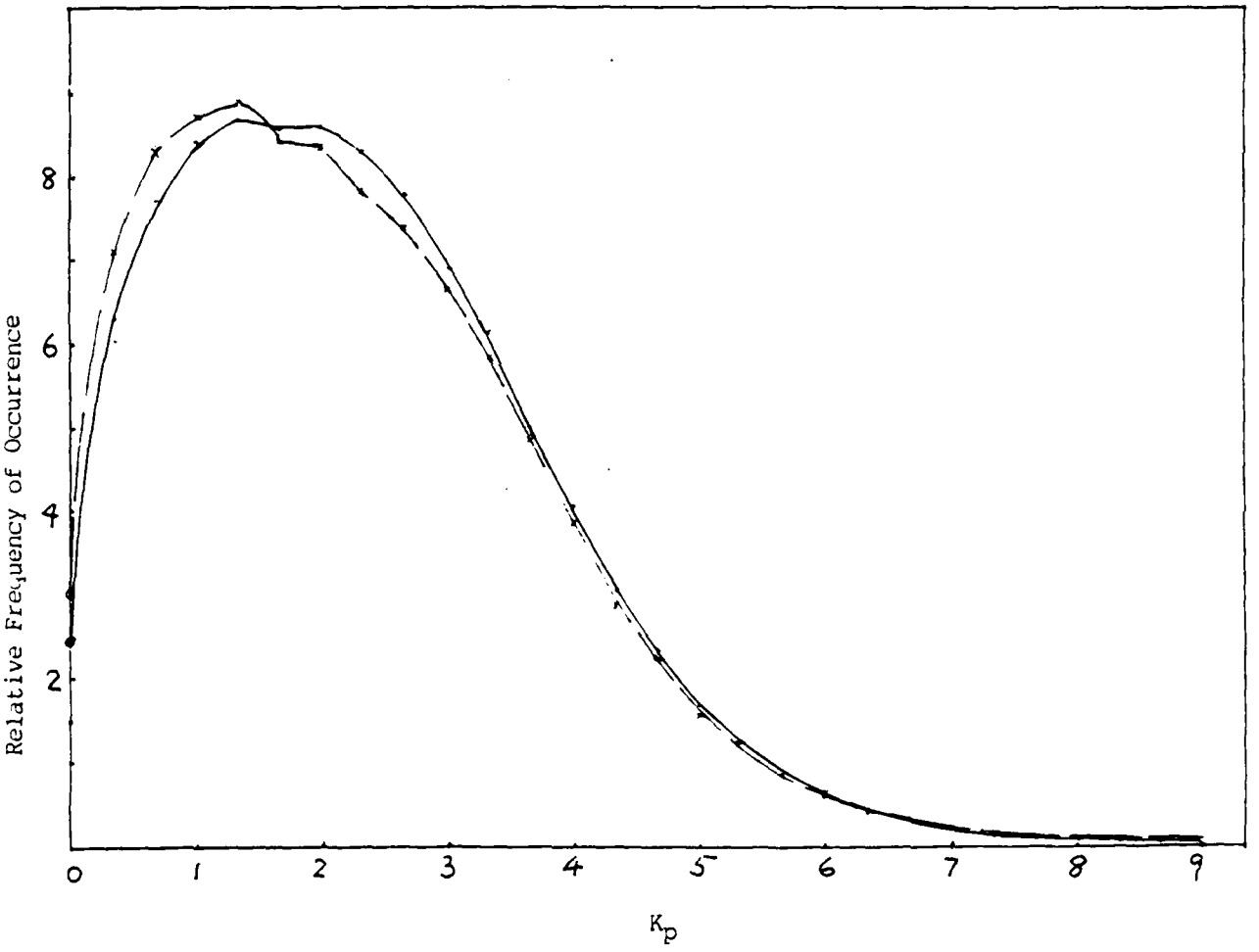

Figure 1. Relative Frequency of Occurrence of the Values of K_p. The solid line is for data from 1 January 1932 through 7 August 1989. The dashed line is for data from 1 January 1932 through 31 December 1971.

its neighboring values. This persistent nature of K_p is similar to that of 1932-1971. Table 3 can be used to construct the data plotted in Figure 2, in which the abscissa is arranged in standard probability format. Each curve is identified by the value of K_p for the present 3-hour interval. The ordinate represents the value of K_p for the succeeding 3-hour interval. It is noted that these curves are very similar to those of Figure 7 in the report by Cage and Zawalick (1972). This is another evidence of persistency, after including the data from 1972 to 1989. By using the definition of magnetic activity level described earlier, the following are some transition (or conditional) probability values.

Probability that a major storm follows right after a minor storm is: 0.1778 (from 1932-89 data)
or 0.1777 (from 1932-71 data)

Probability that a minor storm follows right after an active level is: 0.1793 (from 1932-89 data)
or 0.1773 (from 1932-71 data)

Probability that a major storm follows right after an active level is: 0.04677 (from 1932-89 data)
or 0.04730 (from 1932-71 data)

Thus the transition probabilities change negligibly by including the data from 1972 to 1989.

The average duration of a very major storm, defined as K_p of at least 7, 8, or 9 is calculated as 14.635 hours, with each storm lasting for 6 or more hours. Isolated 3-hour intervals with such K_p values are not included in the calculation.

The active days for 1972-1989 are listed as follows for K_p = 8, 9 only.

For K_p = 9^o,	For K_p = 9-,
August 4, 1972	August 5, 1972
July 13, 1982	July 6, 1974
July 14, 1982	July 13, 1982
Feb. 8, 1986	Sept. 6, 1982
March 13, 1989	Feb. 8, 1986
March 14, 1989	Feb. 9, 1986
	Sept. 12, 1986
	March 13, 1989 (2)

For K_p = 8+,
June 20, 1972
Aug. 4, 1972
Aug. 5, 1972 (2)
Aug. 9, 1972
April 1, 1973
July 6, 1974
May 3, 1976
May 1, 1978
Aug. 28, 1978
April 13, 1981
July 25, 1981 (2)
July 13, 1982
Sept. 6, 1982 (3)
Sept. 22, 1982
Jan. 10, 1983
April 21, 1985
March 13, 1972

For K_p = 8^o,
Sept. 14, 1972
Nov. 1, 1972
Sept. 15, 1974
March 26, 1976 (2)
April 1, 1976 (2)
April 30, 1978
July 4, 1978
Aug. 28, 1978
Sept. 29, 1978 (2)
April 3, 1979
April 25, 1979
April 13, 1981
July 26, 1981
Oct. 14, 1981
March 1, 1982
March 2, 1982
Sept. 6, 1982
Sept. 22, 1982
Feb. 5, 1983
May 24, 1983
Nov. 16, 1984
April 21, 1985
Feb. 8, 1986
April 3, 1988

For K_p = 8-,
May 15, 1972
Aug. 5, 1972
Nov. 1, 1972 (2)
April 1, 1973 (2)
April 14, 1973
May 14, 1973
Sept. 9, 1973
Sept. 15, 1974
Sept. 16, 1974
June 7, 1975
March 26, 1976
May 3, 1976
May 14, 1976
April 21, 1978
May 4, 1978
May 9, 1978
June 29, 1978
July 4, 1978
Aug. 27, 1978
Sept. 29, 1978
April 25, 1979 (2)
Aug. 29, 1979
Dec. 19, 1980
April 13, 1981
July 25, 1981 (2)
Oct. 14, 1981
March 2, 1982
July 14, 1982
Aug. 7, 1982 (2)
Sept. 22, 1982 (2)
Feb. 4, 1983 (2)
May 24, 1983
June 13, 1983
Aug. 8, 1983
April 4, 1984
April 27, 1984
Sept. 4, 1984
Nov. 19, 1984
Feb. 7, 1986 (2)
Feb. 8, 1986
Feb. 9, 1986
Oct. 10, 1988
March 13, 1989
March 14, 1989 (3)

Note: Numbers inside the bracket indicate the number of intervals, if more than one, on that day. There are eight intervals per day.

Table 2. Frequencies of K_p Indices (Cumulative), 1932 to 1971 and 1932 to 1989. K_p takes only the integer values 0 to 9.

K_p	32-71 original frequencies	32-71 reduced to sum 10,000.	32-89 original frequencies	32-89 reduced to sum 10,000.
0	11859	1015	14765	877
1	30331	2595	41849	2487
2	28782	2463	42789	2542
3	23319	1995	35126	2087
4	13342	1141	20217	1201
5	5885	503	8828	525
6	2155	184	3101	184
7	781	67	1091	65
8	337	29	442	26
9	89	8	104	6
SUM	116880		168312	

Table 3. Conditional Frequency Distribution of All K_p Indices (K_p taking on only the values 0 through 9) that occurred in 3-hour interval following that of a given value of K_p, 1932-1989.

K_p	0	1	2	3	4	5	6	7	8	9	Row SUM
0	7336	5973	1198	226	30	8	0	0	0	0	14771
1	6087	21166	10961	3001	517	87	20	7	0	0	41846
2	1164	11317	17558	9875	2402	388	66	11	4	0	42785
3	168	2931	10326	13760	6299	1396	209	30	7	1	35127
4	16	415	2396	6671	7127	2924	567	83	17	1	20217
5	0	40	308	1376	3147	2762	955	195	42	3	8828
6	0	4	34	191	603	1038	872	305	51	3	3101
7	0	0	4	21	80	198	347	308	125	8	1091
8	0	0	0	6	12	26	62	136	158	42	442
9	0	0	0	0	0	1	3	16	38	46	104
Colum SUM	14771	41846	42785	35127	20217	8828	3101	1091	442	104	Total: 168312

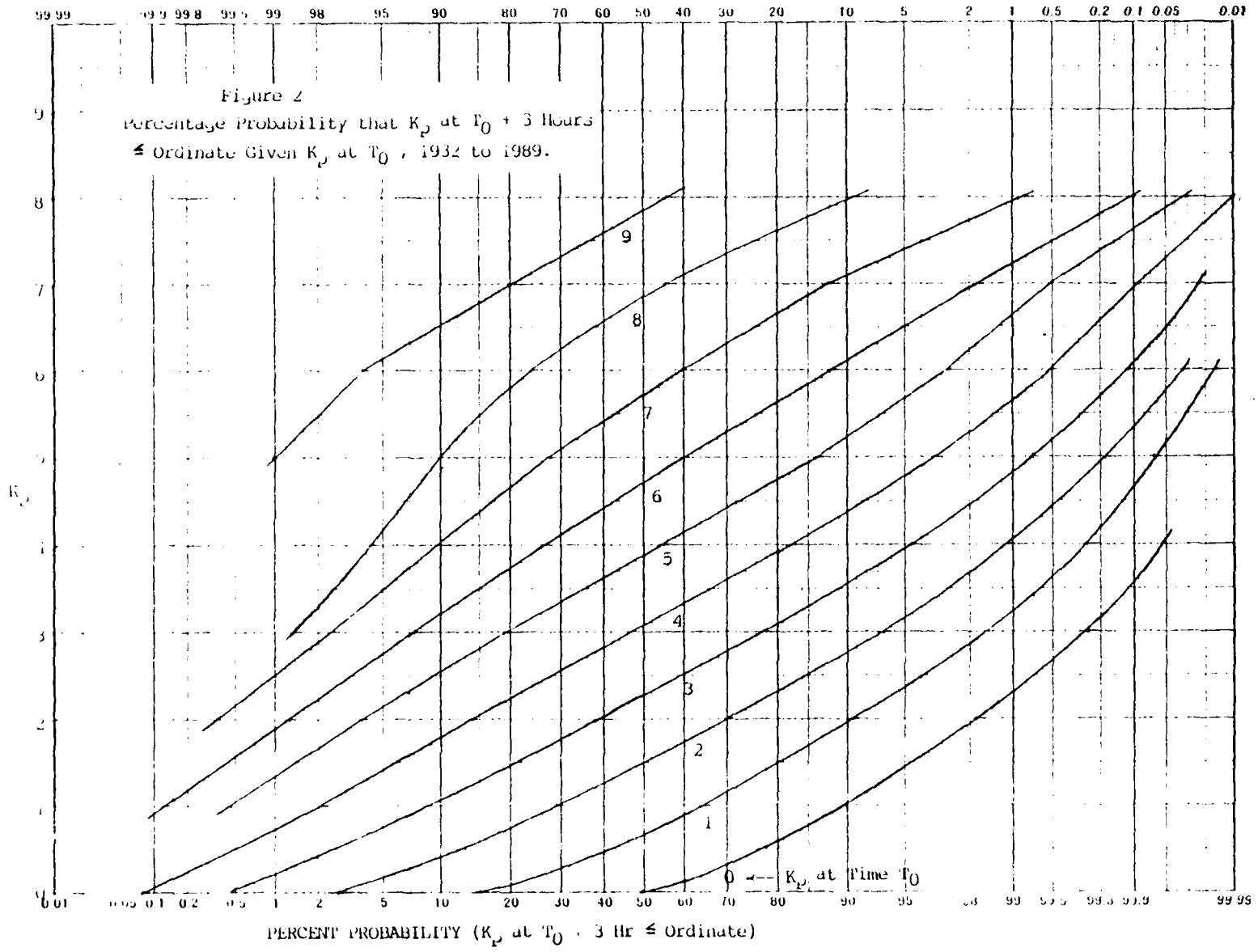

Figure 2

Percentage Probability that K_p at T_0 + 3 Hours ≤ Ordinate Given K_p at T_0 , 1932 to 1989.

IV. ANALYSIS OF THE a_p INDICES

The K_p indices are related to a good approximation to the a_p indices by the equation,

$$K_p = 4 \log_{10} a_p - 1.6 \qquad (1)$$

Thus K_p which is a unitless quantity is more compressed than a_p since a_p is greater than one in practice. With a larger dynamic range, a_p can give us a better indication of variations in geomagnetic indices. The relative frequency of occurrence of a_p for 1932 to 1989 is shown in Figure 3. By using the definitions of magnetic activity levels suggested by Jurgen Buchau of Ionospheric Effects Branch, the probability of occurrence of each activity level can be computed as follows.

a_p range	Magnetic activity level	Probability
0 - 7	quiet	0.2735
8 - 15	unsettled	0.2532
16 - 29	active	0.2312
30 - 49	minor storm	0.1421
= 50	major storm	0.0999

Although there are differences in the probability values as compared to those discussed in previous section, the general conclusion is that the probability is more than 0.5 for the magnetic activity level to be quiet or unsettled, and there is less than 10% of the time for the major storm to occur.

Table 4 provides a tabulation of yearly average K_p and yearly a_p values where a_p is computed by Eq. (1) given above.

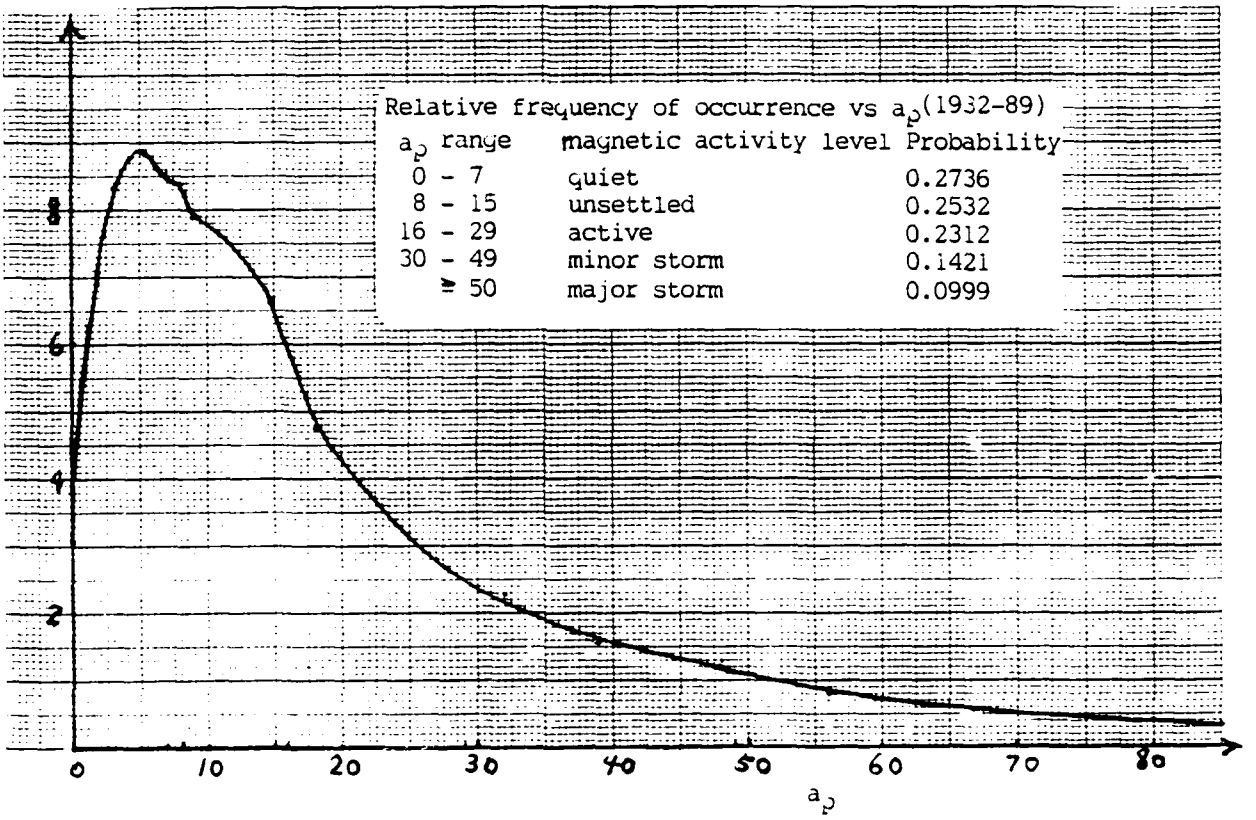

Figure 3. The Relative Frequency of Occurrence of a_p for 1932 to 1989.

Table 4

Yearly Average K_p Values & Average a_p Values

Year	Av. K_p	Av. a_p	Year	Av. K_p	Av. a_p
1932	2.06	8.22	1962	2.17	8.76
1933	1.88	7.41	1963	2.08	8.32
1934	1.44	5.75	1964	1.85	7.29
1935	1.66	6.53	1965	1.56	6.17
1936	1.68	6.61	1966	1.81	7.12
1937	2.07	8.27	1967	1.99	7.90
1938	2.27	9.28	1968	2.30	9.44
1939	2.45	10.29	1969	1.99	7.90
1940	2.35	9.72	1970	2.03	8.08
1941	2.41	10.06	1971	2.03	8.08
1942	2.29	9.39	1972	2.07	8.27
1943	2.58	11.09	1973	2.60	11.22
1944	1.94	7.67	1974	2.93	13.57
1945	1.86	7.33	1975	2.38	9.89
1946	2.50	10.59	1976	2.23	9.07
1947	2.70	11.89	1977	2.14	8.61
1948	2.47	10.41	1978	2.50	10.59
1949	2.36	9.77	1979	2.44	10.23
1950	2.63	11.42	1980	2.08	8.32
1951	3.07	14,71	1981	2.57	11.03
1952	2.93	14.86	1982	3.05	14.54
1953	2.48	10.47	1983	2.82	12.74
1954	2.11	8.46	1984	2.85	12.96
1955	2.04	8.13	1985	2.34	9.66
1956	2.62	11.35	1986	2.15	8.66
1957	2.72	12.02	1987	2.08	8.32
1958	2.73	12.09	1988	2.25	9.17
1959	2.87	13.11	1989	2.79	12.52
1960	2.92	13.49			
1961	2.20	8.91			

Note: a_p is computed from K_p from the equation

$K_p = 4\log a_p - 1.6$.

V. SPECTRAL ANALYSIS OF GEOMAGNETIC INDICES AND RELATED NUMBERS

The modern spectral analysis has provided us a powerful analysis tool for geophysical signals. For the geomagnetic indices listed in Table 4, both FFT and Burg's maximum entropy spectral analysis are used to determine the power spectra. Figure 4a shows the plots of K_p and a_p. Figure 4b and Figure 4c show respectively the Burg's and FFT spectra. The main spectral peak at 0.03 does not appear to correlate with known geophysical activity. A small spectral peak around frequency slightly less than 0.1 may correspond to the period for the sunspot numbers. For the active years indicated by sunspot numbers, the geomagnetic indices tend to be larger. However the correlation is not strong from the spectral analysis. Further work requires the study of daily variations of K_p and a_p and associated power spectra. Such study may give a better indication of the periodicity of geomagnetic indices.

The sunspot numbers and solar flux data have also been examined by using the spectral analysis. Figure 5 shows plots of the yearly sunspot numbers and FFT and Burg's spectra. The periodicity determined as 10.87 years per cycle is reasonably accurate. By using the latest 50 years of sunspot numbers, the periodicity determined by using the Fougere's nonlinear maximum entropy spectral analysis (Fougere 1977) and the Broyden's optimization in maximum spectral analysis (Chen and Costa 1986) is the same at 10.872 years per cycle. For the 50 sunspot numbers beginning with year 1770, both techniques give an estimate of 11.74 years per cycle.

For the solar flux, the daily solar flux data for 1978 as shown in Figure 6a provide a periodicity at 1/0.005 = 200 days per cycle which is not consistent with the expected 154 days per cycle periodicity. The chirp-z-

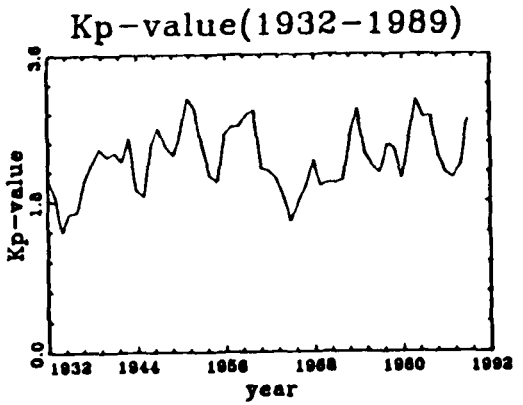

Figure 4a

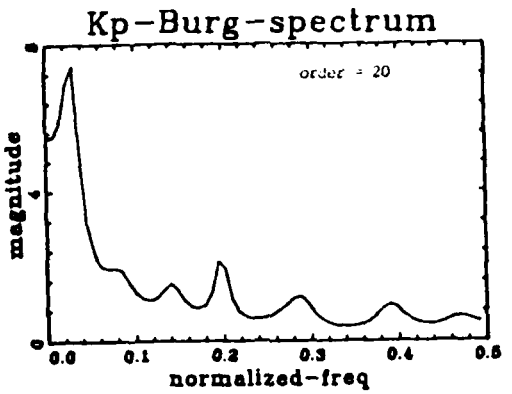

Figure 4b

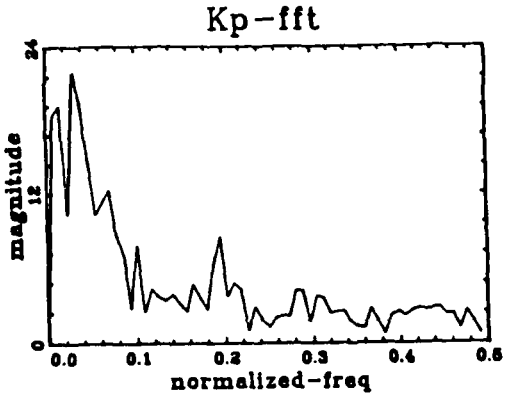

Figure 4c

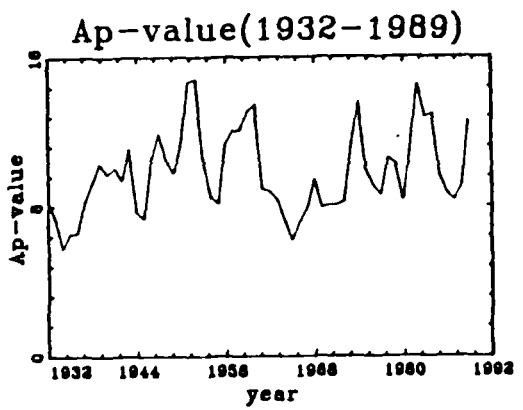

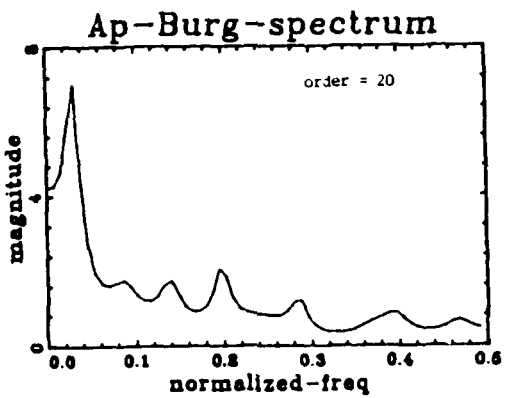

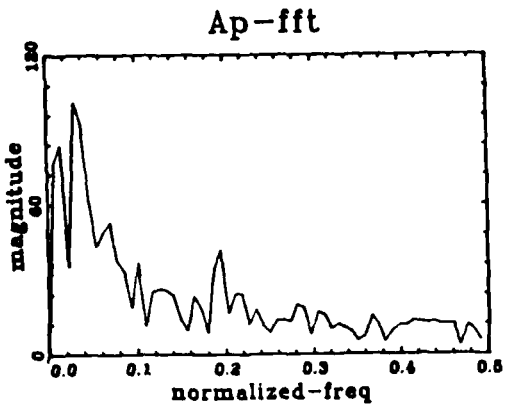

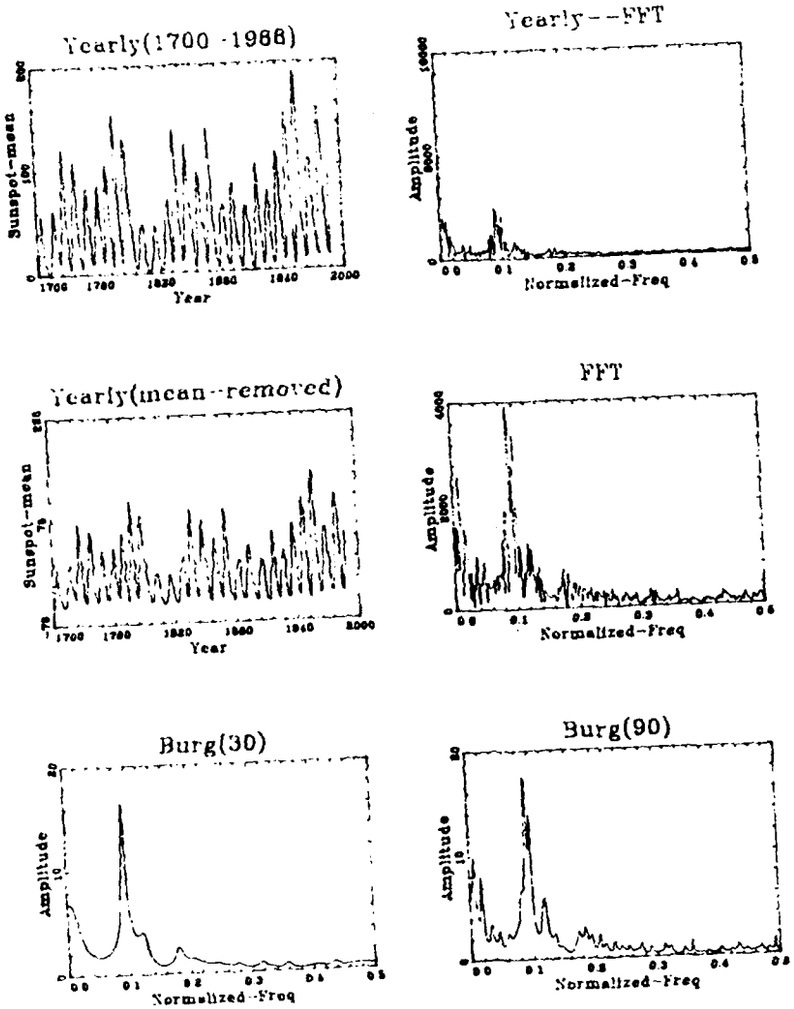

Sunspot numbers and their spectra. Burg(x) means Bury's spectrum of order x. From the spectral peak of Burg's spectrum, the periodicity is determined as 10.87 years per cycle.

Figure 5

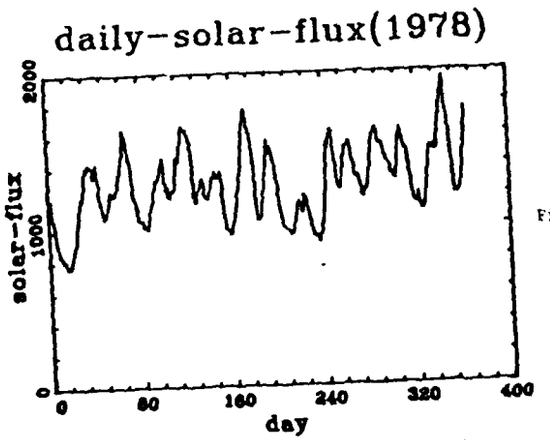

Figure 6a

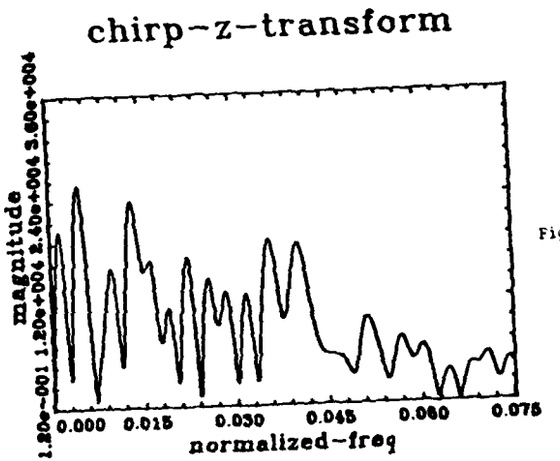

Figure 6b

transform, as shown in Figure 6b, is used in this case. For the yearly solar flux, both the Fougere's method and the Broyden's method provide an estimate of 1/0.09519 = 10.505 years per cycle. Thus there is a much better correlation between the sunspot numbers and the solar flux data.

VI. RECOMMENDATIONS:

There are many unanswered questions in the discussions presented above. A continued and in-depth study is strongly recommended. Specifically, the following topics are recommended for further study.

a. The semiannual and diurnal variations of K_p and a_p. As mentioned earlier the study may help to correlate better the periodicity of geomagnetic indices with sunspot numbers.

b. Additional study of conditional probability of occurrences of K_p and a_p. Although the conclusion may not be significantly different, based on my preliminary analysis of conditional probability at T_o + 27 days given the indices at T_o, a detailed study can provide more quantitative difference.

c. Computation of mean duration of each magnetic activity level. One calculation was given earlier, but the durations for other activity levels remain to be computed. The use of musical diagrams can be helpful and a computer algorithm needs to be developed to read the musical diagrams to determine the mean duration and periodicity. Such diagrams appear to show better periodicity than the listed yearly K_p values.

d. More detailed spectral analysis is needed to analyze a much larger amount of data so that a more reliable periodicity estimates can be obtained. This would require the development of a better spectral estimation software package than we currently have.

REFERENCES

1. Caye, A.L. and E.J. Zawalick, "A Discussion of the Geomagnetic Indices K_p and a_p , 1932 to 1971", Technical Report AFCRL-72-0693, Nov. 1972.

2. Pazich, P.M., "Conditional Probabilities of the Geomagnetic Index A_p", Technical Report AFGL-TR-76-0034, Feb. 1976.

3. Fougere, P.F., "A solution to the Problem of Spontaneous Line Splitting in Maximum Entropy Power Spectrum Analysis", Journal of Geophysical Research, 1977, pp. 1051-1054.

4. Chen, C.H. and A.H. Costa, "An Interactive and Data-Adaptive Spectrum Analysis System", Proc. IEEE International Conference on Systems, Man and Cybernetics, Atlanta, Georgia, Oct. 1986. A more complete version of the paper is in the technical report by the authors, "Interactive Maximum Entropy Spectral Analysis of Personal Computers", SMU-ECE-TR-8, Southeastern Massachusetts University, Dec. 4, 1986.

1989 USAF-UES SUMMER FACULTY RESEARCH PROGRAM/

GRADUATE STUDENT RESEARCH PROGRAM

Sponsored by the

AIR FORCE OFFICE OF SCIENTIFIC RESEARCH

Conducted by the

Universal Energy Systems, Inc.

FINAL REPORT

CUMULUS PARAMETERIZATION IN NUMERICAL PREDICTION MODELS: PROPOSAL FOR A NEW PARCEL-DYNAMICAL APPROACH

Prepared by:	Phanindramohan Das
Academic Rank:	Professor
Department and	Department of Meteorology,
University:	Texas A&M University
Research Location:	Geophysics Laboratory, Atmospheric Sciences
	Division, Atmospheric Prediction Branch
	Hanscom AFB, MA 01731
USAF Researcher:	Dr. Donald Norquist
Date:	15 September 1989
Contract No:	F49620-88-C-0053

CUMULUS PARAMETERIZATION IN NUMERICAL PREDICTION MODELS: PROPOSAL FOR A NEW PARCEL-DYNAMICAL APPROACH

by

Phanindramohan Das

ABSTRACT

The available cumulus parameterization schemes are based on: (i) Kuo's single class of undiluted towers and its modifications; (ii) Arakawa and Schubert's ensemble of cumuli with varying tops under quasi-equilibrium large-scale forcing; (iii) Lindzen's ensemble of cumuli with varying tops as well as bases; and (iv) Bett's systematic adjustment toward a quasi-equilibrium atmosphere. Physically the Arakawa-Schubert scheme is most nearly complete; but it is both difficult to implement and prone to undesirable heating in the lower atmosphere. The physical basis of the Kuo scheme is obscure, while those of Lindzen, and Betts are ad hoc.

A new concept for a cumulus parameterization scheme is proposed and will be based on the physics and dynamics of an undiluted tower; it will use moisture convergence to determine cloud coverage and compensatory subsidence for cumulus heating. A microphysical scheme will determine precipitation formation and fallout. The scheme will be closely tied to the convective available potential energy (CAPE), appropriately corrected for the negative buoyancy due to condensed water loading.

ACKNOWLEDGMENTS

The great benefit I have derived from this study primarily has been possible due to the sponsorship of the Air Force System Command and the Air Force Office of Scientific Research, but the the very friendly working environment provided by the Atmospheric Prediction Branch of the Atmospheric Science Division, Geophysics Laboratory (AFSC), has contributed to my accomplishment to an immense extent. While everyone in these organizations must be thanked for their contributions to this research, I have especial pleasure in acknowledging the day-to-day help I received from Dr. Donald Norquist, without which, in retrospect, I would have been severely handicapped. I also acknowledge the friendliness and the technical suggestions of Dr. Ken Yang. Finally, and not in the least measure, the very pleasant supervisory environment maintained by Dr. Donald Chisholm made me enjoy my work so much more.

The other bunch of nice people I must thank are those with Universal Energy Systems, Inc., and Dr. A. S. Jursa at the Geophysics Laboratory, whose amiability was a constant source of assurance.

I. INTRODUCTION:

Convective clouds, and the precipitation resulting from them, need to be represented in all weather and climate prediction models, since they dominate the weather of the tropics, as well as that of the temperate region in the spring and summer. However, the horizontal dimension of a convective cell is on the order of ten kilometers, while the weather stations for routine observations are separated by distances on the order of hundreds of kilometers. Consequently, the observing systems and the numerical weather prediction (NWP) models based on them are incapable of resolving individual convective clouds. On the other hand, since many convective clouds form simultaneously over a given region, it is considered possible to represent the change caused by them as a statistical average. This representation is accomplished through a system of parameters developed from the detailed knowledge of the convective, or cumulus, clouds, and is popularly (as well as technically) known as cumulus parameterization.

My research in the area of convective clouds started as early as the mid-fifties through my involvement with the radar detection of convective storms at Calcutta Airport, progressed through my dissertation work at the University of Chicago during the early sixties, and has remained a principal academic pursuit of mine to this day. While developing theoretical frameworks of convective cloud research, I pioneered the development of time-dependent one-dimensional models for the study of downdrafts in cumuli. Since then I have personally worked as well as supervised work on models of convective clouds for about twenty years.

However, until my involvement in the SFRP this summer I had not looked at cumulus parameterization as a research problem, although having taught courses in synoptic meteorology, I have had an ideal preparation for studying the interaction of convective clouds with synoptic systems. This preparation must have contributed to my assignment to the Atmospheric Prediction Branch, Atmospheric Sciences Division of the Geophysics Laboratory (AFSC), hereinafter referred to as GL.

II. OBJECTIVE OF THE RESEARCH EFFORT:

The methodology of cumulus parameterization in numerical prediction models initially has been developed by meteorologists who have been interested primarily in large-scale processes and guided by their intuition based on rather simple principles. As the computer technology advanced, higher level of sophistication has been progressively introduced in the parameterization schemes, but mainly in terms of intuitive perceptions of how ensembles of cumuli should behave and interact with the large-scale atmosphere: the physics of individual cumuli, when incorporated in these representations, has remained rather rudimentary. The resulting prediction of weather under predominantly convective conditions, while being successful to various degrees, has not attained a high level of reliability in all geographical locations and under all conditions of convective potential. The experiments performed with the GL Global Spectral Model (GSM) reinforces this general picture, although, so far, relatively simple schemes have been used. Centers of numerical weather prediction, globally, are currently in the process of assessing the potential of the available parameterization schemes, and

the Atmospheric Prediction Branch at GL, being no exception, is continually having these schemes reviewed by scientists who do not have a commitment to any of the existing schemes. My being available as a participant in the 1989 Summer Faculty Research Program (SFRP) provided the scientists at GL with an additional opportunity in this continuing pursuit.

The principal effort to be undertaken by me under the SFRP, as part of the development at GL, was to examine all the available cumulus parameterization schemes with a view to arriving at a choice for future use in the GSM. A specific problem to be addressed was why the Kuo (1965) parameterization, as modified by Krishnamurti, et al. (1976), being rather simplistic as it is, works as well as it does, compared to some of the sophisticated schemes developed later. As this examination progressed, it became obvious that there is scope for developing a parameterization scheme which, while building upon the experience of the schemes presently in use, takes advantage of the knowledge that have been gained by the cumulus dynamicists and modelers. An intriguing fact that emerged from the review of the previous studies was that schemes based on quite distinctly disparate assumptions, such as (i) single species of deep cumuli (Kuo, 1965), (ii) ensembles of cumuli with a common base but varying heights of tops (Arakawa and Scubert, 1974) and (iii) ensembles of cumuli with varying heights of bases and tops (Lindzen, 1980), appeared to produce essentially similar results overall, although there are differences in detail. A further source of curiosity is that one of these schemes imply entrainment of environmental air into the cloud, while the other two assume undiluted

clouds. Obviously it does not matter whether entrainment is included in the scheme or not so long as some other factors are properly represented. The three important factors appear to be (i) the moisture and (ii) the mass fluxes that are processed by the cumuli, and (iii) the precipitation that reaches the ground. Of these (i) and (ii) can be assessed from large-scale processes, while (iii) depends on the microphysics of the clouds. The last factor has been addressed only partially by Hack, et al., (1984). Time is ripe, it appears, for a more rigorous cloud-physical approach to cumulus parameterization, which will include the above three factors in an internally consistent fashion. To design such an approach emerged to be one of the principal goals of the research under the 1989 SFRP.

III. THE PHYSICAL GOAL OF CUMULUS PARAMETERIZATION:

Cumulus parameterization is a component of the more general problem, namely, that of the conversion of latent heat into sensible heat and potential energy, and the redistribution of moisture in the atmosphere. The physical formulation of this problem starts by evaluating the moisture entering a vertical column of the atmosphere, per unit time, by (large-scale) horizontal convergence and surface evaporation as:

$$M_t = -\int_{z_o}^{z_t} \nabla_o(\rho q \mathbf{v})\, dz + \rho_o C_d\, (q_o - q),$$

where ρ is the air density, q, the specific humidity, $\mathbf{v}$, the horizontal velocity, C_d, the drag coefficient of the surface, and z is the vertical coordinate, with z_o and z_t, respectively, referring to the earth's surface and the top of the atmosphere. M_t is disposed of as two final products:

(i) precipitation reaching ground at the rate R, and

(ii) moisture left behind in the atmosphere in the quantity $M_t - R$.

M_t is "observable" in terms of large scale parameters (either measured or predicted) and R is measurable. If we define a parameter, b:

$$b = \frac{M_t - R}{M_t},$$

we clearly have

$$LR = \int_{z_o}^{z_t} \frac{\partial}{\partial t}(\rho s)\, dz,$$

where L is the latent heat of vaporization, s ($= c_p T + gz$) is the static energy, and

$$bM_t = \int_{z_o}^{z_t} \frac{\partial}{\partial t}(\rho q)\, dz.$$

In writing the above we have raised three obvious questions:

(i) What is the correct vertical profile of $\partial s/\partial t$ corresponding to LR?

(ii) What is the correct vertical profile of $\partial q/\partial t$ corresponding to bM_t?

(iii) What is the value of b?

In addition, we have the final question: Once the cloud scale quantities are known, how are they to be translated into (horizontally) large-scale quantities?

Answering the above questions is the goal of a parameterization scheme. However, in the above, the meteorology of the processes by which the conversion (of latent heat to static energy) occurs has not been identified. Fundamentally these processes can be divided into two categories: (i) large-scale precipitation under convectively stable conditions and (ii) convective precipitation. Noting further that precipitation is the crucial process we can subdivide convective processes into two categories:

(1) Shallow convection, which is principally nonprecipitating, causes no net heating of the atmosphere, but redistributes heat and moisture. In this respect, shallow convection acts more like eddy diffusion; and

(2) deep convection, which is the principal process by which convective precipitation is caused. Consequently, deep convection is a process by which net heating of the atmosphere occurs. Of course, it also redistributes heat and moisture.

The questions asked earlier can again be asked, now specifically about the convective processes, and the answers obtained in terms of cumulus

parameterization. The following discussion concentrates on the parameterization of deep convection.

IV. A BRIEF OVERVIEW OF THE AVAILABLE PARAMETERIZATION SCHEMES:

For facilitating the overview, we may recall that cumulus parameterization is dependent on a model of the cloud, which includes parameters such as vertical and horizontal scales, and the cloud lifetime. These parameters, in their turn, are determined by physical and dynamical processes inside and around the cloud. The knowledge of how these parameters are determined in natural clouds is at best fragmentary; consequently only simple cloud models are used in cumulus parameterization.

As already remarked, the first effort at cumulus parameterization was due to Kuo (1965). The cloud model adopted by him treated the active cloud and its environment as a single system so that there was no need for treating cloud-environment interactions (e.g., entrainment). The temperature (T_c) and specific humidity (q_c) in this model cloud was determined by those in an "undiluted tower", that is by a moist adiabat through the cloud base conditions. The horizontal scale of (fractional area, a, occupied by) the cloud, and cloud lifetime (t) were related through

$$M_t = a\, M_c/t,$$

where M_c is the moisture processed in a cloud column of unit cross section per unit time. One can write

$$M_c = I_\theta + I_q;$$

where

$$I_\theta = \text{moisture used in heating} = \int_{z_b}^{z_t} (c_p/L)\,(T_c - T)\,\rho dz,$$

and

$$I_q = \text{moisture used in moistening} = \int_{z_b}^{z_t} (c_p/L)\,(q_c - q)\,\rho dz.$$

Precipitation rate is determined indirectly from

$$R = I_\theta\,/\tau,$$

in which τ needs to be disposed of. Kuo used the observed duration of the developing stage of the cloud to determine t. The heat realized in the precipitation was vertically apportioned through the relation:

$$\frac{\partial s/\partial t}{\text{moisture processed per unit time}} = \frac{\text{heating per unit mass in a layer}}{\text{moisture processed in cloud lifetime}},$$

or

$$\frac{\partial s}{\partial t} = \frac{c_p(T_c - T)}{M_c} M_t = \frac{a}{\tau} c_p(T_c - T).$$

If $\tau \sim \Delta t \sim 30$ min

$$s_{t+\Delta t} = s_t + ac_p(T_c - T),$$

and a similar expression for moistening, that is, the increase of q with time.

Kuo (1965) scheme has been found to work well in hurricane simulations and in the tropics. However, in more general situations it causes an excessive drying of the atmosphere since I_θ appears to be the dominant

term in the expression for M_c. In a later study Kuo (1974) changed his cloud model from an undiluted tower to one with entrainment to be specified by two parameters which were to be determined experimentally. More importantly, (large scale) moisture convergence was partitioned by invoking the b parameter:

$$R = (1 - b)M_t; \qquad \int_0^{z_t} \frac{\partial q}{\partial t} \rho dz = bM_t.$$

However, no method was specified for determining b. The method of vertical apportionment also was changed:

$$\frac{\partial s}{\partial t} = L(1 - b)M_t \frac{(q_c - q)}{\langle q_c - q \rangle}$$

where $\langle q_c - q \rangle$ is the pressure-weighted vertical average over the depth of the cloud.

There has been little direct impact of the entrainment formulation of Kuo (1974) on later developments; on the other hand, Krishnamurti, *et al.* (1976) were strongly influenced by the new method of vertical apportionment as well as the partitioning of moisture convergence by the b parameter. As a matter of fact, Krishnamurti et al. provided a method, albeit based on an ad hoc assumption, for the determination of b. It also is noteworthy that they changed the method of computing moisture convergence which was treated as concomitant with mass convergence. It appears that current formulations of Kuo parameterization is, to a great extent, a combination of Kuo (1965, 1974) and Krishnamurti, et al. (1976). Later variations on the Kuo

scheme, while laden with complex sophistication, have mostly been ignored by operational prediction models.

In the Kuo and Kuo-type parameterization schemes described above, the process by which the cloud affects the large-scale properties is left unspecified. The cloud model itself is internally contradictory: the undiluted tower is talked of as if it were an imporous pipe through which heat and moisture flows from the cloud base to the top, and also as one which mixes the heat and moisture horizontally at all levels. Consequently, the idea of a single species of clouds as undiluted towers has been replaced by one in which the cumulus population is assumed to consist of ensembles differentiated by varying bases and tops. In a picture, originally envisioned by Ooyama (1971), the cumulus population has the same base, and ensembles are characterized by varying tops such that the ensemble with a given top is assumed to detrain into the layer in which the top exists, the clouds in different ensembles supplying heat and moisture to different layers. This idea has been developed by Arakawa and Schubert (1974) who specify the distribution of the tops of cumuli through an entrainment parameter.

The complex system of equations that result from the formulation of Arakawa and Schubert is closed by making two assumptions: (i) The vertical mass flux in the large scale environment is equal to the total mass flux through the cloud population (the so-called quasi-equilibrium assumption); and (ii) heating of the atmosphere, level for level, is determined by cumulus-induced subsidence; while moistening occurs primarily through detrainment. Precipitation formation in the clouds is

treated in terms of cloud models. Including further assumptions on cloud processes, Arakawa and Schubert develops a model which can be considered physically complete, while there may be questions on individual assumptions. However, as opined by Lindzen (1980), the system of equations based on the Arakawa-Schubert model is hard to solve. Interestingly, this complex scheme does not produce results much superior to that produced by the conceptually simpler Kuo schemes.

Apparently frustrated by the heuristic and ad hoc nature of the Kuo-type schemes and the complexity of the Arakawa-Schubert formulation, as well as the failure of both to produce satisfactory results, efforts have been directed toward developing models based on the observed behavior of the atmosphere. One such approach, offered by Lindzen (1980), is to divide the atmosphere into two parts, one below and the other above the level of minimum equivalent potential temperature characteristic of the tropical atmosphere. It is then assumed that the mass converging in a layer of the lower part of the atmosphere will rise into the upper part to a level at which the equivalent potential temperature of the layer of origin is matched. The readjustment caused by the consequent overturning should then adjust the atmosphere to a stratification characteristic of the observed equilibrium atmosphere. Interestingly, schemes based on this very simple approach appears to give results comparable to Kuo scheme modified by Krishnamurti, *et al.*, and the Arakawa-Schubert methods (Geleyn, *et al.*, 1982). However, as admitted by Lindzen, the method is *ad hoc* ; as a matter of fact, it takes cumulus parameterization backwards in the sense that it relies entirely on

intuition rather than on the knowledge, gathered over the years, of the physics and dynamics of convective clouds .

Another method, developed by Betts (1986) and tested by Betts and Miller (1986), is simultaneously to relax the instantaneous temperature and moisture fields "towards observed quasi-equilibrium thermodynamic structures," with relaxation times dependent on the model characteristics. This approach as that of Lindzen "sidesteps all the details of how the subgrid-scale cloud and mesoscale processes maintain the quasi-equilibrium structure we observe."

The purely empirical approaches of Lindzen as well as Betts, apparently practical for the tropics where quasi-equilibrium conditions are often available, are likely to fail in the extratropical regions where the atmosphere is mostly in a state of transition. In other words, the search for a cumulus parameterization scheme, consistent with the present-day knowledge of cumulus physics and dynamics, must continue.

V. PROPOSAL FOR A NEW PARAMETERIZATION SCHEME:

The concept of a cumulus parameterization scheme being presented hereunder is purported to incorporate some of the principal features of the presently available ones. It is noteworthy that all the parameterization schemes, except for that of Kuo, use the vertical mass flux, rather than the moisture flux, as the factor determining the horizontal coverage of cumulus activity and its effect on the large-scale atmosphere. Such an approach is likely to work in the tropics

since, as argued by Charney (1963, 1969), all the vertical mass flux in the tropics appears to be due to the cumulus-induced motion. However, this is not likely to be the case in extratropical convective systems, or even tropical convective systems induced by interaction with the tropical systems. Consequently, in a puristic approach one must distinguish between the roles of moisture and mass convergence. In the proposed scheme, moisture convergence determines the areal coverage of the cumulus, while the cumulus-induced mass flux is the cause of heating in compensatory subsiding motion.

The scheme, while resorting to some minor assumptions of an *ad hoc* nature, is rigorously tied to a simple cloud model. Only deep convection is considered in this scheme: an examination of the problem of shallow convection is postponed till a later study. The physical assumptions underlying the scheme are as follows:

1. Single class of undiluted towers of vertically variable radius: In view of the apparent success of the Kuo-type schemes as well as the comments made by Lindzen (1980), a complex cloud model may not be warranted. Since the products of the cloud are ultimately mixing with the large-scale environment, entrainment of environmental air, as assumed by Kuo (1965), need not be explicitly considered. The effect of entrainment on buoyancy and vertical velocity is crucially dependent on the horizontal dimension of the cloud, which is too uncertain to be considered in an unequivocal manner, especially in a preliminary effort.

2. Simultaneously occurring clouds in different parts of their life cycle: In the Arakawa-Schubert and Lindzen schemes, the need for clouds of various depths has been recognized, apparently for the purpose of modifying all the layers of the atmosphere by the cumulus processes. Unfortunately, there is no physically established distribution function for cloud depths. On the other hand, even for single species of deep clouds, there are cloud cells in different stages of their life cycles. Thus the following cloud events will be simultaneously occurring but for different clouds: (a) developing clouds, signifying upward mass flux and moisture convergence; (b) dissipating clouds, signifying falling precipitation, evaporation of precipitation in the lower part and mixing of the cloud with the environment in the upper part; and (c) mature clouds, having the characteristics of developing clouds in the uppermost layers and dissipating clouds in the lowermost layers.

The cloud model consistent with the above physical picture will consist of two one-dimensional, steady-state, nonentraining parcel models: one for the developing phase and the other for the dissipating phase. The depth of the developing cloud will be determined by the convective available potential energy (CAPE), the computation of which will include correction for the negative buoyancy due to the condensed phase (Das, 1964; Seitter and Kuo, 1983). Fractional area covered by the clouds will be determined so as to have the available moisture convergence to pass vertically through the developing cloud. The vertical mass flux through the cloud will be balanced, level by level, by compensatory

large-scale flux induced by the upward mass flux through the clouds so that there is no cumulus-induced large-scale pressure change.

Precipitation formation and fallout, in the dissipating phase, will be determined by a steady-state solution of a cloud-to-precipitation conversion equation, with a vertical distribution of the conversion parameter analogous to that of Hack, et al. (1984), tuned in by trial and error; the microphysical processes envisioned by the cumulus physicists are too complex for direct application.

Large-scale heating will be effected primarily by the the compensatory subsidence induced by clouds as indicated above. This heating will be modulated by the mixing of the dissipating cloud with the environment inasmuch as there is cooling due to evaporation of residual cloud water and heating (or cooling) due sensible heat excess (or deficit) of the cloud. Especially in the lower part of the cloud, cooling due to the evaporation of precipitation will be an additional important process.

Large-scale moistening due to cumuli will be through a straightforward mixing algorithm. The ideas for developing such an algorithm are contained, for example, in Anthes (1977).

VI RECOMMENDATIONS:

a. This research has produced a concept of cumulus parameterization which needs to be tested in three steps: one, develop the mathematical-physical structure for the concept and a corresponding numerical

algorithm; two, test the algorithm semiprognostically, that is, by using a four-dimensional data set to initialize a one time-step prediction which, in turn, can be verified against the observations taken at a later time in the same data set; and three, test the algorithm by integrating it into a large-scale model.

b. At the time of writing this report, the first step mentioned above has been in progress for some time. I intend to apply for a minigrant for the purpose of completing the first two steps.

c. The review undertaken in this research has demonstrated that the state of the science of cumulus parameterization is in a rather unsatisfactory state inasmuch as there is inadequate understanding of how a cumulus or a group of cumuli modify its large-scale environment. Presently, research on convective systems concentrates more on their internal dynamics than on the influence they bring to bear on their environment. Obviously there is scope for a reorientation of the goal of convective dynamics research.

REFERENCES

Anthes, R. A., A Cumulus Parameterization Scheme Utilizing a One-dimensional Cloud Model. Mon. Wea. Rev., 1977, vol. 105, pp. 270-286.

Arakawa, A, and W. H. Schubert. Interaction of a Cumulus Cloud Ensemble with the Large-Scale Environment. Part I. J. Atmos. Sci., 1974, vol.**31**, pp. 674-701.

Betts, A. K., A New Convective Adjustment Scheme. Part I: Observational and Theoretical Basis. Quart. J. Roy. Meteor. Soc., 1986, vol. **112**, pp. 677-691.

Betts, A. K., and M. J. Miller. A New Convective Adjustment Scheme. Part II: Single Column Tests Using GATE Wave, BOMEX, ATEX and Arctic Air-mass Data Sets. Quart. J. Roy. Meteor. Soc., 1986, vol. **112**, pp. 693-709.

Charney, J. G., A Note on Large-Scale Motions in the Tropics. J. Atmos. Sci., 1963, vol. **20**, pp. 607-609.

Charney, J. G., A Further Note on Large-Scale Motions in the Tropics. J. Atmos. Sci., 1963, vol. **26**, pp. 607-609.

Das.,P., Role of Condensed Water in the Life Cycle of a Convective Cloud. J. Atmos. Sci., 1964, vol. **21**, pp. 404-418.

Geleyn, J.-F., C. Girard, and J.-F. Louis, 1982: A Simple Parameterization of Moist Convection for Large-Scale Atmospheric Models. Beitr. Phys. Atmosph., vol. **55**, pp. 325-334.

Hack, J. J., W. H. Schubert, and P. L. Silva Dias, A Spectral Parameterization for Use in Numerical Models of the Tropical Atmosphere. Mon. Wea. Rev, 1984, vol. **112**, pp. 704-716.

Krishnamurti, T. N., M. Kanamitsu, R. Godbole, C.-B. Chang, F. Carr, and J. H. Chow, Study of a Monsoon Depression (II), Dynamical Structure. J. Meteor. Soc. Japan, 1976, vol. **54**, pp. 208-226.

Kuo, H.-L., Further Studies of the Parameterization of the Influence of Cumulus Convection on Large-Scale Flow. J. Atmos. Sci., 1974, vol. **31**, pp. 1232-1240.

Ooyama, K., A theory on parameterization of cumulus convection. J. Meteor. Soc. Japan, 1971, vol. **39**, pp. 369-379.

Seitter, K. L., and H.-L. Kuo. The Dynamical Structure of the Squall-line Type Thunderstorms. J. Atmos. Sci., 1983, vol. **40**, pp. 2831-2854.

1989 USAF-UES SUMMER FACULTY RESEARCH PROGRAM
GRADUATE STUDENT RESEARCH PROGRAM

Sponsored by the
AIR FORCE OFFICE OF SCIENTIFIC RESEARCH
Conducted by the
Universal Energy Systems, Inc.

FINAL REPORT

Estimating Characteristics of Chemical Explosions in New England and Eastern Kazakhstan Using Local and Regional Seismic Data

Prepared by:	Alan L. Kafka, Ph.D. ; Matthew Jacobson-Carroll
Academic Rank:	Associate Professor ; Graduate Student
Department and University	Geology and Geophysics Boston College
Research Location:	GL/LWH Hanscom AFB Bedford, MA 01731
USAF Researcher:	Dr. John Cipar
Date:	30 September 1989
Contract No:	F49620-88-C-0053

Estimating Characteristics of Chemical Explosions in New England and Eastern Kazakhstan Using Local and Regional Seismic Data

by

Alan L. Kafka
and
Matthew Jacobson-Carroll

ABSTRACT

One of the problems associated with monitoring a comprehensive nuclear test ban treaty is that of discriminating between small explosions and earthquakes based on seismic data. Chemical explosions are used routinely in the mining and construction industries in both the United States and the Soviet Union. These chemical explosions usually occur at very shallow depths (a few tens of feet), and probably are all shallower than a few hundered meters. Most nuclear explosions are detonated at depths of less than about one kilometer, and the deepest underground nuclear explosions are a few kilometers deep. On the other hand, most earthquakes occur deeper in the earth's crust. Thus, accurate estimation of the depths of seismic sources can be helpful in discriminating earthquakes from explosions. During the past several years, the Principal Investigator (PI) for this summer project has been studying the use of short-period Rayleigh waves (Rg) as a depth discriminant for seismic sources in New England. The research that we conducted this summer was primarily an extension of the PI's research on Rg as a depth discriminant. In addition, we investigated other aspects of estimating characteristics of chemical explosions from local and regional seismic data. The primary goal of our research this summer was to record seismic data at field sites located at near-regional distances from quarry blasts.

Acknowledgements

We thank the Air Force Systems Command and the Air Force Office of Scientific Research for sponsoring this research. Universal Energy Systems, Inc. provided assistance for the administrative aspects of this research program.

This work would not have been possible without the support of John Cipar, James Battis and James Lewkowicz of the Geophysics Laboratory. The cooperation of personnel at the San-Vel quarry in Littleton, MA is greatly appreciated. In particular, we thank John Trotter (superintendent of the San-Vel quarry) for his patience and logistical support. We also thank the following people on the research staff of the Geophysics Laboratory who helped with field and technical work: Joseph Craig, Janet Johnston, Katharine Kadinsky-Cade, Steve Mangino, Charles Taylor, Raymond Willemann and Lorraine Wolf. Susan D'Annolfo was an excellent field partner, and it was a great experience for both of us to work with her on this project.

I. INTRODUCTION:

One of the basic problems associated with monitoring a comprehensive nuclear test ban treaty is that of discriminating between small explosions and earthquakes based on local and regional seismic data. Chemical explosions are used routinely in the mining and construction industries in both the United States and the Soviet Union. Although the specific depths of these industrial explosions are often unknown, they usually occur at very shallow depths (a few tens of feet), and probably are all shallower than a few hundered meters. Most nuclear explosions are detonated at depths of less than about one kilometer, and the deepest underground nuclear explosions are on the order of a few kilometers deep. On the other hand, most earthquakes occur deeper in the earth's crust, and earthquakes in the upper kilometer are probably not very common. Thus, accurate estimation of the depths of seismic sources can be helpful in discriminating earthquakes from explosions.

During the past several years, the Principal Investigator (PI) for this summer research project has been studying the use of short-period Rayleigh waves (Rg) as a depth discriminant for seismic sources recorded in New England (Kafka, 1988, 1989a, 1989b). Using seismic data recorded by the New England Seismic Network (NESN; a regional seismic network operated by Boston College) we have been able to use New England as a "laboratory" for Rg wave propagation in various geological regions (Figures 1, 2 and 3). In addition, data recently recorded in eastern Kazakhstan, USSR by the National Resources Defense Council (NRDC) in the vicinity of the Soviet Test Site makes it possible to compare Rg waves in New England with Rg waves in eastern Kazakhstan.

For the small chemical explosions that are routinely recorded in New England (m_{bLg} 1.0 to 1.5), methods that use Rg as a depth discriminant appear to be applicable to seismograms recorded at

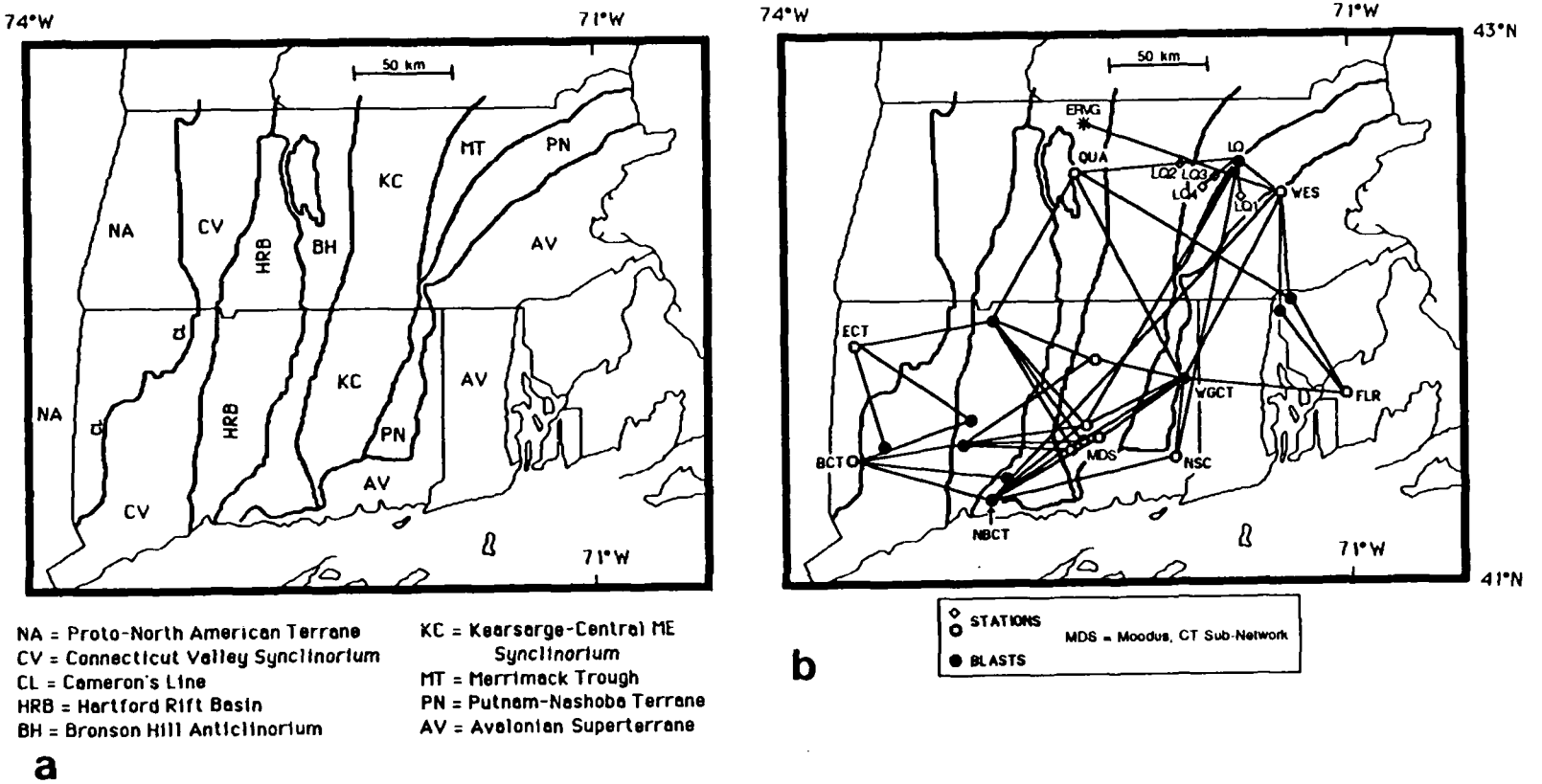

Figure 1: Map of southern New England showing (a) boundaries of lithotectonic terranes and other major geological features of the southern New England Appalachians, and (b) propagation paths of Rg waves discussed in this paper. In (b), solid circles are quarry and construction blasts, open circles are seismic stations of the New England Seismic Network (operated by Weston Observatory), and open diamonds are field stations installed (previous to this study) to record quarry blasts located at the San-Vel quarry in Littleton, MA (LQ). Rg paths are from numerous studies summarized by Kafka (1988). ERVG indicates the epicenter of the Erving, MA earthquake of June 14, 1984.

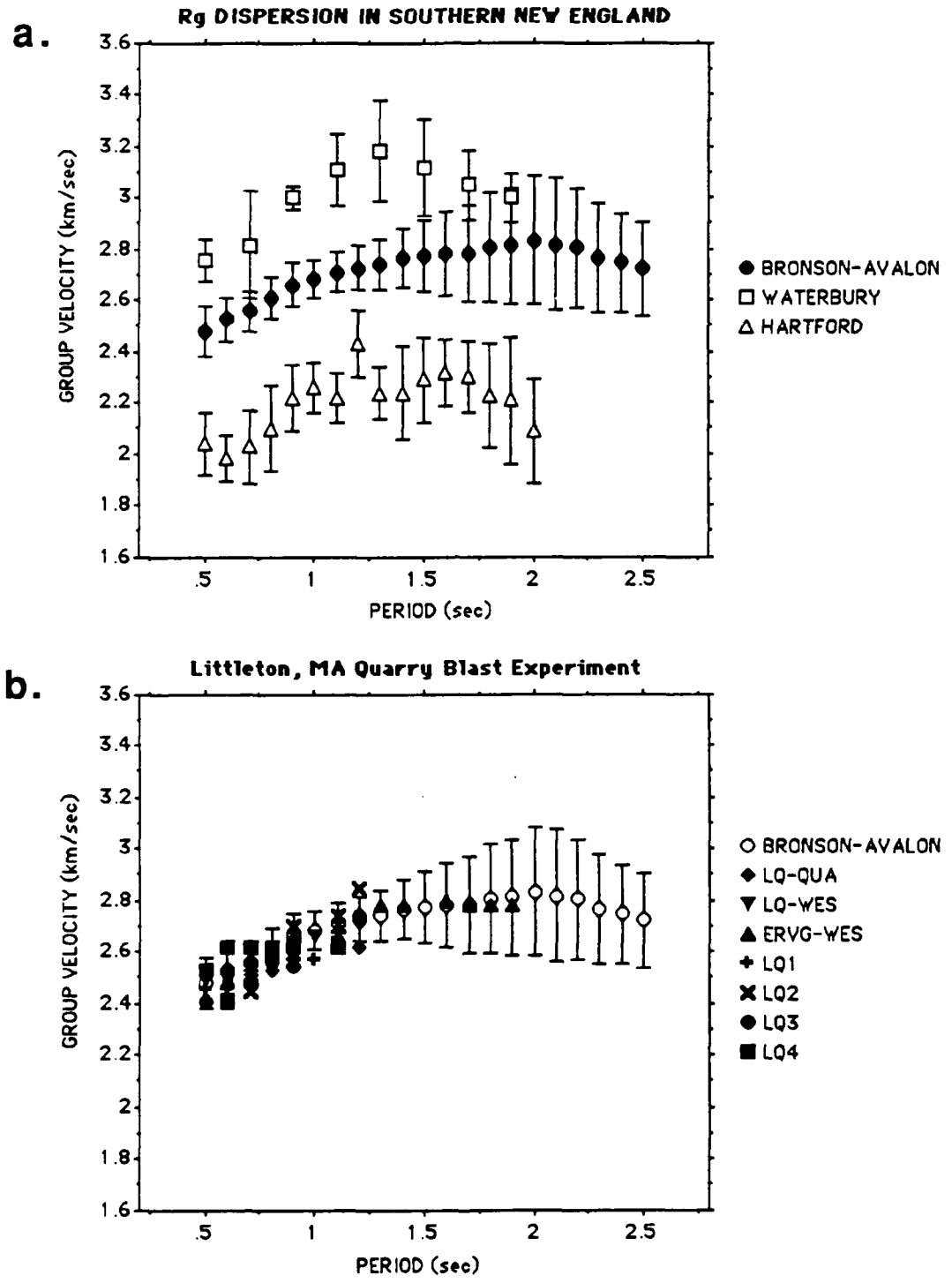

Figure 2: (a) Rg dispersion data for southern New England from various studies summarized by Kafka (1988). Mean and standard deviation is shown for the Bronson-Avalon (BADR), Waterbury, the Hartford dispersion regions. These statistics represent a subset of the paths shown in Figure 1, but all of the data from the paths in Figure 1 are consistent with the classification shown here. (b) Comparison of Rg dispersion from field data recorded in 1987 from the San-Vel quarry with dispersion in the BADR, and with dispersion data for the path from the Erving, MA earthquake to WES.

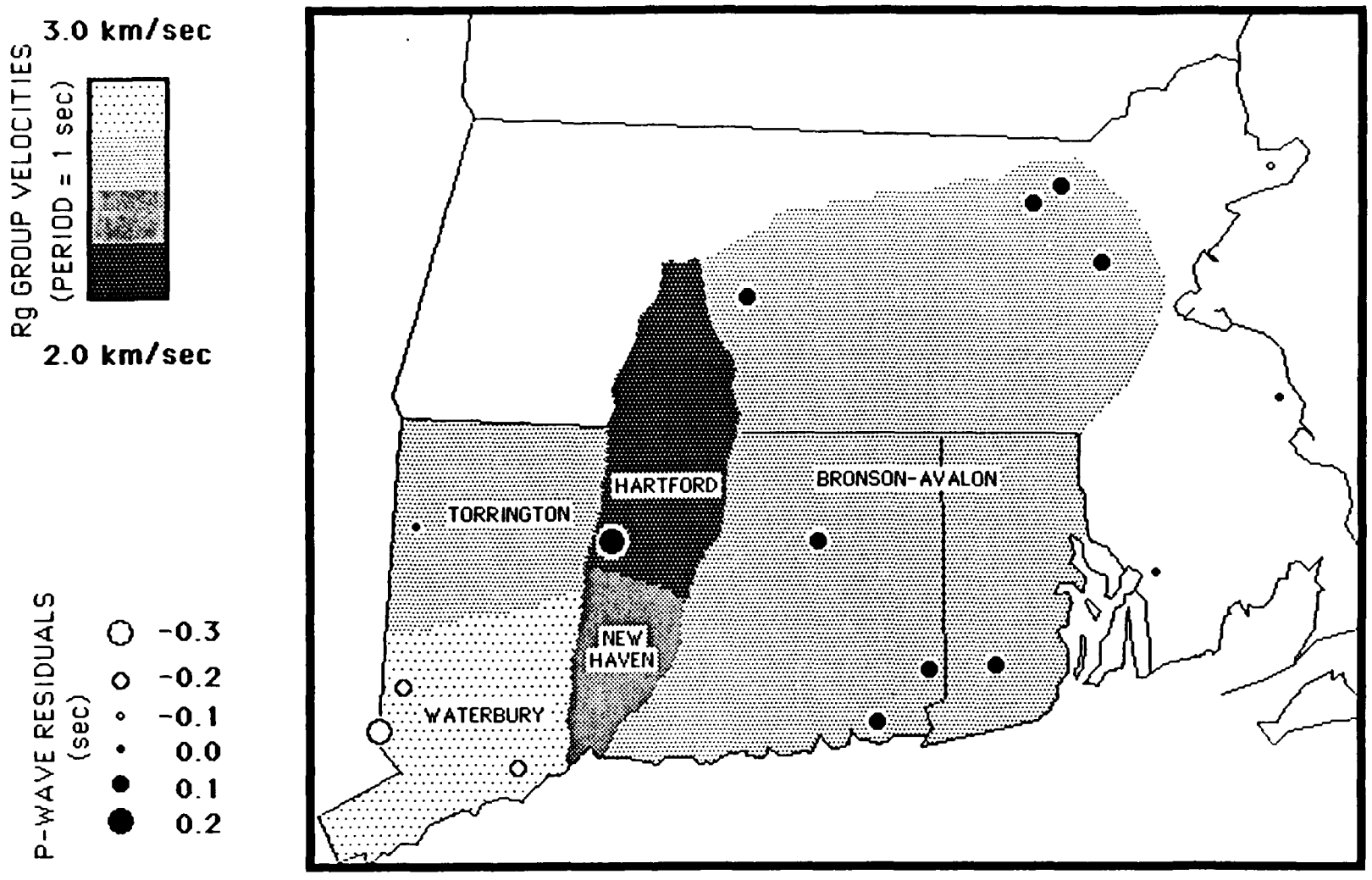

Figure 3: Map of Rg dispersion regions and teleseismic P-wave residuals in southern New England. Teleseismic residuals (indicated by dots and circles) are from Taylor and Toksoz (1979) and Peseckis and Sykes (1979)

epicentral distances ranging from about 20 km to at least 170 km. The presence of Rg on a seismogram indicates that the source occurred in the upper few kilometers of the crust. Thus, the problem of developing a method for using Rg as a depth discriminant is essentially the problem of deciding how to determine if Rg is present on a seismogram. The specific methods that have been developed by the PI for determining the presence of Rg on a seismogram are described in Kafka (1989a and 1989b).

The research that we conducted this summer at the Geophysics Laboratory (GL) was primarily an extension of the PI's research on Rg waves as a depth discriminant. In addition, we investigated other aspects of estimating characteristics of chemical explosions from seismograms recorded at local and regional distances.

II. OBJECTIVES OF THE RESEARCH EFFORT:

a. During the past several years, field data have been recorded from chemical explosions in New England by personnel from Boston College's Weston Observatory in cooperation with personnel from GL as well as a number of other institutions. We have focused our attention on the San-Vel quarry in Littleton, MA (Figures 4, 5 and 6) because that quarry is conveniently located near Weston Observatory and the GL and because the operators of that quarry have been very cooperative. The primary goal of our research this summer was to record additional seismic data from quarry blasts in the San-Vel quarry.

Rg waveforms are affected by variations in the geology and shallow crustal structure along the propagation path as well as by variations in source characteristics. To separate the effects of the source and path on Rg waveforms, we have been investigating Rg wave propagation in New England, with particular attention on southern New England. As part of this summer research project, we

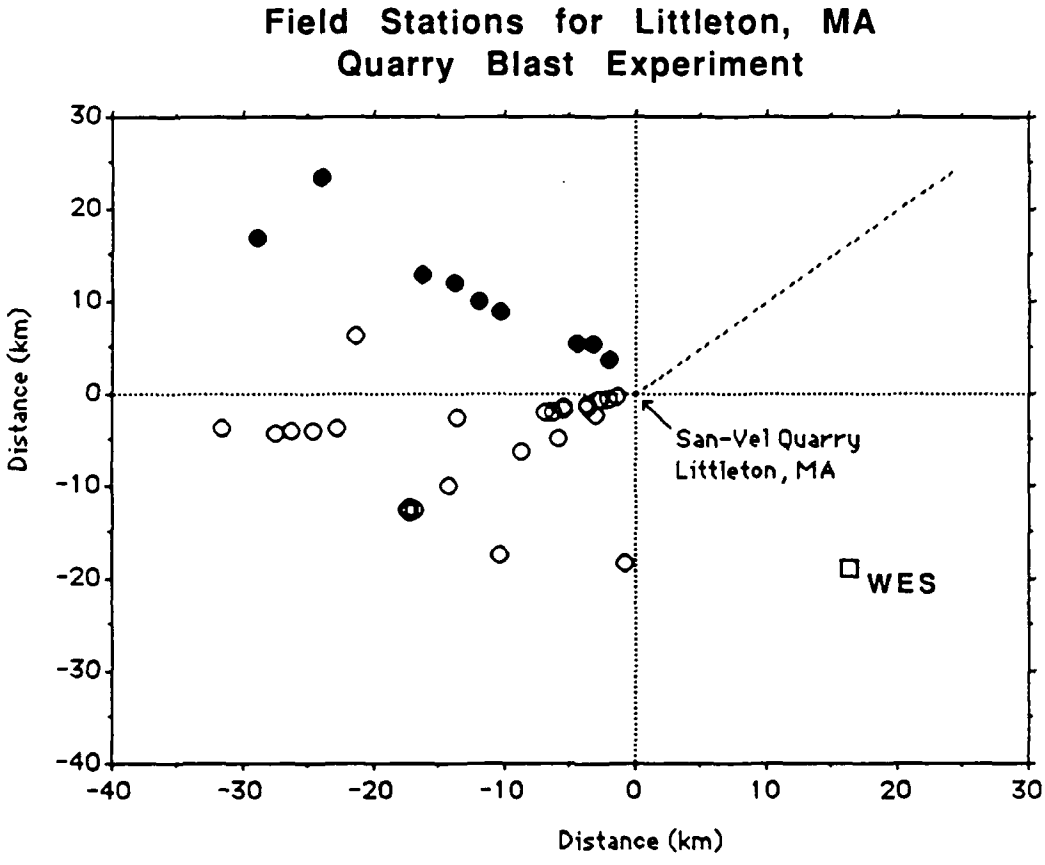

Figure 4. Field stations installed to record quarry blasts detonated at the San-Vel quarry in Littleton, MA. Open circles indicate stations installed in 1987 and 1988. Closed circles indicate stations installed as part of this study. During the last phase of this study, stations were installed along the direction indicated by the dashed line.

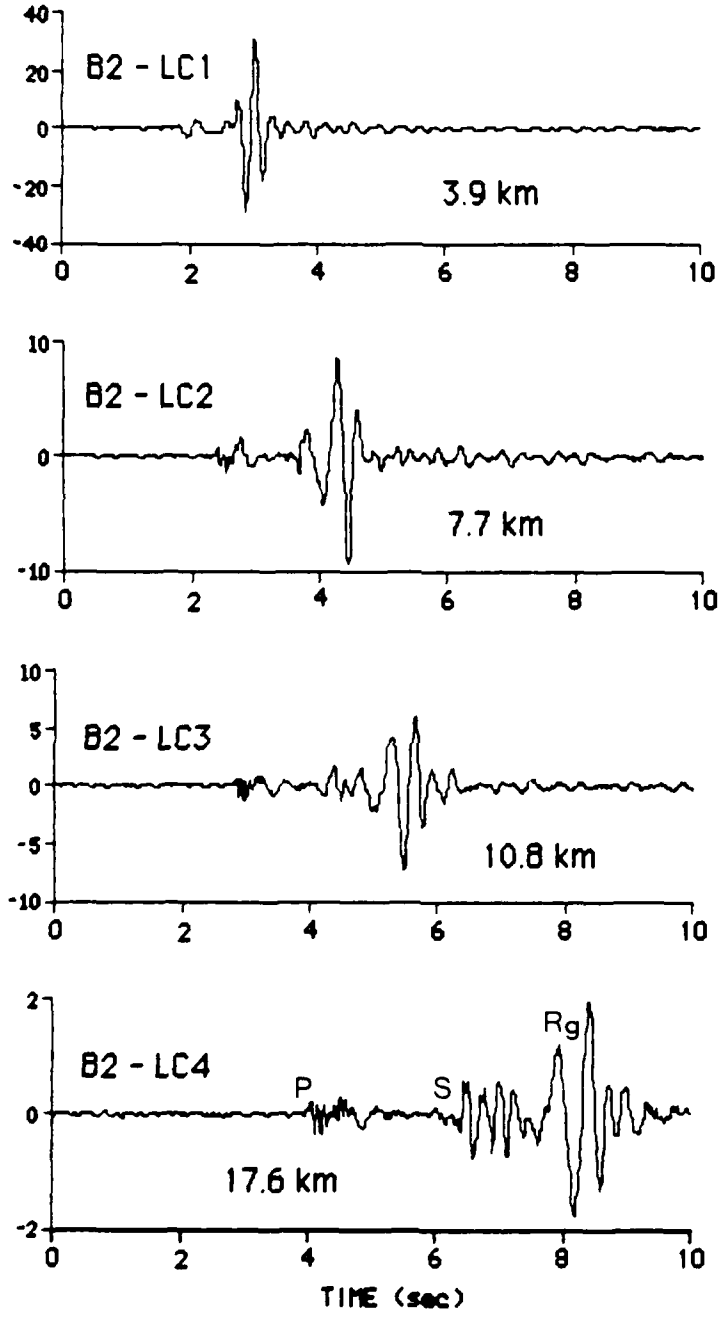

Figure 5: Seismograms of a San-Vel quarry blast recorded as part of a July 21, 1987 field experiment. These seismograms were recorded along a line extending southwest of the quarry. Distances from the shot are given (in km) for each trace.

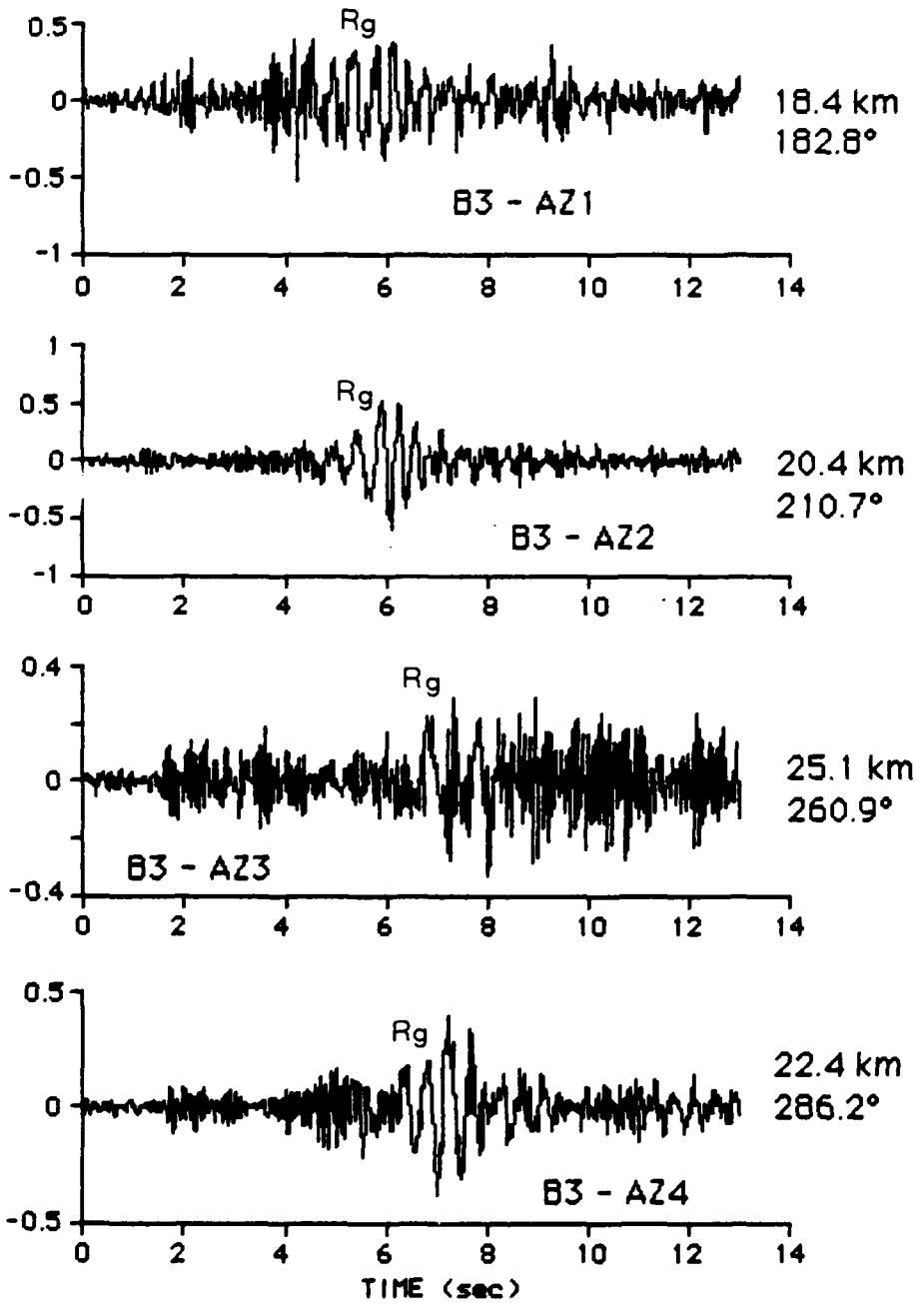

Figure 6. Seismograms of a San-Vel quarry blast recorded as part of a July 29, 1987 field experiment. These seismograms were recorded at four different azimuths around the quarry (at distances of 18 to 25 km) to investigate the radiation pattern of the blast. Azimuths (measured from north) are given (in deg) for each trace.

investigated the variation of Rg waveforms for quarry blasts located at the San-Vel quarry and recorded at NESN station WES (Figure 4). The purpose of this aspect of our research is to get a better idea of the variation of Rg waveforms generated by quarry blasts. To augment the NESN data, we installed field stations near the sources as well as at near-regional distances (about 15 to 40 km from the source).

Another objective of this research was to begin a systematic investigation of all available information regarding the characteristics of quarry blasts and other chemical explosions in New England. We obtained information from blasting logs maintained by quarry operators to begin cataloguing information such as source depth, configuration of blasting holes, total number of pounds of explosives detonated, and maximum number of pounds of explosives per delay. Based on this information, we will be able to investigate the effects of these source characteristics on local and regional seismograms.

b. An important aspect of this research is to compare seismograms of explosions in New England with those recorded in the vicinity of the Soviet Test site in eastern Kazakhstan. We have obtained a data tape from the Center for Seismic Studies which contains digital seismograms recorded at stations operated by the National Resources Defense Council (NRDC) in the vicinity of the Soviet test site. Those seismograms have been transeferred to the Boston College VAX computer, and we are beginning to process the NRDC data using the methods that we are developing for estimating depth from observed Rg waves. The NRDC seismograms will be studied to compare the excitation and propagation of Rg waves in eastern Kazakhstan with that in New England. The work conducted this summer on this aspect of our research is a pilot study for a Research Initiation Program grant proposal.

III.

a. Rg as a Depth Discriminant

The strongest Rg signals recorded by the NESN are generally in the period range of about 0.5 to 1.5 sec. In that period range Rg displacement is essentially confined to depths shallower than 5 km, with most of the Rayleigh wave energy in the upper 2 or 3 km. Sources deeper than about 4 km would not be expected to generate strong Rg signals. Thus, if Rg can be clearly identified on a seismogram, the souce is most likely very shallow (less than 3 km). Observed Rg waves can, therefore, be used as a depth discriminant, provided that the Rg phase can be identified and distinguished from other phases. Kafka (1989a) suggested a method for identifying the Rg phase which involves comparing amplitudes in the arrival-time window where the Rg wave energy is expected to arrive with amplitudes in the arrival-time window where S and Lg waves are expected to arrive. The amplitudes in the various arrival time windows are measured for specific periods using a narrow bandpass filter (NBF) analysis (Dziewonski et al., 1969). This method of identifying Rg is currently being tested for events recorded in New England. An important aspect of this research is to apply the same method to seismograms recorded by the NRDC in the vicinity of the eastern Kazakhstan test site, and to compare the effectiveness of the method in the two different regions.

b. 1989 SFRP/GSRP Experiments in Southern New England

In the beginning of the summer we met with the San-Vel quarry operators to set up procedures for obtaining information about the characteristics of the blasts (such as the amount of explosives detonated, the location of the blasts in the quarry, and the times of the blasts). We also spent time in the field, familiarizing ourselves with the geological characteristics of the area and obtaining

permission from land owners for setting up specific recording sites on their property. Based on these preparatory steps, we recorded blasts detonated on June 26 and July 7 at the San-Vel quarry to test our recording and analysis procedures.

Our first complete field experiment of this summer's project was conducted on July 11 using GL's Terra-Technology DCS-302 portable seismic recorders. We installed a line of portable seismic stations extending northwest of the San-Vel quarry (Figures 4 and 7). During July, we also met with the operators of the San-Vel quarry to obtain detailed information about shot times, locations of the shots within the quarry, and the amount of explosives used in a given shot. Using this information, we are analyzing data recorded in the past from the San-Vel quarry at NESN stations along with data recorded in the field this summer to investigate the relationship between characteristics of the quarry blast sources and characteristics of seismograms recorded at a distance.

By the end of the summer we completed two additional field experiments along the line extending northwest of the San-Vel quarry. We successfully recorded and archived sixteen vertical-component seismograms from nine sites. Horizontal components were also recorded at all sites, but we have so far only archived the vertical components because we are primarily interested in the vertical component of the Rg wave. Additional data were recorded, but some of the field data still remain to be transferred from field data cassettes to the mainframe computer.

Most of the field data recorded from San-Vel quarry blasts are from stations installed at sites to the west of the quarry (Figure 4). NESN station WES routinely records data to the southeast of the quarry. Thus we decided that it was important to complete the azimuthal coverage by installing stations to the northeast of the quarry. Our last experiment of the summer involved recording along

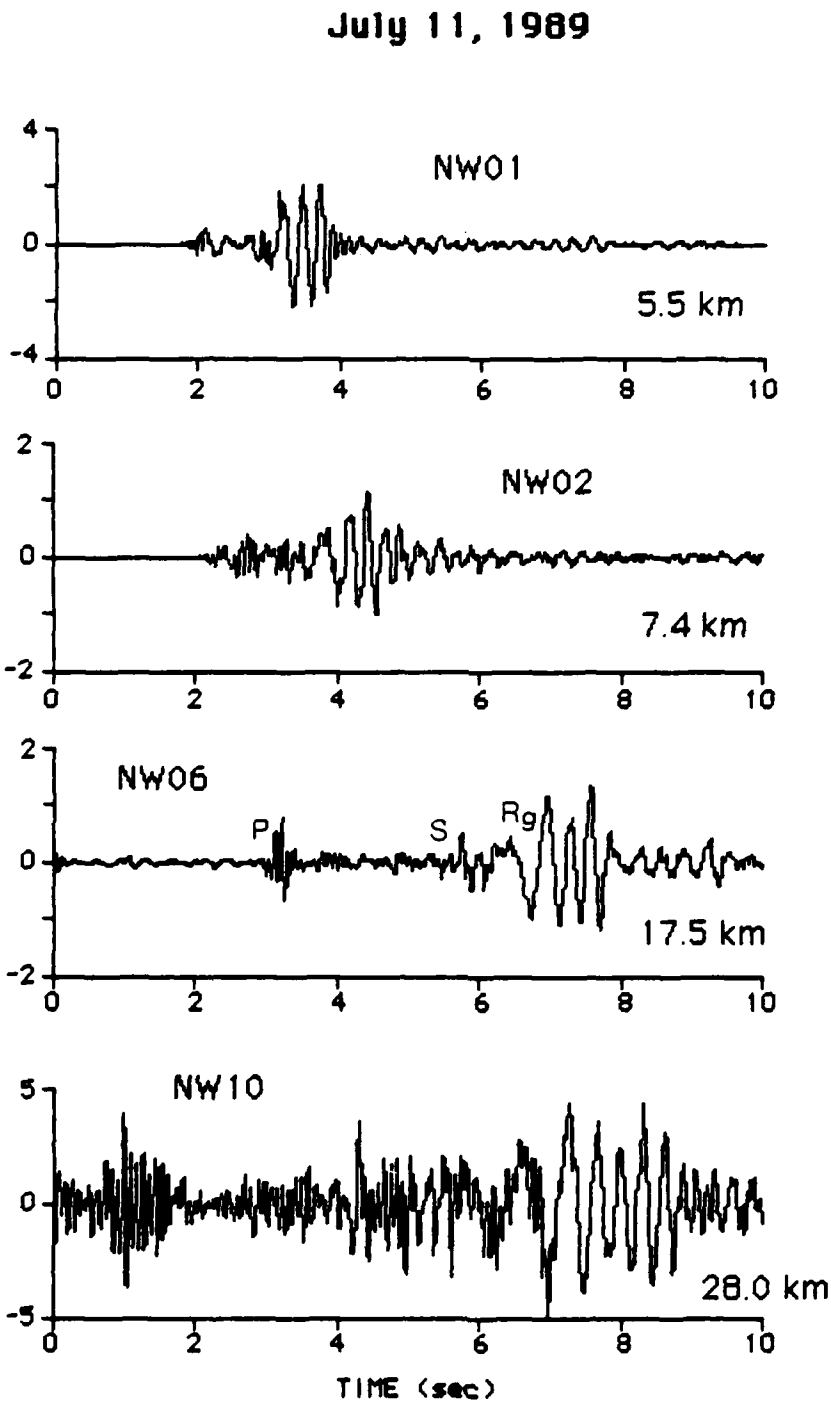

Figure 7: Seismograms of a San-Vel quarry blast recorded as part of a July 11, 1989 field experiment conducted this summer. These seismograms were recorded along a line extending northwest of the quarry. Distances from the shot are given (in km) for each trace.

a line extending northeast of the San-Vel quarry (dashed line in Figure 4). We are currently transferring data recorded at two sites along that line from field data cassettes to the Boston College VAX computer. We hope to continue our work this fall and next spring to obtain more complete recording along that northeast line.

We are also analyzing data recorded at NESN stations from numerous additional blasts detonated at the San-Vel quarry as well as blasts detonated at two other quarries in eastern Massachusetts (the Keating quarries, one located in Lunenburg, MA and the other in Dracut, MA).

c. Seismograms Recorded in Eastern Kazakhstan

We have begun to analyze seismograms of quarry blasts in the vicinity of the Soviet Test Site (obtained from the NRDC data tapes). Figure 8 shows the seismogram of a blast located at the Karagayly quarry recorded at NRDC station KKL (a distance of 27 km). Using a location and origin time for that blast obtained from Thurber et al. (1989), we analyzed the dispersion of the Rg waves using the same methods that we are now routinely using in New England. The results suggest that Rg velocities along that path are quite similar to those of the Bronson-Avalon dispersion region in southern New England (Figure 2 and 3).

To compare the seismogram shown in Figure 8 with seismograms of quarry blasts recorded in New England, we deconvolved the NRDC seismogram to ground motion and then convolved it through the NESN instrument response curve. This gives an estimate of what the Karagayly blast might have looked like if it were recorded by one of the NESN stations. It is interesting that the Karagayly blast, when processed in this manner, looks quite similar to the San-Vel quarry blast. We will process additional seismograms from the NRDC data

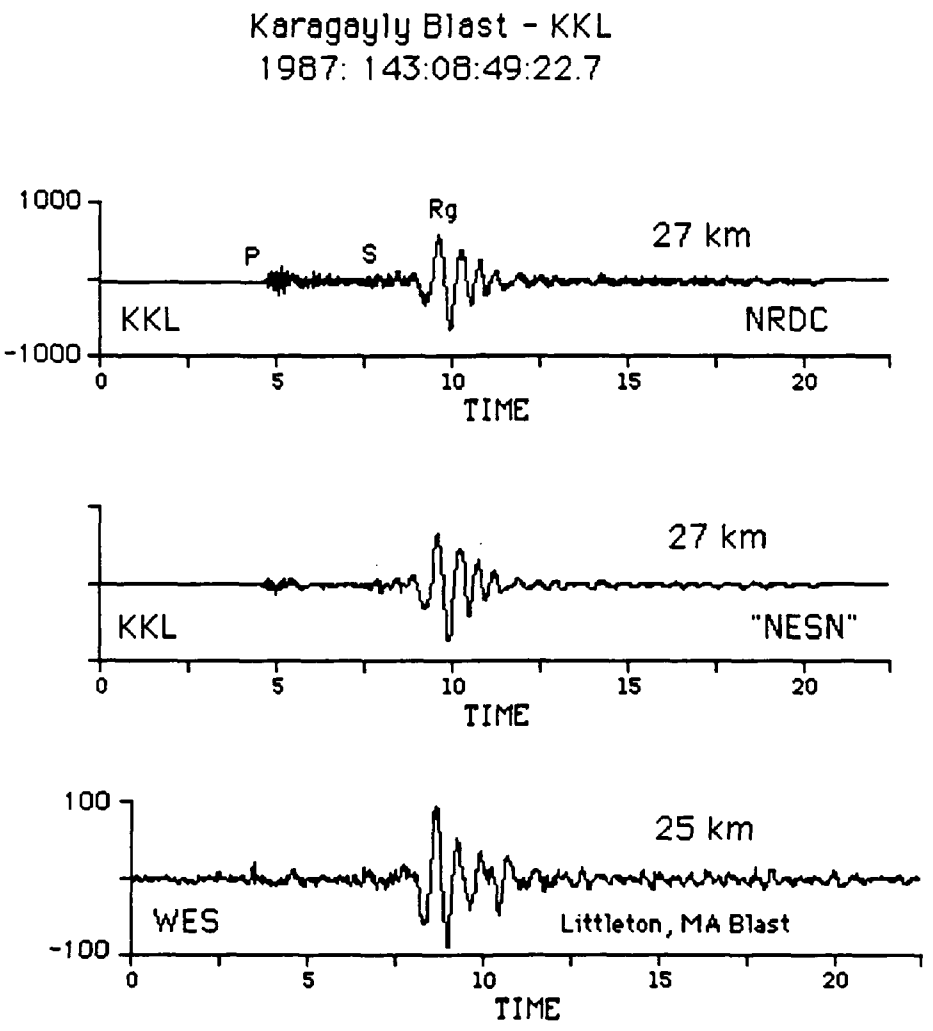

Figure 8: Comparison of seismograms from a quarry blast in eastern Kazakhstan and a quarry blast in New England. The New England quarry blast (lower seismogram) was located at the San-Vel quarry in Littleton, MA and recorded at station WES, a distance of 25 km. The eastern Kazakhstan blast (upper seismogram) was located at Karagayly and recorded at NRDC station KKL (Karkaralinsk), a distance of 27 km. The middle seismogram is the Karagayly blast after being deconvolved to ground motion and then convolved with the NESN instrument response.

tape to investigate the variation of Rg velocities and waveforms in eastern Kazakhstan.

IV. RECOMMENDATIONS:

a. Although there are some practical problems associated with using Rg as a depth discriminant, regional seismograms a generally complex, and it is unlikely that any regional discriminant will work in all cases. It seems clear that, in any region where event depth must be determined from a limited number of seismic observations, some measure of the presence (or absence) of Rg wave energy on seismograms should be considered as a possible depth discriminant.

b. The Rg methods being developed as part of this study should be tested on seismograms of as many blasts and earthquakes as possible. These tests should be conducted on seismic data recorded in New England and in eastern Kazakhstan, as well as in other areas.

c. It is important to continue recording seismograms of quarry blasts in New England to develop an extensive data base that could be used to investigate the characteristics of seismograms recorded from small explosions.

REFERENCES

Dziewonski, A.M., S. Bloch and M. Landisman (1969). A technique for the analysis of transient seismic signals, Bull. Seis. Soc. Am., 59, 427-444.

Kafka, A.L. (1988). Earthquakes, geology and crustal features in southern New England, Seism. Res. Let., 59(4), 173-181.

Kafka, A.L. (1988). Investigation of Rg waves recorded from earthquakes and explosions in New England, 10th Annual Defense Advanced Research Projects Agency/ Air Force Geophysics Laboratory Symposium, San Antonio, TX, May 1988, 24-30.

Kafka, A.L. (1989a). Rg as a depth discriminant for earthquakes and explosions: A case study in New England, 11th Annual Defense Advanced Research Projects Agency/ Air Force Geophysics Laboratory Symposium, Fallbrook, CA, May 1989, 32-39.

Kafka, A.L. (1989b). Rg as a depth discriminant for earthquakes and explosions: A case study in New England, submitted to Bull. Seism. Soc. Am. (accepted pending revisions).

Peseckis, L., and L.R. Sykes (1979). P-wave residuals in the northeastern United States and their relationship to major structural features (abstract). EOS, Trans. Am. Geophys. Un., 60, 311.

Taylor, S.R. and M.N. Toksoz, (1979). Three-Dimensional Crust and Upper Mantle Structure of the Northeastern United States, J. Geophys. Res., 84, 7627-7644.

Thurber, C., H. Given and J. Berger (1989). Regional seismic event location with a sparse network: Application to eastern Kazakhstan, USSR, (preprint), submitted to Journal of Geophysical Research.

1989 USAF-UES SUMMER FACULTY RESEARCH PROGRAM/

GRADUATE STUDENT RESEARCH PROGRAM

Sponsored by the

AIR FORCE OFFICE OF SCIENTIFIC RESEARCH

Conducted by the

Universal Energy Systems, Inc.

FINAL REPORT

A STUDY OF THE WATER VAPOR CATION-NEUTRAL REACTIONS

Prepared by:	C. Randal Lishawa, Ph.D.
Academic Rank:	Assistant Professor
Department and	Department of Physics and Engineering
University:	Utica College of Syracuse University
Research Location:	Geophysics Laboratory (AFSC)
	Space Physics Division
	Spacecraft Interactions Branch (PHK)
USAF Researcher:	Edmond Murad, Ph.D., Rainer Dressler, Ph.D.
	and James Gardner, Ph.D.
Date:	August 14, 1989
Contract No:	F49620-88-C-0053

A STUDY OF THE WATER VAPOR CATION-NEUTRAL REACTIONS

by

C. Randal Lishawa, Ph.D.

ABSTRACT

The charge transfer, atom pickup, and proton transfer cross-sections for the reaction $H_2O^+(D_2{}^{18}O^+) + H_2O(D_2{}^{18}O)$ were measured over center-of-mass energies from approximately 1 eV to approximately 25 eV. The cross-sections for the charge transfer process decreased from about 16 x 10^{-16} cm^2 at 1 eV to about 8 x 10-^{16} cm^2 at 3 eV. The charge exchange cross section then remained constant to 25 eV.

The cross-section for proton transfer reaction behaved similarly with the cross-section falling from about 4 x 10^{-16} cm^2 at 1eV to about 1.0 x 10^{-16} cm^2 at 3 eV. The proton transfer cross section then fell slowly to about 0.3 x 10^{-17} cm^2 at 25 eV.

The cross-section for hydrogen pickup fell from about 1.3 x 10^{-16} at 1 eV to about to 0.2 x 10^{-16} cm^2 at 3 eV before leveling out until 25 eV.

Time-of-flight measurements for the charge exchange products show that the products are produced at near thermal energies. For the atom pickup products, the time-of-flight measurements show distinctly forward peaked distributions at product ion energies at about 80% of the primary ion energy. The proton transfer time-of-flight measurements showed two peaks in the spectra, the first is attributed to a very fast $^{18}OD^+$ product and a second slow (near thermal energy) peak attributed to the transfer product.

Acknowledgements

I wish to thank the Air Force Systems Command, the Air Force Office of Scientific Research and Universal Energy Systems, Inc for the sponsorship and assistance in completing this project.

The summer experience was a very positive experience because of the opportunity for close interaction with the staff of the Spacecraft Contaminations Branch (PHK) of the Space Physics Division of the Air Force Geophysics Laboratory. In particular I would like to thank Dr. Edmond Murad and Dr. Rainer Dressler for many helpful discussions and suggestions on this project. Dr. Jim Gardner has been especially helpful in all aspects of the operation of the equipment and the laboratory and deserves much credit for the success of the project. When equipment problems occurred, Mr. Dick Salter was invaluable in arriving at quick and efficient solutions to the problems. All of these people deserve and receive my heartfelt thanks.

I must also thank my family, my wife Chris and my two sons Adam and Christopher, who were unable to accompany me to the Boston area this summer and had to put up with the many hardships caused by my absence.

A STUDY OF THE WATER VAPOR CATION-NEUTRAL REACTIONS

I. INTRODUCTION

The ceramic tiles providing heat protection for the Space Shuttle absorb large quantities of water prior to launch from Cape Canaveral, Florida. Once in orbit, this water is outgassed into the Space Shuttle environment forming a contaminant cloud that travels with the shuttle throughout the mission and into re-entry. Water vapor is also released into the Space Shuttle environment as a combustion product from thruster firings, as well as evaporating from released waste water. The Space Shuttle velocity of about 7.7 km s^{-1} corresponds to a translational energy of approximately 5.6 eV for the H_2O vapor. The reactions of these energetic chemical entities in the Space Shuttle environment may interfere with experiments being performed during the mission and with communications. The Shuttle Glow is probably the best known example of this type of physical/chemical interaction.

Recent measurements of the plasma surrounding the Space Shuttle have revealed ion densities greater than ambient densities.[1,2] Mass spectroscopic measurements show that the local environment of the Space Shuttle contains relatively large quantities of H_2O^+ and H_3O^+.[1,2] These ions are thought to originate in charge transfer reactions between ambient atmospheric ions and H_2O vapor in the Space Shuttle cloud.[3,4,5,6] The ionic water products formed in such reaction have energies similar to that of the neutral H_2O. These H_2O^+ ions therefore remain in the Space Shuttle environment and may react further with the H_2O vapor in the cloud.

Attempts to model the Space Shuttle local environment[3-6,7] require a knowledge of the relevant rate coefficients as a function of the relative collision energy. In order to study the ion-molecule reaction of H_2O^+-H_2O, reactants are isotopically labelled. The reaction channels examined in this study are:

1) Charge Exchange Reactions

$$H_2O^+ + D_2{}^{18}O \rightarrow H_2O + D_2{}^{18}O^+ \qquad (1a)$$

$$D_2{}^{18}O^+ + H_2O \rightarrow D_2{}^{18}O + H_2O^+ \qquad (1b)$$

2) Atom Pickup Reactions

$$H_2O^+ + D_2{}^{18}O \rightarrow DH_2O^+ + {}^{18}OD \qquad (2a)$$

$$D_2{}^{18}O^+ + H_2O \rightarrow HD_2{}^{18}O^+ + OH \qquad (2b)$$

3) Proton (Deuteron) Transfer Reactions

$$H_2O^+ + D_2{}^{18}O \rightarrow OH + HD_2{}^{18}O^+ \qquad (3a)$$

$$D_2{}^{18}O^+ + H_2O \rightarrow {}^{18}OD + DH_2O^+ \qquad (3b)$$

and

4) the reaction channel leading to the dissociation of the primary ion (collisional dissociation).

$$D_2O^+ + H_2{}^{18}O \rightarrow OD^+ + H_2{}^{18}O + D \qquad (4a)$$

$$D_2{}^{18}O^+ + H_2O \rightarrow {}^{18}OD^+ + H_2O + D \qquad (4b)$$

Previous studies of the water vapor ion-neutral reaction have been conducted by Turner and Rutherford[8], by Ryan[9,10,11], by Fluegge[12], in flowing afterglow studies by Bolden[13], and in ion cyclotron resonance studies by Huntress[14]; but the latter two studies can only determine thermal rate constants. The study by Turner and Rutherford[8] examined the energy dependence of the reaction

$$H_2O^+ + H_2O \rightarrow H_3O^+ + OH$$

which deals with the proton transfer and atom pickup channels simultaneously. Ryan's work on this same reaction is at ion energies less than 1 eV in a high pressure, single-source mass spectrometer and as such does not yield detailed cross section data in the 1 eV to 25 eV energy range examined in this study.

My research interests have been in the area of experimental chemical reaction dynamics using molecular beam techniques. My work on the inelastic collisions of metastable argon has included studies on N_2 and H_2in crossed-supersonic molecular beam systems.[15,16] My work has also included the application of classical trajectory methods to computer simulations of ion-dipole collisions. Other work has included INDO calculations on the structure of the SiO_4 molecule and the development of microprocessor-based air monitoring systems for the U. S. Army.

II. Objectives

This study provides the information on the translational energy dependence of the reaction cross sections, as well as information on the kinetic energy

distribution of the products for the ion-neutral reactions of H_2O that may then be used in theoretical models of the Space Shuttle environment.

III. Experimental

1. General

The experimental apparatus consists of a modification of a tandem mass spectrometer described previously[17,18,19] and illustrated in Figure 1. An electron-impact source operating at 35 V is used to produce the primary ion beam (H_2O^+, $D_2{}^{18}O^+$, or D_2O^+). The ionized gas is then accelerated through a 150 V potential and passed through a Wien velocity filter (Colutron Research), producing a mass selected ion beam.

Decelerating potentials are then applied to slow the ion beam to the desired translational energy before entering the collision cell. The collision cell is a 2.7 mm long gold-plated cell. The "target gas" water vapor ($D_2{}^{18}O$, H_2O or $H_2{}^{18}O$) is introduced into the collision chamber at pressures less than 1.33 Pa (10^{-3} Torr) to provide single-collision reactions. The target gas pressure is measured with a capacitance manometer (MKS Baratron 390H).

The translational energy of the primary beam is measured by ramping a retarding potential on a set of grids located after the collision cell. This signal is then smoothed before taking the derivative of the retardation curve. The beam energy is taken as the minimum of the derivative curve.

The reaction cross sections for reactions (1a, 2a, and 3a) are measured as a function of electron energy in order to check for the presence of undesired excited metastable states in the primary beam. As the measured cross sections are constant with respect to source electron energy, we do not believe that significant numbers of metastables species are present in primary beam.

There has also been a study[20] of the lifetimes of excited states ($^1A \rightarrow {}^1B$) of the H_2O^+ ion showing the lifetimes to be about 800 ns for all of the measured states. This is at least an order of magnitude less than the time required for the ion to travel from the source to the collision cell. This also indicates that the metastable population in the beam should be negligible.

The product ions exiting the collision cell are focused by a hemispherical grid onto the entrance to a 22.5 cm ELF quadrupole mass spectrometer. The mass-analyzed ions are then detected with a channeltron electron multiplier, and the detector pulses are amplified before being counted and stored by an AT-type microcomputer-based data acquisition system.

APPARATUS

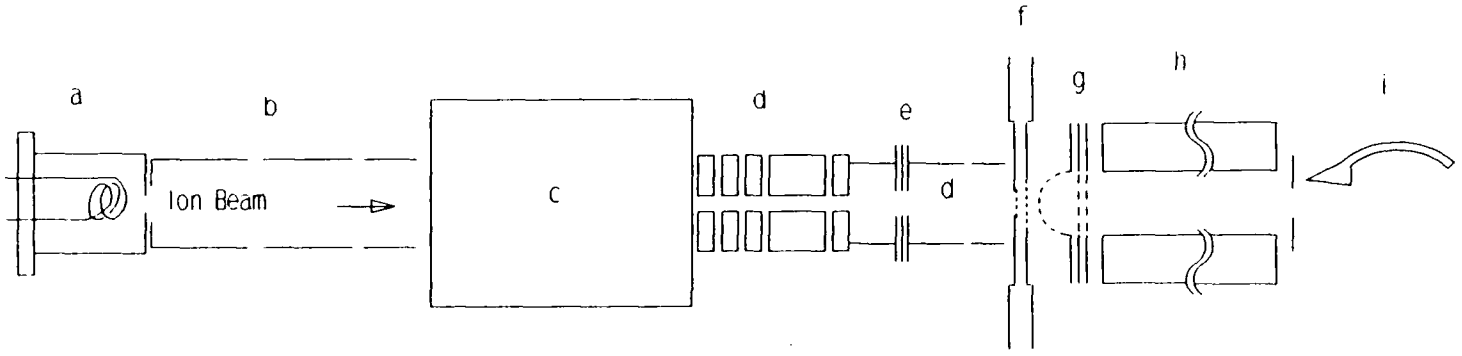

Figure 1. Schematic illustration of the tandem mass spectrometer used in these experiments.

a) Ion Source
b) Acceleration Lens
c) Wien Velocity Filter
d) Deceleration Lenses
e) Deflector Electrode
f) Collision Chamber
g) Collection and Acceleration Grids
h) Quadrupole Mass Filter
i) Channel Electron Multiplier

note: Elements not drawn to scale

All spectra were obtained at the lowest resolution consistent with resolving the desired mass peaks. This reduces potential problems associated with mass-dependent detector efficiencies. Figure 2 is a sample of the mass spectra obtained in these experiments.

As there is no detectable attenuation of the primary beam, the cross section is calculated from

$$\sigma = I_s/I_p nl$$

where I_s and I_p are the intensities of the secondary ion signal and the primary beam signal, respectively, n is the target gas density, and l is the effective interaction length. The ratio of I_s to I_p is obtained by taking the ratio of the integrated areas of the relevant mass peaks in the mass spectra.

IV. RESULTS

1. Charge Exchange Reactions.

The energy dependence of the cross section is shown in Figure 3 for the two charge exchange reactions (1a and 1b). As the center of mass energy increases, the cross section shows a rapid decrease until an energy of about three electron Volts (eV) and then falls slowly over the rest of the energy range studied.

The time-of-flight spectra (Figure 4) show a single broad peak at all energies studied with product translational energies of about 0.1 eV. The peaks exhibit the broad distributions in time characteristic of thermal ions.

2. Atom Pickup Reactions.

The energy dependence of the cross section is shown in Figure 5 for the two atom pickup reactions (2a and 2b). These cross sections also fall off very rapidly as the energy increases to about three eV, and then decline slowly (or remain constant) over the remaining energies studied.

The time-of-flight spectra (Figure 6) for these reaction products are very sharply peaked, with temporal distributions only slightly wider than the primary beam distribution. The peaks in the distributions lie at approximately 80% of the primary ion energy for reaction 2a and near 90% for reaction 2b.

3. Proton (Deuteron) Pickup Reactions.

The energy dependence of the cross section is shown in Figure 7 for the two charged-particle pickup reactions (3a and 3b). The cross sections here also fall off rapidly with increasing energy up to about three eV and then level off over the rest of the energy range studied.

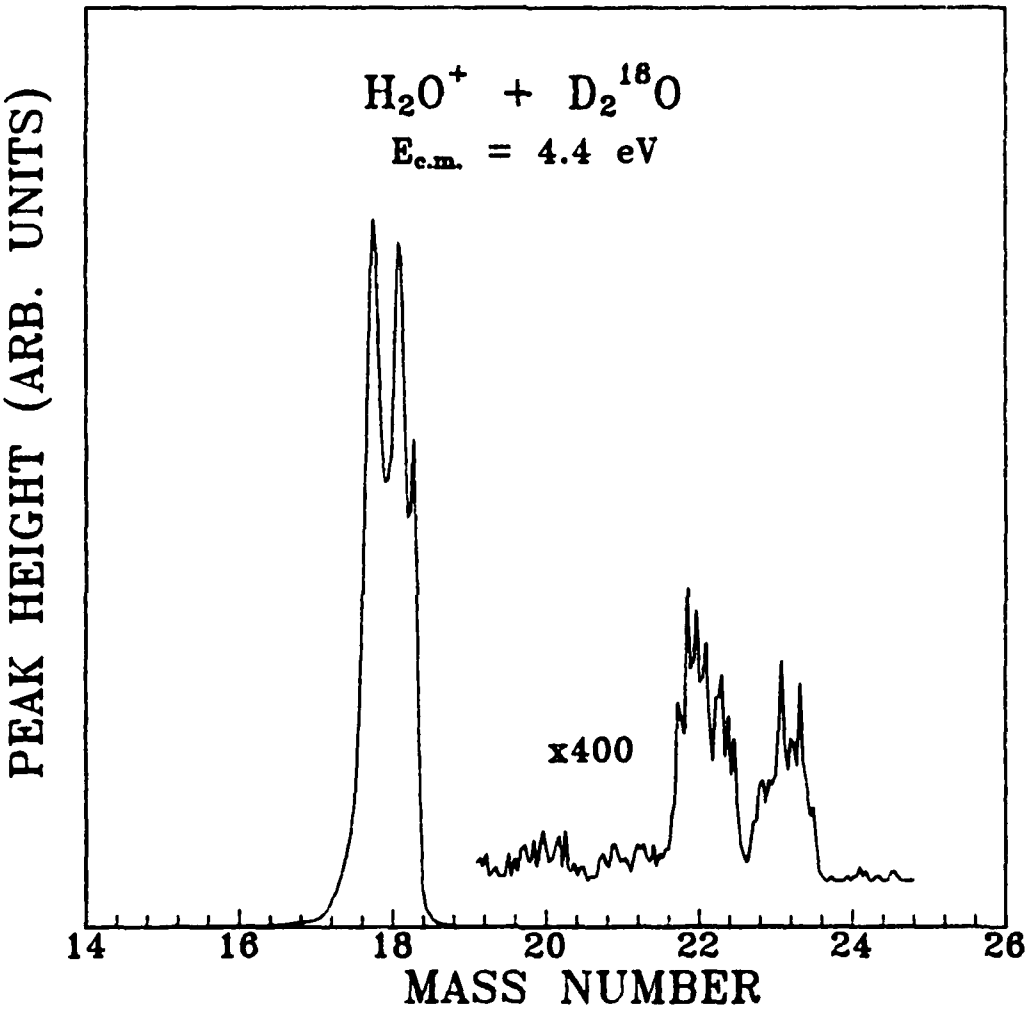

Figure 2. Example of mass spectra used to calculate the cross sections measured in these experiments.

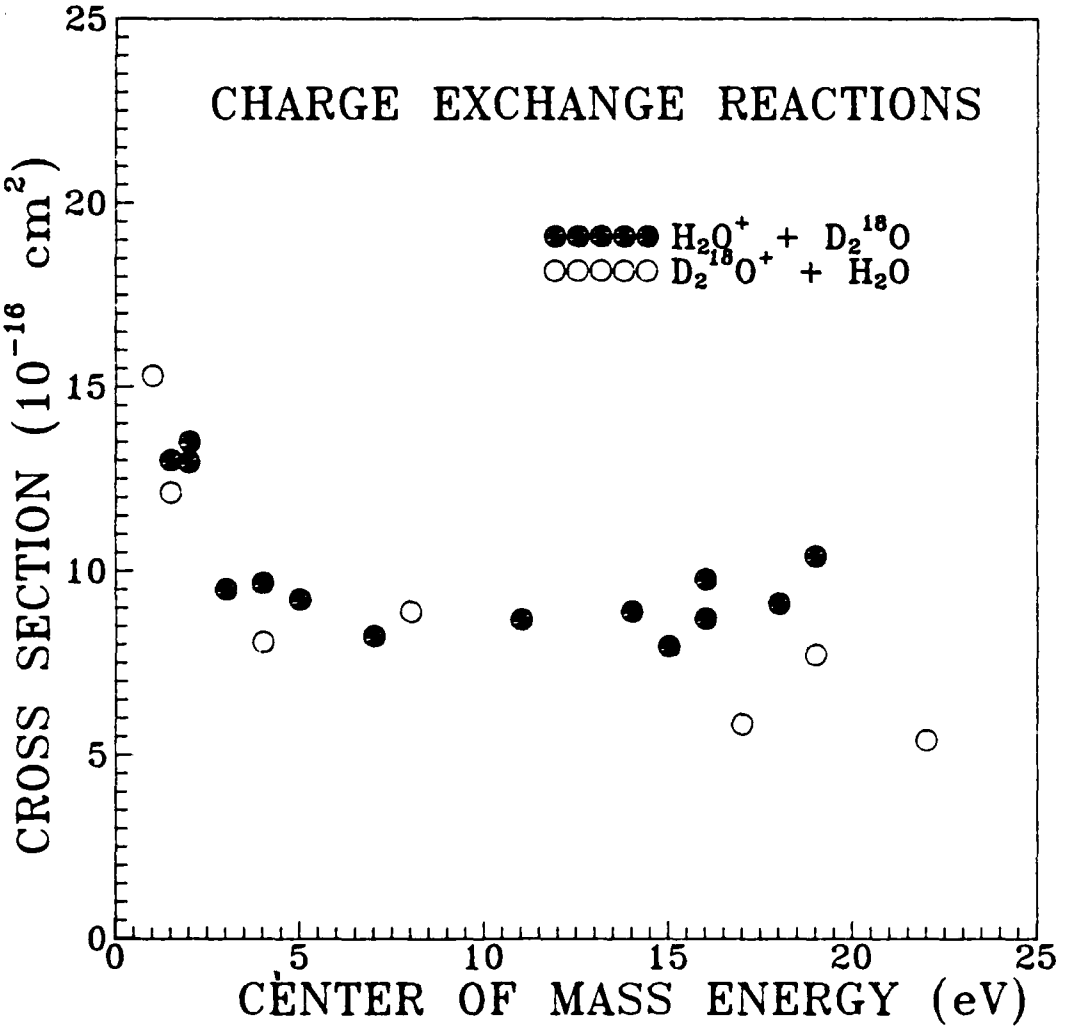

Figure 3. The energy dependence of the charge exchange cross section. The filled-in circles are for reaction 1a. The open circles are for reaction 1b.

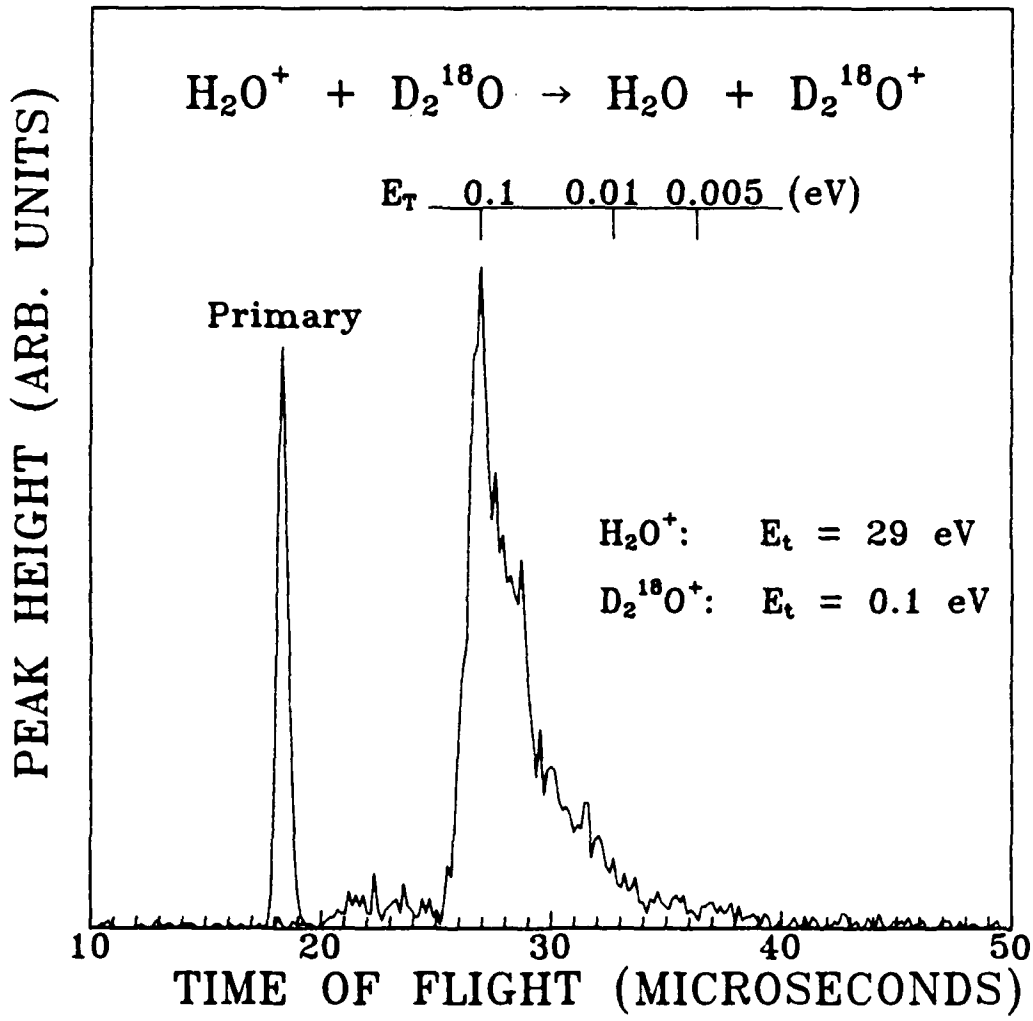

Figure 4. The time of flight spectra for the charge exchange product showing the broad time distribution and low kinetic energy characteristic of thermal ions.

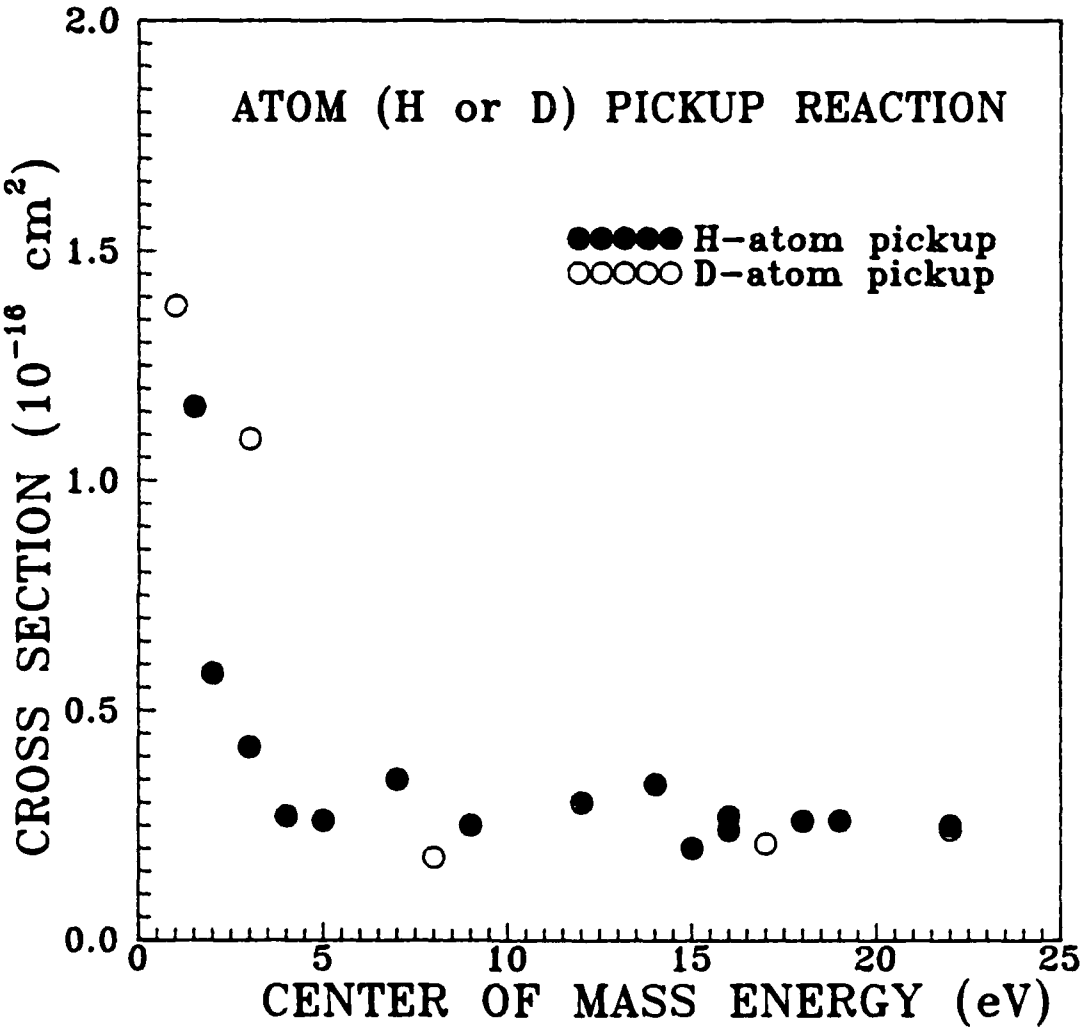

Figure 5. The energy dependence of the atom pickup cross section. The filled-in circles are for reaction 2a. The open circles are for reaction 2b.

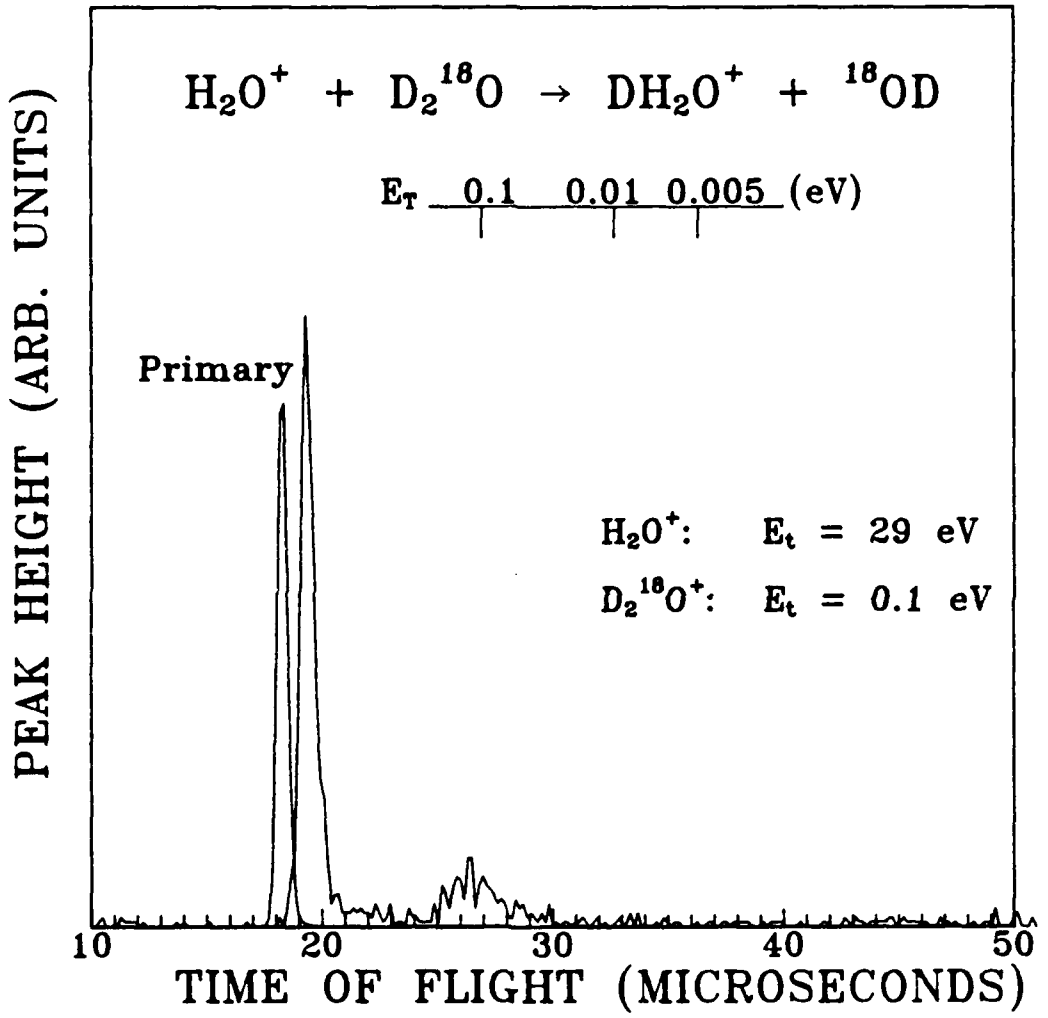

Figure 6. The time of flight spectra for the atom pickup product showing the narrow time distribution and high kinetic energy characteristic of forward scattered ions.

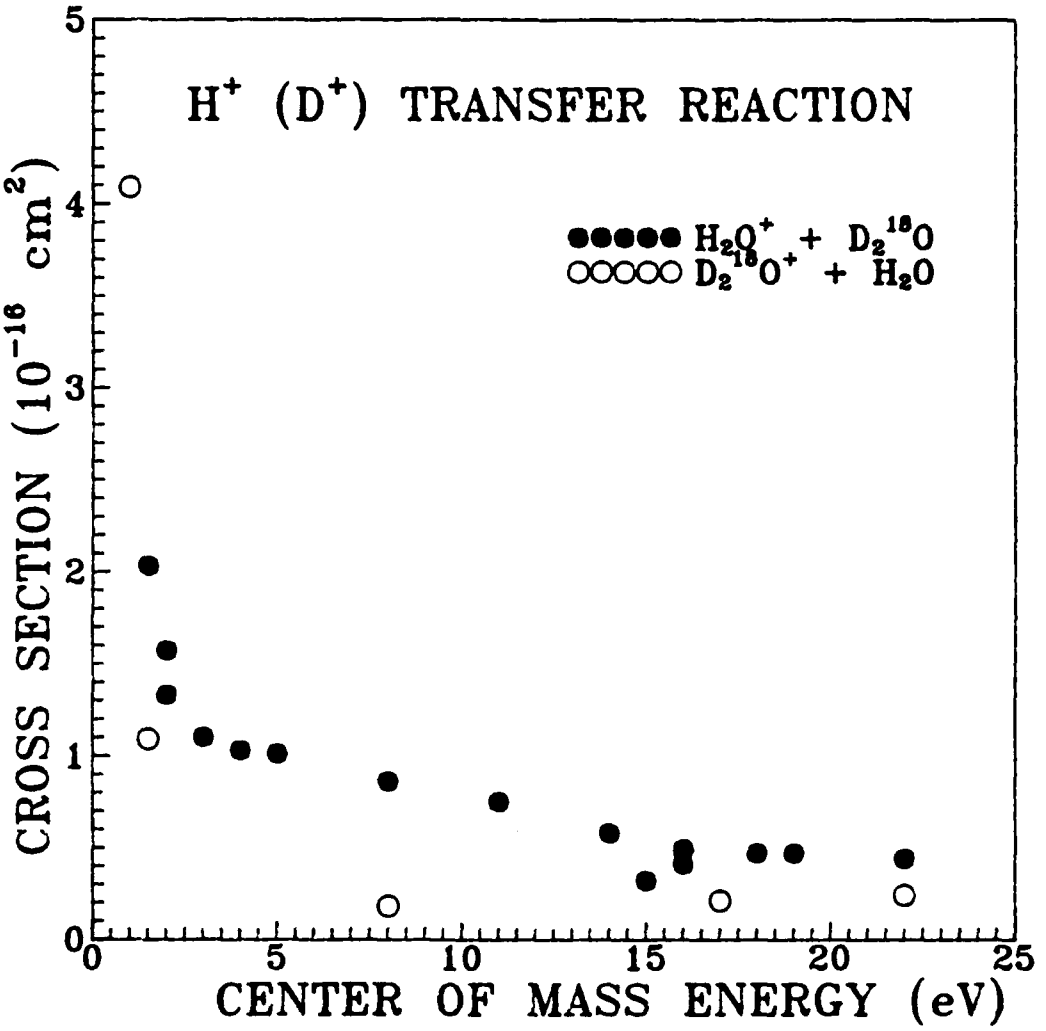

Figure 7. The energy dependence of the proton (deuteron) exchange cross section. The filled-in circles are for reaction 3a. The open circles are for reaction 3b.

The time-of-flight spectra (Figure 8) for the pickup reaction show broad distributions for reaction 3a with the product translational energies about 0.085 eV. For reaction 3b (Figure 9), where the product ion is DH_2O^+ (mass 20), we again see the broad thermal peak, but at primary ion energies above 8 eV, we see a second peak growing in with a very sharp, very fast (arrival time approximately that of the primary beam). We associate this peak with the appearance of a new reaction channel (the ion dissociation channel) yielding $^{18}OD^+$ (mass 20).

4. Ion Dissociation

The complete energy dependence of the cross section for this channel has not been determined, but a three values of the cross section in the energy range have been measured. These values are given in Table I

Ion Energy	Cross Section
13 eV	5.0×10^{-17} cm^2
18 eV	8.5×10^{-17} cm^2
29 eV	6.5×10^{-17} cm^2

The time-of-flight spectra show an ion velocity distribution nearly identical to that of the primary ($D_2{}^{18}O^+$) beam. The product ion beam may even be slightly faster than the primary beam (although still at a lower energy). The possibility that this peak is due to primary beam leaking through the mass filter was checked by removing the water vapor from the collision cell and rechecking the time of flight spectra. No peak was observed when the target gas was absent. We conclude that this very fast product must be the result of a reaction between the primary and target gases.

IV. DISCUSSION

The results of these experiments can be explained in terms of the spectator stripping model[21]. This model describes the system in which a light particle (X), such as an a proton or hydrogen atom, is transferred from a parent particle (A-X) to a second receiver particle (B) with no transfer of momentum accompanying the transfer of mass. This can be written symbolically as

$$A\text{-}X + B \rightarrow A + B\text{-}X$$

For the case where the parent molecule is moving past the receiver, the ratio of

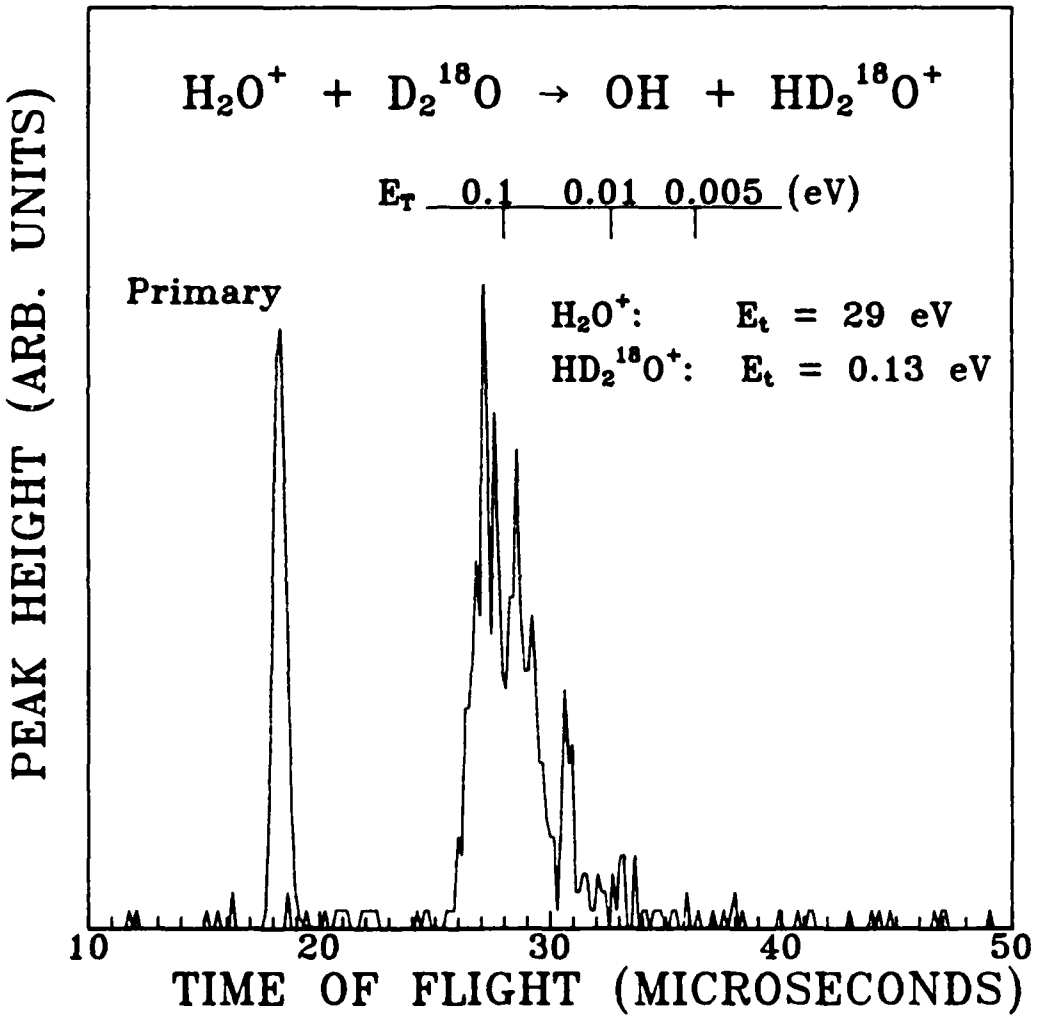

Figure 8. The time of flight spectra for the proton (deuteron) exchange product showing the broad time distribution and low kinetic energy characteristic of thermal ions.

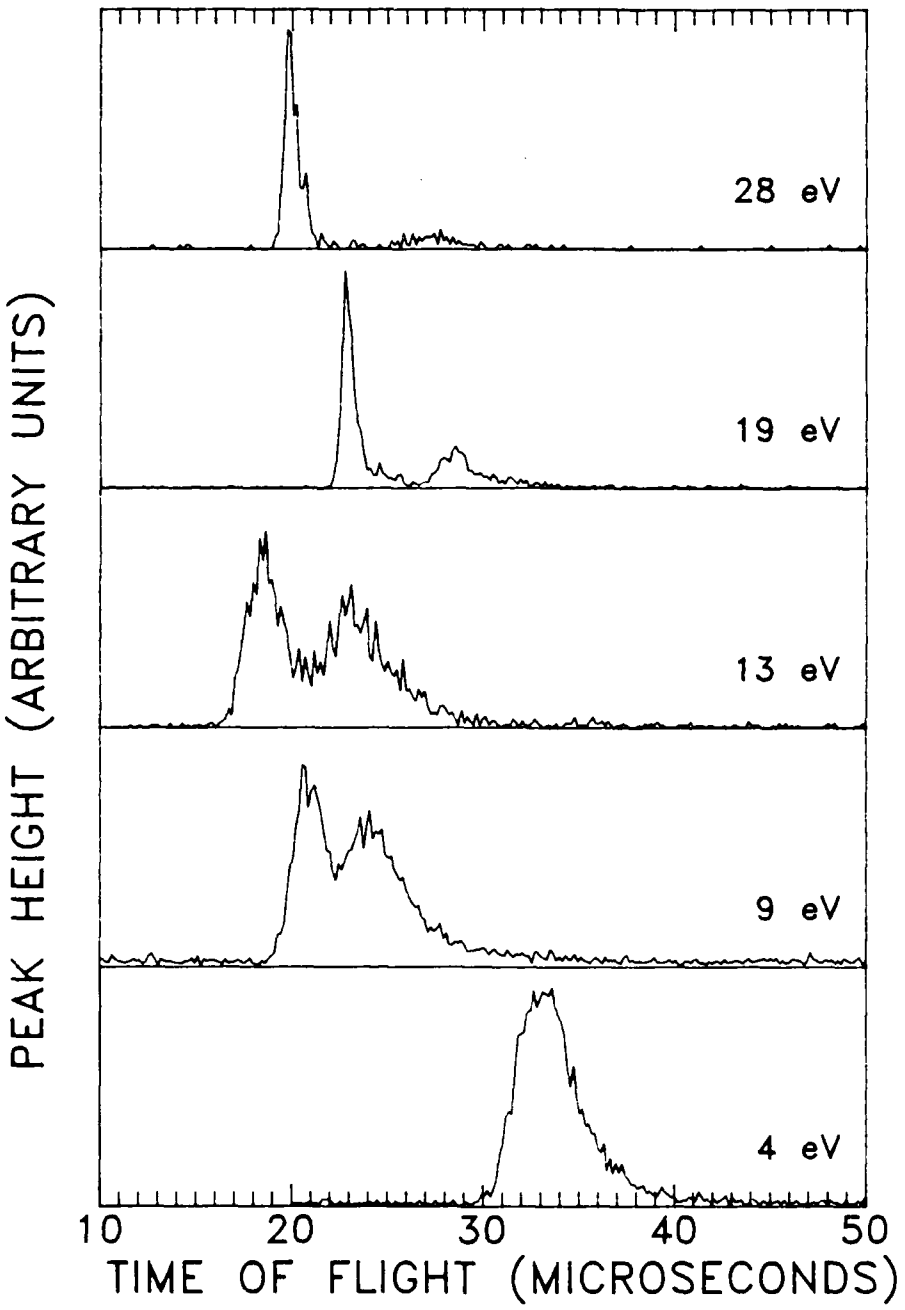

Figure 9. The time of flight spectra showing the onset of the fast peak associated with the ion dissociation channel.

the translational energy of the receiver to the translational energy of the parent is given by the simple equation

$$\frac{E_r}{E_p} = \frac{m_A\, m_B}{m_{AX}\, m_{BX}}$$

This simple model predicts the ratio of the translational energy of the reactant H_2O^+ ion to the translational energy of the product DH_2O^+ ion in the atom pickup reactions (2a) to be 0.82. The observed ratio averages 0.80 and varies from 0.84 to 0.74 over the center-of-mass energy range 16 eV to 2.7 eV, with the higher energy data nearest the predicted value.

The prediction for reaction 2b is 0.90 with observed values ranging from 0.7 at low primary ion enrgies (9 eV) to nearly 1.0 at high primary ion energies (49 eV) with an average value of 0.86, in good agreement with theory.

For a second case, where the parent molecule is the stationary spectator and the second molecule (B) is moving with known energy, this mechanism predicts that the translational energies of the product ions should be approximately thermal, as is observed in the case the proton (deuteron) transfer reactions (3a and 3b).

The ionic dissociation channel also fits the Spectator Stripping model. In this channel, the $^{18}OD^+$ product continues to travel after collision with essentially the same, or even slightly higher, speed as the primary. This is shown in Figure 14, where the time-of-flight of the product is slightly faster than the primary with essentially the same distribution of speeds as the primary beam.

VI. SUGGESTIONS FOR FURTHER RESEARCH

Further work on this system should follow two lines. First, further experimental work should be conducted on the ion dissociation channel observed in this study. This could possibly be accomplished by the use of other isotopes of water to study the reaction

$$D_2O^+ + H_2{}^{18}O \rightarrow OD^+ + H_2{}^{18}O + D$$

In association with this study, careful consideration of the effect the collision cell potential has on the reaction should be included, as it was discovered that at the higher potential, significant amounts of the primary beam would leak through the mass filter. Is this because of lower selectivity at the higher translational energies? If so, how does this affect the cross section measurements at higher translation energies?

A second line of investigation that should be followed is the application of the spectator stripping model to the description of the product ion translational energy. In particular, the model has been reformulated by Herman et al.[22] to take into account the long-range intermolecular forces which will accelerate the ions as they approach and depart the reaction site. This formulation does not in itself provide direct information as to the time-of-flight distribution of the ions in any particular experiment. Determination of the time of flights using this model can be done by calculating of classical trajectories using the various dipole orientations and experimental geometries as the input.

VI. REFERENCES

1. R.S. Narcisi, E. Trzcinski, G. Federico, L. Wlodyka, and D. Delorey, AIAA-83-2659, 183 (1983).

2. J.M. Grebowsky, M.W. Pharo, III, H.A. Taylor, Jr., and I.J. Eberstein, Planet. Space Sci., 35,501 (1987).

3. D.E. Hunton and J.M. Calo, Planet. Space Sci., 33, 945 (1985).

4. E. Murad, Planet. Space Sci., 33, 421 (1985).

5. D.E. Hastings, N.A. Gastonis, and T. Mogstad, J. Geophys. Res., 93, 273 (1987).

6. G.E. Caledonia, J.C. Person, and D.E. Hastings, J. Geophys. Res. to be published.

7. J.B. Elgin, M.M. Perviaz, D.C. Cooke, M. Tautz, and E. Murad, J. Geophys. Res. Lett., 16, 139 (1989).

8. R.B. Turner and J.A. Rutherford, J. Geophys. Res., 73,6751 (1968).

9. K.R. Ryan, J. Chem. Phys., 52, 6009 (1970).

10. K.R. Ryan and J.H. Futrell, J. Chem. Phys., 42. 824 (1965).

11. K.R. Ryan and J. H. Futrell, J. Chem. Phys., 43, 3009 (1965).

12. R.A. Fluegge, J. Chem. Phys., 50, 4373 (1969).

13. R.C. Bolden and N.D. Twiddy, Faraday Disc., 53, 192 (1972).

14. W.T. Huntress and R.F. Pinnizzotto, J. Chem. Phys., 59, 4742 (1973).

15. C.R. Lishawa, W. Allison, and E.E. Muschlitz, Jr., J. Chem. Phys., 77, 5885 (1982).

16. C.R. Lishawa, J.W. Feldstein, T.N. Stewart, and E.E. Muschlitz, Jr., J. Chem. Phys., 83, 133 (1985).

17. W.B. Maier II and E. Murad , J. Chem. Phys., 55, 2307 (1971).

18. R.A. Dressler, J.A. Gardner, R.H. Salter, F.J. Woldarczyk, and E. Murad, submitted to JCP.

19. J.A. Gardner, R.A. Dressler, and E. Murad, Technical Report for Geophysics Laboratory (in preparation).

20. P. Erman and J. Brzozowski, Phys. Lett., 46A, 79 (1973).

21. Heglein, Lacmann, and Jacobs, Ber. Bunsenges, Physik. Chem., 69, 279, (1965).

22. Z. Herman, J. Kerstetter, T. Rose, and R. Wolfgang, Disc. Faraday Soc., 44, 123, (1967).

1989 USAF-UES SUMMER FACULTY RESEARCH PROGRAM/

GRADUATE STUDENT RESEARCH PROGRAM

Sponsored by the

AIR FORCE OFFICE OF SCIENTIFIC RESEARCH

Conducted by the

Universal Energy Systems, Inc.

FINAL REPORT

ACIDITIES OF IRON HYDRIDE AND VARIOUS TRANSITION-METAL COMPOUNDS; REACTIONS OF IRON AND IRON CARBONYL ANIONS

Prepared by:	Amy E. Stevens Miller and Thomas M. Miller
Academic Rank:	Assistant Professor, Professor
Department and	Chemistry & Biochemistry, Physics & Astronomy
University:	University of Oklahoma
Research Location:	Geophysics Laboratory, Ionospheric Physics Division
USAF Researcher:	Dr. John F. Paulson
Date:	1 August 1989
Contract No:	F49620-88-C-0053

ACIDITIES OF IRON HYDRIDE AND VARIOUS TRANSITION-METAL COMPOUNDS; REACTIONS OF IRON AND IRON CARBONYL ANIONS

by

Amy E. Stevens Miller and Thomas M. Miller

ABSTRACT

Four projects were carried out:

1. A number of transition-metal acids were synthesized, and their gas phase acidities were bracketed by determining proton transfer reaction rates with of negative ions of known basicity. One of these compounds, $HCo(PF_3)_4$, proved to be stronger than any other known acid in the gas phase.

2. Proton transfer rates for Fe^- reacting with a variety of acids were measured. The gas phase acidity of FeH was determined to be between that of propionic acid (ΔH_{acid} = 347.3 ± 2.3 kcal/mol) and acetic acid (ΔH_{acid} = 348.5 ± 2.3 kcal/mol).

3. Ion-molecule reaction rate coefficients were measured for $Fe(CO)_n^-$ (n = 0-4) interacting with methyl halides. Nucleophilic displacement occurs when energetically possible, yielding $Fe(CO)_nCH_3$ and a halide anion. If this reaction channel is energetically closed, ligand exchange may occur. The reaction rates measured in projects 2 and 3 are the first to be measured with the atomic iron negative ion.

4. Collision-induced dissociation of $Fe(CO)_n^-$ (n = 1-4) with He was studied in an attempt to determine the carbonyl bond energies. Because of the difficulty of calibrating the collision energy scale, the results are estimated to be uncertain by about 0.5 eV.

Acknowledgments

We wish to thank the Air Force Systems Command and the Air Force Office of Scientific Research for sponsorship of this research, and Universal Energy Systems for administering the program. This research has also been sponsored by the National Science Foundation (EPSCoR), and the Petroleum Research Fund administered by the American Chemical Society (to A.E.S.M.).

We especially thank our colleagues at the Geophysics Laboratory, Drs. John Paulson, Albert Viggiano, Robert Morris, and Mr. Fred Dale, and Dr. Michael Henchman of Brandeis University. We could not have carried out this work without benefit of the discussions, assistance, and interest they donated.

I. INTRODUCTION:

The authors of this report carry out research in chemical physics at the University of Oklahoma. One of us (A. E. S. M.) is a chemist specializing in gas-phase ion-molecule reactions of transition-metal complexes, and has extensive experience in preparative inorganic and organometallic chemistry. The other of us (T. M. M.) is a physicist specializing in low energy electron interactions with atoms and molecules. Both of us have had experience measuring ion-molecule reaction rate coefficients, and in determining the electron binding energy and structure of negative ions.

The research described in this report is an outgrowth of our mutual interests. The transition-metal acids described herein are very strong acids in the gas phase, and are of possible use to the USAF as electron scavengers in plasmas (for example, in rocket plumes). At the University of Oklahoma we have been making measurements of electron attachment rates for these compounds. It is important in the general interpretation of our electron attachment results to know the gas phase acidities of the transition-metal compounds. We were able to use the GL/LID ion-molecule flow reactor for this purpose. This collaboration with GL/LID was particularly appropriate since the strongest gas phase acids known prior to this research were those determined by GL/LID scientists (Henchman et al., 1985).

II OBJECTIVES OF THE RESEARCH EFFORT:

Our principal goal for the 1989 SFRP research was to determine the acidities of transition-metal compounds in the gas phase, by comparison with other known strong acids.

Since the setup for the syntheses of the transition-metal acids, and the syntheses themselves, required roughly one month, our initial work with the GL/LID ion-molecule flow reactor utilized commercially available $Fe(CO)_5$ to produce the ions $Fe(CO)_n^-$ (n = 0-4). Reactions of all five of these ions with methyl halides gave us information on the strengths of the iron-carbonyl and iron-methyl bonds. Additionally, measurements of the kinetics of proton transfer from various acids to Fe^- were examined to determine the gas phase acidity of FeH.

In the course of producing $Fe(CO)_n^-$ ions, it was found that collision-induced dissociation thresholds for CO loss correspond approximately to previously reported

(Compton and Stockdale, 1976) ligand bond energies for the $Fe(CO)_n^-$ ions. This is remarkable, since the apparatus was not specifically designed for such work, and an effort was made to use the collision-induced dissociation to determine these bond energies more accurately.

III. EXPERIMENTAL METHOD

These experiments were carried out on a Selected Ion Flow Tube (SIFT) at the Geophysics Laboratory. This apparatus has been described earlier (Viggiano and Paulson, 1983). The variable temperature capability of the apparatus was not used in the present study; all measurements were made at 297 K. Briefly, ions are created in an electron-bombardment ion source and mass selected before injection into a flow tube reactor. The ions are swept down the flow tube by helium buffer gas, which flows at a speed of about 14,000 cm/s at a pressure of 0.4 torr. After a total flight path of 100 cm, ions on the axis of the flow tube are sampled into a high vacuum region, mass analyzed, and detected with a particle multiplier.

A very small amount of reactant gas (roughly one part per thousand parts of helium buffer) was introduced through perforated ring inlets at either of two points along the flow tube. Two reaction distances (50.3 and 35.4 cm) were always used, since the "end correction" associated with non-uniform gas mixing near the inlet must be determined. In the present experiments the end correction was typically -16 cm, implying that a considerable distance is required for the reactant gas to mix uniformly with the helium buffer. This end correction results in effective reaction distances of about 34 and 19 cm for the two inlets.

The ion velocity is greater than the bulk helium velocity, by a factor of 1.5 for these conditions, because the sampled ions have traveled the length of the flow tube on axis, hence at the peak of the parabolic velocity profile of the buffer gas. The ion velocities for this work were measured by a time-of-flight technique. In most of the experiments described here, the ion velocity was typically 20,000 cm/s. In some of the work, the vacuum pump was throttled, and the helium flow reduced to keep the flow tube pressure at 0.395 torr, giving an ion velocity of about 12,000 cm/s. The slower ion speed results in longer reaction times, and thus lower flow rates of reactant gas are required. This is a considerable advantage when only a gram or less of neutral reactant is available (as was typical for the metal compounds which we synthesized), or when the vapor pressure of

the reactant is low. Lower end corrections (-7 cm) also resulted with the slower helium flow.

Concentration of neutral reactants were measured by comparing the flow of the neutral using a heat-transfer type flow meter (MKS) to the rate of helium flow and the known helium pressure in the flow tube. It was necessary to estimate the heat capacities of the metal compounds we synthesized, based on the heat capacities of metal carbonyls, in order to use the flow meters with neat sample gas. For the metal hydride reactions we also used mixtures of the metal hydride reactant (4 - 18%) in argon gas, and the resulting rate constants indicated that there is an additional 10% uncertainty in the metal hydride data due to the flow measurements.

Reaction rate coefficients are then calculated from the exponential attenuation of the primary ion signal as a function of neutral reactant concentration, using a reaction time determined using the effective reaction distances and the ion velocities. Diffusion also attenuates the ion density, but is negligibly affected by the presence of the reactant. Thus the effect of diffusion was not included in the calculation of reaction rate coefficients reported here. The rate coefficients determined here are considered accurate to $\pm$ 25% for the reactions with $Fe(CO)_n^-$, and $\pm$ 35% for the metal hydrides..

In the proton transfer experiments to determine the acidity of transition-metal compounds, many different negative ions were produced in the ion source from a variety of parent species. The halogen negative ions were produced by dissociative electron attachment to methyl halides or halogenated methane. $CCl_3CO_2^-$ was produced from trichloroacetic anhydride; $CF_3COCHCOCH_3^-$ from 1,1,1-trifluoro-2,4-pentanedione; $CHCl_2CO_2^-$ from methyl dichloroacetate; $CHF_2CO_2^-$ from difluoracetic acid; PO_3^- from dimethylphosphite; $CF_3SO_3^-$ from trifluorosulfonic anhydride; FSO_3^- from a mixture of SF_6 and SO_2; NO_2^- from NO; and HCO_2^- from formic acid. A few other negative ions were produced incidentally by collision-induced dissociation (e.g., CHF_2^- from $CHF_2CO_2^-$.

For the experiments with $Fe(CO)_n^-$ ions, $Fe(CO)_5$ vapor was introduced into the ion source, where dissociative electron attachment produced mainly $Fe(CO)_4^-$. Barely usable amounts of $Fe(CO)_3^-$, $Fe(CO)_2^-$, and $Fe(CO)^-$ could also be extracted from the ion source. However, it proved far more effective to make these ions by injecting $Fe(CO)_4^-$ at sufficient energy to dissociate it. Using collisional dissociation to produce the primary ions creates additional concern about long-lived electronic or vibrational excited states. We made no specific tests for excited states in this work. The ion source

operates at high pressure (about 1 torr) which should inhibit excited states to some extent. Additionally, no evidence of excited states of negative ions has been observed in previous work using this apparatus.

Only $Fe(CO)_4^-$ could be studied in the absence of other $Fe(CO)_n^-$ ions, by injecting it at low enough energy to leave it undissociated. The complication of several $Fe(CO)_n^-$ ions in some instances made the determination of product branching ratios for multiple reaction products difficult. However, the multiple ions do not affect the determination of rate coefficients for reactions, since these are determined solely by primary ion loss.

$Fe(CO)_5$ vapor in the ion source repeatedly resulted in sudden failure of the source after 2 or 3 days of running. The precise cause of the failure is not known, but the source became coated with a black residue during this time, due to thermal dissociation of $Fe(CO)_5$. A cooler electron filament (thoriated iridium) allowed longer operation of the source than a hotter rhenium filament. Using a 10% mixture of $Fe(CO)_5$ in Ar was preferrable to pure $Fe(CO)_5$.

IV. RESULTS AND DISCUSSION

a. Acidity of Transition-Metal Compounds. Table I lists the reactions studied and the resulting reaction rate coefficients and product branching ratios.

Table II presents an acidity scale for the reference acids. The locations on the ladder for the transition-metal compounds are also indicated. An important result of this research is the identification of $HCo(PF_3)_4$ as the strongest gas phase acid now known. The 300 K electron attachment rate coefficient for $HCo(PF_3)_4$ has been measured to be 1.2×10^{-8} cm^3/s (determined by us at the University of Oklahoma, and independently by R. W. Crompton at the Australian National University). Thus it is shown that this strongest of all gas phase acids undergoes electron attachment only in approximately 1 out of every 20 collisions with an electron. This is in sharp contrast to the other strong acids, as CF_3SO_3H, which attach the electron at near collision frequency (Adams et al., 1986).

We also found that $Re(CO)_5^-$ rapidly charge transfers with WF_6, implying that the electron affinity (EA) of $Re(CO)_5$ is less than that of WF_6, 3.4 eV (Viggiano et al., 1985). This finding is consistent with an estimate of $EA[Re(CO)_5] = 2.4 \pm 0.2$ eV reported by Meckstroth and Ridge (1985).

b. Acidity of FeH. Table III lists the results of reactions of Fe^- with various acids. Table IV shows how these results are interpreted in terms of the gas phase acidity of FeH. The present data correct a previous study of the acidity of FeH (Sallans et al., 1985). We also obtained data for the $Fe^- + HCO_2H$ reaction as a function of ion kinetic energy, and find that the proton transfer channel becomes dominant at several tenths of an eV energy.

c. Reactions of $Fe(CO)_n^-$ (n = 0-4) with CH_3X (X = F, Cl, Br, I). Reaction rate coefficients and ionic products are presented in Table IV. Also included for comparison are collisional rate coefficients calculated from classical trajectory theory for ion-polar molecule collisions (Su and Chesnavich, 1982). The simplest interpretation of these data is as follows. (1) Nucleophilic displacement, resulting in a halide negative ion product or leaving group, occurs when energetically possible, and indeed the rate of reaction seems to depend on the ergicity of the reaction. The fact that the observed reaction rates increase as the available energy in the reaction increases may be interpreted in terms of the model of a transition state barrier to nucleophilic displacement (Pellerite and Brauman, 1983). (2) If nucleophilic displacement is not energetically possible, ligand exchange occurs, in which CH_3X replaces <u>two</u> CO ligands, presumably by CH_3 and X respectively. The only exceptions to interpretations (1,2) are an association channel seen with $Fe(CO)_2^- + CH_3F$, and the cases in which no reaction is observed to take place, notably for $Fe(CO)_4^-$. The observation of no reaction for $Fe(CO)_4^-$ with the methyl halides, and the loss of two CO ligands in other reactions is in agreement with a recent report by Jones et al. (1989).

These observations are offered as the simplest interpretation rather than as absolute, because the energetics of these reactions cannot be quantified without knowing $Fe(CO)_n$ and $Fe(CO)_n$-CH_3 bond strengths. The available energy in each reaction is given in Table V in terms of the unknown bond energies. Electron affinities were taken from Leopold and Lineberger (1986), Engleking and Lineberger (1979), and Miller (1989), and CH_3-X bond strengths from Lias et al. (1988).

If lack of reaction is taken as a sign of endothermicity (and not activation energy), the Fe^- data imply that the Fe-CH_3 bond strength lies between 0.16 eV (3.6 kcal/mol) and 1.64 eV (38 kcal/mol). This wide range encompasses the value of 1.45 eV (33.4 kcal/mol) recently calculated by Bauschlicher et al. (1989). A value of 10 kcal/mol may be estimated from the acidity of FeH determined by us, and comparing it to the correlation between methyl affinities and proton affinities for a variety of negative ions.

However, that correlation does not include any transition metal species, for which effects such as metal to carbon d to p backbonding, or agostic bonding may act to increase the CH_3 relative to H bond strengths. Similarly, under the endothermicity assumption, the $Fe(CO)^-$ and $Fe(CO)_2^-$ data imply that both D[Fe(CO)-CH_3] and D[$Fe(CO)_2$-CH_3] are about 1.1 eV (25 kcal/mol).

d. Collision-Induced Dissociation. Measured laboratory and center-of-mass energy thresholds for the dissociation of various negative ions in collisions with helium are listed in Tables VI and VII. The respective energies expected on the basis of previous work are also given. The thresholds measured in this work have considerable uncertainties associated with them, due primarily to (1) energy scale calibration, to correct for contact potentials, and (2) indistinct thresholds as a result of thermal motion of the helium target. Efforts were made to solve problem (1) by dissociating NO_3^-, SF_6^-, and SF_5^- under the same conditions as the $Fe(CO)_n^-$. The SF_6^- and SF_5^- dissociation energies are not known well enough to be very useful in this regard. Problem (2) may be handled by computer modeling, at a later date.

Knowledge of these negative ion bond energies is quite important, for if corresponding electron affinities are known, a thermochemical cycle yields bond strengths in the neutral molecules - generally difficult to measure directly for radical species. In Table VIII, iron-carbon bond energies in neutral $Fe(CO)_n$ are derived from the collision-induced dissociation results of Table VII and $Fe(CO)_n$ electron affinities. These results are very tentative; further analysis of the data is needed, as indicated above.

One puzzle is illustrated in Table IX. In a separate experiment, $Fe(CO)_4^-$ was injected and thresholds for loss of 1-4 carbonyl groups were measured. These thresholds occur at much lower kinetic energies than expected from the data of Table VII. The implication is that either (a) the $Fe(CO)_4^-$ is excited, or (b) the method is flawed - perhaps there are multiple collisions, or the point at which collisions take place is mass dependent due to focusing differences.

V. RECOMMENDATIONS:

a. The results of each of the studies described above should be published in the scientific literature as soon as possible.

b. Electron attachment measurements must be made (at the University of Oklahoma) for the transition-metal acids studied in this work. We wish to examine related molecules, e.g., how do the attachment rates for $HCo(CO)_4$ and $HCo(PF_3)_4$ compare? We wish to build up a body of attachment data for as many of the transition-metal acids as feasible, to reveal periodic-table trends. It is very important for proper interpretation of the results that these attachment data be accompanied by mass identification and branching ratios of the negative ion products. The attachment results take on much greater significance now that the SFRP research has allowed us to determine acidities for these compounds - even if only approximately, in some cases.

The work on synthesizing more of a variety of transition-metal acids and superacids must be continued as well. Obtaining pure samples is very important for the electron attachment experiments, and helpful - though not essential - for further proton transfer experiments at GL.

It is easy to think of additional experiments which would allow us to further characterize these systems. The determination of the temperature dependence of the electron attachment rates would indicate how much rearrangement of the molecule is necessary for electron attachment. Experiments at very high temperatures could show whether electron attachment can take place before thermal dissociation of the parent occurs. Photodetachment experiments with the negative ions resulting from electron attachment [e.g., $Co(PF_3)_4^-$] would tell us the electron binding energies. Collision-induced dissociation experiments would reveal the ligand bond energies.

Further work should be done on collision-induced dissociation, particularly with species for which the bond energies are already accurately known, to better assess the method. Electron affinities (published and unpublished) are known for $Fe(CO)_n$, $Ni(CO)_n$, $W(CO)_n$, $Cr(CO)_n$, and $Re_2(CO)_n$. An important contribution to inorganic chemistry could be made if these bond energies could be determined.

We also intend to work with halogenated species, e.g., $BrCo(CO)_4$. The syntheses are much easier than for the corresponding acids, and the electron attachment rates and branching ratios should be very interesting.

REFERENCES

Adams, N. G., Smith, D., Viggiano, A. A., Paulson, J. F., and Henchman, M. J., J. Chem. Phys., 1986, Vol. 84, p. 6728.

Bartmess, J. E., private communication, 1987.

Bauschlicher, Jr., C. W., Langhoff, S. R., Partridge, H., and Barnes, L. A., J. Chem. Phys., 1989, Vol. 91, p. 2399.

Compton, R. N., and Stockdale, J. A. D., Int. J. Mass Spectrom. Ion Phys, 1976, Vol. 22, p. 47.

Engleking, P. C., and Lineberger, W. C., J. Am. Chem. Soc., 1979, Vol. 101, p. 1569.

Henchman, M., Viggiano, A. A., Paulson, J. F., Freedman, A., and Wormhoudt, J., J. Am. Chem. Soc., 1985, Vol. 107, p. 1453.

Jones, M. T., McDonald, R. N., Schell, P. L., and Ali, M. H., J. Am. Chem. Soc., 1989, Vol. 111, p. 5983.

Leopold, D. G., and Lineberger, W. C., J. Chem. Phys., 1986, Vol. 85, p. 51. Some of the data obtained in this study (quoted in Table IX) are are unpublished.

Lias, S. G., Bartmess, J. E., Liebman, J. F., Holmes, J. L., Levin, R. D., and Mallard, W. G., J. Phys. Chem. Ref. Data, 1988, Vol. 17, Supplement No. 1, Gas Phase Ion and Neutral Thermochemistry.

Meckstroth, W. K., and Ridge, D. P., J. Am. Chem. Soc., 1985, Vol. 107, p. 2281.

Miller, T. M., in Handbook of Chemistry and Physics, 70th Edition, ed. R. C. Weast, 1989, p. E-65.

Pellerite, M. J., and Brauman, J. I., J. Am. Chem. Soc., 1983, Vol. 105, p. 2672.

Sallans, L., Lane, K. R., Squires, R. R., and Freiser, B. S., J. Am. Chem. Soc., 1985, Vol. 107, p. 4379.

Su, T., and Chesnavich, W. J., J. Chem. Phys., 1982, Vol. 76, p. 583.

Viggiano, A. A., and Paulson, J. F., J. Chem. Phys., 1983, Vol. 79, p. 2241.

Viggiano, A. A., Paulson, J. F., Dale, F., Henchman, M., Adams, N. G., and Smith, D., J. Phys. Chem., 1985, Vol. 89, p. 2264.

Table I. Reaction rate coefficients (in units of 10^{-9} cm^3/s) measured at 297 K. The reactions are proton transfer except in a few cases noted where additional products were observed. The reactant negative ions are listed in order of increasing acidity of their proton-bonded parent.

Negative Ion	Neutral Reactant				
	$HRe(CO)_5$[a]	$HMn(CO)_5$	$HMn(CO)_x(PF_3)_y$[b]	$HIr(PF_3)_4$	$HCo(PF_3)_4$
F^-	2.1[c]	2.1	-	-	-
CCl_3^-	-	1.1	-	-	-
HCO_2^-	1.1	-	-	-	-
NO_2^-	1.1	-	-	-	-
Cl^-	1.5	1.5	-	-	-
$CHF_2CO_2^-$	0.3	-	-	-	-
$CF_3COCHCOCH_3^-$	<0.01[d]	-	-	-	-
$CHCl_2CO_2^-$	<0.01[d]	-	-	-	-
Br^-	<0.001[d]	1.0	0.62	>0.15[f]	-
$CCl_3CO_2^-$	-	1.0	-	-	-
I^-	<0.001[d]	<0.001[d,e]	0.46	>0.05[f]	0.56
PO_3^-	-	-	0.61	0.4[g]	0.69
FSO_3^-	-	-	0.02	0.1[g]	0.62
$CF_3SO_3^-$	-	-	<0.002[d]	0.0003[h]	0.58

[a]Additional reaction rates (in parentheses) were measured for $HRe(CO)_5$ proton transfer reactions with the following ions: $CHCl_2^-$ (1.1), CHF_2^- (1.6), CF_3O^- (0.5), and CF_3^- (1.4).
[b]78% $HMn(CO)_3(PF_3)_2$ and 22% $HMn(CO)_2(PF_3)_3$ indicated by products from both Br^- and I^- reactions.
[c]65% proton transfer, 35% association at 0.395 torr.
[d]No reaction observed within the limit given.
[e]At a center-of-mass interaction energy of 0.88 eV, $Mn(CO)_5^-$ product ions were observed, but the rate coefficient was still too small to measure with the limited reactant pressure available.
[f]Impurities were present so the actual rates for pure $HIr(PF_3)$ are probably greater. Only the $HIr(PF_3)_4$ proton transfer channel was active.
[g]Impurities were present which produced low mass products (i.e., not containing Ir) in addition to the proton transfer channel for $HIr(PF_3)_4$. Thus, the rate coefficient given is not particularly meaningful.
[h]Pure sample.

Table II. Acidity scale used for the determination of the gas phase acidity of transition-metal compounds in this work, with the relative positions of the transition-metal hydrides also given. The acidity data (in kcal/mol) are from Bartmess (1987), except as noted.

Acid	ΔH_{acid}	ΔG_{acid}
HF	371.5 ± 0.2	365.7 ± 0.5
$CHCl_3$	357.1 ± 6.3	349.3 ± 6.0
HCO_2H	345.2 ± 2.3	338.2 ± 2.0
HNO_2	338.2 ± 4.3	330.5 ± 4.6
HCl	333.4 ± 0.2	328.0 ± 0.5
$HRe(CO)_5$	position according to this work	
CHF_2CO_2H	330.0 ± 2.3	323.5 ± 2.0
$CF_3COCH_2COCH_3$	328.4 ± 4.1	322.0 ± 2.0
$CHCl_2CO_2H$	327.3 ± 2.6	320.8 ± 2.0
HBr	323.5 ± 0.1	318.2 ± 0.4
CCl_3CO_2H	319.9 ± 2.9	312.8 ± 2.0
$HMn(CO)_5$	position according to this work	
HI	314.4 ± 0.1	309.3 ± 0.4
HPO_3	311[a]	
H_2SO_4	a	
FSO_3H	a	
$HIr(PF_3)_4$, $HMn(CO)_3(PF_3)_2$, $HMn(CO)_2(PF_3)_3$	position according to this work	
CF_3SO_3H	a	
$HCo(PF_3)_4$	position according to this work	

[a]Viggiano et al. (1989).

Table III. Reaction rate coefficients (in units of 10^{-9} cm^3/s) and product branching ratios for Fe^- interacting with various acids, at 0.395 torr and 297 K.

Reactant Acid	Reaction Rate Coefficient	Ionic Products
H_2S	1.6	90% FeS^- 10% $FeSH^-$
CH_3CO_2H	0.47	none observed[a]
$CH_3CH_2CO_2H$	0.52	50% $CH_3CH_2CO_2^-$ 30% $(32 \pm 2\ amu)^-$ 20% $FeCH_3CH_2CO_2H^-$
HCO_2H	0.60	65% FeH_2^- 20% HCO_2^- 15% $FeHCO_2H^-$
$CH_3COCH_2COCH_3$	not measured	$FeCH_3COCH_2COCH_3^-$

[a]Presumably associative detachment, but an H^- product cannot be ruled out as it would not be detected by us due to diffusive loss and poor mass-analysis sensitivity at 1 amu.

TABLE IV. Reaction rate coefficients determined by the present work at 297 K. The rate coefficients are in units of 10^{-9} cm^3/s and are estimated accurate to ± 30%. Calculated collisional rate coefficients are given in parentheses. The ionic products of the reaction are given in the final lines of each entry.

Primary Ion	Reactant CH_3F	CH_3Cl	CH_3Br	CH_3I
Fe^-	<0.001[a] (2.2)	0.75 (2.0) Cl^-	1.4 (1.8) Br^-	2.2 (1.6) I^-
$Fe(CO)^-$	<0.001[a] (2.0)	0.020 (1.9) Cl^-	0.61 (1.6) Br^-	1.2 (1.4) I^-
$Fe(CO)_2^-$	0.12 (2.0) 55% $Fe(CH_3F)^-$ 25% $Fe(CO)_2(CH_3F)^-$ [b]20% $Fe(CH_3F)_2^-$	0.82 (1.8) $Fe(CH_3Cl)^-$	0.66 (1.5) Br^-	1.2 (1.3) I^-
$Fe(CO)_3^-$	<0.005[a] (1.9) $Fe(CO)(CH_3Cl)^-$	0.25 (1.7) $Fe(CO)(CH_3Br)^-$	0.49 (1.4)	0.78 (1.2) [c]$Fe(CO)(CH_3I)^-$
$Fe(CO)_4^-$	<0.001[a] (1.9)	<0.001[a] (1.7)	<0.001[a] (1.4)	<0.001[a] (1.2)

[a]No reaction was detected, within this uncertainty.
[b]Cannot be a primary product of the reaction, but the secondary reaction was so fast that we were unable to identify the precursor.
[c]This product was inferred, not observed; there was no ion product below the 200 amu limit of this experiment.

TABLE V. Exothemicity of the nucleophilic displacement reactions, in eV. D_n represents $D[Fe(CO)_n\text{-}CH_3]$, for n = 0-4. Below each entry, the reaction efficiency (observed rate divided by the calculated collisional rate) for nucleophilic displacement is given.

Primary Ion	Reactant CH_3F	CH_3Cl	CH_3Br	CH_3I
Fe^-	D_0 - 1.64 no reaction	D_0 - 0.16 0.37	D_0 + 0.15 0.78	D_0 + 0.45 1.34
$Fe(CO)^-$	D_1 - 2.66 no reaction	D_1 - 1.17 0.011	D_1 - 0.86 0.38	D_1 - 0.56 0.84
$Fe(CO)_2^-$	D_2 - 2.71 ligand exchange	D_2 - 1.22 ligand exchange	D_2 - 0.92 0.45	D_2 - 0.62 0.91
$Fe(CO)_3^-$	D_3 - 3.41 ligand exchange	D_3 - 1.92 ligand exchange	D_3 - 1.61 ligand exchange	D_3 - 1.31 ligand exchange
$Fe(CO)_4^-$	D_4 - 3.89 no reaction	D_4 - 2.40 no reaction	D_4 - 2.10 no reaction	D_4 - 1.80 no reaction

Table VI. Thresholds (in eV) observed for collision-induced dissociation. These thresholds are not yet corrected for energy scale shifts and broadening due to thermal motion of the helium target gas. All data were obtained at a target pressure of 0.395 torr, except for Run 2 (0.275 torr). For Run 4, SF_6 was in the ion source along with $Fe(CO)_5$. For Runs 5 and 6, NO was in the ion source along with $Fe(CO)_5$.

Data Run Number	System	E(Lab)	E(CM)	Best Available Bond Strength[a]
1	$NO_3^- \rightarrow NO_2^-$	57.5	3.48	3.8 ± 0.1
2	$NO_3^- \rightarrow NO_2^-$	59.7	3.62	3.8 ± 0.1
3	$Fe(CO)_4^- \rightarrow Fe(CO)_3^-$	21.0	0.50	0.4 ± 0.3
	$Fe(CO)_3^- \rightarrow Fe(CO)_2^-$	26.9	0.75	2.6 ± 0.3
	$Fe(CO)_2^- \rightarrow Fe(CO)^-$	29.4	1.02	0.9 ± 0.3
	$Fe(CO)^- \rightarrow Fe^-$	57.7	2.63	2.2 ± 0.3
4	$SF_5^- \rightarrow F^-$	49.0	1.50	1.90 ± 0.56
	$SF_6^- \rightarrow SF_5^-$	16.4	0.44	1.25 ± 0.38
	$Fe(CO)_4^- \rightarrow Fe(CO)_3^-$	21.5	0.51	0.4 ± 0.3
	$Fe(CO)_3^- \rightarrow Fe(CO)_2^-$	23.0	0.64	2.6 ± 0.3
	$Fe(CO)_2^- \rightarrow Fe(CO)^-$	24.4	0.84	0.9 ± 0.3
5	$NO_3^- \rightarrow NO_2^-$	51.8	3.14	3.8 ± 0.1
	$Fe(CO)_4^- \rightarrow Fe(CO)_3^-$	22.3	0.55	0.4 ± 0.3
6	$NO_3^- \rightarrow NO_2^-$	51.4	3.11	3.8 ± 0.1
	$Fe(CO)_4^- \rightarrow Fe(CO)_3^-$	24.9	0.59	0.4 ± 0.3
	$Fe(CO)_3^- \rightarrow Fe(CO)_2^-$	27.7	0.77	2.6 ± 0.3

[a]The NO_3^-, SF_6^-, and SF_5^- thermochemical data are from Lias et al. (1988). The $Fe(CO)_n^-$ data are from the appearance potentials of Compton and Stockdale (1976).

Table VII. Collision-induced dissociation thresholds for $Fe(CO)_n^-$, using NO_3^- and SF_5^- thresholds to calibrate the energy scale. Further improvement may come later by modeling the thermal motion of the helium target gas. The E(CM) results are estimated accurate to $\pm$ 0.5 eV.

System	E(Lab)	E(CM)	Best Available Bond Strength[a]
$Fe(CO)_4^- \rightarrow Fe(CO)_3^-$	34.3	0.82	0.4 ± 0.3
$Fe(CO)_3^- \rightarrow Fe(CO)_2^-$	38.2	1.06	2.6 ± 0.3
$Fe(CO)_2^- \rightarrow Fe(CO)^-$	40.2	1.39	0.9 ± 0.3
$Fe(CO)^- \rightarrow Fe^-$	68.5	3.12	2.2 ± 0.3

[a]Compton and Stockdale (1976).

Table VIII. Fe-C bond strengths (in eV) derived from the collision-induced dissociation results using the relation $D[CO\text{-}Fe(CO)_n] = D[CO\text{-}Fe(CO)_n^-] + EA[Fe(CO)_n] - EA[Fe(CO)_{n-1}]$. The uncertainties in this work include $\pm$ 0.5 eV for $D[CO\text{-}Fe(CO)_n^-]$, and the EA uncertainties listed below.

Species	EA	Fe-CO Bond Strength, This Work	Fe-CO Bond Strength[a]
Fe	0.151 ± 0.003[b]	-	-
Fe(CO)	1.164 ± 0.010[b]	2.1 ± 0.5	1.0 ± 0.3
$Fe(CO)_2$	1.22 ± 0.04[b]	1.3 ± 0.6	1.0 ± 0.3
$Fe(CO)_3$	1.915 ± 0.085[b]	0.4 ± 0.6	1.4 ± 0.3
$Fe(CO)_4$	2.4 ± 0.3[a]	0.3 ± 0.9	0.2 ± 0.4
$Fe(CO)_5$	c	-	2.4 ± 0.5

[a]Engleking and Lineberger (1979).
[b]Leopold and Lineberger (1986).
[c]$Fe(CO)_5^-$ not stable with respect to CO loss.

Table IX. Collision-Induced dissociation thresholds (in eV) for $Fe(CO)_4^-$ + He, resulting in the loss of 1-4 carbonyl ligands. The energy scale has been corrected as in Table VII, and the thresholds are considered uncertain to ± 0.5 eV.

System	E(Lab)	E(CM)	Cumulative Bond Energies, Table VII	Appearance Potentials[a]
$Fe(CO)_4^- \rightarrow Fe(CO)_3^-$	34.8	0.83	0.82	0.4 ± 0.3
$Fe(CO)_4^- \rightarrow Fe(CO)_2^-$	59.1	1.41	1.88	3.0 ± 0.3
$Fe(CO)_4^- \rightarrow FeCO^-$	73.6	1.75	3.27	3.9 ± 0.3
$Fe(CO)_4^- \rightarrow Fe^-$	122.3	2.92	6.39	6.1 ± 0.3

[a]Compton and Stockdale (1976).

1989 USAF-UES SUMMER FACULTY RESEARCH PROGRAM/

GRADUATE STUDENT RESEARCH PROGRAM

Sponsored by the

AIR FORCE OFFICE OF SCIENTIFIC RESEARCH

Conducted by the

Universal Energy Systems, Inc.

FINAL REPORT

ACIDITIES OF IRON HYDRIDE AND VARIOUS TRANSITION-METAL COMPOUNDS; REACTIONS OF IRON AND IRON CARBONYL ANIONS

Prepared by:	Amy E. Stevens Miller and Thomas M. Miller
Academic Rank:	Assistant Professor, Professor
Department and	Chemistry & Biochemistry, Physics & Astronomy
University:	University of Oklahoma
Research Location:	Geophysics Laboratory, Ionospheric Physics Division
USAF Researcher:	Dr. John F. Paulson
Date:	1 August 1989
Contract No:	F49620-88-C-0053

ACIDITIES OF IRON HYDRIDE AND VARIOUS TRANSITION-METAL COMPOUNDS; REACTIONS OF IRON AND IRON CARBONYL ANIONS

by

Amy E. Stevens Miller and Thomas M. Miller

ABSTRACT

Four projects were carried out:

1. A number of transition-metal acids were synthesized, and their gas phase acidities were bracketed by determining proton transfer reaction rates with of negative ions of known basicity. One of these compounds, $HCo(PF_3)_4$, proved to be stronger than any other known acid in the gas phase.

2. Proton transfer rates for Fe^- reacting with a variety of acids were measured. The gas phase acidity of FeH was determined to be between that of propionic acid (ΔH_{acid} = 347.3 $\pm$ 2.3 kcal/mol) and acetic acid (ΔH_{acid} = 348.5 $\pm$ 2.3 kcal/mol).

3. Ion-molecule reaction rate coefficients were measured for $Fe(CO)_n^-$ (n = 0-4) interacting with methyl halides. Nucleophilic displacement occurs when energetically possible, yielding $Fe(CO)_nCH_3$ and a halide anion. If this reaction channel is energetically closed, ligand exchange may occur. The reaction rates measured in projects 2 and 3 are the first to be measured with the atomic iron negative ion.

4. Collision-induced dissociation of $Fe(CO)_n^-$ (n = 1-4) with He was studied in an attempt to determine the carbonyl bond energies. Because of the difficulty of calibrating the collision energy scale, the results are estimated to be uncertain by about 0.5 eV.

1989 USAF-UES SUMMER FACULTY RESEARCH PROGRAM/

GRADUATE STUDENT RESEARCH PROGRAM

Sponsored by the

AIR FORCE OFFICE OF SCIENTIFIC RESEARCH

Conducted by the

Universal Energy Systems, Inc.

FINAL REPORT

CO_2(4.3μm) VIBRATIONAL TEMPERATURES AND LIMB RADIANCES UNDER SUNLIT CONDITIONS IN THE 50-120 KM ALTITUDE RANGE

Prepared by:	Dr. Henry Nebel
Academic Rank:	Professor
Department and University:	Physics Department, Alfred University
Research Location:	Geophysics Laboratory/Optical & Infrared Technology Division/ Infrared Backgrounds Branch Hanscom AFB, MA 01731
USAF Researcher:	Dr. Ramesh D. Sharma
Date:	22 September 1989
Contract No:	F49620-88-C-0053

CO2(4.3μm) VIBRATIONAL TEMPERATURES AND LIMB RADIANCES UNDER SUNLIT CONDITIONS IN THE 50-120 KM ALTITUDE RANGE

by

Henry Nebel

ABSTRACT

Vibrational temperature profiles as functions of altitude under sunlit conditions have been calculated for the 4.3 μm, 2.7 μm and 2.0 μm absorbing states of carbon dioxide which contribute to 4.3 μm radiation. These calculations have been performed using a non-equilibrium line-by-line infrared radiation transport code (ARC) developed at the Geophysics Laboratory. The vibrational temperature profiles are then used to calculate integrated radiance from the 4.3 μm bands of CO_2 in a limb view for the 50-120 km altitude range. The calculated radiances are in good agreement with day-time measurements obtained by the Spectral Infrared Rocket Experiment (SPIRE)*.

*Stair, A.T., et. al., J. Geophys. Res. 90, 9763-9775 (1985).

ACKNOWLEDGEMENTS

I am grateful for the sponsorship of the Air Force Systems Command and the Air Force Office of Scientific Research, and particularly for the hospitality of the Optical and Infrared Technology Division of the Geophysics Laboratory (GL) during the summer of 1989. I appreciate the hospitality and guidance of Dr. Ramesh D. Sharma of GL with whom I worked closely during my stay. I thank Dr. Robert Joseph of Arcon Corporation for assistance in revising the computer code and Armand Paboojian of Arcon Corporation for computer-generated graphs of the vibrational temperature profiles. I thank Universal Energy Systems, Inc. for administration of the Summer Faculty Research Program.

Finally, I thank Dr. Peter Wintersteiner of Arcon Corporation for many useful discussions and suggestions, and for assistance in implementing the infrared radiance code. This research would not have been possible without his assistance.

I. INTRODUCTION:

There has been increasing interest recently in radiative transfer in the infrared spectral region under non-equilibrium conditions in the atmosphere (1-5). Under these conditions, local thermodynamic equilibrium (LTE) may not be assumed to apply, i.e. collisions among molecules are not frequent enough to bring a parcel of air into equilibrium before radiative deexcitation occurs. This is generally the situation in the earth's upper atmosphere (above 60 km). An infrared radiance computer code has been developed at the Geophysics Laboratory (GL) by Dr. Ramesh Sharma of GL and Dr. Peter Wintersteiner of Arcon Corporation. This code treats absorption, emission, and transmission of infrared radiation through the atmosphere under non-equilibrium conditions. One component of the code (RAD) calculates excited state population densities and the corresponding vibrational temperature profiles assuming various mechanisms of excitation and deexcitation, and also assuming the population densities are constant in time. Another component of the code (NLTE) uses the vibrational temperature profiles to calculate total integrated band radiance for various viewing geometries. These calculations are done on a line-by-line basis, whereas most previous calculations of this type were based on band models (1,2,5).

II. OBJECTIVES OF THE RESEARCH EFFORT:

In past summers I applied the AFGL non-equilibrium radiance code to the 4.3 micron band of carbon dioxide. Vibrational temperature profiles were obtained as functions of altitude and used to calculate infrared radiance through the atmosphere in a limb viewing geometry. This was done for the four major isotopic forms of CO_2 under night-time conditions (6,7) and also under terminator conditions where the limb view line-of-sight is partially sunlit and partially in darkness (8). My objective for this summer was to do the calculation for day-time conditions where the entire line-of-sight is sunlit in order to compare with day-time measurements obtained by the Spectral Infrared Rocket Experiment, or SPIRE (9). The following modifications to previous work were required:

1. Inclusion of solar absorption as an excitation mechanism, where the sun is at higher angles than is the case for terminator conditions.

2. Inclusion of various higher order transitions where a molecule makes a transition from one excited state to a lower excited state, emitting a 4.3 micron photon. Some of the higher vibrational states are excited by 2.7 and 2.0 micron radiation, and this is then followed by emission at 4.3 microns.

Integrated radiance in a limb view for the 4.3 micron band is calculated using the above modifications, and the results are compared with the day-time SPIRE measurements mentioned previously.

III. APPROACH:

In order to do this calculation, one first determines which excited vibrational states are responsible for emission at 4.3 microns. For each such level, a vibrational temperature profile must be calculated as a function of altitude. "Vibrational temperature" is an indication of excited state population density. It is determined by assuming various mechanisms for excitation and deexcitation of the level in question, and also assuming the population densities are constant in time. For the sunlit case treated here, solar absorption must be included as one of the excitation mechanisms. Solar absorption coefficients are calculated as a function of altitude by a computer program called SABS. These are then fed into either program RAD or program VPMP (discussed below) in order to calculate a vibrational temperature profile. This profile is then used as input to program NLTE which calculates integrated radiance in a limb view as a function of tangent height (see Fig. 3). The results are compared with the daytime SPIRE measurements referred to above.

IV. THEORETICAL DEVELOPMENT:

An energy level diagram including the vibrational states required for this calculation is shown in Fig. 1. The notation for the vibrational levels is that of the HITRAN database generated at the Geophysics Laboratory (10). The first, second and fourth digits represent the three quantum numbers of the vibrational modes of excitation. The 4.3 micron absorption or emission band results from transitions between states with one ν_3 quantum and corresponding states with no ν_3 quanta (other quantum numbers being equal for the upper and lower states). The present

calculation determines emission in the 4.3 micron band in a limb view as a function of tangent height (see Fig. 3).

Vibrational temperatures for the 00011 and 01111 states have been obtained using program RAD described above. In the case of the 00011 state (sometimes referred to as the 001 state indicating the three vibrational quantum numbers only), there is rapid collisional transfer between this state and the first excited vibrational state of N_2; thus the populations of both these states are treated as unknowns in the calculation. The mechanisms assumed for excitation and deexcitation of these two states are shown in Fig. 2. All radiative absorption as well as spontaneous emission, is in the 4.3 micron band. Coefficients for airglow absorption and spontaneous emission are calculated by program RAD. Solar absorption coefficients are calculated by a program called SABS. Rate constants for the collisional interactions have been taken from reference 5. Each of the two excited states is assumed to have a population density which is constant in time. Thus the sum of the excitation rates is set equal to the sum of the deexcitation rates for each state. The result is two coupled linear equations in the population densities of the excited states in question. These equations are combined to form a 2x2 matrix equation which is solved by the computer code yielding the population densities of the $CO_2(001)$ state and the $N_2(1)$ state. The vibrational temperatures are then calculated by means of the formulas

$$[CO_2(001)]/[CO_2(000)] = \exp(-h\nu/kT_{001})$$

and

$$[N_2(1)]/[N_2(0)] = \exp(-h\nu/kT_{N2})$$

where [ ] represents a population density, T_{001} and T_{N2} are the vibrational temperatures of the $CO_2(001)$ state and the $N_2(1)$ state respectively, h and k are the Planck and Boltzmann constants respectively, and ν is the frequency associated with the transition in each case. These equations define the vibrational temperatures. The calculation may be done for each altitude required for a particular problem, resulting in a vibrational temperature profile as a function of altitude. This vibrational temperature profile is then used to calculate total band radiance in a limb view, the geometry of which is shown in Fig. 3. Program NLTE calculates integrated radiance in a limb view for each spectral line within the band for selected tangent heights (see Fig. 3), and then sums the results to obtain total band radiance. The results may then be

compared with experimental data obtained from a rocket or a satellite. Results have been obtained under sunlit conditions for the principal isotopic form of carbon dioxide ($^{12}C^{16}O_2$) labeled 626, as well as for the three most important minor isotopic forms ($^{13}C^{16}O_2$, $^{16}O^{12}C^{18}O$, $^{16}O^{12}C^{17}O$) labeled 636, 628, and 627 respectively. Solar absorption coefficients were calculated assuming a solar elevation angle of 12°, which closely corresponds to the conditions of the first sunlit scan of the Spectral Infrared Rocket Experiment, or SPIRE (9), for 50-100 km tangent heights.

A similar calculation has been done for the 01111 state, which can absorb at 4.3 microns from the 01101 state and can also spontaneously emit 4.3 micron radiation to the 01101 state. This calculation has been done for the 626 and 636 isotopic forms only, since the others are expected to contribute very little to the limb radiance. In addition, contributions from higher lying states have also been considered in this study. The states in groups 1 and 2 (see Fig. 1) can absorb at 2.7 microns as well as at 4.3 microns, while those in group 3 can absorb at 2.0 microns. All of these states can subsequently emit at 4.3 microns, and thus contribute to the 4.3 micron integrated limb radiance. Vibrational temperatures for these states have been calculated using a program called VPMP, which neglects the airglow contribution compared to solar absorption. This is a reasonable assumption for two reasons. First, solar flux is stronger at 2.7 and 2.0 microns than it is at 4.3 microns. Secondly, the branching ratios for emission from these states strongly favors 4.3 micron emission which means very little 2.7 or 2.0 micron airglow will be present.

V. RESULTS:

Vibrational temperatures for the 00011 state for all four isotopic forms of CO_2 are shown in Fig. 4 while those for the 01111 state for the 626 and 636 isotopic forms are shown in Fig. 5. Vibrational temperatures for the three groups of higher lying states computed by program VPMP are shown in Fig. 6.

Integrated radiance in a limb view as computed by program NLTE is shown for the 00011 state in Fig. 7 and for the 01111 state in Fig. 8, along with experimental values from the Spectral Infrared Rocket Experiment (9). Contributions from each of the isotopic forms of CO_2 are shown as separate curves. Integrated radiances from the higher lying states are shown in Fig. 9.

Adding the contributions to the limb radiance from all the states considered results in the calculated values shown in Fig. 10. As can be seen in that figure, the agreement with day-time measurements from the SPIRE mission is excellent.

VI. CONCLUSIONS:

The infrared radiance computer code developed at the Geophysics Laboratory is an accurate and efficient vehicle for modelling infrared radiative transfer through the atmosphere under non-equilibrium conditions. Using the code to calculate vibrational temperature profiles and limb view integrated radiances for the 4.3 micron band of carbon dioxide under sunlit conditions results in excellent agreement with measurements obtained by the Spectral Infrared Rocket Experiment (9).

VII. RECOMMENDATIONS:

It is recommended that the infrared computer code (ARC) be applied to CO_2 4.3 micron radiation under terminator conditions where the limb view line-of-sight is partially sunlit and partially in darkness due to the sun being below the horizon. This problem has been treated in a preliminary way (8), but the solar flux absorption coefficients could not be calculated for a below-horizon sun, and the higher lying states considered here were not included. Both these limitations can now be overcome.

It has been assumed that the hydroxyl radical (OH) plays no role in the kinetic equations for excitation and deexcitation of the $CO_2(001)$ state. It is well known that hydroxyl exists in the upper atmosphere (11), and it has been suggested (12) that interactions involving the OH radical will have a significant effect on $CO_2(001)$ vibrational temperatures. It is recommended that the effect of hydroxyl be investigated by including it in the kinetic equations and re-calculating vibrational temperature profiles and integrated radiances. Comparison with experimental results can then be made as before.

Finally it is recommended that the four isotopic forms of CO_2 be coupled in such a way that vibrational temperatures for all four forms be calculated simultaneously. Preliminary results indicate that this will not affect the present results significantly; nevertheless it needs to be done for completeness and in order to obtain a more reliable $N_2(1)$ vibrational temperature profile.

REFERENCES

1. Kumer, J. B., and T. C. James, "$CO_2(001)$ and N_2 Vibrational Temperatures in the $50 \lesssim z \lesssim 130$ km Altitude Range", J. Geophys. Res. 79, 638-648 (1974).

2. Shved, G. M., G. I. Stepanova, and A. A. Kutepov, "Transfer of 4.3 μm CO_2 Radiation on Departure from Local Thermodynamic Equilibrium in the Atmosphere of the Earth", Izvestia, Atmospheric and Oceanic Physics, 14, 589-596 (1978).

3. Sharma, R. D., and P. P. Wintersteiner, "CO_2 Component of Daytime Earth Limb Emission at 2.7 Micrometers", J. Geophys. Res. 90, 9789-9803 (1985).

4. Solomon, S., J. T. Kiehl, B. J. Kerridge, E. E. Remsberg, and J. M. Russel III, "Evidence for Nonlocal Thermodynamic Equilibrium in the ν_3 Mode of Mesospheric Ozone", J. Geophys. Res. 91, 9865-9876 (1986).

5. López-Puertas, M., R. Rodrigo, J. J. López-Moreno, and F. W. Taylor, "A non-LTE radiative transfer model for infrared bands in the middle atmosphere. II. CO_2(2.7 and 4.3 μm) and water vapor (6.3 μm) bands and $N_2(1)$ and $O_2(1)$ vibrational levels", J. Atmos. Terr. Phys. 48, 749-764 (1986).

6. Nebel, H., "$CO_2(001)$ Vibrational Temperatures in the 50 to 150 km Altitude Range", Final Report/ 1986 USAF-UES Summer Faculty Research Program (1986).

7. Nebel, H., R. D. Sharma, and P. P. Wintersteiner, "Night-Time $CO_2(001)$ Vibrational Temperatures in the 50 to 150 km Altitude Range", Eos. Trans. AGU, 68, 1389 (1987).

8. Nebel, H., R. D. Sharma, J. R. Winick, R. Picard, P. P. Wintersteiner, and R. A. Joseph, "CO_2(001) Vibrational Temperatures and Limb-View Infrared Radiances Under Terminator Conditions in the 60-100 km Altitude Range", Eos. Trans. AGU, 69, 1346 (1988).

9. Stair, A. T., R. D. Sharma, R. M. Nadile, D. J. Baker, and W. F. Grieder, "Observations of Limb Radiance With Cryogenic Spectral Infrared Rocket Experiment", J. Geophys. Res. 90, 9763-9775 (1985).

10. Rothman, L. S., R. R. Gamache, A. Goldman, L. R. Brown, R. A. Toth, H. M. Pickett, R. L. Poynter, J.-M. Flaud, C. Camy-Peyret, A. Barbi, N. Husson, C. P. Rinsland, and M. A. H. Smith, "The HITRAN Database: 1986 Edition", Appl. Opt. 26, 4058-4097 (1987).

11. Baker, D. J, T. Conley, and A. T. Stair, "On the Altitude of the OH Airglow", Eos Trans. AGU, 58, 460 (1977).

12. Kumer, J. B., A. T. Stair, N. Wheeler, K. D. Baker, and D. J. Baker, "Evidence for an $OH^* \xrightarrow{VV} N_2^* \xrightarrow{VV} CO_2(\nu_3) \longrightarrow CO_2 + h\nu(4.3\,\mu m)$ Mechanism for 4.3 μm Airglow", J. Geophys. Res. 83, 4743-4747 (1978).

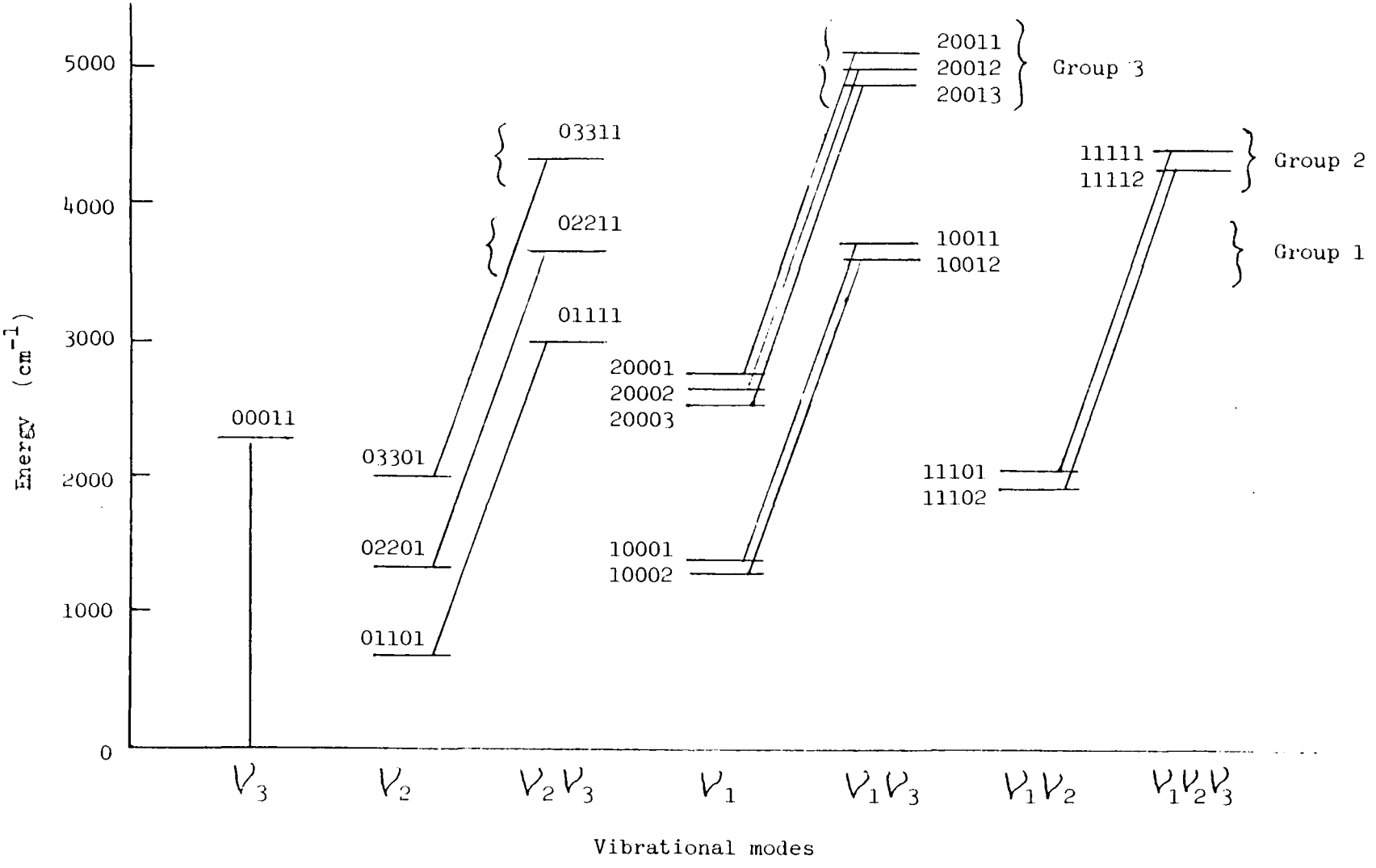

Fig. 1. Vibrational levels and 4.3 micron transitions considered. Absorption at 2.7 and 2.0 microns not shown.

Mechanisms for the $CO_2(001)$ state:

Spontaneous Emission:

$$CO_2(001) \longrightarrow CO_2(000) + h\nu$$

Solar and airglow pumping:

$$CO_2(000) + h\nu \longrightarrow CO_2(001)$$

V-V transfer with N_2:

$$CO_2(001) + N_2(0) \rightleftharpoons CO_2(000) + N_2(1) + 18\ cm^{-1}$$

V-T transfer to $CO_2(030)$:

$$CO_2(001) + M \rightleftharpoons CO_2(030) + M + 346\ cm^{-1}$$

V-T transfer with oxygen atoms:

$$CO_2(001) + O \rightleftharpoons CO_2(000) + O + 2349\ cm^{-1}$$

V-V transfer with O_2:

$$CO_2(001) + O_2(0) \rightleftharpoons CO_2(010) + O_2(1) + 128\ cm^{-1}$$

Mechanisms for the $N_2(1)$ state:

V-V transfer with CO_2:

$$CO_2(001) + N_2(0) \rightleftharpoons CO_2(000) + N_2(1) + 18\ cm^{-1}$$

V-V transfer with O_2:

$$N_2(1) + O_2(0) \rightleftharpoons N_2(0) + O_2(1) + 775\ cm^{-1}$$

V-T transfer with M (N_2 or O_2):

$$N_2(1) + M \rightleftharpoons N_2(0) + M + 2331\ cm^{-1}$$

V-T transfer with oxygen atoms:

$$N_2(1) + O \rightleftharpoons N_2(0) + O + 2331\ cm^{-1}$$

Fig. 2. Mechanisms for population of $CO_2(001)$ and $N_2(1)$ states.

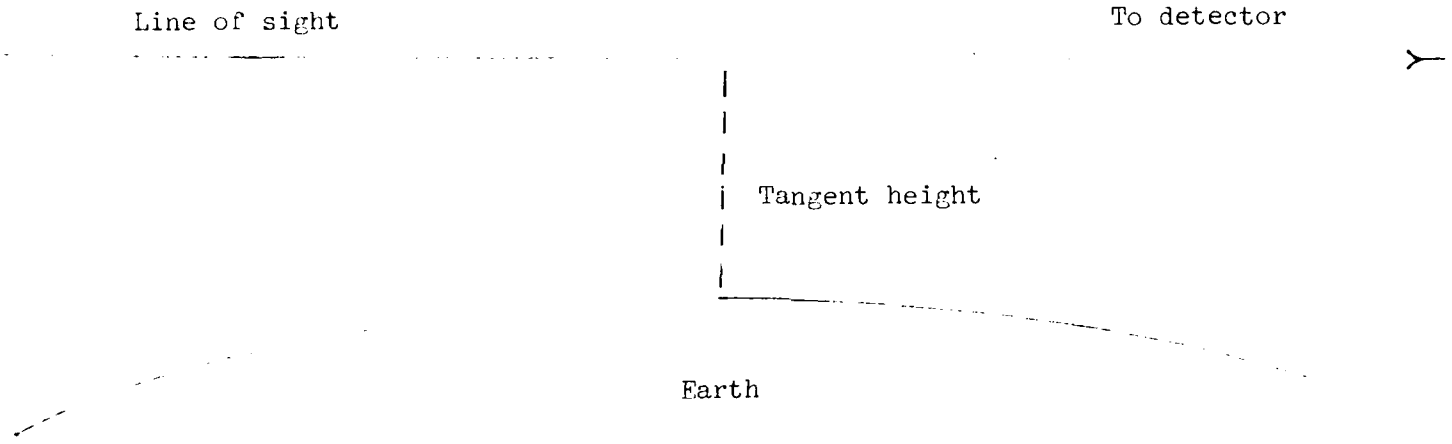

Fig. 3. Limb viewing geometry.

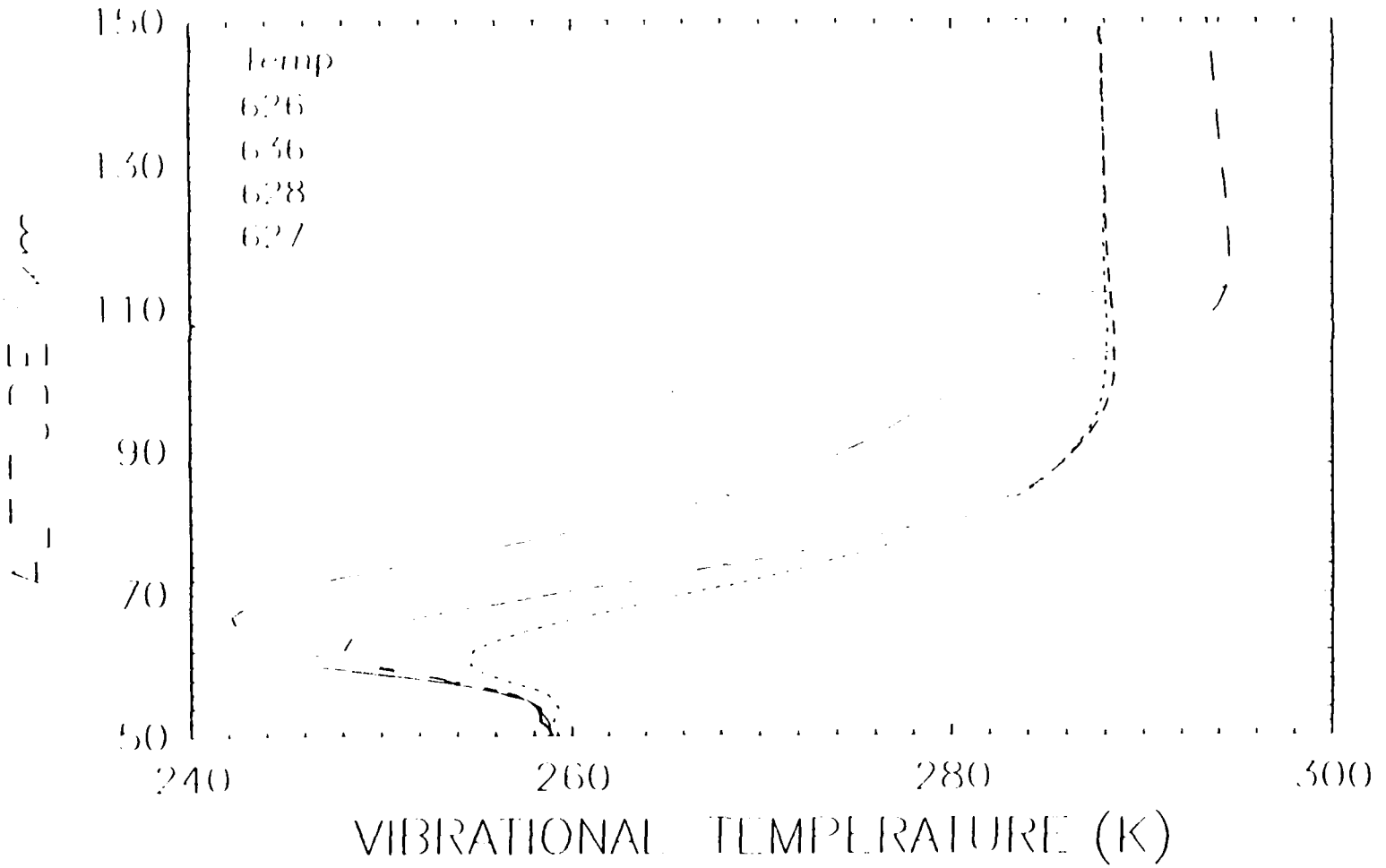

Fig. 4. Vibrational temperatures for 00011 state.

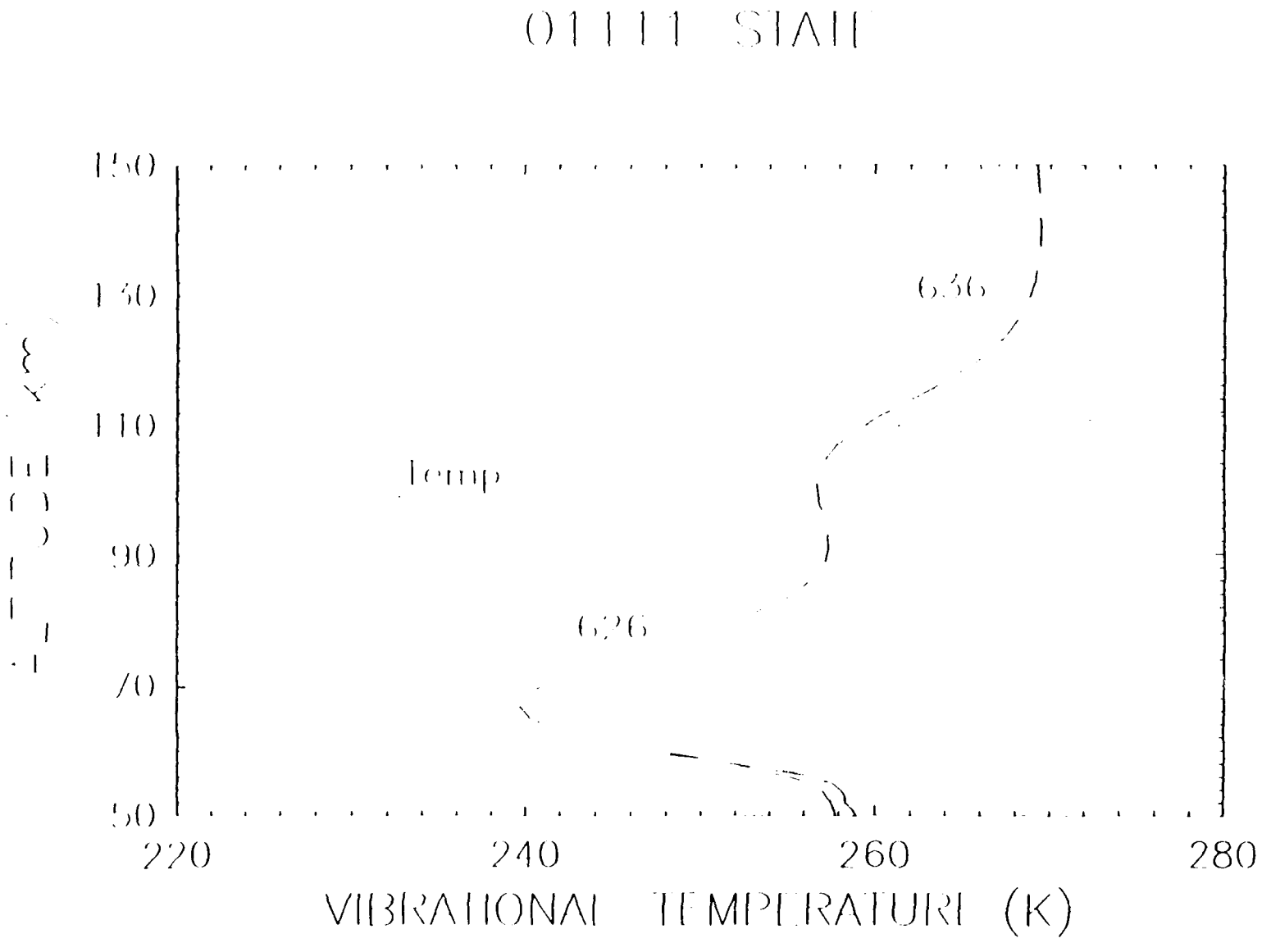

Fig. 4. Vibrational temperatures for 01111 state.

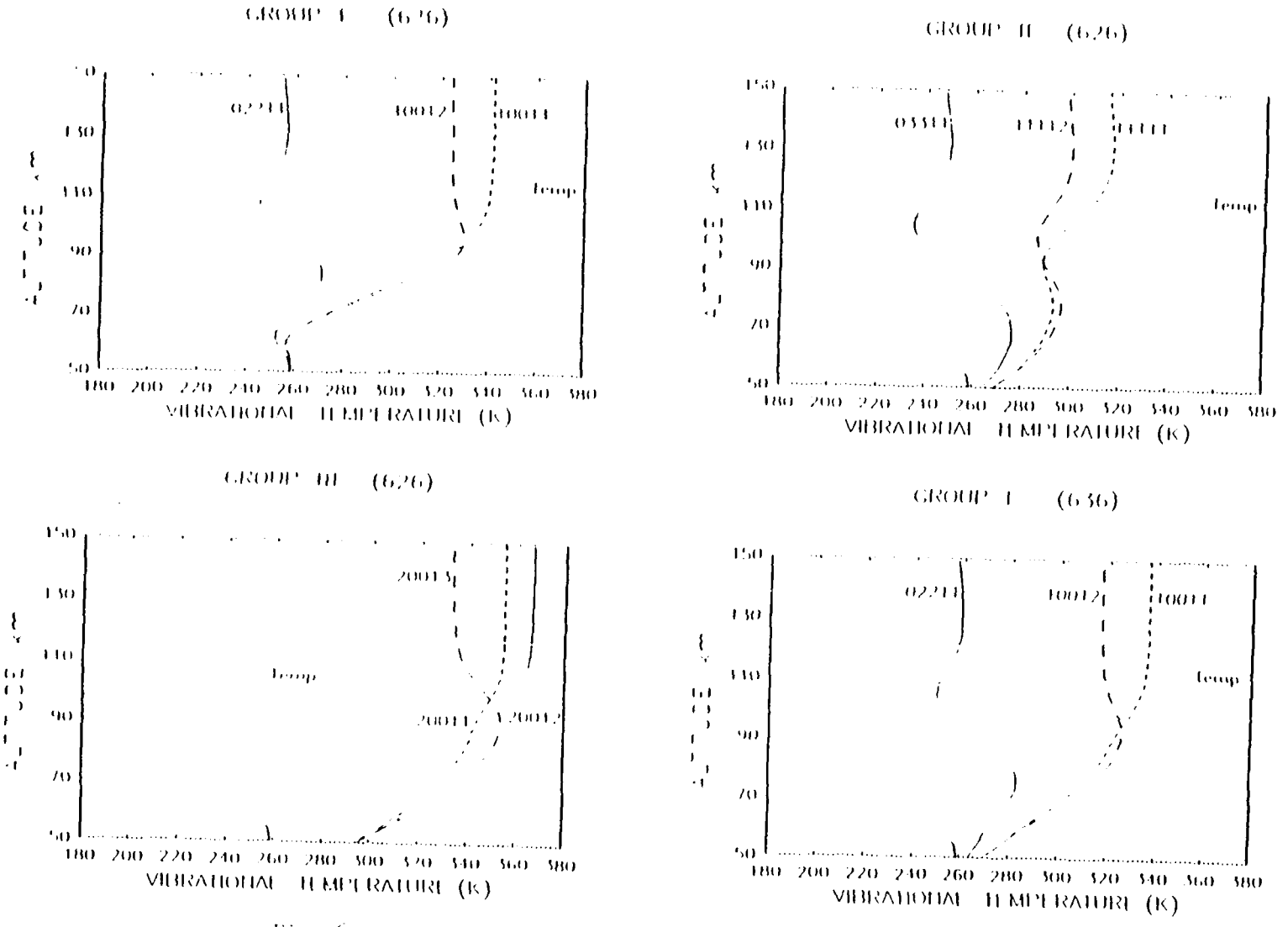

Fig. 6. Vibrational temperatures for higher lying states.

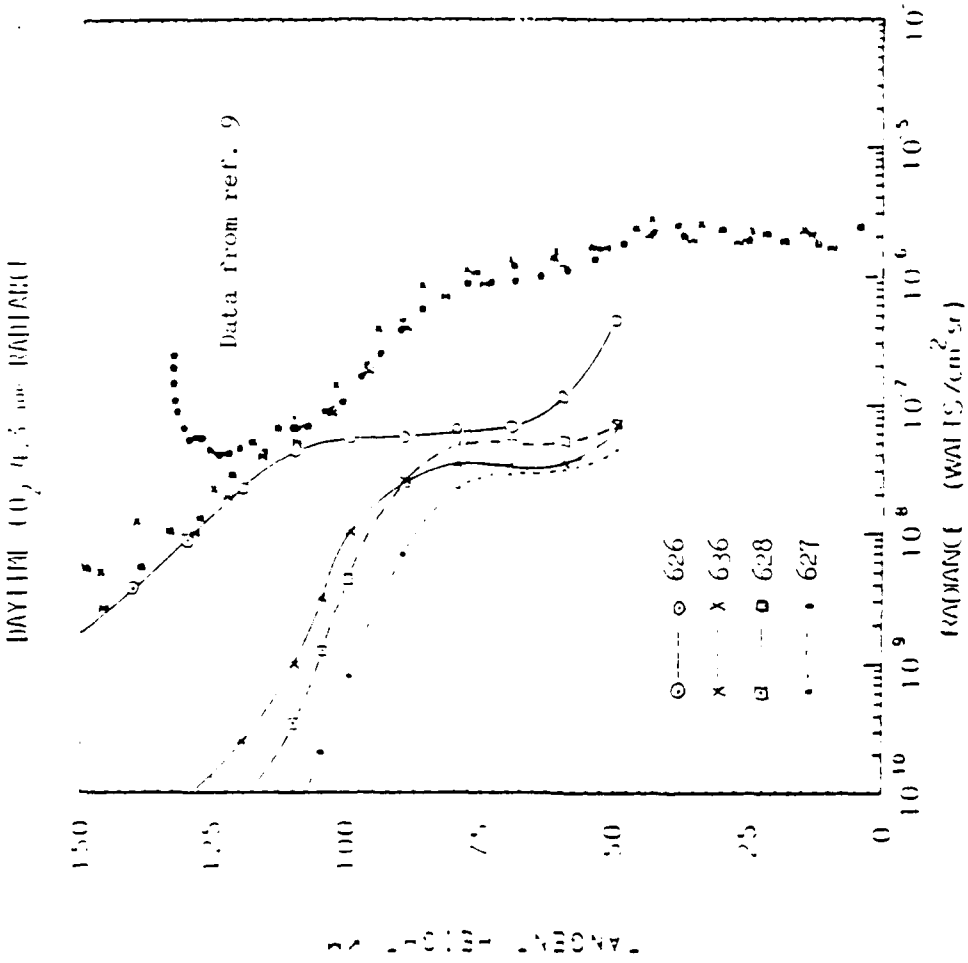

Fig. 7. Integrated radiances for 00011 state.

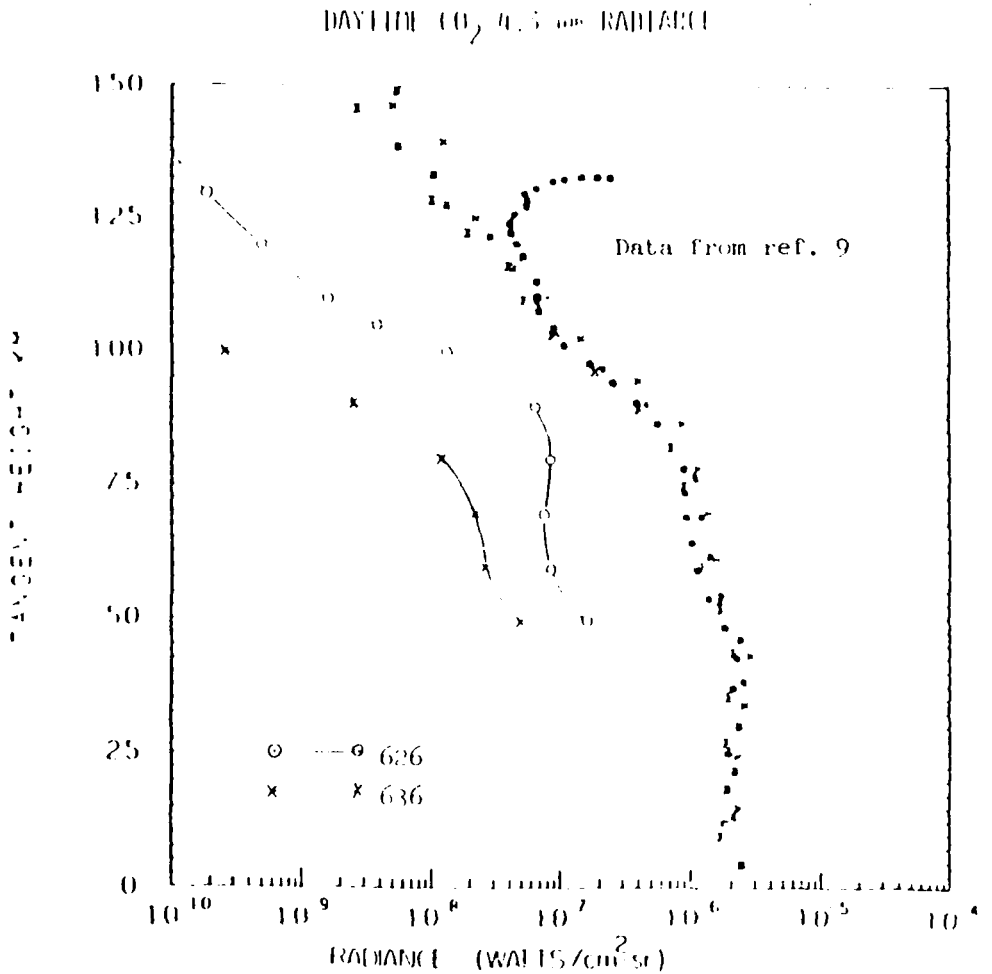

Fig. 8. Integrated radiances for 01111 state.

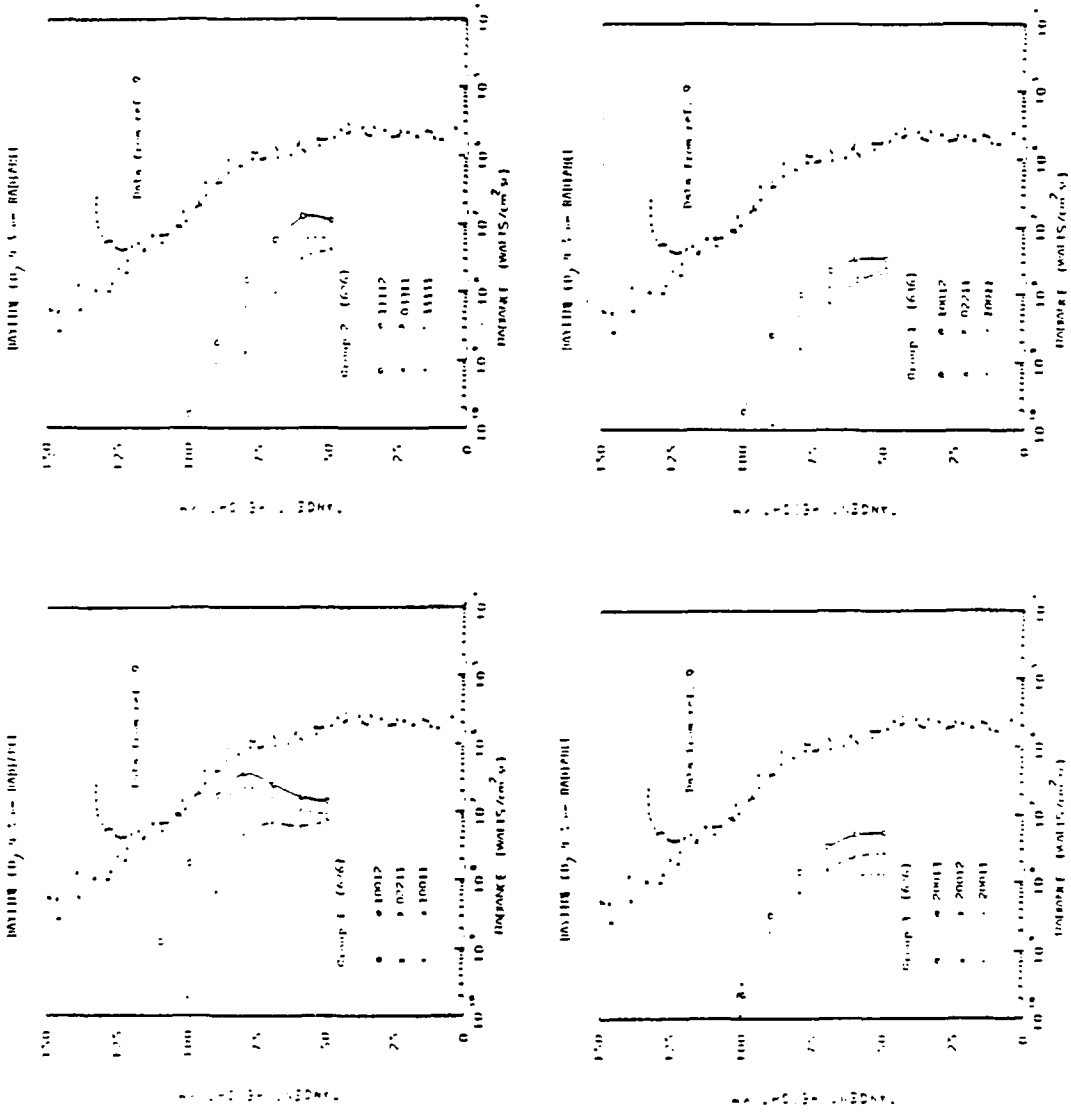

Fig. 9. Integrated radiances for higher lying states.

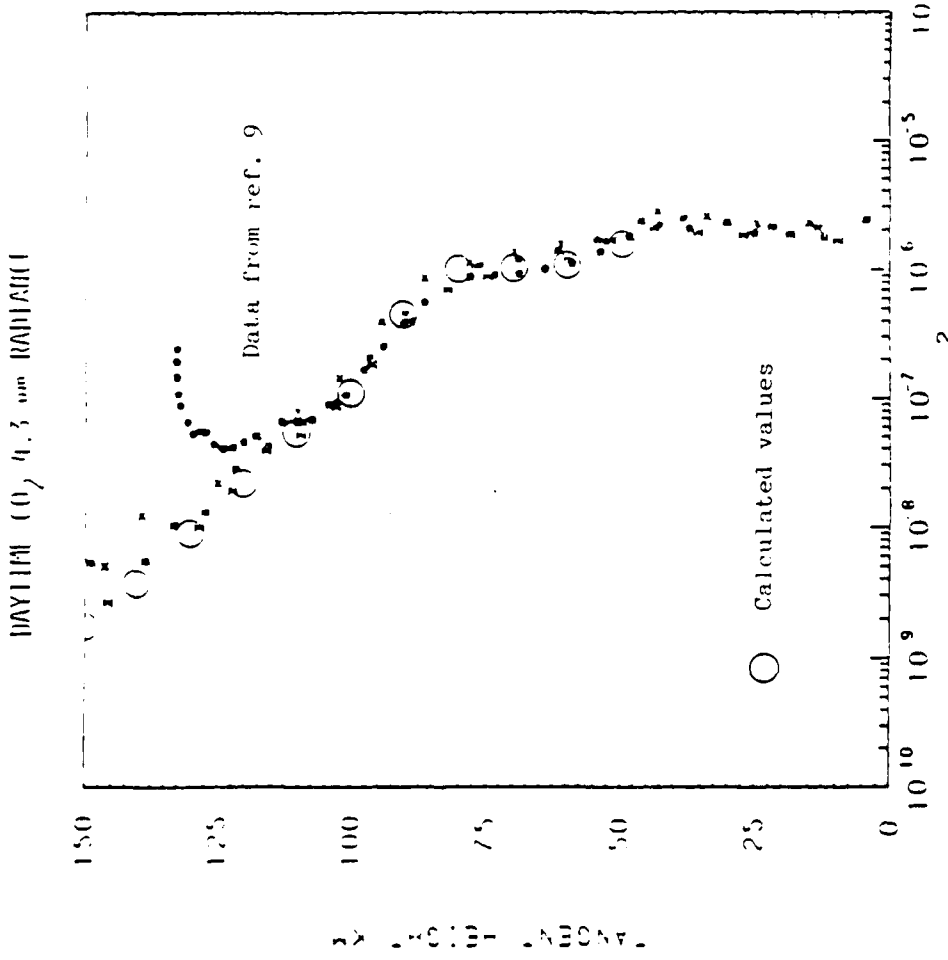

Fig. 10. Total integrated radiance.

1989 USAF-UES SUMMER FACULTY RESEARCH PROGRAM/

GRADUATE STUDENT RESEARCH PROGRAM

Sponsored by the

AIR FORCE OFFICE OF SCIENTIFIC RESEARCH

Conducted by the

Universal Energy Systems, Inc.

FINAL REPORT

ESTIMATING SOLAR FLARE PROTON FLUENCES FROM 1850 WITH TRITIUM DATA

Prepared by: Hugh Nutley. Ph. D.

Academic Rank: Professor

Department and University: Electrical Engineering, Seattle Pacific University

Research Location: USAFGL/PHG
Hanscom AFB, MA 01731

USAF Researcher: Margaret A. Shea

Date: 22 June 89

Contract No: F49620-85-C-0013

Estimating Solar Flare Proton Fluences From 1850 With Tritium Data

by

Hugh Nutley. Ph. D.

ABSTRACT

Arrangements were made to get annual samples from 1850 of a high geomagnetic latitude glacier. These samples will give an estimate of solar flare proton fluences based on the tritium in them. Furthermore, the measuring of tritium by mass spectrometer was studied and also correlations between tritium concentrations, above-ground nuclear explosions, and proton fluences was investigated. Finally, a more exact method of calculating ^{14}C production by solar flare protons and galactic cosmic rays was found so that a student can do the calculation for his honors project this fall. Tritium and ^{14}C are similarly produced and knowledge of one is useful in understanding production of the other.

Acknowledgements

I thank the Air Force Systems Command and the Air Force Office of Scientific Research for sponsorship of this research and Universal Energy Systems for their help and clear instructions in completing all administrative details.

Don Smart is deeply appreciated for arranging the excellent word processor, a typewriter, an empty desk, and an empty room as well as for helping me send a number of facsimiles to Japan. He and Peg Shea were very supportive and provided me with a copy of their good paper on major solar proton events, a copy of the BRYNTRN transport model document which will be very helpful in my future papers, and a copy of the Joan Feynman paper on solar proton events. I especially appreciate Peg Shea's close reading of my reports, her supportive comments, and her positive recommendation on my Research Initiation Program application. I also thank Ed Cliver for reading my reports and his friendly attention to my project. Other researchers, librarians, and secretaries at the AFGL too numerous to mention were thoughtful and helpful; I did some good work I think and I am a better researcher and teacher as a result of this experience because the people of the laboratory helped me.

I. INTRODUCTION:

Major proton events originating in solar flares occur at random and have random fluences above any energy threshold. As a result, these events may cause unacceptable numbers of single event upsets in spacecraft electronics, or of military communications disruptions, or of electrical power grid shutdowns. Therefore the Air Force necessarily must seek to predict the probability and severity of future proton events in order to defend the nation despite those problems.

My mentors, Dr. Margaret A. Shea and Dr. Donald Smart of the AFGL, Space Physics Division (PHG), are experts in the study of proton events and they were interested in my suggestion, presented in Nutley and Voth (1987), for estimating the size of large events. In the paper, we calculate that one large proton event such as that of August 1972 will make many times as much tritium, ^3H, as is created by a whole year of galactic cosmic rays. (We calculated 67 times as much for that flare.) The 12.5 year half-life tritium scavenges out of the stratosphere, where it is produced, in a half-life residence time of about 20 months and out of the troposphere in about 10 days. If the tritium scavenges out as HTO snow at high geomagnetic latitudes in mountainous regions, it may pack into glacial ice that does not melt during summer months. Then the tritium is locked in the ice and may be removed years later. Given sufficient sensitivity for detecting tritium, it may be counted even 10 or 12 half lives

later. In short, one can estimate solar flare proton fluences even 150 years after the event.

To prepare for this work I took a BS in physics at MIT, where I graduated in the top 10% of my class, and a PhD in experimental nuclear physics at the University of Washington. In 1985, 1986, and 1987 I studied extreme value analysis of solar flare proton events while I was a Summer Faculty Fellow and then consultant for the Jet Propulsion Laboratory, California Institute of Technology. Before coming to the AFGL, I had negotiated with the Japanese Polar Research Institute to accompany their team to Greenland in May of 1989 in order to take ice core samples. I planned to count tritium in those samples with Dr. John Lupton, Research Professor of Oceanography at the University of California, Santa Barbara using his mass spectrometer.

II. OBJECTIVES OF THE RESEARCH EFFORT:

At present, fluence values for solar flare protons before 1956 are essentially unknown. And those values estimated between 1956 and about 1965 are only indirectly obtained from ground measurements of RF attenuation and of cosmic ray intensity from neutron monitors. In contrast, the more recent fluences and flux values measured with space vehicles in the past 24 years are well known. But MANY annual maximum values are needed for an extreme-value analysis which could confidently predict future fluences. Therefore, my long range goal in the 1989 Summer Faculty Research Program (SFRP) was to determine the largest fluence values for solar flare protons during as many years as possible. And my method of estimating those proton fluences was by measuring tritium concentrations in a high geomagnetic latitude glacier as described in the introduction to this report. It is true that immense quantities of tritium were injected into the stratosphere by above-ground nuclear fusion explosions beginning in 1952. But even if the recent tritium record is swamped, the previous record in frozen HTO is not. And one can hope to measure the bomb tritium pulses as a check on the method.

Before I arrived at the AFGL I had been negotiating for almost two years with Dr. Fumihiko Nishio of the Japanese National Polar Research Institute for permission to accompany their team to Greenland in May of 1989 to take ice core samples. I expected to do the necessary calculations for the trip early in the SFRP and

then return after taking the samples. To pay for the coring effort, I also had negotiated with a funding agency for two years. Early in my SFRP Dr. Nishio wrote that the Japanese government had not allocated sufficient funds to include me on their team. I found that the average cost for each member was $10,000 and, unfortunately, I had less money than that available to offer them.

When I could not go with the 1989 Japanese team I sought another way to get the cores. The University of Kansas Space Technology Center informed me that they will attempt an ice coring trip to high latitudes in Canada or Greenland in June and July of 1990. They assure me that they will take samples for me and then I can do the tritium analysis at the University of California, Santa Barbara. I have applied for a UES RIP grant and am negotiating with the Research Corporation and my university for the other necessary funds.

In addition to arranging for ice core samples, during this SFRP I essentially reached three short-term goals toward my long term goal of estimating past large proton fluences. The three goals were to answer the questions: 1) How does one measure tritium concentrations with a mass spectrometer? 2) What are the correlations between solar flare proton fluences, above-ground nuclear explosions, and existing tritium measurements in ice cores? and 3) ^{14}C, like tritium, is produced in the atmosphere by solar flares and by galactic cosmic rays. How much?

III. MASS SPECTROMETER MEASUREMENT OF TRITIUM:

Early tritium measurements involved concentrating the activity and then counting beta decays. More recently, scientists have increased measurement sensitivities two orders of magnitude by careful use of mass spectrometers, cold traps, and special glass containers that retard the leakage of gas. In short, now it is not decays which are measured but the entire population of daughter nuclei collected over a time as long as a year.

Early in the development of mass spectrometers for noble gas analysis, Reynolds (1956) found his machine unsuitable for helium measurements because atmospheric helium diffused through Pyrex walls into the spectrometer. In the early 1970's, Clarke, Jenkins, and Top (1975) made a mass spectrometer using Corning 1720 glass, with a very low diffusion rate for helium or hydrogen gas, which reached a detection limit of about 0.1 tritium unit (T. U.). That was equal to the best possible with the earlier enrichment and beta counting method. (One T. U. is a $^{3}H/^{1}H$ ratio of 10^{-21}.) Beginning in the late 1970's and continuing to the present, cold traps have been added to the low diffusion glass, which is now Corning 1720 or Corning 1724, to drop the detection limit two orders of magnitude to 0.001 T. U. for a 1-year storage time. (See Reynolds et. al. (1977), Jenkins et. al. (1983), and Lott and Jenkins (1984) for typical details.)

Oceanographers, such as John Lupton at the University of California, Santa Barbara who has agreed to help me on solar flare research, regularly use a mass spectrometer for analysis of tritium. To observe the detecting process, during my SFRP I visited the tritium counting laboratory of D. E. Lott at Woods Hole Oceanographic Institute, Woods Hole, MA which is like that of John Lupton in Santa Barbara. The counting proceeds:

1) Samples are introduced, with little contact with the atmosphere, into one of two different kinds of purged, clean containers: a length of copper tubing clamped at both ends or a flint glass, 1-liter bottle. The bottle cap seal is polyethylene which can keep tritium from leaking through for months, if needed.

2) Next, a small, measured amount (90 ml) of the sample is placed into a Corning 1720 or 1724 aluminosilicate glass ball having 200 ml. volume. After filling, the ball is connected to about 50 ml of LN-cooled graphite through about 20 cm of the Corning 1720 or 1724 glass tubing. A flow of water vapor carries with it all the helium, argon, and other gases leaving the tritium in the glass ball in the form of HTO. The graphite with its absorbed gases is sealed off by fusing the glass tubing; also the glass ball with the HTO is sealed by fusing. Later both containers are measured for helium content to ensure that the proper things in the proper amount are there.

3) The ball, now containing only tritium and no helium is placed in a deep freeze to ensure that no He leaks into the sample.

4) After a year, the ball is warmed up and then shaken for a

half hour to ensure that the headspace contains all the helium. Then the gas is sent through two traps at 55K and 10-70K; the first removes all gases but helium and neon while the second removes those and then sends them out one at a time as the trap is cycled to higher temperatures. Before gas is sent through the spectrometer, ^{4}He is measured with a Faraday Cup and ^{3}He is simultaneously measured with an electron multiplier to ensure that there is not too much.

5) Finally, if the pressures are in the correct range so that they won't swamp the spectrometer, the gas is allowed to enter and ^{3}H is effectively measured to a sensitivity of 0.001 T. U.

IV. TRITIUM, BOMB YIELD, AND SOLAR PROTON FLUENCE CORRELATIONS:

Several physical processes follow the injection of high energy protons into the atmosphere from solar flares or galactic cosmic rays. As considered in Section V below, ^{14}C is produced, and, as considered throughout this report, ^{3}H is produced. But also, above-ground nuclear explosions produce both ^{14}C and ^{3}H. To help determine correlations between tritium and explosion yield and between tritium and solar flares, Tables I and II below exhibit data available at present. In Table I the solar flare proton fluences are from Shea and Smart (1989) and Feynman (1989). Where they differ, in only three cases before there was satellite data, both estimates are given. Also in Table I, the nuclear yields are my estimates of the probable smallest and largest

values from Carter and Moghissi (1977). Table II gives tritium concentrations in antarctic firn corrected for decay from the year of deposition.

There are three years in Table II for which the tritium concentrations are higher at every station than for preceding and later years at those stations: 1973, 1969 and 1966. The 1973 peak clearly follows from the large solar flare fluences of August 1972. There was little nuclear yield in 1972 and probably not much in 1971. The 1969 peak clearly follows principally from the large nuclear fusion yields in the southern hemisphere in 1968. (Also there was a small continuing contribution from solar flare protons in 1968 and 1967.) It is reasonable that the ^{3}H would scavenge out of the stratosphere within a year when it need not diffuse to the other hemisphere.

The tritium peak in 1966 is harder to understand. There were no significant flares in 1965, 1964, or 1962, possibly none in 1963, and that in 1966 occurred September 2 according to Shea and Smart (1969). Nuclear explosions were not large in 1964 and 1965 and the large ones in 1966 occurred, according to Carter and Moghissi (1977), October 4 (at $21^{o}S$ $137^{o}W$) and December 28 (at $40^{o}N$ $90^{o}E$). It is true that there is uncertainty in the literature; both the number and yield of reported explosions are underestimates, according to Carter and Moghissi (1977). But the more obvious explanation of the 1966 tritium peak lies in the very large nuclear yields of 1961 and especially 1962. These were

principally Russian tests at 75°N and the diffusion times and scavenging out of the stratosphere would be expected to take 4 years. In a similar way, the high tritium count at the south pole in 1960 can be explained by the large American and Russian tests of 1956 through 1958 which were exploded in more southern latitudes on average.

V. CALCULATING ^{14}C PRODUCTION:

As is the case for ^{3}H, most of the ^{14}C in the atmosphere is made in a two-step process involving (p,n) reactions on nitrogen and oxygen and, finally, neutron reactions on nitrogen, principally. Therefore, the calculation for ^{14}C production which I am suggesting for my honors student, Mr. Tim Coleman, will parallel the calculation for ^{3}H production in the paper of Nutley and Voth (1987). The steps of the calculation are:

1) The target gas (N_2 or O_2) is randomly selected.
2) The energy of a proton is randomly selected from either the distribution of the August 1972 solar flare or that of galactic cosmic rays as is desired.
3) Use the cross sections for absorption of protons in Wilson (1989) and production of neutrons by (p,n) reactions in Silberberg and Tsao (1977) to find the probability of creating a neutron given a proton of the energy selected in step 2. Then compare a third random number with the calculated probability to

find if a neutron is indeed created. If it is, its energy is known.

4) Using the most modern ^{14}N (n,p) ^{14}C and ^{16}O (n,^{3}He) ^{14}C cross section tables from the National Nuclear Data Center at Brookhaven, calculate the number of ^{14}C nuclei produced by the neutron of energy found in step 3.

5) Compare the production by solar flare protons and galactic cosmic rays.

VI. RECOMMENDATIONS:

a. Ice cores from a high latitude glacier that does not melt in the summer should be sought in the northern hemisphere where most of the nuclear explosions occurred. For layers in the top 35 years, tritium in the cores should more clearly reflect the northern hemisphere explosions than is the case with Antarctic cores. For deeper layers, the tritium concentrations should give an estimate of solar flare proton fluences perhaps as early as 1850. To accomplish this task, I have applied for a Research Initiation Program grant from the Universal Energy Systems, Inc. and I have encouragement and forms from the Research Corporation to apply for a nearly matching grant to that of the UES. Finally, I am applying to my university for additional funds to pay for page costs, phone and copy fees, and cold weather equipment. See the tentative budget in Table III.

b. Section IV of this report on correlations between tritium, nuclear explosion yields, and solar flare proton fluences should be extended to include the few existing measurements of tritium in northern latitudes. Then a paper on the topic should be submitted for publication.

c. The calculation should be performed of ^{14}C production described in Section V using the new BRYNTRN code and the newest possible cross section values. Then a paper should be submitted for publication estimating the total global ^{14}C produced by solar flare proton fluences in contrast with active sun and quiescent sun galactic cosmic rays. An interesting topic for inclusion in that paper may be a comparison between ^{3}H and ^{14}C global production. An excellent physics major at my university is eager to begin the calculation for his honors thesis.

Table I.

YEAR	FLUENCE	ATMOSHPERIC YIELD (MT) at latitude:			TOTAL (MT)
	(10^{10} p/cm^2)	N:45-90°	0-45°	S: 0-45°	
1945			.06		0.06
1946			.04		0.04
1947		----------	----------	----------	0.00
1948			.10		0.1
1949		.02			0.2
1950		----------	----------	----------	0.00
1951		.04	.2/.3		0.2/0.3
1952			11./20.	.1/.9	11./21.
1953		1./10.	.25	.2/1.8	1.5/12.
1954		1./10.	16./55.		17./65.
1955		2.6/40.	.17		2.8/40.
1956	.22	2./40.	11./60.	2./3.6	15./104.
1957	.46/.1	5./80.	8./40.	1./2.	14./122.
1958	.66/1.1	21./90.	21./122.		42./212.
1959	2.1	----------	----------	----------	0.00
1960	3.5		.1		0.1
1961	.18	82./180.	.02		82./180.
1962	--------	94./190.	18./77.		110./270.
1963	.34/.01	----------	----------	----------	0.00
1964	--------		.02		0.02
1965	.02		.02		0.02
1966	.1		.44/2.	.27/.37	0.7/2.4
1967	.2		3.	.06	3.
1968	.2		3.	1.5/2.7	4.5/5.7
1969	.3		3.		3.
1970	.05		3.	2.3/2.6	5.3/5.6
1971	.2		.02	.3/1.2	0.3/1.2
1972	1.1		.1/.2		0.1/0.2
1973	.005		2./3.		2./3.
1974	.06		.2/1.		0.2/1.
1975	.001	----------	----------	----------	0.00
1976	.01	----------	----------	----------	0.00
1977	.07	----------	----------	----------	0.00
1978	.7	----------	----------	----------	0.00
1979	.1	----------	----------	----------	0.00
1980	.02	----------	----------	----------	0.00

Table II.

YEAR	TRITIUM IN T. U. AT LATITUDES: (GEOMAGNETIC LATITUDES)								
	41°S* (43°S)	67°S* (77°S)	68°S* (74°S)	70°S* (79°S)	72°S* (81°S)	73oS* (81°S)	76°S* (66°S)	90°S! (79°S)	90°S! (79°S)
1954								70	
1955								(70)	
1956		25	120	40	110	55		130	
1957		50	190	60	215	60		360	
1958		60	160	75	115	25		580	
1959		50	250	60	125	50		340	560
1960	18	45	165	85	190	55		1080	1000
1961	14	55	50	50	80	60		260	280
1962	20	60	190	110	85	105		320	375
1963	44	125	110	180	155	80		480	1030
1964	64	180	190	330	485	150		900	1140
1965	51	70	140	205	350	320		1580	1690
1966	75	415	300	335	450	850	615	1900	2780
1967	48	220	150	250	210	(500)	310	1080	1590
1968	44	200	170	215	250	340	380	1020	720
1969	53	210	280	320	670	550	430	1680	2030
1970	41	90	105	260	370	330	330	480	840
1971	38	75	150	275	215	250	210	1360	780
1972							250	400	410
1973							275	1900	780
1974								180	220
1975									220
1976									125
1977									190

* From Merlivat (1978)

! From Jouzel (1979)

Table III.

Proposed Budget

		Seattle Pacific	Research Corporation	Universal Energy Sys.
a)	Equipment and Supplies			
	Sample Containers/Carrying Case			
	1990 (140 @ 40 + 300)		$5,900	
	Cold Weather Gear			
	1990 (tent, clothing, etc)	$1,800		
b)	Stipends			
	1990 Principal (11 weeks)			$7,200
	1991 Student (2 months)		2,200	
	1991 Principal (10 weeks)		7,000	
c)	Other			
	Otain Samples in Canada or Greenland			
	1990 U of Kansas Space Technology Center			10,000
	Outgas Samples			
	1990 UCSB			1,600
	Mass Spectrometer			
	1991 UCSB		2,500	
	1990 Phone, Copy Costs	250		
	Travel in U. S.			900
	Motels in U. S.			300
	1991 Phone, Copy Costs	250		
	Journal Page Fee	650		
	Travel in U. S.		400	
	Housing in U. S.		500	
		$2,950	$18,500	$20,000
		(7%)	(45%)	(48%)

TOTAL BUDGET: $41,450.

REFERENCES

Carter, M. W. and Moghissi, A. A., Three Decades of Nuclear Testing, Health Phy., 1977, Vol. 33, pp. 55-71.

Clarke, W. B., Jenkins, W. J., and Top, Z., Determination of Tritium by Mass Spectrometric Measurement of ^3He, Int. J. App. Rad. Isot., 1976, Vol. 27, pp. 515-522.

Feynman, J., Armstrong, T., Dao-Gilbner, L., and Silverman, S., A New Proton Fluence Model, Spacecraft and Rockets, 1989, accepted for publication.

Jenkins, W. J., Lott, D. E., Pratt, M. W., and Boudreau, R. D., Anthropogenic Tritium in South Atlantic Bottom Water, Nature,Lond., Vol. 305, No. 5929, 1983, pp. 45-46.

Jouzel, J., Merlivat, L., Pourchet, M., and Lorius, C., A Continuous Record of Artificial Tritium Fallout at the South Pole, Earth Planet. Sci. Lett., Vol. 45, 1979, pp. 188-200.

Lott, D. E. and Jenkins, W. J., An Automated Cryogenic Charcoal Trap System for Helium Isotope Mass Spectrometry, Rev. Sci. Instrm., 1984, Vol. 55(12), pp. 1982-1988.

Merlivat, L., Jouzel, J., Robert, J., and Lorius, C., Distribution of Artificial Tritium in Firn Samples From East Antarctica, IAHS-AISH PUBL. 118, 1978, pp. 138-145.

Nutley, H. and Voth, M. D., Estimating the Anomalously Large Fluences of Solar Flare Protons with Tritium Data From 1900 to 1952, J. Geophys. Res., 1987, Vol. 92, No. A10, pp. 11179-11182.

Reynolds, J. H., High Sensitivity Mass spectrometer for Noble Gas Analysis, Rev. Sci. Instru., 1956, Vol. 27, No. 11, pp. 928-934.

Reynolds, J. H., Jeffery, P. M., McCrory, G. A., and Varga, P. M., Improved Charcoal Trap for Rare Gass Mass Spectrometry, Rev. Sci. Instrm., 1977, Vol. 49(4), pp. 547-548.

Shea, M. A. and Smart, D. F., A Summary of Major Solar Proton Events, Sol. Phy., in press.

Silberberg, R. and Tsao, C. H., Cross Sections for (p,xn) Reactions, and Astrophysical Applications, Astrophy. J. Supp., 1977, Vol. 35, pp. 129-136.

Wilson, J. W., et. al., BRYNTRN: A Baryon Transport Model, NASA TP 2887, 1989, Langley Res. Cent.

1989 USAF-UES SUMMER FACULTY RESEARCH PROGRAM/

GRADUATE STUDENT RESEARCH PROGRAM

Sponsored by the

AIR FORCE OFFICE OF SCIENTIFIC RESEARCH

Conducted by the

Universal Energy Systems, Inc.

FINAL REPORT

Electric Fields in the Middle- and Low-Latitude Ionosphere and Plasmasphere

Prepared by:	Craig E Rasmussen
Academic Rank:	Research Assistant Professor
Department and	Center for Atmospheric and Space Sciences
University:	Utah State University
Research Location:	Geophysics Laboratory PHG Hanscom AFB, MA 01731
USAF Researcher:	Nelson Maynard
Date:	19 September 1989
Contract No:	F49620-88-C-0053

Electric Fields in the Middle- and Low-Latitude Ionosphere and Plasmasphere

by

Craig E Rasmussen

ABSTRACT

Previous research has effectively shown that middle- and low-latitude electric fields are primarily caused by neutral winds in the dynamo region of the ionosphere. These electric fields are important because they are indicative of tidal motion in the Earth's atmosphere and of coupling processes between the thermosphere and the ionosphere. Middle- and low-latitude electric fields are also of interest to the Air Force at this time because of the Combined Release Radiation Effects Satellite (CRRES) which will be making measurements in the Earth's plasmasphere and radiation belts. This report describes research related to middle- and low-latitude electric fields which was done at the Geophysics Laboratory in conjunction with the Summer Faculty Research Program. The research was primarily divided into two areas: Electric field data from the double probe, vector electric field instrument (VEFI) on the DE 2 spacecraft were examined in the magnetic latitude range from 30° to approximately 50°. Electric fields in this latitude range are typically of the same order as instrumental errors so the amount of reliable data is often limited. Thus, a new technique was evaluated to see if the amount of useful data could be increased. This new technique showed promise but further evaluation is necessary. The other area of research involved an extensive review of the scientific literature related to mid- and low-latitude electric fields. This review was done in order to devise a research program which can be undertaken in support of the CRRES program.

I. INTRODUCTION:

Electric fields have been measured in the Earth's space environment by several spacecraft. Scientific studies which have utilized these data have primarily concentrated on electric fields in the polar and high-latitude regions. This is principally because of the large electric fields that exist there and the importance of these fields to various processes in the Earth's ionosphere and thermosphere. However, middle- and low-latitude electric fields are also important as they are indicative of diurnal tides in the Earth's atmosphere and the coupling of these winds to the ionosphere. These low-latitude electric fields are substantially smaller than the fields at higher latitudes and are more difficult to measure. Middle- and low-latitude electric fields are of particular interest to the Air Force at this time because of the Combined Release Radiation Effects Satellite (CRRES) which will be making measurements in the Earth's plasmasphere and radiation belts.

Scientists associated with the magnetospheric branch at the Geophysics Laboratory have done extensive research regarding electric fields in the magnetosphere and the plasmasphere and their coupling to the ionosphere (e.g., Burke et al., 1982; Maynard et al., 1983, 1988). My own research interests in the past couple of years have centered on the plasmasphere. These interests include the refilling of the plasmasphere following magnetic storms and the subsequent evolution and formation of the plasmapause (Rasmussen and Schunk, 1988a). A three-dimensional numerical model has been created to theoretically study densities within the plasmasphere and the diurnal response of the plasmasphere to convection electric fields (Rasmussen and Schunk, 1989). Also of interest are the generation mechanism of ionospheric electric fields and the coupling of the ionosphere and the magnetosphere via field-aligned currents (Rasmussen and Schunk, 1988b; Rasmussen and Schunk, 1987).

This report describes research done at the Geophysics Laboratory as part of the 1989 Summer Faculty Research Program. Objectives of the research are described in the next section followed by a description of the two major areas of research. Finally, recommendations for further research are made in the concluding section.

II. OBJECTIVES OF THE RESEARCH EFFORT:

One of my primary goals during the summer program was to examine electric field data from the Dynamics Explorer (DE 2) satellite. Maynard et al. (1988) examined electric field data from the double probe, vector electric field instrument (VEFI) on the DE 2 spacecraft to determine the average meridional electric field in the region within 30° of the magnetic equator. Typical average amplitudes of the electric field ranged between 3 and 6 mV/m. These low amplitudes are near the limits of the VEFI probe (the limitations due in large part to a contact potential of unknown and varying magnitude developing on the instrument). Maynard et al. employed a method for estimating the contact potential between the probe and the background plasma, which was valid only in the region within 30° of the magnetic equator. Thus, in order to study electric field data taken at slightly higher latitudes, up to roughly 55°, a different method for estimating the contact potential had to be developed. Therefore, one of my research goals was to evaluate new methods for estimating the contact potential.

Another research goal was associated with the coming flight of the CRRES satellite, which is to make electric field and plasma measurements in the Earth's plasmasphere and radiation belts. Much of my research emphasis relating to electric fields has been on theoretical modeling of high-latitude fields. Since high-latitude fields are primarily of different origin than the fields at lower latitudes, another of my research goals was to become more familiar with electric field sources at middle and low latitudes and with the measurements which had been made in these regions. This study was undertaken with the goal to try and find an area of research which would, not only utilize expertise which I have gained in previous theoretical modeling studies, but which could also be used in support of future plasmaspheric measurements of the CRRES satellite.

An outline of the work done to accomplish these two goals is given in the next two sections.

III. ESTIMATING THE CONTACT POTENTIAL:

a. Approach taken. VEFI electric field measurements are made in the plane containing the orbit of the DE 2 spacecraft. These measurements are made with probes at the end of two booms extending from the satellite. These booms are orientated at an angle of 90° from each other and at some known angle from the Earth's magnetic field. The problem is to be able to estimate the two contact potentials which are associated with the probes on each of the two booms. As long as the magnetic field direction lies in the orbit plane (mostly applicable at middle and low latitudes), advantage can be taken of the fact that electrical conductivity is effectively infinite along the magnetic field and that, therefore, the electric field in the magnetic field direction is zero. This information reduces the number of unknowns from two to one.

Further progress can be made if it is assumed that the contact potentials remained constant over a portion of the spacecraft orbit. For instance, in the first test we made, it was assumed that the contact potentials remained constant during the time it took for the spacecraft to traverse from 30° in one hemisphere, over the pole and back down to 30° in the same hemisphere. Measurements, made at the two ends the traverse, were used to obtain two independent equations containing two unknowns (the two contact potentials). The contact potentials obtained in this manner were then used to plot electric field data along the entire portion of the orbit. A check for consistency with the original assumptions was then made by examining the electric field component along the magnetic field direction, E_z; if this component was near zero then the original assumptions were valid.

b. Results. Orbits of the DE 2 spacecraft were examined to find times when measurements were taken continuously from 30° in one hemisphere, over the pole and back down to 30° in the same hemisphere. 53 orbits were found which satisfied this criterion. Contact potentials were then estimated by the method described above and the electric field component along the magnetic field direction was examined to check to see if it was nearly zero (within ± 2 mV/m). In only 15 orbits, out of the original 53, did the estimated contact potentials produce electric field components E_z which were less than ± 2 mV/m. The data from these 15 orbits were too few to produce reliable statistics.

It was then decided to try a slightly different assumption about the temporal vari-

ation in the contact potentials. Clearly, the contact potentials were frequently varying on a time scale which was small in comparison to the time it takes for the satellite to traverse 120° in latitude. Therefore, it was decided to break the orbit into smaller segments of approximately 10° each. The contact potentials were assumed to be constant over each set of data points which were roughly 10° apart. The contact potentials were then estimated by the method described above for each of the many sets of points. When a running average of these contact potentials were used over sections of the orbit of roughly 20°, it was found that E_z was within ± 1 mV/m for over 50% of the orbits tested.

An example of the electric fields obtained by this latter method is shown in Figure 1. The lower panel shows the parallel electric field component, E_z. As can be seen in the figure, E_z remains very nearly zero from 20° to 50° invariant latitude. At the same time, E_x, the component perpendicular to the magnetic field, changes by 4 mV/m. It should be noted that the first method for estimating contact potentials failed when applied to data from this orbit. Thus, it can be seen that the latter method substantially improves the amount of useful data which can be used for scientific study.

IV. REVIEW OF LITERATURE:

In this section a brief review of a portion of the literature regarding the dynamo generation of middle- and low-latitude electric fields is given. A discussion of measurements as well as theoretical aspects of electric fields in this region of the ionosphere and plasmasphere is included. The focus of this section is on examining potential avenues of future research which can be done in support of the future flight of the CRRES satellite.

There are primarily two sources of electric fields in the plasmasphere. During magnetically active times, relatively large electric fields of magnetospheric origin can penetrate into the plasmasphere. These electric fields are normally shielded from the plasmasphere by space charge which builds up at the inner edge of the ring current (e.g., see review by Wolf, 1975). During magnetically quiet times, the predominant source of electric fields for $L < 3$ has been shown to be the atmospheric dynamo (e.g., Richmond et al., 1976). Atmospheric winds couple with the ionosphere via ion-neutral collisions and drive electric currents, which in turn lead to the creation

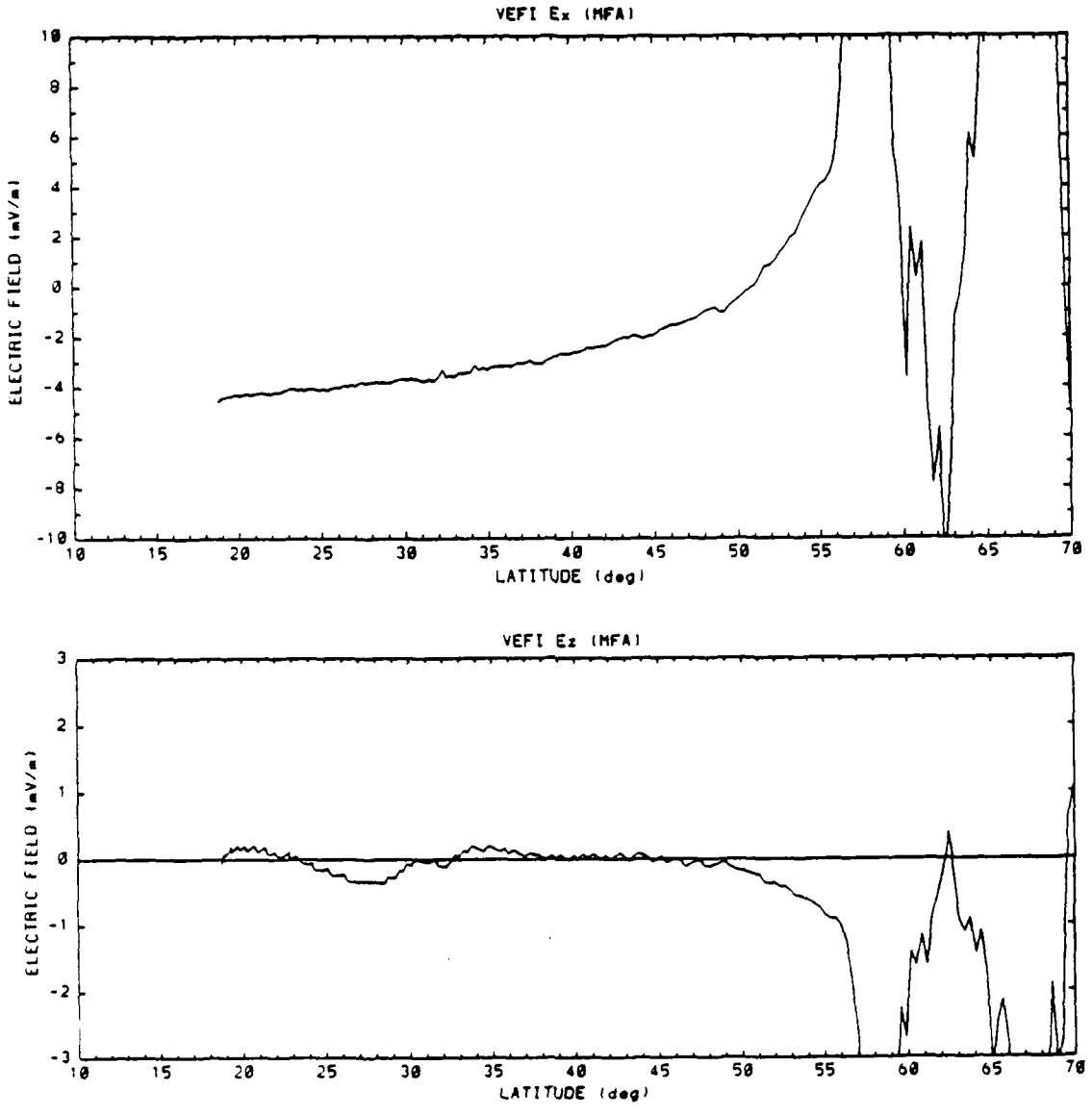

Fig. 1. Perpendicular (top panel) and parallel (bottom panel) components of the VEFI electric field as a function of invariant latitude.

of electric fields.

Equatorial electric fields have been reviewed by Fejer (1981). During magnetically quiet periods, daytime vertical drifts in the F-region are upward with an average velocity of about 20 m/s, corresponding to an eastward electric field of 0.5 mV/m. These drifts reverse at night and are usually slightly larger than the daytime drifts (Woodman, 1970). The east-west drifts are westward during the day with drift velocities of about 50 m/s ($\sim$ 1 mV/m) and eastward at night. Again the nighttime velocities are slightly larger than those during the day. The east-west drifts show little dependence on season, solar cycle, or magnetic activity (Fejer et al., 1981). However, the vertical drifts show a dependence on all three parameters, in particular on magnetic activity (Fejer, 1986).

At latitudes above the magnetic equator, ionospheric electric fields are directly coupled to the plasmasphere because of the very high electrical conductivity along magnetic field lines. Maynard et al. (1988) examined over 300 passes of the DE 2 spacecraft to obtain an empirical model of the meridional electric field (east-west drifts) between $\pm 30°$ magnetic latitude. They found a diurnal pattern similar to the patterns obtained by radar measurements in the F-region ionosphere (Fejer et al., 1985), although the magnitude was somewhat higher that the ionospheric measurements. The meridional electric field in the plasmasphere was found to vary substantially with latitude in the early morning sector, with the field reversing direction near 30°. Coley and Heelis (1989) performed a similar study using drift meter data on the DE 2 satellite and found very good agreement with the radar measurements of east-west drifts, but somewhat less with the vertical drifts. Both Maynard et al. and Coley and Heelis found that the ion and neutral drifts displayed similar diurnal patterns, emphasizing the coupling between the thermosphere and the ionosphere in the equatorial region.

Finally, Richmond et al. (1980) developed an empirical model of quiet-day electric fields. By incorporating observations from several incoherent scatter radars, this model is applicable over the region between $\pm 60°$ magnetic latitude. This model includes seasonal and, to some extent, longitudinal variations in the electric field as well.

During magnetically quiet times, the middle- and low-latitude electric fields show a repeatable diurnal pattern (albeit with some variability). The relatively consistent diurnal pattern is linked to the diurnal and semi-diurnal tides of the neutral atmo-

sphere. This can be seen by examining the dynamo equations, which describe the coupling between the thermosphere and the ionosphere. The principal equation,

$$\mathbf{J} = \sigma \cdot (\mathbf{E} + \mathbf{u} \times \mathbf{B}) \tag{1}$$

relates the current density J to the electric field E, where σ is the tensor conductivity. The latter term in (1) is the induced emf due to the motion of the neutral gas ($\mathbf{u}$) with respect to the geomagnetic field ($\mathbf{B}$). It is assumed that the electric field is electrostatic,

$$\mathbf{E} = -\nabla\Phi \tag{2}$$

and that current is conserved,

$$\nabla \cdot \mathbf{J} = 0 \tag{3}$$

Finally, because of the high conductivity along magnetic field lines, it is assumed that magnetic field lines are equipotentials, i.e.,

$$E_z = 0 \tag{4}$$

where E_z is the parallel (to $\mathbf{B}$) component of the electric field. Given a model of the conductivities and the neutral wind, along with appropriate boundary conditions, these equations can be solved for the electric potential Φ.

There have been several theoretical studies which have solved the dynamo equations to model electric fields and currents in the middle- and low-latitude ionosphere. Tarpley (1970) showed that the electrical currents created by the diurnal, (1,-2) tidal mode winds give rise to geomagnetic Sq variations which are similar to observations. The (1,-2) mode is generated by in situ absorption of UV and EUV radiation and is important in the E- and lower F-region ionosphere, where the Pedersen and Hall conductivities are the highest. Stening (1973) used the same tidal mode to model electric fields and found reasonable agreement between the calculated and the observed electrostatic field near the equator, but found less agreement at higher latitudes. A peak in the electric field was predicted near sunset due to variations in conductivity. This peak is frequently observed in electric field measurements.

Richmond et al. (1976) demonstrated that the diurnal (1,-2) mode is significantly influenced by the ion drag force. When the (1,-2) mode is modified to take into

account ion drag, they found that this wind mode accounted for most of the middle- and low-latitude electric fields. However, they found the best agreement with observations during the daytime, when the diurnal (1,-2) mode was combined with the semidiurnal (2,4) mode. Furthermore, they demonstrated that a magnetospheric source cannot account alone for the observed electric fields and currents. Forbes and Lindzen (1977) found that the (2,2) mode, in conjunction with the strong diurnal component of conductivity, may also be important. Both Richmond et al. and Forbes and Lindzen found less agreement with the observations at night and suggested that F-region winds may play an important role at night.

As discussed above, dynamo electric fields are primarily driven by diurnal and semidiurnal tides. However, magnetic storms and substorms can also have a large effect on the neutral atmosphere through Joule heating of the thermosphere. The disturbed wind patterns created by storm activity can last for several hours. This is in comparison to the 10's of minutes it takes for the Alfvén layer to shield high-latitude electric fields from the plasmasphere. Of particular interest, then, is what happens to electric fields in the plasmasphere in the latter stages of a magnetic storm. Blanc and Richmond (1980) have shown that energy input to the thermosphere during magnetic disturbances alters the global thermospheric circulation and consequently alters the generation of electric fields and currents at middle and low latitudes by ionospheric wind dynamo action. They referred to this as the disturbance dynamo.

Subsequent to these predictions, Fejer et al. (1983) found that equatorial east-west electric fields are sometimes perturbed 16–24 hours after the onset of geomagnetic storms. They found that disturbance dynamo electric fields decrease and sometimes even reverse the quiet-time pattern of electric fields during both daytime and nighttime. Foster and Aarons (1988) recently found evidence of disturbance dynamo fields at higher latitudes in Millstone Hill radar observations. In a modeling study of low latitude electric fields during a magnetically active period, Spiro et al. (1988) found that the duration of perturbed fields at low latitudes could only be explained when disturbed thermospheric winds were considered.

V. RECOMMENDATIONS:

In this section recommendations are made for future action on the results of research undertaken this summer. Suggestions are made for continuing a small-scale effort to examine electric field data from the DE 2 spacecraft and to initiate a modeling program to study the disturbance dynamo.

As explained above, a new method to estimate the contact potential on the electric field probes was developed. Initial results of this method showed promise. However, it should be pointed out that other mechanisms, in addition to contact potentials, can lead to measurement errors. Thus, it is suggested that electric field data obtained by this new method be checked to see if it generally fits previous measurements and also fits our theoretical understanding of electric fields in the plasmasphere.

As discussed above, on magnetically quiet days, middle and low-latitude electric fields are caused by tides active in the Earth's atmosphere and generally follow a diurnally reproducible pattern. It is suggested that data from roughly 200 orbits be reduced to eliminate the contact potential and then binned according to magnetic latitude and local time. These data could then be compared with, for instance, the empirical model of Richmond et al. (1980). At this point a further determination could be made as to the likelihood that further work would lead to publishable results.

On the theoretical side, it is suggested that a program be initiated to model the disturbance dynamo. Spiro et al. (1988) have shown that the disturbance dynamo is of critical importance in understanding the time it takes for substorm electric fields to decay at low latitudes. However, as the Spiro et al. study used only a very crude model of neutral winds, further study is needed to understand the impact of the disturbed thermosphere on electric field generation.

Specifically, it is suggested that the electric field model developed at Utah State University (see Rasmussen and Schunk, 1987) should be modified to include neutral winds. This modification is relatively minor as it only requires the addition of an extra term in (1); no major changes in numerical methods are required. The modified model could then be used to study dynamo electric fields, given an appropriate wind pattern. NCAR thermospheric general circulation model (TGCM) wind patterns exist for two days encompassing a quiet period followed by a magnetic storm

(Crowley et al., 1989). The Crowley et al. study was the first realistic time dependent simulation to incorporate upward propagating tides and is, thus, ideal to use to model the disturbance dynamo fields. Winds from the NCAR TGCM are considerably more realistic than the idealized tidal modes used in previous dynamo modeling studies. Although Richmond and Roble (1987) have previously used TGCM winds to model dynamo electric fields, they did not include auroral zone heating or magnetospheric convection in the TGCM model runs. The planned study would therefore be the first to use realistic, time dependent winds to model the effect of the disturbed thermosphere on dynamo-generated electric fields. Furthermore, this time-dependent study would also be important because it would provide a realistic estimate of dynamo electric fields in the plasmasphere during magnetically active conditions, separate from the magnetospheric electric fields which also exist in the plasmasphere during disturbed conditions.

ACKNOWLEDGMENTS

I wish to thank the Air Force Systems Command and the Air Force Office of Scientific Research for sponsorship of this research. Universal Energy Systems should also be credited for their administration of the summer faculty research program. Special mention should be of the support and the help of Nelson Maynard and Bill Burke. Many others in the magnetospheric branch of the Geophysics Laboratory should also be thanked for many stimulating conversations and for their technical assistant. All helped to make my stay a thoroughly enjoyable experience.

REFERENCES

Blanc, M., and A.D. Richmond, "The Ionospheric Disturbance Dynamo," J. Geophys. Res., 1980, Vol. 85, pp. 1669–1686.

Burke, W.J., M.S. Gussenhoven, M.C. Kelley, D.A. Hardy, and F.J. Rich, "Electric and Magnetic Field Characteristics of Discrete Arcs in the Polar Cap," J. Geophys. Res., 1982, Vol. 87, pp. 2431–2443.

Coley, W.R., and R.A. Heelis, "Low-Latitude Zonal and Vertical Ion Drifts Seen by DE 2," J. Geophys. Res., 1989, Vol. 94, pp. 6751–6761.

Crowley, G., B.A. Emergy, R.G. Roble, H.C. Carlson, Jr., and D.J. Knipp, "Thermospheric Dynamics During September 18–19, 1984: I. Model Simulations," J. Geophys. Res., 1989, in press.

Fejer, B.G., "The Equatorial Ionospheric Electric Fields. A Review," J. Atmos. Terr. Phys., 1981, Vol. 43, pp. 377-386.

Fejer, B.G., "Equatorial Ionospheric Electric Fields Associated with Magnetospheric Disturbances," Solar Wind-Magnetosphere Coupling, edited by Y. Kamide and J.A. Slavin, pp. 519-545, Tokyo, Japan, Terra Scientific Publishing Company, 1986.

Fejer, B.G., D.T. Farley, C.A. Gonzales, R.F. Woodman, and C. Calderon, "*F* Region East-West Drifts at Jicamarca," J. Geophys. Res., 1981, Vol. 86, pp. 215–218.

Fejer, B.G., M.F. Larsen, and D.T. Farley, "Equatorial Disturbance Dynamo Electric Fields," Geophys. Res. Lett., 1983, Vol. 10, pp. 537–540.

Fejer, B.G., E. Kudecki, and D.T. Farley, "Equatorial *F* Region Zonal Plasma Drift," J. Geophys. Res., 1985, Vol. 90, pp. 12,249–12,255.

Forbes, J.M., and R.S. Lindzen, "Atmospheric Solar Tides and Their Electrodynamic Effects—III. The Polarization Electric Field," J. Atmos. Terr. Phys., 1977, Vol. 39, pp. 1369–1377.

Foster, J.C., and J. Aarons, "Enhanced Antisunward Convection and *F* Region Scintillations at Mid-Latitudes During Storm Onset," J. Geophys. Res., 1988, Vol.

93, pp. 11,537–11,542.

Maynard, N.C., T.L. Aggson, and J.P. Heppner, "The Plasmaspheric Electric Field as Measured by ISEE 1," J. Geophys. Res., 1983, Vol. 88, pp. 3981–3990.

Maynard, N.C., T.L. Aggson, F.A. Herrero, and M.C. Liebrecht, "Average Low-Latitude Meridional Electric Fields From DE 2 During Solar Maximum," J. Geophys. Res., 1988, Vol. 93, pp. 4021–4037.

Rasmussen, C.E., and R.W. Schunk, "Ionospheric Convection Driven by NBZ Currents," J. Geophys. Res., 1987, Vol. 92, pp. 4491–4504.

Rasmussen, C.E., and R.W. Schunk, "Multistream Hydrodynamic Modeling of Interhemispheric Plasma Flow," J. Geophys. Res., 1988a, Vol. 93, pp. 14,557–14,565.

Rasmussen, C.E., and R.W. Schunk, "Ionospheric Convection Inferred From Interplanetary Magnetic Field-Dependent Birkeland Currents," J. Geophys. Res., 1988b, Vol. 93, pp. 1909–1921.

Rasmussen, C.E., and R.W. Schunk, "A Three-Dimensional Time-Dependent Model of the Plasmasphere," J. Geophys. Res., 1989, in press.

Richmond, A.D., and R.G. Roble, "Electrodynamic Effects of Thermospheric Winds from the NCAR Thermospheric General Circulation Model," J. Geophys. Res., 1987, Vol. 92, pp. 12,365–12,376.

Richmond, A.D., S. Matsushita, and J.D. Tarpley, "On the Production Mechanism of Electric Currents and Fields in the Ionosphere," J. Geophys. Res., 1976, Vol. 81, pp. 547–555.

Richmond, A.D., M. Blanc, B.A. Emery, R.H. Wand, B.G. Fejer, R.F. Woodman, S. Ganguly, P. Amayenc, R.A. Behnke, C. Calderon, and J.V. Evans, "An Empirical Model of Quiet-Day Ionospheric Electric Fields at Middle and Low Latitudes," J. Geophys. Res., 1980, Vol. 85, pp. 4658–4664.

Spiro, R.W., R.A. Wolf, and B.G. Fejer, "Penetration of High-Latitude-Electric-Field Effects to Low Latitudes During SUNDIAL 1984," Ann. Geophysicae, 1988, Vol. 6, pp. 39–50.

Stening, R.J., "The Electrostatic Field in the Ionosphere," Planet. Space Sci., 1973, Vol. 21, pp. 1897–1910.

Tarpley, J.D., "The Ionospheric Wind Dynamo, 2, Solar Tides," Planet. Space Sci, 1970, Vol. 18, pp. 1091–1103.

Wolf, R.A., "Ionosphere-Magnetosphere Coupling," Space Sci. Rev., 1975, Vol. 17, pp. 537.

Woodman, R.F., "Vertical Velocities and East-West Electric Fields at the Magnetic Equator," J. Geophys. Res., 1970, Vol. 75, pp. 6249–6259.

1989 USAF-UES SUMMER FACULTY RESEARCH PROGRAM

Sponsored by the

AIR FORCE OFFICE OF SCIENTIFIC RESEARCH

Conducted by the

Universal Energy Systems, Inc.

FINAL REPORT

Review and Assessment of Carbon Dioxide Pressure Broadening Data

Prepared by: Robert E. Willis, Ph.D.

Academic Rank: Associate Professor

Department and University: Physics and Earth Sciences, Mercer University

Research Location: GL/OPI
Hanscom AFB
Bedford, Massachusetts 01731-5000

USAF Researcher: Laurence S. Rothman

Date: 25 August 1989

Contract No: F49620-88-C-0053

REVIEW AND ASSESSMENT OF CARBON DIOXIDE PRESSURE BROADENING DATA

by

Robert E. Willis

ABSTRACT

A review was conducted of all journal articles published since 1965 that relate to the pressure broadening of carbon dioxide absorption lines. For each broadening species, the published data were compared by vibrational band, branch (P, Q and R) and experimental technique. Various systematic differences between branches and bands as a result of technique are reported. Recommendations are made concerning which data to use for the HITRAN database. Comparison of all data gave a broadening coefficient of O_2, relative to N_2, of 0.85. The variation of halfwidth with temperature was also reviewed, and recommendations made for values of the temperature coefficient n. Theoretical calculations of both halfwidths and n are compared to the experimental values.

Acknowledgements

I wish to thank the Air Force Systems Command and the Air Force Office of Scientific Research for the sponsorship of this research. Universal Energy Systems aided me in all administrative aspects of this program; they were especially helpful with the logistics of the pre-summer visit.

Many people at the OPI branch helped make my time there enjoyable and rewarding. Dr. Laurence S. Rothman provided encouragement and help with my computer programming. Jim Chetwynd, Lt. Scott Shannon and Frank Kneizys also gave willing help. A special thanks is owed to Ms. Nancy Lott-Schlicher for her editing and typing of this report.

I. INTRODUCTION

The HITRAN database is a catalogue of spectroscopic parameters of molecular species commonly found in the earth's atmosphere. As many as seven parameters are provided for each of nearly 348,043 absorption lines in the spectral range 0 to 17,900 cm^{-1}.

One of the more important molecules included in HITRAN is carbon dioxide and the pressure-broadened or Lorentzian halfwidth is a very significant parameter for those who apply the HITRAN database in studies of atmospheric transmission. Over the past twenty years, many researchers have studied the pressure-broadening of carbon dioxide absorption lines due to carbon dioxide itself, nitrogen, oxygen and occasionally other gases. A number of vibrational bands have been investigated using a wide variety of experimental techniques. There is considerable scatter in the published data; which data is better and whether there are significant differences between bands or as a result of techniques, is not clear. Furthermore, the published data show a great variation in how the halfwidth changes with temperature.

My research background is in the microwave spectra of gases. However, I have also studied the pressure-broadening of carbon monoxide lines in the infrared region. This experience led to my assignment to the Infrared Physics

Branch of the Optical and Infrared Technology Division of the Geophysics Laboratory.

II. OBJECTIVES OF THE RESEARCH EFFORT

The shape of a spectral absorption line widens with increasing pressure. Both experimentally and theoretically the shape of an isolated line broadened solely as a result of collisions is described mathematically by the Lorentz function with the halfwidth at half maximum being directly proportional to the total pressure. The broadening effect on lines of a given molecule varies with the species of the colliding molecule and the rotational state of the absorbing molecule. This broadening effect is included in the HITRAN database by listing for each rotational level J the value at atmospheric pressure of the collision-induced halfwidth, γ, in units of cm^{-1}/atm. These values are all for a temperature of 296 K, since the halfwidth at a fixed pressure decreases with temperature. The effect of temperature is included by giving a value for the exponent n in the semi-empirical formula

$$\gamma(T) = \gamma(T_o)\ (T_o/T)^n. \qquad (1)$$

Over the last twenty years there have been a great many experimental studies of the pressure-broadening of carbon dioxide absorption lines by various gases, in various IR bands and as a function of temperature. Several theoretical studies have also been published on this subject. There is a considerable scatter among the results of these studies, though they all show the same general pattern for the

variation of γ with rotational level. It is not certain whether γ should be taken to be the same for all vibrational transitions having the same rotational level J, or whether there is a small variation between bands or between the P, Q and R branches of a given band. There may also be systematic variations in the results caused by the different experimental techniques. Finally, there is considerable disagreement on the value of the temperature coefficient n.

My assignment as a participant in the 1989 Summer Faculty Research Program was to determine which data among published experimental and theoretical values should be included in the HITRAN database. First, I was assigned to discover if there was a significant difference in γ between bands or between branches of the same band, and whether there was a systematic difference between the results of different techniques. When calculating average values for the HITRAN tape, should some data be omitted and should some be given a greater weight than others? Secondly, I was also to determine the best value to use for the temperature coefficient n for each broadening species for which adequate data exists. An additional task was to find out what is known about the shift with increasing pressure of the center frequency of carbon dioxide lines.

III.

Every article published since 1968 that related to these questions was read with careful attention given to the

details of the experimental technique. All published values of γ and n were assembled into a notebook and arranged according to the broadening gas and the vibrational band, with a brief description of the experimental technique included. Next, all the halfwidth values were entered into separate tables for each band. Each row of a table corresponds to a value of J", the rotational quantum number of the lower vibrational state, and each column is the data reported in a particular paper. Columns for the different branches P, Q and R, were grouped together. All data was normalized to 296 K using equation (1) and n = 0.75.

All the self-, nitrogen- and oxygen-broadened data were entered into Fortran programs that printed the values out in columns similar to those described above and calculated various averages for each value of J". These data tables were also fed into a graphing program called Grapher which allowed plotting the halfwidth values from each paper with a different symbol. For self broadening and N_2 broadening, the following graphs were prepared: 9.4μ P branch, 9.4μ R, 10.4μ P, 10.4μ R, all other perpendicular transitions, nu-3 band, hot band and high-frequency (3.0 - 1.6μ) transitions. These graphs made systematic differences between investigators especially evident and were a great aid in deciding which data to discard and how to weight other data in calculating averages. Overlaying of transparencies of these graphs gave a vivid depiction of any differences between the bands. There is not sufficient data for broadening by other species to justify preparing a graph.

The next section details a comparison between the bands and branches of the average halfwidth for each value of J".

IV. HALFWIDTHS

SELF BROADENING The average value of the halfwidth γ due to all investigators was calculated for each band and each value of J". For the laser transitions, the amount of data allowed a comparison between the P and R branches by averaging them separately. For the other bands, values for the P and R branches were contrasted when the same investigator measured both branches. For many of the bands no significant comparison to other bands could be made because the data for a particular band comes from only one paper and any difference with other bands may have resulted from a systematic experimental error. For these cases, composite averages were calculated for perpendicular transitions other than the laser transitions and hot band parallel transitions. These average halfwidths were then compared to those of the laser, the nu-3 and the high frequency transitions measured by Valero and Suarez. A summary of what differences were found between branches and bands follows.

For the 9.4 micron band, the average halfwidth of the P branch was greater than that of the R branch by 0.0038 cm^{-1}. Such comparisons will be indicated by writing "$\gamma(P) > \gamma(R)$". The value of 0.0038 is a weighted average calculated by multiplying the difference in average halfwidth at each J value by the number of data points for that J value, summing over all J values and dividing by the total number of data

points. In all comparisons involving the 9.4 micron band, the early results of McCubbin and Mooney(2) and Devir and Oppenheim(5) were omitted from the calculation because their values are much lower than those of anyone else.

Summary of Comparison of P and R Branches

9.4 micron band, $\gamma(P) > \gamma(R)$ by 0.0038 cm^{-1} for 71 data points.

10.4 micron band, $\gamma(P) > \gamma(R)$ by 0.0029 cm^{-1} for 146 data points but R branch halfwidths > P by 0.0030 for 4 common J values measured by Young and Chapman(8).

11101-10002 band, $\gamma(R) > \gamma(P)$ by 0.0001 cm^{-1} for 5 J values measured by Henry et al(39).

$\gamma(R) > \gamma(P)$ by 0.0010 cm^{-1} for 4 lines measured by Dana et al(31).

Nu-3 band: There are five papers on the R branch, but only Johns(37) studied the P branch. Because the values are low, the data of Tubbs and Williams(34) were left out of the R branch average. $\gamma(P) > \gamma(R)$ by 0.0007 cm^{-1} for 18 lines of the common isotopic species and $\gamma(P) > \gamma(R)$ by 0.0023 cm^{-1} for 11 lines of $^{13}CO_2$, both measured by Johns.

$\gamma(P) > \gamma(R)$ when average R branch values are compared to P data of Johns.

01111-01101 band, $\gamma(P) > \gamma(R)$ by 0.0003 cm^{-1} for 17 lines measured by Johns.

$\gamma(P) > \gamma(R)$ by 0.0008 for 8 lines measured by Dana and Valentin(54).

10011-10002 band, $\gamma(R) > \gamma(P)$ by 0.0003 cm^{-1} for 5 lines

measured by Henry et al.

For the four high-frequency transitions studied by Valero and Suarez(45-48), $\gamma(P) > \gamma(R)$ by 0.0007 for a total of 87 common J" values.

In summary, there is a tendency for halfwidths in the P branch to be larger than in the R branch but only by 0.003 cm^{-1} for the laser bands and less than 0.001 cm^{-1} for all other bands. In contrast, the published data shows a significantly larger halfwidth for lines of the Q branch. Twelve Q branch lines were measured by Eng and Mantz(25) and six by Gentry and Strow(33). They were careful to account for overlapping of these closely-spaced lines. For the 15 lines that could be compared, $\gamma(Q) > \gamma(P,R)$ by 0.0105 cm^{-1}. When the data is weighted by the number of studies for each J" value, the difference is 0.0094 cm^{-1}.

A comparison of the average halfwidth in the various vibrational bands was made using only those lines for which at least two values had been measured in each band. The halfwidths in the 10.4 micron band exceeded those of the 9.4 micron band by an average of 0.0071 cm^{-1} in a weighted average involving 218 data points. Abubakar and Shaw(30) used a low resolution Fourier transform spectrometer and a whole band analysis to measure halfwidths up to J=40 on several bands. In their results, the 10.4 micron band is also larger than the 9.4 micron band by 0.0071 cm^{-1} with the difference being about 0.0010 for low J. Their halfwidths for the 11101-10002 band are less than their 10.4 micron

values by 0.0009 cm^{-1}. With the P and R branches averaged together for all techniques, a comparison to the average halfwidths of the nu-3 (4.3 micron) band gives:

-10.4 micron greater by 0.0024 cm^{-1} for 15 lines.

-9.4 micron less by 0.0088 cm^{-1} for 15 lines.

-Average of all other perpendicular transitions less by 0.0017 cm^{-1} in a weighted average of 121 data points.

-Average of all parallel hot bands less by 0.0020 cm^{-1} in a weighted average of 114 data points.

-High-frequency transitions measured by Valero and Suarez, averaged together, were greater by 0.0010 cm^{-1} for 19 J values.

Johns studied the nu-3 transition in the isotopic species $^{13}C^{16}O_2$, measuring 19 P branch and 13 R branch lines. For the 16 lines that can be compared to his values for the common isotopic species, the C-13 halfwidths average 0.0025 cm^{-1} larger with a standard deviation of .0017.

NITROGEN BROADENING The same comparisons as for self broadening were made and are summarized below-

9.4 micron band: $\gamma(P) > \gamma(R)$ by 0.0034 cm^{-1} for 14 data points.

10.4 micron band: $\gamma(P) < \gamma(R)$ by 0.0009 cm^{-1} for 72 data points. For 18 lines of common J values measured by Boulet et al(10), there was no difference between the branches.

Nu-3 band: Again only Johns(37) measured the P branch. For average of 25 common J values, $\gamma(P) > \gamma(R)$ by 0.0008

cm^{-1} . When average of all R branch data is compared to Johns P branch values, $\gamma(P) > \gamma(R)$ by 0.0016 cm^{-1}. In general, this is the same as the difference for self broadening.

11101-10002 band: $\gamma(P) > \gamma(R)$ by 0.0020 cm^{-1} for 3 common lines measured by Dana et al(31).

High frequency (10011, 30013, 30012-00001) bands: Difference between branches < 0.0001 cm^{-1} for 64 lines that could be compared.

In summary, the difference between the P and R branches is much less than for self broadening except for the nu-3 band where the difference is about the same. Similarly, the Q branch is much closer to the P and R branches for nitrogen broadening. The halfwidths for a total of 34 Q branch lines have been measured, but for the majority, there are no P or R values with which to compare. For the 15 lines that could be compared, $\gamma(Q) > \gamma(P,R)$ by only 0.0015 cm^{-1}.

Comparison of halfwidths between the bands using lines measured at least twice:

9.4 micron < 4.3 micron by 0.0071 cm^{-1} for 59 data points.

10.4 micron < 4.3 micron by 0.0001 cm^{-1}, 117 data points.

Other perpendicular transitions-

< 4.3 micron by 0.0018 cm^{-1}, 101 data points.

Higher frequency parallel transitions-

< 4.3 micron by 0.0026 cm^{-1} for 98 data points.

These differences are very much like those for self broadening.

OXYGEN BROADENING A total of only 73 halfwidths have been reported and there is no data for the 9.4 micron band or any combination bands. On average, the halfwidth of each oxygen-broadened line is less than the corresponding nitrogen-broadened line by 0.0102 cm^{-1}, with the difference greater for low J and around 0.007 cm^{-1} for the J = 60 - 80 lines measured in the nu-3 band. Of more significance, the average relative broadening coefficient ($\gamma(CO_2 - O_2)/\gamma(CO_2 - N_2)$) is 0.867. This implies that the relative broadening coefficient for dry air is 0.96.

The two comparisons between branches that can be made indicate the same trend for the P branch halfwidths to be slightly larger than the R branch, the difference being 0.0037 cm^{-1} for four common lines of the 10.4 micron band measured by Arie et al(22) and 0.0006 cm^{-1} for 6 common lines in the 11101-10002 band measured by Dana et al(31).

The only comparisons of one band to another shows:

10.4 micron > 4.3 micron by 0.0034 cm^{-1} for 22 data points.

11101-10002 < 4.3 micron by 0.0009 cm^{-1} for 11 data points.

Bulanin et al(14) reported an average halfwidth for the 9.4 and 10.4 micron bands combined. A comparison of their values to the other data for the 10.4 band indicates that the half-widths in the 9.4 band are less by 0.010 cm^{-1}, consistent

with the results of the more thoroughly studied species.

OTHER BROADENERS For broadening by helium 31 halfwidths have been reported in the laser transitions. For ten comparisons, $\gamma(P) > \gamma(R)$ by 0.0014 cm^{-1} and the 9.4 band halfwidths are smaller than the 10.4 band by 0.0064 cm^{-1}, consistent with the studies reported above. The relative broadening coefficient compared to nitrogen is 0.782.

Valero and Suarez(47 & 48) studied broadening by argon for the 30013 and 30012 transitions from the ground state. There is no significant difference between the P and R branches. A comparison to their nitrogen-broadened data for the same transitions gives a relative broadening coefficient of 0.808 for J" = 8 - 28. Other data was rejected because of a wide scatter in values. Rosenmann et al measured two lines of the nu-3 band broadened by water vapor. Comparison to nitrogen gives a relative broadening coefficient of 2.11.

THEORETICAL STUDIES In 1969, Yamamoto et al(51) calculated the halfwidths of carbon dioxide lines using the Anderson-Tsao-Curnette theory. Their predictions were well below the great number of values measured since that time. In papers published in 1979 and 1984, Robert and Bonamy(52, 53) modified the ATC theory by including a realistic parabolic trajectory for close collisions and an anisotropic atom-atom potential. Rosenmann et al(50) used the RB theory to calculate CO_2 line broadening by CO_2, N_2 and O_2. For all three, their results are about 10 percent higher than the average experimental values, coming into closer agreement at high J.

Their values give a relative broadening coefficient for oxygen of 0.853 which again implies a coefficient for dry air of 0.96.

COMPARISON OF TECHNIQUES It was hoped that one outcome of this study would be a clear assessment of the accuracy and consistency of different experimental techniques. A meaningful comparison could be made only when lines within the same band were measured by different techniques. Unfortunately, most lines within a given band were measured by the same technique. For example, nearly all the data on the laser bands was taken with a CO_2 laser tuned to the line center while most of the data for the nu-3 band was taken with grating spectrometers. For bands in the one and two micron range, the only good data was taken by Valero and Suarez with a Fourier transform spectrometer. A variety of techniques have been used to study other transitions, but the data in any one band is scant. Q branch lines have been measured primarily with tunable diode lasers. The difficulty in making comparisons is compounded by the variety of factors that vary even for the same technique such as the pressure in the sample cell, the resolution of the instrument, whether the instrument function was apodized and whether a Voigt or Lorentz shape was assumed for the line. One general conclusion is that since 1980, whatever the technique, there has been increasingly careful attention paid to sources of error. The Voigt function is now used exclusively for the line shape, instrument functions are now carefully apodized

and the contributions from the far wings of adjacent lines are subtracted out. Most of the data for the laser bands were taken prior to 1980 which probably explains the wide scatter in these values.

Since lines in the laser bands were largely measured by the same technique, the difference between the 9.4 and 10.4 micron bands must be real. The same difference occurred in the whole-band analysis of Abubakar and Shaw. Four lines measured with a TDL were 0.0045 cm^{-1} wider than the average laser values while the whole band analysis gave halfwidths that were slightly smaller. The well-studied nu-3 band shows the best consistency of results, but most of this data was taken with spectrometers. 16 lines studied with a TDL were 0.0026 cm^{-1} less than the spectrometer values. In the (nu-2 + nu-3) - nu-2 band, lines measured with a TDL averaged 0.0030 cm^{-1} less than the spectrometer data. In perpendicular bands, Fourier transform data was less than that from a TDL by 0.0020 cm^{-1} for 12 lines and less than spectrometer values by 0.0019 cm^{-1} for 20 lines. At least for these cases, the Fourier transform spectrometer gives slightly smaller halfwidths. Comparing only within the same band, grating spectrometer values are larger than TDL and FT averaged together by 0.0030 cm^{-1} for 45 lines. Thus, the reported nu-3 halfwidths might be slightly larger than what would be obtained by other methods.

VI. TEMPERATURE COEFFICIENT

Reported values of n in equation (1) vary from 0.5 to

over 1.0. For self broadening, most of the data is for the 10.4 micron band and the high frequency bands studied by Valero and Suarez. The method based on a laser tuned to the line center is quite insensitive here with reported values of n ranging from 1.02 to the 0.515 claimed by Robinson(17) to give the best fit to his data. Leaving out the early study of the nu-3 band by Tubbs and Williams (γ values too low), the average of 22 values is 0.698. From the data of Suarez and Valero, 76 n values were calculated for J" = 2 - 40 with the average being 0.614. These n values have a fantastic scatter and a tendency to be lower in the mid-J range. If they are averaged in as one value for each J, the average n becomes 0.658. Finally, a weighted average using 1.0 as the weight for TDL and transform data, 0.5 for a laser locked to the line center and 0.3 for a laser not locked gives n = 0.662.

For broadening by nitrogen, there are only eight values for laser transitions, but 20 for nu-2 and 16 for nu-3. Valero and Suarez again studied the 30013-00001 and 30012-00001 bands at two temperatures, but their results show even more scatter than for self broadening and give an average n of 0.513. Averages calculated as above give 0.755 without the data of Valero and Suarez and 0.703 when their data is weighted as one number for each J. For broadening by oxygen, the average n for ten laser lines(22, 14) is 0.840 and for 11 lines in the nu-3 and nu-1 + nu-3 bands(40), it is 0.72. The average for oxygen is 0.777. For broadening by water vapor, Rosenmann et al(41) got 0.770 for two lines of the nu-3

band. For broadening by helium, Bulanin et al got 0.773 for six lines and Brimacombe and Reid(15), 0.58, all in the 10.4 micron band.

The theoretical calculation reported by Bonamy et al arrived at the expression

$$n = (7/12) + M \qquad (2)$$

where M depends in a complicated way on the broadening species, rotational quantum number and the temperature itself. The experimental values of n tend to be slightly larger for low temperature studies and smaller for high temperature studies.

VII. RECOMMENDATIONS:

There are several differences that are consistent for a large amount of data and should be included in the database. For self-broadening, the P branch halfwidths are larger than the R branch by 0.003 cm^{-1} in the laser bands and 0.001 cm^{-1} in the other bands. For nitrogen broadening, the difference is 0.001 cm^{-1} for all bands. For both broadeners, γ in the 9.4 band is less than in the 10.4 band by 0.007 cm^{-1}. For the non-laser transitions, γ in the nu-3 band was smaller than in other bands by 0.002 cm^{-1} for both self and nitrogen broadening. The true difference might be more as the nu-3 band has been studied with standard spectrometers which gives larger halfwidths than diode laser or transform spectrometers.

The laser bands have been studied almost exclusively with lasers tuned to the line center, and there is a large

scatter in the reported values. These halfwidths need to be measured more accurately. Of the data in articles referenced in this report, that of McCubbin and Mooney, Devir and Oppenheim, Tubbs and Williams and Meyers et al should not be used in determining halfwidth values for HITRAN. Published data not referenced was rejected early in this study. Data from diode lasers and transform spectrometers should be given more weight than that from standard spectrometers. When possible, use only data from studies in which there was a deconvolution of the instrument function. These are listed in the references under numbers 28-30, 35-37 and 58.

For the temperature coefficient n, use 0.70 for self broadening and 0.75 for nitrogen and oxygen broadening. For halfwidths in oxygen and dry air, use 0.85 and 0.96 of the nitrogen-broadened values respectively.

The pressure shift of the center frequency is negligible. A thorough study of this phenomenon by Soohoo et al showed shifts < 0.0002 cm^{-1}/atm for all isotopic species in CO_2 and < 0.0001 cm^{-1}/atm in N_2. There was no significant change with J. Shifts reported by Bulanin et al and Brimacombe and Reid are consistent with these values.

APPENDIX A

MAY BE OBTAINED FROM

UES OR

THE AUTHOR

1989 USAF-UES SUMMER FACULTY RESEARCH PROGRAM/
GRADUATE STUDENT RESEARCH PROGRAM

Sponsored by the

AIR FORCE OFFICE OF SCIENTIFIC RESEARCH

Conducted by the

Universal Energy Systems, Inc.

FINAL REPORT

NON-UNIFORM CLOUDS

Prepared by:	John G. Wills
Academic Rank:	Professor
Department and	Physics Department
University:	Indiana University
Research Location:	Geophysics Laboratory/LYS Hanscom AFB MA. 01731-5000
USAF Researcher:	Kenneth Hardy
Date:	25 Aug. 1989
Contract No.	F49620-88-C-0053

Non-Uniform Clouds

by

John G. Wills

ABSTRACT

Calculations of light propagation through non-uniform clouds are time consuming. This is because they involve computations in three space dimensions. But such calculations are essential if one is to model the realistic flow of light energy through the atmosphere.

In an approach similar in spirit to the nuclear optical model, the results of a Monte Carlo simulation of light scattering by a cube are parameterized so that the multiple scattering can be represented as a single scattering.

Various shapes of non-uniform clouds can then be constructed by stacking these cubes, and cubes for clear atmospheric areas, in any desired manner. The calculation of the scattering of light by a cloud then only involves a single scattering by each cube. This approach is much faster than the Monte Carlo simulation of the full cloud.

The method has been tested on large cubic clouds, on horizontal layer clouds and on vertical column clouds. The results are the same as full Monte Carlo calculations of these same clouds.

Examples of scattered clouds have been performed to examine the cloud-cloud interaction in the scattering of light in a non-uniform cloud field. The amount of upwelling light is found to be a non linear function of the fraction of cloud cover.

Acknowledgements

I wish to thank the Air Force Systems Command and the Air Force Office of Scientific Research for their sponsorship of this research. Also Universal Energy Systems was very helpful and efficient in handling the administrative aspects of this effort.

The personnel at the Geophysics Laboratory have provided a stimulating environment in which to work. I want to especially thank Kenneth Hardy, Chief of the Satellite Meteorology Branch and Larry Thomason for their support and use of their computer facility.

I. INTRODUCTION:

The Satellite Meteorology Branch of the Geophysics Laboratory (GL/LYS) is interested in understanding the propagation of light through clouds. This knowledge is essential for weather observation and prediction. It is vital to the understanding of the transport of solar energy to the earth in daytime and radiation losses at night. This information also plays an important role in formulating the requirements of an optical communication system between a satellite and the earth.

My training is in theoretical physics. In particular I have been involved in the use of scattering theory and numerical analysis in a variety of areas. These include problems in nuclear physics, elementary particle physics and atomic physics. I have taught extensively at both the graduate level and the undergraduate level. The courses taught include electromagnetic theory, mathematical methods, physical optics, and quantum mechanics including scattering theory.

Most recently my research efforts have involved either the study of meson spectra in the quark model (Lichtenberg 1989) or the investigation of the scattering of light by clouds (Wills 1988,1989). The work on clouds has been a part of a U.S. Navy, submarine laser communication (SLC) project (Waldman 1989). There, the multiple scattering of light through the atmosphere, through clouds and finally through the water had to be understood to specify the conditions necessary for the establishment of a satellite to submarine communications link. During that effort the need for faster methods of calculating the scattering of light by non-uniform clouds became clear. It is this effort in the scattering of light that forms the

connecting link between my interests and the research enterprise of the Geophysics Laboratory (McGinty 1987).

II. OBJECTIVES OF THE RESEARCH EFFORT

The work reported in this document is directed toward providing a high speed approach to obtaining transmission and reflection information for light scattering by non-uniform clouds. A computer program has already been written to calculate the Monte Carlo scattering from a cube and to parameterize the results. The principal objective of this research is to construct a program that will use these parameterized results to examine a variety of cloud patterns. The various cloud patterns will be constructed by stacking cubes that have differing optical properties, including a clear atmosphere, in a manner that will represent the desired cloud field. A photon entering a particular cube will scatter just once, but with a distribution that is obtained from that cube's multiple scattering history. Effects to be examined will include cloud to cloud scattering.

III. NON-UNIFORM CLOUDS

It is easy to program a computer to do a Monte Carlo simulation of photons scattering through a non-uniform cloud (Marchuk 1980). But the computer time necessary to get good results is so long that it is impractical to do a general survey of the transmission and reflection of light by a variety of non-uniform clouds using this approach. However, a general survey is necessary if one is to develop a sound basis for understanding the interaction of light with realistic cloud patterns.

There is a similar problem in nuclear physics. The scattering of a nucleon from a variety of nuclei would also involve repeated multiple scattering calculations. Even though such calculations have been done, the vast majority of nucleon-nucleus scattering calculations utilize the optical potential (Hodgson 1963). The optical potential is a single scattering interaction that has been constructed to simulate the multiple scattering effects. The use of the optical potential has made it practical to investigate the scattering of a nucleon from many nuclei. This has allowed one to gain an insight into the general features of nuclear scattering and the structure of nuclei that is exceedingly valuable and that would have been difficult to obtain without the optical potential.

The approach used here is similar in spirit but quite different in practice from the optical potential. In the nuclear problem, the nucleus is nearly spherical and is very small compared to laboratory dimensions. This suggests the use of spherical coordinates, and the outgoing radiation emanates essentially from a point. In the cloud problem the size of a uniform region of a cloud is of the same order of magnitude as the size of the cloud itself and clouds are far from spherical. Cartesian coordinates are more natural. Instead of constructing an optical potential, a Monte Carlo solution to the scattering of photons by a uniform cube has been done and the results parameterized. The size of the uniform cube used is arbitrary, and can easily be modified, but a linear dimension of the order of 1 km seems to be reasonable. This is large enough to include multiple scattering, while being small enough to reasonably represent a uniform portion of a cloud. Several such calculations are done to provide the

results for cubes with a variety of optical parameters. Then these cubes are stacked up as required to construct any desired cloud formation. The computer program that evaluates the scattering for each cube and performs it's parameterization is called CUBE. The way the probability distribution is constructed can best be illustrated by considering only the face the photons exit through and ignoring the angular and position information. Suppose using 1000 photons one found

+Z	-Z	+X	-X	+Y	-Y
450	50	200	60	120	120.

Here +Z denotes the positive Z face of the cube, and 450 photons exited that face. The next step is to sum these results

+Z	-Z	+X	-X	+Y	-Y
450	500	700	760	880	1000.

If one picks a uniformly distributed random number between 0 and 1000, one would say that the photon exited the +Z face if the number was between 0 and 449. If the number was between 760 and 879 the +Y face would be indicated. Similar calculations are made for the position and angle information.

Figure 1a shows a cube with four position bins on each face. An incident and exit photon are shown along with their zenith and azimuth angles. In figure 1b one sees the numbering system for the four bins on the +Z face of the cube. The coordinates x' and y' are the coordinates of a point in that plane. The x', y', and the outward normal to the plane are picked to form a right handed coordinate system. In figures 1c,1d and 2a through 2c, the numbering system for the other five faces is displayed.

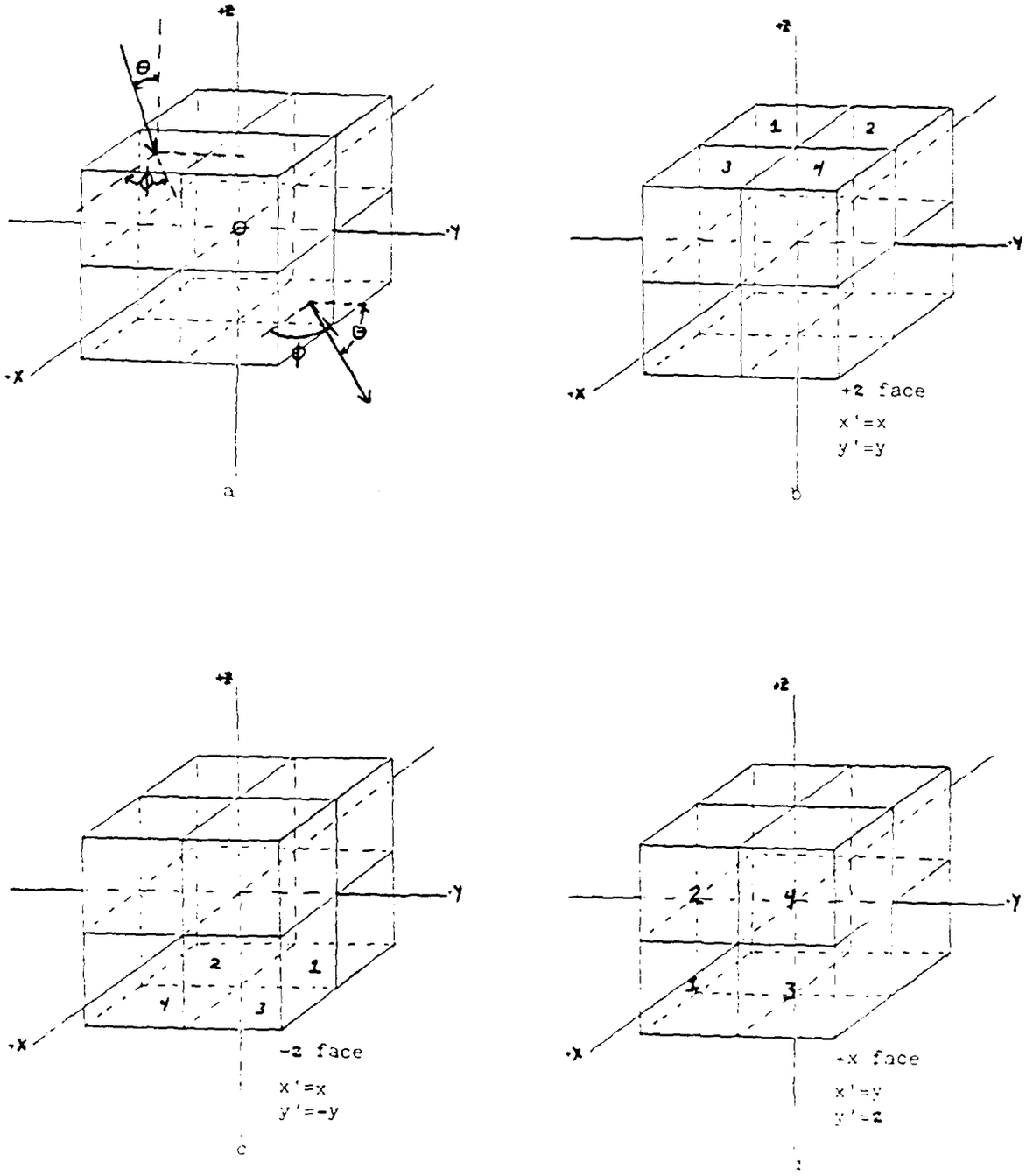

Figure 1

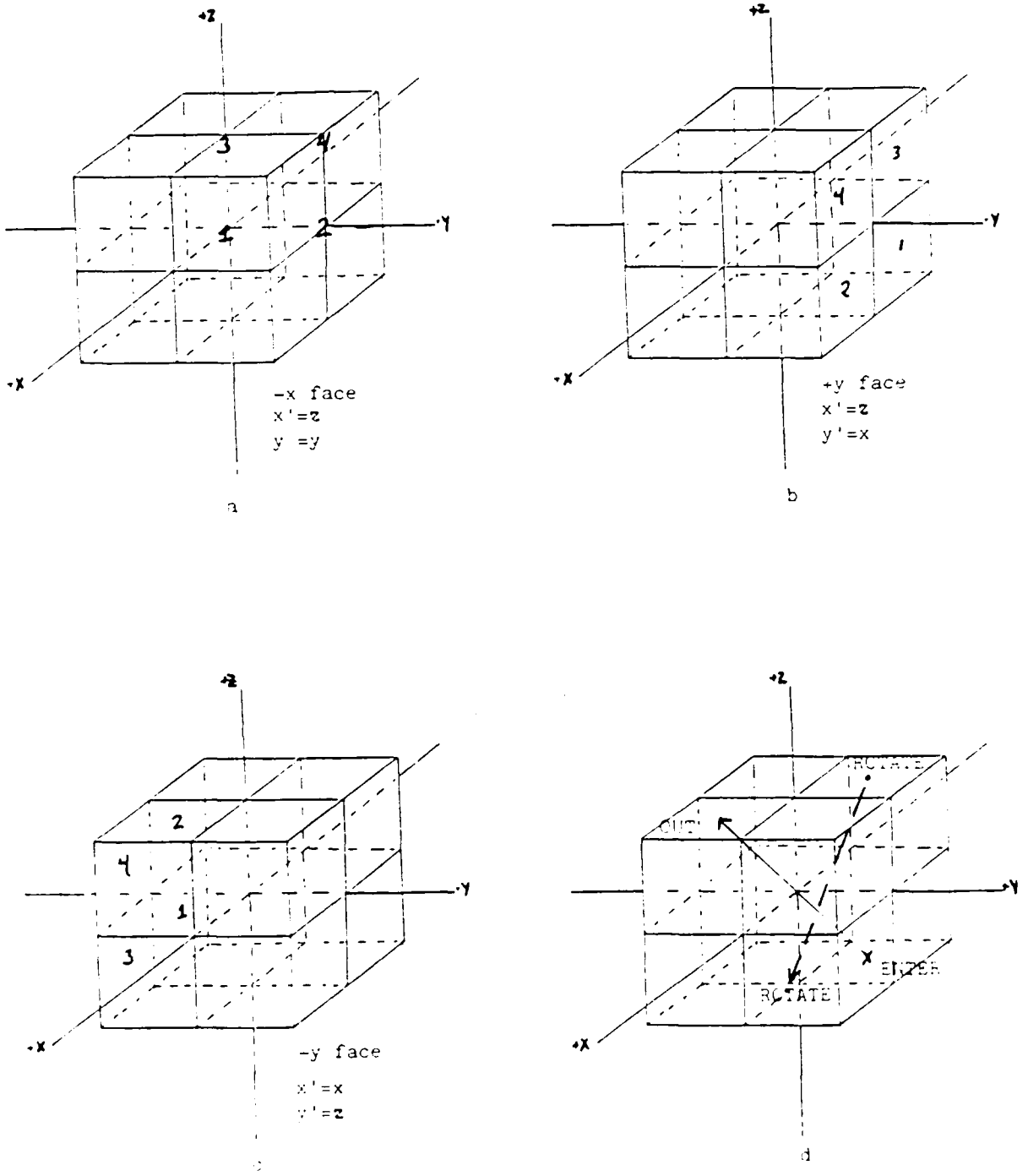

Figure 2

Each of these faces can be made congruent with the +Z face by at most two rotations. Figure 2d illustrates a photon entering the +Y face of the cube. This position is related to the position on the +Z face shown by the dot, by the rotations mentioned above. If a randomly chosen number selects the direction shown by the dashed arrow, from the stored probability distribution, then the true exit point is given by the inverse rotations and is displayed as the solid arrow.

The essense of these computations is that the scattering from the complete cloud field is performed by sucessive single scatterings from the constituent cubes, using each cube's stored multiple scattering history. That is, only one scattering takes place per cube but the photons path length, exit point and exit direction comes from the previously calculated and stored probability distribution for that cube.

To illustrate the calculation speed in one simple case, a cubic cloud 10 km on a side was represented by 1000 identical 1 km cubes. The solution for the 10 km cube, with this new method, took 8 seconds on the GL/LYS Vax while a direct Monte Carlo calculation required 92 seconds, for the same number of photons. The results of the two calculations agreed. A program named BCC was used for this calculation and can handle any cloud field that can be constructed out of several cube types. BCC is the acronym for Broken Cloud Cover.

In another calculation two cube types were used. One had a photon mean free path of 0.05 km to represent a cloud and the other had a mean free path of 10.0 km to simulate free space. Both cubes had a Henyea-Greenstein parameter of 0.875. The incident radiation was downward

from the zenith. The amount of upwelling radiation (counts) was determined as a function of cloud cover. The shape of the cloud is shown in figure 3. The results of the calculation are shown in figure 4.

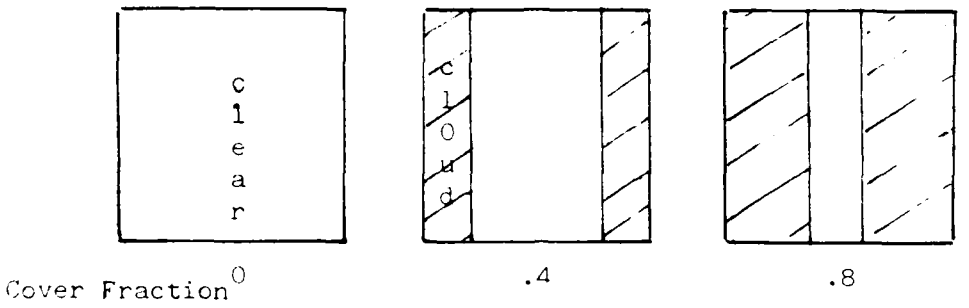

Figure 3

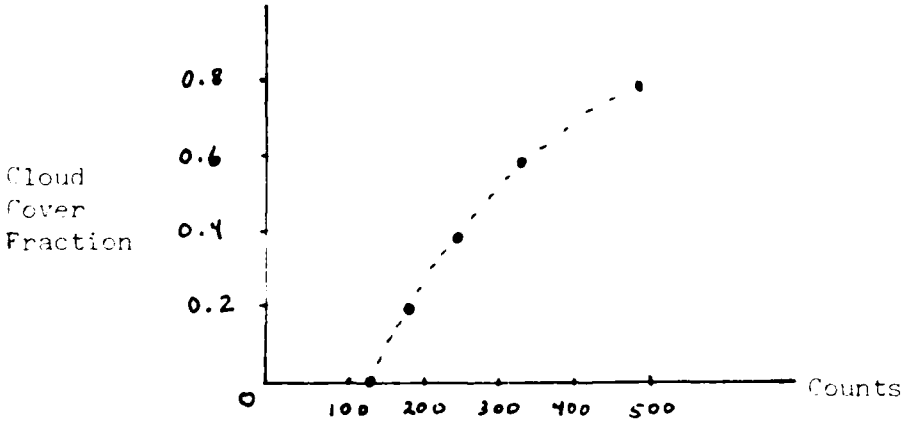

Figure 4

It is clear from figure 4 that as the cloud cover increases the the amount of upwelling light increases faster than linearly. This effect agrees with the data shown by Hawkins (1986). This effect is caused by cloud to cloud scattering. A photon leaving one cloud, that would have proceeded to the ground, can now intercept another cloud and scatter upwards.

IV. RECOMMENDATIONS

This research has provided a fast, new, method of examining the properties of non-uniform clouds. It is recommended that this approach be applied to an even wider variety of cloud shapes and types than was possible in this brief research period. The current programs provide as output the number of photons leaving each face of the cube. It is recommended that one also extract the position and direction of each photon so that distributions in position and angle can be obtained.

Currently the programs do not include the effect of real absorption in the cloud. This effect should be added. It can be added without increasing the number of basic cubes by including the number of collisions as part of the output. This will also provide the path length for the photons, which can be used in the program BCC to provide signal distortion data. The role of reflection of the light from the ground has not yet been included. It also needs to be added. In the current version of the program BCC it is assumed that the initial photons enter the top of the cloud field. This requirement should be relaxed so that the photons can enter from any direction. This would make the program more useful for large zenith sun angles and would allow the incident light to originate at the ground.

The approach used in these calculations could be extended to handle problems where the scattering is by non-uniform particles. This technique is not limited to spherical scatterers. Then cirrus clouds containing ice crystals could be examined.

There is another variation of the program BCC that may further

increase the computation speed. If there are large regions of clear space between the clouds, the combination of a direct Monte-Carlo calculation for those regions and the cube approach for the more cloudy regions may be the best technique.

REFERENCES

Hawkins,R.S. ,Cumulus Cloud Cover From Meteorological Satellites,Presentations at the Fourth Tri-Service Clouds Modeling Workshop,Air Force Geophysics Laboratory, 1986,pp. 199

Hodgson,P.E. ,The Optical Model of Elastic Scattering, Oxford, Claredon Press, 1963

Lichtenberg,D.B.;Predazzi,E.;Roncaglia,R.;Rosso,M.;Wills,J.G., Testing Static Quark-Antiquark Potentials With Bottomonium,Z. Phys. C,Vol. 41,1989 pp. 615

Marchuk,G.I. ,The Monte Carlo Method in Atmospheric Optics, Springer Verlag,1980

McGinty,A.B. ,Editor,Air Force Geophysics Laboratory, Report On Research, AFGL-TR-87-0188, 1987

Waldman,C.H., Optical Transmission Through Clouds, unpublished report prepared for Titan Systems Inc., 1989

Wills,J.G., Scattering By Non-Uniform Clouds I, unpublished report prepared for the San Diego State University Foundation(1988). This report contains the initial idea of using a parameterized cube.

Wills,J.G., Scattering by Non-Uniform Clouds II, unpublished report prepared for the ASEE/Navy summer program (1989). This report concerns the writing of the program CUBE and some preliminary efforts on what has become the program BCC.

Final Report

1989 USAF-UES SUMMER FACULTY RESEARCH PROGRAM/

GRADUATE STUDENT RESEARCH PROGRAM

Sponsored by the

AIR FORCE OFFICE OF SCIENTIFIC RESEARCH

Conducted by the

Universal Energy Systems, Inc.

FINAL REPORT

Design Considerations in the Implementation of ACT Programmable Transversal Filters

Prepared by:	Charles J. Alajajian
Academic Rank:	Assistant Professor
Department and University:	Electrical and Computer Engineering Dept. West Virginia University
Research Location:	RADC/DCCD Griffis AFB Rome, NY 13441-5700
USAF Researcher:	Richard Hinman
Date:	19 Sept 89
Contract No:	F49620-89-C-0053

Design Considerations in the Implementation of ACT Programmable Transversal Filters

by

Charles J. Alajajian

ABSTRACT

A well known computer program by Parks et. al. was used to design finite-impulse response (FIR) filters with linear phase for a programmable transversal filter (PTF) based upon acoustic charge transfer (ACT) technology. The program employs the Remez exchange algorithm to minimize the weighted Chebyshev error in approximating a desired ideal frequency response.

Because the programmable filter hardware cannot represent the FIR filter coefficients exactly (currently, only to 6 bit accuracy using fixed-point numbers), a quantizer subroutine was developed in order to simulate the finite wordlength effects.

The non-destructive (current) sensing (NDS) electrode structures that are utilized in the physical device result in an undesirable rolloff in the frequency response of the actual filter. An analytic expression for the transfer function and impulse response of an NDS tap has been derived in the literature [15]. This undesirable degradation in the frequency response was cancelled by predistorting the filter response so that its passband compensates for the deterioration [7].

Acknowledgements

I would like to thank the Air Force System Command and the Air Force Office of Scientific Research for sponsorship of this research. The assistance of Dr. Rod Darrah and the fine staff at Universal Energy Systems for their expert handling of the administrative and directional aspects of the summer program is gratefully acknowledged.

In addition, I would like to personally thank Peter Leong, Director of the Communications Technology Branch, for extending a warm welcome to me and my family and for his encouragement in this work. John Graniero and Col. Reid, Director of Communications, John Ritz, of the Directorate of Plans & Programs, and Chief Scientist, Dr. F. I. Diamond made me feel welcome and offered their support.

I profited a greal deal from regular, stimulating technical discussions with Rick Hinman, of DCCD, who provided background into the operation of ACT programmable transversal filters and their application in frequency hopping high frequency communication systems. I also appreciated helpful discussions with John Patti and Rich Smith.

Jim Cutler, Al Emondi and Steve Tyler unselfishly shared their PC's with me, and Jim Cutler was always willing to offer assistance with PC or software related problems. Toni Greci provided helpful assistance in the laboratory and Jim Reichart and others went out of their way to help.

The professional and cheerful secretarial support rendered by Pauline Romano and Connie Watkins is greatly appreciated.

I. INTRODUCTION

Acoustic charge transfer devices (ACT) offer a number of very attractive advantages over charge-coupled devices (CCD) or surface acoustic wave (SAW) devices in the realization of programmable transversal filters (PTF). Like a CCD, the ACT may be thought of as an analog tapped delay line having digital control, which can perform in analog form, all the operations of a digital system [16]. Compared to the CCD, the ACT boasts superior bandwidth and charge transfer efficiency. It has the distinct advantage over SAW devices that the active digital controlling electronics and the passive charge transfer device may be integrated on a monolithic substrate [16].

The Communications Technology Branch of the Rome Air Development Center is particulary interested in effectively utilizing state-of-the-art PTF's based on ACT devices as the solution to problems in existing communication systems. Typical problems arising in communication systems include the cosite interference problem in airborn receivers and the need for suppression of narrowband interference in frequency hopping high frequency communication systems. Many of the proposed algorithms for solving these problems utilize an adaptive scheme which usually requires an adaptive FIR filter. Thus, the need for a programmable filter arises. Because a complete PTF can be realized on a monolithic chip using ACT technology, it is well suited for use in airborn receivers because of its small size and weight.

My research interests have been in the areas of circuits, systems, and digital signal processing, particularly computer-aided techniques and numerical methods for the analysis, design and testing of electronic circuits and systems.

II. OBJECTIVES

The primary objective of the research effort was to design linear phase FIR filters of lengths (less than or equal to 256) and filter types (predominantly bandpass and bandreject filters) for an ACT PTF, and to use computer simulation to predict the performance of the actual prototype hardware in the laboratory.

Presently, a prototype PTF, built primarily for demonstration purposes, consists of a tapped delay line with 64 taps, which permits filter lengths ≤ 64;

the unused taps are set to zero. The technology exists to extend the length of the tapped delay line. To determine whether the current filter length is adequate for the aforementioned communication applications, bandpass and bandreject filters of varying lengths were to be designed and their frequency response evaluated. Thus, the objective was to have the in-house capability of rapidly designing FIR filters to achieve a desired frequency response, and computer-aided techniques were seen as a viable solution to this problem.

In the prototype PTF the tap weights are internally represented only to 6 bit accuracy using fixed point arithmetic. It is well known that coefficient quantization errors result in a perturbation of the zeros of the FIR transfer function from their nominal positions, which in turn introduce errors in the frequency response. Thus, computer simulation was used to predict the frequency response when the coefficients (unit sample response) were represented by 6 and 8 bits. This was to ascertain whether future versions of the PTFs should use additional bits to represent the tap weights (with a resulting decrease in the frequency response error), and whether or not this would warrant the additional cost, increase in area consumed by the chip, and time delay in redesign and production.

The frequency response of the non-destructive sensing (NDS) electrodes falls off with frequency which will degrade the PTF response, unless provision is made for cancelling its effect in designing the filter. Predistortion was to be used to solve this problem.

The last objective was to test the prototype PTF in the laboratory, to determine the degree of agreement between theory and experiment.

III. DESIGN OF LINEAR PHASE FIR FILTERS

a. In order to design linear phase FIR filters, a widely used filter design program which implements the P-M algorithm [1, 8] was used. The program uses the Remez exchange algorithm to design linear phase FIR digital filters with minimum weighted Chebyshev error in approximating a desired ideal frequency response [3].

b. A slightly modified version of the program EQFIR [8], which appears in [6],

was saved as an ASCII file on a $5\frac{1}{4}$" floppy disk using a popular word processor. A FORTRAN compiler, Microsoft, Version 4.01 [18], was installed on a IBM PC clone, and used to compile the program. The input to the program is read from the terminal and the output is stored in files on a floppy disk. The program prompts the user for the filter length, type, number of bands, band edges, desired value in each band and weight in each band. Further modifications were made to the program which now questions the user whether or not cancellation of the voltage or current NDS electrode response is desired; otherwise, the program assumes the same form as in [6].

The P-M program yields only the coefficients (unit-pulse response h(n)) of the FIR filter. Thus, it is necessary to take the discrete Fourier transform (DFT) of the impulse response, and use a plotting program to display the frequency response. To increase the resolution of the plot so as to give a more accurate picture of the frequency response $H(\omega)$, the impulse response was padded with additional zeros to make the total sequence length 256; this parameter is easily modified within the program if additional resolution is required.

Graph-In-The-Box-Analytic (GIA) [19] was used to display the data files AMP.GIA, LAMP.GIA, PHASE.GIA, AMPN.GIA, LAMPN.GIA and PHASEN.GIA which contain the following frequency response data: magnitude, log magnitude and phase all plotted vs. frequency. To prevent overflow, the unit-pulse response samples are all divided by the scale factor $G=\max_n (h(n))$, to give the scaled unit-pulse response [6]

$$\tilde{h}(n)=\frac{h(n)}{G} \qquad (1)$$

Filenames whose primary part (i. e., not the extension) ends in the letter N contain the frequency response data corresponding to $\tilde{h}(n)$; filenames with the extension GIA are compatible with the program GIA [19].

IV. FIR FILTER DESIGN TO ACHIEVE A DESIRED FREQUENCY RESPONSE

a. The frequency response of a lowpass FIR Chebyshev filter [8,12], is characterized by its amplitude response in the passband ($f_{p_1} \le f \le f_{p_2}$) and in the stopband, ($f_{s_1} \le f \le f_{s_2}$). In the passband, the response generally oscillates between $(1+\delta_p)$ and $(1-\delta_p)$ and in the stopband, between $+\delta_s$ and $-\delta_s$. The extension to bandpass filters is straightforward and may be found in

[8,13]. In design, the quantities of interest are the (peak-to-peak) passband ripple A_p in decibels (dB)

$$A_p = \log \frac{(1+\delta_p)}{(1-\delta_p)} \qquad (2)$$

and the minimum stopband attenuation A_s in decibels

$$A_s = -20\log\delta_s \qquad (3)$$

as well as the transition bandwidth of the filter, which, for a lowpass filter is $\Delta f = f_s - f_p$. The actual filter length N is a complicated function of δ_p, δ_s and Δf. Herrmann has proposed a formula [5,11] which yields $\hat{N}$, an estimate of N, which is reproduced here for convenience.

$$\hat{N} = \frac{D_\infty(\delta_p,\delta_s) - f(\delta_p,\delta_s)(\Delta f)^2}{\Delta f} + 1 \qquad (4)$$

where $D_\infty(\delta_p,\delta_s)$ and $f(\delta_p,\delta_s)$ are defined by

$$D_\infty(\delta_p,\delta_s) = [0.005309(\log\delta_p)^2 + 0.07114(\log\delta_p) - 0.4761](\log\delta_s) - [0.00266(\log\delta_p)^2 + 0.5941(\log\delta_p) + 0.4278] \qquad (5)$$

$$f(\delta_p,\delta_s) = 11.012 + 0.51244(\log\delta_p - \log\delta_s) \qquad (6)$$

b. In a spread-spectrum system, typically a filter with a maximum passband ripple of 1 dB, ($A_p = 1$ dB; $\delta_p = 0.05750$) yields acceptable performance. Constrained by the prototype PTF to have length 64, Herrman's equations were used to obtain A_s and the transition bandwidth; the resulting design to be later verified by computer simulation.

In the design of filters with multiple transition bands, the P-M algorithm may fail, especially in the transition regions so that certain precautions are necessary [2,13]. Thus, the transition bands were made equal to avoid any overshoot in the response [2,13].

Equations (4), (5) and (6) were entered into a popular spreadsheet along with the appropriate parameters. It should be emphasized that all frequencies are entered in hertz and are normalized with respect to the sampling frequency. With $\delta_p = 0.05750$ ($A_p = 1$ dB), the combination of $\delta_s = 0.01$ ($A_s = 40$ dB) and transition bandwidth $\Delta f = 0.025$ in Herrmann's formula yields $\hat{N} \approx 64$.

For a bandpass filter the passband is contained between $f_1 \le f \le f_2$. The two stopbands are contained between $(0 \le f \le f_{s_1})$ and $(f_{s_2} \le f \le 0.5)$, respectively. Let f_o be the geometric mean between f_1 and f_2. Then

$$f_o = \sqrt{f_1 f_2} \tag{7}$$

Define the fractional bandwidth as

$$f_b = \frac{f_2 - f_1}{0.5} \tag{8}$$

Given f_o and f_b, the solution of equations (7) and (8) for f_1 and f_2 is

$$f_{1,2} = \sqrt{f_o^2 + 0.0625 f_b^2} \mp 0.25 f_b \tag{9}$$

Usually, the P-M program will be run several times to get an appropriate filter [6]. It was noted that the program yielded an f_b about 3 times as large as desired. By entering $\frac{1}{3}$ the desired fractional bandwidth entered into equation (9) the desired result was obtained.

A bandpass filter was designed with center frequency $f_o = 0.25$ and $f_b = 0.15$. Table 1 lists the critical frequencies of this filter and the unscaled unit-pulse response h(n), which is written to the file PM.LST. A plot of the frequency response of the predistorted filter appears in a later section.

V. FREQUENCY RESPONSE DUE TO FINITE WORDLENGTH COEFFICIENTS

a. The PTF, with its associated electronics, cannot represent the coefficients of the filter with arbitrary precision and unlimited amplitude; the latter limitation was the rationale for introducing the scaled unit-pulse response.

The error in representing the filter coefficients as finite, fixed-point numbers is now considered. Each infinite-precision coefficient that is represented as a floating-point number on the computer is to be converted into a second, floating-point number whose value is equal to the finite-precision value, closest to the infinite-precision coefficient, that can be represented by a 2's complement fixed-point number having w_c bits [10, 14]. The coefficients are quantized to stepsize of

$$Q = 2^{-(w_c - 1)} \tag{10}$$

Thus, with a sign bit, w_c bits are used to completely define the coefficients. The quantization process is implemented using the truncation function AINT in FORTRAN. Using this function, each coefficient may be quantized by first

dividing its value by Q, truncating the result using AINT, and then multiplying the result by Q. This simple algorithm was implemented in a subroutine so the effects of various wordlengths could be examined.

b: The result of quantizing $\tilde{h}(n)$ for the bandpass filter of Table 1 and the bandreject filter of Table 2 is shown in Figure 1 and Figure 2, respectively.

VI. CANCELLATION OF THE NONDESTRUCTIVE SENSING (NDS) RESPONSE

a. The frequency domain, current sensing response for a simple buried channel traveling wave charge transfer device is given by [15]

$$H_{oi}(F) = e^{-2\pi \frac{d}{\lambda_w}\left|\frac{F}{f_w}\right|} \tag{11}$$

where d is the depth at which a line charge is carried by a traveling wave of wavelength λ_w and frequency f_w and F is the continuous-time frequency variable. For the prototype PTF, $\frac{d}{\lambda_w} \approx .125$ and $f_w \approx 360$ MHz [17]. The PTF is an analog tapped delay line which can perform, in analog form, all the operations of a digital system [16]. The equivalent digital system has a tap-to-tap spacing of 7.68 nsecs, corresponding to a sampling frequency of 130 Mhz. The analog input data to be processed by the ACT has been sampled at a 360 Mhz rate [17]. To determine the transfer function of the equivalent digital system, the relationship between the continuous-time frequency variable F and the discrete-time frequency variable f (given by $F = f_s f$) is substituted into equation (11) to give

$$H_{oi}(f) = e^{-2\pi \frac{d}{\lambda_w}\left|\frac{f_s}{f_w}\right| f} \tag{12}$$

where f_s denotes the sampling frequency. The undesirable rolloff in the frequency response should be cancelled. Equations (11) and (12) give the frequency response of a single electrode. However, in the block diagram representation of the equivalent digital system, $H_{oi}(f)$ appears as a block in cascade with each tap weight. Using standard procedures for manipulating block diagrams, this common block may be "pulled out" of the output summer, so that the equivalent digital system is reduced to the cascade of just two system blocks; the block consisting of the digital tapped delay line (which admittedly is made up of other blocks) and $H_{oi}(f)$ [17]. Predistortion techniques are used to cancel the effects of $H_{oi}(f)$ by requiring that the passband of the digital filter to be designed compensate for $H_{oi}(f)$ so that the

product of the two transfer functions has its passband response within the required tolerance [7]. Because of the flexibility of the P-M program this is readily accomplished by modifying the subroutines EFF and WATE; the former specifies the desired magnitude response as a function of frequency, while the latter permits an arbitrary weighting function to be specified. Thus, for the subroutine EFF, define the desired frequency respone D(f) as

$$D(f)=\begin{cases}|1/H_{oi}(f)|, & 0 \le f \le f_p \\ 0, & f \ge f_s\end{cases} \qquad (13)$$

and, for the subroutine WATE, define the weight function, W(f) as

$$W(f)=\begin{cases}|H_{oi}(f)|, & 0 \le f \le f_p \\ \delta_1/\delta_2|H_{oi}(f)| & f \ge f_s\end{cases} \qquad (14)$$

where δ_1 and δ_2 denote, as before, the desired maximum ripple in the passband and the minimum attenuation in the stopband, respectively [8,12]. The choice of the weighting function in equation (14) ensures that the relative ripple in the passband is a constant [11].

b. The result of compensating for the current sensing response for the bandpass filter of Table 1, is given in Figure 3. A careful study of the magnitude response (in dB) shows a slight increase in the slope in the stopbands, with increasing frequency. Figure 4 shows the magnitude response (not in dB) for the bandreject filter of Table 2; the relative ripple in the passbands is constant, as predicted. Note that these figures depict the frequency response of the predistorted filter, and not that of the cascade of the predistorted filter and the transfer function $H_{oi}(f)$.

VII. LABORATORY MEASUREMENTS

a. A standard transmission fixture was assembled in the laboratory, consisting of a Hewlett-Packard HP-8601A frequency sweep generator, a Hewlett-Packard network analyzer equipped with a "plug-in" magnitude and phase display unit, HP-8412A, and an ANZAC T-1000 power splitter. This fixture was to be used for displaying the frequency response of the prototype PTF and to assess the degree of agreement between theory and experiment.

b. The bandpass filter of Table 1 performed quite well in the laboratory as

predicted by computer simulation. When the tap weights were represented with 6 bit accuracy, simulation of the magnitude response yielded 35 dB of stopband attenuation; this increased to 40 dB when 8 bits were used. In the laboratory 25 dB of stopband attenuation was measured with neglible distortion in both the passband and stopbands. The measured phase was linear over the appropriate frequency intervals as predicted.

The bandreject filter of Table 2 did not perform as well. When the weights were represented with 6 bit accuracy, simulation of the magnitude response predicted about 14 dB of rejection in the stopband, with less than 1 dB passband ripple. The magnitude response as observed in the laboratory showed substantial passband distortion and while the stopband was clearly evident, it exhibited less rejection than predicted; the phase response was well behaved.

VIII. RECOMMENDATIONS

a. Regarding the number of bits used to represent the filter coefficients in the PTF, my recommendation is to increase the number of bits from 6 to 8, because for the filters considered, computer simulation reveals that increasing the number of bits to 8 typically results in an additional 15 dB of attenuation for a filter length of 64. As the filter length increases, the error in the frequency response due to finite wordlength appears to be even more severe, especially in the case of narrow-band filters.

b. In the production of PTFs which utilize ACT technology, frequently, one or more tap weights may be defective. The defective weight(s) may assume a value of one, zero, or any value in between. As a result, the PTF will not exhibit the correct response. Due to the inability to address, or alter the value of the defective tap(s), compensation techniques are required to cancel the effect(s) of the defective tap(s) such that the desired response, or the response to within some gain constant over the frequency spectrum is obtained. I propose to develop an algorithm, which, given the location and value of the defective tap weights, will adjust a subset of the remaining tap weights so as to yield an acceptable response.

REFERENCES

Conference and journal publications:

1. J. H. McClellan, T. W. Parks and L. R. Rabiner, "A Computer program for Designing Optimum FIR Linear Phase Digital Filters," Proc. IEEE Trans. Audio and Electroacoust., Vol. AU-21, December 1973, pp. 506 - 526.

2. L. R. Rabiner, J. F. Kaiser and R. W. Schafer, "Some Considerations in the Design of Multiband Finite-Impulse-Response Digital Filters," IEEE Trans. Acoust. Speech, and Signal Processing, Vol. ASS1-22, Dec. 1974, pp. 462 - 472.

3. L. R. Rabiner, J. H. McClellan and T. W. Parks, "FIR Digital Filter Design Techniques Using Weighted Chebyshev Approximation," Proc. IEEE, Vol. 63, April 1975, pp. 595 - 610.

4. D. M. Kodek, "Design of Optimal Finite Wordlength FIR Digital Filters Using Integer Programming Techniques," IEEE Trans. Acoust. Speech, Signal Processing," Vol. ASS1-28, June 1980, pp. 304 - 308.

5. O. Herrmann, "On the Approximation Problem in Nonrecursive Digital Filter Design," IEEE Trans. Circuit Theory; Vol. 18, May 1971, pp. 411 - 413.

Textbooks:

6. T. W. Parks and C. S. Burrus, Digital Filter Design, New York, NY, Wiley Interscience, 1987.

7. P. P. Vaidyanathan, "Design and Implementation of Digital FIR FIlters" in D. F. Elliott, Ed., Handbook of Digital Signal Processing, San Diego, California, Academic Press Inc., 1987.

8. J. H. McClellan, T. W Parks and L. R. Rabiner, "FIR Linear Phase Filter Design Program," in Programs for Digital Signal Processing, New York, NY, IEEE Press, 1979.

9. C. M. Rader, "FOUREA - A Short Demonstration Version of the FFT," in Programs for Digital Signal Processing, New York, NY, IEEE Press, 1979.

10. U. Heute, "A Subroutine for Finite Wordlength FIR Filter Design," in Programs for Digital Signal Processing, New York, NY, IEEE Press, 1979.

11. J. G. Proakis and D. G. Manolakis, Introduction to Digital Signal Processing, New York, NY Macmillan Publishing Co., 1988.

12. N. K. Bose, Digital Filters: Theory and Applications, New York, NY, Elsevier Science Publishing Co, Inc., 1985.

13. D. J. DeFatta, J. G. Lucas and W. S. Hodgkiss, Digital Signal Processing: A System Design Approach, New York, NY, John Wiley & Sons, 1988.

14. R. Kuc, Introduction to Digital Signal Processing, New York, NY , McGraw-Hill, Inc., 1988.

15. Charles E. Warren, Nondestructive Sensing in Burried Channel Travelling Wave Charge Transfer Devices, Masters Thesis, University of Illinois at Urbana-Champaign, 1985.

16. A. Papoulis, Circuits and Systems, New York, NY, Holt, Rinehart and Winston Inc., 1980.

17. Richard Hinman, Personal communication, RADC/DCCD, Rome, NY.

18. Microsoft FORTRAN Optimizing Compiler: Language Reference, Redmond, WA, Microsoft Corporation, 1987.

19. Graph-In-The-Box Analytic Owner's Handbook, Greenwich, CT, New England Software, Inc., 1988.

```
C*****************************************************************
                FINITE IMPULSE RESPONSE (FIR)
              LINEAR PHASE DIGITAL FILTER DESIGN
                 REMES EXCHANGE ALGORITHM
                      BANDPASS FILTER

                    FILTER LENGTH =  64

                  ***** IMPULSE RESPONSE *****
                H(  1) =  -.39544916E-02 = H( 64)
                H(  2) =   .65617359E-02 = H( 63)
                H(  3) =   .38076136E-02 = H( 62)
                H(  4) =  -.14813226E-02 = H( 61)
                H(  5) =  -.17188692E-02 = H( 60)
                H(  6) =   .18228935E-02 = H( 59)
                H(  7) =   .85176686E-03 = H( 58)
                H(  8) =   .67136340E-04 = H( 57)
                H(  9) =   .16086345E-02 = H( 56)
                H( 10) =  -.29311624E-02 = H( 55)
                H( 11) =  -.53538378E-02 = H( 54)
                H( 12) =   .72436801E-02 = H( 53)
                H( 13) =   .10505826E-01 = H( 52)
                H( 14) =  -.12962755E-01 = H( 51)
                H( 15) =  -.17065528E-01 = H( 50)
                H( 16) =   .19997310E-01 = H( 49)
                H( 17) =   .24794704E-01 = H( 48)
                H( 18) =  -.28115112E-01 = H( 47)
                H( 19) =  -.33398144E-01 = H( 46)
                H( 20) =   .36929077E-01 = H( 45)
                H( 21) =   .42397701E-01 = H( 44)
                H( 22) =  -.45947827E-01 = H( 43)
                H( 23) =  -.51282454E-01 = H( 42)
                H( 24) =   .54609610E-01 = H( 41)
                H( 25) =   .59429188E-01 = H( 40)
                H( 26) =  -.62315267E-01 = H( 39)
                H( 27) =  -.66293793E-01 = H( 38)
                H( 28) =   .68521612E-01 = H( 37)
                H( 29) =   .71349725E-01 = H( 36)
                H( 30) =  -.72769156E-01 = H( 35)
                H( 31) =  -.74239862E-01 = H( 34)
                H( 32) =   .74720201E-01 = H( 33)

                          BAND  1        BAND  2        BAND  3
LOWER BAND EDGE            .0000000       .2375000       .2875000
UPPER BAND EDGE            .2125000       .2625000       .5000000
DESIRED VALUE              .0000000      1.0000000       .0000000
WEIGHTING                10.6481482      1.0000000     10.6481482
DEVIATION                  .0107777       .1147622       .0107777
DEVIATION IN DB          -39.3495066       .9436445   -39.3495066

EXTREMAL FREQUENCIES--MAXIMA OF THE ERROR CURVE
     .0000000     .0175781     .0341797     .0517578     .0683594
     .0849609     .1015625     .1181641     .1337891     .1503906
     .1660156     .1816406     .1953125     .2070313     .2125000
     .2375000     .2501953     .2625000     .2875000     .2923828
     .3041016     .3187500     .3333984     .3490234     .3646484
     .3802734     .3958984     .4125000     .4281250     .4437500
     .4603516     .4759766     .4916016
```

Figure 1

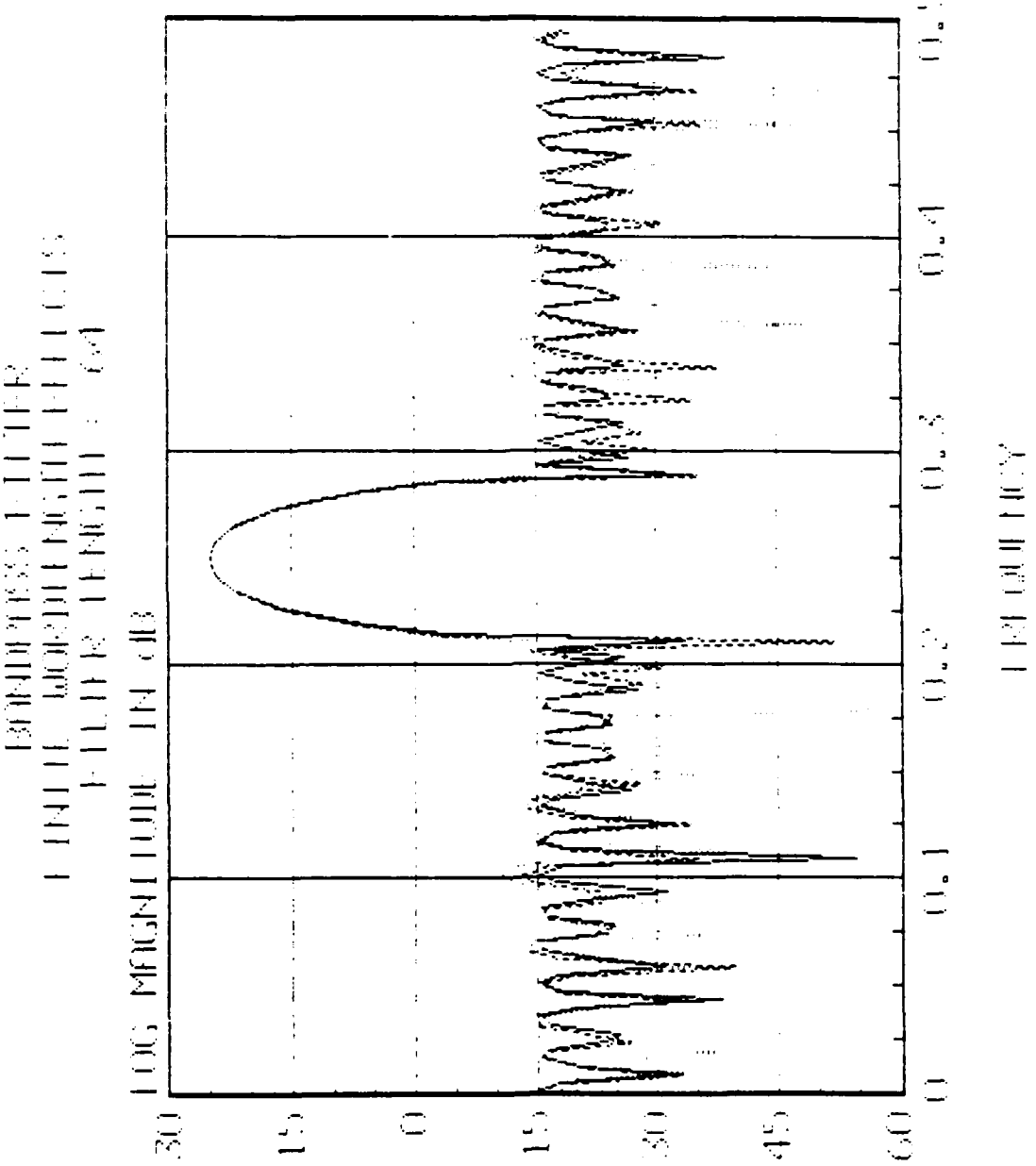

FINITE IMPULSE RESPONSE (FIR)
LINEAR PHASE DIGITAL FILTER DESIGN
REMES EXCHANGE ALGORITHM
BANDPASS FILTER

FILTER LENGTH = 63

***** IMPULSE RESPONSE *****

H(1)	=	-.11355930E-02	= H(63)
H(2)	=	.17634256E-01	= H(62)
H(3)	=	-.32807797E-02	= H(61)
H(4)	=	.32933405E-01	= H(60)
H(5)	=	-.14175649E-02	= H(59)
H(6)	=	-.21880871E-01	= H(58)
H(7)	=	-.32557532E-03	= H(57)
H(8)	=	.17934951E-01	= H(56)
H(9)	=	-.55518374E-03	= H(55)
H(10)	=	-.14153609E-01	= H(54)
H(11)	=	-.40882636E-04	= H(53)
H(12)	=	.83238450E-02	= H(52)
H(13)	=	-.81298488E-03	= H(51)
H(14)	=	.10796381E-02	= H(50)
H(15)	=	.24770931E-03	= H(49)
H(16)	=	-.13874858E-01	= H(48)
H(17)	=	-.12507392E-02	= H(47)
H(18)	=	.30151305E-01	= H(46)
H(19)	=	.38183626E-03	= H(45)
H(20)	=	-.48443086E-01	= H(44)
H(21)	=	-.17436080E-02	= H(43)
H(22)	=	.68176255E-01	= H(42)
H(23)	=	-.63814840E-04	= H(41)
H(24)	=	-.86881786E-01	= H(40)
H(25)	=	-.24957504E-02	= H(39)
H(26)	=	.10437600E+00	= H(38)
H(27)	=	-.24831882E-02	= H(37)
H(28)	=	-.11660672E+00	= H(36)
H(29)	=	-.90551341E-02	= H(35)
H(30)	=	.12898905E+00	= H(34)
H(31)	=	-.75996257E-01	= H(33)
H(32)	=	.10491011E+01	= H(32)

	BAND 1	BAND 2	BAND 3
LOWER BAND EDGE	.0000000	.2375000	.2875000
UPPER BAND EDGE	.2125000	.2625000	.5000000
DESIRED VALUE	1.0000000	.0000000	1.0000000
WEIGHTING	1.0000000	10.6481482	1.0000000
DEVIATION	.0645616	.0060632	.0645616
DEVIATION IN DB	.5434162	-44.3459921	.5434162

EXTREMAL FREQUENCIES--MAXIMA OF THE ERROR CURVE

.0000000	.0166016	.0341797	.0507813	.0683594
.0849609	.1025391	.1201172	.1367188	.1542969
.1718750	.1884766	.2041016	.2125000	.2375000
.2414063	.2501953	.2589844	.2625000	.2875000
.2953125	.3109375	.3285156	.3451172	.3626953
.3802734	.3968750	.4144531	.4310547	.4486328
.4652344	.4828125	.5000000		

Table 2

Figure 2

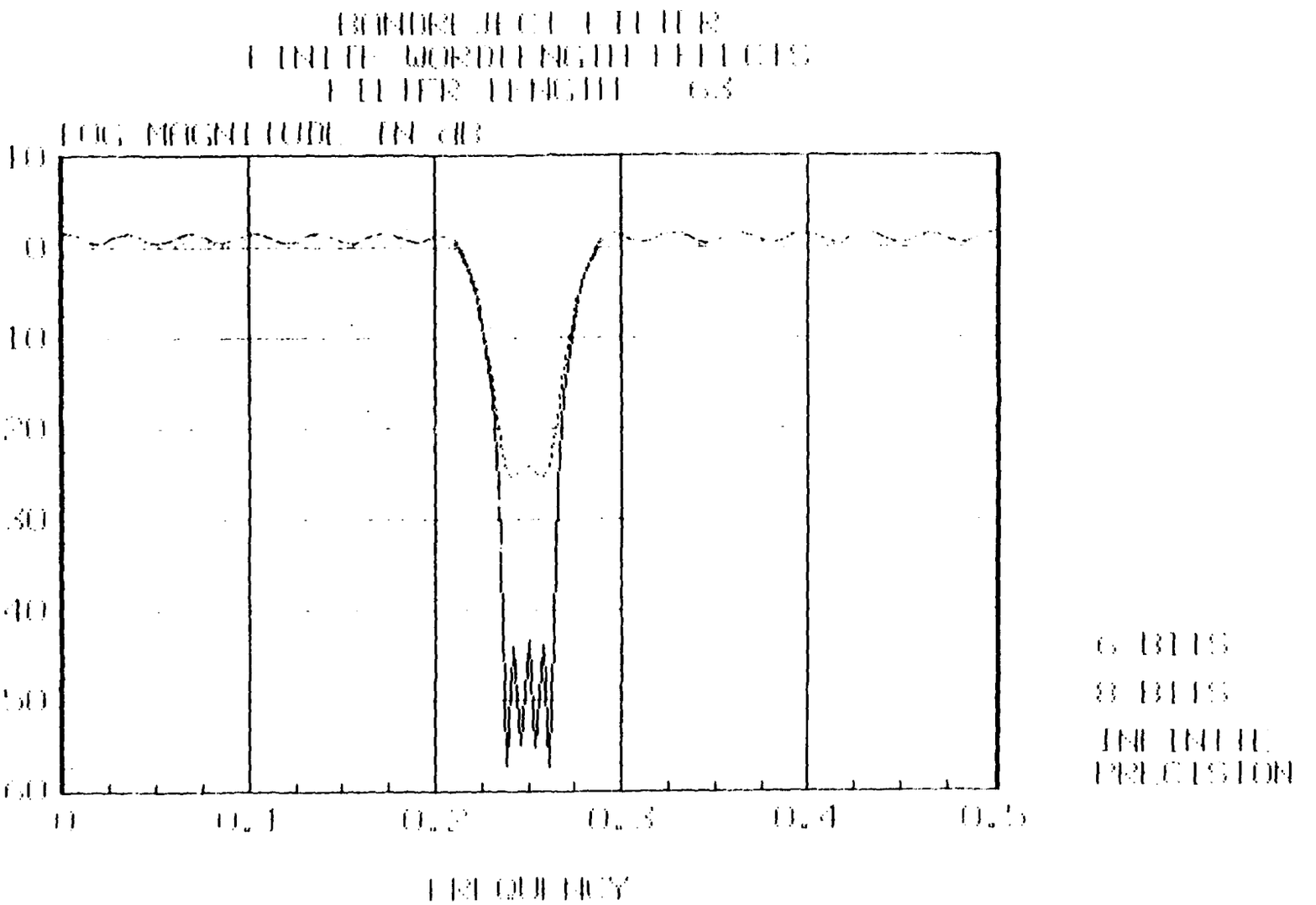

Figure 3

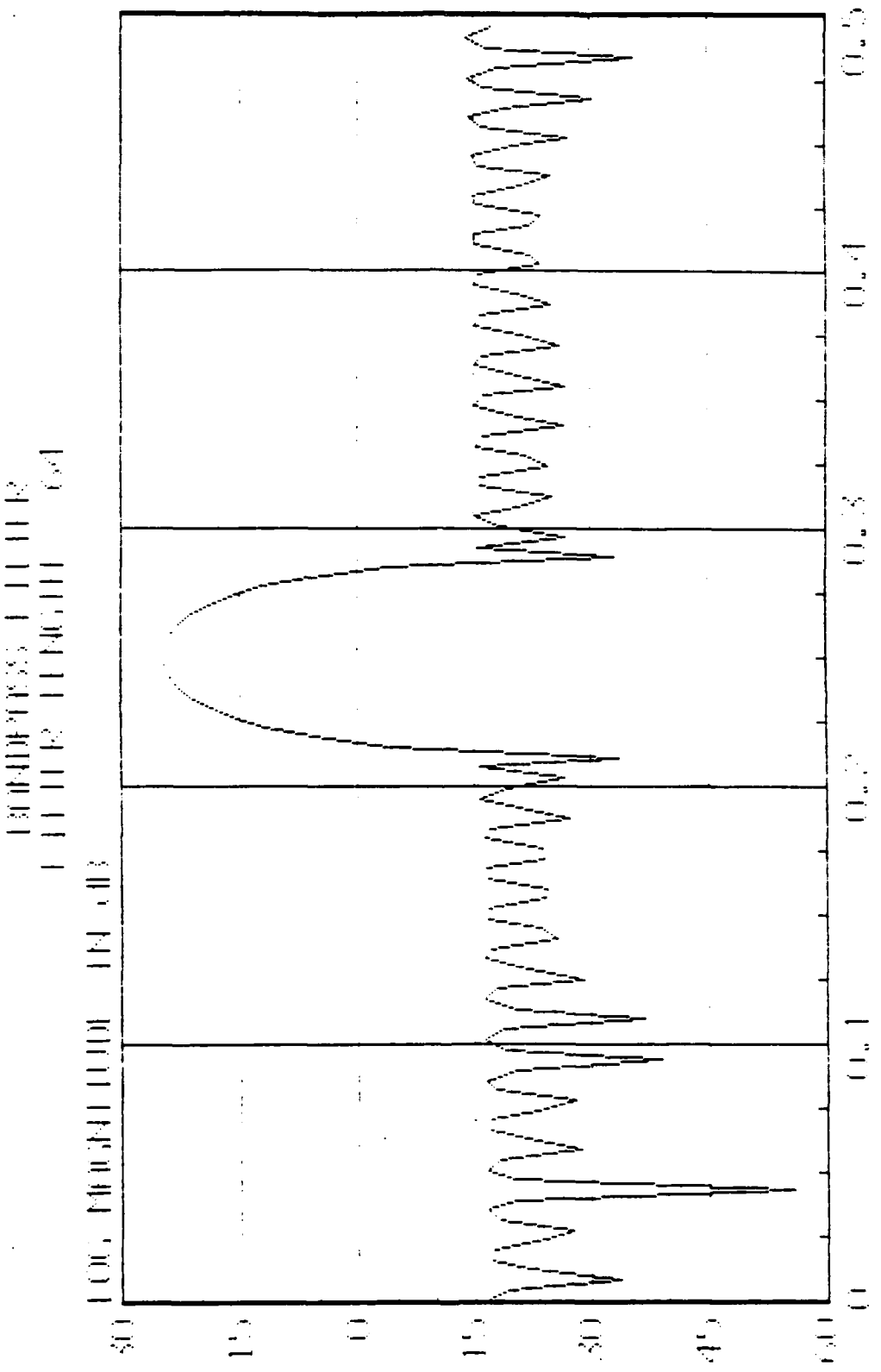

Figure 4

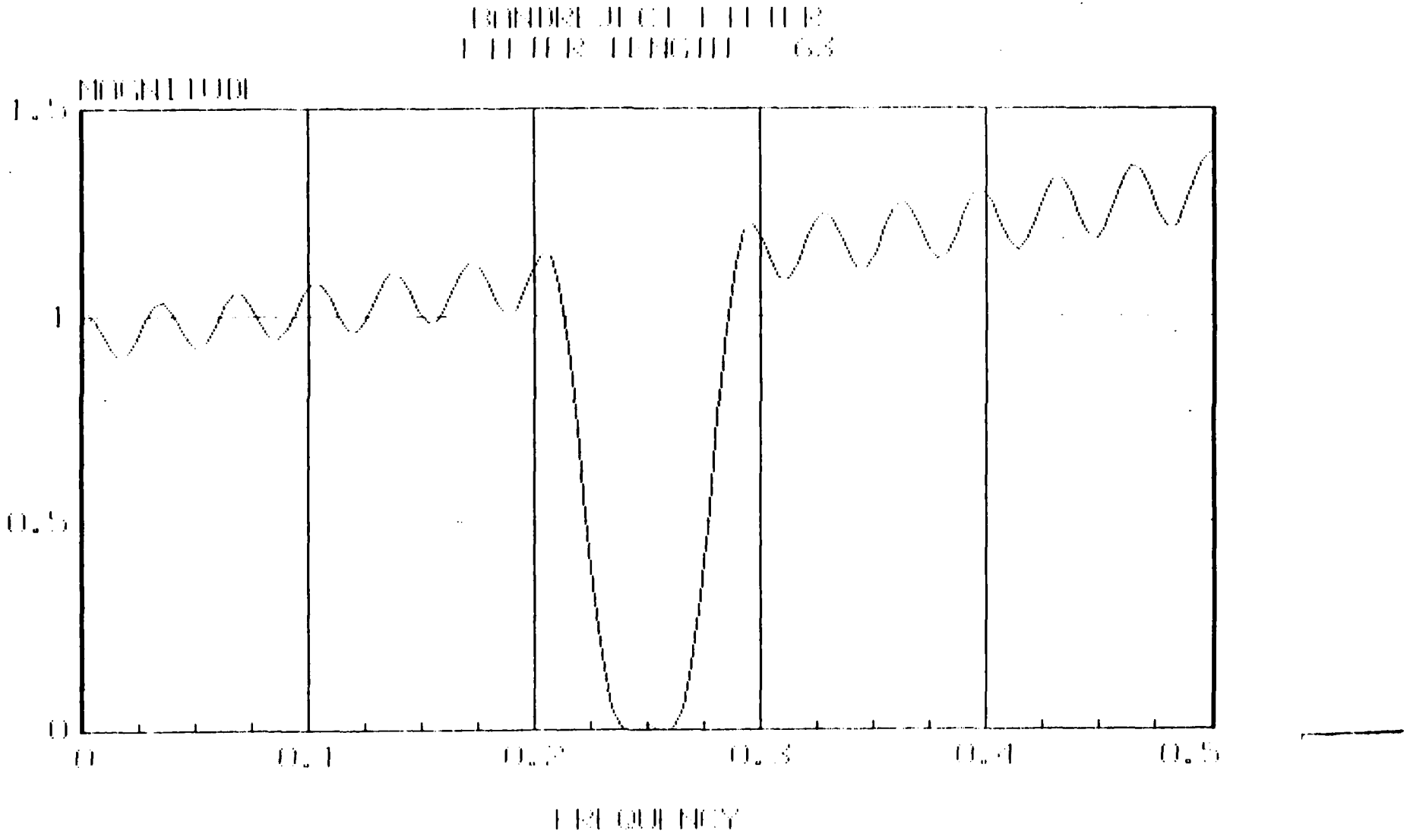

1989 USAF-UES SUMMER FACULTY RESEARCH PROGRAM/

GRADUATE STUDENT RESEARCH PROGRAM

Sponsored by the

AIR FORCE OFFICE OF SCIENTIFIC RESEARCH

Conducted by the

Universal Energy Systems, Inc.

FINAL REPORT

Automating Finite Element Reliability Assessment of Microelectronic Components

Prepared by: Ian R. Grosse, Ph.D.

Academic Rank: Assistant Professor

Department and University: Mechanical Engineering Department, University of Massachusetts

Research Location: Rome Air Development Center (RBES), Griffiss AFB, NY 13441

USAF Researcher: William J. Bocchi

Date: 6 Sep 1989

Contract No.: F49620-88-C-0053

Automating Finite Element Reliability Assessment of Microelectronic Components

by

Ian R. Grosse

ABSTRACT

This report details an investigation of two related research areas of critical importance for finite element reliability assessment of microelectronic components. The first area was automatic finite element mesh generation. For this task, two software codes, **AMEKS** and **FASTQ** , were obtained for evaluation purposes from the artificial intelligence and engineering analysis groups at Sandia National Laboratories. The **FASTQ** software was successfully ported to the Computer Aided Systems Engineering Branch's VAX computer located at Rome Air Development Center, while various machine and software incompatibilities prevented porting of the LISP-based **AMEKS** code to the AI Lab's TI-Explorer workstation despite much effort. The **FASTQ** software demonstated powerful two-dimensional meshing capabilities and was easily interfaced to the commercial finite element code used by the Computer Aided Systems Engineering group. For the second research area, various adaptive meshing algorithms were studied, and a new adaptive meshing algorithm was developed. The algorithm and how it can be implemented with **FASTQ** and a commercial finite element code is discussed in the report.

Acknowledgements

I wish to thank Rome Air Development Center and the Air Force Office of Scientific Research for sponsorship of this research. I also thank Universal Energy Systems for their help in all administrative and directional aspects of this program.

I found both the technical and personal aspects of my research experience very rewarding. It was a pleasure to work with Bill Bocchi, my technical focal point who, together with Doug Holzhuer and Dale Richards, provided much support, technical expertise, direction, and friendship. I would also like to extend my thanks to Elaine Baker, Gretchen Bivens, Peter Rocci, Ginger Ross, Claire Thiem, Jim Vaccaro, and Paul Yaworsky for their help.

Special thanks must be bestowed on Sandia National Laboratories, and in particular, to John Mitchiner and Laurie Phillips of the AI group and to Ted Blacker of the Engineering Analysis group. Their contributions in terms of not only software and documentation but also support and ideas were invaluable.

Finally, I would like to thank the management staff at Rome Air Development for providing me this research opportunity, especially Ed Jones, Tony Feduccia, and Jack Bart.

1 Introduction

Over the past few years, the Computer Aided Engineering Systems Branch (RBES) at Rome Air Development Center has successfully employed the finite element method for reliability assessment of electronic components. Detailed finite element modeling and analysis of semiconductor chips, leads, weld joints, etc., has yielded accurate predictions of the location and magnitude of critical stresses and temperatures in the microelectronic component. Based on these results, failure modes can be predicted and the reliability of the product assessed. While there is no substitute for statistical and empirical reliability prediction methods, finite element analysis of electronic components can supplement other reliability prediction methods by offering a deeper understanding of the physics of design-related failure modes. With this insight the engineer can then make design changes to improve the reliability of the device, if necessary.

The finite element reliability prediction method is particularly useful as a reliability design tool for proposed new technology or custom devices where one does not have the benefit of extensive (or any) experimental data. Often, these devices are quite costly and time consuming to develop and manufacture. It is critical, therefore, that design-related reliability problems be revealed and corrected early in the prototype design phase, before expensive tooling and processing costs have been incurred. Finite element analysis of the device can give the designer and engineer the knowledge needed to make the best possible design decisions in the absence of hard experimental data.

However, reliability assessment via the finite element method has been greatly limited by the substantial amount of labor-intensive work required for accurate finite element analysis. Typically, it may take an engineer several weeks to build an initial detailed finite element model of the electronic device on the computer. Moreover, the numerical results will often indicate critical regions of the device which must be remod-

eled in greater detail to obtain an accurate solution for these regions. Accordingly, finite element modeling and analysis is inherently an iterative process. A flow diagram of this process is shown in Figure 1. Several iterations are usually required before accurate results can be obtained. The most labor-intensive and time-consuming activities are the geometric model generation and finite element mesh generation stages. In contrast, the finite element solver is fully automated and highly optimized to obtain the stress and/or temperature distribution in the component in typically a few CPU hours or less on a small minicomputer such as a VAX 11/750. On faster machines, such as RISC based engineering workstations, the computational time is in the order of minutes or even seconds. This computational time will only decrease as faster machines and algorithms (i.e. parallel processing) continue to emerge.

2 Objectives

Clearly, the bottleneck in finite element reliability analysis is the labor-intensive finite element modeling process and the number of modeling and analysis iterations required to obtain a sufficiently accurate solution. The objectives of this research will specifically address ways to improve the efficiency of these two processes.

In terms of improving the finite element modeling efficiency, the first objective was to bring in-house, install, and evaluate state-of-the-art automatic mesh generator software which would dramatically reduce the amount of human required for finite element mesh generation. Two related software codes, AMEKS and FASTQ, were selected for evaluation. Both codes were developed recently at Sandia National Laboratories in response to their finite element modeling needs and made available to RADC.

To minimize the number of analysis required to obtain an accurate solution, an adaptive meshing scheme is needed. An adaptive meshing scheme is simply an algo-

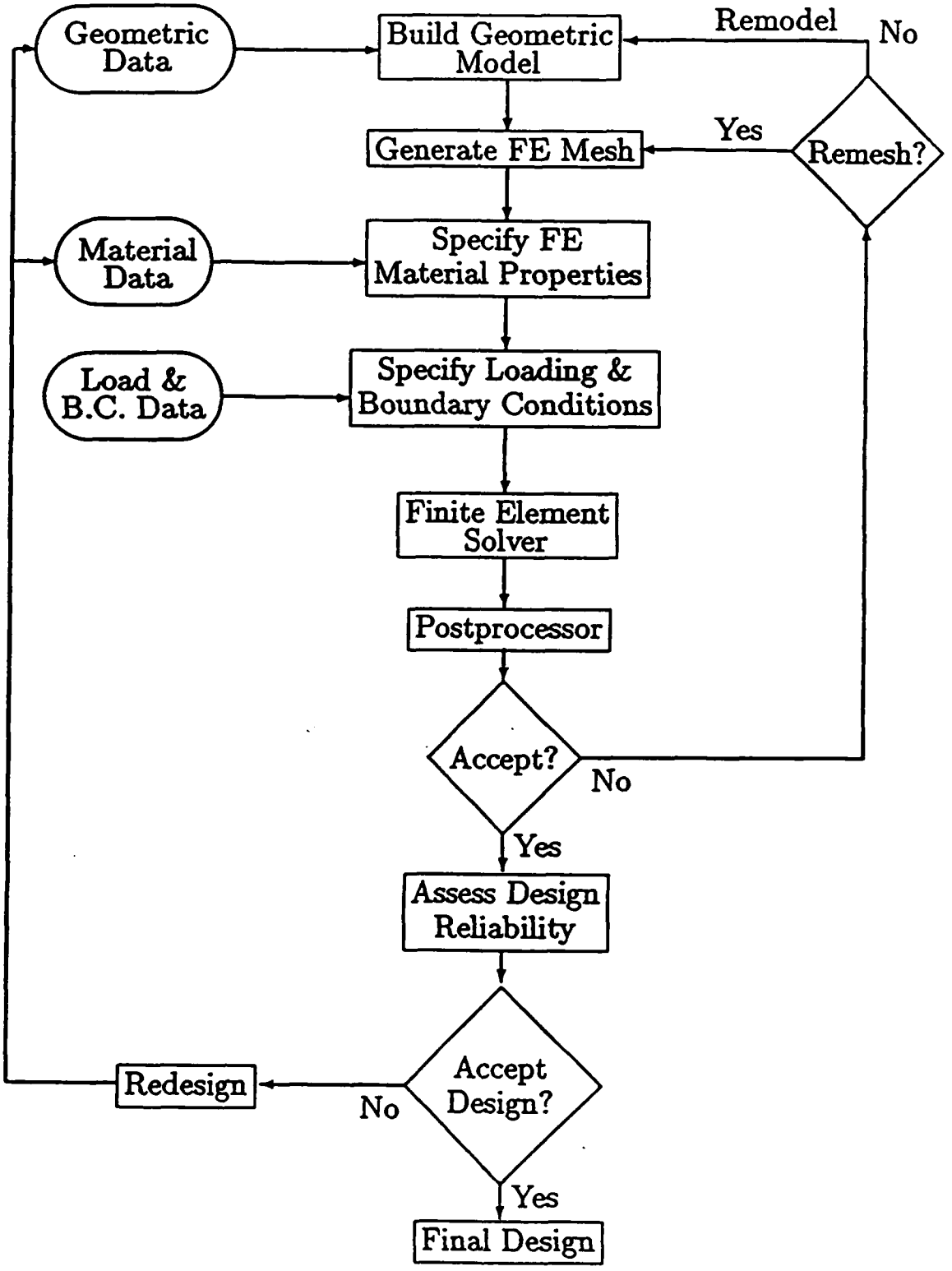

Figure 1: Current Finite Element Reliability Assessment Process

rithm by which the results (i.e. stress or temperature distribution) of a finite element analysis can be used to remesh or refine the finite element model to improve the level of accuracy of the solution. Hence, the second objective was to propose an adaptive meshing scheme which could interfaced with the NISA results and the automatic mesh generation software. It was important that the adaptive meshing scheme be applicable to both heat transfer and stress finite element analyses.

Finally, the last objective of this summer research appointment was to offer specific recommendations and steps the RBES group should take toward realizing the long-term goal of fully automated finite element modeling and analysis of electronic devices.

3 Automatic Mesh Generation

FASTQ is a large FORTRAN 77 code, developed primarily by Ted Blacker at Sandia National Laboratories, which has the capability to automatically mesh a two-dimensional (2D) object with either four-noded, eight-noded, or nine-noded quadralateral elements. Until recently, FASTQ's automatic meshing algorithms were all based on parametric mapping techniques. These techniques required that the analyst first decompose the general-shaped 2D object into regions that map well into the parametric space. A task was then undertaken by the artifical intelligence group at Sandia, lead by Dr. John Mitchiner, to automate the region decompostion task required by FASTQ. This led to the development of AMEKS (Automated MEshing Knowledge System), a knowledge-based expert system for automatic decompcsition of 2D bodies into meshable regions. AMEKS is built on Common Lisp and the KEE[1] shell and runs on Symbolics computers.

Since no Symbolics computers were available in the RADC AI laboratory, consider-

[1] KEE is a software product of Intellicorp.

able effort was expended to convert the AMEKS code to the TI-Explorer LISP based computer under KEE in order to evaluate and hopefully improve the software. However, the conversion effort revealed a great many more incompatibilities in the code than originally anticipated. First, the use of Symbolics dynamic window functions in AMEKS were incompatible with the TI-Explorer window functions. The Symbolics dynamic window functions were replaced with the closest functionally-equivalent TI-Explorer window functions which sometimes meant a loss of window functionality. The incompatibile window function calls were primarily in the following lisp files: ameks-core, eroder, create-objects, and save-objects.

Once these incompatibilities were resolved, the system was able to load the LISP files, knowledge bases, and bring up the AMEKS control menu. However, KEE-related errors occurred after reading in an object data file as AMEKS attempted to decompose the object into subregions. This errors could not be resolved, despite consultation with the AMEKS's programmers and many debugging attempts. In view of these ongoing portability problems and the inordinate amount of time being spent on the AMEKS software, a decision was made to abandon the porting of the AMEKS code to the TI-Explorer. A tape was made of the TI-Explorer current version of the TI-Explore AMEKS code for possible future use.

Parallel with the AMEKS porting effort, the FASTQ code, version 1.4X, as well as device drivers for various TEKTRONIC graphics terminals and FASTQ example input data files, were obtained and installed on the RBES VAX 11/750 computer. Because the software was developed on a VAX computer, there were only minor compatibility problems which were quickly resolved. This version of the code includes a new non-parametric meshing technique, in addition to the parametric mapping techniques (a different meshing technique can be specified for each region). The nonparametric mesh-

ing technique creates elements one-by-one along closed-loop paths beginning with the exterior boundary and preceding inward. In this manner, rows of elements are "paved" into the region. If the region contains holes, then rows of elements are also paved in a similar manner on these interior boundaries. A algorithm detects overlapping elements, and a pull back technique is then implemented to correct these problems. The user can specify different nonuniform element sizes along individual line segments that form the region boundary. Version 1.4X also contains a new region "size" command which can be used to control the element size throughout the region. After the region is meshed, several different smoothing methods or mesh restructuring schemes can be applied to reduce element distortion.

The big advantage of FASTQ's paving technique is its ability to mesh most general-shaped 2D regions. The object need not be decomposed into primitive regions as required by the parametric mapping techniques. Hence, the paving technique obviates much of the need for AMEKS. However, multi-regions may still be desireable for meshing purposes, especially for composites and other multi-material bodies (devices).

Figure 2 shows both the initial FASTQ model of a two-material wafer for a 3-D computer and the resulting finite element mesh obtained from FASTQ. The finite element mesh consists of 1305 four-noded elements and 1376 nodes. The input data required by FASTQ, which can be either keyed in interactively or read from a data file, is listed in the table below. Note the simplicity and the brevity of the data required by FASTQ. It took only five minutes to enter this data and roughly 10 minutes of CPU time on a VaxStation 3100 for FASTQ to obtain the resulting mesh. The FASTQ commands are documented in a user's manual obtained from Ted Blacker of Sandia National Laboratories. The geometry is input into FASTQ in an hierarchical boundary representation format- points, lines, sides, regions, and body. A digitizing tablet may

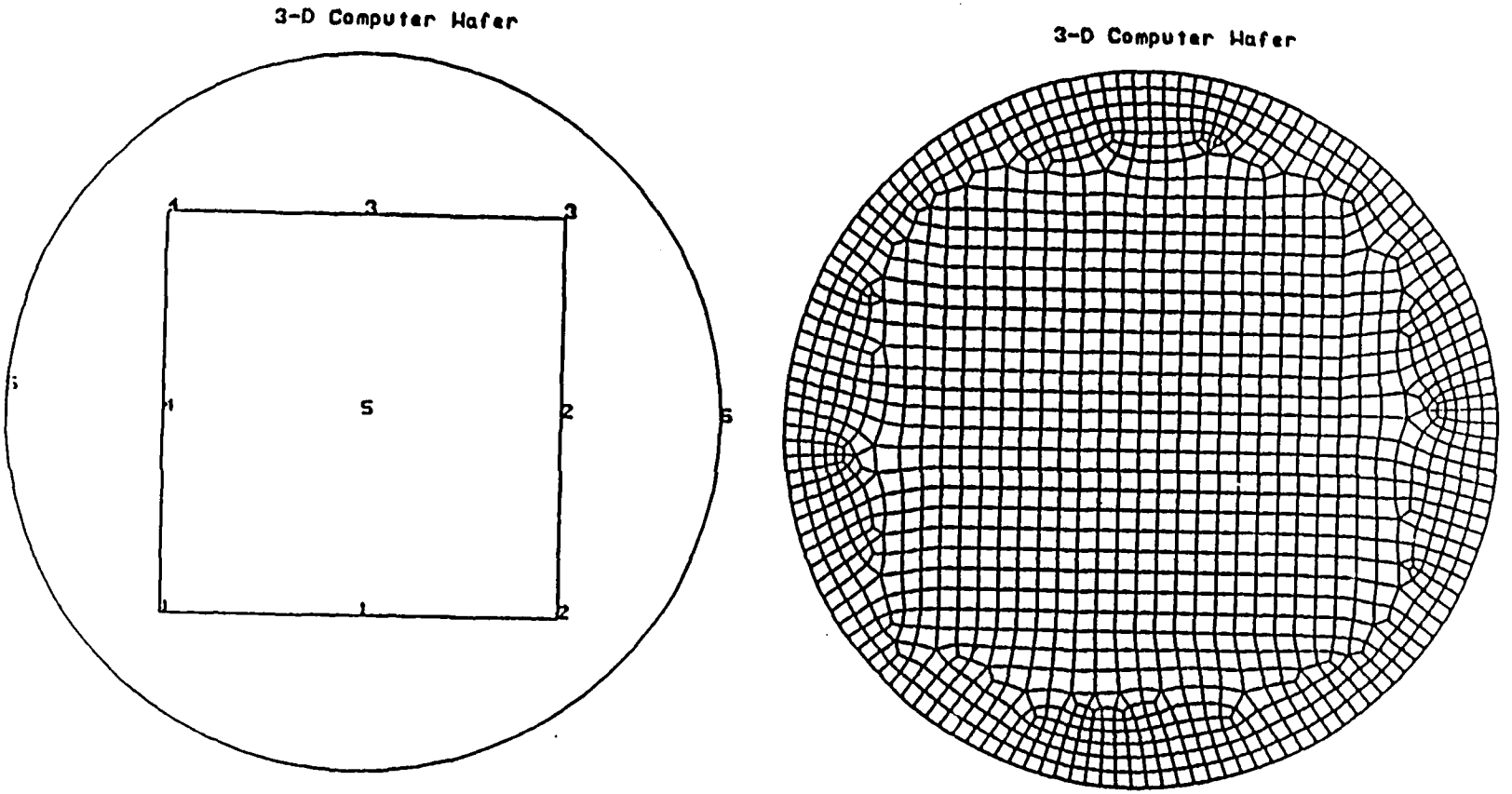

Figure 2: Initial FASTQ Model and Resulting Finite Element Mesh of Wafer

```
title
3-D Computer Wafer
point   1   0     0
point   2   5     0
point   3   5     5
point   4   0     5
point   5   2.5   2.5
point   6   7.0   2.5
line    1   str   1   2   0   20   1.0
line    2   str   2   3   0   20   1.0
line    3   str   3   4   0   20   1.0
line    4   str   4   1   0   20   1.0
line    5   circ  6   6   5   140  1.0
region  1   1     -5
region  2   2     -1  -2  -3  -4
hole    1   2
scheme  1   x5s
scheme  2   M
body    1   2
exit
```

Table 1: **FASTQ** Input Data File for 3-D Computer Wafer

also be used to input the data directly from a drawing. Meshes generated by **FASTQ** can be interfaced to NISA in the following manner. In the meshing module of **FASTQ**, a NASTRAN output file is written using the N command. Then, **FASTQ** is exited and the NASTRAN/NISA2 conversion program is executed to convert the NASTRAN file format to a NISA2 file format. This file can then read by the NISA2 preprocessor Geometry Database (GDB) which is used to complete the finite element model and write a complete NISA2 output file. This conversion process takes only a few minutes and could easily be automated so that a NISA2 data file could be written from the mesh module of **FASTQ**.

4 Automatic Adaptive Remeshing

For automatic adaptive remeshing, the finite element analysis results are used to estimate the discretization error distribution throughout the finite element model. This discretization error is due to the fact that the continuum is represented by a finite number of elements and should be distinguished from computer roundoff (truncation) errors and errors due to modeling assumptions. Based on this error estimate and user-specified accuracy requirements, the finite element model is adapted to yield a more "optimal" mesh. Adaptive meshing techniques can be classified into three categories:

1. **Nodal Point Optimization:** In this approach neither the connectivity of the finite element mesh or the order of the finite elements is changed. The new mesh contains the same number of nodes, elements, and nodal connectivity used to define each element. However, the nodal locations are moved to obtain a more optimal solution. The repositioning of the nodes may be based on a local error estimate or on the minimization of the total potential energy with respect to the nodal coordinates.

2. ***h* Refinement:** This is the most common type of mesh refinement scheme. It is often practiced in an intuitive manner by analysts without any formal error estimate computations. Ideally, error estimates are used to increase the number of elements and nodes locally and/or globally to obtain a more optimal mesh. The order of the element (linear, quadratic, etc.) remains unchanged.

3. ***p* Refinement:** This is a relatively new method where the number of elements and element shape remain the same. Instead, the order of the element is increased by the addition of midside and interior nodes. Higher order elements used higher order polynomials to represent the displacement or temperature field. The accu-

racy of the solution improves because of the additional nodal degrees of freedom in the new mesh.

Each method has its own advantages and disadvantages. Nodal point optimization can be computationally inexpensive and relatively simple to implement. The most optimal mesh can be obtained for a fixed number of degrees of freedom. However, there is no guarantee that the number of degrees of freedom in the mesh is sufficient to satisfy the accuracy requirements of the user. The *h* refinement method has the advantage of being applied locally and/or globally to force the solution error to within acceptable bounds. However, mesh restructuring is required which usually dictates the need for a robust automatic mesh generator. The *p* refinement method has shown promising results compared to the *h* refinement method. However, it is more difficult to implement and requires access to the finite element source code which is not required by the other two techniques. Additional discussion and some specific implementations of these methods can be found in the papers presented by Babuska et al. (1986) and the text of Zienkiewicz and Taylor (1989).

Due to the availability of a good automatic 2D mesh generator in the FASTQ code and the lack of source code access to the NISA finite element code makes, an *h* refinement adaptive meshing strategy was selected for automatic remeshing. First, in the following section a new error estimator is presented which can be applied to both stress and thermal finite element results.

4.1 A Generalized Error Estimator

The approach taken is similar to Zhu and Zienkiewicz's approach (1987) for obtaining a stress error estimate.

To avoid confusion, the following notation convention is used. All vector quantities

are enclosed by curly braces { } and matrices by square brackets [ ]. Nodal variables, such as nodal temperatures, are indicated with an overbar, while finite element field variables, such as the temperature distribution, are indicated with an overhat. The subscript e is used to denote an element quantity.

Let $\{\hat{\sigma}\}$ denote the finite element stress field which is, in general, discontinuous across interelement boundaries. Let $\{\sigma^*\}$ denote a higher-order approximation to the true stress field which is continuous across interelement boundaries. An estimate of the stress error is given by the difference of these two fields. To obtain $\{\sigma^*\}$, Zhu and Zienkiewicz imposed a weighted residual equality between the finite element stress vector field $\{\hat{\sigma}\}$ and the "smooth" stress vector field $\{\sigma^*\}$ used to approximate the true stress vector field

$$\int_V [N_\sigma]^T (\{\sigma^*\} - \{\hat{\sigma}\})\, dV = \{0\} \tag{1}$$

where the integration is carried out over the volume V of the entire body and $[N_\sigma]$ is the nodal shape function matrix used to interpolate the smooth stress field from stress nodal values, denoted by $\{\overline{\sigma}^*\}$:

$$\{\sigma^*\} = [N_\sigma]\{\overline{\sigma}^*\} \tag{2}$$

The individual shape functions contained in the matrix $[N_\sigma]$ are identical to the shape functions used to interpolate the displacement field from nodal values. Thus, if linear finite elements are used, then matrix $[N_\sigma]$ will contain linear functions of the spatial coordinates.

Substituting for $\{\sigma^*\}$ from Eq. (2) into Eq. (1), solving for $\{\overline{\sigma}^*\}$, and substituting back into Eq. (2) yields the following expression which is used to compute $\{\sigma^*\}$

$$\{\sigma^*\} = [N_\sigma][A]^{-1} \left(\int_V [N_\sigma]^T \{\hat{\sigma}\} \right) dV \tag{3}$$

where

$$[A] = \int_V [N_\sigma]^T [N_\sigma] dV \tag{4}$$

If a body contains multiple materials, then the stress field may not necessarily be continuous across intermaterial boundaries. Thus, the continuity requirement used to obtain to the smooth stress field $\{\sigma^*\}$ must be relaxed. This is done by applying Eq. (1) independently to each material region:

$$\int_{V_i} [N_\sigma]^T (\{\sigma^*\} - \{\hat{\sigma}\}) dV_i = \{0\} \quad , i = 1, 2, \ldots, nummat \tag{5}$$

where V_i denotes the volume of the i^{th} material region and *nummat* equals the number of material regions. Using the same derivation as above yields the following formula for the smooth stress vector field for each material region:

$$\{\sigma^*\}_i = [N_\sigma][A]_i^{-1} \left(\int_{V_i} [N_\sigma]^T \{\hat{\sigma}\} \right) dV_i \tag{6}$$

where

$$[A]_i = \int_{V_i} [N_\sigma]^T [N_\sigma] dV_i \tag{7}$$

Using the difference between $\{\sigma^*\}_i$, an approximation to the true stress field, and the finite element stress field $\{\hat{\sigma}\}$, an error estimate can be obtained element by element for each material region.

There are two disadvantages with the stress-based error estimator. First, it is computational expensive to compute because stress is a vector quantity. For example, the matrix $[A]_i$ has size $3N_i \times 3N_i$ and $6N_i \times 6N_i$ for 2D and 3D. respectively, where N_i is number of nodes in material region i. Secondly, matrix and vector sizes are a function of the dimensionality of the problem which increases the programming complexity of the algorithm.

A more desireable error estimator would be based on a scalar quantity, such as the strain energy density (SED) function u given by

$$u = \frac{1}{2}\{\epsilon\}^T [D]\{\epsilon\} \tag{8}$$

where $\{\epsilon\}$ is the strain vector and $[D]$ the constitutive material matrix. The same continuity requirements imposed on the stress vector must also apply to the SED function to obtain a higher order approximation to the SED function, denoted by u^*, used to approximate the true strain energy density. Thus, one has

$$\int_{V_i} [N_u]^T (u^* - \hat{u})\, dV_i = \{0\} \quad , i = 1, 2, \ldots, nummat \tag{9}$$

where $[N_u]$ are the shape functions used to interpolate the smooth SED field u^* from nodal values. Following the same steps as above, one can easily derive the following formula for the SED function estimator:

$$u_i^* = [N_u][A]_i^{-1} \left(\int_{V_i} [N_u]^T \hat{u} \right) dV_i \tag{10}$$

where

$$[A]_i = \int_{V_i} [N_u]^T [N_u]\, dV_i \tag{11}$$

The analogous scalar function to the SED function in thermal analysis is the energy function given by

$$u = \frac{1}{2}\{a\}^T [\mathcal{K}]\{a\} \tag{12}$$

where $[\mathcal{K}]$ is the thermal conductivity matrix and $\{a\}$ is the vector of temperature gradients

$$\{a\} = \begin{Bmatrix} T_{,x} \\ T_{,y} \\ T_{,z} \end{Bmatrix} \tag{13}$$

Thus, this error estimator can be easily generalized to thermal analysis, in addition to other field problems.

For each element e, a least square error estimator for u_e can be computed:

$$\|e\|_{u_e} = \left[\int_{V_e} (u_e^* - \hat{u}_e)^2 \, dV_e\right]^{1/2} \tag{14}$$

In the following section an adaptive remeshing scheme is proposed based on this error estimator.

4.2 An Adaptive Remeshing Scheme

The total root mean square error is given by

$$E_{rms} = \left(\frac{\|E\|_u^2}{m}\right)^{1/2} \tag{15}$$

where m = total number of elements and

$$\|E\|_u^2 = \sum_{e=1}^{m} \|e\|_{u_e}^2 \tag{16}$$

For any element e, it is required that the element error estimator be less that some small percentage of the total root mean square error

$$\|e\|_{u_e} < \bar{\eta} E_{rms} \equiv \bar{e}_m \tag{17}$$

where typically $0.01 \leq \bar{\eta} \leq 0.05$. Let

$$\xi_e = \frac{\|e\|_{u_e}}{\bar{e}_m} \tag{18}$$

If $\xi_e > 1$, then the element size h should be decreased. Conversely, if $\xi_e < 1$, then the element size can be increased. If $\xi_e = 1$ for all elements, then the error distribution is uniform.

To obtain appropriate values by which to increase or decrease element size h, the asymptotic convergence rate criteria is invoked at the element level. If the order of the assumed polynomial used to approximate the field variable is p, then one can expect a convergence rate of order $O(h^{p+1})$ since higher order terms have been omitted from the assumed field. Similarly, the convergence rate for derivatives of the field variable, such as strains or temperature gradients, will have a convergence rate of order $O(h^{p+1-l})$, where l is the order of differentiation required to obtain the derivative variables. In 2D and 3D elasticity and thermal analysis, $l = 1$ since the strains and temperature gradients are given by the first derivatives of the field variable. Since the scalar u is given by the product of these derivatives, one can expect a convergence rate of order $O(h^{2(p+1-l)}) = O(h^{2p})$. Thus, it is assumed that

$$\|e\|_{u_e} \propto h_e^{2p} \tag{19}$$

Denoting the current mesh with the pre-superscript i, the requirement that ${}^{i+1}\xi_e = 1$ together with the above equation yields

$$\frac{{}^{i}\xi_e}{{}^{i+1}\xi_e} = {}^{i}\xi_e = \frac{{}^{i}h_e^{2p}}{{}^{i+1}h_e^{2p}} \tag{20}$$

Thus,

$${}^{i+1}h_e = \xi_e^{-1/2p}\, {}^{i}h_e \tag{21}$$

Using eq. 21, a mesh density distribution for a new mesh can be obtained throughout the model. The distribution can be used by the automatic meshing program FASTQ in its meshing algorithm to obtained an optimal mesh.

5 Recommendations

The first step towards automated finite element reliability assessment of electronic devices is the automation of finite element mesh generation. While a number of 2D

automatic mesh generators exist today, the new meshing algorithm implemented in the FASTQ code was seen to be particularly robust, easy to use, and is extendable to 3D problems. It was clear that the amount of time required to mesh a nontrivial 2D object, such as a the computer wafer of Figure 2, was significantly less using the FASTQ software than by using current commercial finite element mesh generators which require a substantial amount of user interaction. Therefore, it is recommended that the FASTQ code be immediately utilized for finite element meshing of nontrivial 2D geometries. To facilitate this process, it is recommended that the FASTQ code should be modified to directly output NISA2 data files. FASTQ should also be immediately used for 3D problems which can be modeled by the extrusion of 2D meshes into the third dimension.

Secondly, it is recommended that a FORTRAN 77 code be developed for automatic remeshing. The code would read as input a NISA2 results file and generate a new optimal mesh based on the accuracy requirements using the generalized error estimator and adaptive remeshing algorithm presented above and the FASTQ code itself for meshing. The addition of this computational tool will provided the Air Force the capability of automating for 2D problems the most time consuming steps of finite element reliability assessment: the initial mesh generation and subsequent mesh refinement stages.

The final recommendation is to pursue a long term goal of automating 3D finite element reliability assessment of electronic devices. This will require a significant committment on the Air Force's part but has a tremendous potential for increasing the reliabilty of new technologies, reducing new technology developmental time. and thereby dramatically reducing their developmental costs. The research this summer indicates that both the FASTQ meshing technique and the adaptive remeshing algorithm are extendable to 3D. However, the complexity of 3D devices dictates the use of a higher-level modeling tool, such as a solid modeler incorporated into an expert knowledge-based system for

electronic devices, and the use of a higher-level meshing tool. It is envisioned that the FASTQ code, adaptive meshing software, and the reliability assessment software would function as low-level procedures executed by these knowledge-based computational systems.

6 References

Babuska, I., Zienkiewicz, O.C., Gago, J., and Oliveira, E.R. (1986), *Accuracy Estimates and Adaptive Refinements in Finite Element Computations*, Wiley & Sons, New York.

Zienkiewicz, O.C., and Taylor R.L. (1989), *The Finite Element Method* 4th Ed., McGraw-Hill, New York, pp. 398-435.

Zhu, J.Z. and O.C. Zienkiewicz, "Adaptive techniques in the finite element method," *Comm. Appl. Num. Methods*, Vol. 4, 197-204, 1988.

1989 USAF-UES SUMMER FACULTY RESEARCH PROGRAM

Sponsored by the

AIR FORCE OFFICE OF SCIENTIFIC RESEARCH

Conducted by the

Universal Energy Systems, Inc.

FINAL REPORT

DESIGN FOR TESTABILITY: FROM COMPONENTS TO SYSTEM

Prepared by:	John Hadjilogiou, Ph.D., P.E.
Academic Rank:	Professor and Head
Department:	Electrical and Computer Engineering
University:	Florida Institute of Technology
Research Location:	Rome Air Development Center Griffiss AFB, NY 13441
USAF Researcher:	Jerome Klion
Date:	30 Sept. 1989
Contract No:	F49620-8-C-0053

DESIGN FOR TESTABILITY: FROM COMPONENTS TO SYSTEM

BY

JOHN HADJILOGIOU

ABSTRACT

The purpose of this study is to illustrate the interrelationships between various component/system design implementations and overall testability related features.

Inherent to every design are considerations, such as power, percentage of detection, diagnostic capabilities, ease of testability, acquisition time, reliability, maintainability, availability, and life-cycle costs. The documentation of these interrelationships and their cost trade-offs will ease the task of the design engineer with the selection and determination of system specifications and attributes.

Testability features, together with the functional description of the system and other design features, must be addressed at the beginning of the design cycle for a successful product. Integrating testability into a system should result in maintainability improvement, which in turn, will increase its availability. This is true provided these added testability features did not appreciably degrade the original system's reliability. Every effort must be made to keep the reliability of the testable system to its original (prior to the testability integration features) reliability level.

ACKNOWLEDGMENTS

I would like to express my appreciation and gratitude to Mr. Jerome Klion, Chief of the Reliability and Maintainability Techniques Branch at RADC, and the focal point for this research work. He created a professional atmosphere and provided me with direction and the tools for a successful summer research experience.

Mr. Klion's staff at RADC were extremely helpful and cooperative. I felt priviledged to have the opportunity to work and interact, on a daily basis, with such a wonderful group of committed individuals. I would also like to express my appreciation to Mr. John A. Ritz, from the Directory of Plans and Programs Division, for his direction and guidance. Special thanks should also go to Mr. John H. Bart, Technical Director of Reliability and Compatibility and Mr. Anthony J. Feduccia, Chief of Systems Reliability and Engineering Division, for their valuable support.

The services rendered to me by Universal Energy Systems, Inc. were extremely satisfying. The support received from the United States Air Force Summer Faculty Research Program (SFRP) was much appreciated since, without their financial assistance, this research work would not have been completed nor would it be available to interested institutions.

Finally, I would like to express my appreciation and gratitude to my family who accompanied and supported me throughout this effort.

I. INTRODUCTION

Teamwork, cooperation, innovation, and proper initial system specification are the requirements for a successful product. The various design attributes of the system must be clearly specified by the system engineer. In addition to performing its intended function the system must be reliable, testable, affordable, and meet the requirements and demands of the customer. Quality is defined by the customer's requirements. In the initial specification, the system must also itemize reliability, maintainability, testability, and availability quantitative requirements.

A practicing engineer must also address two considerations in the initial phase. These engineers must select components that meet specific quality ratings for reliability considerations, and they must enforce design rules from other successful mature projects for improving fault avoidance. Appendix E contains design rules that engineers are encouraged to follow. These rules were derived from previous mature designs and are documented in the literature. This initial list will be updated on a quarterly basis and will be supplemented with additional rules.

Design reviews are an effective method of fault avoidance. Periodic design reviews, appropriately conducted, will detect and correct initial specification mistakes, contradictions, and possible omissions. Cooperation, innovation, and knowledge are the important ingredients for a successful design. Fault tolerance considerations should also be part of the initial design phase to address unavoidable critical random faults. Hardware, software, information, and time redundancy techniques are used for fault tolerance and are summarized in Appendix F. The fault-tolerant system is capable of continued operation with little or no service degradation and without corruption of data. Demands for high system availability require some type of fault tolerance.

The initial design also requires addressing quantitative factors, such as cost, chip and board area, power considerations, and reliability requirements. The success of any product design is heavily dependent on the proper trade-offs and implementations of these requirements. The availability of alternatives is crucial to the success of a design.

Several efforts are underway to automate these procedures. Success is still heavily dependent on the ingenuity of the designer because the thorough understanding of a large and complex set of interrelated concepts and their effects on performance, reliability, and usefulness is necessary. For example, experiments have shown that the reliability of manufactured tested circuits are almost independent of the number of electronic gates on a chip. Thus, a single chip containing a large number of gates is more reliable than a large number of less complex chips. Accomplishing a design objective with the minimum amount of chips will require the specification of all the testability and reliability requirements at the beginning of any design. It facilitates the process of securing the reliability of the easily tested system to that of the system that was in use prior to testability features integration.

Failure rates, mean-time-to-failure, mean-time-between-failure, failure coverage, and other reliability analysis attributes will not be outlined in this document but will be integrated in the design of line-replacement module in Appendix D. However, the design engineer addresses these concepts in the initial design specification.

At the end of the design cycle and during the implementation phase, the design engineer should address and document ways of modifying the design for added features. Furthermore, ways to improve the present fault-avoidance and fault-tolerance attributes for future products should be documented. This procedure is becoming a requirement for a successful business operation—to improve, expand, and conquer through knowledge, planning, cooperation, and innovation.

II. OBJECTIVES OF THE RESEARCH WORK

The objective of this research work is to study and document the interrelationships between the various components/system implementations and their overall testability features.

During the course of this summer faculty research program (SFRP) the testability features of components and systems was studied together with current design philosophies. A more detailed analysis of each implementation was also studied and documented in the six appendices. Due to lack of space these appendices are

available from the author and will be fully published as an RADC report.

III. TESTABILITY CONSIDERATIONS

A system must be tested to guarantee its functionality, and for a system to be testable it must be designed with this criteria in mind. Fault modeling and reduction, test pattern generation, fault simulation, fault coverage evaluation, and production of the fault dictionary are the processes normally involved for testing systems.

Built-in testing and external testing are the two major approaches used to examine a system; a combination of these two approaches is the technique most commonly used today. External testing, when referring to a chip, means that the testing mechanism is outside the chip, may be at the board level or system level, or outside the system. Board level external testing means that the testing mechanism is at either system level or outside the system, and at the system level, it means that a tester resides outside the system. A system and its components are usually designed with the help of built-in test techniques and testers. It is further refined in such a way as to have the capability for the system to test its boards and interconnections among the boards, the boards to test its chips and interconnections among the chips, and chips to test the components within themselves. Chips and boards may also have the capability to self test. Self testing has received much attention in recent years, and the technology is here to support it, as shown in Appendix C.

Concurrent built-in test techniques allow the system to be monitored while it continues to perform the intended function. Several of the fault- detection techniques can work under this mode. In the nonconcurrent built in test approach, the system must leave the normal mode of operation and enter into the test mode before testing can be performed. Most of the fault detection techniques fall under this category.

The functional type of testing attempts to verify that the system under test possesses the functional characteristic of the intended design. This is extremely useful when the internal details of the circuit are not known and structural testing cannot be

accomplished. It is also useful to obtain test information during the early stages of the design phase so that a determination can be made if design mistakes exist within the system. On the other hand, fault type of testing determines if faults exist within the physical structure, as well as attempts to isolate/locate the fault. A fault can be present, and the system can still pass the functional test. Under some failure conditions, the intended function is correctly performed, but other events are incorrectly activated. Parametric type of testing determines if certain parameters of the system under test are within the required ranges. The switching time of a logic gate is an important parameter for digital circuits.

During the normal design phase, the designer will produce a set of functional vectors to be used as a verification tool. These functional vectors are used in a fault simulation to obtain the percentage of total fault coverage. Depending on the quality of these functional vectors and the design rules used to implement the circuit, this percentage of coverage will range between 40% and 85% of the total faults. Additional structurally related test vectors must then be generated to bring this coverage up to the pre-specified minimum value.

All these types of testing can be performed at or below the operational speed of the system. When testing is performed below its operating speed it is referred to as static test, and if it is performed at its operational speed it is referred to as dynamic test. In general, built-in test structures that are custom made and integrated into the system are capable of performing dynamic testing, and the general purpose testers, external to the system, are capable of performing static testing.

Test pattern and the corresponding fault-free response is produced by either software-based or hardware-based methods. In the software-based method, the test pattern vectors are generated in advance along with the corresponding fault-free response vectors and stored in memory. Compacting these responses is an effective way of reducing the storage space and the number of comparisons. Test programs are normally produced automatically by test generation algorithms/programs. This is a deterministic testing method and requires excessive memory space, time to generate patterns, time to apply patterns, and time to compare with the fault-free response. In the hardware-based method, test pattern vectors are normally generated by pseudorandom techniques and

are simultaneously applied to the circuit under test and to a known good/gold circuit. Comparing output responses determines the status of the circuit. However, this random type of testing requires a good/gold circuit and must adhere to strict synchronization rules for output comparison. It also requires applying an excessive number of input patterns for any acceptable fault coverage. Compacting output responses will alleviate some of the synchronization and good/gold requirements but unfortunately do not reduce the length of the input pattern. Compact testing, due to ease of implementation, is well suited for built-in testing.

IV. TESTING COMBINATIONAL SYSTEMS

Fault testing of a system ascertains the existence of faults, while extra testing is normally required for isolation. The faulty conditions can be determined by observing the relationship between inputs and outputs. This should also be true for redundant systems. If not, additional input, output lines, and possible internal gates, must be inserted for testability purposes.

Test, test vector, test pattern, and fault-detection test usually have the same meaning and denote a specific input pattern to be applied to the system for testability purposes. When an input pattern, which is capable of covering one or more faults, causes the output to behave differently than when it was implemented, this input pattern detects at least one fault. Test pattern generation is the process of collecting a minimum set of input patterns to detect a certain percentage of detectable faults. One hundred per cent detection is desirable but, for most applications, due to time limitations or complexity requirements of the built-in testing, a lesser percentage of detection is accepted.

For the input pattern to detect a fault it must first activate the fault, and then propagate its effect to the output lines. The process of activating the fault is known as controllability, and the process of propagating its effect to the output lines is referred to as observability. Thus certain input bits of the input test vector activate the fault and certain other sets of input bits propagate its effect to the output. However, these two sets of input bits do not have to be mutually exclusive. The ease of controllability and the ease of observability normally relates to the ease of testability. The

proper addition of input lines, output lines, and extra gates improves the controllability and observability of the design. Proper partitioning also has a tremendous effect on testability.

There are several techniques that are easy to understand and master that are now available for test pattern generation for combinational circuits. These techniques have been around for many years, but improvements are continuously appearing in the literature with their software implementation. Several of these packages are available for the personal computers, and the more sophisticated packages are available for popular workstations.

A summary of these concepts and combinational testing techniques, with illustrative examples, appears in Appendix A. These concepts and techniques are used extensively throughout the testability cycle and should be mastered by every design engineer. The truth-table approach, path sensitization, D-algorithm, PODEM algorithm, and FAN algorithm are some of the most popular combinational testing techniques.

For ease of implementation most of the testing techniques are applied to the system in the preset approach/experiment mode. In this mode, all the predefined input patterns are applied to the system, and based on the response, a decision is made about the system's status. The testing time is independent of the output responses. With this approach the hardware requirement is less sophisticated, but the length of the testing sequence is longer. If the time for testing is the governing factor, an adaptive approach will be better. In the adaptive approach, every output is observed prior to applying the next input, which is a great saving on the length of the input testing sequence for the expense of more sophisticated hardware.

The fault-simulation approach is an effective way of obtaining the required test vectors for a pre-specified fault coverage. The input pattern is applied to the simulation of the fault-free system and is also applied to a simulation of the faulty system, which contains the faults that need to be detected. If the outputs of the fault-free and faulty systems differ, the present input pattern is retained as a test pattern for the faults contained in the faulty system. The process continues until the pre-specified fault coverage is achieved. An illustrative example of the two fundamental

methods of generating test patterns using the simulation approach is also shown in Appendix A.

If the duration of the fault testing is not significant, then the fault- pattern generation effort and the hardware required to store these vectors can be eliminated by replacing it with a simple linear feedback shift register (LFSR) structure that generates random vectors. The time- consuming process of fault pattern generation is eliminated at the expense of less fault coverage per input pattern. However, for VLSI systems and high-fault coverage requirements, this approach takes an enormous amount of time. It is better to apply input random patterns for the detection of approximately the first 70–90% of the faults and then use a deterministic approach for the remaining faults. This combined approach takes advantage of the simple implementation of the linear feedback shift register to generate random vectors that will detect most of the faults and later switches to the deterministic approach for storing and applying the additional, relatively smaller amount of patterns to achieve the required fault coverage. However, this design philosophy has been challenged in recent months by several researchers. They are claiming [1] that changing from random to deterministic, both the total test generation time and total number of tests are increased. The comparison made was on a small sample, and they only considered LFSR-generated random vectors rather than weighted or biased vectors. The weighted and biased random vectors have some very interesting features for test pattern generation.

Random input vector patterns are extensively used in the various testing modes. Every design engineer must be familiar with the implementation and application of linear feedback shift registers. Work is presently under way at Florida Institute of Technology [2] to design simple structures capable of generating on-line deterministic vectors rather than storing them. The success of this research work will have a tremendous impact on the architecture of testing devices, boards, and systems, with large savings in total generation time and total number of tests. Testing speeds will also be increased over existing techniques.

The application of input testing vectors produces output vectors for testing purposes. One simple solution is to store all these vectors and compare them with those of the fault-free system. Using this approach we have collected sufficient data to make intelligent testing conclusions. If there is sufficient time, space, and

power, this can be an acceptable solution for the application at hand. However, this luxury is usually not available, and it is necessary to resort to one of the existing compact approaches. The most popular and proven approach is to compact a set of vectors into a single vector. This is the signature-[3] analysis technique in which the vectors are compressed, using a simple structure, into a single, multiple-bit vector known as signature. The signatures of the fault-free system are compared with the system under test to determined its fault status. The structure used to generate the signature is known as signature analyzer and usually is nothing more than a linear feedback shift register.

V. TESTING SEQUENTIAL SYSTEMS

In the previous section and in Appendix A, several testability techniques are outlined that are applicable to combinational systems. Combinational systems, however, do not have many practical applications without incorporating some kind of feedback mechanism. Through feedback mechanisms, information can be stored for future processing or design counters for controlling various operations. A sequential system is a combinational circuit with feedback.

Several attempts have been made to extend the approaches developed for the combinational to the sequential systems with varying success. The sequential approaches developed worked for some very small systems, but as soon as the system complexity increased, these approaches became very difficult to implement. The test generation problem for general sequential circuits is very difficult and, for all practical purposes, unsolvable at this time. Poor controllability and observability of the memory elements are the major sources of difficulty. The original state assignment of the sequential machine also has an effect on the ease of testability. Research work [4] is presently under way to optimize state assignments for ease of testability.

Not only must it be verified that the sequential system provides the correct primary outputs for a given set of primary inputs, but the occurrence of the proper state transitions must be verified. Complete testing of a sequential system requires the verification of all possible primary inputs for all the possible initial

states. This is a formidable task, and from the practical point of view is impossible to be attained. Partitioning the sequential system and taking advantage of the existing combinational testing approach is the way these systems are now being tested. Several elegant techniques are available and are characterized as structural approaches for design for testability (DFT) of sequential systems.

Ad hoc and structural approaches are the two basic DFT techniques. Ad hoc techniques are heuristic techniques that are more of an art than science. They are mainly based on proper circuit partitioning and on the addition of extra input and output lines for ease of controllability and observability. The design philosophy is that well-structured smaller circuits with extra pins are easier to test than larger ones with less pins. The success of these techniques heavily depends on the past experience and the cleverness of the designer. Some of these ad hoc techniques are included in Appendix E along with other design rules.

Structural design techniques characterize ways of designing self-testable circuits and testing those structures with built-in tests and external automatic test equipment. DFT techniques, with their design guidelines and their ease of automation, are rapidly becoming part of every product.

VI. STRUCTURAL DESIGN FOR TESTABILITY TECHNIQUES

Structural design techniques require a set of general rules and guidelines that will help improve the ability to test sequential circuits and provide standardization of the design. When the feedback paths are effectively broken in the sequential circuits, the state of the machine can be controlled and observed. The combinational section is also tested using standard combinational methods.

The main purpose of DFT is to optimize the observability and controllability of the circuit under various constraints. Scan design, detailed in Appendix B, is one of the accepted and widely applied DFT techniques. In a scan design, each scan memory element can become a control/observation point. Controllability/observability no longer depends on the number of pins on the package or levels of logic within the design. However, every time the scan path is

increased by one, the number of input pins is increased by two. Some memory elements are augmented with multiplexed inputs that have a scan mode input in addition to their functional input. The extra space and performance penalties of full scan design can be reduced using partial scan. As illustrated in Appendix B, partial scan is a promising method for designing circuits with reduced test input vectors and acceptable test coverage.

One of the approaches presently used is to select the scan memory elements after performing the sequential testability analysis. The scan chain includes the minimum number of memory elements that will detect the faults not covered by the testability analysis for a given percentage of coverage. The test coverage and scan overhead is dependent on the testability analysis used. Different testability analysis results with different overhead and test coverage for the same circuit under test. Another approach is to first apply functional tests, and then apply a combinational testability analysis to detect the remaining faults not covered by the functional tests. The corresponding minimum number of memory elements are the scan elements for the chain. Again, for this approach, the number of chain elements and test coverage are dependent on the functional test performed. Both of these approaches are also dependent on the structure of the sequential circuits. Researchers are working on new techniques to further improve partial scan by attempting to minimize space overhead and length of the test pattern while at the same time, keeping the fault coverage at a high number.

Scan techniques are also applicable at board- and system-level testing. An extension of the circuit/chip scan is the boundary scan. It allows the signals at the chip boundaries to be controlled and observed by placing memory elements that can be scanned next to each primary input and output terminal. These scanned memory elements are the elements of the boundary scan cell.

Several researchers have performed experiments using boundary scan. It has received the attention of the Joint Test Action Group (JTAG) and is now the IEEE Standard P1149.1. This started as an attempt to include as many levels of design as possible, beginning with IC fabrication and ending with the system test. It has been well received and is being used by designers to easily test products independently of the content of the ICs. When fully accepted and implemented it will benefit all levels of design and foster good

design methodologies. Boundary scan will reduce test complexity, increase accuracy, establish guidelines and uniformity, and decrease cost, especially at the board level where testing costs are escalating due to growing circuit and board complexity. However, it adds space overhead because of the extra testing circuitry and possible performance degradation. The challenge is to design products that are easily testable and at the same time minimize these two factors, namely, space and performance degradation.

Built-in Self Technique (BIST) is another aspect of structured DFT that transforms some of the functions of the automatic test equipment into the circuit itself at chip, board, or at system level. Test generation, application, and evaluation are the tasks performed by BIST. Normally, maximum length Linear Feedback Shift Registers (LFSR) are used to generate pseudorandom vectors that are applied to the circuit under test. Multiple input signature analysis registers (MISR) are also used for response compaction.

BIST, together with random patterns generated by LFSR, cannot achieve sufficient high-fault coverage using a practical number of test patterns. Therefore, an extension of this procedure that can be used is the BIST with perturbed deterministic patterns (PDPs) generated by on-chip memory and compressed signatures on chips [5]. The perturbed patterns are generated using a predefined circuit under test-related algorithms. This method integrates the advantages of random-pattern testing, such as low test data volume, low test generation cost, high test quality, as well as those for deterministic patterns test methods, such as high test coverage, low number of patterns, and reduced test time. The objective of the PDR test generations is to produce the required test patterns in minimum test time.

The Built-in Block Observer (BILBO) approach integrates the features of the scan design and those of the pseudorandom generator. It realizes built-in self-test mechanism for highly modular and bus-oriented systems. BILBO's four modes of operation include the normal mode, scan or test mode, signal analyzer mode, and the reset mode. In the normal mode, the circuit logically behaves as if the BILBO circuit was not present, but physically the input travels through at least two gate delays, depending on the physical implementation of BILBO. In the scan or test mode the memory elements can be interconnected as a shift register for scan-in/ scan-out operation or as linear shift register to produce

pseudorandom sequences. In the signal analyzer mode, the memory elements are arranged as a linear feedback structure with parallel inputs. By feeding the output of the circuit under test to the parallel inputs of this feedback shift register, the signature of the unit is formed and can be used to ascertain its status. In the reset mode, all memory elements are set to zero.

The real advantages of BILBO over the regular scan method of LSSD or scan path is in the speed of performing the test process. After entering the initial testing vector, a BILBO structure continuously generates the pseudorandom sequence and another BILBO is collecting the signature. After a certain number of testing patterns, the resulting signature is scanned out for verification. The testing is performed at the process speed with very little overhead time. The only overhead is the time required for the initial vector to scan in on one of the BILBOs and the time required for the scan out of the final signature. The real disadvantage, however, is that the combinational circuit is continuously tested with the random sequences generated by one of the BILBOs. Unfortunately, these random sequences have very low fault coverages for a reasonable amount of testable time. Another disadvantage is the two gate delays during normal operation. These delays decrease the maximum speed under which the circuit can operate.

Several built-in test architectures with parallel signature analysis of the BILBO structure and signature analysis of LFSR structure have been implemented to self-test circuits.

VII. BOARD AND SELF TESTING

Scan design is capable of simplifying the testing of sequential logic circuits. A combination of scan design and LFSR design can be utilized to perform self-testing. Self-testing can be characterized as either internal or external, depending on the positioning of the LFSRs. External testing does not mean the use of external sophisticated testing configurations but merely means that the LFSRs are residing outside the unit in question. As can be seen from Appendix C, there are several methods for external testing that all have different architectures and wide applications.

The structure discipline of scan path and/or LSSD, together with BIST techniques, allows a large number of random tests to be generated and applied in a reasonable amount of time with relatively adequate cost coverage. It greatly reduces the costly test generation and application procedures and at the same time offers a means for system-test verification. There are several possibilities for self-testing, ranging from pure random generation to highly deterministic; from off-line to on-line; from concurrent to noncurrent; from observing every output to compaction on a single signature; from applicable to a simple circuit to the entire system.

Internal self-test can be further classified into centralized and distributed types. These architectures are also summarized in Appendix C. The internal self-test integrates the LFSRs into the circuit under test and is included as part of the scan path. It is a dedicated custom solution with the flexibility in realizing various self-test techniques from low levels to higher levels. However, it requires extra overhead over the external case, where some of the LFSRs can be shared by more than one circuit on the board.

VIII. BOARD AND SYSTEM TESTING

By integrating DFT structural design techniques at the initial phase of any system design, testing difficulties are alleviated. Fault diagnosis is required in the testing of board and systems. Diagnosis at the system level is very important for factory testing and field maintenance. On-line testing uses a built-in monitoring circuit to detect failures caused by faults. The process monitor is the central unit for board testing and monitors several tasks at the various phases of the design. It is a form of statistical process control on a chip that keeps the process and the system under control and observes all the system level process changes. It improves the quality through process control.

There is a cost associated with every board-test philosophy. Better test coverage and diagnostics implies more test development costs, more space-board allocation, and more time for testing. Accuracy and misdiagnosis are considerations that must also be addressed. Some boundary scan implementations will have a number of testing benefits. It will reduce and hopefully eliminate the need for one- and two-sided board probing. It will facilitate the application of topologically derived tests for test interconnection

faults, which will reduce the need to do board level for simulation to developing tests for manufacture faults.

As can be seen from Appendix C, the ATE cost and complexity can be dramatically decreased using BIST techniques. Deterministic test data and storage requirements are reduced, and test running times are shorter. All BIST structures are transparent during normal system operation. Every circuit is checked at separate times by applying test patterns to its input and compacting its set of responses into a signature register. Parallel/concurrent test patterns can also be applied to two or more circuits simultaneously for minimizing the testing time. This can only be done for compatible tests, which means that these tests should not cause any conflict in the configuration of the BIST structure.

Several quantitative and qualitative measurements that need to be addressed early in the design phase at the system/board level. These requirements are similar to those for a single chip. Fault coverage, for example, needs to receive great attention. This is especially true when a decision must be made between two alternative test measures. An implementation technique that enhances fault coverages, the speed of the test pattern applications, and response evaluations must be rated more favorably. System/board space overhead, quantified by the percentage of useable circuits dedicated to self test over the total space, is a measure that needs consideration. Another concern is the number of additional input/output pins. System performance must not be degraded due to the BIST technique that is chosen.

By addressing all of the above requirements at the beginning of the design cycle and after several design iterations and repartitionings, an acceptable solution will be found. The implementation of boundary scan within ICs will make designs more testable, producible, and structured and will remove last-minute ad hoc modifications for fast fixing. This can only be accomplished by good communication and interaction between the circuit designer and test engineer.

A draft on "Standard Test and Boundary-Scan Architecture," sponsored by the Test Technology Technical Committee of the IEEE Computer Society, is on its fifth revision. It defines a test access port and boundary-scan architecture for digital integrated circuits and for the digital portions of mixed analog/digitally integrated

circuits. This publication seeks to provide a solution to the problem of testing assembled printed circuit boards and other products based on highly complex, digitally integrated circuits and high-density surface mounting technology. It also will provide a means of accessing and controlling design to test features built into these digitally integrated circuits. Such features might include scan paths and self-test functions, as well as other features intended to support service applications in the assembled products.

In addition to the above considerations, there is strong emphasis by the military to increase system reliability and decrease maintainability for the future weapon systems. In the U.S. Air Force, this is being implemented through directives that state that all newly procured systems must meet the incentives of R&M 2000. This directive places reliability and maintainability on equal status with cost, schedule, and performance and an immediate goal of procuring systems that are twice as reliable and require half as much maintenance as its predecessor system. It should be noted that although R&M 2000 requirement is an Air Force initiative, other branches of the service are also incorporating its goals.

To achieve these incentives, stringent quantitative BIST requirements are being imposed on the contractors of these weapon systems.

A typical set of BIST requirements includes:

1. All system fault detection and isolation to the line replaceable unit or line replaceable module shall be accomplished using BIST. No external test equipment is permitted.
2. BIST shall be capable of detecting 98% of all failures.
3. BIST shall be capable of isolating all detectable failures to the faulty line replaceable unit or module 98% of the time.
4. BIST false alarm shall be less than 1%.
5. BIST test time shall not exceed 10 seconds.
6. BIST test modes shall include power-up, continuous and initiated.

When the complications are taken into account, along with modern technology's use of high-density packaging, such as gate arrays, VHSIC/VLSI devices, and ASICs, satisfying the above criteria becomes a formable task.

Appendix D, "BIST Implementation for a Line Replacement Module" in an airborne, uninhabited fighter environment, gives guidelines for such an accomplishment. The temperature environment ranges from 25-125° C. MIL-HDBK-217E reliability models are used to derive an expression that considers the failure rate contributions caused by device electronic failures and those caused by package-related failures. Using failure rate information to arrive at an acceptable BIST design, it will become obvious that BIST implementation cannot be entirely embedded inside each circuit package. Partial scan and partial boundary schemes, along with ad hoc techniques, are attractive alternatives to be incorporated into the testability system guidelines.

IX. RECOMMENDATIONS

The stated objectives were extensively studied and documented in this report. In addition, some of the described testability techniques were applied for comparison purposes to a simple benchmark circuit.

To complete this summer work, additional benchmark circuits must be selected and the stated testability techniques must be further developed for automation purposes. This will require the proper application of software engineering principles to the already documented material.

An additional extension of this summer work, is to obtain a reconfigurable structure for generating deterministic test vectors. The success of this effort will significantly reduce the amount of additional overhead circuitry needed to generate the test vectors. This will definitely be considered as a breakthrough in the area of testability.

REFERENCES

[1]. Abramovici, M., and D.T. Miller, "Are Random Vectors Useful in Test Generation?" Proceedings of the First European Test Conference, pp 22-25, Paris, April 1989.

[2]. Merlino, D.H. "Deterministic Test Vector Generation Using Feedback Shift Registers," Ph.D. Dissertation, Florida Institute of Technology.

[3]. Bardell, P.H., W.H. McAnney, and J. Sanir, "Built-In-Self-Test for VLSI," John Wiley and Sons, Englewood Cliffs, N.J., 1987.

[4]. Devadas, S., H.K.T. Ma, and A.R. Newton, "Redundancies and Don't Cares in Sequential Logic Synthesis," Proc. of International Test Conference, pp 491-500, Washington, DC., August 1989.

[5]. Wu, D.M., and J. Waiculauski, "Built-In Self Test Using Perturbed Deterministic Patterns," Proc. of the First European Conference pp 398-492, Paris, April 1989.

APPENDICES A, B, C, D, E, F

-- Due to lack of space, these appendices can be obtained directly from the author.

-- The complete text will be published as a Rome Air Development Center (RADC) technical report available in February, 1990.

1989 USAF-UES SUMMER FACULTY RESEARCH PROGRAM

Sponsored by the

AIR FORCE OFFICE OF SCIENTIFIC RESEARCH

Conducted by the

Universal Energy Systems, Inc.

FINAL REPORT

Development of a High Resolution Research Facility

Prepared by:	Henry F. Helmken, Ph.D.
Academic Rank:	Professor
Department and	Electrical Engineering
University:	Florida Atlantic University
Research Location:	RADC/EE Hanscom AFB Lexington, MA
USAF Researcher:	Ray Cormier
Date:	August 15, 1989
Contract:	F49620-88-C-0053

High Resolution Research Facility

by

Henry F. Helmken

Abstract

In order to improve the performance of Over The Horizon (OTH) radar, communication and direction finding systems, Rome Air Development Command is interested in developing a national High Frequency (HF) test facility. At the facility, experiments aimed at understanding the nature of clutter, especially auroral clutter, would be carried out. It would also serve as field site for testing new hardware concepts. In order to quantify the requirements, a report has been prepared which outlines a phased approach to the establishment of such a facility. In addition to the report, several hardware changes to the existing test equipment at Ava, N.Y. and Verona, N.Y. were tested via computer simulation and laboratory experiment.

Acknowledgements

I wish to thank the Rome Air Development Center and the Air Force Office of Scientific Research for the sponsorship of the 1989 ASAF-UES Summer Faculty Research Program.

In particular I would like to thank Mr. John Ritz for his administrative help. I am particularly indebted to Mr. Ray Cormier, Mr. Bertus Weijers and Lt. Anthony Gould for their patience and understanding in explaining the present HF system at Verona and Ava as well as the requirements for an HRRF. Bertus very generously supplied me with documentation on existing world wide HF arrays and helped test some new hardware concepts. I would also like to thank SSGT Mark St. John for his help in establishing computer account and Lt. Joseph Fortney for running some antenna analysis programs.

I. Introduction

In the area of ionospheric research, there is a need to develop an experimental test bed that can serve as a dedicated national facility to investigate High Frequency (3 MHz to 30 MHz) propagation phenomena. The results from such a facility will have a direct bearing upon Over The Horizon (OTH) radar development, military communications and direction finding systems.

Rome Air Development Command (RADC) has been operating an experimental High Frequency (HF) test facility at Ava, N.Y. and Verona, N. Y. for several years. The goal of the summer research effort was to describe a plan whereby these facilities could be transformed, in a phased approach, to a national facility. An investigation was also made of some recent technological developments that could be applied to improve the existing test equipment.

For many years, I have been involved with the development and operation of experimental radio frequency measurement systems. These systems typically involve antennas, radio frequency sources, data receivers, control computers and data storage devices. Numerous computer programs to assist in the

data analysis have also been developed.

II. Objective of the Research Effort

The primary goal of the summer effort was to assist RADC/EE by preparing a report describing the development of a High Resolution Research Facility (HRRF) which would study High Frequency (HF) propagation phenomena. The study was to include both transmission and receiving sites. In addition, methods to improve existing measurement capabilities were also to be investigated.

OTH Radars operate in the 3 MHz to 30 MHz band. They cover from 1000 km to 3000 km in range and track moving targets such as airplanes. As with any radar, a high power pulse is emitted in a known direction and some of the energy is backscattered by targets into a receiving antenna array. The received signal is measured and processed to locate and track targets. In addition to targets, backscattering also occurs from clutter sources such as the ground reflection and ionospheric irregularities. Man made and natural noise also mask the target. The desired signal can be 40 dB below the clutter level and as much as 80 dB below the noise level. Hence wide dynamic range must be obtained if the target is to

be recovered from the received signal.

III. HRRF Requirements

Since the primary purpose of the HRRF will be to assist OTH development, the first task item was to become familiar with the present OTH systems and their limitations. Familiarity was also gained with the design and operation of existing HF experimental arrays.

As indicated above, the major factor limiting OTH radar performance is clutter and noise interfering with the desired signal. Hence the primary goal of the HRRF will be to measure and characterize clutter and noise.

Desired radar targets can be 40 dB to 50 dB below the local clutter level. To achieve the necessary subclutter visibility, design of effective signal processing systems require accurate clutter models. Numerous clutter models have been proposed but further validation is still required. In some models, clutter is thought to arise from field aligned E and/or F layer irregularities in the ionosphere, other models postulate specular backscatter or backscatter into receive antenna sidelobes. In Northerly directions, specific

attention must be directed towards the study of auroral clutter. This would encompass identification of clutter sources, origin of spectral broadening and statistical analysis of clutter location, intensity, size and duration. High resolution, both in azimuth and elevation are required to discriminate among these models.

IV. HRRF Requirements and Design

The basic requirement is for a high power directional HF transmission site and at a suitably distant location, a high angular resolution (azimuth and elevation) receiving array and data collection facility. Their separation must be sufficient to avoid high power transmissions contaminating the received signal. Since man-made and natural electrical noise are limiting factors, a quiet a site as possible should be selected.

The transmitting site should have power (e.g. 600 kW or higher) and azimuth beamwidth (2.5°) comparable to current OTH radars. Current OTH systems operate over the 3 MHz to 30 MHz band. Elevation coverage is governed by a simple dipole radiation pattern and is typically 30° to 40°. Some of the transmission and receiving patterns should be capable of overlapping existing OTH coverage areas so as to jointly

measure backscatter phenomena.

The proposed receiving site would ultimately contain 3 rows of linear arrays. Cost estimates were prepared for array lengths of 1400 m, 2400 m and 3600 m. The arrays would be aligned East-West so as to yield North-South look directions. North looking is necessary for auroral measurements. Twerp antenna elements would permit easy switching between North and South look directions.

The plan is to begin with the present transmitting facility at Ava N.Y. and the 700 m receiving array at Verona, N.Y. and evolve them in a phased approach to a national test facility.

The initial phase will concentrate on developing the receivers and outlining the data collection and storage methods to be used in all subsequent phases. It will also involve transmitter upgrades and receiving array site selection. A number of very specific receiver requirements were cited.

The next phase will involve site preparation and constructing to its final length, a single row of the receiving array. Subsequent phases would add the second and

third rows.

The report was completed and submitted on August 11, 1989

V. Additional Items

An additional effort involved a study on upgrading the present transmitter system at Ava, N.Y. to perform some joint experiments with the existing East Coast Radar System (ECRS). The result of the study was a recommendation to construct a rhombic antenna pointing in the direction common to ECRS segment 1 and the Verona receiving array. The antenna is rhombic in shape with a major axis length of approximately 400 m and supported on towers 30 m above the ground. This suggestion was acted upon and construction of the new antenna has begun.

Conventional HF receivers coherently covert incoming signals to base band where the Inphase and Quadrature components are sampled by two Analog to Digital Converters (A/D). Recent work at the Naval Research Laboratory by Waters et al. demonstrated that sufficient phase accuracy can be achieved by sampling the Intermediate Frequency (IF) of the receiver with a single A/D and converting the data to

baseband in software. Thus the last down conversion is eliminated which increases the dynamic range of the system and also avoids the D.C. offset problem between two A/D converters. The only limitation of the technique is that one must observe the well defined relationship between the bandwidth of the system and the IF center frequency. The concept of direct IF sampling was successfully simulated on a computer.

Pseudo-random Noise (PN) codes have been used to investigate multipath propagation problems. The maximum Signal to Noise Ratio (SNR) is governed by code length. However, it was felt that Complementary Codes (CC) could yield higher SNR ratio because they have 0 close-in sidelobes. To test this as well as demonstrate direct IF sampling, the 455 kHz IF from the standard Air Force RACAL HF receiver was modeled in software and modulated with PN and Complementary code sequences. The results are shown in the following two figures. The first is a 63 chip PN sequence and exhibits a 20 dB SNR. The second is a 32 chip CC sequence and exhibits a 35 dB SNR.

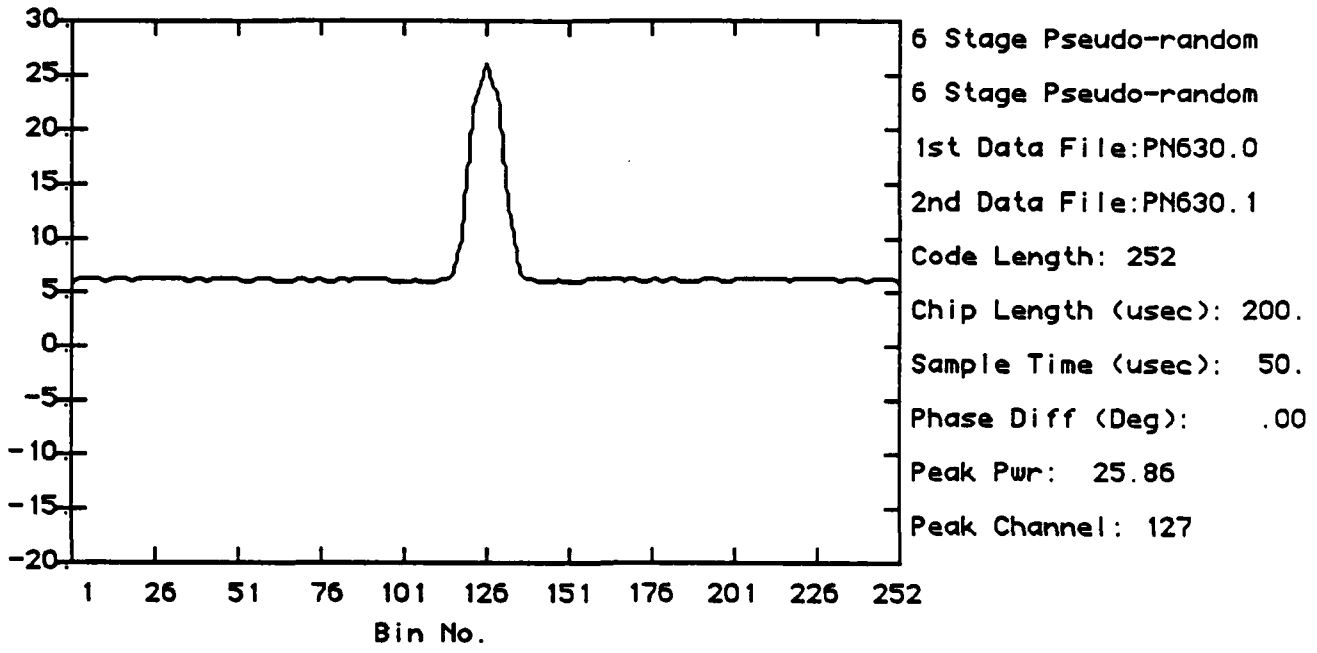

Figure 1. 63 Chip PN Sequence

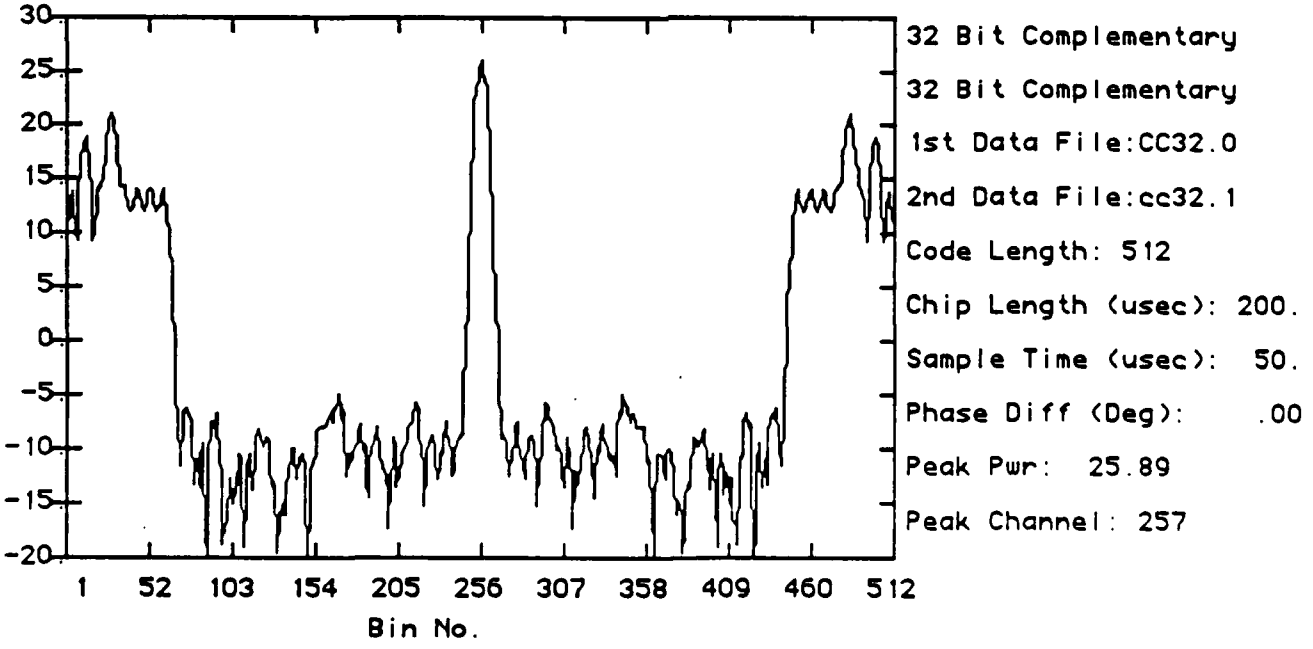

Figure 2. 32 Chip Complementary Code Sequence

The availability of 30 MHz Direct Digital Synthesizers (DDS) offers the opportunity of direct code modulation under computer control. As a replacement for existing waveform generators, a single circuit card could provide a fully modulated waveform at the desired HF frequency.

With the advent of long baseline and multi-row receive arrays, phase front distortions caused by Faraday rotation in the ionosphere is of increasing importance. An experiment to measure these effects was outlined. Data measurements will make use of the previously mentioned digital techniques. A SRF proposal is being prepared to measure the distortion on a propagation path from Ava N.Y. to Boca Raton. FL (1900 km).

VI. Recommendations

There is a clear need for a national test facility to study and characterize HF propagation phenomena. The approach taken in the report begins with existing RADC facilities and gradually expands them to fulfill this requirement.

Direct sampling at IF has been demonstrated as an improvement in HF receiver design. It is hoped that this technique will be used in future receiver designs.

Complementary Codes offer a significant improvement in SNR over PN codes. There use in multipath measurements should be considered. Direct Digital Synthesizers offer a very easy way to implement code sequences both in the laboratory and as waveform generators for the transmitter.

As very long baseline arrays are now being planned, phase front distortion must be investigated further. An experiment to study this over a 1900 km path will be proposed as an SRF follow on.

1989 USAF-UES SUMMER FACULTY RESEARCH PROGRAM / GRADUATE STUDENT RESEARCH PROGRAM

Sponsored by the
AIR FORCE OFFICE OF SCIENTIFIC RESEARCH

Conducted by the
Universal Energy Systems, Inc.

FINAL REPORT

ITERATIVE V&V: A MODEL FOR VERIFICATION AND VALIDATION IN THE RAPID PROTOTYPING LIFE CYCLE

Prepared by:	Stuart H. Hirshfield
Academic Rank:	Associate Professor of Computer Science
Department/University:	Mathematics and Computer Science Hamilton College, Clinton, NY 13323
Research Location:	Rome Air Development Center (RADC/COAD) Griffiss AFB, NY
USAF Researcher:	Robert Kruchten
Date:	August, 23, 1989
Contract No:	F49620-88-C-0053

ITERATIVE V&V: A MODEL FOR VERIFICATION AND VALIDATION IN THE RAPID PROTOTYPING LIFE CYCLE

by
Stuart H. Hirshfield

ABSTRACT

This paper addresses the role of verification and validation (V&V) techniques in the rapid prototyping (RP) model of software development. Unlike software developed by more traditional means (i.e., according to the "waterfall" model), RP software is characterized by evolving requirement specifications, informal intermediate-level (detailed requirements, design) documentation, and an increased reliance on functional testing as a means for both evaluating and influencing system development. These differences dictate to a large degree which V&V activities can be applied at different stages of development, and how they can be applied. While conventional V&V techniques are by and large still applicable, the order and manner in which they are applied is project dependent. That is, an RP life cycle necessitates more operational changes to V&V activities than theoretical ones, and the changes are dictated by the particular RP model used to develop the software. This paper proposes a general V&V scheme that is customized both operationally and theoretically to the RP model, and can be adapted to any RP development effort.

ACKNOWLEDGEMENTS

I gratefully acknowledge the Air Force System Command, the Air Force Office of Scientific Research, and Dr. Fred Diamond, Chief Scientist of RADC, for affording me this exceptional opportunity. Most of all, I wish to express my utmost gratitude to Mr. Robert Kruchten, my Effort Focal Point, who first interested me in the project and supported me in every way possible throughout.

I. INTRODUCTION

A single phrase that accurately captures my research interests and expertise is "applied Artificial Intelligence." In the last ten years, I have published, spoken and conducted a variety of projects in Software Engineering, mostly devoted to software life cycle models and design methodologies. My graduate training was in Artificial Intelligence (AI), originally in natural language processing and recently in Expert Systems. To my good fortune, these interests come together in the mission of the Decision Aids group at Rome Air Development Center (RADC/COAD).

This group conducts a number of programs related to the development and deployment of automated expert systems to support battle management and planning. This mission requires in-depth understandings of both the AI techniques used to design and build such decision aids and the software engineering techniques used to evaluate and render the aids deployable. I have worked with the group in the past, most notably on a project wherein we developed (and published) a software architecture to support sophisticated levels of interaction ("cooperation") between existing decision aids. Needless to say, our research interests and capabilities overlap considerably.

II. OBJECTIVES OF THE RESEARCH EFFORT

One of COAD's current pressing technology issues is: How are complex decision aids verified and validated? Indeed, verification and validation (V&V) is being increasingly recognized as a significant and profound research problem throughout the AI and Software Engineering communities. We continue to develop, deploy and rely upon sophisticated expert systems in all walks of life. Such systems are intended to model human behavior in a broad range of mostly subjective tasks. Their outputs are not always straightforward functions of their inputs. How, then, do we know when a program's output - i.e., its judgment about a particular situation - is correct? Should the program

make the same decisions as a human? Which human? Aren't humans often wrong?

These questions are not new to software developers. They can be seen as instances of the more general question of how one specifies and evaluates software requirements. Requirements specifications are the basis for all conventional V&V activities. Without a detailed specification against which the correctness of a system's behavior can be judged, V&V is difficult, if not impossible. Unfortunately, for many complex systems (and particularly those that model human expertise) a sufficiently detailed requirements specification may be as difficult to formulate as a complete implementation of the system.

The V&V problem is further compounded by the fact the experts systems, including decision aids, are being developed increasingly based upon new, innovative software technologies. It was once the case the computer-naive users were the only ones who had difficulty specifying system requirements (which explains, in part, the need for systems analysts and the modelling tools and techniques developed to support them). Today, the complexity of software is such that even experienced users require support to accurately articulate system requirements. Non-traditional high-level languages and complete software development environments have been developed to support explicitly the knowledge acquisition demands and logical processing requirements of expert system developers. The complexity of the attendant knowledge bases and the demand of intricate, but "friendly" user interfaces have led developers to adopt non-traditional strategies (software life cycles) which allow for systems to be built and tested incrementally.

While these non-traditional software technologies support the development of sophisticated expert systems, they do not directly lend themselves to traditional V&V techniques. The software V&V techniques (including what is commonly called "program testing") that have evolved over the past 20 years coincident with the field of Software Engineering were implicitly bound to software technologies of the time. Indeed, procedural

programming languages and the waterfall life cycle model can be seen as the theoretical background of most Software Engineering practices, including testing, today. As we now come to rely on different programming languages and upon different life cycle models as means for developing mission-critical, safety-related systems, we see more than ever the need for V&V techniques that reflect these new technologies.

This paper, then, focuses on one small part of the V&V problem. In it, I concentrate on the role of V&V techniques in the rapid prototype (RP) life cycle model. The next section describes briefly the RP life cycle, emphasizing its differences from the traditional waterfall model. Traditional approaches to V&V are briefly summarized in Section IV, with an eye towards their utility in the RP model. In Section V, I propose a general V&V scheme which applies standard techniques in novel ways to the RP model. The scheme is general in the sense that, like the RP model, it must be tailored to a given software development effort to reflect the system-level functional requirements, the number of prototypes, and the mapping of requirements to prototypes. Finally, in Section VI, the findings are summarized, recommendations are made for implementing the proposed model, and suggestions are put forth for further research.

III. THE RAPID PROTOTYPE LIFE CYCLE

For many years the predominant software development life cycle has been the phased refinement (or, "waterfall") model. According to this model, all software functionality is specified as the first phase of development. Subsequent phases (high-level and detailed designs) add levels of detail to the requirements specification without substantially changing it until a single version of the system can be implemented as code, tested, (i.e., modified so that errors are not present) and maintained. Despite our many attempts to render this model as an "engineering" discipline, it has shown itself to be highly impractical.

This impracticality stems primarily from two implicit assumptions: (1) that requirements can be identified, articulated and frozen prior to development, and (2) that most formal V&V activities are directed at the source code description of the system and are intended to "fix" the system, not change its focus in any substantive way. Practical experience has shown both of these assumptions to be naive at the very least, and often misguided. It is naive to assume that the end-users of a system, particularly those that are not themselves experienced software developers, could anticipate and specify with any degree of certainly all of a system's critical functionality without having any experience with it. Further, systems developed according to the waterfall model have proven to be very expensive to maintain in large part because of the lack of responsiveness of source code to the inevitable changes in requirements that are recognized during the formal test phase.

The rapid prototype (RP) model is gaining acceptance as a potential response to the shortcomings of the waterfall model. Its goals (not unlike any life cycle model) are to reduce the time required, and the the expense in building useful, responsive software systems. It is based on the philosophies of incremental development and increased end-user involvement in assessing system capabilities as they emerge. More specifically, RP is an evolutionary model[1] which calls for the use of prototypes (scaled-down, executable versions of various aspects of the proposed system) in building a fully functional system. Each prototype addresses certain of the system's critical features and is evaluated for those features by the end user with the intention of influencing subsequent prototypes. A "system level" view is maintained throughout development. That is, users evaluate a prototype by using it, not by reviewing formal or informal descriptions or design documents, and by comparing the behavior with the behavior they expect. If

[1] Note that prototypes may be "throw away" efforts. That is, a prototype can be developed as a means for demonstrating the feasiblity of a particular approach, or the tractability of a particular sub-problem, with the intention of discarding the prototype after its purpose has been achieved. In such cases, the prototype contributes conceptually but not tangibly to subsequent development efforts. We will restrict our attention to the evolutionary prototype model.

a prototype fails to perform according to expectations, the user identifies the inconsistencies and works with the developer to refine and/or revise the requirements. The updated requirements serve as the basis for designing a subsequent prototype. Thus, changes in requirements trigger changes not in a final product, but in a single prototype.

The changes that are dictated reflect the types of evaluation that are performed on a given prototype. Linden and Owre [10] classify prototypes as being directed to: functionality (implementing a critical system function), user interface (evaluating the user interface in terms of actual tests with representative users), performance (test the system for critical response times), design (used for evaluating the effectiveness of a design), and operational concerns (testing a majority of a system's functionality in an operating environment that resembles closely its target environment). A given prototype may be evaluated according to more than one of these dimensions, of course, depending on its role in the development plan.

The focus of the RP model is, thus, notably different from that of the waterfall model. The RP approach concentrates on the most difficult problems in systems development - identifying requirements and responding to changes in them. It does this by incorporating verification and validation activities into the life cycle so that they can influence development in an appropriate way—by providing timely and directed feedback to the developer. In the waterfall model V&V is, in the best cases, a burdensome task that can add time and expense to a development effort and impose change on an unresponsive implementation. More often, it can be a mock formality that identifies problems when it is too late to address them in an economically feasible manner. In the RP model, V&V is an integral, fruitful part of the iterative development cycle.

Note, too, that the RP model is decidedly less prescriptive than the waterfall model, which in its strictest form directs developers through a fixed sequence of activities. The results of prototype evaluation in the RP model have the potential to alter system requirements and thus affect dramatically

the remainder of the development process. Even more important is the fact that the RP model is a general one. Each RP development is a unique instance of the general RP philosophy in which the number of prototypes, the focus of each prototype, and the relation of each prototype to the final system varies. What the RP model prescribes is not a lock-step procedure, but rather a top-down methodology for developing precise and correct requirement specifications. Early prototypes address quite intentionally only high-level, critical system requirements. These requirements get refined and revised, becoming increasingly tractable and testable, based on experience using the prototypes. Indeed, RP is closer to a true software development methodology by virtue of its formalizing the requirements specifications and evaluation procedures.

To be sure, the potential benefits of the RP methodology depend essentially on the ability, first, to evaluate critically a prototype's behavior and then to modify a prototype with less effort than would be required of a production version of a system. This is partly addresed by the fact that, by definition, prototypes do not include all of the functionality of a final system, and thus represent less of an investment of time. Also, a variety of automated tools have recently be developed [9,11,14] which claim to support prototype development and experimentation. Some provide high-level, executable requirement specification languages. Others provide programming environments with extensive support of modularity (which helps in mapping requirements to source code), code reuseability and adaptability, and user interface development. It is interesting to note that few, if any, of these tools address explicitly and directly V&V activities.

IV. VERIFICATION AND VALIDATION

Boehm [2] describes software verification as the task which addresses the question "Am I building the product right?". Verification consists of evaluating the intermediate products of a development effort so as to ensure that each meets the requirements prescribed for it in such a way as to

maintain the "traceability" of system requirements. That is, tests and analyses performed on intermediate products should address low-level requirements that are clearly linked to the system-level requirements from which they were derived.

Software validation is concerned with the more global question "Am I building the product right?". Validation occurs, in the waterfall model, at the end of the development effort and is applied to final (or, nearly final) products to ensure that high-level system requirements have been satisfied. Errors and unfulfilled requirements detected at this stage are often the most difficult and costly to remedy. Taken together, verification and validation activities claim to address the problem of resolving software problems and high-risk issues as early as possible in the development process.

V&V techniques evaluate products in terms of their completeness (does it address all requirements imposed upon it?), consistency (are the notations and terminology used to describe the product internally consistent? do they conflict in meaning or purpose with other products?), feasibility (can the system or component being described be operated and maintained so as to justify the development effort?), and testability (can, for example, a realistic means be established for determining whether or not a requirement has been satisfied?).

Early V&V models were what Gelpering and Hetzel [7] refer to as "phase models." That is, testing was regarded as a distinct phase of the life cycle, usually occurring at or near the end of development. Today's "life cycle models" of V&V readdress the role of testing, moving it to the beginning of development and stressing its importance throughout development. Correspondingly, the focus of V&V techniques has shifted from the detection and fixing of requirement, design, and implementation faults to the prevention of them.

Individual V&V techniques can be categorized according to many criteria. For our purposes, they can be classified as either static, dynamic, or formal. "Static" techniques do not in general require automated execution of the product being evaluated. They do, though, usually assume that the

product being evaluated (which could be a requirement specification, a design document, or source code) is expressed in at least a "semi-formal" notation. Indeed, in some cases even though the product is not executed, the analysis itself is automated. Examples of static techniques include reviews, walkthroughs, inspections, pre-compilers, cross-referencing of documents, and state error analysis (e.g., interface checkers).

"Dynamic" techniques, on the other hand, involve product execution and, so, most often focus on testing code. Techniques describe how to choose test data and how to analyze program output. Test can be directed toward program function, performance efficiency, stress (exercising the program at and beyond its intended operational limits to see how it will perform), and structure. Symbolic execution, expression testing, data flow testing, branch testing, coverage testing, path testing, integration testing and acceptance testing are all examples of dynamic techniques.

The third class of V&V techiques, "formal," also concentrates more on programs than on other software products. Based upon the formal semantics of the language it is written in, a program can be regarded as a mathematical proof asserting that its input will be transformed into the desired output. Input-output assertions, weakest preconditions, and structural induction are the most prevalent methods used to analyze programs in this way. The nominal advantage of such formal techniques is that by defining what a program is to do without describing the details of how it is to do it (which is precisely what these techniques stress), it is possible to develop a relatively precise and unambiguous specification. Unfortunately, current formal methods have been found to have only limited practical utility because of their complexity.

Nearly all of the V&V techniques mentioned above are considered "white box" techniques. That is, each requires detailed knowledge of the product being evaluated and each is intended to address a particular class of faults. "Black box" testing, on the other hand, evaluates a software product as a unit and is concerned only that the product satisfies its requirements,

without regard to how it does so. The argument has been advanced over the years that neither type of testing is by itself sufficient and that both are necessary to develop confidence in software. It is safe to say that this is still the case, and that this is the reason we continue to talk about both verification (white box testing) and validation (black box testing), as opposed merely to "testing."

V. ITERATIVE V&V

In originally considering the problem of how to accomplish V&V in the RP life cycle model, I noted that much of the information upon which conventional V&V techniques rely (low-level specifications, formal design documents, pseudocode) may not be available for analysis, if indeed they exist at all, in an RP development effort. I thus focused my attention on ways to accomplish V&V without them.

The most obvious (and unsatisfactory) choice is to some how improve our skill at soliciting low-level requirement specifications from users prior to system development. Experience has shown us that such attempts are ill-fated. In fact, the RP model is a response to this concern. As part of its goal of facilitating system development, RP provides an iterative, top-down method for specifying requirements because users of complex systems usually do not know what they want a system to accomplish until they have experience with it or with similar systems.

The idea, though, of spelling out requirements formally is not a bad one. It is simply very difficult to do, particularly early in the development process. A variation on this theme is to define formal requirements specification languages and to use them as the basis for developing more formal analysis procedures, along the line of those used for testing source code. This idea has been demonstrated recently with some success using non-procedural languages for expressing requirements.

Both of these approaches, and others I considered as well, are based on the assumption (in retrospect, an incorrect one) that standard V&V

techniques, particularly white box methods, would simply not apply to RP development. In doing so, I fell victim to a common misconception about the RP model—that it is compatible with only black box testing techniques. The fact that the RP model does not explicitly refer to intermediate level products does not mean they are not defined. They are—or, at least, can be—defined in any RP development effort. Unlike in the waterfall model, such products will be defined at different stages in the development process for each system. The intermediate links between high-level specifications and low-level code evolve as part of the prototyping process and get filled in before final system evaluation occurs. Ultimately any and all of them can be subjected to analysis and white box testing. It seems, then, that both high-level functional testing techniques and many established low-level, white box testing techniques are applicable in the RP model. The problem is not one of developing new techniques, but rather one of effectively applying exiting ones.

One promising approach follows quite naturally from a combined understanding of the RP model and the goals of V&V. It is important first to note that, contrary to common impression, RP is not an unstructured activity. It is, as mentioned before, a general one, but when applied with rigor and care, RP yields a detailed system development plan. As part of the development plan, all of the following should be specified: (1) high-level requirements of the system, (2) the number and sequence of prototypes to be implemented, and (3) a mapping of the system requirements to the prototypes—i.e., a description of which prototype is initially to address each requirement. This final, and often overlooked, point is essential to achieving the verification goal of tracing code to requirements.

Furthermore, our standard definitions of V&V do not make sense in the context of the RP model for two reasons. First of all, black box testing (validation) occurs repeatedly, once for each prototype, and not only at the end of the development process. Secondly, the process of white box testing and of linking intermediate level software products in terms of their

requirements is non-linear. That is, whereas coding always follows design, which always follows requirements specification in the waterfall model, such is not the case in RP. While one prototype may address a low-level coding concern (e.g., the efficiency of a particular algorithm), a subsequent one might focus on the overall system design. Similarly, the effectiveness of different parts of the design may be addressed in different prototypes. All we know with respect to requirements in a carefully planned RP system is (1) that they will all be addressed by the final product, and (2) the relationships between system level requirements and the lower level specifications that implement them is strictly hierarchical—i.e., every low level requirement should be derived from a system level requirement.

These insights lead us to revise slightly the definitions of validation and verification so that they are consistent with RP development. Validation ("Am I building the right product?") can be thought of as testing software at the end of a prototype development cycle to ensure that it meets its requirements. Verification ("Am I building the product right?") involves evaluating each prototype to ensure that it meets the requirements set for it in some previous prototype cycle (not necessarily the previous cycle). The goal of V&V in the RP model is still to identify and resolve software problems, but it is accomplished by the timely evaluation of prototype models for the purpose of identifying and articulating requirements for subsequent planned prototype models. Our model, which I have dubbed "Iterative V&V" for reasons that will soon be obvious, reflects these new definitions, and prescribes both how rapid prototyping should be accomplished in general, and the role of V&V in the RP model.

To accomplish V&V in an RP development effort, do the following:

(1) Define the high-level system requirements.
(2) Classify each requirement as being most closely related to the system's functionality, performance, user interface or design.
(3) Define the number and sequence of prototypes to be developed.
(4) Associate each system requirement with one or more prototypes, thereby

indicating which prototypes are to address which requirements.

(5) Review the mapping established in (4) to ensure that every requirement is addressed explicitly by either a prototype of the final version of the system, and that the number of prototypes is sufficient to allow for effective feedback between prototypes.

(6) For each prototype,

a. Validate it—i.e., perform black box testing to ensure it satisfies its requirements.

b. Verify it—i.e., perform white box tests that address the individual requirement types as defined in (1), above. [For example, if two of the prototype's requirements involve, respectively, evaluating the system design and the efficiency of particular algorithm, then verification consists, in part, or performing design reviews and conducting timing tests on the algorithm in question.]

c. Revise and refine requirements based on an analysis of steps 6a and 6b. For each new requirement formulated, note

1. its "ancestor"—i.e., the requirement from which it was derived,
2. its type, as in step (2), above, and
3. the prototype (or final version) that it is to be addressed in.

Step (1) in our model is nothing new, except that the iterative, top-down nature of the RP process frees one from worrying early on about specifying too much detail. Step (2) is important because it dictates what type of white box testing will be performed when verifying individual requirements. Step (6c) is the one that guarantees traceability and, in some sense, is the most critical to the model. It exploits the notion that RP is a top-down requirements methodology and that requirements, whenever in the development process they are identified, are linked either to some previous intermediate-level requirement or, at the very least, to one of the original system-level goals.

Whereas the V&V model for the waterfall life cycle could be

paraphrased as "Verify this, verify that, . . ., then validate," V&V in the RP model is more accurately "Verify and validate, verify and validate . . .". Also note that the iterative nature of V&V in the RP model dictates that all testing be accomplished early enough to impose changes in requirements on a subsequent prototype. This implies that these testing cycles must be built into the system development plan from the beginning.

VI. RECOMMENDATIONS

While the Iterative V&V model is both tractable and well-suited to the RP life cycle, it leaves many significant problems unresolved. I address these problems below, in no particular order, to put the proposed model in a broader perspective and to identify a collection of research problems that could justifiably be pursued in the near future.

The success of Iterative V&V rests in large part on the ability to do effective black box functional testing. Black box testing was recognized long ago by Turing in a 1950 paper [15] which considered whether a program could be written that exhibited intelligence. In it he posed the question of how we would know that such a program had satisfied its rather vague primary requirement. He resolved the problem by postulating an operational equivalent (the Imitation Game, a.k.a. the "Turing Test") for the original requirement, and proposed testing the system according to the rules of the new game.

With real software systems it is not usually easy to develop an operational model which can be used to guide system testing. Indeed, most of the detailed work, both practical and theoretical, in testing models has been accomplished at the code level, and is decidedly white box in nature. the testing community as a whole is still groping for confidence-inspiring (or even comparable) black box techniques. The Iterative V&V model places additional responsibility on black box testing because of the successive validations performed on each prototype. As we gain experience with it, black box methods and models will hopefully evolve.

Indeed, the same can be said for the RP model as a whole. As a development methodology, it is still immature. Its motivation is primarily practical, with little theoretical background. Because of the lack of theory, tools to support RP development are few and far between. As Hamlet [8] points out, it is premature to expect sound testing methods or tools without strong theoretical backing. As our base of experience with RP grows, such backing may develop and subsequently lead to more thorough and effective V&V strategies.

The fact that effective V&V is difficult is not a reflection on the RP model. The inherent weaknesses of all testing strategies must be recognized. There are both theoretical and practical limitations indicating, in a nutshell, that, as Hamlet says, "in the worst case, all fail." The software testing community has expended great energy developing systematic, even automated techniques (e.g., branch testing) of unknown value. There are no guarantees that errors will be found by standard techniques, and no guarantees that because a test detects nothing, there are no errors. Formal verification, in theory, is a far more valuable approach. Until, though, its practical limitations can be overcome (and it becomes more useful at a system level), its remains an area in need of additional research.

Along these lines, Musa and Ackerman [12] have proposed a statistics-based approach which recognizes the inherent limitations of all software testing. The correctness of a program is reported as a probability that the program will perform according to specification for a certain period of time. This approach is interesting in that it closely parallels hardware testing, and may ironically be the logical conclusion of the push to make software development an engineering discipline.

Finally, a note about expert systems and, in particular, decision aids is in order. The weaknesses of our V&V methods are compounded when we apply them to programs that are required to perform like humans in some task. Given our relative lack of V&V sophistication, every attempt to keep humans "in the loop" should be made when considering the use of a decision

aid in mission critical situations. We call them "aids"—and not "decision makers"—for good reason. Until we have more confidence in our V&V methods, decision aids should be endowed with extensive explanatory facilities which allow them to demonstrate how judgments are made so that each decision can be documented (thus helping system level testing theory), reviewed, and analyzed.

My recommendations for pursuing these lines of research can be summarized as follows:

(1) Continue to promote RP as a development methodology, and do so formally. That is, insist that projects adopt RP from the outset (the development and V&V plans should reflect it) and apply Iterative V&V with rigor. Ideally, each project should be fully documented from a process standpoint by an independent reviewer, and subsequently analyzed with the ultimate goal of developing an RP theory.

(2) Support research which focuses on black box, functional testing. As software complexity grows, we will become increasingly dependent on such methods.

(3) Support the development of RP development environments containing automated tools that support requirements definition and tracing in meaningful and useful ways.

REFERENCES

1. Beizer, B., Software Testing Techniques, New York, von Nostrand Reinhold, 1983.
2. Boehm, B. W., "A Spiral Model of Software Development," Computer, May, 1988, pp. 61-72.
3. ibid., "Verifying and Validating Software Requirements and Design Specifications," IEEE Software, January, 1984, pp. 75-88.
4. Dunham J., "V&V in the Next Decade," IEEE Software, May, 1989, pp. 47-54.
5. Dunn, R., Software Defect Removal, New York, McGraw-Hill, 1984.
6. Fairley, R., Software Engineering Concepts, New York, McGraw-Hill, 1985.
7. Gelperin, D., B. Hetzel, "The Growth of Software Testing," Communications of the ACM, June, 1988, pp. 687-695.
8. Hamlet, R., "Introduction to Special Section on Software Testing," Communications of the ACM, June, 1988, pp. 662-667.
9. Jordan, P. W., K. S. Keller, R. W. Tucker, D. Vogel, "Software Storming: Combining Rapid Prototyping and Knowledge Engineering," IEEE Computer, May, 1989, pp. 39-50.
10. Linden, T. A., S. Owre, "Verification and Validation of AI Software," Mountain View, CA, Advanced Decision Systems, TR-3209-01, March, 1989.
11. Luqi, "Software Evolution through Rapid Prototyping," IEEE Computer, May, 1989, pp. 13-27.
12. Musa, J., A. F. Ackerman, "Quantifying Software Validation: When to Stop Testing," IEEE Software, May, 1989, pp. 19-30.
13. Radatz, J. W., "Analysis of IV&V Data," Rome Air Development Center, Griffiss AFB, NY, Technical Report RADC-TR-81-145, June, 1981.
14. Tanik, M. M., R. T. Yeh, "Rapid Prototyping in Software Development," IEEE Computer, May, 1989, pp. 9-12.
15. Turing, A., "Computing Machinery and Intelligence," Mind 59, October,

1950, pp. 433-460.

16. Wallace, D., R. Fujii, "Verification and Validation: Techniques to Assure Reliability," IEEE Software, May, 1989, pp. 8-9.
17. ibid, "Software Verification and Validation: An Overview," IEEE Software, May, 1989, pp. 10-18.

1988 USAF-UES SUMMER FACULTY RESEARCH PROGRAM/

GRADUATE STUDENT RESEARCH PROGRAM

Sponsored by the

AIR FORCE OFFICE OF SCIENTIFIC RESEARCH

Conducted by the

Universal Energy Systems, Inc.

FINAL REPORT

CAPABLE NEURAL NETWORKS FOR APPLICATIONS IN DATA ANALYSIS

Prepared by:	O. G. Jakubowicz
Academic Rank:	Assistant Professor, PhD.
Department and	Electrical and Computer Engineering
University:	State University of New York at Buffalo
Research Location:	Rome Air Development Center
	IRD/IRDP
	Griffis AFB
	Rome, NY 13441
USAF Researcher:	Major Bob Russell/Bob Herrmann
Date:	October 20, 1988
Contract No.:	F49620-87-R-0004

CAPABLE NEURAL NETWORKS FOR APPLICATIONS IN DATA ANALYSIS

by

O. G. Jakubowicz, PhD.

ABSTRACT

A summary of desirous neural network properties for automatic aids for intelligence analysts was derived. A neural network system which is capable of all of the desired properties was modeled. A working computerized prototype was constructed in a short period of time that exhibited some of the properties (generalization, noise tolerance, translation, relational distortion and partly rotation invariance). The other properties, autolearning, autoassociative restoration, focus of attention and segmentation, have been demonstrated in a parent system, the Neocognitron. The intermediate layers are organized into Kohonen-like feature maps to aid the generalization property and the 'bubbles' of localized activity formation. A vision-like Y cell preprocessor acts to pick out the areas of a larger 80x80x6 (for 6 types of input) input space that have the highest possibilities of containing pre-defined 'interesting', sought after patterns of tactical activity. Output values represent the probability of particular patterns being present in the input. Together with an accompanying man machine interface program the computerized system can be used for demonstration purposes of a robust, multi-talented neural net for data analysis. In its present form it could also be easily interfaced to the Intelligent Analyst Associate system when it is ready.

ACKNOWLEDGEMENTS

I would like to thank the Air Force Systems Command and the Air force Office of Scientific Research for this opportunity to perform this research. I would also like to thank the Rome Air Development Center and the Intelligence and Reconnaissance Division for picking me to develop the system mentioned here. Sue Espy of Universal Energy Systems, Inc. gave me friendly logistical information when needed.

I would like to thank the people I met at RADC for being friendly and helpful in their various roles. First Major Bob Russell was an inspiration in directing me to an exciting application area and at the same time conversant in the area of neural nets. Bill Woody and Bob Herrmann were always available for technical consultation in the computer lab which was especially helpful in several pinch situations.

I. INTRODUCTION:

Neural networks are computational programs and devices that can perform low and high level biological or intelligent operations. They are showing theirselves to be a benificial solution method to problems because of their rich base of cooperative sciences from which development can proceed from.

These includes computer science, psychology, neurophysiological and anatomical biology, statistical and Hamiltonian physics and electrical engineering. The rapid growth of computational power and Very Large Scale Integrated Circuit technology is also opening the doors to implementations.

Simple networks can perform pattern recognition and clustering duties. Single layered networks can perform Gaussian maximum-likelihood classifiers and optimum minimum-error classifiers for binary patterns corrupted by noise. Arbitrary decision region segmentation can be performed straightforwardly by three-layered feed-forward nets. However unlike most classification methods (Parzan estimators is one notable exception) many neural can be continuously updated or adapt to additional inputs or changing environments while being used. The automatic learning which neural networks utilize frees the human designer from sizable amounts of the programming of fine details. Most neural net models operate on distributed representations of

input/output and internal information. This usually leads to excellent tolerance and classification in the presence of noise and fault-tolerance graceful degradation properties when damage amounting to lost connections or processors occurs.

The Rome Air Development Center and other facilities of the Defense agencies are interested in extracting important messages and events out of an excessive and continual barraige of input sources in this maturing and dynamically changing age of information. The state of situations ranging from jet combat attack to international monitoring must be detected, determined, analyzed and responded to. This is the exact strong-point of the neural network technology. Once detected important and relevant current situations must be presented to the human operator or some further electronic system in a meaningful format.

I have been involved with massively parallel processes of intelligent behavior for five years. My area of research is in utilizing and exploring current sensory-motor brain functioning neural nets in order to derive general brain processing principles for neural networks. The aim is to later extrapolate these principles into hypotheses of how higher infomational and situational recognition and reasoning process. This coincided well with RADC's twofold interests of 1) becoming more informed in neural network technology and 2) recognizing and processing "significant items" within a large database or high rates of data (message) input. My assignment was well placed with the Technology

Development section of the Intelligence, Reconnaissance and Data Processing Division at the Rome Air Development Center.

II. OBJECTIVES OF THE RESEARCH EFFORT:

Intelligence analysts suffer from a high rate of intelligence information coming under his scrutiny. Furthermore these analysts usually remain at their particular assignment for a relatively short period of time, often a year or two. Much information is not assimilated quickly and much previous knowledge and training is not being used by deluged analysts in these rapid turnover positions. Therefore we run into the problems of inefficiency and incompleteness in the world of the intelligence analyst.

My first assignment was to determine if a computerized implementation of current neural network techniques would be an aid in overcoming these problems. My job was to determine in what ways could neural nets aid an analyst for say a Foreign Technology Division project and to determine if the current neural net state of the art is sufficient to perform such a function. In particular it was determined that the ability of neural networks to recognize 'interesting' patterns would aid an analyst in attending to any overlooked input data. Also the usual neural net properties of generalization and partial invariance to noise is ideal for handling the analyst's varying and imprecise data. Furthermore the neural net property of autoassociative restoration is

easily capable of suggesting missing features to an analyst. Additionally functions of automatic focus of attention and segmentation in neural nets are suited for working with real world data where inter-mixed or overlapping patterns are encountered. Finally the fact that neural nets are implemented as numerical algorithms allows rapid processing on array processor boards or similar peripherals.

My second goal was to develop in the time alloted a neural net system that could both be used as a demonstration of one or more neural network types and at the same time capable of performing some of the above mentioned functions. In particular a network that recognizes tactical patterns in 2-dimensional maps irrespective of translation, distortion or (currently) slight rotation was constructed. Furthermore architectural principles were maintained in this network that would allow with further development the incorporation of all of the properties benificial to an intelligence analyst as mention in the first goal above. An actual demonstration of such a system is presented in a related but distinctly different domain (hand character recognition) in Fukushima's papers. The recognition neural net system developed this summer can straightforwardly be modified to possess these capabilities using university facilities with funding from the research initiation program.

III. GOALS AND RESULTS OF THE REQUIREMENTS AND CAPABILITY STUDY:

a. A few weeks were used to review the prominent neural net models and to become familiar with the Intelligent Analyst Associate system (IAA) in order to ascertain which neural net capabilities would be benificial to the IAA analyst. The results of this requirements study is expressed in the following. What we need for a IAA analyst's aid is a hybrid neural net/knowledge base analysis system, designed primarily to recognize previously-seen patterns in timelines and map locations. It should also have a learning component to automatically store new inputs into its knowledge base. A follow on effort would involve having the network search for interesting relationships without previous training of the network by an analyst. The primary purpose of this system is to try to build some machine-based corporate knowledge of applications of enemy doctrine, and to alert the analyst when such applications of doctrine are noticed.

As a simple example, suppose that an analyst had previously trained the system with the information that in the Czechoslovakian invasion, when the Czechs blew up some Soviet tanks, the Soviets responded by sending in helicopter gunships within 20 minutes, and continued to send in copters until there was no more noticable anti-tank activity in the area. Now when the analyst is evaluating a battle in the Afghanistan war, and sees the Afghans blow up several tanks, the system would alert the analyst to a possibilty of Soviet helicopters arriving within 20 minutes, and would interpret the existence of Soviet helicopters during that time period as a probable response to the tank attacks.

In addition a neural net aid would be helpful if it could search for potentially 'interesting' relationships where part of a previously-seen significant cause-effect-result event is seen but not all of it. The system should indicate to the analyst what the unseen part of the event entails and in what time and/or location it might be found.

b. In brief it was decided that the almost ubiquitous neural net property of autoassociation (pattern restoration of completed patterns from incomplete) was the main effect that such an analyst would require. In addition the equally customary properties of generalization and the related tolerance to noise supports the use of neural nets in the first place to such a real world application area. Other problems that arise in time-line or 2-D map displays are translational displacement and relational distortion of patterns. Relational distortion here means that two or more subparts of an input test pattern are displaced relative to each other when compared to the training exemplar. Most neural networks do not tackle the problem of translation invariance and rarely is there a neural network that deals with relational distortion. Neural nets often can handle noise where some elements of an input pattern are missing or have corrupted amplitudes but most often not relational distortion. Neural nets which don't handle translationally displaced patterns can have a partial fix by finding a mechanism to align the input but they require that a starting and ending point are easily detectable. Considering the example that words are often run into one another with no quit periods between spoken words we see that this is not always possible in many

real world problem domains. Furthermore in the recognition of patterns in a 2-D spatial map problem the IAA analyst needs to be able to recognize rotated patterns. A real world application such as the IAA analyst aid would require segmentation and focus of attention capabilities to recognize a pattern properly when two or more are present simultaneously (see Fukushima's papers).

A neural net system that does solve for translated, relationally distorted and even partially rotated patterns is the Fukushima Neocognitron. More recently autoassociative versions of the Neocognitron have been developed which are able to reconstruct the missing components of a testing exemplar. When two or more 'interesting' patterns are in the input plane at the same time the system can select or temporarily focus its attention and consider only one pattern at a time, even if they are overlapping or share components. This striking ability is precisely what a real world analyst requires.

IV. GOALS AND RESULTS OF A NEURAL NET DEVELOPMENT AND DEMONSTRATION:

a. A second goal was to start the development of a system that would be able to perform all or most of the desired functions arrived at in the first goal. Knowing that this would be a large effort we focused on performing only the translational, distortional, scale, partially rotational and noise invariant properties in a situational pattern recognition system. The system is also to be used as a demonstration

of several neural net theories or models. The other four properties of predicting unseen parts of significant events (autoassociation), automatic derivation of 'interesting' events from a large data base, and focus of attention and segmentation are to be left to a 'research initiative program' follow up effort. This network was constructed in an open ended architecture that can readily accommodate the additional system features and components mentioned earlier.

b. At the high level the network has multi-levels of condensing data representation with overlapping input windows as in the Fukushima Neocognitron. However the levels theirselves each have an ordered feature map representation of data unlike the Neocognitron. The discovery of the principles of construction and representation of data in relationally ordered feature maps has been primarily accredited to Teuvo Kohonen of the Helsinki University of Technology. The propagation of activity rules in the network are also not the same as the ones used in the Neocognitron but rather are more akin to the popular linear associator rules as also usually used in Kohonen feature maps. The advantages of this approach are discussed and then the network is described in detail.

As pointed out earlier the idea of multiple small windows and the integration of information over many such spatially collocated input windows to upper levels of layers of nodes provides the network with the traits of translation, scale and distortion invariance. These forwardly activity propagating nodes are readily situated to act as

gates for backward retracing activity which can terminate at a final layer of cells that is identical to the input space. Backward connections have not been implemented yet. This final pattern would be an autoassociatively reconstructed and restored image of the input situational pattern. This capability has been experimentally demonstrated by Fukushima and his co-workers for visual input in recent papers of extensions of the Neocognitron. Furthermore his new system will be able to perform 'focus of attention' and 'segmentation'.

Focus of attention is the ability of choosing and considering only one compound input object at a time when several are simultaneously present in the input. Segmentation is the ability to delineate one compound object at a time when there are several juxtaposed or superimposed objects present in the input. These are two input situations common in everyday real life and data bases which most neural net systems have not matured to handle yet.

Nature has deemed the formation of ordered feature maps as important in the brain. Numerous such maps on the neocortex have been found beginning with the spatially ordered primary sensory areas. Each of these areas typically encompasses about 1 cm . Kohonen has for the first time isolated the biological mechanisms that account for the automatic development of feature maps and has presented them in the form of a simple algorithm. The method produces optimal feature detectors and places them into an order according to their most significantly correlated relationships. Therefore excellent feature

detectors for the patterns in the plane below are produced. When neurons in the detector plane are learning they also aid nearby neurons to learn simultaneously and the fact that neighboring neurons are closely related feature detectors provides higher processing planes with greater easily interpretable input information.

An automatic learning rule which is an extension to the Kohonen learning rule was developed for use in this new network. In analogy with the more or less symmetry of the lines and blobs receptive fields of simple cells in the primary visual cortex windows which have symmetric input patterns were chosen to be the training exemplars in our network. Once these training exemplars were chosen then the standard Kohonen learning rules for finding the output winner and updating the weight matrix were used. Then this same weight matrix can again be used by all the windows at its level as usually done in the standard Neocognitron. Having symmetric input is here defined as when the average x and y coordinate of all thresholded inputs is near the center of a layer's window receptive field.

In the actual computerized model the input is represented in one 80x80 character plane in the C computer language. A 'T' at any location represents a tank or battalion of tanks at that spatial location. A 't' represents a battalion of troops and a 'c' represents a communications node at the spatial location. Therefore spatially ordered objects or situations of military importance are represented in the input.

Propagation of activity upwards in the network procedes along two independent paths corresponding first to the fast Y complex cells in the neocortex first and secondly up the slower X simple cells co-mingled together. Though popularly assumed but not yet biologically verified nor nullified our network assumes that the Y cells which only provide a rough spatial resolution are used to guide the X cells in their processing with the later performing fine spatial resolution.

The rough Y cell subsystem is implemented is follows. At an interval of every 7 input cells a 20x20 receptive field to a Y cell is considered. This means that the 20x20 receptive fields overlap and that a 12x12 plane of Y cells will be able to cover the entire 80x80 input character plane. We allowed our network to be able to search a maximum of 10 'interesting' patterns, spatially related combinations of the input objects T's, t's and c's. Therefore there are actually 12x12x10 Y cells; one Y cell that will respond to any 20x20 area containing the input objects neccessary for each of the 'interesting' sought for patterns. A simple learning algorithm for each type of Y cell automatically determines the weights to the afferent connections when the training set of the 10 or less 'interesting' patterns are presented. The percentage of T's, t's and c's to the entire pattern are determined and taken as the weights in the Y subsytem. Whenever that same pattern or some larger convolution of it is present in a testing situation then the output of that Y cell will be 1.0 . If part of that pattern is only presented then the Y cell will only have a corresponding partial output.

As of this time we have been experimenting with learning and recognizing 6 17x17 input patterns. The learning rule is being experimented with and the system recognizes the correct pattern about 93 % of the time. The alloted ten week time period for the project was not enough for all the required debugging and development, especially since the machine used could only operate at about .1 mflops. If patterns are displaced they also are recognized with the same accuracy. Distortion and changes in size have not been experimented yet at the conclusion of the 10 weeks. However there is a follow-on effort being conducted to optimize the system.

V. RECOMMENDATIONS:

a. Any RADC effort in neural networks should keep in mind the wide range of remarkable properties that neural networks are capable of exhibiting. The first goal of discovering what neural network traits would be most important for intelligence analysis causes this report to emphasize the importance of involved architectures with forward, lateral and backward activity propagation in neural nets. Neural nets are needed not only to recognize patterns but also to associate output patterns, evaluations or even decisions. Their capability for autoassociative restoration of incomplete patterns is useful for suggesting unseen factors in the input. Their capability for generalization and noise tolerance is useful for real world situations where the input is varying. The function of focus of attention is

neccessary in the presence of complex input. And the property of segmentation is remarkably advantageous when inputs are overlapping.

The second result from my summer work is the demonstration program. This can both easily be used to demonstrate some capabilities of an advanced neural network system and with a small amount of tailoring be used as a first draft to a back end for the IAA system or possibly even other systems. The development of the system to exhibit some other advance features and to handle large scale IAA problems is the subject for the follow on research initiative program effort.

b. As mentioned in the previous sections the incorporation of the other versatile properties would be the substance of further research. These again include autoassociation, auto-learning, focus of attention and segmentation. A more friendly and powerful man machine interface should be created that will include functions such as modify and include small patterns into various locations on the input map. The identification of rotated versions of patterns needs to be developed. The current suggestion is that training at four to eight rotated versions of each pattern might suffice to demonstrate rotation invariance. Another area of follow-on research is the study of scaling the system up for actual use in a real IAA analyst aid system. A large version of this network will require much number crunching resources and would undoubtedly require one or more array processing or multi-processor (transputer ?) boards.

c. High architecture neural nets developed to the point of exhibiting multiple advanced properties offer many capabilities that other electronic and computational methods do not exhibit. These human intelligence like properties can aid the intelligence analyst. Many useful tasks should be implementable with the aid of some 10 to 20 boards for workstations (most popularly with SUN computers) some of which are presently commercially available. Several more advanced boards will soon be available which can perform 50 to 100 Mflops. Some of these boards consist of 16 to 48 transputers with 20 or more megabytes of RAM while others have specially developed components. In order to solve real world problems you need involved neural networks. In order to use these high architecture neural networks you need many megaflops of processing speed, fast interconnections between subprocessors and many megawords of fast data storage.

REFERENCES

1. Fukushima,K., "Neocognitron: A Hierarchical Neural Network Capable of Visual Pattern Recognition," Neural Networks, April 1988,No.2.

2. Kohonen,T., Self-Organization and Associative Memory, Berlin -Heidelberg-New York-Tokyo, Springer-Verlag Publishers, 1988.

APPENDIX

For those who wish to experiment with the network as a demonstration the following will be of help. There are two programs. Executing "mmi" will bring up self explanitory prompts that will ask if a new data base of input patterns will be created or if you wish to execute the already existing set of patterns. Then the user will be prompted to create the set item by item one pattern at a time. Once these "interesting", "important" patterns are decided on, then the user can enter a "q" to exit the program. The second program "recog" can be executed with a parameter of either 1 or 2. 1 means to learn the new patterns and two means to see which types of patterns the input map contains. The results are sent as output to the screen.

FINAL REPORT

1989 USAF-UES SUMMER FACULTY RESEARCH PROGRAM

GRADUATE STUDENT RESEARCH PROGRAM

Sponsored by the

AIR FORCE OFFICE OF SCIENTIFIC RESEARCH

Conducted by the

Universal Energy Systems, Inc.

A STUDY OF INTERACTING TUNNELING UNITS WITH POSSIBLE APPLICATION TO HIGH TEMPERATURE SUPERCONDUCTORS

Prepared by:	Michael W. Klein*
Academic Rank:	Professor
Department:	Physics Department
University:	Worcester Polytechnic Institute
Research Location:	Rome Air Development Center Hanscom Air Force Base, MA 01731
USAF Researcher:	Alfred Kahan
Date:	July 24, 1989
Contract No:	F49620-88-C-0053
Project No:	210

* This is a joint report by **Michael W. Klein**, Summer Faculty Research Fellow and **Timothy P. Mavor**, Graduate Student.

A Study of Interacting Tunneling Units with Possible Application to High Temperature Superconductors

Dr. Michael Klein and Timothy Mavor, Graduate Student

ABSTRACT

Most amorphous and glassy materials exhibit anomalies in their low temperature thermal properties. Very similar anomalies were observed in a number of high temperature superconductors. Whereas it is believed that these anomalies arise from the presence of tunneling states in the solid, so far there is no microscopic model for these tunneling states. Recently I examined a system of tunneling dipoles distributed in alkali halides and found that they give glasslike properties at low temperatures. Thus dilute tunneling dipoles present a microscopic model for glasslike properties. The purpose of this research to derive the thermal properties of dilute quadrupoles and examine whether they can explain the temperature-dependent variation of the sound velocity of some high T_c superconductors.

ACKNOWLEDGEMENT

I wish to thank the Air Force Office of Scientific Research for awarding me a Summer Research Fellowship and for sponsoring this research. I also wish to acknowledge Universal Energy Systems Inc. for their help in expediting the administrative aspects of this program; for their "instant response" with the fax machine, without which my Graduate Student Assistant, Mr. Timothy Mavor, may not have received his appointment.

My special thanks to Alfred Kahan of the Rome Air Development Center for having made my stay at Hanscom Air Force Base a most pleasant one; for having introduced me to a wealth of literature on high temperature superconductivity; for having spent a good deal of time to keep me informed of the newest literature in the field and for patiently explaining the structure of some of these high-temperature superconducting materials. I also thank him for having introduced me to the outstanding Science Library at Hanscom Air Force Base, which enabled me to track down a number of references not usually available.

The universal complaint of faculty members at Colleges is the constant demand on their time in teaching, committee work and research. One often longs for some free time to sit back and reflect on one's research in depth. I am grateful to the Air Force Office of Scientific Research and to Universal Energy Systems Inc. for having provided me with the opportunity to do so during this Summer.

A STUDY OF INTERACTING TUNNELING UNITS WITH POSSIBLE APPLICATION TO HIGH TEMPERATURE SUPERCONDUCTORS

1. BACKGROUND INFORMATION

There has been a good deal of recent interest in the properties of tunneling states. This interest arises because the experimentally observed low temperature anomalies in amorphous and glassy materials[1,2] can be explained by assuming the presence of tunneling states.[3,4] Amorphous materials are of a good deal of practical importance in technology and their understanding presents a serious challenge to the experimental as well as theoretical physicist.

Experiments on glasses and amorphous materials exhibit low temperature anomalies in their specific heat,[3-4] thermal conductivity, thermal expansion, dielectric relaxation and sound propagation and absorption. To explain these anomalies it was proposed that the "glassy"[5] system is made up of two-level tunneling states (TLS)[3,4] with a random distribution of barriers. An assumed phenomenological constant density of states gives many of the experimentally observed properties of glasses.

There is a great deal of experimental support for the existence of tunneling states in glasses. However, all attempts to obtain a microscopic description for the tunneling states or for the constant density of states have had very limited success. The early experiments concentrated mostly on amorphous insulators. More recent[6] ones found that the glassy anomalies are also present in amorphous metals.

In addition to most amorphous materials, there are a number of other systems that exhibit "glasslike" properties at low temperatures. Dilute concentrations of tunneling electric dipoles[7-8], (for example Li^+ in KCl)

or strain dipoles (for example CN^- dissolved in KCl) also show low temperature glasslike anomalies. In fact there are a whole classes of impurities which when dissolved in alkali halides show glasslike properties of one form or another.[9-14]

More recently there has been a good deal of evidence in the literature for glassy properties in a number of high temperature superconductors. Evidence for possible glassy properties have been seen in the sound velocity[15-19], in the thermal conductivity[20-21] and in the specific heat.[21] It is the observation of the glassy properties of some of the high temperature superconductors that has motivated this research.

In an attempt to identify the origin of the low-energy excitations in tunneling units, I studied[22] the microscopic properties of very dilute two-level Ising-model tunneling dipoles which interact via a $1/r^3$ interaction. I derived a set of microscopic relations for the thermal properties of the tunneling dipoles. From the microscopic derivations I obtained a constant density of excitation energies E for low E in agreement with experimental results observed in glasses. Later on[23] I treated multiorientational tunneling dipoles (for example Li^+ in KCl) and obtained the specific heat, the thermal expansion, the the complex dielectric susceptibility[24] for the tunneling dipoles. Again these results are consistent with those observed in glasses. Thus the tunneling dipole problem[24] serves as a first microscopic model for one particular glass system.

OBJECTIVES OF THE RESEARCH

The objective of the research during the tenure of the Fellowship is to formulate an approach which may explain the glasslike properties of some of the high temperature superconductors. As is outlined in the intro-

duction, there is currently no microscopic theory which explains the universal properties of amorphous materials or the glasslike properties of high temperature superconductors, or any other materials. I have been able to develop a microscopic theory for tunneling dipoles distributed in alkali halide crystals. This microscopic theory gives, at least for the tunneling dipole system, glasslike properties from fundamental considerations. However tunneling electric dipoles do not effect the sound velocity (or elastic constant) appreciably. Therefore the solution of the dipole problem is not likely to explain the observed sound velocity variations in superconductors. Tunneling strain dipoles or "quadrupoles" (for example CN^- ions distributed in alkali halides) will, on the other hand, effect the following physical quantities: (i) the elastic constant and thereby the temperature dependence of the sound velocity; (ii) the real and imaginary part of the dielectric constant; (iii) the specific heat; (iv) the thermal expansion; (v) the thermal conductivity. Therefore the effort was concentrated to understand the dilute quadrupole problem.

RESEARCH PERFORMED

We considered the simplest interacting strain quadrupoles. In distinction to electric dipoles which can have two (up or down) orientations, the strain quadrupoles must have four or more orientations.[25] Thus a pair of strain quadrupoles have at least 4 x 4 or sixteen orientations. In this sense the simplest quadrupole problem becomes mathematically much more complicated then the electric dipole problem.

We have been able to derive an effective quadrupole (QP) Hamiltonian. This Hamiltonian depends on the tunneling matrix element D and the quadrupole-quadrupole (QQ) interaction J_{ij} between two QP's located at

sites i and sites j (i and j are arbitrary positions which the QP may occupy in the solid). The quadrupoles are assumed to interact via a strain interaction and are assumed to be randomly and uniformly distributed in the solid. Thus the QQ interaction is a random variable. We derived the probability distribution of the QQ-interaction. From the QP Hamiltonian we set up the sixteen by sixteen matrix for a single pair of QP and solved for the strain dependent eigenvalues of the system.

We then obtained the eigenvalues of a pair of quadrupoles in the presence as well as in the absence of an external strain field. From the eigenvalues we have obtained the partition function and the the d.c. strain susceptibility. Any fixed pair of quadrupoles have a well defined interaction between them. The quadrupoles are assumed to be randomly distributed, and to obtain the thermal properties of the whole system one has to average over the distribution of the quadrupole interactions.

Using the strain dependent eigenvalues we derived expressions for the partition function of the system in the limit as the ratio of the number of quadrupoles to the total number of atoms in the solid is small. This is called the dilute quadrupole limit. From the partition function we can derive the complex strain susceptibility. The real part of the strain susceptibility is directly related to the sound velocity, whereas the imaginary part is related to the sound absorption (or the internal friction). The complex susceptibility was derived assuming a Debye relaxation of the quadrupoles over the barrier formed by the QQ interaction itself. Such a mechanism was found to cause the relaxation in electric dipoles and are assumed to cause the relaxation in the quadrupoles also.

From the quadrupole susceptibility for a single pair of quadrupoles we obtain the susceptibility of the system by integrating over all pairs. Our results show that there is a term in the sound velocity which is proportional to the temperature. This seems to be consistent with sound measurements in a number of glasses as well as some high T_c superconductors.

We have evaluated the low temperature variation of the sound velocity for a number of frequencies. We find that the strain susceptibility, and thereby the sound velocity, is proportional to T ln$X$, where X is the. frequency. Our work has not yet progressed far enough to determine whether we can explain the variation of the sound velocity in the high T_c superconductor.[15]

RECOMMENDED FURTHER WORK

Preliminary investigation shows that quadrupoles distributed in a crystal give some "glasslike" properties at low temperatures. This is quite encouraging and indicates that it may be scientifically profitable to obtain other thermal properties of the quadrupoles. These properties are: (i) the specific heat; (ii) the thermal expansion; (iii) the thermal conductivity and (iv) the dielectric susceptiblity. When these results are obtained one should examine whether experiments on the glassy properties of quadrupoles are consistent with the theoretical predictions obtained from the quadrupole Hamiltonian.

In addition to the dealing with the dilute quadrupole problem above this research suggest that it would be useful to treat the more concentrated quadrupole problem in a mean field approximation (exact treatments of this quantum mechanical problem are presently not available). This will be part of the effort for next year's research of the writer of this report.

REFERENCES

[1]. Amorphous Solids, edited by W. A. Phillips, (Springer Verlag, Berlin, 1981).

[2]. S. Hunklinger and W. Arnold, in Physical Acoustics Vol. 12, edited by W. P. Mason and R. N. Thurston, (Academic Press,New York, 1976), p.155.

[3]. P. W. Anderson, B. I. Halperin and C. Varma, Phil. Mag. 25, 1(1972).

[4]. W. A. Phillips, J. Low Temp. Phys. 7, 351(1972).

[5]. Materials which have properties similar to amorphous solids and glasses, but are not usually considered considered glasses will be denoted as "glasslike".

[6]. S. Hunklinger and J. Raychaudhuri, in Progress in Low Temperature Physics Vol 9, edited by D. F. Brewer (North Holland , Amsterdam-New-York, 1986) and references therein.

[7]. R. C. Potter and A. C. Anderson, Phys. Rev. B24, 4826(1981).

[8]. R. C. Potter and A. C. Anderson, Phys. Rev. B24, 677(1981).

[9]. D. Moy, R. C. Potter and A. C. Anderson, J. Low Temp. Phys. 52, 115(1983).

[10]. W. Kanzig, H. R. Hart and S. Roberts, Phys. Rev. Lett. 13, 543(1964).

[11]. A. T. Fiory, Phys. Rev. B4, 614(1971).

[12]. M. W. Klein, C. Held, and E. Zuroff, Phys. Rev. B13, 3576(1976).

[13]. M. W. Klein, B. Fischer, A. C. Anderson and P. J. Anthony, Phys. Rev. B17 4997(1978).

[14]. U. T. Hoechli, Phys. Rev. Lett. 48, 1494(1982).

[15]. M. J. McKenna, A. Hikata, J. Takeuchi, C. Elbaum, R. Kershaw and A.Wold, Phys Rev. Lett. 62 1556(1989)

[16]. B. Golding, N. O. Birge, W. H. Haemmerle, R. J. Cava and E. Rietman Phys. Rev. B36, 5606(1987).

[17]. A. Jezowski, J. Klamut, R. Horyn and K. Rogacki, Superc. Sci. Tech. 2, 96(1988)

[18]. S. D. Peacor and C. Uher, Phys. Rev. B39, 11559(1989).

[19]. S. J. Burns, A. Goyal, and P. D. Funkenbusch, Phys. Rev. B39, 11457, 1989.

[20]. P. Esquinazi, C. Duran, C. Fainstein and M. Nunez Regueiro, Phys. Rev B37, 545(1988).

[21]. For a recent review article on the specific heat see S. E. Stupp and D. M. Gindsberg, Physica C158, 299(1989).

[22]. M. W. Klein, Phys. Rev. B29, 5825(1984); B31, 2528(1985).

[23]. M. W. Klein, Phys. Rev. B35, 1397(1987).

[24]. M. W. Klein, Phys. Rev. B40, 1918(1989).

[25]. Three orientations might be sufficient, but it is simpler to choose quadrupoles with orientations along the x and y axis.

1989 USAF-UES SUMMER FACULTY RESEARCH PROGRAM/

GRADUATE STUDENT RESEARCH PROGRAM

Sponsored by the

AIR FORCE OFFICE OF SCIENTIFIC RESEARCH

Conducted by the

Universal Energy Systems, Inc.

FINAL REPORT

DESIGN OF A PRACTICAL BINARY PHASE-ONLY OPTICAL CORRELATOR

Prepared by:	William L. Kuriger
Academic Rank:	Professor
Department and University:	School of Electrical Engineering and Computer Science, University of Oklahoma
Research Location:	Photonics Center Rome Air Development Center Griffiss Air Force Base, New York
USAF Researcher:	Andrew R. Pirich
Date:	28 July 1989
Contract No:	F49620-88-C-0053

DESIGN OF A PRACTICAL BINARY PHASE-ONLY OPTICAL CORRELATOR

by

William L. Kuriger

ABSTRACT

Procedures were investigated for designing optical correlators based on binary phase-only filters. Implications of the procedures were investigated by use of computer simulations. The report contains correlator and filter design information and samples of simulation results. It is a reduced version of a report submitted at the research location.

DESIGN OF A PRACTICAL BINARY PHASE-ONLY OPTICAL CORRELATOR

W. L. Kuriger

I. INTRODUCTION

Optical correlators are devices that can be used to indicate by optical means the presence or absence, and if present, the location, of a particular pattern in an image. In the standard or VanderLugt form of optical correlator, an input image is impressed on a beam of coherent light, and the transform of the image is taken by use of a suitable lens. At the transform plane, the beam with the image transform is passed through a spatial light modulator containing the transform of the desired pattern, in effect multiplying the two transforms. The transform of this product is taken by a second lens, producing at the output plane an intensity distribution which is the correlation of the image with the desired pattern. The major advantage of doing the pattern comparison in the Fourier plane rather than in the image plane is translation invariance, obviating any need for mechanical motion to search for the location of the target object within a larger image.

II. OBJECTIVES OF THE RESEARCH EFFORT

The objective of the research effort is to develop design information for optical correlators utilizing phase-only filters.

III. SYSTEM DESIGN CONSIDERATIONS

In this section formulas are presented for the design of a standard correlator system. It is assumed that a sampling-type SLMs (Semetex MOSLM, liquid crystal device, deformable mirror device, etc.) are used both to form the input image and the filter. Any numbers used as examples are based on the assumption that a Semetex 128x128 MOSLM is used at both the input and filter planes. Results for other devices would be similar.

Assume the standard Vanderlugt correlator architecture is to be employed. Assume that an SLM with pixel size dx1 is used at the input, and an SLM with N2xN2 pixels of size dx2 is used at the output. The Fourier transform lens must have a focal length such that the input's zero order is precisely imaged on the transform-plane SLM. The required lens focal length is given by the product of N2 times dx1 times dx2, divided by the wavelength. This equation can be derived from either a sampling theory or diffraction grating viewpoint (they are essentially equivalent).

For 128x128 MOSLMs, N2 is 128, and dx1 and dx2 are 76 microns. Assuming the HeNe 632.8 nm wavelength is employed, the necessary focal length is f = 1.168 m.

A configuration that allows use of off-the-shelf lens sizes and permits control of system size is shown in Figure 1. A diffraction analysis of the configuration has been done, resulting in the design procedure and formulas included in the Figure.

If a linearly polarized laser beam is applied to the input SLM, it is converted into a pattern in which pixels are polarized either by a positive or a negative angle. Since an amplitude-modulated wavefront is wanted at this point, conventional practice is to follow the SLM by an analyzer oriented to block one of the polarizations produced by the SLM. At the transform plane, the effect of this analyzer so oriented is to remove the dc component. It is thus possible to dispense with this analyzer if the dc component (a focussed spot at the coordinate origin) can be blocked at the transform plane, either by use of physical stop or by operating the transform-plane SLM in its ternary phase-amplitude mode. There is a slight advantage in optical throughput if this is done. Not only is the loss associated with the polarizer no longer there, but the signal amplitude is

proportional to twice the sine of the SLM polarization rotation angle, rather than to one times the sine of twice the angle. The difference is negligibly small for the small (about +\- 5 degree) rotations produced by the available MOSLM, however.

The optical signal into the transform-plane MOSLM is linearly polarized. The filter MOSLM then causes each pixel of the phasefront to be advanced or retarded in polarization, by the rather small amount characteristic of the MOSLM. The transform-plane MOSLM must be followed by an analyzer set to block the polarization of the incoming wave. This produces the desired phase-only filtering effect.

For purposes of calculating optical losses, assume that a correlator system consists of a laser, detector array, 2 MOSLMs, 2 polarizers, and 4 lenses. Further assume that each lens is 90 per cent efficient and each polarizer is 62 per cent efficient. Major losses occur in the MOSLMs via five different effects: Bulk material loss, vignetting loss, diffraction loss, surface reflections, and the fact that only a component of the output can be used.

From manufacturer's data, the bulk material loss is probably on the order of 50 per cent. A vignetting loss occurs because pixel extent is less than pixel spacing. The active area of a MOSLM pixel is a square 56 microns on a side, while the pixel separation is 76 microns. Thus only .54 of each pixel represents transparent area. There is a diffraction loss because the MOSLM acts as a two-dimensional diffraction grating, scattering light into many higher orders (only the 0 order is used). To obtain an estimate of how much light is scattered into higher orders, the amount of power scattered into a number of lower- numbered orders was calculated. From this calculation, a reasonable

estimate of the diffraction loss is 50 per cent. The material used in the MOSLM has a refractive index of n = 2.35, so there should be a power reflection of 16 per cent at each surface. If the polarization rotation angle of the MOSLM is +/- 5 degrees, the useful portion of the signal intensity is proportional to the square of the sine of 5 degrees, a factor of 0.0076. Assuming the 5 degree figure is typical, the power out of the Semetex unit will be about .0007 of the input power.

For the overall system, the power to the detector will be attenuated by about 7 orders of magnitude. There are still two other factors to consider. Since the input MOSLM's function is to create a black and white picture, the amount of white is picture dependent. We will assume that the input scene threshold is set so that half of the pixels are white, a reasonable choice if the picture is to present maximum information. The other factor to be considered is the extent to which the input laser intensity is required to be uniform over the extent of the input MOSLM aperture. There is a straightforward tradeoff between the uniformity of a gaussian beam segment and the fraction of the beam that can be used. If the relative intensity of the beam at an edge of the useful portion is x times the peak intensity, the fraction of the beam power that can be used is 1 - x. Thus if it is required to hold the variation in beam intensity to 10 per cent over the MOSLM surface, only the central 10 per cent of the beam can be used. What is a reasonable estimate of the necessary beam uniformity? Fortunately, the correlators envisioned are not at all sensitive to this parameter. It does not seem unreasonable to use the central 50 per cent of the gaussian beam, with an intensity at the edges that is only 50 per cent of that at the beam center.

Based on all the above considerations, the light incident on the detector should be about 8 orders of magnitude below the laser's output power. Thus a 10 mW HeNe laser would be expected to deliver about 0.1 nW to the entire detector array. Some typical numbers gleaned from manufacturer's literature for a 128x128 CCD array suggest that a reasonable estimate for a minimum detectable signal would be 40 nW for a 0.1 ms exposure, averaged over the entire detector aperture. It thus appears that the system as envisioned would be too lossy to be usable if two MOSLMs (the major loss element) are used, unless units with greater rotation angles are employed. Fortunately, devices with greater rotation angles do seem to be becoming available.

IV. FILTER DESIGN

The choice of where to place a target image on a scene for the construction of a filter is affected by two considerations. One is simply that the location of a correlation spot is determined by the location of a target relative to its location in the image from which a filter was made. Thus it is very convenient to use a central image when constructing a filter. A correlation spot will then be (except for inversion) at the same location as the target.

The other factor arises from the fact that a binary POF is inherently ambiguous. Unless special tricks are employed, a binary POF will correlate equally well with a target and with its mirror image. If it is important to separate the true (correlation) output from the false (convolution) output, the target should be placed so that it is completely off the scene center. If not, then there is no reason not to center the target when constructing the filter.

The choice of image placement for filter construction is

also closely intertwined with the choice of thresholding-line angle used in the binarization of a binary POF. In a binary phase-only filter based on a device like the Semetex MOSLM, the filter's pixels can assume values of +1 or -1 (or 0, if the MOSLM's ternary phase-amplitude mode operation is allowed). How is the decision made to assign +1 or -1 to an individual pixel? Each entry in the Fourier transform array for the target is a point on the complex plane. Consider that the complex plane is bisected by a line, the thresholding-line, with all phasors on one side being assigned +1 and all on the other side assigned -1. The problem is now reduced to finding the optimum thresholding-line angle. By use of the Farn-Goodman algorithm, the optimum angle was calculated for the centered plane image and found to be 0 degrees (the optimum angle for a plane image completely in one quadrant was found to be 21 degrees). Any centered image's transform will have a large component clustered about the positive real axis, resulting in an optimum thresholding angle very close to zero.

The Semetex MOSLM has a ternary phase-amplitude mode. In this mode, an individual pixel is nucleated but not saturated. The pixel then contains several oppositely-oriented magnetic domains, and it tends to scatter light into higher orders. Individual pixels can thus have a positive polarization rotation, a negative rotation, or an off state: +1, 0, and -1. SLM devices that lack this facility can still be used in a reduced-bandwidth mode by use of an iris to block higher spatial frequencies. How can this additional freedom be gainfully employed?

Consider first that spatial frequencies are to be subjected to a low-pass filtering. This simply means that the POF will consist of an active center portion surrounded by a wide band of

zeros (or equivalently, that these outer pixels are blocked by a mechanical iris). The effect is the same as though the fine detail in an image had been smoothed over. There is a loss in the discrimination ability of the POF and an increase in its tolerance to rotations and scale changes. The correlation peak is reduced in amplitude and broadened. Low-pass filtering can be used to make a correlation peak's height and amplitude vary from that of a POF to that of a matched filter and on to a fully uniform correlation plane output. Conversely, high-pass filtering can be used to make a correlation peak narrower (a matched filter followed by a high-pass filter can equal a POF, for example). Since POFs already often have correlation peaks less than one pixel in extent and are very sensitive to scale and rotation changes, a high pass operation is seldom useful.

The use of a reduced-bandwidth POF is desirable in two situations. One is the case where it is desired to trade target specificity for less sensitivity to scale or rotation changes or partial obfuscations. For example, it might be desired to conduct a coarse search of a set of scenes, with closer looks (that is, correlations with POFs with greater spatial bandwidths) taken whenever a suspected match is found. The second situation occurs for very noisy scenes, as might be obtained with a great amount of enlargement, for instance. Since high spatial frequencies will tend to add more noise than signal information, cutting them out can improve performance in this situation.

The approach considered above involved low-pass filtering on spatial frequencies. There is another approach that may be useful for a ternary phase-amplitude mode. Filter pixels can be assigned values of +1 or -1 if their amplitude is above a preset threshold, and assigned 0 otherwise. A filter made in this

fashion is known as a TPAF (ternary phase-amplitude filter). Note that a TPAF could be realized with a Semetex MOSLM, but not with a mechanical iris. Simulations with plane targets in this study gave TPAF results very much like reduced-bandwidth POF results.

With regard to all types of sensitivity, the bad news is that there is no free lunch. A Fourier transform correlator is inherently capable of being invariant to precisely two parameters, no more. In a standard correlator configuration, the invariant parameters are x and y translation. This invariance has to be given up to obtain any other invariances. The good news is that a continuous tradeoff exists between target specificity and partial invariances, that is, reduced tolerances to particular distortions. A POF design can thus be tailored to fit any desired situation.

A very different and interesting approach that yields complete rotation invariance as well as position invariance, at a cost of a rather drastic reduction in specificity, is to base the filter design on a rotationally symmetric component of the target. The zero-order rotationally symmetric component of any image is simply the best-fit circle. For the airplane image used in the simulations in this study, this circle is probably the optimum circularly symmetric component. Its use in the simulations gave rather complex results. Multiple correlation peaks were always obtained, and especially complex correlations resulted if circles larger than optimum were used.

One major technique for dealing with scale and rotation sensitivity is the use of composite filters, that is, filters with multiple images stored on them. Thus if a target is sought with size and orientation within specified limits, there is a tradeoff

available to a designer between the number of different filters required and the number of images put on each filter. Simulations with multiple image filters suggest that correlation peak degradation is not severe if the rotated images are not too different. Because of this consideration, a recommended design procedure, assuming a target is to be located when its size and orientation are only known within specified limits, is to place several (perhaps 3 to 5) different rotations of the image on a single filter, and prepare several such filters at different scales.

V. SIMULATIONS

A set of programs was written to permit simulating correlator operation for various images and filters. The program package is designed for use with 128 x 128 pixel matrices, since this is the resolution of the Semetex magnetooptic spatial light modulator available for laboratory verification of designs suggested in this report.

The binarized plane image used throughout this simulation series is shown in Figure 2a. The representation for the plane rotated 8 degrees downward is shown in Figure 2b. The distortion caused by the limited resolution is clearly evident. In the simulations that follow, centered plane means that the plane is in the center of the scene. Offset plane means that the plane is located entirely in one quadrant, normally the lower right quadrant.

Binarized white noise has been added in a number of the simulations. In every case where noise is added, the noise intensity is such that on the average, every fourth pixel is changed in value.

Each correlation simulation has marked on it Cor.Pk.

(correlation peak intensity), PSR (peak to sidelobe ratio), and SNR (signal to noise ratio), but not all these quantities were calculated in each case. A correlation peak value is given for each simulation, but a PSR is more appropriate to a noise-free case and an SNR is more appropriate to an added-noise case, so in most cases only one or the other is calculated. The PSR is defined as the ratio of the correlation peak intensity to the average response for everything but the top half of the correlation peak. The SNR is the standard definition, the ratio of the peak correlation intensity to the average noise intensity.

Figure 3 is a comparison of a BPOF, CPOF (continuous phase-only filter), and an MF (matched filter). The relative correlation peak intensities are 23.7, 51.5, and 1.0, respectively. The BPOF is an approximation to the CPOF, and the cost of approximating is about half the intensity in this instance. The MF response is quite different in character, much shorter and broader. The PSRs for the three filters are 1590 (32 dB), 3900 (35.9 dB), and 218 (23.4 dB), respectively. Since this is a noise-free case, no SNR (signal to noise power ratio) is calculated.

Figure 4 is the same as Figure 3, except this time noise has been added, of sufficient intensity that on the average every fourth pixel's value is changed. The BPOF's correlation peak intensity is now 9.8, and the PSR and SNR are both 39.2 (15.9 dB). Corresponding values for the CPOF are 15.2 for the correlation peak and 58.7 (17.7 dB) for both the PSR and SNR. Numbers for the matched filter response are 0.55 for the correlation peak, 8.1 (9.1 dB) for the PSR, and 590 (27.7 dB) for the MF.

In the correlations of Figure 5, the BPOF's active area is reduced to its central 32x44 portion, so only 1408 of the

filter's 16,384 pixels are used. The bandwidth was selected to include 4 sinc function cycles of the plane's envelope in the x and y directions. The response of a reduced-bandwidth BPOF is much like that of a matched filter. TPAFs were constructed for several threshold values. The responses look much like those obtained for reduced-bandwidth POFs.

Figure 6 shows results from simulations using 3-plane composite filters. The results indicate that, at least for this particular target, the penalty for including several rotated images in one filter is not severe.

VI. CONCLUSIONS

1. Phase-only filters in optical correlators are a remarkably versatile tool. Filter designs can be tailored to fit a wide variey of situations.
2. A target can be reasonably discriminated from clutter if its extent is at least 10s of pixels, and preferably 100s of pixels.
3. The theoretical base for phase-only filtering is fairly complete, except that no general results regarding geometry are yet available. Several areas are in need of further development (composite-filter encoding, tradeoffs involved in filter bandwidth limiting, etc.).
4. New SLM devices just now becoming available or presently being developed will produce dramatic improvements in the capabilities of optical correlators.
5. Because of the need to address and write onto SLMs, any practical optical correlator will be a hybrid, a computer plus optical device combination. The computer capability needed is quite modest if the computer is not called upon to process data.

VII. RECOMMENDATIONS

1. While the basic theory of phase-only filtering is fairly

complete, further development is needed in a number of areas.

2. There is a need to do simulations involving the types of background clutter typical of real scenes.

3. There is an urgent need to develop hardware correlators to verify simulations and explore limitations.

ACKNOWLEDGMENTS

The sponsorship of the Air Force Systems Command, Air Force Office of Scientific Research, and Rome Air Development Center is gratefully appreciated. I also very much appreciated the opportunity to work with my mentor, Andrew R. Pirich of the Photonics Center, RADC.

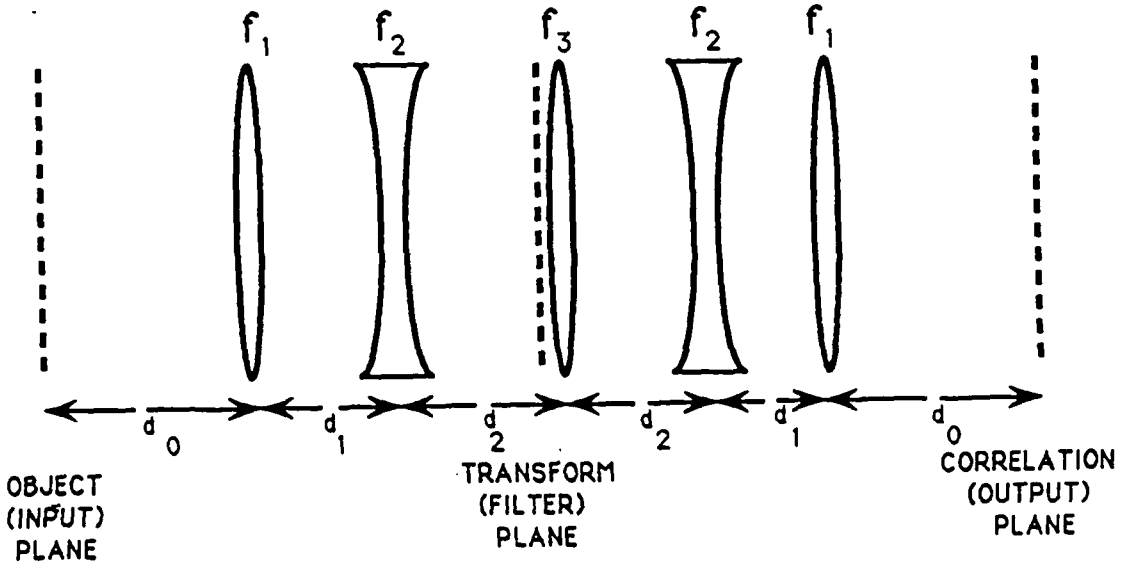

Design equations: A known value for $f_{equiv} = \frac{N_3 \Delta x_1 \Delta x_2}{\lambda}$ is assumed.

1. Choose a positive f_1 and a negative f_2.

Then $d_1 = f_1 + f_2 - \frac{f_1 f_2}{f_{equiv}}$; $d_2 = \frac{1 - \frac{d_1}{f_1}}{\frac{1}{f_1} + \frac{1}{f_2} - \frac{d_1}{f_1 f_2}}$

2. Choose a positive $f_3 \geq \frac{0.5 d_2^2}{w_1 - d_2}$, for $\frac{1}{w_1} = \frac{1}{d_1} + \frac{1}{d_2} - \frac{1}{f_2}$,

& solve for d_0 via

$$\frac{1}{d_0} = \frac{2 w_1^2 f_3}{d_1^2 [2 f_3 (d_2 - w_1) - d_2^2]} - \frac{1}{d_1} + \frac{1}{f_1} + \frac{w_1}{d_1^2}$$

Special cases: For $d_0 = 0$, $f_3 = \frac{0.5 d_2^2}{w_1 - d_2}$

For $f_3 = \infty$ (no f_3), $\frac{1}{d_0} = \frac{w_1^2}{d_1^2 (d_2 - w_1)} - \frac{1}{d_1} + \frac{1}{f_1} + \frac{2 w_1}{d_1^2}$

Figure 1. Flexible correlator geometry and design equations.

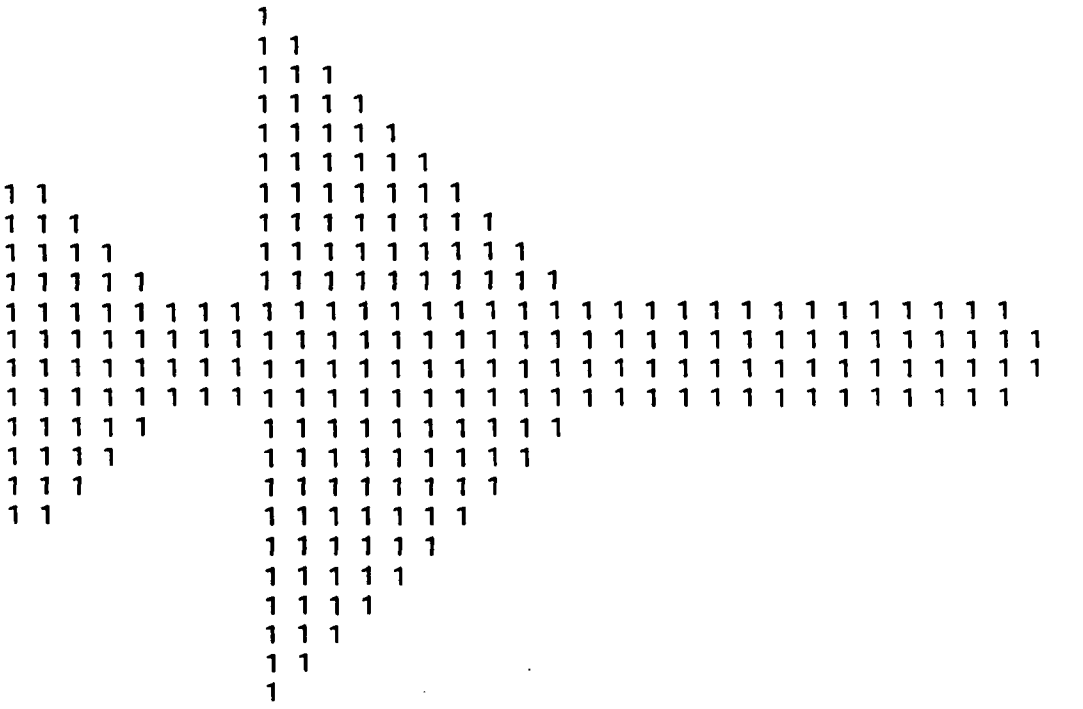

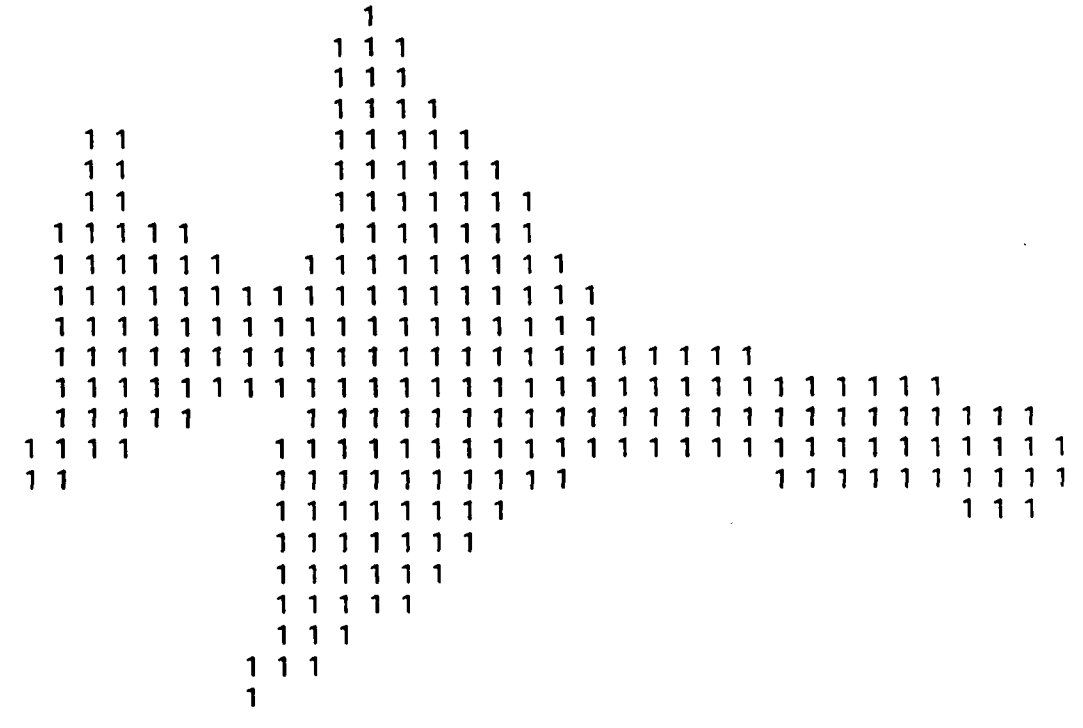

Figure 2. (a) Binarized plane image used throughout the simulation series.
(b) Image of plane rotated 8 degrees downward.

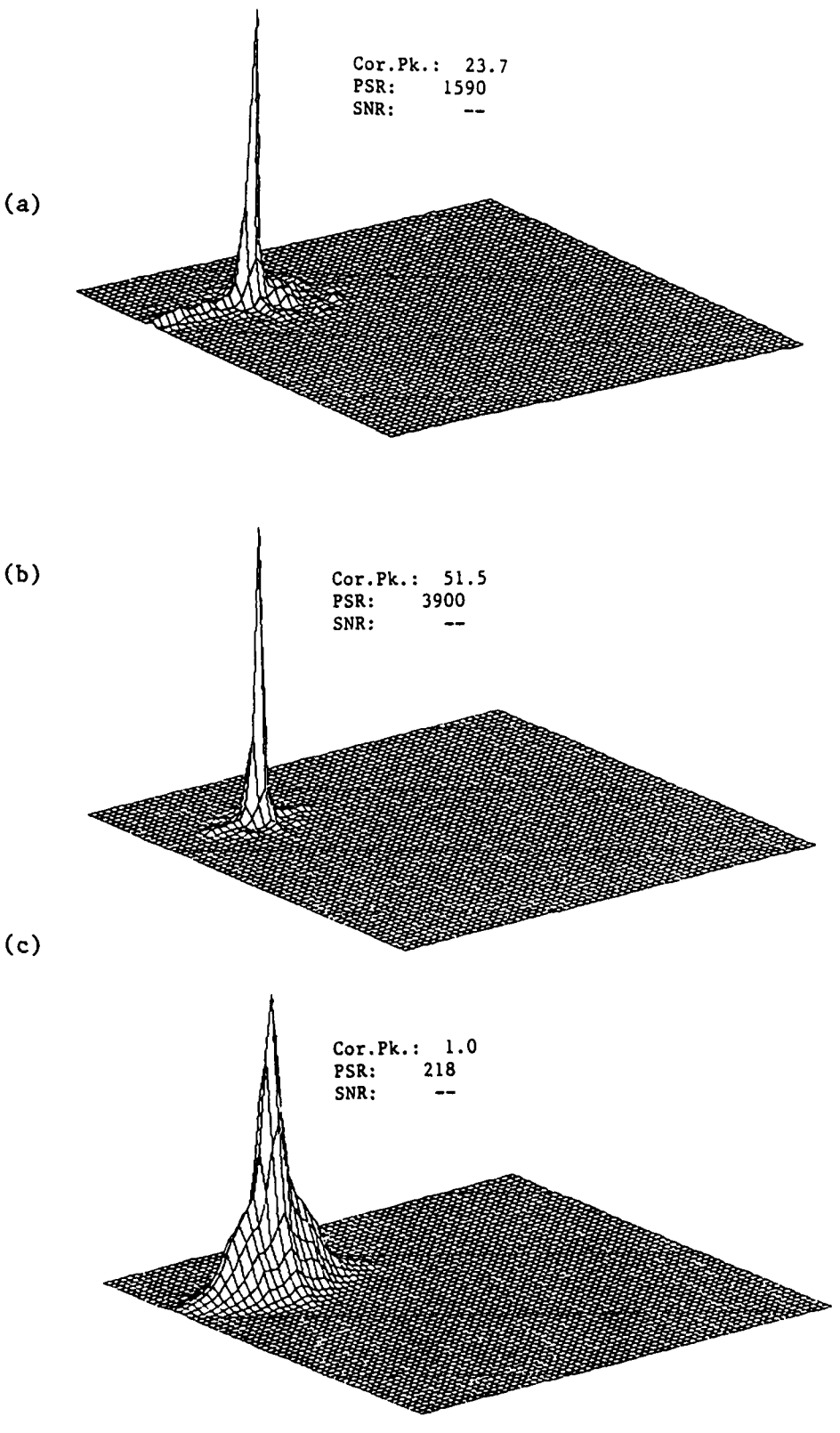

Figure 3. Correlations of an offset plane image with an (a) BPOF, (b) CPOF, and (c) MF for a centered plane image. Each graph is normalized to the same amplitude.

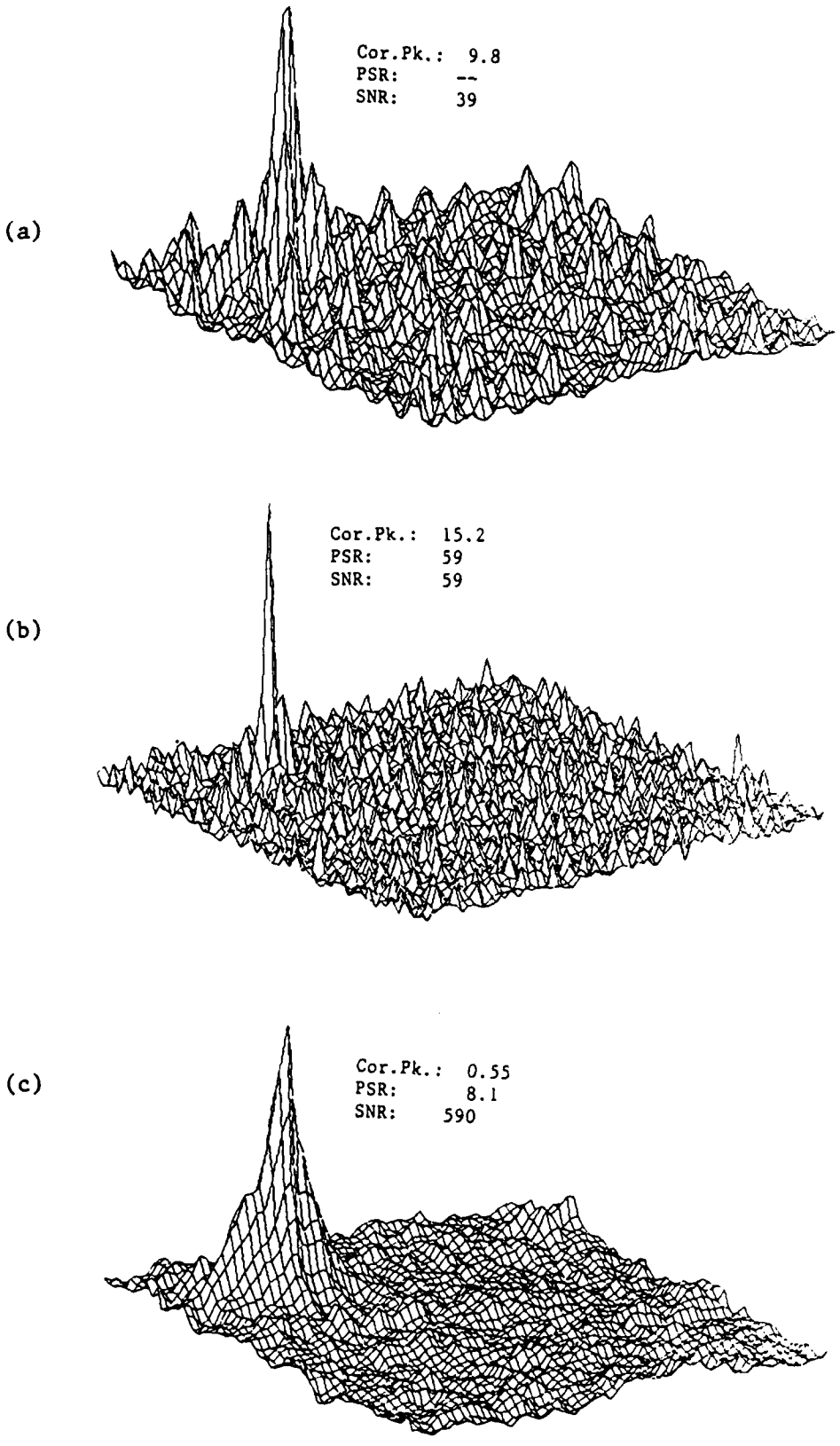

Figure 4. Same as Figure 13, but with noise added.

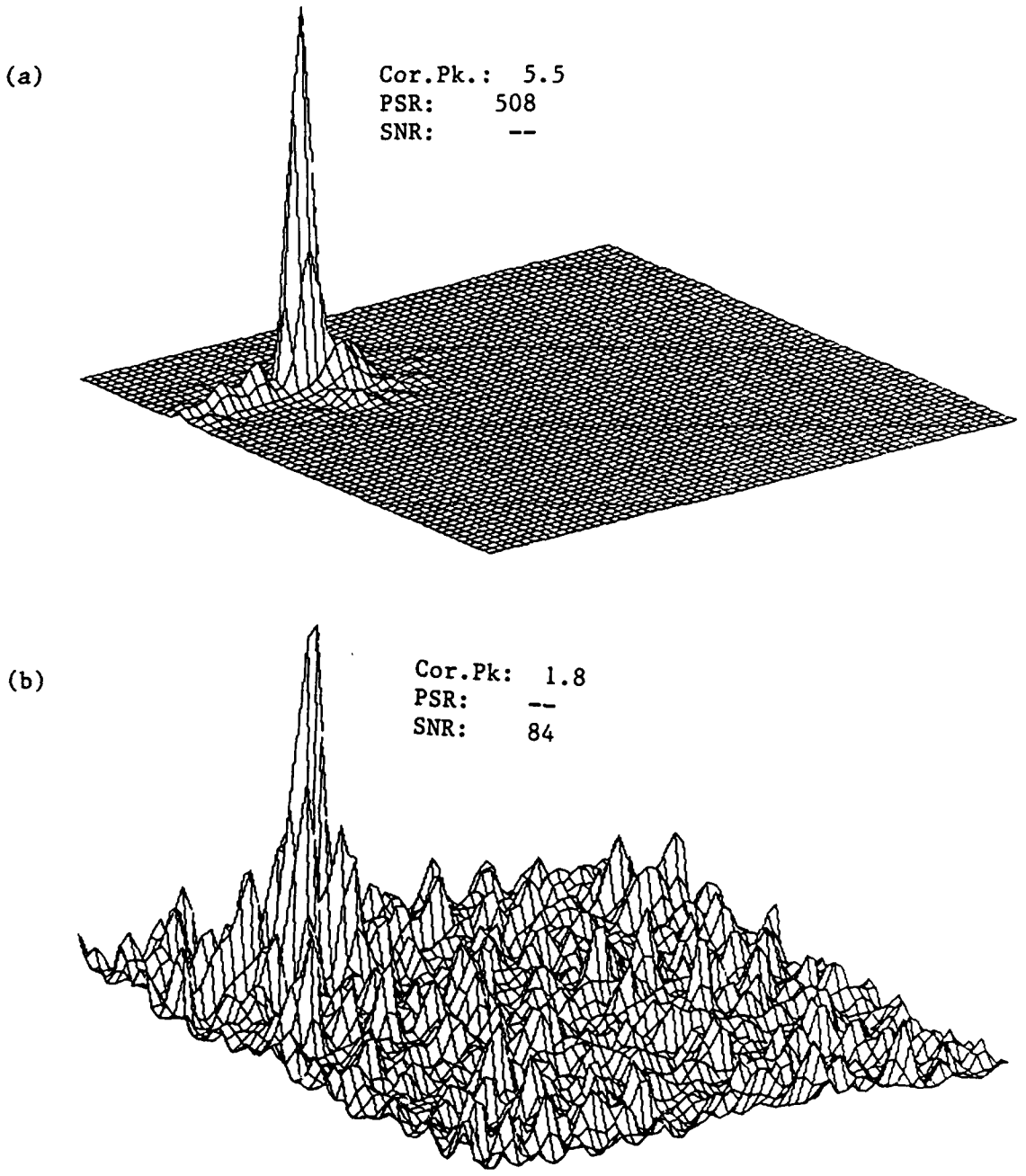

Figure 5. Correlation of an offset plane image with a reduced-bandwidth BPOF for (a) noise-free case, and (b) added noise case.

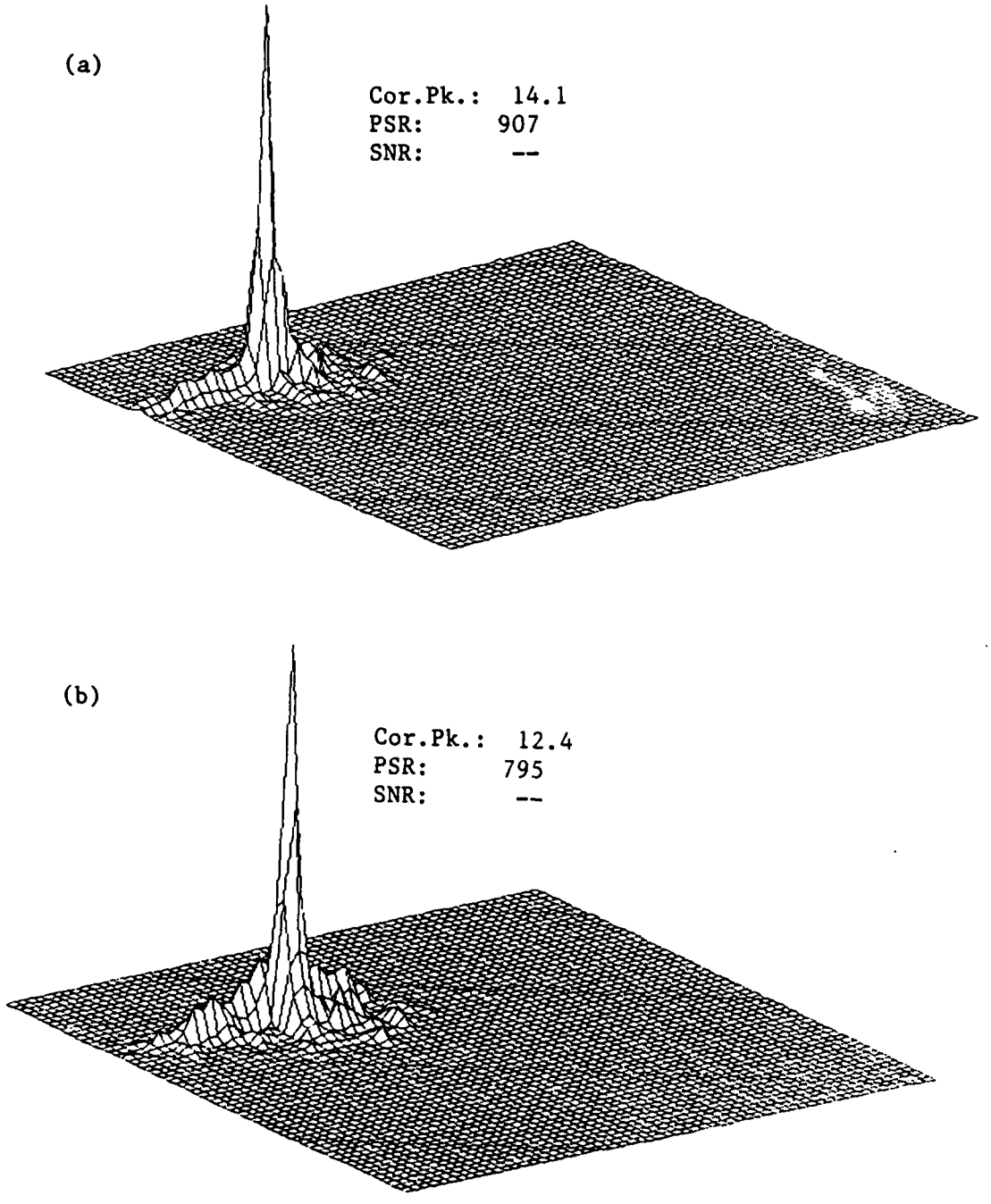

Figure 6. Correlations of (a) an offset plane, and (b) an offset plane rotated downward 8 degrees, with a composite BPOF made from a centered plane, one rotated 8 degrees downward, and one rotated 8 degrees upward.

1989 USAF-UES Summer Faculty Research Program/
Graduate Student Research Program

Sponsored by the
AIR FORCE OFFICE OF SCIENTIFIC RESEARCH
Conducted by the
Universal Energy Systems, Inc.

FINAL REPORT

A Computer Model for Temporal Frequency Spectrum of Vegetation Clutter Return

Prepared by:	Jay K. Lee / Lynda Tomlinson
Academic Rank:	Assist. Professor / Grad. Student
Department and University:	Electrical and Computer Engineering Syracuse University
Research Location:	Rome Air Development Center Griffis AFB Rome, NY 13441
USAF Researcher:	Michael Wicks
Date:	August 15, 1989
Contract No:	F49620-88-C-0053

A Computer Model for Temporal Frequency Spectrum of Vegetation Clutter Return

by

Jay K. Lee and Lynda Tomlinson

ABSTRACT

A computer model that incorporates polarization information is developed for predicting the temporal frequency spectrum of the clutter return from forest vegetation at C-band and S-band based on the geometric and physical parameters of the vegetation.

It is assumed at these frequencies the predominant backscattering occurs from leaves in the forest canopy. A multiple scattering model that incorporates vegetation density, moisture content of leaves and correlation lengths as adjustable parameters is used to calculate the radar cross section of the stationary canopy for both horizontal and vertical polarization.

The temporal frequency spectrum of the backscattered radiation is estimated under windy conditions, by assuming the leaf velocity in the direction of incident radiation is described by a quasi-harmonic oscillation.

The effect of adjustable parameters on the resulting spectrum is anaylzed.

ACKNOWLEDGMENTS

We would like to thank the Rome Air Developement Center, the Air Force Office of Scientific Research, and Universal Energy Systems for this research opportunity.

Several individuals at RADC contributed significantly to our research effort and overall experience. We would like to thank Michael Wicks, Russell Brown, and Vincent Vannicola for their technical guidance. Ronald Blackall and Zenan Pryk were especially helpful and patient in their instruction on use of the computer system used at RADC and the quirks of Vax C. We would especially like to thank James Michels for his hospitality and many interesting technical discussions. We would also like to thank Cliff Tsao, Anthony Lovaglio, and Anthony Lattanzio for their interest and for helping us to feel confortable at RADC.

I. INTRODUCTION:

An important goal in the design of a radar system is the reduction of radar clutter. A significant portion of this clutter in many rural areas can be attributed to moving forest vegetation.

Numerous clutter models have been developed based on assumed statistical properties of the target and clutter returns, most assuming those returns to be stationary and homogeneous. On the other hand, very few vegetation clutter models have been developed based on the statistical and physical properties of the vegetation.

The Signal Processing Section at RADC is interested in developing a clutter model based on the physical properties of the vegetation to be used to help evaluate the models based on the statistical properties of the clutter returns.

II. OBJECTIVE OF THE RESEARCH EFFORT:

The objective of this research effort is the developement of a model based on the physical characteristics of forest vegetation that incorporates polarization information and is capable of predicting the spectral content of the clutter return and the backscattered power received by an MTI radar operating at S-band or C-band. Various probabilistic models for clutter and target scattering have been proposed and developed, but most are based on hypothesized characteristics of the return signal rather than the electromagnetic properties of the vegetation.

The computer model developed uses the concepts from a static model presented by Fung and Ulaby in 1978 [1] and the clutter model of Rosenbaum and Bowles, presented in 1974 [2].

III. MODEL AND ANALYSIS

A. Model Assumptions

The computer model developed for analyzing the clutter spectrum of forest vegetation is constrained by the following assumptions.

1. There is a negligable return from ground reflections, branches, and trunks.
2. The leaves have no azimuthally preferred orientation.
3. The movement of the leaves in the direction of incident radiation is a quasi-static oscillation where the phase, frequency of oscillation and displacement magnitude are mutually independent, wide-sense stationary processes. In addition, the displacement magnitude is Rayleigh distributed and the phase is uniformly distributed between $-\pi$ and π.
4. The velocity of the scattering centers (leaves) is a stationary function of time.
5. The wind velocity is a slowly varying function of time. (The velocity of leaves is much smaller than the velocity of wave propagation.)
6. The detailed variation of the leaf canopy is not appreciablly changed under windy conditions. (ie. The permittivity of the canopy is independent and uncorrelated with the leaf movement.)
7. The volume of leaves is normally less than 1% of the total air-leaf volume.
8. When the leaf-air medium is treated as a dielectric, the correlation length of the dielectric constant's correlation function is less than the wavelength.

B. Formulation of Model

The temporal frequency spectrum of the backscattered field, $W_s(w)$, is [6]

$$W_s(w) = \{2n_o P_t \lambda^2/(4\pi)^2\} \int [W_\sigma(\hat{1},\hat{1},w)G^2(\hat{1})/R^4]\, dV \quad (1)$$

where n_o is the intrinsic impedance of free space, P_t is the transmitted power, $G(\hat{1})$ is the gain of the receiver (assumed to be equal to the gain of the transmitter), and R is the range to the incremental volume, dV. $W_\sigma(\hat{1},\hat{i},w)$ is the spectrum of the radar cross section

$$W_\sigma(\hat{1},\hat{i},w) = 2 \int \sigma(\hat{1},-\hat{i},\tau)\exp[jw\tau]d\tau \quad (2)$$

where $\sigma(\hat{1},-\hat{i},\tau)$ is the radar cross section, $\hat{i}$ is the direction of incident radation and τ implies a wide-sense stationary process.

When the permittivity of the volume scatterer and the velocity of the scattering centers are independent and uncorrelated, the radar cross section can be expressed in terms of the radar cross section of the stationary volume scatterer, $\sigma(\hat{i},-\hat{i})$, as shown below.

$$\sigma(\hat{i},-\hat{i},\tau) = \sigma(\hat{i},-\hat{i}) \langle \exp[j\bar{k}_s \cdot \bar{v}\tau] \rangle_v \quad (3)$$

($\langle \cdot \rangle_v$ indicates an average over the variable, $\bar{v}$, $\bar{k}_s$ is the propagation vector of the scattered field, and $\bar{v}$ is the velocity of a scattering center.) Now, (2) is reduced to

$$W_\sigma(\hat{i},\hat{i},w) = 2\sigma(\hat{i},-\hat{i})I_\sigma \quad (4)$$

where I_σ is

$$I_\sigma = \int \langle \exp[j\bar{k}_s \cdot \bar{v}\tau] \rangle_v \exp[jw\tau]\, d\tau. \quad (5)$$

When I_σ is independent of position, the temporal frequency spectrum of the backscattered field is

$$W_s(w) = I_\sigma\{4n_o P_t \lambda^2/(4\pi)^2\}\{\int [\sigma(\hat{1},\hat{1})G^2(\hat{1})/R^4]\, dV\} \quad (6)$$

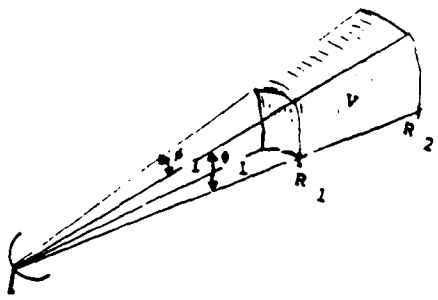

Figure 1: Narrow Beam Monostatic Radars

For a narrow beam radar system, the radar cross section does not vary appreciably over the irradiated volume and can be removed from the integral for the temporal frequency spectrum of the backscattered field. Using the method outlined in [5], the gain function, $G(\hat{i})$, is approximated by the Gaussian function

$$G(\hat{i}) = G(\hat{i}_o)\exp\{-\ln 2[(2\theta/\theta_1)^2+(2\phi/\phi_1)^2]\} \tag{7}$$

where $\hat{i}_o$ is the unit vector from the transmitter to a reference point in the volume, V, θ and ϕ are angles measured from i_o (see Figure 1), and θ_1 and ϕ_1 are the half-power beamwidths in the θ and ϕ directions.

Substituting (7) into (6) results in the following simplified expression

$$W_s(w) = I_\sigma \{n_o P_t \lambda^2 G^2(\hat{i}_o)\pi\theta_1\phi_1/[2\ln 2(4\pi)^3]\} \{\int_{R_1}^{R_2}[\sigma(\hat{i},\hat{i})/R^2]dV\} \tag{8}$$

where the gain, $G(\hat{i}_o)$, can be approximated by [5]

$$G(\hat{i}_o) = \pi^2/\theta_1\phi_1 \ . \tag{9}$$

The scattering matrix, [S], for two general orthogonal polarizations is shown below.

$$[S] = \begin{bmatrix} S_{11} & S_{12} \\ S_{21} & S_{22} \end{bmatrix} \tag{10}$$

The radar cross section is related to the scattering coefficient by the relationship [7]

$$\sigma_{jk}(\hat{i},\hat{i}) = 4\pi R^2|S_{jk}|^2 = 4\pi R^2\alpha_{jk} \tag{11}$$

Substituting (9) and (11) into (8) results in the simplified expression for the temporal frequency spectrum of the backscattered field,

$$W_s(w) = \{I_\sigma n_o P_t \lambda^2 (R_2-R_1)\alpha_{jk}\ \pi\}/[16\ln 2] \approx 13.35\{I_\sigma P_t \lambda^2 (R_2-R_1)\alpha_{jk}\} \tag{12}$$

In order to compute I_σ the velocity of the scattering centers must be known. For the case where the scattering centers are modeled as quasi-harmonic oscillators, the velocity, $\bar{v}(\bar{r},t)$, in the direction of incident radiation is

$$v(\bar{r},t) = v_o \cos[\Omega t + \xi] \tag{13}$$

where v_o, Ω, and ξ are wide sense stationary, time independent, random functions of $\bar{r}$.

Integrating (13) from t=0 to t=τ yields

$$\int_o^\tau v(\bar{r},t)\, dt = p_o \{\sin[\Omega\tau + \xi] - \sin\xi\}, \tag{14}$$

where p_o is v_o/Ω. For the backscatter case, the time dependent term in (3) can now be expressed as

$$\langle \exp[j\bar{k}_s \cdot \bar{v}\tau] \rangle_v = \langle \exp[j2k \int_o^\tau v(\bar{r},t)\, dt \rangle_v \tag{15}$$

where k is the propagation constant of free space. Using the identity

$$\exp[j2kp_o \sin(\Omega\tau + \xi)] = \sum_{n=-\infty}^{\infty} J_n(2kp_o)\exp[jn(\Omega\tau + \xi)] \tag{16}$$

(where J_n is an nth order Bessel function of the first kind) and substituting (14) into equation (15) results in the following equality.

$$\langle \exp[j\bar{k}_s \cdot \bar{v}\tau] \rangle_v = \langle \exp[j2kp_o \sin\xi] \{\sum_{n=-\infty}^{\infty} J_n(2kp_o)\exp[jn(\Omega\tau + \xi)]\} \rangle_v . \tag{17}$$

Substituting (17) into (5) and interchanging the integration and averaging processes results in the following expression for I_σ in terms of the random functions p_o, Ω, and ξ:

$$I_\sigma = \langle \exp[j2kp_o \sin\xi] \{\sum_{n=-\infty}^{\infty} J_n(2kp_o)\exp[jn\xi] \int \exp[j(n\Omega+w)\tau] d\tau\} \rangle_v . \tag{18}$$

Performing the integration in (18) reduces the expression for I_σ to

$$I_\sigma = 2\pi \langle \exp[j2kp_o \sin\xi] \{\sum_{n=-\infty}^{\infty} J_n(2kp_o)\exp[jn\xi]\ \delta(n\Omega+w)\} \rangle_v . \tag{19}$$

When p_o, Ω, and ξ are mutually independent, the averaging over the distribution of v is equivalent to a sequential averaging over the distributions of p_o, Ω, and ξ. Assuming a uniform distribution for ξ,

$$f(\xi) = \begin{cases} 1/(2\pi) & -\pi < \xi < \pi \\ 0 & \text{elsewhere} \end{cases} \tag{20}$$

results in the following equality

$$\langle \exp[j2kp_o \sin\xi + jn\xi] \rangle_\xi = J_n(2kp_o). \tag{21}$$

Now, (19) can be rewritten as

$$I_\sigma = 2\pi \{ \sum_{n=-\infty}^{\infty} \langle J_n^2(2kp_o) \rangle_{po} \langle \delta(n\Omega+w) \rangle_\Omega \}. \tag{22}$$

For the case where p_o is Rayleigh distributed,

$$f(p_o) = \begin{cases} (1/p^2) p_o \exp[-\frac{1}{2}(p_o/p)^2] & p_o \geq 0 \\ 0 & p_o < 0 \end{cases} \tag{23}$$

(p_o=p at the maximum of the distribution) and Ω has the following arbitrary distribution,

$$f(\Omega) = \begin{cases} P(\Omega) & \Omega \geq 0 \\ 0 & \Omega < 0 \end{cases} \tag{24}$$

(22) is reduced to [2]

$$I_\sigma = 2\pi \exp[-4k^2p^2] \{ I_o(4k^2p^2)\delta(w) + \sum_{n=1}^{\infty} I_n(4k^2p^2)[P(w/n)+P(-w/n)]/n \}. \tag{25}$$

where $I_n(\cdot)$ is an nth order modified Bessel function of the first kind.

The physical interpretation of (25) is evident upon noting that $P(\Omega)$ describes the distribution of scattering center resonance frequencies. There are essentially two parts. The summation term represents the spectrally modified portion of I_σ due to the movement of the scattering centers. This function is symmetrically distributed about the origin. The $\delta(w)$ term is the unmodified portion of I_σ that would not contribute to the detected, received power in an MTI radar system. The $\delta(w)$ singularity is the result of assuming a monochromatic transmitted signal. For the case where p=0, there is no movement of the scattering centers and the spectrally modified portion of I_σ disappears. An increase in p implies an increase in movement of the scattering centers and a larger portion of I_σ becomes spectrally modified.

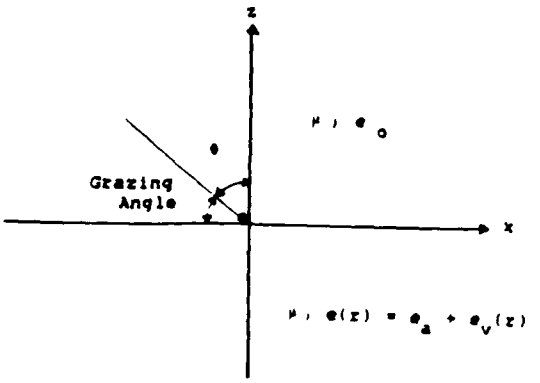

Figure 2: Geometry of the Stationary Model

The radar cross section for the stationary forest canopy is modeled as an inhomogeneous half-space of leaves and air using the method presented by Fung and Ulaby [1] (see Figure 2). The leaf-air half-space has the following random, wide-sense stationary permittivity function with a constant mean, e_a and a fluctuating part, $e_v(r)$.

$$e(r) = e_a + e_v(r) \qquad (26)$$

The method used to determine the scattered field in the air region (z>0) is summarized below. A more thorough treatment of the procedure can be found in [3] or [4](pages 1072 to 1079).

First the half-space Green's functions are determined in the homogeneous medium (z>0) as well as in the random medium (z<0). Then the effective propagation constants for the coherent (or mean) electric fields are determined using Dyson's equation under the assumptions of monochromatic excitation and that the correlation functions for both the real and imaginary parts of the permittivity in the random medium are the same and are statistically independent. Using the assumptions that the correlation function is cylindrically symmetric (ie, isotropic in the xy plane) and the correlation length is very short, the effective propagation constants for the coherent fields are determined using a perturbation approach with first-order correction term.

This analysis gives rise to two effective propagation constants. The first, k_{e1}, is a propagation constant with small losses and the second, k_{e2}, is highly lossy and represents propagation in a transition layer near the boundary z=0. They are given by

$$k_{e1} \approx [k_a^2-k^2\sin^2\theta]^{1/2} - j(I/l_z)/\{[k_a^2-k^2\sin^2\theta]^{1/2}\,[k_a^2-k^2\sin^2\theta+(1/l_z)^2]\} \quad (27)$$

and

$$k_{e2} \approx -I/\{[k_a^2-k^2\sin^2\theta]^{1/2}\,[k_a^2-k^2\sin^2\theta+(1/l_z)^2]\} - j/l_z \quad (28)$$

where l_z is the correlation length in the z-direction (under the assumption that $kl_z<<1$), θ is the angle of incidence (from zenith), k is the free-space propagation constant and k_a is the average propagation constant in the random medium,

$$k_a = 2\pi f[\mu\epsilon_a]^{1/2} \quad , \quad (29)$$

(μ is the permeability of free space and f is the frequency). The term, I, is the double integral

$$I=[k^4l^2\epsilon_e/(4\pi)] \iint [1+l^2(k\sin\theta+k_x)^2+l^2k_y^2]^{-3/2}[k_a^2-k_x^2-k_y^2]^{-1/2}dk_x dk_y \quad (30)$$

where ϵ_e is the variance of the fluctuating part of the permittivity, l is the azimuthal correlation length, and k_x and k_y are integration variables corresponding to propagation constants in the x and y directions. This integral is transformed into cylindrical coordinates. A second order binomial expansion is used to simplify the $[\cdot]^{-3/2}$ term. The integration is performed over an angular interval of 0 to 2π and a radial interval of 0 to $|k_a|$, reducing (30) to

$$I=[k^4l^2\epsilon_e/(4\pi)]\{|k_a|\pi[2-3k^2l^2\sin^2\theta-2|k_a|^2l^2+|k_a|^4l^4 +10|k_a|^2k^2l^4\sin^2\theta+15k^4l^8|k_a|^4\sin^4\theta/4]\} \quad (31)$$

The magnitude of the coherent electric field in the random medium has the form

$$Ea = A\exp[-jkx\sin\theta] \{\exp[jk_{e1}z]-[(1-jk_{e2}l_z)/(1-jk_{e1}l_z)]\exp[jk_{e2}z]\} \quad (32)$$

where A varies as a function of incident polarization.

This amplitude term is calculated by matching boundary conditions at z=0 for both horizontal polarization, A_h (the electric field is y-directed), and vertical polarization, A_v (the electric field is perpendicular to the direction of propagation and to the y-direction).

The amplitude terms are

$$A_h = \frac{2k\cos\theta}{\{k\cos\theta + k_{e1} - (1-jk_{e2}l_z)(k\cos\theta+k_{e2})/(1-jk_{e1}l_z)\}} \quad (33)$$

and

$$A_v = \frac{2k\cos\theta}{\{k\cos\theta + k_{e1}/e_{e1} - (1-jk_{e2}l_z)(k\cos\theta+k_{e2}/e_{e1})/(1-jk_{e1}l_z)\}} \quad (34)$$

where e_{e1} and e_{e2} are the following relative effective permittivities

$$e_{e1,2} = \sin^2\theta + k^2_{e1,2}/k^2 \ . \quad (35)$$

In the final step of this method, the average power in the homogeneous medium is calculated and the backscattering coefficients are determined. With this method, the cross-polarization terms do not significantly contribute to the backscattered power and the backscattering coefficients are given by

$$\alpha_{hh} = 2k^6 \epsilon_s l^2 \cos^2\theta I_s \ |A_h/[k\cos\theta + (k_a^2 - k^2\sin^2\theta)^{1/2}]|^2 \cdot [1+(2kl\sin\theta)^2]^{-3/2} \quad (36)$$

and

$$\alpha_{vv} = 2*k^6 \epsilon_s l^2 \cos^2\theta I_s \ |A_v/[ke_a\cos\theta + (k_a^2 - k^2\sin^2\theta)^{1/2}]|^2 \cdot [1+(2kl\sin\theta)^2]^{-3/2} \quad (37)$$

where ϵ_s is the sum of the variances of the real and of the imaginary part of the relative permittivity. The term, I_s, is

$$I_s = l_z(1-\mathrm{Re}[D])/[\mathrm{Re}[D](1-2\mathrm{Re}[D]l_z + |D|^2 l_z^2)] \approx l_z/\mathrm{Re}[D] \quad (38)$$

where Re[D] is the real part of D,

$$\mathrm{Re}[D] = \mathrm{Re}\{j[k_{e1} + (k_a^2 - k^2\sin^2\theta)^{1/2}]\} \approx -\mathrm{Im}[k_{e1}] - \mathrm{Im}[k_a]/[1-(k^2\sin^2\theta/\mathrm{re}[k_a]^2)]^{1/2} \quad (39)$$

and Im[·] signifies the imaginary part.

The average relative permittivity of the forest canopy is determined by using the mixing formula

$$e_a = (e_l V_l + V_a)/V \ . \qquad (40)$$

where V_l is the volume of leaves, V_a is the volume of air and V is the total volume of the canopy. The probability of occurrence for the relative permittivity of a leaf, e_l, is V_l/V and the probability of occurrence for the relative permittivity of air (assumed to be 1) is V_a/V.

The leaf is modeled as a mixture of water granules dispersed in a solid material. The relative static permittivity is

$$e_m = 5 + 51.56 \{M/[(dw/ds)(1-M)+M]\} \qquad (41)$$

where M is the moisture content of a single leaf measured on a wet weight basis and dw/ds is the ratio of the density of water to the density of the solid material. The de Loor-Meijboom model,

$$e_l = [5.5+(e_m-5.5)/(1+f^2\tau^2)] - jf\tau(e_m-5.5)/(1+f^2\tau^2) \qquad (42)$$

is used for computing the relative permittivity of the leaf at microwave frequencies. In this model, f is the frequency being considered and τ is the relaxation time of water. The product $f\tau$ is approximated by $1.85/\lambda$ where λ is the wavelength of the excitation in cm.

The variance of the real part of the relative permittivity, c^2_{er}, is estimated to be

$$c^2_{er} \approx (Re[e_l]-Re[e_a])^2 V_l/V + (1-Re[e_a])^2 V_a/V \qquad (43)$$

and the variance of the imaginary part, c^2_{ei}, is estimated to be

$$c^2_{ei} \approx (Im[e_l]-Im[e_a])^2 V_l/V + Im[e_a]^2 V_a/V \qquad (44)$$

From (43) and (44), the variances, ϵ_e and ϵ_s, are given by

$$\epsilon_e = c^2_{er} - c^2_{ei} \qquad (45)$$

and

$$\epsilon_s = c^2_{er} + c^2_{ei} \qquad (46)$$

IV. DISCUSSION

Two parameters in the expression for the temporal frequency spectrum (see(12)) are dependent on the physical parameters of the forest canopy. The scattering coefficient of the stationary canopy, α_{jk}, affects the magnitude of the return as a function of transmission frequency and angle of incidence, and the parameter, I_σ, generally affects the shape of the spectrum.

The magnitude of the backscattering coefficients, α_{hh} and α_{vv}, do not differ significantly from one another for the cases of interest, so all plots are derived using α_{hh}.

The assumed correlation lengths of the fluctuating permittivity in the azimuthal (l) and vertical directions (l_z) affect the magnitude of the scattering coefficients. The vertical correlation length is dependent on the thickness of the leaf and the inclination of the leaves. Its order of magnitude is some fraction of a millimeter. The azimuthal correlation length is chosen so that kl is less than 1. Its value is based on a comparison of the theoretical scattering coefficient to measured data. Figures 3 and 4 illustrate that an increase in the correlation lengths generally increases the magnitude of the scattering coefficient. For this model to be valid the following inequality must be satisfied:

$$\epsilon^3[k^2(l^2+lz^2)]^4 << 1,$$

where ϵ is the variance of the relative permittivity.

The relative volume of leaves is always taken to be a fraction of a percent for this model. The behavior of the scattering coefficient with varing leaf ratio is shown in Figure 5. As the grazing angle is decreased the magnitude of α_{hh} drops much more rapidly for the higher leaf ratio.

There also appears to be a slight increase in α_{hh} with decreasing volume ratio. However, this is probably the result of assuming a planar boundary between the air and the forest canopy.

The ratio of water density to solid density in the leaf does not appear to appreciably affect the magnitude of the scattering coefficient as illustrated in Figure 6. It is chosen to be in the range of 3 to 6 based on measured data presented by Fung and Ulaby [1].

Figure 7 illustrates the affect of percent moisture in the leaves. This parameter is a function of the time of year as well as the climate of a region. The magnitude of the scattering coefficient is generally increased (as expected) with increasing moisture content.

The summation term in (25) for computing I_σ converges rapidly and 10 terms are used to approximate the semi-infinite series. For this model the impulse term is ignored because only the spectrally modified terms are relavent. In the weak wind limit ($kp<<1$), the summation term is adequately represented by the first term. Using the small argument approximation for the modified Bessel function this is approximately

$$4\pi k^2 p^2 \exp(-4k^2p^2)\,[P(w)+P(-w)].$$

The proper choice for $P(\Omega)$ can be determined by comparing normalized measured data taken in weak wind with normalized theoretical data plots of I_σ using appropriate choices for $P(\Omega)$. Since no measured data is available at these frequency bands, data taken using an L-band system [2] is used to compute two probability density functions that may be appropriate candidates.

Figure 8 is a normalized plot of I_σ showing the different effect of two different choices for $P(\Omega)$. The plot is normalized with respect to the magnitude of the spectrum at a frequency of 1 Hz.

The power law density is obtained by curve fitting measured data points in [2] then numerically integrating the function over the w>0 region.

Figure 9 is another normalized plot of I_g illustrating the affect of changing p in (25). An increase in p implies an increase in windspeed.

V. COMMENTS AND RECOMMENDATIONS

As shown in Figure 9, the choice of $P(\Omega)$ dramatically affects the shape of the spectrum at low frequencies. Measured data should be taken under low wind conditions in order to accurately determine $P(\Omega)$ and to validate the model.

No cross-polarization terms appear in the scattering matrix of this model. This is primarily the result of assuming the major scatters to be an azimuthally symmetric distribution of leaves and of using the first-order approximation in the perturbation approach. If cross-polarizations are shown to exist in the experimental data, a correction can be added by considering the contribution of branches or by making the second-order approximation. References [8], [9], and [10] have information that may be useful in modifying the model.

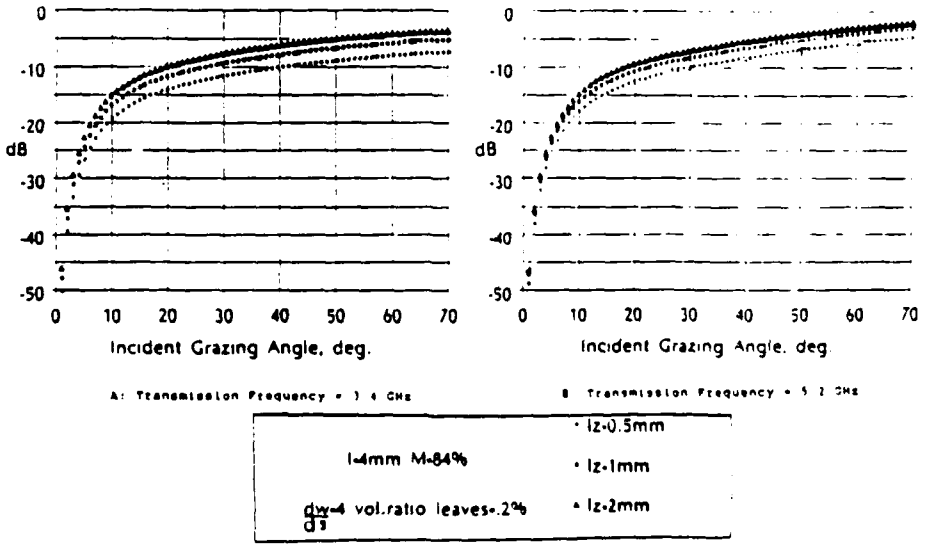

Figure 3: Scattering Coefficient as a Function of Incident Angle and I-Directed Correlation Length

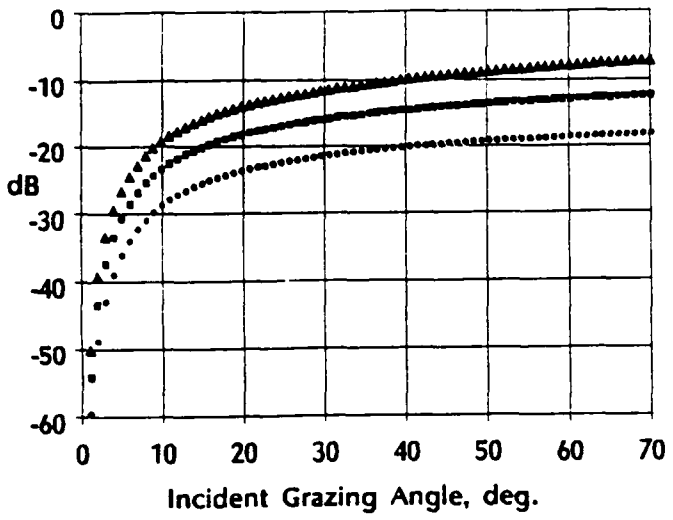

A: Transmission Frequency = 3.4 GHz

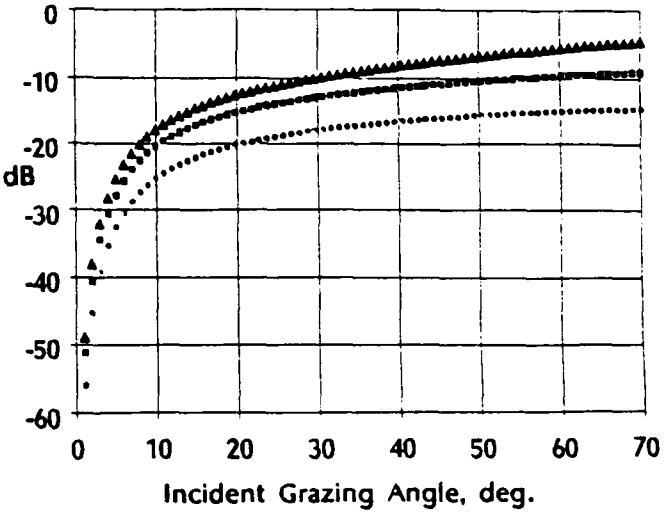

B: Transmission Frequency = 5.2 GHz

lz-0.5mm M-84%

$\frac{dw\text{-}4}{ds}$ vol.ratio leaves-.2%

• l-1mm
• l-2mm
▲ l-4mm

Figure 4: Scattering Coefficient as a Function of Incident Angle and Azimuthal Correlation Length

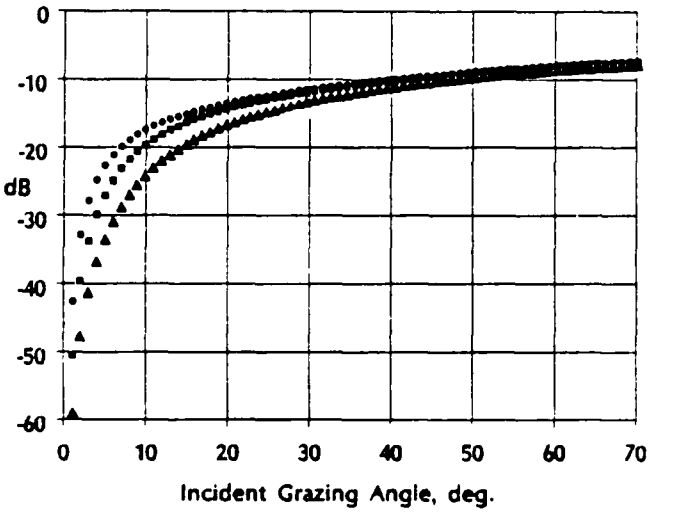

A: Transmission Frequency = 3.4 GHz

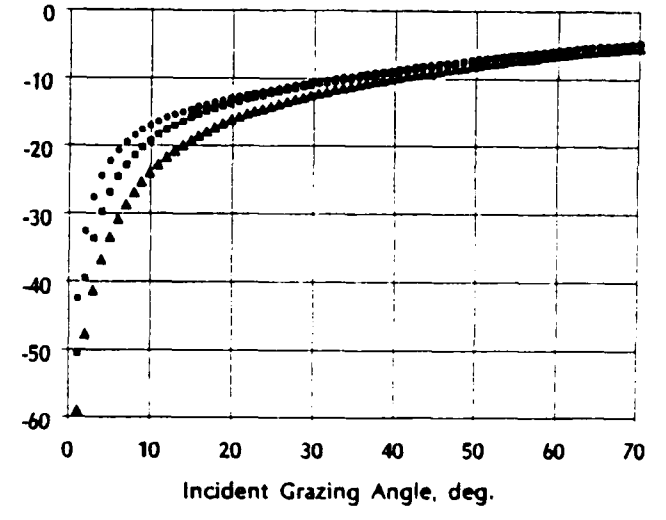

B: Transmission Frequency = 5.2 GHz

l-4mm lz-0.5mm
M-84% $\frac{dw\text{-}4}{ds}$

• vol leaves/vol-0.0005
▪ vol leaves/vol-0.002
▲ vol leaves/vol-0.008

Figure 5: Scattering Coefficient as a Function of Incident Angle and Volume Ratio of Leaves

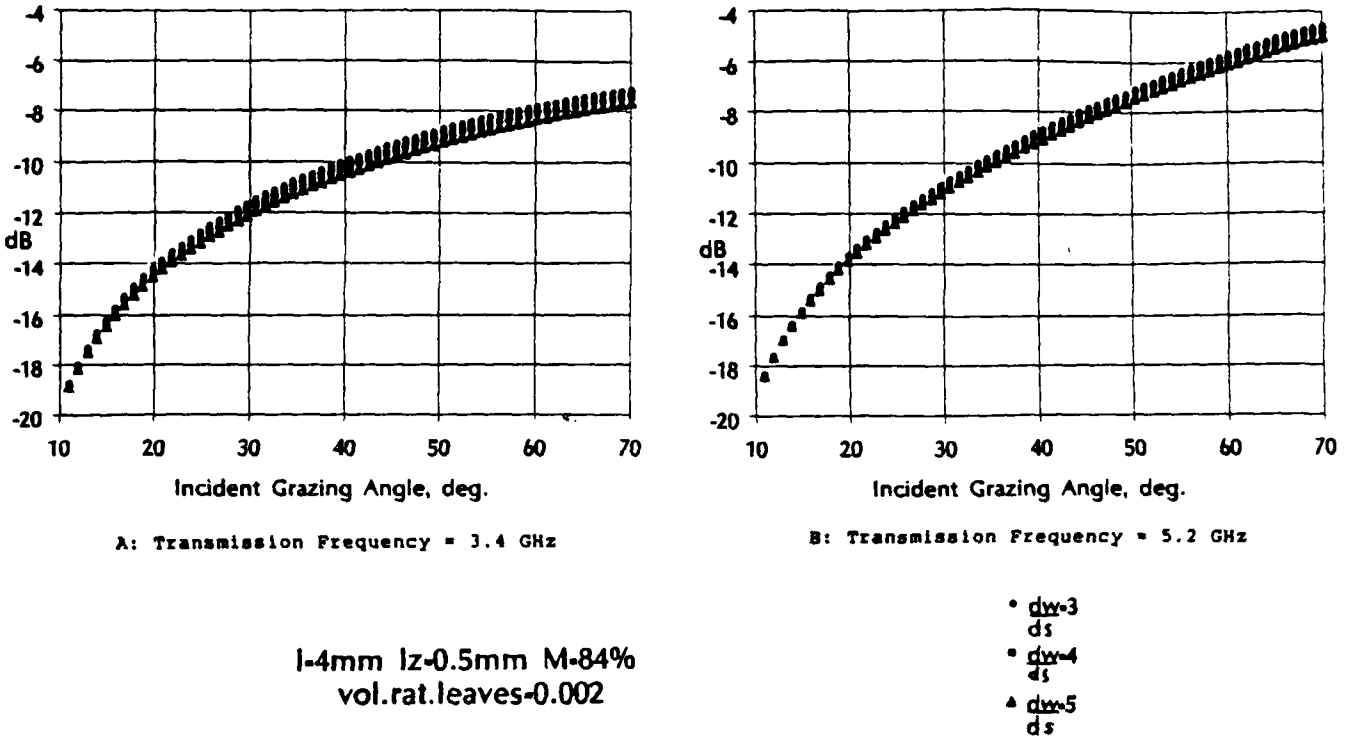

Figure 6: Scattering Coefficient as a Function of Incident Angle and the Ratio of Water Density to Solid Density

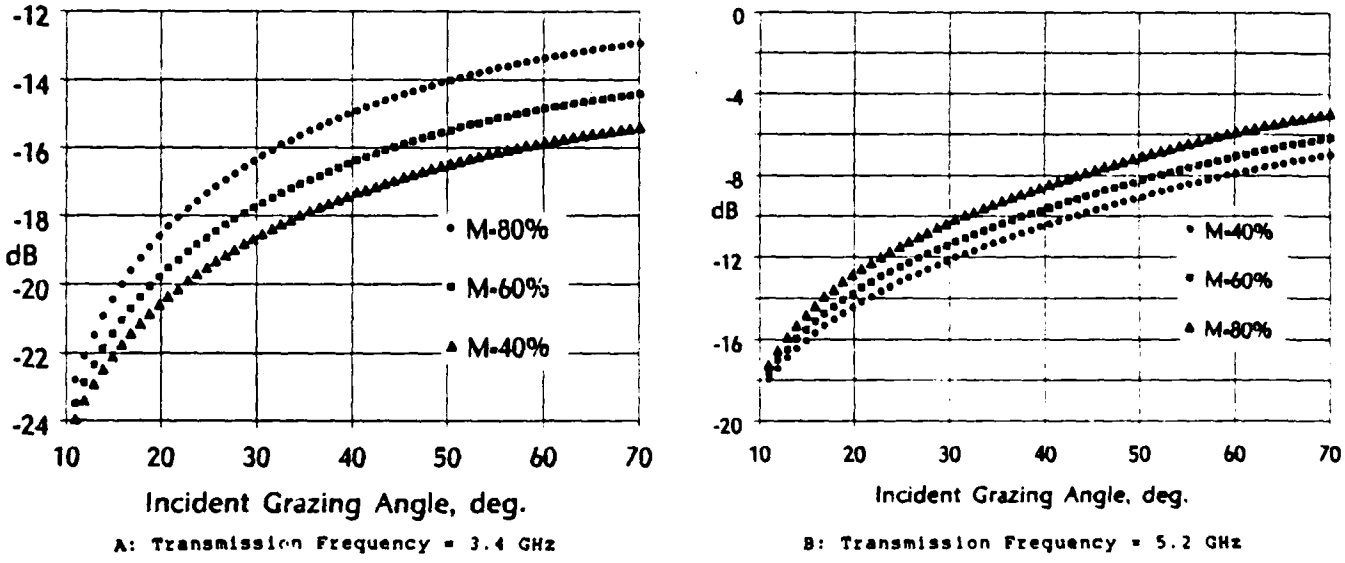

Figure 7: Scattering Coefficient as a Function of Incident Angle and Percent Moisture in Leaves

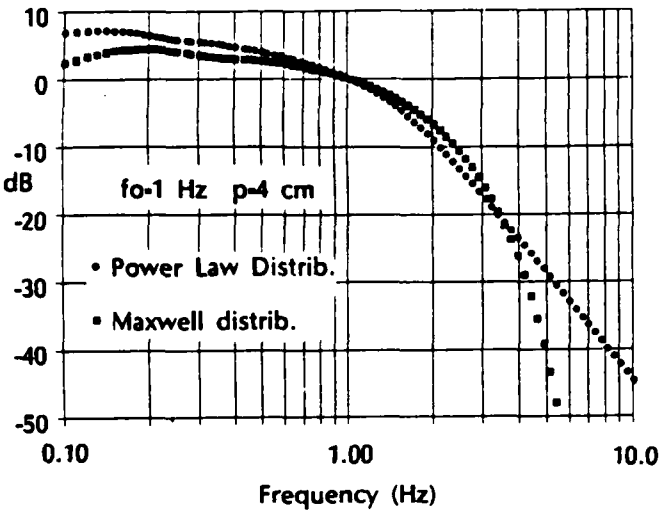

A: Transmission Frequency = 3.4 GHz

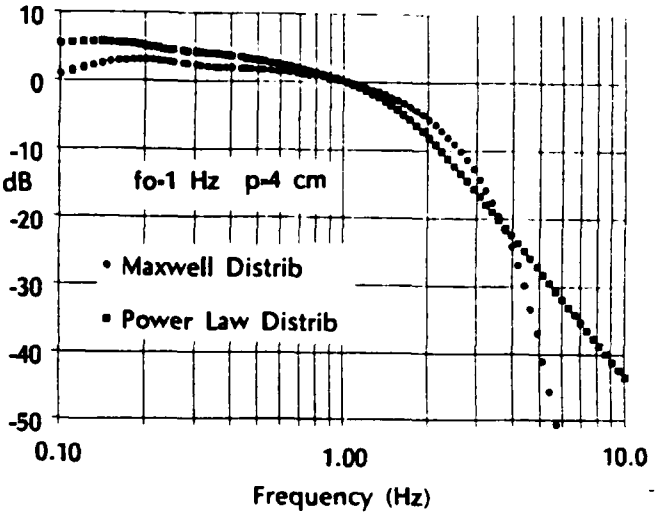

B: Transmission Frequency = 5.2 GHz

Figure 8: Normalized Temporal Frequency Spectrum for Two Choices of P(Ω)

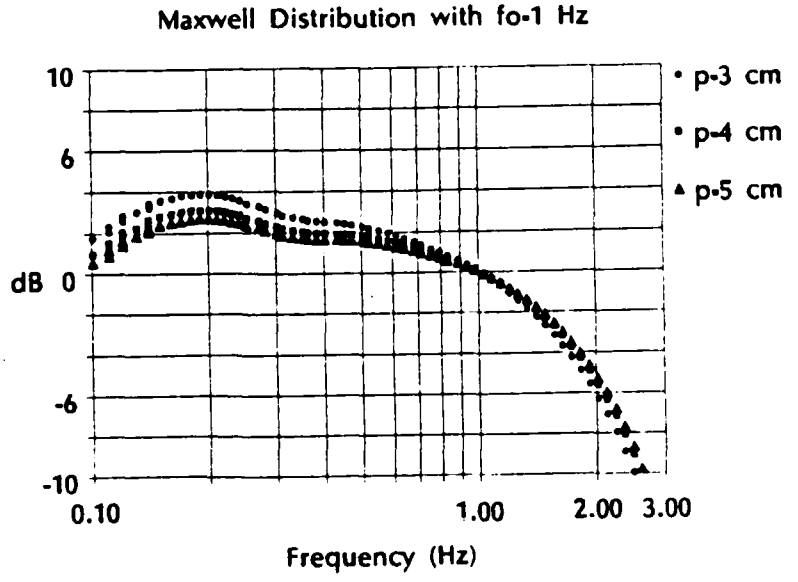

Transmission Frequency = 5.2 GHz

Figure 9: Normalized Temporal Frequency Spectrum for Three Different Wind Conditions

REFERENCES

[1] A.K. Fung and F.T. Ulaby, "A scatter model for leafy vegetation," IEEE Trans. Geosci. Electron., vol. GE-16, no. 4, pp. 281-285, Oct 1978.

[2] S. Rosenbaum and L. Bowles; "Clutter return from vegetated areas," IEEE Trans. Antennas Propagat., vol. AP-22, no. 2, pp. 227-236, March 1974.

[3] A.K. Fung and H.S. Fung; "Application of first-order renormalization method to scattering from a vegetation-like half-space," IEEE Trans. Geosci. Electron., vol. GE-15, no. 4, pp. 281-285, Oct 1977.

[4] F.T. Ulaby, R.K. Moore, and A.K. Fung, Microwave Remote Sensing: Active and Passive, Vol III, Artech House Inc.,1986, Dedham, Mass.

[5] Akira Ishimaru, Wave Propagation and Scattering in Random Media, Vol I, Academic Press, 1978, NY.

[6] Akira Ishimaru,Wave Propagation and Scattering in Random Media, Vol II, Academic Press, 1978, NY.

[7] Ruck, Barrick, Stuart and Krichbaum, Radar Cross Section Handbook, Vol 2, Plenum Press, 1970, NY.

[8] H.S. Tan, A.K. Fung and H. Eom, "A second-order renormalization theory for cross-polarized backscatter from a half space random medium," Radio Science, vol. 15, no. 6, pp. 1059-1065, Nov.-Dec 1980.

[9] G.S. Brown and J.C.Curry, "A theory and model for wave propagation through foliage," Radio Science, vol 17, no. 5, pp. 1027-1036, Sept-Oct 1982.

[10] H.J. Eom and A.K. Fung; "Scattering from a random layer embedded with dielectric needles," Remote Sensing of the Environ., vol. 19, pp. 139-149, 1986.

1989 USAF-UES SUMMER FACULTY RESEARCH PROGRAM

Sponsored by the
AIR FORCE OFFICE OF SCIENTIFIC RESEARCH

Conducted by the
Universal Energy Systems, Inc.

FINAL REPORT

Material Effects in Photoconductive Frozen Wave Generators

Prepared by:	Robert M. O'Connell
Academic Rank:	Associate Professor
Department and	Electrical and Computer Engineering
University:	University of Missouri-Columbia
Research Location:	RADC/EEAC
	Hanscom AFB, MA 01731
USAF Researcher:	J. Bruce Thaxter
Date:	29 Sept. 89
Contract No:	F49620-85-C-0053

Material Effects in Photoconductive Frozen Wave Generators

by

Robert M. O'Connell

ABSTRACT

Material effects in photo-conductive frozen wave generators fabricated in semiconductor-based microstrip transmission line have been studied from three perspectives: frozen wave propagation in the line; the spacing between switches in a frozen wave generator and their maximum number; and the switching behavior of the gap-switch itself, which is modeled as a lumped-element, modified Ebers-Moll equivalent circuit.

Frozen wave propagation is influenced by both the static relative dielectric constant ϵ_r and the electrical conductivity σ_d of the semiconductor substrate and by the electrical conductivity σ_c of the strip conductor of the microstrip line. The maximum number of switches in a frozen wave generator is limited by the recombination lifetime τ of light-induced carriers in the semiconductor substrate. This directly affects both the center frequency and the bandwidth of the frozen wave. The switch spacing depends on both ϵ_r and τ. The behavior of the photoconductive switch depends on the dielectric constant ϵ_r , band gap E_g, absorption behavior (quantum efficiency η and absorption coefficient β), and reflectively r of the semiconductor, on the lifetimes τ and mobilities μ of charge carriers in the semiconductor, and on the injection efficiency η_i of the strip conductor/semiconductor junction. Some of these relationships have yet to be determined, especially in the saturation regime.

Finally, the analysis has also shown that in all three cases, there is a complicated interplay between geometric factors and material properties which might best be studied numerically using pre-existing simulation software.

ACKNOWLEDGMENTS

I wish to thank the Air Force Systems Command and the Air Force Office of Scientific Research for sponsoring this program, and to thank Drs. John Schindler and Paul Carr at RADC/EE for selecting me as a participant.

I also wish to thank Rodney Darrah, Sue Espy, Missy Tomlin, and others at Universal Energy Systems for their able and congenial assistance in administrative matters.

Finally, I wish to acknowledge the generous and excellent technical assistance given by Jon Schoenberg, Rich Bell, Nick Kernweis, and especially, Bruce Thaxter, all technical staff members of RADC/EE.

I. INTRODUCTION

Future Air Force system requirements include the need for low cost, lightweight sources of pulsed microwave energy. A typical such pulse is illustrated in Figure 1 along with its amplitude spectrum[1]. Note that the center frequency f_0 of the

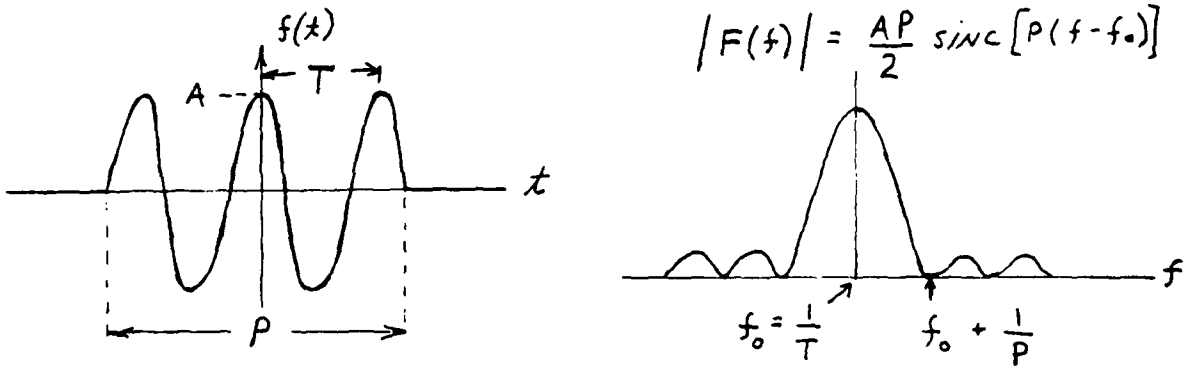

Figure 1. A typical RF or microwave pulse f(t) and its amplitude spectrum F(f).

microwave pulse is determined by the period T of a single cycle of the microwave signal within the pulse and that the amount of energy in the main lobe and its spread Δf (the bandwidth) about f_0 are determined by the temporal width P of the microwave pulse.

The signal of Figure 1 is closely approximated by the pulse train shown in Figure 2, which can in principle be produced very simply with a frozen wave generator[2,3]

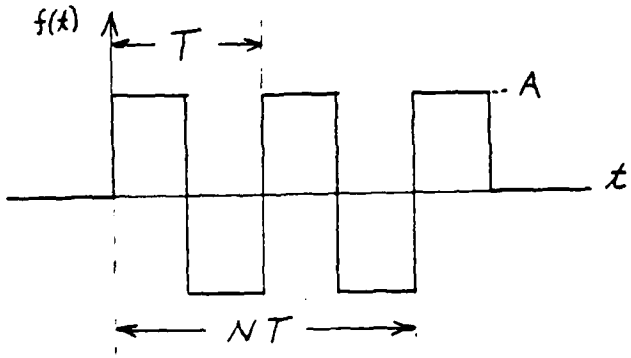

Figure 2. A pulse train which closely approximates the signal of Figure 1.

such as that illustrated in Figure 3. If the switches in Figure 3 are closed

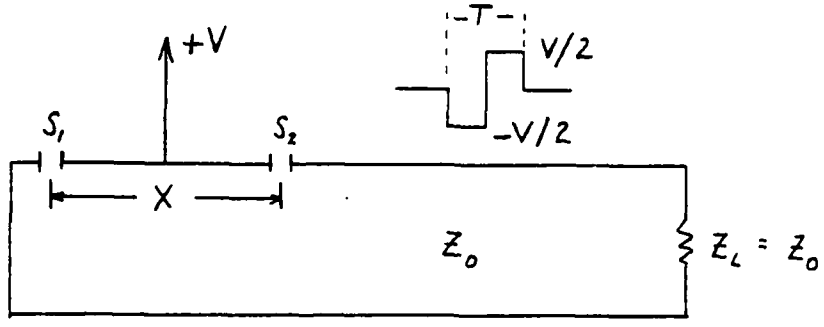

Figure 3. A one-cycle frozen wave generator consisting of two switches S_1 and S_2 embedded in a transmission line which is short circuited at S_1 and terminated in a matched load.

simultaneously and very quickly when the segment between them is charged to +V volts, the wave shown in the figure will be launched. This happens because one half of the energy stored on the charged (+V) line segment travels to the right and the other half travels to the left. This latter half reflects and reverses phase at the short circuit, then travels back through both switches (assuming they are still closed) to join the first half of the signal and form the wave shown in Figure 3. More cycles are added to the wave by using more switches and alternating the polarity of the voltage (±V) on the line segments between successive pairs of switches. Note that half of the period of the wave is determined by the length of line X between the switches and the phase velocity v_p of the wave on the line through the relation

$$v_p \, T/2 = X. \qquad (1)$$

Scientists at RADC/EE are attempting to produce microwave frozen waves as illustrated in Figure 3 by using short gaps in microstrip transmission lines. Since the center frequency of the microwave pulse equals 1/T (this is only approximately true, as we'll see later), gigahertz signals will have nanosecond periods and the switches must close in times much shorter than that. Consequently, the effort is aimed at using state-of-the-art picosecond laser pulses to close the switches by drastically changing the electrical conductivity of the material in the switch (the gap

in the microstrip) from very low to very high (through the photoconductive effect). The obvious choice of material for this is a semi-insulating semiconductor. Thus, a monolithic approach to the project would be to produce frozen waves using photoconductive switches (gaps) in semiconductor-based microstrip.

From these remarks, it is evident that the primary technical areas in the project are microwave transmission, semiconductor optoelectronics, and lasers. I have had the opportunity to do research and teach in all of these areas at various times in the past. For example, an important question in the project is the choice of semiconductor to use in the photoconductive switch/transmission line device. Answering this question requires knowledge of the photoconductive behavior and microwave properties of various materials. During the summer of 1988, I studied photoconductivity in various optical and electronic materials. Also, photoconductivity in semiconductors is one of the subjects I discuss regularly in a course I teach on optical electronics. For these and similar reasons related to the microwave transmission and laser aspects of the research, the project was well-suited to my experiences and interests.

II. OBJECTIVES OF THE RESEARCH EFFORT

At the outset of the project, it was presumed that the frozen wave generators to be built and tested would consist of short gaps in the upper conductors of microstrip transmission lines based on semi-insulating semiconductors. Thus, the material properties of the semiconductor would affect both the behavior of the switch (speed, resistance, etc.) and the propagation characteristics of the transmission line (characteristic impedance, etc.). Accordingly, a major goal of the project was to seek optimum materials for the frozen wave generators.

Toward this end, we established the following preliminary objectives:

1. Determine which properties of materials influence frozen wave generator behavior.
2. Decide on optimum materials for the devices that are eventually to be built.

3. Design, build, and test some simple switches in various promising materials.
4. Design, build, and test some frozen wave generators in various promising materials.

It quickly became apparent during the project that in order to make wise decisions concerning materials, it was necessary to thoroughly understand the behavior of the frozen wave generator and, even more importantly, the basic photoconductive switch. Thus, as the project wore on, three new objectives evolved, which essentially replaced the original ones. They are as follows:

1. Learn how material properties affect the propagation of a frozen wave traveling in microstrip.
2. Learn how material properties affect the spacing and number of switches in the frozen wave generator.
3. Learn how material properties affect the behavior of the photoconductive switches themselves.

In the next section, the approaches taken toward achieving these objectives and the results obtained will be described and discussed.

III. APPROACHES AND RESULTS

A. Material effects on frozen wave propagation in microstrip

The important materials-related properties of microstrip transmission line, a cross-section of which is illustrated in Figure 4, are its characteristic impedance Z_0, effective relative dielectric constant ϵ_{re}, dielectric attenuation constant α_d, and strip conductor attenuation constant loss α_c. Z_0 is important for impedance matching considerations and α_d and α_c are important for loss considerations. The importance of ϵ_{re} will be discussed in the next section.

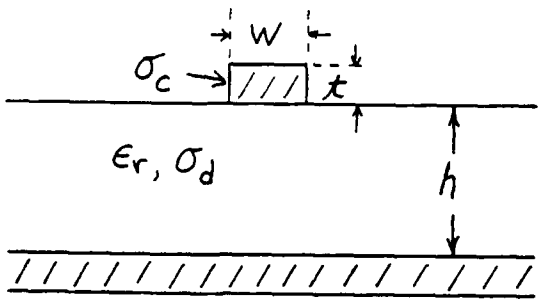

Figure 4. Microstrip cross-section, illustrating the width W and thickness t of the upper strip conductor and the dielectric or semiconductor substrate thickness h. ϵ_r is the relative dielectric constant of the substrate and σ_c and σ_d are the electrical conductivities of the strip conductor and substrate, respectively.

Highly accurate approximate analyses of the structure in Figure 4 have been performed, and complete tabulations of the rather cumbersome results are widely available[4,5]. For our purposes, it is only necessary to indicate the functional dependances of Z_0, ϵ_{re}, α_d, and α_c, which are as follows:

$$Z_0 = Z_0 (\epsilon_r, f, w/h, t/h, h), \quad (2a)$$

$$\epsilon_{re} = \epsilon_{re} (\epsilon_r, f, w/h, t/h, h), \quad (2b)$$

$$\alpha_d = \alpha_d (\epsilon_r, \sigma_d, w/h, t/h), \quad (2c)$$

$$\alpha_c = \alpha_c (\epsilon_r, \sigma_c, w/h, t/h), \quad (2d)$$

where f refers to frequency and the other quantities in the parentheses are defined in Figure 4. Thus, for a given material system, there is a rather complicated interrelationship among frequency, waveguide geometry, and the material properties (ϵ_r, σ_d, and σ_c), which must be considered. This can be done using commercially available software[6], in which the equations suggested by Equations 2a-2d are programmed.

B. Material effects on the spacing and number of switches in the frozen wave generator

The elementary concept that velocity times time equals distance leads to the equation

$$X = v_p \, T/2 \ , \tag{1}$$

which was stated in the Introduction. It relates the period T of one cycle of a frozen wave pulse train to the phase velocity v_p of the wave on a transmission line and the spacing X of the switches that comprise the frozen wave generator. Since, in microstrip[5] ,

$$v_p = c / \sqrt{\epsilon_{re}} \tag{2}$$

where c = the free space speed of light, Equation (1) can be rewritten as

$$X = cT / 2 \sqrt{\epsilon_{re}}. \tag{3}$$

As promised in the last section, this equation shows the importance of the effective relative dielectric constant ϵ_{re} in device design. Also, since ϵ_{re} depends on the relative dielectric constant ϵ_r of the substrate (as stated in functional Equation (2c)), it follows that Equation (3) also shows that the substrate material affects the switch spacing. The exact behavior of this dependence would require the use of the exact equation represented by (2c) in (3).

To appreciate the relationship between material properties and the number of switches in the generator, it is necessary to consider the amplitude spectrum of the frozen wave. (The number of switches is one more than the number of cycles in the frozen wave.) As illustrated in Figure 1, if the frozen wave were a truly sinusoidal pulse train, the relation

$$f_0 = 1/T \tag{4}$$

would be exactly correct and Equation (3) could be rewritten in the convenient form

$$X = c / 2 \sqrt{\epsilon_{re}}\ f_0 \ . \qquad (5)$$

Furthermore, as is also illustrated in Figure 1, as the width P of the pulse train increases, its energy becomes concentrated in an increasingly narrower band of frequencies Δf centered on f_0 .

If these results were also exactly true of the frozen wave shown in Figure 2, it would follow that the number of cycles N in the frozen wave would only affect the bandwidth of the signal, i.e., by associating NT with P (see in Figures 1 and 2) the bandwidth would decrease with increasing N. As we will show, however, N also affects the center frequency of the square wave pulse train, so that Equation (4) must be replaced by a functional equation of the form

$$f_0 = f_0\ (N,\ 1/T\ ) \ . \qquad (6)$$

Using this form, Equation (5) should also be a rewritten as

$$X = c / \sqrt{\epsilon_{re}}\ f_0\ (N,\ 1/T) \ . \qquad (7)$$

If f(t) and $f_1(t)$ represent the signal in Figure 2 and one of its cycles, respectively, f(t) can be expressed as

$$f(t) = \sum_{n=1}^{N} f_1\ (t - (n-1)\ T) \ . \qquad (8)$$

By the Shifting Theorem of spectral analysis, the Fourier transform $F(\omega)$ of f(t) can be written as

$$F(\omega) = F_1(\omega) \sum_{n=1}^{N} e^{-j\omega(n-1)T} \ , \qquad (9)$$

where $F_1(\omega)$ is the transform of $f_1(t)$. It is straight-forward to show that

$$F_1(\omega) = \frac{A}{j\omega}\,(1 - e^{-j\omega T/2})^2$$

$$= jAT\, e^{-j\omega T/2}\, \frac{\sin^2 \omega T/4}{\omega T/4} \quad . \tag{10}$$

Also, using information in Reference 7, we can write

$$\sum_{n=1}^{N} e^{-j\omega(n-1)T} = \sum_{n=0}^{N-1} e^{-j\omega nT} = \frac{1 - e^{-j\omega NT}}{1 - e^{-j\omega T}}$$

$$= e^{-j\omega T(n-1)/2}\, \frac{\sin \omega TN/2}{\sin \omega T/2} \quad . \tag{11}$$

Finally, using Equations (10) and (11), we can express the amplitude spectrum $| F(\omega) |$ as

$$| F(\omega) | = AT \left| \frac{\sin^2 \omega T/4}{\omega T/4} \; \frac{\sin \omega TN/2}{\sin \omega T/2} \right| \quad . \tag{12}$$

Plots of this equation would show that the main lobe of $| F(\omega) |$ is centered on a frequency f_0 that is somewhat to the left of 1/T and approaches 1/T with increasing N. Furthermore, $| F(\omega) |$ becomes more symmetrical about f_0 with increasing N with a bandwidth proportional to 1/N. Thus, the behavior of $| F(\omega) |$ for the square wave pulse train is similar to that of the sinusoidal pulse train when N is large.

To briefly illustrate these points, note that for N=1 the second factor of Equation (10) is 1 and the first factor plots as shown in Figure 5. Differentiation

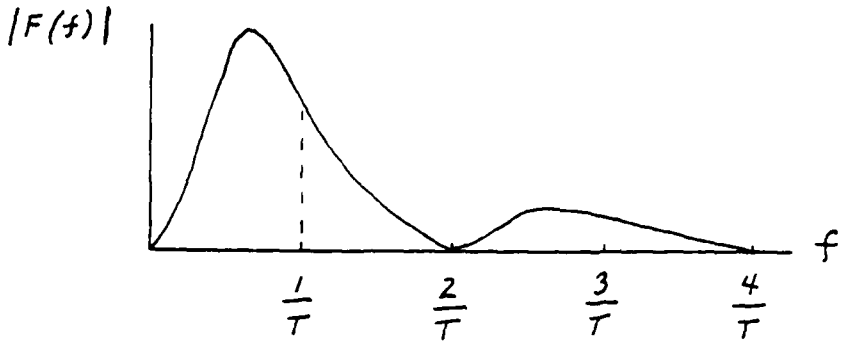

Figure 5. Plot of Equation (10) for the case N = 1, which is also the first factor in Equation 10.

of the first factor in Equation (10) to determine the frequency of the main lobe results in the transcendental equation

$$\tan \omega T/4 = 2\, \omega T/4 \quad , \tag{13}$$

which can be solved iteratively to give

$$f_0 = 0.7417 \; / \; T \; . \tag{14}$$

For N > 1, the plot of Figure 5 must be multiplied by the second factor in Equation (10). Plots of this factor for N = 2 and 3 are shown in Figure 6. It is apparent

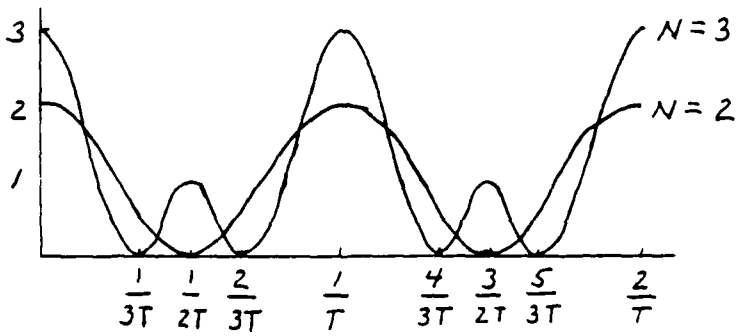

Figure 6. Plots of the second factor in Equation (10) for the cases N = 2 and 3.

that the product of the curve in Figure 5 with each of these curves will have a peak frequency which approaches 1/T as N gets larger. Also, the resultant spectrum

becomes more symmetrical about f_0 with increasing N and has a bandwidth proportional to 1/N.

We have now shown how both the center frequency f_0 and the bandwidth Δf of the square pulse train form of frozen wave depend on the number of cycles N in the frozen wave or, equivalently, on the number of switches N + 1 in the frozen wave generator. It remains to explain how the device material enters the picture. As discussed in the Introduction and illustrated with the help of Figure 3, in order for the frozen wave to form properly, all the switches in the generator (N+1) have to remain closed while all of the segments of the wave work their way to the left and right, and ultimately leave the generator, traveling to the right. If N is large, which would be desirable if a narrow-band, high-power signal were required, this could require a fairly long switch closure time. Since the switches are to be made of an illuminated semiconductor, this means that the recombination lifetime τ of the substrate material has to be sufficiently long. Thus, the recombination lifetime of the substrate material limits the number of switches in the frozen wave generator. Furthermore, since the center frequency f_0 of the main lobe of the signal spectrum varies with N as discussed above, τ affects f_0 as well as Δf.

C. Material effects on photoconductive switches

Having considered the transmission medium and the number and spacing of switches in a frozen wave generator, we now consider the behavior of the photoconductive switches themselves. One important aspect, the recombination lifetime τ of the switch and its influence on the number of switches, was discussed in the last section, although not in any quantitative way. The results of the present section should make it possible to, among other things, decide how many switches can be used in a given generator using a given material system.

Our approach to studying a single photoconductive switch is to model it for use in the well-known SPICE simulation program. An appropriate switch model would include both material and device parameters for the switch. Such a model, embedded between segments of transmission line, could be analyzed with SPICE. The analysis would include the full range of device behavior from the unilluminated OFF state through the transient leading to the illuminated ON state and finally

through the transient leading back to the OFF state.

The first decision to be made was whether the switch model could be composed of lumped rather than distributed elements. Since the length of a typical switch (the size of the gap in the strip conductor of the microstrip line) is of the order of (at most) tens of microns, and since the wavelength of a gigahertz signal in typical microstrip is of the order of centimeters, a lumped-element model was appropriate for the present work. However, when higher frequencies (the millimeter-wave regime) are considered, the lumped-element model will have to be revised.

To illustrate some of the logic that led to the lumped-element switch model, Figure 7 shows a cross-section of a typical photoconductive switch (the gap) in

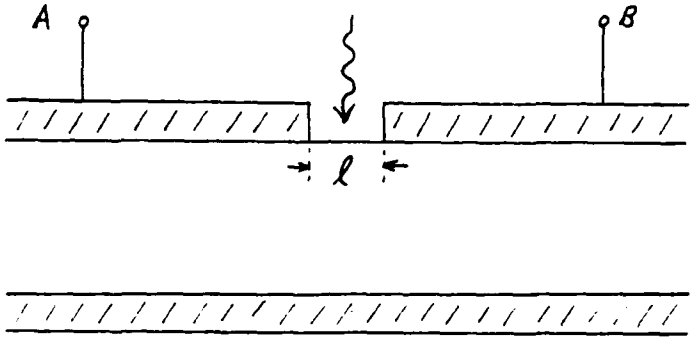

Figure 7. Cross-section of an illuminated photocondutive switch in microstrip. ℓ is the length of the gap in the strip conductor.

microstrip. Note first that there is clearly a capacitance C_g between the electrodes on either side of the gap. Secondly, when the gap is illuminated, the increased conductivity of the semiconductor will allow (and control) an electrical current between A and B. Thus there is also a light-controlled variable resistor between the electrodes. Furthermore, because the photoconductive effect is at work, a photoconductive gain is also possible. Finally, because the substrate is semi-insulating, the metal semiconductor contacts where the strip electrode meets the substrate at the edges of the gap are probably significantly non-ohmic[8], i.e., they probably form shottky diodes.

We observed such non-ohmic behavior in a preliminary measurement on a photoconductive switch fabricated from semi-insulating GaAs mounted in a coplanar waveguide made of alumina. In the measurement, one side of the switch

(terminal B in Figure 7) was terminated in 50Ω and the other side of the switch (terminal A in Figure 7) went to a 50Ω oscilloscope. When the gap was illuminated with a laser pulse, a negative electrical pulse was observed on the oscilloscope. This signal can only be explained if there is a rectifying contact between electrode A and the substrate; electrons produced by the absorbed photons thus see a down-hill potential and generate the observed signal via the photovoltaic effect[9]. Incidentally, when terminal B was terminated in either a short or an open, the oscilloscope signal was modified as would be expected by the reflected signals.

The above ideas suggest that the switch be modelled as a phototransistor with a variable resistor between the junctions and a shunt capacitor, as shown in Figure 8. The shunt capacitor C_g has been analyzed by Maeda[10] and is a function

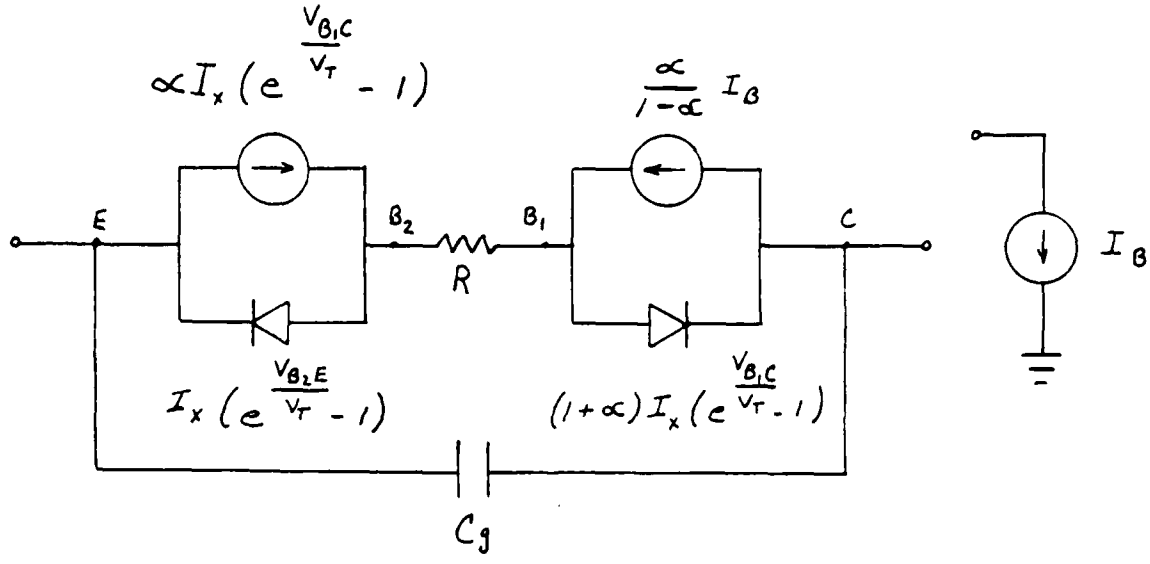

Figure 8. Lumped-element model of the photoconductive switch.

of the static relative dielectric constant ϵ_r of the semiconductor as well as geometric factors. Values of 20-50 fF are typical. The junctions are modelled using a symmetric Ebers-Moll model[11] to allow any bias (forward or reverse) across each junction. Capacitances associated with the junction should automatically be accounted for by the SPICE program. Note that if the junctions are non-rectifying, the diodes become short circuits and the model becomes a parallel resistor/capacitor combination, as discussed by Auston[8] .

The Ebers-Moll model introduces the parameters α and I_x. These parameters are somewhat complicated functions of both geometry and material properties.

including the lifetimes and mobilities of charge carriers and the band gap (or intrinsic density) of the semiconductor. Exact functional forms for these parameters remain to be established.

The remaining parameters in the model, I_B and R, are functions of the time varying optical power in the pulsed laser that is used to close the switch. I_B is the light-induced photocurrent, which can be expressed as[12]

$$I_B = \frac{e\eta\,(1-r)\,P(t)}{h\nu} \tag{16}$$

where e is the electron charge, r is the reflectivity of the semiconductor at the wavelength of the light pulse, $h\nu$ is the photon energy in the beam, P(t) is the optical power that reaches the semiconductor, and η is the quantum efficiency for conversion of photons to electron-hole pairs. Both η and r are material properties.

An expression for R can be developed[13] by approximating the illuminated volume between terminals A and B in Figure 7 as a parallelepiped as illustrated in Figure 9. The dimensions, ℓ, w, and d represent, respectively, the length of the

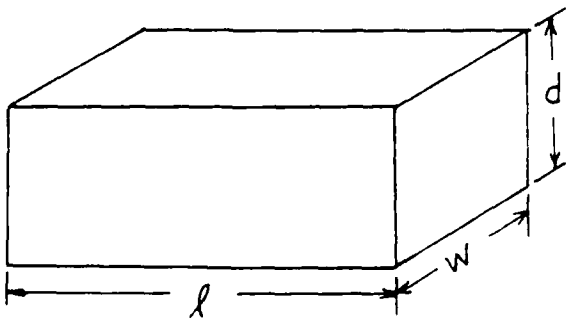

Figure 9. Geometry used to approximate the illuminated volume in a photoconductive switch. ℓ = gap length, w = strip conductor width, d = effective absorption depth of the light.

gap (see Figure 7), the width of the strip conductor (see Figure 4), and an effective or average absorption depth of the light. The depth d is often approximated by $1/\beta$, where β is the absorption coefficient of the material at the laser wavelength[12].

The resistance R of the model in Figure 9 can be expressed as

$$R = \ell / \sigma(t)wd \quad , \tag{17}$$

where $\sigma(t)$ is the electrical conductivity of the material. Since the material is assumed to be semi-insulating, $\sigma(t)$ can be written as

$$\sigma(t) = e(\mu_n + \mu_p)\, n(t) \quad , \tag{18}$$

where μ_n and μ_p are the electron and hole mobilities, respectively, and n(t) is the concentration of free electron-hole pairs. n(t) can be written as the sum of intrinsic (n_i) and light-induced ($\Delta n(t)$) quantities as

$$n(t) = n_i + \Delta n(t) \quad , \tag{19}$$

so that Equation (17) becomes

$$R = \frac{\ell}{wd\, e(\mu_n + \mu_p)\, [n_i + \Delta n(t)]} \quad . \tag{20}$$

Using the results of Reference 13, $\Delta n(t)$ can be expressed as

$$\Delta n(t) = e^{-\gamma t} \int_0^t e^{\gamma t} \frac{\eta(1-r)\, P(t)}{h\nu\, wld}\, dt \, , \tag{21}$$

where

$$\gamma = 1 / \tau + (1-\eta_i) / t_t \quad . \tag{22}$$

In Equation (22), τ is the recombination lifetime of excess carriers in the material, η_i is the contact injection efficiency (a function of both the strip conductor and the semiconductor, which we have not yet ascertained), and t_t is the transit time (l/v_d,

where v_d is the drift velocity, which depends on charge carrier mobilities).

If we define

$$F[P(t)] = e^{-\gamma t} \int_0^t e^{\gamma t} P(t)\, dt \qquad (23)$$

for shorthand purposes, substitution of Equation (21) into Equation (20) yields

$$R(t) = \frac{\ell}{ewd(\mu_n + \mu_p)\left[n_i + \frac{\eta(1-r)}{h\upsilon wld} F[P(t)] \right]} \qquad (24)$$

It should be evident from the discussion in this section that the behavior of the photoconductive switch is a very complicated function of geometry and materials, including both the strip conductor (injection efficiency) and the semiconductor. The semiconductor properties that come into play are its relative dielectric constant ϵ_r, intrinsic density n_i or band gap E_g, lifetimes τ and mobilities μ of carriers, quantum efficiency η and absorption coefficient β, and reflectivity r. The easiest and most efficient way to consider the roles of these material parameters is to analyze different material/switch configurations using a simulation program such as SPICE.

Although the model presented here should be valid for analysis through the entire cycle of operation (from OFF to ON to OFF), some caution is needed in the ON state when the optical intensity is apt to be great enough to cause saturation or high-level injection effects. In such case, many of the material parameters vary from their well-known "constant" values. For example, mobilities are known to drop significantly at high intensities[14]. Thus, using the model correctly during the ON state will require a proper understanding of how the material properties behave under conditions of high level injection.

IV. RECOMMENDATIONS

Of the three areas studied during the project, the behavior of the photoconductive switch is by far the most complicated and the least understood. Thus, in general, the physical behavior of the switch needs to be studied further and the results used to improve the circuit model discussed above. As the switch model improves, it will be possible to identify optimum material systems from the point of view of the switch. The properties of those materials can then be used with simulation software to optimize the waveguide geometry for frozen wave propagation and to optimize the number of switches in the generator and determine their proper separation. This process should be interactive with the experimental effort to build and test such devices.

In order to improve the photoconductive switch model, the following specific tasks are recommended:

1. Improve the lumped-element circuit model to include:
    a. effects of materials and geometry on the behavior of the injection efficiency and the parameters α and I_x of the metal-semiconductor junction.
    b. the effects of high-level injection on, for example, carrier lifetimes and mobilities.
    c. a more accurate description of the spatial absorption of laser pulse light by the material of the gap-switch and its effect on R(t).
2. Develop a high-frequency (e.g., millimeter-wave) switch model that includes:
    a. distributed circuit elements.
    b. appropriate high-frequency parasitic effects.
    c. high-frequency effects of certain geometric factors.

REFERENCES

1. Haykin, Simon, Communication Systems, 2nd ED., New York, NY, John Wiley and Sons, 1983, p. 29.
2. Proud, J.M., and Norman, S.L., "High-Frequency Waveform Generation Using Optoelectronic Switching in Silicon," IEEE Trans. Microwave Theory Tech., Vol. MTT-26, 1978, p. 137.
3. Lee, C.H., Li, M.G., Chang, C.S., Yurek, A.M., Rhee, M.J., Chauchard, E., Fischer, R.P., Rosen, A., and Davis, H., "Optoelectronic Techniques for Microwave and Millimeter-Wave Applications," Proc. IEEE-MTT-S International Microwave Symposium, St. Louis, MO, 1985, p. 178.
4. Gupta, K.C., Garg, R., and Bahl, I.J., Microstrip Lines and Slotlines, Dedham, MA, Artech House, 1979, p. 88.
5. Bahl, I.J., and Bhartia, P., Microstrip Antennas, Dedham, MA, Artech House, 1980, p. 309.
6. SUPERCOMPACT, for example, is one such software package.
7. Proaksis, J.G., and Manolakis, D.G., Introduction to Digital Signal Processing, New York, NY, Macmillan, 1988, p. 246.
8. Auston, D.H., Chapter 4 in Lee, C.H., ed., Picosecond Optoelectronic Devices, New York, NY, Academic Press, 1984.
9. Bube, R.H., Photoconductivity of Solids, New York, NY, John Wiley and Sons, 1960, p. 78.
10. Maeda, M., "An Analysis of Gap in Microstrip Transmission Lines," IEEE Trans. Microwave Theory Tech., Vol. MTT-20, 1972, p. 390.
11. Muller, R.S., and Kamins, T.I., Device Electronics for Integrated Circuits, 2nd Ed., New York, NY, John Wiley and Sons, 1986, p. 294.
12. Sze, S.M., Physics of Semiconductor Devices, 2nd ED., New York, NY, John Wiley and Sons, 198[illegible], p. 745.
13. Nunnaly, W.C., and Hammond, R.B., Chapter 12 in Lee, C.H., ed., Picosecond Optoelectronic Devices, New York, NY, Academic Press, 1984.
14. Lee, C.H., Chapter 5 in Lee, C.H., ed., Picosecond Optoelectronic Devices, New York, NY, Academic Press, 1984.

1989 USAF-UES SUMMER FACULTY RESEARCH PROGRAM

Sponsored by the

AIR FORCE OFFICE OF SCIENTIFIC RESEARCH

Conducted by the

Universal Energy Systems, Inc.

FINAL REPORT

Parrallel Processing for Associative Semantic Space Analysis

Prepared by:	Sally Yeates Sedelow, Ph.D.
Academic Rank:	Professor; and Adjunct Professor
Department and	Computer Science Department; Graduate Institute of Technology (Electronics and Instrumentation), English
University:	University of Arkansas/Little Rock; University of Arkansas
Research Location:	RADC/COES Griffiss AFB New York 13441-5700
USAF Researcher:	Douglas A. White
Date:	15 Aug 89
Contract No:	F49620-88-C-0053

PARALLEL PROCESSING FOR ASSOCIATIVE SEMANTIC SPACE ANALYSIS

by

Sally Yeates Sedelow

ABSTRACT

Associative semantics refers to the "definition" of a word through its association with other semantically closely-related words. For the natural languages (e.g., English), which are the focus of this research, thesauri provide the most readily available whole-language compendia for associative semantics. Through research extending over more than twenty-five years, my research groups have determined Roget's International Thesaurus, 3rd edition (1962) to be a reliable guide to English semantic space when our mathematical model (Bryan, 1973, 1974) is employed (Brady, 1988; Patrick, 1985; S. Sedelow, 1969, 1985, 1987; S. Sedelow with Mooney, 1988; S. Sedelow and W. Sedelow, 1969, 1988, 1989, 1986 (The Lexicon...), 1986 (Thesaural...); W. Sedelow, 1985, 1987, 1988; W. Sedelow and S. Sedelow, 1969, 1987; Talburt and Mooney, 1989 (Determination...), (The Decomposition...); Warfel, 1972). Efforts to get at structural components of the Thesaurus through programming conventional computers have posed major difficulties. The focus of this research has been to explore the appropriateness of parallel processing for our mathematically-guided analysis of associative semantic space.

Acknowledgements

Thanks are due to the US Air Force Systems Command and to the Air Force Office of Scientific Research for sponsorship of this research, to the Rome Air Development Center for its support, and to Universal Energy Systems for efficiently looking after the general administrative components of the program.

As supervisor for this research project, Douglas A. White was extremely supportive and facilitative, providing good ideas as to promising intersections between this research and Air Force interests. Special thanks also go to Don Gondek and Sharon Walter for introductions into the parallel processing "net". Dr. Diamond and Mr. Urtz provided helpful introductions to research at RADC and John Ritz, Sam DiNitto, and Bob Ruberti saw to it that administrative support was available as needed. I'm very grateful to the entire COES research and secretarial staff for arranging everything from computer accounts to paycheck delivery (not to mention stimulating conversations on professional matters); Captain Mike Baldwin (on reserve assignment) and Michelle Kubis (a summer student) produced a fine flat version of the densely packed Thesaurus file. Thanks, too, to all the folks at the Northeast Parallel Architecture Center (NPAC), including the excellent instructors at the Summer Institute. Joe Meehan, who knows how to Star in C, provided proof that parallel processing has great promise for this research; Walter Sedelow generously contributed much time to the review of relevant research in the fields of associative semantics and parallel processing.

I. INTRODUCTION

An associative semantic topology for an entire natural language has the potential to serve as the foundation for the building of domain-transcendent knowledge-based computer/information systems. At present computer-based systems having a substantial natural-language knowledge base component invoke only very cumbersome knowledge representations of semantic (meaning) relationships, which, per force, reduce any such systems to very restricted domains. Hence, under current circumstances knowledge-based expert systems, intelligent tutoring systems, and natural language interfaces of all sorts require inefficient and costly extensive pre-processing and on-the-fly structuring so as to make the resulting relatively small vocabularies perform in meaningful ways. In contrast, the research standing behind this project always has been focused on getting at semantic relationships in _whole languages_ by using culturally-validated, already available compendia of such relationships. (Most simply, cultural validation means that through time many people use and understand such compendia.) Dictionaries and thesauri traditionally have been major repositories of whole-language semantic information--dictionaries through definitions and thesauri through associations with other semantically-related words. Our research has emphasized the associative semantics route represented by thesauri and, after a comparative study (S. Sedelow and W. Sedelow, 1969) of three such compendia (_Roget's International Thesaurus, 3rd Edition_, _Roget's University Thesaurus_, and _Webster's Dictionary of Synonyms_), the _International Thesaurus_ was selected for computer input, editing (Harris, 1973), and analysis.

As part of that analysis, our graduate student, Robert Bryan (1973 and 1974), developed a mathematical model for both the explicit hierarchical structure and the implicit structure provided by the occurrence of any given word in several different places (multilocality property) in the _Thesaurus_. For example, "restfulness" occurs with words associated with _quiescence_ as well as with words associated with _comfortableness_. Among other constructs, Bryan's model defines Chains,

Stars, and Neighborhoods, which provide principled guides for navigating both cross-hierarchically and hierarchically within the Thesaurus. As to the explicit hierarchy, the lower levels (in contrast to the very general and more arbitrary upper levels) have been most useful for our purposes; in the implicit hierarchy, the more tightly restricted chains (Types 9 and 10), as well as Stars and Neighborhoods, have proved most promising.

Empirical studies of the Thesaurus demonstrate that it might be accurately regarded as the skeleton for English-speaking society's collective associative memory (Frege, 1892). We have tested this assumption of explicit and implicit lower hierarchy level validity in a number of ways: A. the determination of when the initial characters in an English word are functioning as a prefix; our working hypothesis was that when a possibly prefixed word form and its possible stem occur close together within the Thesaurus they probably can be considered as a stem and prefixed form; (This assumption was borne out in a large majority of cases, while at the same time the Thesaurus correctly showed, e.g., that the words "vent" and "prevent" cannot be grouped together as stem and prefixed form. Thus, as a measure of 'semantic distance' between English words, the Thesaurus is useful in a satisfying way in this test (Warfel, 1972; S. Sedelow, 1969; S. Sedelow, Chum, 1985; ASIS, 1985, 1988)); B. early experiments with content-analytic programs using the Thesaurus showed that it provides semantic clustering conformal with experience and expectations as to usage patterns (S. Sedelow and W. Sedelow, 1969); C. starting from a low level (the semi-colon groups, indicated by semi-colon boundaries) with the syntactic subset comprising verbs, navigation of 'chains' based on the topological model (Bryan, 1973, 1974); Patrick, 1985; S. Sedelow and W. Sedelow, 1986) produced distinctions among homographs--a very important achievement, given the pervasiveness of semantic ambiguity in multi-domain natural language knowledge bases, user queries, and system responses, and thus of problems involving disambiguation; D. a distribution of the so-called Chinese simplicia,

as categorized by Karlgren (1929), against categories in Roget's showed semantic gaps conformal with observations made more 'anecdotally' by scholars comparing aspects of Chinese and English (e.g., book and private conversation of Alfred Bloom (1981, etc.: S. Sedelow, 1979, "The Interlingual..."; W. Sedelow, 1987, "The Interlingual..."); E. research exploring the interaction between the Thesaurus and abstracts of articles in the 1985 SCAMC (Symposium on Computer Applications in Medical Care) Proceedings, which produced a conceptual overview of the abstracts based on intersections between textual context and theasurus concepts--for which the results are quite satisfactory (Brady, 1988); F. a distribution of the UNIX Spelling Dictionary against terms occurring in the Thesaurus shows a very high correlation with the grouping of entries in the Thesaurus as to semi-colon group, paragraph, category, etc. (That is, terms in the dictionary "pile up" in those areas in the Thesaurus which also have large numbers of terms.) A distribution of the Oxford Advanced Learner's Dictionary against the Thesaurus also has produced a similar very high correlation; G. inasmuch as the sentence "Time flies like an arrow" is a classic in discussions of ambiguity, it is worth noting that the Thesaurus, again interacting with the text of the sentence (Brady, 1988), produces the reading that often seems to come to mind first, i.e., the speed with which time goes by.

The studies of the Thesaurus cited above--studies which range over many different kinds of problems/applications and many types of text--indicate that it is appropriate to conclude that the initial, working assumption as to the potential usefulness of a culturally validated resource such as Roget's has been substantiated with specific reference to Roget's. We do not claim that the Thesaurus is 'perfect'--we can ourselves generate examples of desirable structural modifications and additions that are well-grounded theoretically--but it has performed very well in a number of tests over rather widely-ranging discourse domains. Thus, it seems very worthwhile and promising now (1) to make more directly accessible the formal semantic connectivity structures

implicit in the Thesaurus and (2) to define/elucidate further both implicit and explicit structures. In order to achieve these two goals, more efficient, powerful computing than anything to which we have had access is necessary. This specific RADC research effort focused on parallel processing and its possible relevance for our research work generally.

II. Objectives of the Research Effort:

The first objective was to investigate parallel processing modes/architectures with a view toward determining which, if any, looked promising for analysis of the Thesaurus.

The second objective was to determine the availability of programming languages for likely candidate machines, as well as to discover what types of algorithm development would be required.

The third objective was to test empirically the use of a parallel computer for a thesaurus-focused task to which a serial computer already had been applied, and thus to enable comparisons.

III. Results Obtained:

As to architectures, preliminarily it should be noted that, following Miller (1988) and Quinn (1987), the definition of parallel processing used here is as "a type of information processing that emphasizes the concurrent manipulation of data elements belonging to one or more processes solving a single problem" (Miller, p. 4). Miller distinguishes between this type of concurrency and pipelining, which "increases concurrency by dividing a computation into a number of steps, while parallelism is the use of multiple resources to increase concurrency. A parallel computer is a computer designed for the purpose of parallel processing" (Miller, pp. 4-5).

Again relying upon Miller and Quinn and, in turn, their sources, two major classes of possibly usable parallel machines are identified: (1)

the Single-Instruction stream, Multiple-Data stream (SIMD) computers, and (2) the Multiple-Instruction stream, Multiple-Data stream (MIMD) computers. SIMD machines "are generally designed to exploit the fine-grained parallelism of tasks...where the same operation is performed on many different...elements" (Miller, p. 12). Miller, citing Siegel (1984), notes that an MIMD machine

> typically consists of n processing elements (PEs), n memory modules, and an interconnection network. Each of the n PEs stores and executes its own program. (Therefore, there are multiple instruction streams as opposed to the SIMD architecture that consists of only a single instruction stream.) Each PE fetches its own data on which to operate. (Thus, there are multiple data streams, as in the SIMD system.) The interconnection network provides communications among the processors and memory modules. While in an SIMD system all active PEs use the interconnection network at the same time (i.e., synchronously), in an MIMD system, because each PE is executing its own program, inputs to the network arrive independently (i.e., asynchronously)... Whereas all active PEs operate in a synchronous lockstep way in SIMD machines, PEs in an MIMD machine operate asynchronously with respect to each other. With this increased flexibility comes an increase in overhead costs to perform process synchronization and design programs for each of the n PEs (there may not be a single program, as in SIMD operation). Miller, p. 15.

Consultation of available literature on parallel processing, as well as consultation with administrators and users of commercially available parallel computers both at the Rome Air Development Center and at the Northeast Parallel Architectures Center (NPAC), housed at Syracuse University, led us to conclude that among the machines accessible to us this summer (MIMD machines including several types of Encore Multimax computers and an Alliant FX/8; SIMD-type Connection Machine 1 and Connection Machine 2), the Connection Machine was most appropriate, at

least for initial experimentation. With its large number of processors (at NPAC, both the CM 1 and the CM 2 are configured with 32k processors, but the CM 2 can have up to 65k processors) and sizable memory attached to each processor (on the CM 1 4k bits and on the CM 2 64k bits), the Connection Machine is appropriate for the type of data base represented by the Thesaurus and to the type of operations to be performed on the Thesaurus.

Having settled upon a particular machine, the choice of programming languages was constrained to those available for that machine. It is now possible to program the Connection Machine in an extension of Lisp (*Lisp), of C (C*), and of Fortran (CM.Fortran and, soon, Fortran 8x). Thanks to an NPAC two-week summer institute on the Connection Machine, a sense of the capabilities of each of these languages was established. In all cases the extended languages are designed to take advantage of at least some of the special properties of the Connection Machine and its implications for program structure (for example, programs in *Lisp are much less recursive than standard Lisp programs for serial processors, since one instruction operates simultaneously on many data elements). It is quite likely that at some point the Thesaurus research will imply use of each of the available languages; for immediate experimentation, C* was chosen, in part because the algorithm we wanted to replicate was originally implemented in C.

For the third objective, the empirical test, Joe Meehan, a Laboratory Support Specialist/Senior Programmer at The National Center for Toxicological Research (Jefferson, Arkansas) and a graduate student in Computer Science at The University of Arkansas/Little Rock, produced in C* a portion of the program for identifying the Type 10 chains of the Bryan model reported on in Talburt and Mooney (1989). A preliminary to identifying the Type 10 chains consists of locating categories in the Thesaurus (for this research task, semi-colon groups were the categories) which have so-called strong links (two words in common) and words which are also strongly linked (two categories in common). In

order to make that task more tractable, Talburt and Mooney point out that

> a simple reduction is to scan across each horizontal line of the T-graph [used to represent words, on the horizontal axis, and categories, on the vertical axis] (i.e. word sets) and eliminate any word group that consists of only one entry. Similarly, categories of only one entry can also be eliminated. There is possible interaction in that the elimination of single-entry words may create single-entry categories which can be eliminated, but which in turn may create more single-entry words, and so on. (Talburt and Mooney, 1989)

Although exact comparison timings are not possible, this reduction phase of the Type 10 identification took many hours (days, really) on a dedicated, large AT style microcomputer. Meehan's C* program on the Connection Machine required from three to five minutes (depending upon the work load on the host computer), of which two to four minutes were required to input the data from the host computer (a Vax 8800) and approximately one minute was required for the reduction operation. For the CM implementation, each entry in the Thesaurus (approximately 199,000) was assigned to its own processor (one is not restricted to the literal number of processors in the CM; virtual processors can be declared) and counts were achieved by having entries send messages to, e.g., the category in which they occurred. Thus, the total number of messages comprised the count for each category and the first stage of the reduction (elimination of single-entry categories and single-entry word types) was accomplished. Successive reductions continued in this manner; in fact, although there obviously was a loop, only seven iterations of the reduction loop occurred--and it should be noted that, in contrast to the serial program, which was halted when the reductions were no longer large enough to be significant, the CM program performed all possible reductions.

IV. Recommendations:

Both the "off-line" investigation (including the two-week Connection Machine Institute) and the empirical test suggest that parallel processing and, at least for research in the immediate future, a SIMD machine such as the Connection Machine are appropriate to utilize for this research on associative semantic space.

The next steps should be (1) To complete replication of the research directed toward identifying Type 10 chains (the reduction replication resulted in a non-significant difference--3--in the number of candidate entries for such chains--90,822 as opposed to 90,819 at the stage where computing was halted in the serial algorithm); (2) To develop algorithms for identification of other structural components, e.g., Type 9 chains, for implementation on the Connection Machine; practically speaking, such work has been impossible on the computing resources available to us. Parallel processing would appear to provide the resources necessary to make visible the formerly hidden implicit structural skeleton of the Thesaurus. At the least, it reveals major, useful components of that skeleton applicable to disambiguation and, in general, for placing words with multiple meanings and connotations within their appropriate semantic sub-spaces, as determined by the context in which they occur.

REFERENCES

Bloom, Alfred H., Linguistic Shaping of Thought: A Study in the Impact of Language on Thinking in China and the West. New Jersey, Laurence Erlbaum, 1981.

Brady, John, "ICSS (Interlingual Communication Support System) and a Wittgensteinian Language Game," Proceedings, European Studies Conference, University of Nebraska, Omaha, NE, 1988, pp. 20-27.

Bryan, Robert, "Abstract Thesauri and Graph Theory Applications to Thesaurus Research," in S. Sedelow, et al., Automated Language Analysis, 1972-1973, University of Kansas, Lawrence, KS, 1973, pp. 45-89.

Bryan, Robert, "Modelling in Thesaurus Research," in S. Sedelow, et al., Automated Language Analysis, 1973-1974, University of Kansas, Lawrence, KS, 1974, pp. 44-59.

Frege, G., "Uber Sinn und Bedeutung" (Eng. Trans.: On Sense and Reference), in P. Geach and M. Black, eds., Frege, Philosophical Writings, 1892; 1952, Oxford University Press.

Harris, Herbert R., "The Conversion of Roget's International Thesaurus to an Automated Data Base," in S. Sedelow, et al., Automated Language Analysis, 1972-1973, University of Kansas, Lawrence, KS, 1973, pp. 5-27.

Karlgren, Bernhard, Sound and Symbol in Chinese, Han-Shan Tang Ltd., New York, State Mutual Book, 1929.

Miller, Susan E., A Survey of Parallel Computing, RADC, Air Force Systems Command, Griffiss AFB, NY, Amherst Systems, Inc., 1988.

Patrick, Archibald, An Exploration of an Abstract Thesaurus Instantiation, M.S. Thesis, Computer Science, University of Kansas, Lawrence, KS, 1985.

Quinn, M. J., Designing Efficient Algorithms for Parallel Computers, New York, McGraw-Hill, Inc., 1987.

Roget's International Thesaurus, Third Edition, New York, Thomas Y. Crowell, 1962.

Roget's University Thesaurus, New York, Thomas Y. Crowell, 1963.

Sedelow, Sally Yeates, "Computational Lexicography," Computers and the Humanities, 19:2, 1985, pp. 97-101.

Sedelow, Sally Yeates, "Computational Literary Thematic Analysis: The Possibility of a General Solution," in Carol Parkhurst, ed., Proceedings, 48th ASIS Annual Meeting, 1985, 22:359-362.

Sedelow, Sally Yeates, "An Interlingual Communication Support System (ICSS) Example Re Chinese/English Classroom Instruction," Proceedings, Methods III, International Conference on Foreign Language Teaching, University of Northern Iowa, Cedar Falls, 1987, pp. 115-120.

Sedelow, Sally Yeates, "Prefix," in S. Sedelow, et al., Automated Language Analysis, 1968-1969, University of North Carolina, Chapel Hill, NC, 1969, pp. 12-25.

Sedelow, Sally Yeates, with Donna Weir Mooney, "Knowledge Retrieval from Domain-Transcendent Expert Systems: II. Research Results," Proceedings, 51st ASIS Annual Meeting, 1988, 25:209-212.

Sedelow, Sally Yeates and Walter A. Sedelow, Jr., "The Application to Business/Industry of the Domain-Transcendent Expert System Building Methodology," in R. Vedder, et al., eds., Proceedings, Conference on the Impact of Artific al Intelligence on Business and Industry, Information Systems Research Center, University of North Texas, Denton, 1988, pp. 98-105.

Sedelow, Sally Yeates and Walter A. Sedelow, Jr., "Artificial Intelligence, Expert Systems, and Productivity," in Whitney and Ochsman, eds., Psychology and Productivity: Bringing Together Theory and Practice, New York, Plenum Press, 1989, pp. 51-68.

Sedelow, Sally Yeates and Walter A. Sedelow, Jr., "Categories and Procedures for Content Analysis in the Humanities," in George Gerbner, et al., eds., The Analysis of Communication Content, New York, John Wiley & Sons, Inc., 1969, pp. 487-499.

Sedelow, Sally Yeates and Walter A. Sedelow, Jr., "The Lexicon in the Background," in Winfred Lehmann, ed., Computers and Translation, 1.2, 1986, pp. 73-81.

Sedelow. Sally Yeates and Walter A. Sedelow, Jr., "Thesaural Knowledge Representation," Proceedings, Waterloo University (Ontario) Conference on Lexicology, 1986, pp. 29-43.

Sedelow, Walter A., "The Interlingual Communication Support System (ICSS): Underlying Concepts and Procedures," Proceedings, Methods III, International Conference on Foreign Language Teaching, University of Northern Iowa, Cedar Falls, 1987, pp. 109-114.

Sedelow, Walter A., "Knowledge Retrieval from Domain-Transcendent Expert Systems: I. Some Concepts from Cognitive Robotics," Proceedings, 51st ASIS Annual Meeting, 1988, 25:205-208.

Sedelow, Walter A., "Semantics for Humanities Applications: Context and Significance of Semantic 'Stores'," in Carol Parkhurst, ed., Proceedings, 48th ASIS Annual Meeting, 1985, 22:363-366.

Sedelow, Walter A., Jr., and Sally Yeates Sedelow, "Semantic Space," in Winfred Lehmann, ed., Computers and Translation, 1987, 2:231-242.

Siegel, H. J., Interconnection Networks for Large-Scale Parallel Processing: Theory and Case Studies, Lexington, MA, Lexington Books, 1984.

Talburt, John R. and Donna M. Mooney, "Determination of Strongly-Connected Components in Abstract Thesauri by the Method of Quartets," Proceedings, Workshop in Applied Computing, Oklahoma State University, Stillwater, OK, 1989 (In Press).

Talburt, John R. and Donna M. Mooney, "The Decomposition of Roget's International Thesaurus into Type-10 Semantically Strong Components," 1989 (Ms.)

Warfel, Sam, "The Value of a Thesaurus for Prefix Identification," in S. Sedelow, et al., Automated Language Analysis, 1971-1972, University of Kansas, Lawrence, KS, 1972, pp. 31-49.

Webster's Dictionary of Synonyms, Springfield, MA, G & C Merriam Co., 1942.

1989 USAF-UES SUMMER FACULTY

RESEARCH PROGRAM

Sponsored by the

AIR FORCE OFFICE OF SCIENTIFIC RESEARCH

Conducted by the
Universal Energy Systems, Inc.

Final Report

Characterization of an Optical Switch

Prepared by :	Khaja F. Subhani, Ph. D.
Academic Rank:	Associated Professor
Department and University:	Electrical Engineering Lawrence Technological University
Research Location:	RADC/OP Rome Air Development Center Griffiss AFB, NY 13441
RADC/OP Researcher:	Richard Michalak, Ph. D.
Date:	September 10, 1989
Contract Number:	F49620-88-C-0053

CHARACTERIZATION OF AN OPTICAL SWITCH

B Y

KHAJA F. SUBHANI

ABSTRACT

Numerous theoretical models exists for predicting multiple quantum well laser operation. It comprises of single cavity, with simplest device geometry based on one dimensional analysis. Preliminary investigations reveals that three dimensional modelling is essential for accurate characterization of an optical switch with realistic geometry and with different laser cavities of complex nature. A simple model to predict switching action based on the concept of laser bistability representing laser beam propagation within the cavities is also presented. Finally, directions for the follow-up research work to be performed at the parent institution are highlighted.

ACKNOWLEDGEMENTS

I wish to thank the Air Force Systems Command and the Air Force Office of the Scientific Research for sponsorship of this research. Universal Energy Systems must be mentioned for their concern and directional aspect of this program.

My experience at the Photonic Laboratories of the RADC was rewarding and enriching because of many different influences Dr. Henson provided me with support and encouragement throughout this investigation. Dr. Machalak provided a truly enjoyable working atmosphere and am grateful for the freedom I enjoyed during the course of this research work. Thanks also due to Dr. Parker, for many useful and enjoyable conversations, cooperation and understanding throughout this work.

INTRODUCTION

Recent advances in semiconductor growth techniques have made it possible to grow semiconductor hetero structures with atomic scale quantum size effects which significantly modify the electronic and optical properties of Quantumwell structures (QWS) compared with those of parent bulk compound [1-6]. More efficient emission characteristics resulting from the reduced dimensionality have utilized low-threshold index-guided lasers for both high-power laser arrays and opto-electronic integration [7-24]. For optoelectronic integration many coupled semiconductor lasers should be fabricated on a single chip. GaAs/AlGaAs multiple quantum-well (MQW) lasers have demonstrated reliability and higher efficiency. Monolithic integrated optical circuit building blocks including straight and bent waveguides, splitters, grating couplers, and laser based logic gates, memory elements recently demonstrated the compatibility of information processing on a single chip using GaAs/AlGaAs MQWs [5].

My research interest has been in the area of semiconductor devices and digital optical signal processing. My past experience related to the development of theoretical and computer modelling of devices, laser beam propagation in the nonlinear medium, is complimentary to the GaAs/AlGaAs MQWS contributed to my assignment for characterizing the Monolithic Integrated Optical Switch.

II. OBJECTIVES OF THE RESEARCH EFFORT

The Digital Optical Signal Processing (DOSP) group within the Photonic Laboratories of the RADC are in the process of developing in-house expertise through numerous programs initiated recently. However, there is no method available for characterizing the optical switch under investigation. It is expected that DOSP will collect experimental data once the fabrication equipment is operational. This involve large number of samples to be tested before any conclusions are drawn for optimal performance of the switch. Computer modelling is an alternative approach for device parameter variation to be investigated. Furthermore, once a comprehensive model is available, an exhaustive search could be made by simply sweeping over the various parameter values to generate the performance data. From this finding an optimal model for the switch can be identified for experimental testing and verification purposes.

My assignment as a participant in the Summer Faculty Research Program (SFRP) was to investigate the techniques for characterizing the Monolithic Integrated Optical Switch. Over the last 4-5 years various theoretical and numerical simulations has appeared for modelling MQWs lasers based on GaAs/AlGaAs. However, these models deals with ideal geometry and one dimensional simulations. The optical switch model of our interest comprises of two or more laser beams interaction within a complex geometrical form. Furthermore,

no such work has been done to our knowledge, to characterize the Optical Switch using multiple lasers with complex geometry. Thus, it was decided that an investigation into the development of more specific models should be under taken during the latter portion of my SFRP and to continue at my institution with funding from the Mini Grant program.

III. MONOLITHIC INTEGRATED OPTICAL SWITCH

This device consists of three rib waveguide lasers, each of which has one cleaved and one etched facet. The main or quenched laser interests both side or quenching lasers. Thus main laser shares a part of its gain volume with each of the side lasers.

The main laser is 4 micron wide and nominally 85 micron long. The side lasers are 20 micron wide and approximately 200 micron long. The logic gate was operated as an inverter by pulsing the main laser and only one side laser. Pulsing both side lasers produces the NOR/NAND logic function by adjusting side laser currents, appropriately. The NOT, NOR, and NAND functions were also obtained with the main laser driven cw at room temperature. Preliminary investigation reveals the following performance data of the Optical Switch fabricated at Cornell University.

1) Threshold current for switching as an inverter is 35 milli amps;
2) I/O intensity contrast is poor;
3) Fan-out is zero;
4) Inverter transfer function characteristics are poor.

For details see reference [5].

IV. CHARACTERIZATION OF THE OPTICAL SWITCH

1. QUANTUM WELL MATERIAL PROPERTIES

The two dimensional nature of electron motion in quantum well hetero-structure produces several unique and important features in semiconductor lasers. Quantum confinement of electrons or holes arises from a potential well in the band edges when the well width Lz is the order the de Broglie wavelength (λ_c) of the carriers. By reducing the active layer thickness Lz to the order of λ_c , a two dimensional quantum well hetero-structure laser is realized. The corresponding density-of-states function due to confined electron motion in the z-direction is given by:

$$\rho_c = \sum_n \left(\frac{m_e^*}{\pi \hbar^2 L_z} \right) H(E - E_{nz}^e) \quad \cdots \quad (1)$$

where H(E) is a unity step function. E_{nz}^e denotes the quantized energy levels with quantum number n. For the case of a symmetrical rectangular potential well of finite depth Vo and width Lz, E_{nz}^e is given by:

$$E_{nz}^e = \frac{\hbar^2 \pi^2}{2 m_e^*} \left(\frac{n}{L_z} \right)^2 ; \quad \text{for } n = 1, 2, 3 \ldots \quad (2)$$

Thus, the electron bound energy states in the conduction band are given by:

$$E^e = E_{nz}^e + \frac{\hbar^2}{2 m_e^*} (k_x^2 + k_y^2) \quad \cdots \quad (3)$$

where $k_i = n\pi/a_i$ and a_i is the lattice constant in the i direction. Since there are heavy and light holes in the

valence band, the hole bound energy states are given by similar equation to (3) with parameter values for effective heavy and light holes respectively. The quantized energy levels are solved using the following eigenvalue equations:

$$\left\{\left(\frac{m_2}{m_1}\right)\left(E_{k_0}-E_{jn}\right)/E_{jn}\right\}^{1/2} = \tan\left\{L_z\left(2m_1 E_{jn}\right)^{1/2}/2\hbar\right\} \quad \cdots (4a)$$

when n = even integer and

$$\left\{\left(\frac{m_2}{m_1}\right)\left(E_{k_0}-E_{jn}\right)/E_{jn}\right\}^{1/2} = -\cot\left\{L_z\left(2m_1 E_{jn}\right)^{1/2}/2\hbar\right\} \quad \cdots (4b)$$

for n is odd.

where m1 is effective mass of carriers in the well region and m2 corresponds to the barrier region. E_{k_0} is the band offset energy referred to conduction band or valence band case.

2. GAIN SPECTRA OF MQW LASER

In the conventional double hetero QW laser, the gain coefficient for photon energy E can be formally expressed as:

$$g(E) = \frac{\pi^2 c^2 \hbar^3}{n_r^2 E^2} \cdot M \int_0^{E-E_g} \rho_c(E-E')\,\rho_v(E'-E) \times \left[f_c(E') - f_v(E'-E)\right] dE' \quad \cdots (5)$$

where n_r is the refractive index, c the velocity of light, E_g the energy gap, and M a constant representing the probability of dipole transition. $f_c(E)$ and $f_v(E)$ are the distribution functions of electron and hole, respectively.

3. THRESHOLD CURRENT

The temperature dependence of double hetero (DH), QW lasers have been theoretically calculated . Arakawa and Sukaki have found theoretically that the threshold current density of a QW laser is proportional to:

$$J_{th} = J_{th}(o)\ exp\,(T/T_o) \quad - - - \quad (6)$$

It has been shown that the threshold current density function of the DH QW lasers can be described by

$$J_{th} = \frac{J_o d}{\eta} + \frac{d}{n\beta\Gamma}\alpha_i + \frac{d}{n\beta\Gamma}\left(\frac{1}{L}\right) ln\left(\frac{1}{R}\right) \quad - - - \quad (7)$$

with the gain current relation assuming the linear form

$$g_{max} = B\,(\,J_{nom} - J_o\,)$$

In the above equations, d is the active layer thickness in micrometers, η the internal quantum efficiency at the threshold, α_i includes all internal optical losses, Γ is the optical confinement factor, L the cavity length, R the power reflectance of the mirror, g_{max} the gain coefficient, β the gain factor, J_{nom} the nominal current density for a 1 micron thick active layer and unity quantum efficiency, and J_o the value of J_{nom} at which $\beta\, g_{max}$ is linearly extrapolated to zero.

V. PRELIMINARY INVESTIGATIONS

1. THE MAIN LASER

The main laser of the optical switch comprises of cavity region of one piece gain volume at the MQWS lave. From its cross sectional view, it is evident that the current spreading causes nonuniform exposure of MQWS layers affecting the laser characteristics. Thus a realistic geometry has to be considered for characterization of the main laser.

2. THE SIDE LASERS

Gain volume associated with the side lasers cavity region comprises of three parts: directly pumped active region, indirectly pumped active region (gain volume shared by the main laser), and unpumped region. Figure (1) represents various cross sectional views of the switch under study. Lasing action takes place at MQWS level. Geometry of the side lasers and associated mirrors position also causes non uniform distribution of the electric field at MQWS level besides the current spreading effect leading to nonuniform current distribution density as mentioned before. Electrode geometry and etched mirror positions will leads to a complex boundary value problem to be solved. Thus, results of the three dimensional modelling of the optical switch is expected to reveal critical parameters for its performance evaluation. To our knowledge models does not exists for such type of the cavity. This requires including the concepts such as losses associated with the unpumped

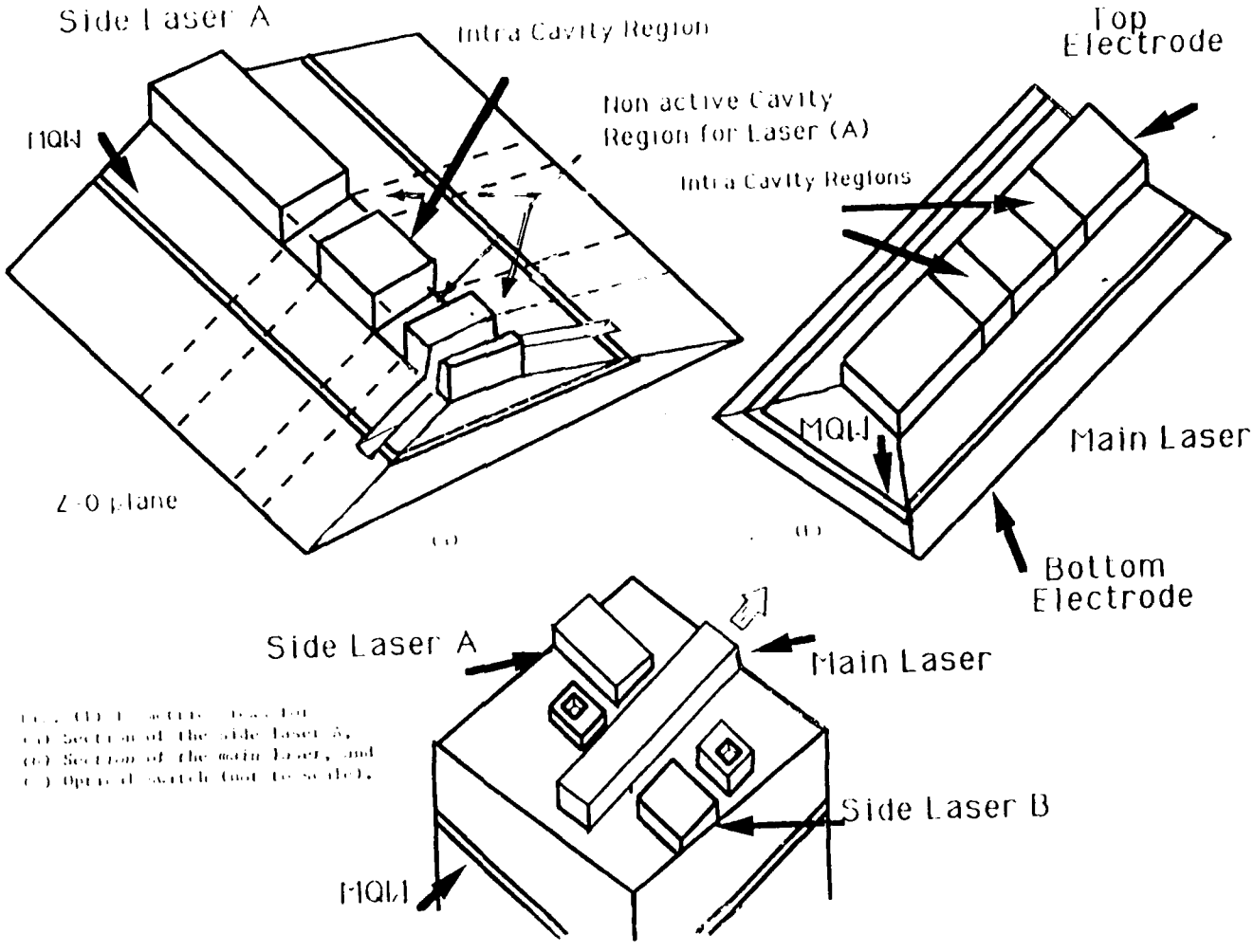
Side Laser A
Intra Cavity Region
MQW
Non active Cavity
Region for Laser (A)
Intra Cavity Regions
Top
Electrode
MQW
Main Laser
Z-O plane
Bottom
Electrode
Side Laser A
Main Laser
Side Laser B
MQW

portion of the cavity for the estimation of threshold current to turn on the coupled laser.

3. BISTABILITY

Bistability function of the main laser represents quenching action using side laser(s). For an optical switch it is necessary to turn on and turn off the main laser with the help of the side laser(s). An Inverter operation deals with the interaction of two laser beams propagating right-angle to each other within the cavity region of the MQWS layers. This operation can be defined using electromagnetic fields theory for the propagation of the laser beams through wave-guides intersecting normal to each other.

A simple model is developed to predict the switching action of an optical inverter circuit. Electromagnetically speaking, the intracavity region is a well known dielectric slab and there exists TE and TM modes, propagating in the plane represented by the MQWS, and dying off exponentially in the direction normal to the plane (i.e. cladding region). Considering the continuity of transverse electric and magnetic fields at the either sides of MQWS interfaced with the cladding region resulted in:

$$\eta_1 = -\frac{\bar{\sigma}}{\omega_1 \epsilon} + \left\{ 2 (k_{01} x_0)^2 \left(\frac{\epsilon_1' - \bar{\epsilon}'}{\epsilon} \right) \frac{\sigma_1}{\omega_1 \epsilon} \right\} + \ldots \ldots \quad (9)$$

for main laser and

$$\eta_2 = -\frac{\bar{\sigma}}{\omega_2 \epsilon} + \left\{ 2 (k_{02} x_0)^2 \left(\frac{\epsilon_2' - \bar{\epsilon}'}{\epsilon} \right) \frac{\sigma_2}{\omega_2 \epsilon} \right\} + \ldots \ldots \quad (10)$$

for the side laser.

where

$$\bar{\sigma} = (\sigma_1 + \sigma_2)/2 \quad \text{and}$$

subscripts 1 and 2 referred to upper and lower cladding regions

$\bar{\epsilon}' = (\epsilon_1' + \epsilon_2')/2$ real part of the permittivity,

$K_{01,02} = \omega_{1,2}\sqrt{\mu_0 \epsilon}$ for GaAs material of MQWS,

x_0 = width of the intracavity region,

$\omega_{1,2}$ represents frequency of main and side lasers and identical to each other.

In the above equations first term represents rate of decay due to losses in the MQWS. Second term within the brackets represents rate of growth due to carrier gain (population inversion) in the region. For the laser operation to occur the second term must dominate in each of the above two equations. However, for quenching action to take place using side laser for inversion operation $\eta_2 > \eta_1$. Thus, in general when the main laser is turned on when $\eta_1 > \eta_2$ and off when $\eta_2 > \eta_1$.

The above simple model is to be extended to consider the realistic geometry of the switch for electromagnetic wave propagation within the cavities.

VI RECOMMENDATIONS

1. CURRENT AND VOLTAGE DISTRIBUTION ON THE MQWS LAYERS

Current spreading effect and potential distribution on the MQWS layers needs to be investigated, using the actual dimensions of the optical switch inconjunction with the electrodes geometry, etched mirrors position, and orientation of the main and side lasers.

This involve current continuity equation and poission's equation to be solved in three dimension. This include computation of current density and potential distribution data at various planes parallel to the MQW layers. It is expected that the results and conclusion of this investigation will be helpful in predicting the electrodes geometry and relative position of mirrors to accomplish uniform current density and voltage distribution on the MQW layers.

2. MAIN LASER PARAMETER OPTIMIZATION

This involve developing numerical models and simulating on a computer to predict the lasing action. Parameter variation has to be investigated for optimal performance of the laser, which includes laser dimensions, variation in the MQWS such as barrier and well thickness; and overall size of the active material, threshold current, temperature effects, MQWS gain, far field radiation effect, and line width.

3. SIDE LASER MODELLING

Lasing cavity models comprising of 3 different regions has to be considered for predicting the operation of the side laser(s). To our knowledge such model does not exists. As a first step a model based of higher cavity losses can be considered for simulation. Latter on this will be replaced with a model representing exact cavity losses. Once a model is developed its parameter optimization, as mentioned in part 2 of this section VI, has to be investigated.

4. BISTABILITY OF THE MAIN LASER

A vast amount of literature exists on optical bistability and semiconducting lasers. Most of the work has been on bulk devices considering two parallel laser beams interaction and restricted to external cavity region. The optical switch operates on the principles of bistability of semiconductor lasers. The present switch under investigation involves interaction of two beams propagating perpendicular to each other within the lasing cavity region. Furthermore, a detail study of the dynamics of two-mode bistability in the semiconducting lasers is required. Of particular interest to us is the case when the two modes refer to two lasing directions.

5. SWITCHING DELAY

This involves detail modelling and numerical simulation of the switching characteristics of the optical gate. It is basically the time required to deplete carrier in the inverted region of the cavity when the switch is turned off. This model simulation deals with the time dependent carrier gain effect. However, no such models exists so far.

6. EXPERIMENTAL VERIFICATION OF THE MODELS

Experimental work requires fabrication of the devices based on the optimal model studies listed in the section 1-5. At present DOSP group of the RADC is in the process of developing in-house expertise for device fabrication and testing. Furthermore, computer modelling may direct the technology to address issued which are not yet identified.

7. RECOMMENDATION FOR MINI GRANT

For the characterization of the Optical Switch, it is essential that all of the six topics listed above has to be investigated. Limitations associated with the USAF Mini Grant scheme forces to prioratise the topics for detail investigations to be conducted. It is recommended that the first two topics, namely, "Current Density and Potential Distribution" and "Main Laser Parameter Optimization" shall be included in the proposal for funding through the Mini Grant scheme. Remaining topics #3-5 shall also be investigated under expert scientist program of the USAF or direct

funding to an institution such as ours. Furthermore, these studies requires some theoretical models to be developed before numerical simulations are performed.

REFERENCES

1. R. Dingle,"Confined carrier quantum states in utrathin semiconductor hetero-structures," Festkorperprobleme, vol. XV, pp 21, 1975.
2. W. T. Tsang,"Extremely low threshold (AlGa)As graded-index waveguide separate-confinement hetero-straucture lasers grown by molecular beam expitaxy," Appl. Phys. Lett., vol. 40, pp 217, 1982
3. G. H. B. Thompson and P. A. Kirkby,"(GaAl)As lasers with a hetreo-structure for optical confinement and additional hetero-junctions for extreme carrier confinement," IEEE J. Quantum Electron., QE-9, pp 311, 1973.
4. L. A. Coldren, K. Furuya, B. I. Miller, and J. A., Rentschler,"Etched mirror and groved-coupled GaInAsP/InP laser devices for integrated optics," IEEE J. Quantum Electron., QE-18, pp 1679, 1982.
5. W. Grande,"A study of GaAs/AlGaAs semiconductor laser devices for monolithic integrated optical circuits," Ph. D. dissertation, Cornell University, 1989.
6. L. K. Cheng, W. Bosenberg, and C. L. Tang, "Growth and characterization of nonlinear optical crystals suitable for frequency conversion," invited review in progress in Crystal Growth and Characterization, Nonlinear Optical Crystals.
7. L. K. Cheng, W. Bosenberg, F.W. Wise, I. A. Walmsley, "Birefringence-induced polarization counter rotation in a semiconductor laser," App. Phys. Lett. vol. 52, pp 519-521, 1988.
8. T. Fujita, A. Schremer, and C. L. Tang,"Plorization switching in a single-frequency external-cavity semiconductor laser", Appl. Phys. Lett., vol. 51, pp 1487, 1987.
9. T.Fujita, A.Schremer, and C. L. Tang, "Polarization bistability in external cavity semiconductor lasers," Appl. Phys. Lett., vol. 51, pp 392, 1987.
10. W. Grande, W. Braddock, J. R. Shealy, and C. L. Tang, "One step two-level etching technique for monolithic integrated optics," Appl. Phys. Lett., vol. 51, pp2189, 1987.
11. N. K. Dutta,"Calculated threshold current of GaAs quantum well lasers," J. Appl. Phys., vol. 53, no. 11, pp 7211-7214, 1982.
12. D. Kasemset. C. S. Hong, N. B. Patel, and P. D. Dapkus, "Graded barriers single quantum well lasers-theory and experiment," IEEE J. Quantum Electron., vol. QE-19, pp 1025-1030, June 1983.
13. N. K. Dutta, R. L. Hartman, and W. T. Tsang, "Gain and carrier lifetime measurements in AlGaAs single quantum well lasers," IEEE J. Quantum Electron., vol. QE-19, pp 1243-1246, Aug. 1983.
14. A. Sugimura, "threshold currents for AlGaAs quantum well lasers," IEEE J. Quantum Electon., vol. QE-20,

pp 336-343, Apr. 1984.
15. M. Asada, A. Kameyama, and Y. Suematsu,"Gain and intervalence band absorption in quantum well lasers,"IEEE J. Quantum Electron., vol. QE-20, pp 745-753, July 1984.
16. L. C. Chiu and A. Yariv, "quantum well lasers," J. Luminescence, vol. 30, pp 551-561, 1985.
17. P. T. Landsberg, M. S. Abrahams, and M.Osinski,"Evidence of no k-selection in gain spectra of quantum well AlGaAs laser diodes," IEEE J. Quantum Electron., vol. QE-21, pp 24-28, Jan 1985.
18. Y. Yamada, S. Ogita, M. Yamagishi, and K. Tabata, "Anisotropy and broadening of optical gain in a GaAs/AlGaAs multiplequantum-well laser," IEEE J. Quantum Electron., vol. QE-21, pp 640-645, June 1985.
19. Y. Arakawa and A. Yariv,"Theory of gain, modulation response and spectral linewidth in AlGaAs quantum well lasers," IEEE J. Quantum Electron., vol. QE-21, pp 1666 -1674, Oct. 1985.
20. P. W. A. Mc Ilroy, A. Kuroba, and Y. Uematsu, "Analysis and application of theoretical gain curves to the design of multiplequantum well lasers," IEEE J. Quantum Electron., vol. QE-23, pp 960-968, June 1987.
21. S. Colak, R. Eppenga, and M. F. H. Schuumans, "Band mixing effects on quantum well gain," IEEE J. Quantum Electron., vol. QE-23, pp 960-968, June 1987.
22. E. Zielinski, H. Schweizer, S. Hausser, R. Stuber, M. H. Pilkuhn, and G. Weimann,"Systematics of laser operation in GaAs/AlGaAs mutiplequantum well heterostructures"IEEE J. Quantum Electron., vol. QE-23, pp 969-976, June 1987.
23. A. R. Reisinger, P. S. Zory, and R. G. Waters, "Cavity length dependence of the threshold behaviour in thin quantum well semiconductor lasers," IEEE J. Quantum Electron., vol. QE-23, pp 993-999, June 1987.
24. P. Blood, S. Colak, and A.I. Kucharaska,"Temperature dependence of threshold current in GaAs/AlGaAs quantum well lasers," Appl. Phys. Lett., vol. 52 no. 8, pp 599-601, 1988.

1989 USAF-UES SUMMER FACULTY RESEARCH PROGRAM

GRADUATE STUDENT RESEARCH PROGRAM

Sponsored by the

AIR FORCE OFFICE OF SCIENTIFIC RESEARCH

Conducted by the

Universal Energy System, Inc.

FINAL REPORT

Study of a Communication Receiver for Spread Spectrum Signals

Prepared by:	Donald R. Ucci, Ph.D. / Ernest Rho
Academic Rank:	Associate Professor / Graduate Student
Department and	Electrical and Computer Engineering Department
University:	Illinois Institute of Technology
Research Location:	RADC/DCCD
	Griffiss Air Force Base
	Rome, NY 13441
USAF Researchers:	Mr. John P. Patti and Mr. Stephen C. Tyler
Date:	September 28, 1989
Contract No:	F49620-88-C-0053

Study of a Communication Receiver for Spread Spectrum Signals

by

Donald R. Ucci & Ernest Rho

ABSTRACT

A simulation of a Frequency Domain Receiver (FDR) was ported from an IBM-type Personal Computer to a Commodore Amiga Multi-tasking Personal Computer System. The enhanced speed and graphics capability of the Amiga was exploited. This system will serve as a workstation for testing communication systems of the future at RADC.

A simulation of an Adaptive Nonlinear Coherent Processor (ANCP) was performed. The signalling environment was presumed to have present non-Gaussian interferers. It is known that, when the received signal contains highly non-Gaussian components, a receiver based on the likelihood function shows substantial performance improvement over correlation processing. This nonlinear demodulator requires the learning of the interference Probability Density Function (PDF) and subsequent generation of an appropriate nonlinear function. In this study a histogram approach was used for estimation of the PDF and the nonlinearity was generated from this estimate.

Several problems were revealed during software simulation. These included PDF estimation at singular points, appropriate smoothing for the histogram and determination of the optimal number of samples and bins for the PDF histogram.

ACKNOWLEDGMENTS

We express our thanks to the Air Force Systems Command and the Air Force Office of Scientific Research for their sponsorship of the work undertaken in this study. In addition, we are most grateful to Universal Energy Systems, Inc. for their assistance in our research efforts.

We also wish to thank the staff and researchers of the Rome Air Development Center. Most especially we wish to thank our Branch Chief, Mr. Peter K. Leong, for his efforts to make our stay a pleasant and productive one. Our sincerest gratitude goes to Mr. John P. Patti and Mr. Stephen C. Tyler, for their help in defining and guiding our summer research effort. In addition, we thank Mr. James Cutler for his aid with the computer systems that we used in our research. Finally, our thanks to all the other members of RADC who made our stay worthwhile.

I. INTRODUCTION:

In modern communication systems design, especially those used for military communications, efforts must be made to mitigate the problem of interfering signals in the transmission path. These interferers, whether intentional or not, under certain circumstances can substantially degrade the overall communication system performance [1]. Modern research in this area is targeted toward several layers of mitigation techniques such as adaptive nulling of these interferers in an antenna array, and adaptive signal processing methods utilized in the receiver decision making process [2].

The Communication Technology Branch of the Rome Air Development Center (RADC/DCCD) at Griffiss Air Force Base is concerned with the effect of non-Gaussian interference on communication system receiver performance. Specifically, of concern is the degradation caused by pulse type, continuous wave (CW), and wide band jammers. Our work at the laboratory has been focused on methods to improve the receiver performance in the presence of these types of jammers. We have outlined some problems and possible solutions. Some of these were examined during the Summer Research Program while others were designated to be studied in the future through the Mini-Grant Program (Research Initiation Program - RIP). Our research interests have been in the area of adaptive array signal processing and digital communication systems. Dr. Ucci has worked on performance degradation in both the areas of adaptive arrays and digital signal processing. The work is very closely related to the study performed during the summer program. Mr. Rho has recently found interest in adaptive signal processing and adaptive antenna arrays.

program graphics outputs to be compatible with the Amiga system. This proved to be a time consuming process as we needed to learn, by trial and error, the effects of changes we made in the program.

Once this was accomplished the remaining task, i.e., to run the simulation, was relatively simple. In the conversion process we gained a great deal of knowledge about the Amiga system, especially its graphics, which will be used in the future.

V. ADAPTIVE PROCESSING METHODS:

The nonlinear signal processing used in an ANCP is based on the likelihood function which is mainly dependent on statistical detection theory [4]. The study focused on the generally optimal (GO) [1] and the locally optimal (LO) [4,5] demodulators. The former is an exact implementation of the likelihood function and the latter is an alternative implementation which is near optimal for large interference-to-signal power ratio (J/S). The GO demodulation is based on the likelihood function as follows:

$$L_{Gm} = \sum_{k=1}^{N} \log[f(r_k - s_k^m)] \quad \text{for } m=1,...,M, \tag{1}$$

where:

L_{Gm} = GO demodulator likelihood of m_{th} signal transmission,

N = number of independent samples per symbol decision,

$f(\cdot)$ = PDF of the received signal,

s_k^m = normalized sample sequence corresponding to the m^{th},

waveform from the M-ary signal set,

M = number of waveforms in the M-ary signal alphabet,

r_k = k^{th} received signal sample.

The noncoherent LO demodulation, obtained from a Taylor series expansion of the GO demodulator around the signaling point, is based upon computing the following likelihood function:

$$L_{Lm} = \sum_{k=1}^{N} -\frac{f'(r_k)}{f(r_k)} \times s_k^m, \text{ for } m=1,...,M, \tag{2}$$

where:

L_{Lm} = LO likelihood of m^{th} signal transmission,

and

f' = the derivative of f.

Both the LO and GO demodulator require the learning of the interference PDF. Two methods are recommended to estimate the interference PDF for the likelihood function [1]. One is the M-interval polynomial approximation (MIPA) algorithm based on a piecewise polynomial representation of the PDF estimate and the other is the well known histogram approach. As can be seen from Eq. (2) the locally optimal demodulator performs a correlation of the known signal reference s_k^m with a function $g(r_k) = -\frac{f'(r_k)}{f(r_k)}$, for all values of m, and chooses the largest. Thus, the demodulator must obtain the PDF, formulate g, and then correlate this mapped output with each of the known signals. The histogram method is used because it is simple, more easily implementable and provides relatively good results [1].

Our summer study focused upon creating software modules which produce a

PDF histogram estimate and form the function g. The shape of the raw histogram can be quite rough and smoothing is recommended [1]. Smoothing is performed in software by a module which performs a convolution with a Gaussian pulse which is truncated appropriately. For certain types of PDF's, (that is, those which exhibit singularities), smoothing can distort the PDF substantially. This will be discussed further in the results and recommendation sections. The function, g, was implemented by digitally performing the derivative of $f(r_k)$ and then taking the ratio of this value with $f(r_k)$ itself. This constituted a third software module that we implemented. All these modules performed as expected.

VI. RESULTS:

A. Simulation Transference Results

As a result of porting the FDR program to the Amiga system two items were observed. The first was speed enhancement. The speed gain over the original Amiga system using a BASIC interpreter was at least a factor of four and about twice as fast as the IBM type machine (note: the Amiga system used only 4 colors or 2 bit planes while the IBM type system used 8 colors or 3 bit planes). Secondly, the graphics of the Amiga system was better because it had higher resolution capabilities. Also, in modifying the graphics portion of Mr. Tyler's program, we were able to use the capability of the Amiga to display output curves on two separate screens, which could be pulled down or brought forward for viewing as needed.

B. ANCP Results

The software modules created for the ANCP were tested by simulation and qualitative curves were created. We present several results here.

First we tested the functionality of the modules by using ideal histograms for both a Gaussian and an inverse square root noise density functions. That is, we generated histograms and associated nonlinear functions of ideal PDF's of the form e^{-x^2} and $\frac{1}{\sqrt{1-x^2}}$. These are shown in Fig. 1 a, b, c, and d for the equivalent of 256 histogram bins. Figures 1 a and b illustrate the PDF and nonlinear transform for the Gaussian density, respectively. As can be observed, the optimum nonlinear function, in this case is linear. That is,

$$g_G = -\frac{f'}{f} = -\frac{(-2x)e^{-x^2}}{e^{-x^2}} = 2x, \text{ for all } x. \tag{3}$$

Figures 1 c and d plot the PDF and transform for a sinusoidal (CW) interferer, respectively. The nonlinear transform for this PDF is

$$g_{CW} = -\frac{x}{1-x^2}, \quad |x| \leq 1. \tag{4}$$

(Note the singularities at the endpoints.)

These plots represent the ideal, theoretical cases. Thus, they provide an optimum measure of performance for comparison with the simulation of real signals.

Figures 2 a, b, c, and d, illustrate the performance of the histogram module for the case of 10,000 sample points, 100 histogram bins, 6 interferers and 99 smoothing filter taps. Figures 2 a and b show the unsmoothed estimators while Figs. 2 c and d

show the smoothed estimates. Notice the rough Gaussian shape and very noisy linear estimate in Figs. 2 a and b, and the improvement shown in the succeeding curves. This illustrates the necessity of smoothing the PDF estimate. (Note: The transform function is not smoothed itself but is obtained from the smoothed PDF.)

In Figs. 3 a, b, c, and d, we demonstrate each module's output for the case of 25,000 samples, 256 bins, 201 taps, and 1 CW interferer. Note in Fig. 3 a, the general shape shown by the ideal curve of Fig. 1 c; however, there is a demonstrable difference in the transform function of Figs. 3 b and 1 d. This noisy PDF needs smoothing. The smoothed estimates are shown in Figs. 3 c and d. Note here, the distortion of the PDF and the consequences sustained by the transform function. It has completely changed character. This is because of the singular endpoints. This anomaly needs to be addressed.

VII. RECOMMENDATIONS:

This study revealed the advantages of utilizing the Amiga system as a platform for simulating communication systems. It also showed some pitfalls of using the ANCP, namely the PDF singularity problem, the noisy estimate and distorted smoothed transform, and the changing characteristic shape of the PDF from non-Gaussian to Gaussian-like for very few interferers (this could be a major deficiency in the approach). All these problems require further examination and simulation.

Investigation of the utility of using a nonlinear processor to mitigate wide-band jammers is a necessity. Since it is desirable to integrate some workable ANCP scheme into the FDR program (which we will explore in the future research),

narrow band jammers can easily be mitigated in the frequency domain by excision. Therefore, the main problem to be studied concerns wide band interferers. Thus far, no research has been performed to quantify the effectiveness of the ANCP on such jammers. Using simulation techniques, it is relatively simple for us to model wide band jammers and determine their effect on system performance.

It is also necessary to model a two-dimensional, i.e. in-phase and quadrature channel, receiver which will ultimately be used in an actual system. This is a straightforward extension of the work we have begun during the summer. In addition, once this is accomplished we can test the system using various, more realistic types of modulation such as Offset Quaternary Phase Shift Keying (OQPSK) and Minimum Shift Keying (MSK). Although it may be true that, in this type of receiver, CW jammer PDF singularities do not appear, this does not necessarily imply that singularities will not occur under different jammer scenarios. Thus, this problem needs to be addressed in this case also.

As an alternative to the histogram approach, the MIPA [1] approach needs to be examined in more detail. There is a tradeoff in the order of the polynomial and the number of bins employed and, thus, the amount of processing which needs to be performed. For example, will a fourth order polynomial used in conjunction with four bins provide better or worse performance than a second order polynomial in eight bins (if one uses the polynomial order times the number of bins as a metric for equivalence, both the above have a value of 16)?

Additionally, other smoothing algorithms need to be examined. The Gaussian pulse may make the smoothed PDF "look" too Gaussian and reduce the

effectiveness of the ANCP on the jammer.

Finally, we must examine methods to optimize the computer code for efficient and fast performance. This entails use of better sorting algorithms, variable type definition, efficient use of memory, and other factors. The above problems and their solution will be proposed in a Mini-Grant application.

REFERENCES

[1] Hazeltine Report No. 6662, Adaptive Nonlinear Coherent Processor Design, Vols. I and II, RADC Contract No. F30602-86-C-0106, October 18, 1988.

[2] Charles Stark Draper Laboratories, Inc. Report No. CSDL-R-2167, Robust Digital Adaptive Transceiver (RDAT), RADC Contract No. F30602-87-C-0149, July 31, 1989.

[3] Charles Stark Draper Laboratories, Inc. Report No. CSDL-R-1787, Robust Digital Adaptive Transceiver (RDAT), RADC Contract No. F30602-83-K-0160, August 1985.

[4] Middleton, David, "Canonically Optimum Threshold Detection," IEEE Transactions on Information Theory, Vol. IT-12, No., April 1966, pp. 230-243.

[5] Spaulding, Arthur D., "Locally Optimum and Suboptimum Detector Performance in a Non-Gaussian Interference Environment," IEEE Transactions on Communications, Vol. COM-33, No. 6, June 1985, pp. 509-517.

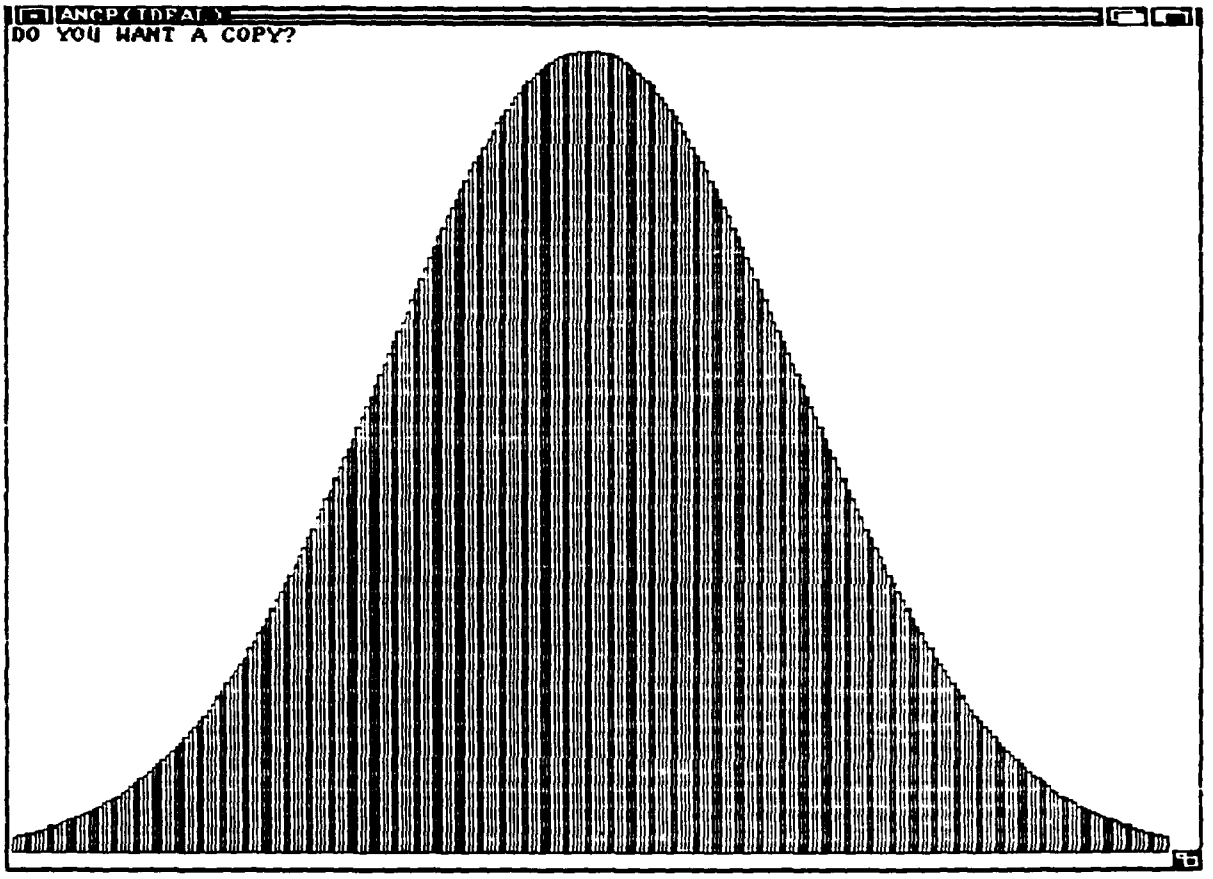

Figure 1a

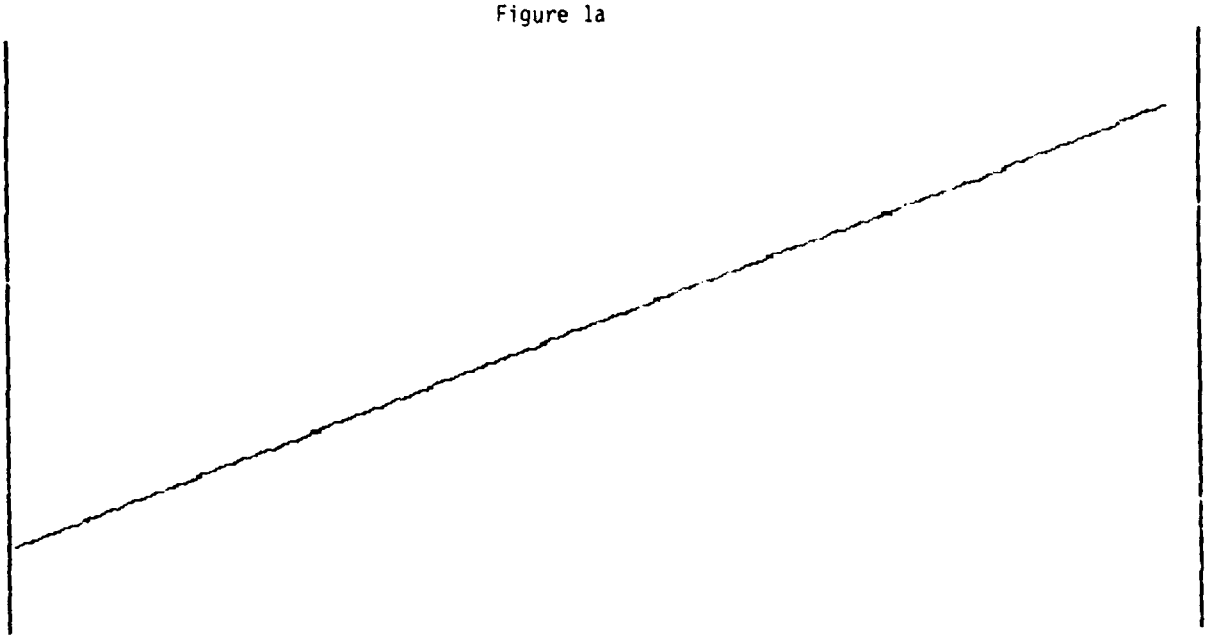

Figure 1b

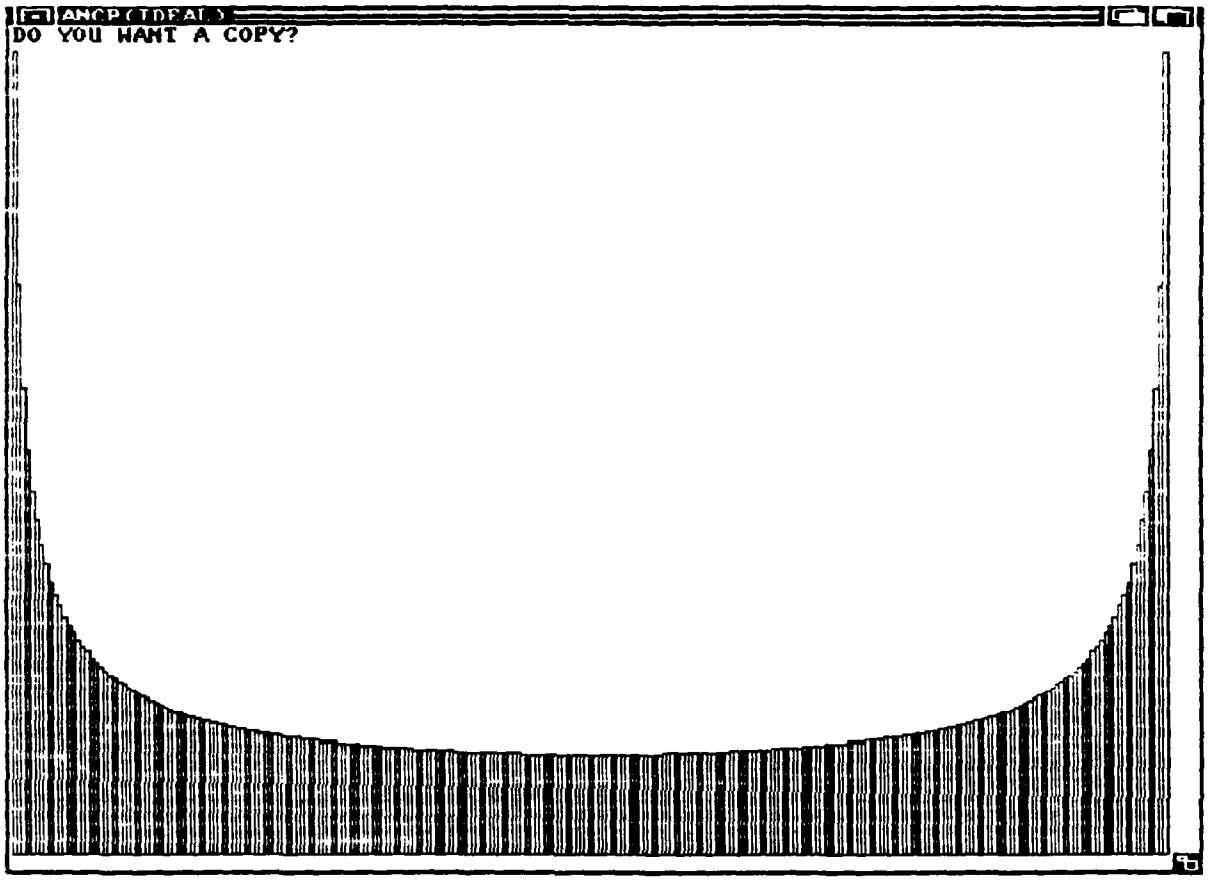

Figure 1c

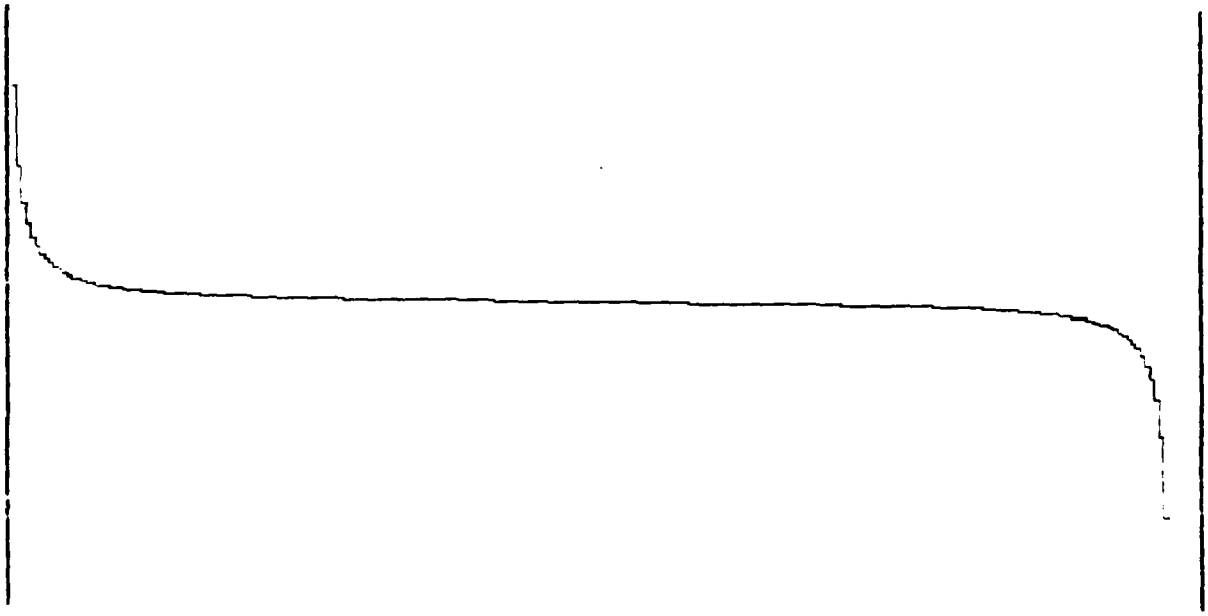

Figure 1d

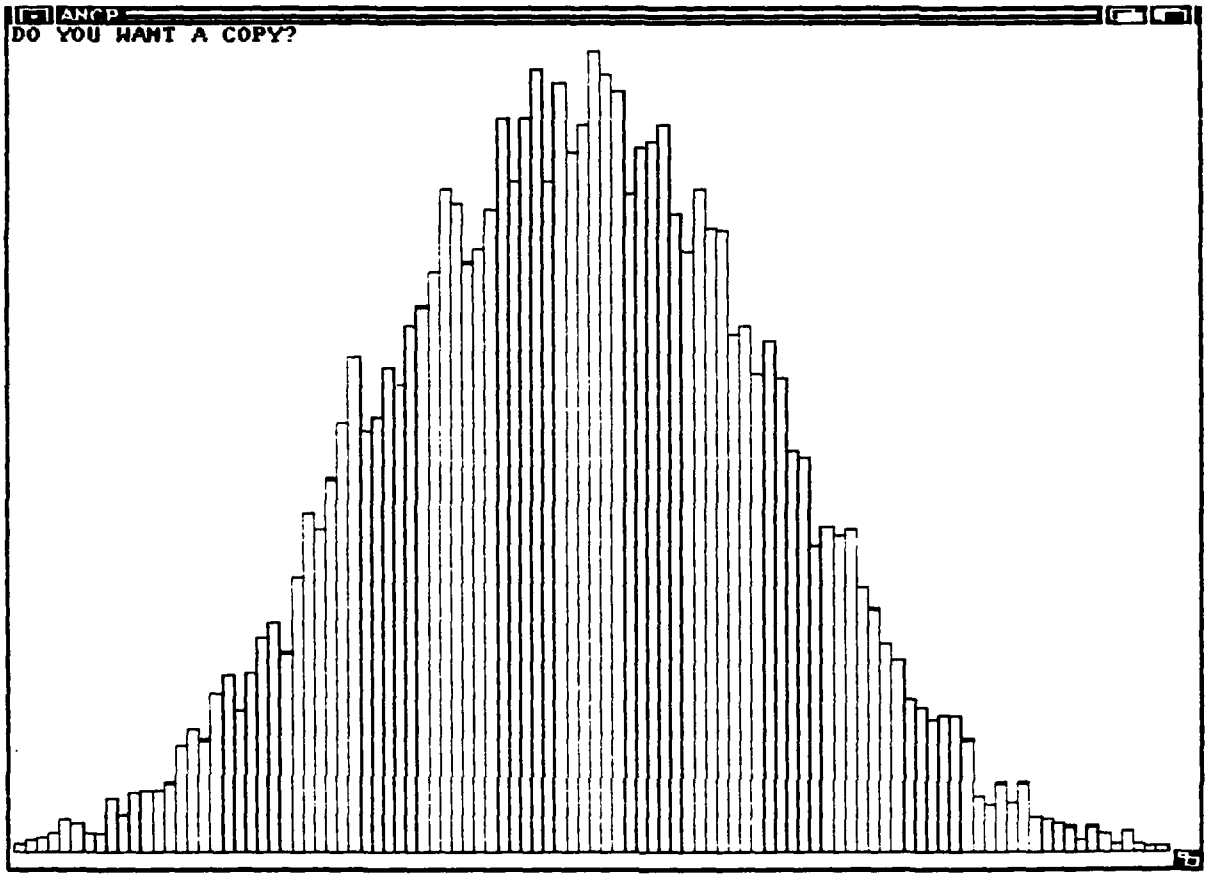

Figure 2a

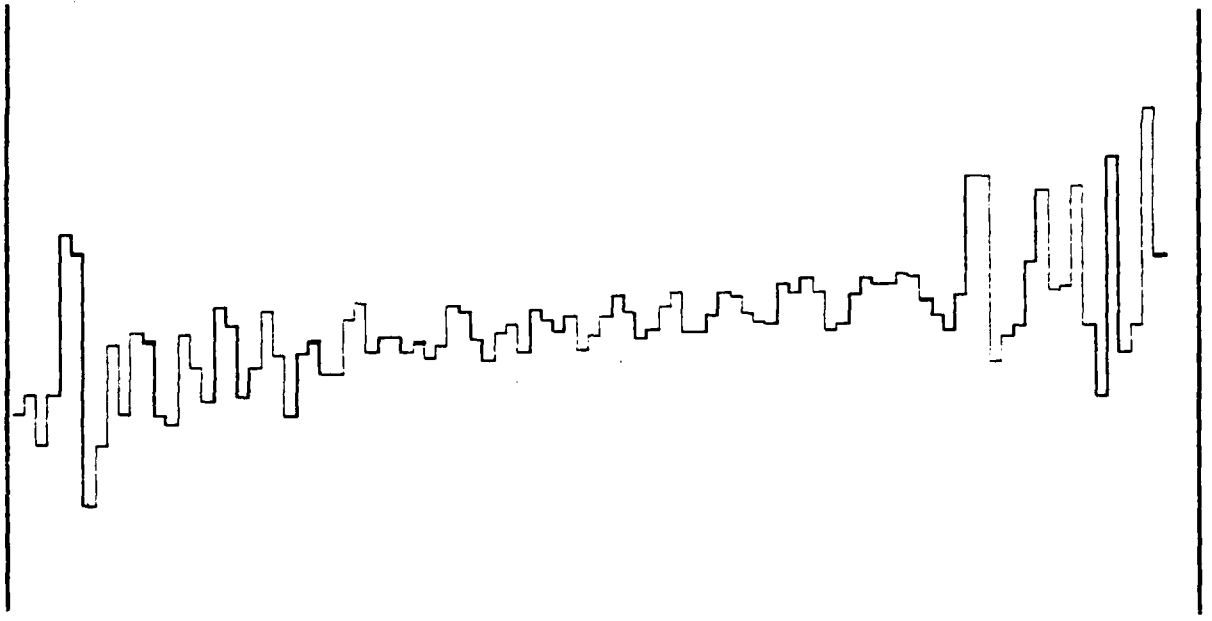

Figure 2b

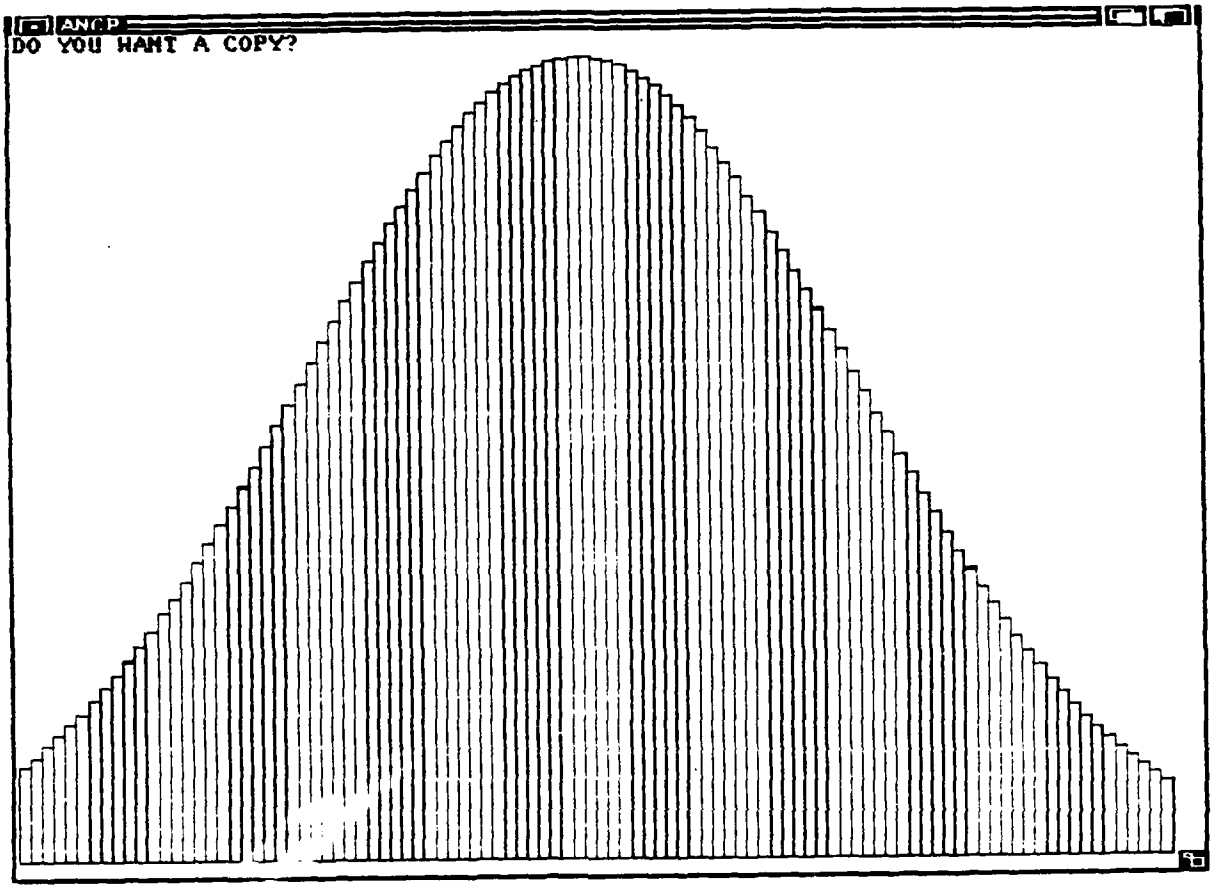

Figure 2c

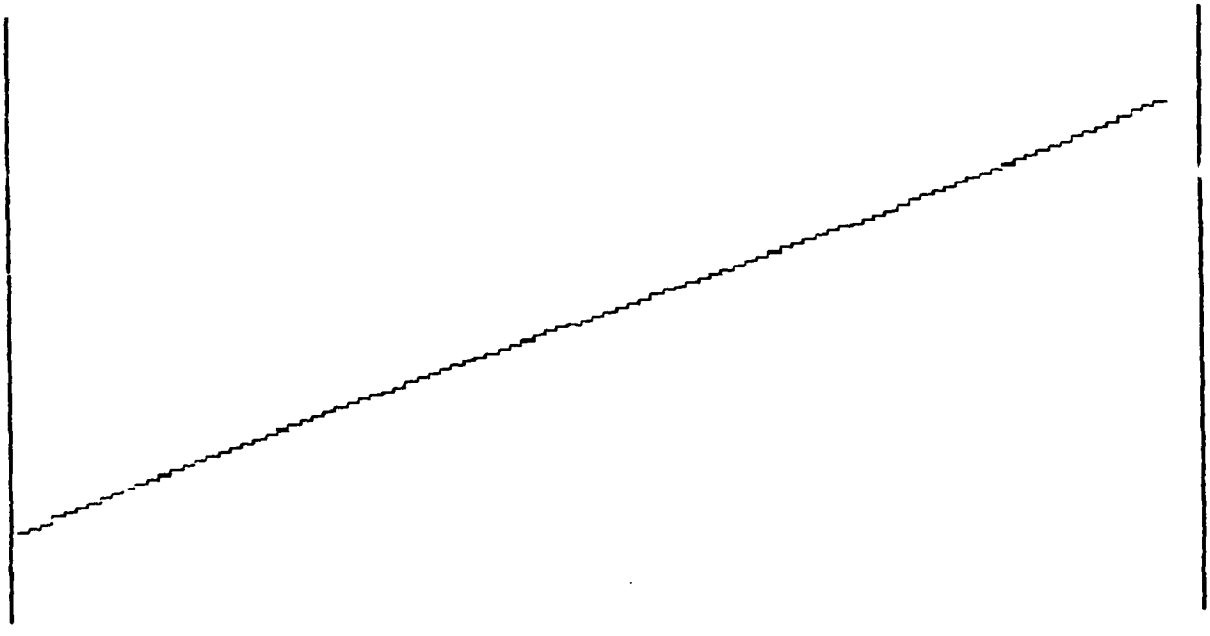

Figure 2d

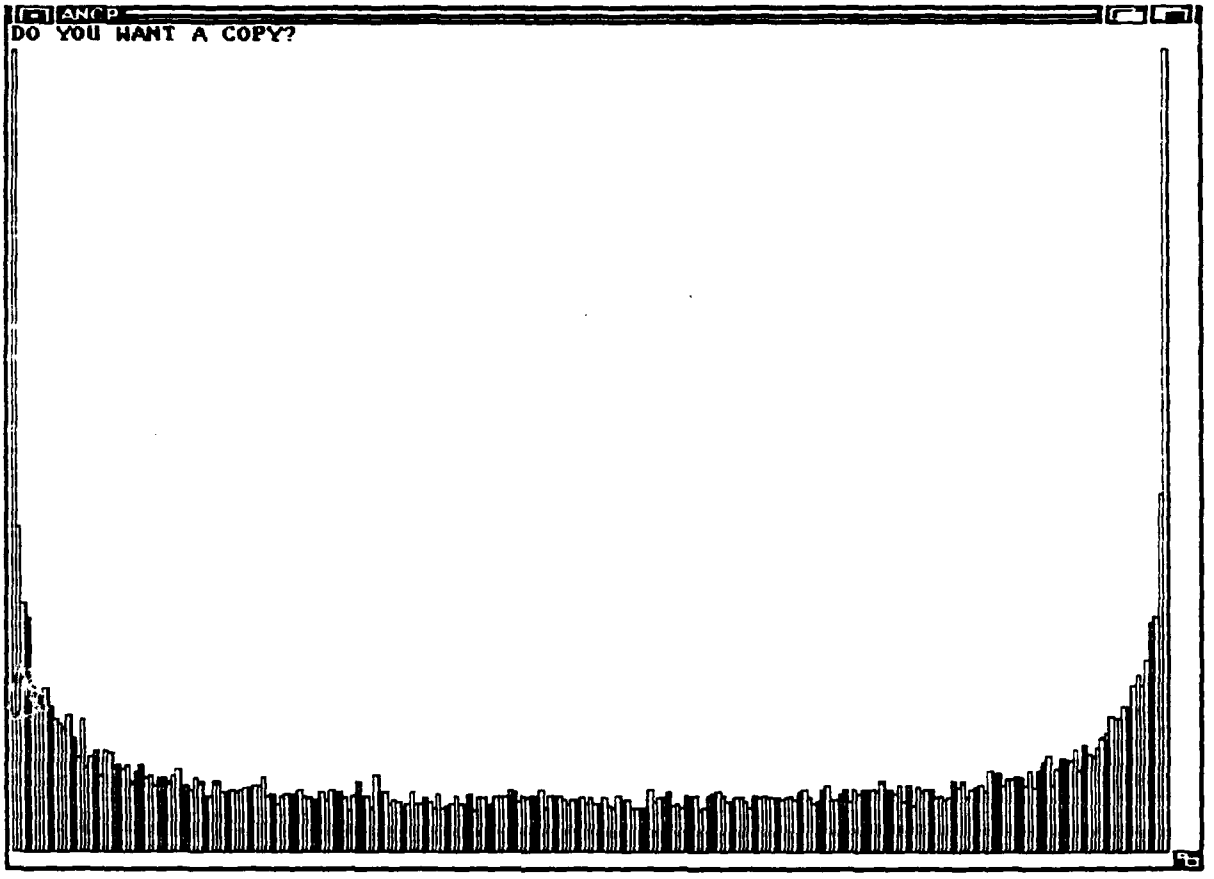

Figure 3a

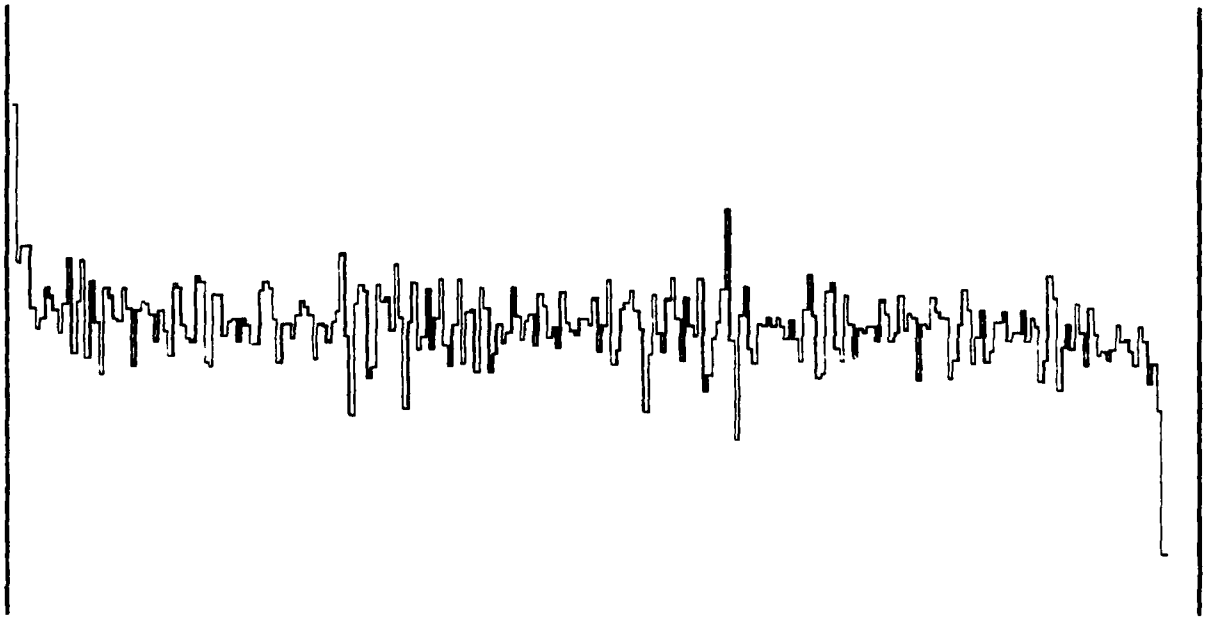

Figure 3b

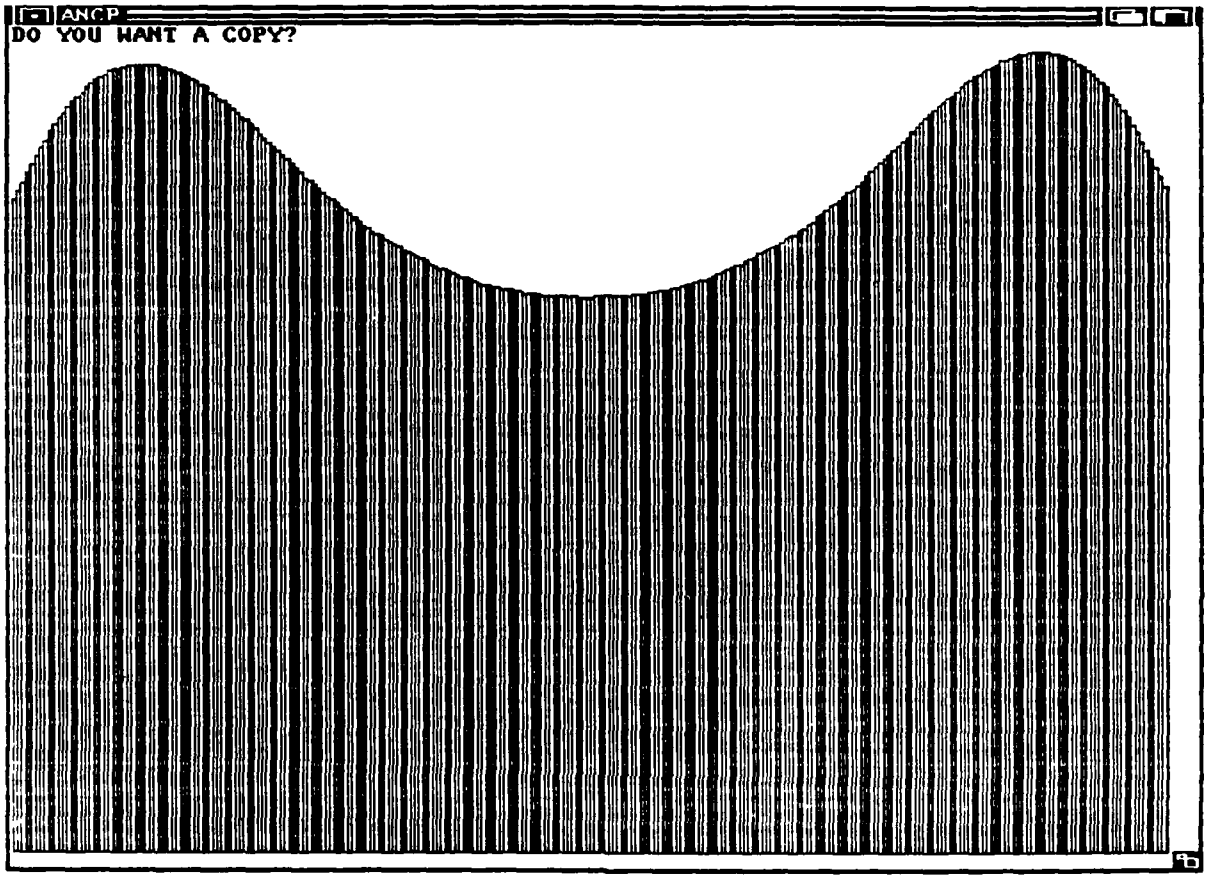

Figure 3c

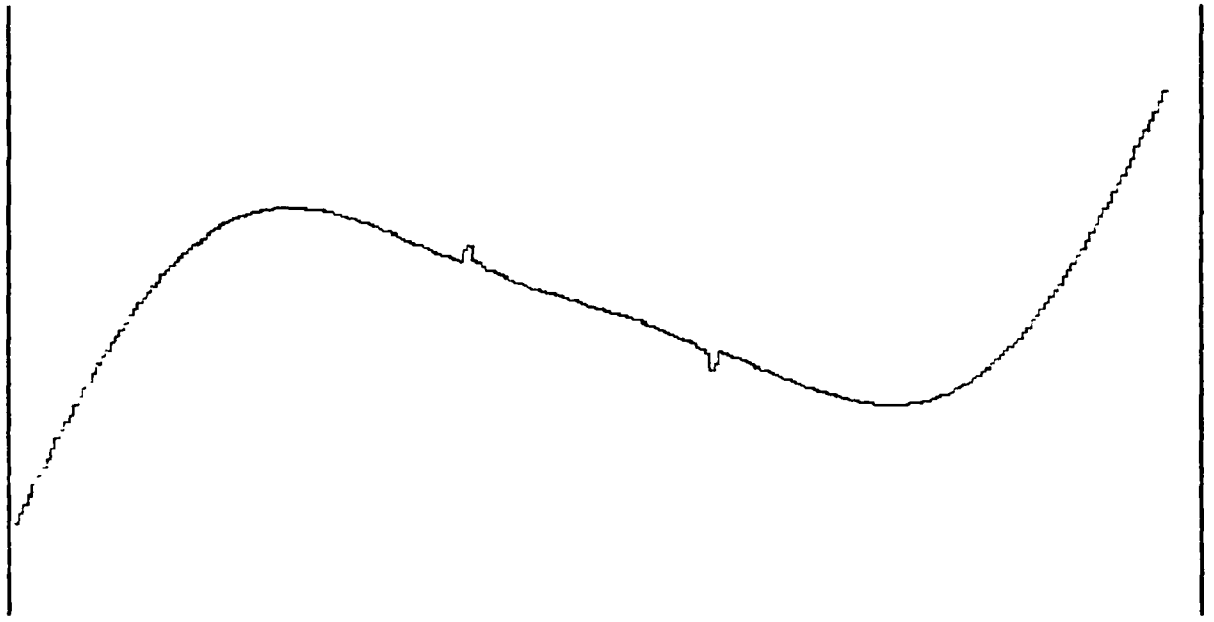

Figure 3d

1989 USAF-UES SUMMER FACULTY RESEARCH PROGRAM

GRADUATE STUDENT RESEARCH PROGRAM

Sponsored by the

AIR FORCE OFFICE OF SCIENTIFIC RESEARCH

Conducted by the

Universal Energy Systems, Inc.

FINAL REPORT

Tactical Command and Control: A Group Problem Solving & Decision Making Process

Prepared by:	William A. Wallace
Academic Rank:	Professor
Department and	Decision Sciences and Engineering Systems
University:	Rensselaer Polytechnic Institute
Research Location:	RADC/COE, Griffiss AFB, New York, 13441-5700
USAF Researcher:	Samuel A. Dinitto, Jr.

Date:	August 18, 1989
Contract No.	F49620-88-0053
Project No.	210

Tactical Command and Control:

A Group Problem Solving and Decision Making Process

by

William A. Wallace

ABSTRACT

The command and control process can be viewed as consisting of problem solving and decision making tasks. Many of these tasks are carried out by groups either in a face-to-face setting or geographically dispersed. This paper provides a conceptual framework for research on the use of decision aid technologies for supporting groups in TAC engaged in problem solving and decision making tasks.

1. Introduction

The process of Command and Control (C2) can be generalized as one of (1) sensing the present and perceiving an anticipated environment; (2) comparing both to a desired state; and (3) if there is a gap, taking action to bring the present or future state in concordance with the desired state. In order to effect this process, one must gather and store data. This data must then be processed in a form that is meaningful and of value in making the decisions needed throughout the C2 process. Information technology has and will continue to be an integral part of this process.

The myth of the commander standing alone, surveying the battle scene, and arriving at a decision to deploy forces is an archaism. In fact, it gives one an erroneous impression of what actually takes place in a combat situation. Commanders make decisions only after gathering what data are available; discussing (processing) it with staff, peers, subordinates, superiors, etc.; comparing it to experience, historical events, rules and procedures etc.; arriving at decision; and, in many cases, acting with others to implement the decision and monitoring its impact. This process involves groups of people ranging from a few in a squadron to many in a strategic command setting. The composition of these groups can vary from staff experts in different weapon systems to line subordinates in the field. The individuals in the group can be colocated and communicate face-to-face, or distributed using a variety of electronic media. The communications can be prearranged, i.e. a meeting or a conference call, or called by plan due to anticipated events. Or they can be ad hoc, driven by the needs of one or more members for information.

We must also recognize that the commander is part of an hierarchical organization with responsibilities to superiors and subordinates. He is also as a member of a "team" of peers either from the same level in the organization or with the same expertise. These relationships further erode the "loner" image of the commander.

The foregoing description of the C2 process is generic, as well as the need for group activity in the process. In this paper, we will focus on a particular C2 process, that of U.S. Air Force Tactical Command and Control (TAC). We will discuss the process and show how it can be categorized into "problem-solving" and "decision-making" activities. The characteristics of group behavior in the context of TAC are discussed next, followed by the role of information technology in supporting group processes. We conclude with a proposed research agenda.

2. USAF Tactical Command and Control*

The TAC process is driven by the prevailing military doctrine, as interpreted by the Joint Force Commander and provided as guidance. Their assessment of enemy and friendly forces, and the natural and man-made environment results in a general apportionment of resources and missions for tomorrows engagement. This process continues with even increasing detail, to the unit commander who must execute today. A crucial step in this process is the detailed documentation of the mission, the Air Tasking Order (ATO). The ATO forms the basis for the air operations undertaken by the unit commander.

The problems faced and the decisions made throughout the TAC process can be categorized into "command" and "control"; those concerned with planning, and those with execution. Airforce doctrine exposes centralized planning with decentralized execution.

3. Requirements for Information

The characteristics of the information needed to support the TAC process are determined by the nature of the decisions. Conventional wisdom states that planning requires aggregate, broad-based data concerning the future, while execution requires current, accurate, specific data.

The need to gather, process and act upon the vast amounts of data available during combat situations will stress the hierarchical organization in both the planning and execution functions of TAC.

* This description of the TAC process draws upon work by Wohl (1981).

An executable plan will have to be based on current, accurate data or the hierarchical organization will be overloaded in attempting to response to requests for deviations from the plan. If not, the plan will only be a "best guess", and rapidly degrade in usefulness, leaving the unit commander with limited knowledge of the overall TAC system. If current, accurate information is unavailable, execution by the unit commander will reduce effectiveness at best or even cause fratricide.

Theories of organization behavior can provide guidance in resolving this stress on the hierarchical structure. The information processing view of an organization would maintain that if the hierarchy is unable, either through its rules and procedures or inherent levels of authority, to respond to the demand for decisions or guidance, it must either increase its capacity to create information or reduce the need. We can accomplish this by (1) providing for lateral processing by establishing teams made of individuals from different components of the organization - these "experts" would have positions of equivalent importance in the organization; and (2) decentralizing decision-making to groups at lower levels of the organization.

Information technology is needed to implement both strategies. Groups consisting of individuals from different components of the organization need to draw upon a common data base, but have the ability to access, process and view data in a way that supports their individual cognitive processes, and enables them to communicate and work together effectively. The goal of decentralization is to have self-sufficient organizational units that are following a set of goals and objectives that enable them to act in concert. However, these units will not have the depth and variety of expertise available in the organization as a whole. In addition, they do not have the coordination mechanisms of the hierarchical structure. Again, information technology can help in the form of (1) decision aids that incorporate the systemized procedures of the hierarchy as well as the expertise of the organization, and (2) communications technologies for rapid, meaningful coordination.

4. Decision Making and Problem Solving

The concepts of decision making and problem solving have not been well defined in the context of command and control. Wohl (1981) recognizes that the C2 decision process is more than just selecting the best option from among a set of alternatives; it also includes the need to create and evaluate hypotheses about the environment and options for dealing with it. This facet of command and control we will call "problem solving".

Solving a problem can be thought of as resolving "a difference between some existing situation and some desired solution" (Pounds 1969); analogous to sensing the environment and comparing it to a desired state, the first two steps in our overview of the C2 process. Step 3, taking the action needed to close the gap, we will call "decision making", selecting and implementing an option.

Research in problem solving uses a paradigm that considers humans as goal-directed beings who apply factual and procedural knowledge in determining how best to achieve their objectives (Smith, 1988). This paradigm , extended by the work of Newell and Simon (1972) and their information processing view of cognition, guided research into how humans store and retrieve data, represent knowledge and make inferences. This research coupled with advances in symbolic programming languages has formed the basis for the design and development of expert systems.

The paradigm for research on decision making is action, a person makes a choice - a course of action. In order to make this choice the decision maker has to have a set of alternatives, be able to assess the alternatives in terms of the future, and have preferences for particular outcomes. Decision Theorists typically characterize an individuals' view of the future by using subjective probabilities, and preferences as single or many-valued utility functions. The process of selection is facilitated by algorithms that determine the feasibility of an alternative given constraints and select the optimal given a utility function. Decision analysis, behavioral decision theory, mathematical programming and optimal control theory are disciplines that adopt

this action - oriented paradigm.

In the command and control setting, "problem solving" describes "command", while "control" matches "decision making". The process of command and control consists, therefore, of groups engaged in problem solving and decision making - groups first thinking in advance of acting, then acting using the advanced thinking.

5. Groups in Problem Solving and Decision Making

Meetings are an inherent part of the day-to-day activities of organizations. Much of the time spent in these meetings is not for problem solving or decision making - the subject of our concern. These meetings consist of (1) two or more people engaged in assessing the current environment, developing a desired state in the future, generating alterative ways of achieving the desired state, evaluating these alternatives and recommending or prescripting one or more courses of action - problem solving or command; and (2) two or more people tasked with selecting and implementing a course of action, and monitoring its impact - decision making or control. The members of a group may or may not be located in the same physical space, but do perceive themselves or are tasked to be part of the problem solving or decision making group.

Military groups engaged in problem solving can be characterized as teams (Weisband et.al., 1988). They are well-organized, structured and have formal operating procedures. The members work toward a common goal, where each one is assigned a role or task to perform based upon expertise. The members must work together effectively for the group to achieve its goal, problem resolution. In command and control, tasks are carried out along functional lines following well-documented procedures. Unless unanticipated situations require extraordinary activity and ad hoc behavior on the part of the group, specialization by function means that data must be shared, and therefore processed in a form understandable and useful to each member in carrying out his or her function. This sharing of information is necessary for the group to accomplish its goal of producing an solution.

Groups involved in military decision making retain the hierarchy of authority. In

command and control, the execution is carried out by the lower levels of the organization, the operating units. The members of these units as well as combat operations are expected to be able to meet and satisfy requirements that are action oriented and based upon "orders", tempered by their experience. Timeliness can be crucial; stress is typically prevalent; and dealing with the exceptional is the norm. Although there may be too much data, little of it can be processed by the units in a form useful for decision making. Information is vital for effective coordination and control. Problem solving and decision making by a group is the result of "the exchange of information among members" (DeSanctis and Gallupe, 1987). This exchange occurs through the medium of communications - face-to-face, document flow, or electronically via voice, visuals or text. Therefore, maintaining and improving the problem solving and decision making of a group requires altering communications in a positive way.

This information exchange view of group activity presumes that the members are, in fact, transmitting and receiving information. In order for this to occur, each member must be able to gather, store and process data into a form that is meaningful, and then be able to transmit the resulting information to other members of the group in a form that is also meaningful to them.

To exchange information effectively, the members of the group must share common understandings and perceptions of the problem solving or decision making activities. They should have a common "mental model" of the system. These models contain the common aspects of each members knowledge and that portion of the knowledge that isn't common that can be communicated.

To the extent that the military provides common goals and common experiences, the groups in command and control should be able to focus their communications on information exchange concerning their view based upon their expertise and analysis of the task at hand.

6. The Nature of the Tasks

The tasks faced by a group determine its informational requirements and the concommitant communications flow. A task can be characterized by its goals, criteria for performance,

procedures for completion, time limits, and consequences and rewards (DeSantics and Gallupe, 1987). If, for example, the group is tasked with generating alternatives, a breath of information is required, but it need not be detailed.

Group problem solving tasks can be categorized by identifying the relevant questions: (1) what is the state of the environment, i.e. where are we, where are the enemies, Description; (2) what is the explanation for that condition, i.e. what is the reason for the enemy's deployment; Diagnosis; (3) what do we really want to do, i.e. do we want to contain or expand the engagement's - Goal-Setting; (4) how do we achieve our goals, i.e. how can we thwart the enemy; Design; (5) what are our options, i.e. how can we respond to a possible offense in that location; Alternative Generation; (6) what will be the likely outcomes, i.e. how will the battlefield look in six hours; Prediction; (7) how good are our options, i.e. how long will it take to move the tankers; Evaluation (Smith 1988, Wohl 1981). In a TAC context, the resolution of these tasks is necessary for completion of an Air Tasking Order.

Decision making tasks are more easily described by action terms: (1) choose an option - which means deciding who will implement; what they will do; when they will start; and where they will start (or where they will go); (2) monitor the process - which means to determine their progress, when to modify and when to terminate, and (3) coordinate with other decision making entities as necessary. These actions are inherent in the implementation by the combat operations and operating units, i.e. Wing Commanders, of an Air Tasking Order.

7. The Effect of Location

Many command and control tasks may be performed by individuals who are separated geographically. These distributed systems are particularly evident in the decision making tasks. For example, effective monitoring will require the sensing and evaluation of data, and the subsequent communication of the information.

Task accomplishment may be inhibited by the lack of face-to-face communications. The ability to exchange information is necessary in order for the group to share a common mental

model. Voice communications may not be sufficient as an exchange medium. It may have to be augumented by computer support in order to share graphics and data bases.

Decision aids can be used to facilitate the information exchange. However, it must be recognized that people will respond differently in face-to-face settings than remote sites communicating via an a electronic means, either voice or computer (Siegel et. al., 1986). The performance of some tasks may be improved particularly where data are best processed by a person on-site, like monitoring. But interpersonal conflict and less efficient communications will reduce the effectiveness and productivity of a dispersed for most problem solving and many decision making tasks.

8. The Role of Decision Aid Technology

Human decision processes, either individually or in groups, are problem focused and dependent upon mental representations, i.e. models. In addition, they are constrained by limitations in mental resources both as individuals and in groups. These limitations are well recognized for individuals, but not as well understood for groups. For example, the complexity of group communications may inhibit the group from reaching a common understanding of the problem, i.e. a shared mental model. The purpose of decision aiding technology should be to help overcome these limitations and extend human processing capabilities - not to merely automate and replace it.

The functions of decision aids can be classified by the types of support they provide human problem solvers and decisions makers. The first six techniques are due to Zachary (1986); while the remaining two are from Benbasat and Nault (1988).

TYPE	FUNCTION
1 Process Models	Computational models that predict behavior of a real-world process.
2. Choice Models	Procedures for selecting an alternative from a set of decision alternatives .

Group Decision & Decsion Type	Process Models	Choice Models	Info. Control Techniques	Analysis & Reasoning Methods	Representation Aids	Human Judgement Amplifying & Refining Techniques	Structuring Techniques	Collaboration Support
Problem								
Description	X		X		X			X
Diagnosis	X			X				X
Goal-Setting				X	X	X		X
Design	X	X		X			X	
Alternative Generation	X		X		X			X
Prediction	X			X		X		X
Evaluation		X		X		X	X	
Decision								
Choice		X	X		X	X	X	
Monitor	X		X		X			X
Coordinate			X		X	X	X	X

TABLE 1
DECISION AIDS AND
PROBLEM SOLVING AND DECISION MAKING
TASKS

3. Information Control Techniques	Storage, retrieval and organization of data, information and knowledge.
4. Analysis and Reasoning Methods	Support reasoning procedures based on representation of a problem.
5. Representation Aids	Provide ways of presenting and manipulating the problem.
6. Human Judgement Amplifying and Refining Techniques	Quantification of heuristic judgement processes.
7. Structuring Techniques	Methods for facilitating group decision making.
8. Collaboration Support	Facilitates for idea generation, processing and displaying for groups.

A decision aid consists of (1) a data and/or knowledge base, (2) an inference engine or model component and (3) a user interface. Knowledge bases provide for both quantitative and qualitative data. Inference engines provide generalized reasoning methods, while models typically employ and manipulate procedural knowledge. The decision aid types 1, 2, 4, and 5 pertain to model components or inference engines with 7 providing modeling features for group activities. Type 3 relates to the data or knowledge base component, while 5 and 8 are user interface and communication components.

Table 1 maps the foregoing classification of decision aids into the tasks of problem solving and decision making. In group settings, the process models used to answer "what-if" questions can be displayed on a common screen with additions or modifications to the model entered by any member. These displays are processed by the representation aids which permit manipulation of the problem representation itself as well as its output. In the design phase, for example, all modelling capabilities are used to determine how to meet a goal-process model to predict, choice models to elicit preferences, analysis of reasoning methods to evaluate, and structured methods to help the group to arrive at a preferred alternative(s).

In decision making it is vital to be able to access data rapidly and accurately, and represent it in a meaningful way to everyone involved in the decision process, who may be

typically separated geographically. Lack of common understanding or a shared mental model can be lethal in a combat situation. In monitoring and coordination the key activity is the ability to communicate with data, voice and visual transmission as well as capabilities for recording electronically such as electronic chalkboards.

The analysis depicted by Table 1 is tentative, but does show how we can relate decision aid technology to the tasks involved in group problem solving and decision making. The remaining section proposes a research agenda for command and control in general, and TAC in particular.

9. A Research Agenda

A major commitment has been made by every service and DOD as a whole to incorporate advances in information technology into the command and control process. Our objective of this research is to reduce the time and personnel involved in the planning and operations in Air Force Tactical Command and Control from hours to minutes, and from many to few. The Advanced Command and Control Environment envisions a small group using advanced information technology to perform both individual and group problem solving and decision making - for both command and control. Problems would arise, be analyzed, decisions made, and implementation ordered and progress monitored by the same small group. The difficulty with realizing the scenario is that the present technological development is focused on supporting individual tasks and presumes that linking the individual decision aids will provide group support. The ability to accomplish individual tasks are necessary but not sufficient to accomplish the goal of a more timely, effective command and control process. We need to understand and support the group activities that are an integral part of this process. We need to know much more about the relations between the technology and the people involved in problem solving and decision making. In the proposed research, we are focusing on those activities where individuals will meet in small groups, both face-to-face and in different locations.

The first step in a research program is to establish bounds on the inquiry, in terms of the

problem. We intend to focus on the Air Force Tactical Command and Control, keeping in mind the possibility of generalizing to other settings such as SAC or SDI, or other services. We believe that this environment offers the best opportunity for effective use of advanced decision aid technology.

The research would start by reviewing descriptions of present an anticipated functions of TAC, identifying where group activities are required (an excellent example is found in TRW 1987). These requirements may be a function of present communications and may change with new technology. In addition, the memeber proximity would be specified face-to-face or dispersed. These group activities would then be categorized generally as either problem solving or decision making, and, if possible, into the tasks, seven for problem solving and three for decision making. A refined version of Table could then be used to select the appropriate decision aids. The result of this analysis is the development of specific TAC group activities classified by task, member proximity and appropriate decision aids; completion of Figure 1 with the entries TAC group activities.

Figure 1 establishes a research framework, i.e. produces testable hypotheses or identifies research requirements. For example one could test the impact of 3D presentation technology on alternative generation using process models, i.e. simulation, in face-to-face group settings.

Assessing the hypotheses could first be done by deductive analysis, using the results of past research, then if promising, in a laboratory setting. Measurement of the (1) problem solving or decision making situation, i.e. characteristics of the task and the group, (2) the group process, i.e. communication and information exchanges, and (3) the output or performance, i.e. decision time, quality of solution, implementability, creativity etc. could be done unobtrusively in a laboratory situation using computer recording, audio and video tapes, and direct observation. Gaming would be a viable way of simulating the command and control group activities. The foregoing could be accomplished in a research environment at RADC with both experienced and inexperienced in TAC personnel. It also could be used to demonstrate prototype decision aids in order to assess

Figure 1

A Research Framework

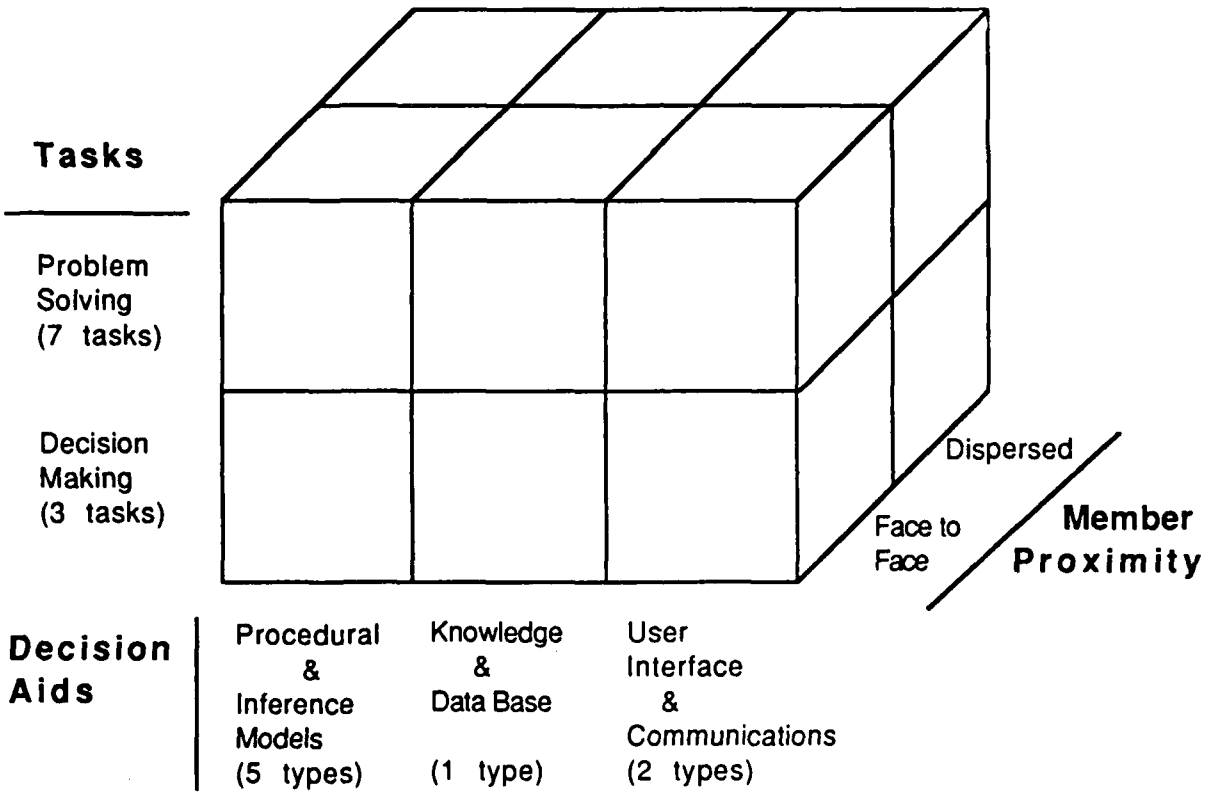

their potential performance for group support in TAC.

Benefits of the proposed research are:

- a determination where group problem solving and decision making tasks must, should and may occur in tactical command and control;
- an identification of the appropriate decision aid technology for face-to-face geographically separated small groups; and
- a determination of the benefits or effectiveness of present or potential group decision aid technology in the overall TAC system; and
- generalizations, where possible, of the foregoing to other command and control environments.

REFERENCES

Benbasat, I. and B.R. Nault, An Evaluation of Empirical Research in Managerial Support Technologies: Decision Support Systems, Group Decision Support Systems, and Expert Systems, Working paper 88-MIS-005, Faculty of Commerce and Business Administration, University of British Columbia, Vancouver, B.C., 1988.

DeSantics, G. and R.B. Gallupe, "A Foundation For The Study of Group Decision Support Systems", Management Science, 33, 5(1987), 589-609.

Newell, A. and H. Simon, Human Problem Solving, Prentice-Hall, Englewood Cliffs, N.J., 1972.

Pounds, W.F., "The Process of Problem Finding", Industrial Management Review, 11(1969), 1-19.

Siegel, J., U. Dubrovsky, S. Kiesler, and T. McGuire, "Group Process in Computer-Mediated Communication", Organizational Behavior and Human Decision Process, 37(1986), 157-187.

Smith, G.F., "Towards a Heuristic Theory of Problem Structuring", Management Science, 34, 12(1988), 1489-1506.

TRW Defense Systems Group, Functional Description (Final): Tactical Expert Mission Planner (TEMPLAR), (DRL A006, Redondo, CA., March, 1987).

Weisband, S.P., J.M. Linville, M.J. Liebhaber, R.W. Obermayer, and J.J. Fallesen, Computer-Mediated Group Process in Distributed Command and Control Systems, Technical Report 795, U.S. Army Research Institute for The Behavioral and Social Sciences, Fort Leavenworth, KA, 1988.

Wohl, J.G. "Force Management Decision Requirements for Air Force Tactical Command and Control", IEEE Transaction on Systems, Man, and Cybernetics, 11, 9(1981), 618-639.

Zachary, W., "A Cognitively Based Functional Taxonomy of Decision Support Techniques", Human-Computer Interaction, 2 (1986), 25-63.

1989 USAF - UES SUMMER FACULTY RESEARCH PROGRAM

Sponsored by

AIR FORCE OFFICE OF SCIENTIFIC RESEARCH

conducted by

Universal Energy Systems, Inc.

FINAL REPORT

Neural Networks for Invariant Pattern Recognition: A Survey of the State of the Art

Prepared by:	James S. Wolper
Academic Rank:	Assistant Professor
Department and University	Department of Mathematics and Computer Science Hamilton College
Research Location:	RADC / IRRA Griffiss Air Force Base Rome, NY 13441
USAF Researchers:	Maj. Bob Russel, Capt. W. Szarek, Mike Hinman

Date:	15 September 1989
Contract Number:	F49620-88-C-0053

Neural Networks for Invariant Pattern Recognition: A Survey of the State of the Art

by

James S. Wolper

Abstract

Several techniques have been proposed for the use of Artificial Neural Systems (Neural Networks) to do Invariant Pattern Recognition. Many of these methods were simulated during a Summer Faculty Research Project. This report classifies the methods, discusses their implementation, and evaluates them.

Acknowledgements

I would like to thank the Air Force Office of Scientific Research for their sponsorship and Universal Energy Systems for their organization of the Summer Faculty Research Program. This work was done by the author while assigned to RADC/IRRA during the AFOSR Summer Faculty Research Program. I was assisted and encouraged by Major Bob Russel, Captain "Buzz" Szarek, Mike Hinman, John Wagnon, Dave Froehlich, Scott Huse, Scott Shyne, and Ken Taylor.

I. Introduction

Pattern Recognition (PR) is an important problem for a wide variety of applications. One of the difficult problems in PR is that of recognizing images which have been transformed in various ways. The most common transformations for visual images are rotation, scaling, and translation; many other transformations are possible. Invariant Pattern Recognition is the ability to correctly recognize a transformed pattern.

Humans are quite good at Invariant Pattern Recognition. For example, I have on my desk an aerial photograph of a KC135 tanker. The photograph was taken from about 1500' above the tanker, at a range of about 1.5NM from the tanker's 8 o'clock position. The image is scaled, deformed, and rotated, yet everybody who looks at the photo immediately classifies it as an "airplane", and experts easily identify its type.

Evaluation of photos of this type is a typical intelligence task. Many analysts have sought to automate this task, but with rather limited success. Image recognition systems are slow and easy to fool; for example, they may fail to classify an image as being an "aircraft" if one of the wings is obscured, even if the rest of the structure is visible.

II. Objectives

The field of Artificial Neural Systems (ANSs) is growing rapidly. ANSs have exhibited humanlike performance in judgment and classification tasks such as recognizing handwritten numerals, interpreting sonar data, and evaluating creditworthiness. ANSs also offer significant speed advantages because they use parallel processing, and are often more robust than other methods. These traits make ANS an attractive design for Invariant Pattern Recognition Systems.

The Intelligence and Reconnaissance Directorate (RADC/IR) is the focal point for ANS research at RADC. RADC/IRR, The Image Systems Division, is investigating the application of ANS methods to many intelligence problems, especially to automated, near-real-time image exploitation. This report describes proposed architectures for ANS systems doing Invariant Pattern Recognition.

III. Artificial Neural Systems

An Artificial Neural System is based on the perceived structure of the human brain. The brain consists of a large number of neurons with many connections between them. These neurons are extremely simple: they receive signals from other neurons, process them in a simple manner, and send out signals. They are slow. None of them seem to have

much memory to speak of. Yet, these simple processors enable us to learn, speak, read, and more.

Psychologists and Neurophysiologists believe that the connections between the neurons contain the memory and programs for the human computer. The evidence for this is that the connection strengths are seen to vary with time and experience.

An Artificial Neural System imitates this architecture. An ANS consists of units (neurons) and connections (weights). Each unit receives signals from the units to which it is connected, changes its internal state (activation), and sends out a signal. The units act in parallel and asynchronously.

Patterns to be learned or processed are represented by various activation levels of the units. For example, a binary image can be represented by assigning one unit to each pixel, and setting a unit's activation to 1 if the corresponding pixel is black and 0 if it is white.

The topology of the network can take several forms. In the Hopfield networks, each unit is connected to every unit (usually excepting itself), and it is often desirable to have the connections be symmetric. In a feedforward network, the units are arranged in layers, and each unit is connected to units in the layers above and below, and to no other unit.

An ANS is capable of "learning". This is done by modifying the connection strengths (weights) in a way that eventually leads to a network that performs the desired task. There are many "learning rules" for various types of networks. For example, the Hopfield networks use a modification of the "Hebb rule", which was proposed by Hebb in 1949 based on physiological evidence. The Hebb rule states that the strength of the connection between two neurons should be increased if they are both in a state of high activation. In the ANS setting, the network is initialized to one of the images to be learned, and the weights are adjusted accordingly.

Most feedforward nets are trained using the back-propagation rule. In this case, the network has "input" units on which the pattern is projected, one or more layers of "hidden" units whose state is unknown to outside observers, and "output" units. The weights are initially random. Then, various patterns are placed on the input units, and the output units are compared to the desired output. The error is used to adjust the various weights, with the error at a hidden unit being a combination of the errors at the units below it.

For a general introduction to ANSs, see the article by Lippmann [L].

IV. Implementing Artificial Neural Systems

Most ANS research is done through simulations, rather than through the use of actual

networks, because general purpose ANS hardware is not widely available. The simulations are done on ordinary 'von Neumann' computers. Thus, the research has two directions: one direction is toward algorithms which will eventually (one hopes) be implemented on genuine hardware networks, and the other is toward the use of ANS as a conceptual tool for the design of systems for ordinary computers.

An example of this first kind of research is the development of an ANS to perform Fourier transforms. A back-propagation network to perform the Fourier transform is $O(n^2)$, as is the ordinary Discrete Fourier Transform. Thus, the simulated ANS model offers no advantage. However, the back-propagation network could be trained by a simulator and then implemented as a VLSI chip, in which case it would be significantly faster.

The second kind of research is the use of, say, a Hopfield network to do noise filtering of an image. This is a new approach to the problem, which is more robust than some of the methods commonly in use. It does not necessarily offer a speed improvement when simulated, although there would be a speed improvement in a hardware implementation of the network.

V. Methods

The algorithms were evaluated by implementation on an IBM-PC/AT compatible computer using programs written in Turbo-C. The C language was chosen because of its widespread availability and its portability. The programs will run, with minor changes, on virtually any processor (the changes are in the display functions).

The main programs are a Hopfield simulator (including constant temperature and simulated annealing modes) and a back-propagation simulator. These use common file formats, enabling easy comparison of performance. The programs were written by the author and John Wagnon, a Summer Graduate Research Fellow.

The DOS operating system imposes a 640K memory limitation on the combined size of the program and data, with a 64K segment size. This effectively limits the image size to 13-by-13 or 14-by-14. Hand-coded images of intelligence targets were used. Sample 13-by-13 images are included in the appendix.

VI. Invariant Pattern Recognition Networks

Three general schemes have been proposed for ANS Invariant Pattern Recognition. These are: preprocessing of images before being fed to an ANS; processing of the raw image

on a single (or nearly single) layer; and multi-layer processing. This report evaluates the following:

Preprocessing schemes:

transformed training set;

complex logarithm input to feedforward network;

moments;

Carpenter/Grossberg CORT-X;

Single layer:

Dotsenko's adjustable thresholds;

Coolan/Kuijk time transformation;

Kree and Zippelius algorithm;

von der Malsburg algorithm;

Multi-layer:

Neocognitron;

Cruz, Cristobal, Michaux, and Barquin.

Preprocessing schemes

Transformed images: This is the simplest scheme of all. A network is trained to recognize the desired image as well as its transforms. Thus, a rotation-invariant system would be trained on the image and several rotated images (sometimes rotated as little as 2°, sometimes as much as 90°). These are generally successful (I implemented a back-propagation system trained on rotated images), but sometimes strain the network's memory capacity. This is especially the case with Hopfield networks. This scheme also involves large training sets, which means that the training is slow.

Another approach is to train the networks on the orbits of a transformation, as in [MR]. The training seems to be quite expensive (at least $O(n^2)$).

Complex logarithm: Application of the complex logarithm function converts rotations and scalings to translations, which are easier to visualize and compute with (for example, Fourier transform is translation invariant). This is a "classical" Image Processing technique [CP].

The simplest use of these properties in the design of a rotation- and scale-invariant recognition system is to use an ANS which has translation-invariance, and to have it classify the complex logarithms of the image (this is mathematically equivalent to transforming into polar coordinates and taking the natural logarithm of r). Translation invariance can be achieved by training a network on the desired images plus their translates. The most likely candidate ANS architecture is a back-propagation system.

The advantage of this technique is that its mathematical basis is already understood by those in the field. There are parallel designs for transforming to polar coordinates (see below), so the pre-processing is speedy. There is some evidence to support a transformation of this type in the human vision system [S].

The disadvantages are that the proposed transformation distorts the image significantly, even if a Fourier transform is not performed. This makes it difficult to go back to the original image, which is sometimes desirable for higher level processing. The back-propagation algorithm is slow. Also, this scheme does not generalize well to other types of image transformations.

Reber and Lyman [RL] propose a layered scheme for implementing this process, which refers back to the optical implementation proposed by Casasent and Psaltis [CP].

It is possible to do the log-polar transformation in hardware, by hardwiring the transformation from the input plane to the transformed plane. Thus, the pixel at point (i, j) would be hardwired to the one at (r, θ), where r and θ are the polar coordinate equivalents of (i, j). I have written a program to simulate this. This procedure has the disadvantage of being difficult to reconfigure.

I have proposed a scheme for "windowing" an image to a desired size. This involves the input plane and 3 linear units. Connections from the pixel at (i, j) in the input plane to the first unit have weight i; those to the second unit have weight 1; and those to the third unit have weight j. It is then easy to calculate the center of mass of the image, which can then be used to window it. This would be a very quick way to implement a parallel interest detector. It also would not need to be reconfigured, because the center-of-mass does not depend on the window size.

Moments: Several researchers, including Kabrisky at AFIT, have proposed ANSs which use various moments to encode invariance. The idea is that one computes a vector of invariant moments, and then trains the network with these. This is closely related to the standard image processing techniques. It suffers from the disadvantage that the original

image, and much of the information that it contains, is discarded.

Flaton and Toborg [FT] propose the use of Gabor transforms [D] followed by a von der Malsburg network. Gabor transforms isolate features of images, and have been proposed as a possible mechanism for human visual processing [D]. This scheme is, however, not intrinsically invariant; it can be made so by using the Fourier-log-polar transform. It is also expensive: after all of the processing, they seem to require an exhaustive search of the database for the best match. It is not obvious whether this kind of search could be done with a Hopfield network or other kind of content addressable memory.

The Gabor transforms could also be used in a Neocognitron-like scheme. I am not aware of any attempts to implement this technique.

Carpenter/Grossberg CORT-X: The Carpenter/Grossberg CORT-X network [CG] uses neural versions of standard filters for edgeenhancement and noise reduction. They then suggest the use of a log-polar-Fourier filter to add invariance. The result of these operations is then the input to an ART 2 network.

This approach is thus very similar to the previous two; the major difference is in the type of network used to classify the feature vectors. One of the graduate interns from SUNY College of Technology has implemented ART 1, and we have not been favorably impressed with either its noise-tolerance or its predictability.

Single layer schemes

Dotsenko's scheme: Dotsenko [D] proposed using a Hopfield-type network to act as an invariant Content Addressable Memory, ie, to do pattern reconstruction. His basic idea was to use the unit thresholds to hold the transformation, and to add terms to the energy function which would force the network to tend toward the correct transformation. After this, it would act like an ordinary Hopfield network.

I attempted to implement Dotsenko's system. There is a way to make it work, namely, to search through the set of remembered patterns in order to find the transformation. But this is extremely costly for a large memory. I was unable to make the network search through the transformations based on the local rules of the Hopfield network.

Coolan/Kuijk time transformation: Coolan and Kuijk determined that a network with delays would learn a one-parameter family of transformations by presenting first the original image, and then its transform. I met with them and saw a demonstration of their system. I implemented it with limited success – the ability of the network to reconstruct

a degraded and transformed image seems to be very sensitive to the image. The network tends to homogenize the image along the transform orbits. This system has the further disadvantage of only learning one transformation, eg, it can handle rotations but not rotations and scalings. I asked Kuijk whether they had had any progress in removing this limitation, and he asked me "Why would anyone want to do that?"

Kree and Zippelius: The Kree and Zippelius scheme [KZ] is a modified Hopfield network, with two additional layers. The image plane has N pixels; there is another N pixel memory plane; and there is an N^2 unit "transform layer". The transformation layer is adjusted while signal feeds back between the image and memory layers. I did not implement this scheme because it requires more memory than we had available.

von der Malsburg: von der Malsburg and colleagues [BLvdM] have proposed several schemes based on restricted network topology. Each of his papers characterizes the previous ones as "impractical". The most recent paper describes a system which will identify a human face after it is told where the eyes, nose, and mouth are.

Multi-layer schemes

Neocognitron: The Neocognitron [F] is a multi-layer feedforward system in which each layer integrates information from the layer below. Its most spectacular achievement was a simulation which was able to correctly identify hand-written numerals, thus demonstrating invariance under change of scale, under distortion, and under translation. The model has the ability to learn in an unsupervised manner.

The Neocognitron does not have intrinsic rotation invariance.

I did not implement a Neocognitron because we did not have sufficient computing capability. I am proposing to implement a Neocognitron through an AFOSR Research Initiative Proposal grant.

Cruz, Cristobal, Michaux, and Barquin: This scheme [CCMB] involves using N slabs of N pixels to achieve translation invariant pattern recognition. Their preprocessing step took 6 hours on a Sun 4 for a 16×16 image.

VII. Recommendations and Conclusions

There are two classes of techniques for Invariant Pattern Recognition using ANS: the unworkable and the expensive. The expensive systems (Neocognitron, Kree and Zippelius) show promise, but are not sufficiently developed for field use. The others either have

disappointing performance or debilitating disadvantages.

The best evidence indicates that the human processing system is a multi-layer system which uses the complex logarithm transformation. This does not mean that this architecture is the best for machine vision: after all, aeronautical engineers do not use flapping wings for propulsion. However, the most successful scheme is of the multi-layer type. These schemes require a tremendous amount of memory.

The single layer schemes require the least hardware for implementation, but these suffer from two disadvantages. First, they are generally based on Hopfield networks, which have limited memory capacity (about $0.15N$, where N is the number of units). Second, Hopfield networks always provide a restored image, even when the initial state is noise. This limitation can be avoided by running the (simulated) network several times. If there really is an image present, the network will provide that image every time; if the initial state is noise, the network will provide several different images.

The preprocessing schemes are time-consuming and generally involve "throwing away" information. Many of these use a back-propagation network, and the design of these networks is still a developing art. In particular, it is difficulty to determine in advance the number of hidden layers and the number of units per layer.

The next breakthrough in this area must be in hardware development. Most ANS research (including most of the methods discussed in this report) is done on "ordinary" computers, ranging in size from PCs to Crays. The most successful system (the Neocognitron) required more than 11,000 processing elements and connections in order to learn 10 patterns. A working intelligence system, which would be required to learn many more patterns, would consequently require many more units. Simulations of such large-scale systems are extremely difficult unless one uses a supercomputer.

Progress can still be made with the currently available equipment (*ie*, workstation class computers). I recommend that work be continued on new techniques to speed the simulations. We made significant improvements in this regard with the Hopfield and back-propagation networks.

RADC/IRR should implement a Neocognitron simulator, and its effectiveness for the analysis of intelligence data should be tested. Another line of investigation would be the addition of rotation invariance to the basic Neocognitron. It should also be modified to handle gray scale, rather than binary, images. I am submitting a proposal through the Research Initiative Program of AFOSR to fund such an implementation.

The two current back-propagation simulators, Bob Russel's and John Wagnon's,

should be combined. Bob's is more user friendly (and hence more useful), but John's uses a faster version of the teaching algorithm and handles larger images. It is my prediction that back-propagation will soon be as important to ANS research as Expert Systems are to AI.

Appendix: Sample Images

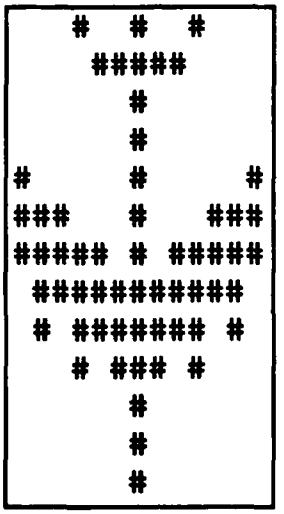

B-52 Bomber

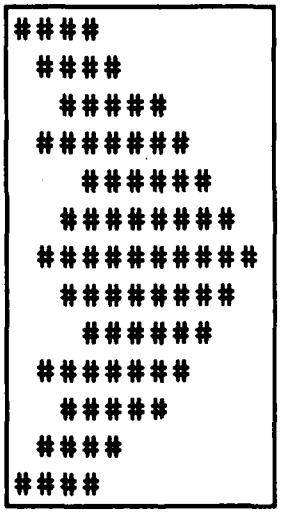

B-2 Bomber

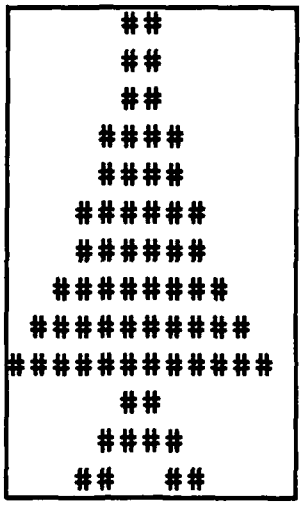

F-15 Fighter

References

Note: This is not a complete bibliography on Neural Networks and Invariant Pattern Recognition.

[BLvdM] Buhman, Lange, and von der Malsburg, "Distortion Invariant Object Recognition by Matching Hierarchically Labeled Graphs", **Proc. Int'l Joint Conf. Neural Networks**, 1989.

[CCMB] Cruz, Cristobal, Michaux, and Barquin, "Invariant Image Recognition using a multi network Neural model", **Proc. Int'l Joint Conf. Neural Networks**, 1989.

[CG] Carpenter and Grossberg, "Invariant Recognition of Cluttered scenes by a self-organizing ART architecture", **Neural Networks** 2(1989).

[CP] Cassasent and Psaltis, "Position, Rotation, ans Scale Invariant optical correlations", **Applied Optics** 15.

[D] Daugman, J. "Uncertainty relation for resolution in space, spatial frequency, and orientation optimized by two-dimensional visual cortical filters", **J. Opt. Soc. Am.** 2 (1987).

[Do] Dotsenko, "Neural Networks: translation-, rotation-, and scale-invariant pattern recognition", **Journal of Physics A** 21(1988).

[F] Fukushima, "Neocognitron: a hierarchical network capable of visual pattern recognition", **Neural Networks** 1(1988).

[KZ] Kree and Zippelius, "Recognition of topological features of graphs and images in Neural Networks", **Journal of Physics A** 21(1988).

[L] Lippmann, "An Introduction to computing with Neural Networks", **Signal Magazine (IEEE)**, April 1987.

[MR] Mas and Ramos, "Invariant perception for symmetry related patterns", **Proc. Int'l Joint Conf. Neural Networks**, 1989.

[RL] Reber and Lyman, "An Artificial Neural System design for Rotation and Scale invariant pattern recognition", **Proc. IEEE Conf. Neural Networks**, 1987.

[S] Schwartz, "Computational Anatomy and Functional Architecture of the Striate Cortex: A spatial mapping approach to perceptual coding", **Vision Res.** 20(1980).

1989 USAF-UES SUMMER FACULTY RESEARCH PROGRAM

Sponsored by the

AIR FORCE OFFICE OF SCIENTIFIC RESEARCH

Conducted by the

Universal Energy Systems, Inc.

FINAL REPORT

OPTICAL BEAMFORMING FOR PHASED ARRAY ANTENNAS

Prepared by:	Henry Zmuda, Ph.D.
Academic Rank:	Assistant Professor
Department and University:	Department of Electrical Engineering and Computer Science Stevens Institute of Technolgy Castle Point on the Hudson Hoboken, NJ 07030
Research Location:	Rome Air Development Center Photonics Research Laboratory Griffiss AFB, NY 13441
USAF Researcher:	Edward Toughlian, 2Lt, USAF
Date:	Sept. 30, 1989
Contract No:	F49620-88-C-0053

Optical Beamforming for Phased Array Antennas

by

Henry Zmuda

ABSTRACT

Microwave carrier generation along with the signal processing required for dynamic beamsteering of a phased array antenna is accomplished using optical components. It is shown that a deformable mirror spatial light modulator can establish an arbitrary optical phasefront which is directly converted to RF phase information by means of an optical heterodyne system. Experimental results which simulate the performance of the actual system are presented. Additionally, a different system is proposed using a spatial light modulator similar to the one above which offers the possibility of achieving extremely wideband response.

ACKNOWLEDGEMENTS

The author wishes to express his gratitude to the Air Force Systems Command and the Air Force Office of Scientific Research for sponsorship of this research. A note of thanks is also extended to Universal Energy Systems, Inc. for their assistance in the administrative aspects of this program. Additionally, the author wishes to thank everyone at the RADC Photonics Center for a most rewarding and enjoyable visit, especially Reinhart Erdman for serving as effort focal point. Most of all sincere thanks are extended to Lt. Ed Toughlian for his insight, guidance, and much more.

I. INTRODUCTION

In recent years a great deal of attention has been given to the problem of adapting optical components to perform various microwave functions. The area perhaps receiving the greatest attention in this regard is that of phased array antenna systems. Conventional electronic methods for large aperature arrays using microwave phase shifters, power splitters and waveguide/coax feed systems are generally impractical due to large size and high loss. An optical system offers the advantage of compact size, lighter weight, less loss and immunity to interference. Perhaps an even more important consideration is that the parallel nature of light allows the designer to exploit creative optical signal processing methods to obtain complex radiation patterns in a rapid and efficient manner [6-8]. An excellent overview of the general theory of phased array antennas has been given by Stark [1] and Mailloux [2]. An overview of various optical schemes for the control of phased array antennas has been given by Soref [4].

The purpose of this report is to present two new methods for dynamic beam steering of phased array antennas using optical components. At the heart of both methods is a class of spatial light modulator known as a deformable mirror device (DMD) [13]. Problems associated with earlier versions of such devices have prevented their practical use in optical systems. As many of these problems have now been resolved, they offer an attractive means for addressing both the high resolution and wideband phased array antenna.

II. OBJECTIVES

The objectives of the summer research program as detailed in this report were:

- Examine various schemes for obtaining all optical signal processing via computer control of dynamic beamforming for phased array antennas.

- Determine, if possible an innovative alternative approach for both wideband and narrowband systems using newly developed photonic components.

- Begin breadboarding some of the proposed ideas for proof-of-concept verification and evaluation.

It is noted here that this research effort was not concerned with the question of antenna pattern systhesis. The focus of the effort as descibed below was to provide an all optical method of producing a sufficiently variable phase shift per element so that an arbitrary array pattern may be realized. Additionally, the specific radiation characteristics of a particular type of antenna and its environment cannot be considered within the framework of this study, since such considerations are unique to a particular application.

III. BANDWIDTH CONSIDERATIONS

To appreciate the bandwidth requirements of a phased array antenna requires an understanding of how the necessary phase and amplitude drive for each element is obtained. Consider an array of N equally spaced uncoupled isotropic radiators scanned to an angle θ_0. All elements are driven with sources of equal amplitudes but each sucessive element has a progressive constant phase lead of β relative to the proceeding element. The situation described here is referred to as a uniform array [17]. Although it is probably the simplest of all situations, it clearly illustrates the nature of the bandwidth problem. For a far field observation point, the total field strength A is proportional to the sum of the fields due to each radiator acting alone,

$$A = \sum_{n=1}^{N} e^{j(n-1)(kd\cos\theta+\beta)} \tag{1}$$

where d is the element spacing and k is the normalized angular frequency ω/c. After some algebra, this can be expressed as

$$A = \frac{\sin[N(kd\cos\theta+\beta)]}{\sin(kd\cos\theta+\beta)} \tag{2}$$

This expression attains a maximum value at the scan angle θ_0 which yields the required phase shift β between elements

$$\beta = kd\theta_0 \tag{3}$$

Clearly the scan angle is a function of frequency. Consequently different frequency components of a modulated carrier will all point in different directions unless the phase shift β varies linearly with frequency as given by (3). Existing microwave phase shifters supply electrical phase increments that are independent of the microwave frequency. In a broadband antenna, this leads to the beampointing error known as "squinting", where the radiation pattern has components in unwanted directions. This undesireable effect limits the effective bandwidth of the array to about 1% of the beamwidth [3]. Squint errors can be eliminated entirely by using delay lines to obtain the desired phase shift. Such time delay beam steering architechtures are however im-

practical for applications which require rapid beam steering. It is for these reasons that switched fiber schemes have received a great deal of attention. A sufficiently long length of optical fiber can achieve the desired RF delay while being much smaller and lighter than its waveguide equivalent [5].

IV. HETERODYNE SYSTEM

Before discussing the antenna system, a brief description of the optical heterodyne process is required. Consider two light sources of slightly different frequencies; $A_{LO}\cos[\omega_{LO}t+\phi]$ and $A_S\cos[(\omega_{LO}+\omega_M)t]$. The subscripts LO and S refer to local oscillator and signal, respectively, ϕ represents an arbitrary optical phase shift, and ω_M a microwave frequency shift. Further consider these two beams travelling an exactly colinear path and incident upon a detector. Since a diode detector responds to the time averaged squared intensity of the incident light, the detected electrical signal will be proportional to

$$(A_{LO}^2+A_S^2)/2 + A_{LO}A_S\cos(\omega_M t+\phi) \qquad (4)$$

The output of the photodiode will thus contain an RF component equal to the optical beat frequency ω_M and an RF phase shift equal in angle to the optical phase shift ϕ. The mixing of two light sources in this way overcomes the difficulty of obtaining substantial variable phase shifts in the RF regime, derived from phase shifts in the order of optical wavelenghts, and readily achieved using only optical components [9-12].

If the beams above are collimated and the phase of the local oscillator beam tailored in a controllable fashion across the wavefront, a detector array can be used to directly obtain the RF signal required for the antenna drive. Such phase control of an optical wavefront can be achieved using a class of spatial light modulator known as a deformable mirror device (DMD). This device may be envisioned as a computer driven NxN array of mirrors each capable of moving independently in a continous fashion at high speed. The excursion is typically on the order of a few

optical wavelengths which is sufficient to produce the required RF phase shift.[1]

The dynamic beamsteering system can be best explained by referring to figure 1. Here a single laser is used to obtain a coherent light source which is split into two paths. A Bragg cell is used to Doppler shift one path (signal) which is then collimated, while the other path (local oscillator) has its collimated phasefront altered as specified by the DMD. The two paths are then recombined, incident on a coherent fiber bundle, and fiber fed to a diode detector on each antenna unit.

A system similar to the one shown in figure 1 was constructed on an optical bench. A 5 mW He-Ne laser operating at λ=632.8 nm was used in conjunction with a deflection type acousto-optic modulator resulting in a frequency up-shift of 40 MHz in the first order diffracted beam. A single mirror was used to simulate the DMD. This mirror was mounted on a positional stage with a piezoelectric drive capable of displacing the mirror with a resolution of a few microns. Both the signal and local oscillator beam were collimated to a diameter of 1 cm. The combined beams were scanned with a 1 mm pupil in front of a silicon photodetector followed by 20 dB of gain. A vector voltmeter was used to measure the phase with reference to the A-O cell driver. This phase as a function of the position along the beam is shown in figure 2 for a relative phase difference between signal and local oscillator of 0, π, and 2π radians. The small variations in phase as the wavefront is scanned result from aberations in the optical components. Note that these variations are independent of the relative phase shift and can be "zeroed out" with the actual DMD in place resulting in a flat phasefront. Slight variations of phase over time were encountered. These however were sub-

---

1 Details concerning the present generation of these DMD's were obtained form Don Gregory of the U.S. Army-MICOM in a private communication.

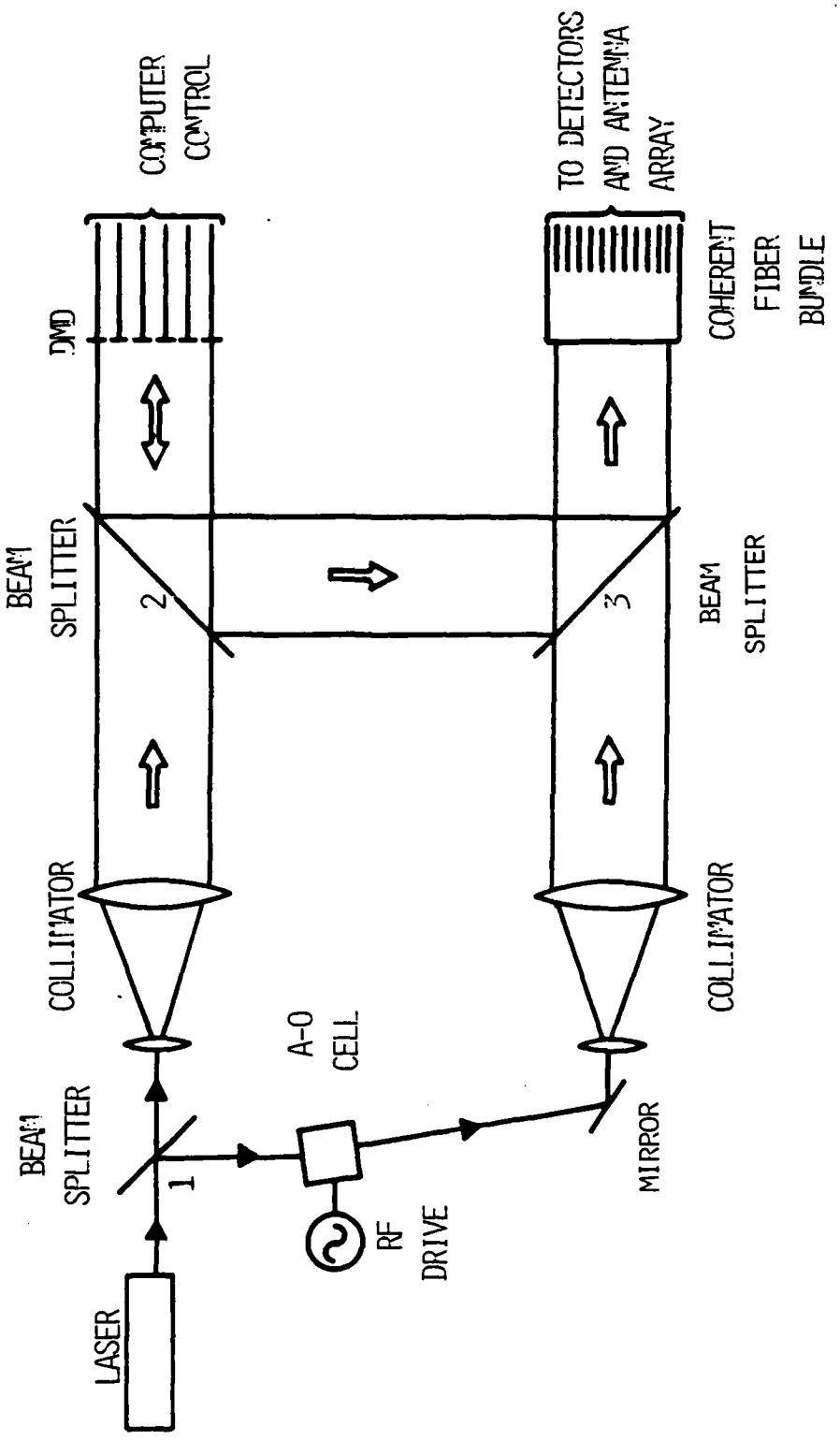

FIGURE 1: Narrowband System

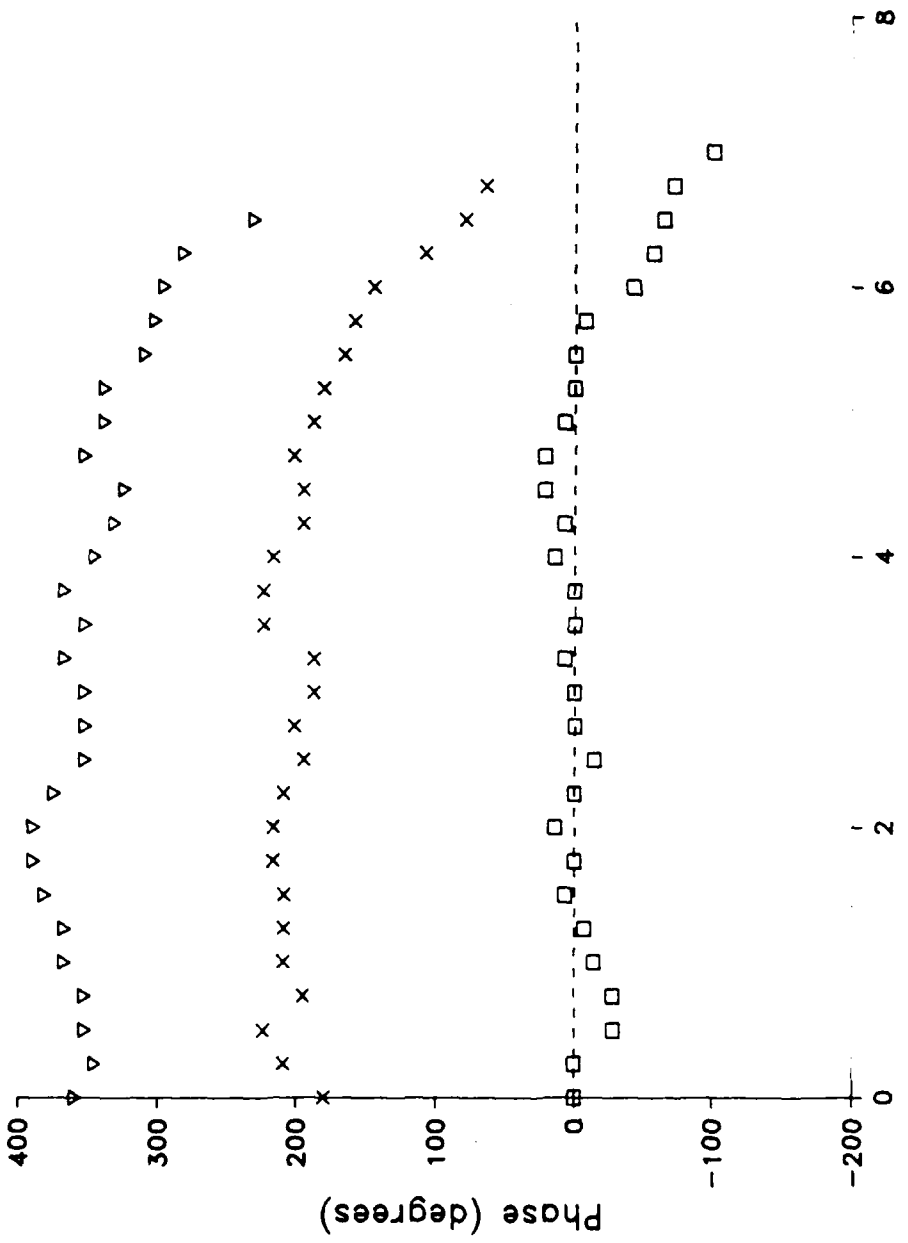

FIGURE 2: Simulated Narrowband Performance

stantially reduced by placing the setup in an enclosure to stabalize temperature and eliminate air currents. Finally it is to be noted that careful alignment of the two beams is required, otherwise severe attenuation will result.

V. WIDEBAND SYSTEM

Since the packing density of a typical DMD is quite high, a large number of radiating elements can be used. As a consequence, the heterodyne system described in the previous section offers the advantage of producing a highly directive, continuously steerable antenna pattern. This system is unfortunately bandwidth limited since the RF phase shift is independent of RF frequency resulting in squint error as discussed in section III. Note however that many of the phased array antenna systems currently found in practice are narrowband, hence this limitation does not necessarily detract from its usefulness. The ability to realize a wideband antenna can be achieved using a DMD similar to the one used in the heterodyne system. In this case the individual mirror elements pivot about a central axis and can be rotated at high speed by a few degrees. An antenna system incorporating this type of DMD is shown in figure 4. Here the laser light is modulated (amplitude or phase) with the desired microwave signal by conventional means and then collimated. The DMD is then used to steer a portion of the collimated beam into a coherent fiber bundle, with one such bundle for each antenna element. Since the fiber feed to each detector can be made an arbitrary length, true time delay steering can be obtained thus eliminating the bandwidth restriction of the heterodyne system. The present system does however offer less resolution. This is due to the fact that the individual mirror elements of the DMD employed here can only pivot in the plane of the paper, and a scheme whereby each mirror could access 2π radians of phase shift would be difficult to obtain in a practical sense. In the present scheme, a NxN DMD can thus only be used to drive N antennas (as compared with N^2 for the previous system.) For each row of the DMD, the

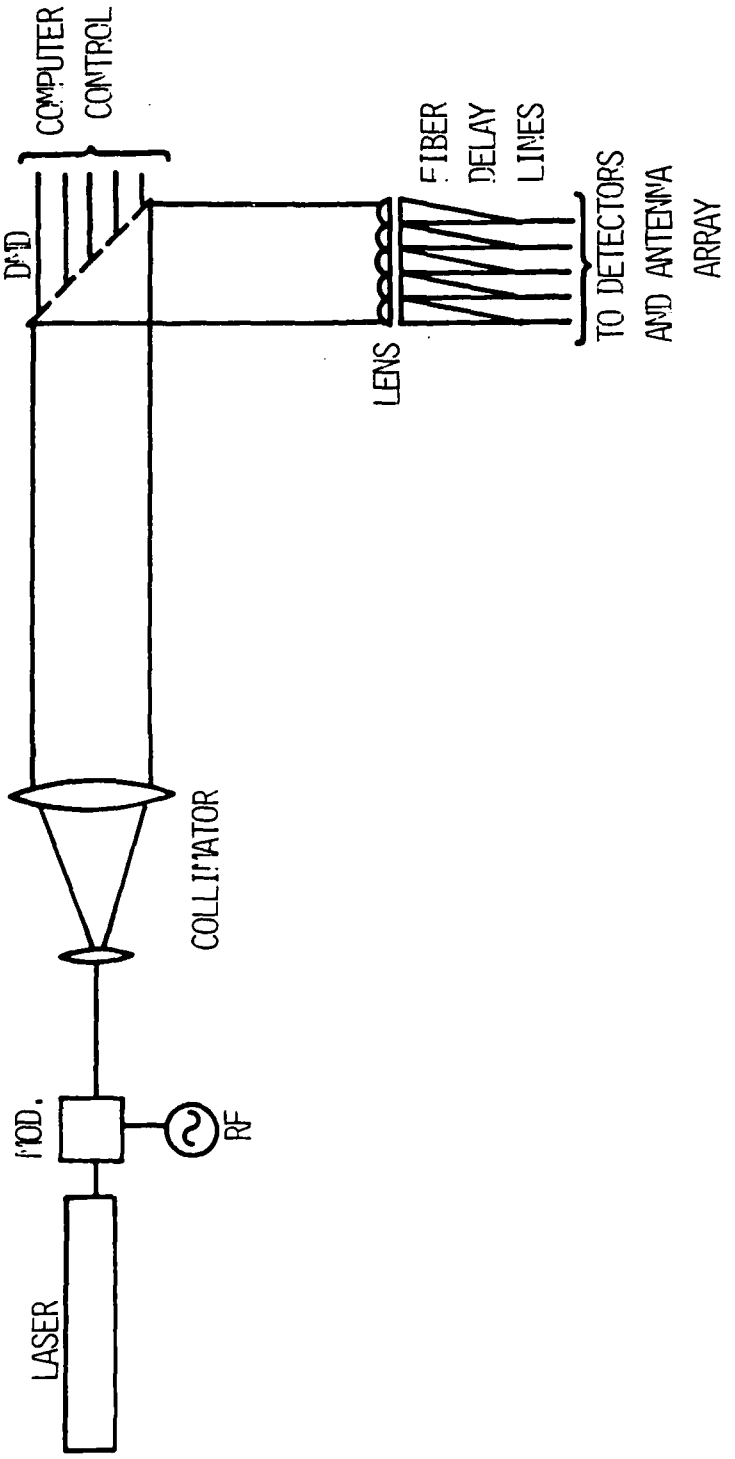

FIGURE 3: Wideband System

elements are ganged together and move in unison in a "venetian blind" fashion, except that each "blind element" can be independently (computer) controlled, with the resulting sheet beam focused into the required delay line by means of a cylindrical lens. In addition, because of the discrete nature of fiber delay scheme, only a discrete angle beam steering system can be obtained. As of the time of this writing, an experimental verification of this system has not been attempted.

VI. RECOMMENDATIONS

The measured results obtained from the heterodyne system are quite encouraging and further investigation will proceed with both systems described in this report. Specific attention will be given to the following points:

a) The major limitation in the heterodyne system described lies in the use of the acoustooptic cell to obtain the required frequency shift. Typical Bragg cells can provide Doppler shifts in the order of tens of megahertz to low gigahertz. Further, the modulation response of a bragg cell is limited since it causes a spatial displacement of the first order beam. Other means for obtaining optical frequency modulation exist, such as using coupled nonlinear optical waveguides [15]. Fabrication considerations however limit the maximum frequency shift attainable this way to a few gigahertz. The most promising and versatile method is one which employs two nominally identical lasers operating at slightly different optical frequencies. A system using two phase locked lasers has been reported where a microwave carrier signal of 100 GHz with a 1 Hz resolution has been obtained [14].

b) Since the delivery date for the next generation of deformable mirror devices is somewhat uncertain, a four-element version of such a device has been initiated by the RADC Photonics Research Center. This approach offers the distinct advantage of allowing a careful evaluation of the system performance to be made before the actual (and intricate) DMD is incorporated into the system. Earlier versions of these devices were frought with significant optical abberation problems. Although many of these problems have been eliminated, an independent evaluation of their performance would prove useful.

c) With specific regard to the wideband system, various aspects and types of modulators need to be considered, and overall optimization of all system components performed [16]. Although optical systems have obvious advantages with regard to size, weight, power efficiency, immunity, etc. over their microwave counterparts, the underlying goal must be to at least meet if not exceed the performance of the electronic system.

REFERENCES

1. Stark, L., "Microwave theory of phased array antennas-A Review," Proc. IEEE, vol. 62, 1661-1701, 1974.

2. Mailloux, R.J.,"Phased array theory and technology," Proc. IEEE, Vol. 70, pp. 246-291, 1982.

3. Frank, J., "Bandwidth criteria for phased array antennas," Proc. Phased Array antenna Symposium, Polytechnic Institute of Brooklyn, June 1970, pp. 243-253.

4. Soref, R.A., "Application of integrated optics and fiber optics to phased-array antennas," RADC-TR-84-176 In-House Report, 1984.

5. Herczfeld, P.R. and A.S. Daryoush, "Fiber-optic feed network for large aperature phased array antennas," Microwave Journal, pp. 160-166, August, 1987.

6. Daryoush, A. et. al., "Optical beam control of mm-wave phased array antennas for communications," Microwave Journal, pp.97-104, Mar. 1987.

7. Koepf, G.A. and J.L. Molz, "Compact optical beam-forming system for large phased-array antennas," IEEE Military Communications Conference, pp. 335-337, Oct. 1984.

8.Koepf, G.A., "Optical processor for phased-array antenna beam formation," SPIE Optical Technology for Microwave Applications, vol. 477, pp. 75-81, 1984.

9. Soref, R.A., "Voltage-controlled optical/RF phase shifter," IEEE J. Lightwave Technology, vol. LT-3, pp. 992-997, 1985.

10. Yariv, A., Optical Electronics, New York, Holt, Rinehart and Winston, 1985.

11. Haus, H.A., Waves and Fields in Optoelectronics, Englewood Cliffs, New Jersey, Prentice-Hall, 1984.

12. Tamburrini, M., et.al., "Optical feed for a phased array microwave antenna," Electronics Letters, vol. 23, pp. 680-681, 1987.

13. Gregory, D.A., et.al., "Optical characteristics of a deformable-mirror spatial light modulator," Optics Letters, vol. 13, pp. 10-12, 1988,

14. Goldberg, L., et.al., "Microwave signal generation with injection-locked laser diodes," Electronics Letters, vol. 19, pp. 491-493, 1983.

15. Heismann, F. and R. Ulrich, "Integrated-optical frequency translator with stripe waveguide," Appl. Phys. Lett., vol. 45, pp. 490-492, 1984.

16. Nees, J., S. Williamson, and G. Mourou, "100GHz traveling-wave electro-optic phase modulator," Appl. Phys. Lett., vol. 54, pp. 1962-1964, 1989.

17. Ma, M.T., Theory and Application of Antenna Arrays, New York, John Wiley, 1974.

1989 USAF-UES SUMMER FACULTY RESEARCH PROGRAM/

GRADUATE STUDENT RESEARCH PROGRAM

Sponsored by the

AIR FORCE OFFICE OF SCIENTIFIC RESEARCH

Conducted by the

Universal Energy Systems, Inc.

FINAL REPORT

AN EXPERIMENTAL PROTOCOL FOR LINE-OF-SIGHT SLEWING, OPTICAL ALIGNMENT AND AFT BODY STATION KEEPING CONTROL EMULATION

Prepared by:	Thomas A. W. Dwyer,III	(1)
	David S. Andreshak	(2)
	Toby B. Martin	(2)
Academic Rank:	Professor	(1)
	Graduate Student	(2)
Department and University:	Aero/Astro Engineering Department University of Illinois	
Research Location:	WL/ARCD Kirtland AFB Albuquerque, NM 87117-6008	
USAF Researcher:	Mr. David Founds	
Date:	4 August 89	
Contract No:	F49620-88-C-0053	

AN EXPERIMENTAL PROTOCAL FOR LINE-OF-SIGHT SLEWING, OPTICAL ALIGNMENT AND AFT BODY STATION KEEPING CONTROL EMULATION

by

Thomas A. W. Dwyer, III
David S. Andreshak
Toby B. Martin

ABSTRACT

This report records the results of an evaluation of the capability of the TACOS pointing and tracking test bed at WL/ARCD for directed energy weapon or space telescope slewing, optical alignment and aft body station keeping control emulation, as well as the adaptation thereto of appropriate parameter estimation and control procedures.

ACKNOWLEDGEMENTS

This work has been made possible with the help of Mr. David Founds, Maj. Terry Hinnerichs, and Lt. Travis Peppler at WL/ARCD. This effort has also gained from the advice of Dr. William H. Bennett of Techno-Sciences, Inc. as well as from the encouragement of Dr. Anthony K. Amos and Lt. Col. V. Claude Cavender of AFOSR.

I. INTRODUCTION

This report outlines the results of an investigation based on a hands on evaluation of avalilable hardware and software, followed by the development on an experimental protcol detailed herein, for the TACOS (Torque Actuator Control Optimization Scheme) facility at WL/ARCD. This activity has been of critical importance for setting up a cooperative experimental program between WL/ARCD and the Aero/Astro Department of the University of Illinois.

In this report the mission and configuration of the TACOS Laboratory is described first. An analytic system model and the sequence of measurements required to identify the necessary system parameters is described next. Finally, two methods of rapid retageting and precision tracking are presented, and shown to be implementable on a properly reconfigured version of the present experimental test bed.

II. OBJECTIVES

The objectives of the research effort reported herein are as follows: (1): Determination of the capability of the TACOS pointing and tracking laboratory at WL/ARCD. (2): Determination of its traceability to directed energy weapons or space telescope rapid retargeting and target tracking. (3): Determination of the required system parameters to be estimated and a procedure for their estimation. (4): Determination of applicable control strategies to demonstrate simultaneous line-of-sight slewing, optical alignment, and aft body station keeping.

II EXPERIMENTAL TEST BED

An appended figure represents the configuration of the TACOS test bed, incorporating modifications herein recommended by us as a result of our cooperation in its development.

At the base is a rotary table mounted on a compressed air bearing that suppresses rotational friction. (The rotary table is monted on a massive concrete block that is itself supported by a 3 point air bearing system for laboratory vibration isolation, but need not be modeled here). Twelve

identical permanent magnet linear motors are presently mounted in series connection along the edge of the rotary table to permit rotating the floating table relative to the concrete base. (We recommend that the number of these motors be reduced to six, to permit increased range of table motion. The required re-machining of the table's mechanical stops once the excess motors are removed has been calculated from our measurements).

An additonal PMI electric servomotor is being procured by our recommendation, to be mounted over and coaxially with the rotation axis of the table. The new motor will permit large angular motion of a pointing and tracking system relative to the table. (This motor and peripherals have been selected as a result of our consultation with the staff at Sandia National Laboratories as well as with colleagues at Texas A&M University).

We recommend that a 6 degree of freedom piezo-electric dynamometer, currently mounted on the table, be re-mounted on a top plate on the vertically oriented shaft of the PMI motor. This will directly measure the net torque acting on a mounting bracket placed on top of the dynamometer assembly. Hence also on any apparatus attached to the bracket.

Presently attached to the top mounting bracket is an aluminum beam, already equipped with transverse accelerometers. We recommend that either force or torque structural actuator(s) also be mounted on the beam. The first specific actuator proposed by us, sufficient for the envisioned experiments, is to consist of a tip mounted transverse VCA (voice coil actuator) or PMA (proof mass actuator), or if possible a torque actuator, for reasons detailed later. For structural control "per se" a PVF2 (polyvinyidene fluoride) strip could be used, although tip control should be available also.

IV. SBL OR SPACE TELESCOPE EMULATION

As configured according to our recommendations set forth above, the TACOS test bed permits the emulation of several aspects of rapid retargeting and precision tracking of a laser beam expander or space telescope. This is outlined here and serves as the justification for our recommended configuration.

A. Line of Sight Control

The first type of application of this test bed is to demonstrate line-of-sight control. In this setting the central mounting bracket and dynamometer block represents a primary mirror of an optical beam expander or telescope and its mounting, the orientation of which can be commanded to point to and track a moving target. (In addition to the apparatus described in the previous section, a centrally mounted mirror can be used to reflect a low-powered laser beam against an externally mounted detector, to serve as a target model such a laser source is in fact part of the original WL/ARCD design).

B. Alignment Control

The second type of application is to demonstrate alignment control. In this setting the beam represents the connecting structure between the primary and secondary mirrors of a laser beam expander or telescope, while a beam tip load (mechanically represented largely by the mass of a tip-mounted actuator itself) accounts for the secondary mirror mass. The control objective is then to maintain the relative orientation between the primary and secondary mirror stand-ins. Presuming significant slew-induced beam deflection, alignment correction can be carried out during slewing by activley rotating a tip-mounted mirror. (For this purpose the tip-mounted actuator discussed in the previous section may more appropriately be of torque type than force type).

C. Aft Body Control

The third type of application is to demonstrate coordinated fore body-aft body control. In this setting the air bearing-mounted rotating table and its tangential motors represents a space-based platform. That is either a SBL aft body or a space telescope-carrying spacecraft, together with its attitude control system. Due to the small angular travel of the rotating table, even with the reduced number of motors and narrowed mechanical stops as recommended. It is recommended that table control be used to emulate station keeping rather than agile slewing maneuvers. It is the motor mounted at the center of the table that will emulate large angle maneuvers.

Aft body station keeping interaction with laser beam expander or telescope slewing maneuvers distinguishes between the behavior of space-based and ground based lasers or telescopes, and has not to date been adequately addressed in ground experiments. (We mention in passing that this difference was initially a source of difficulty with the computer control of the STS Remote Manipulator System, inasmuch as the space shuttle reaction to robot motion caused significant undershoot in attempts to retrieve external objects).

D. Non-Co-Located Control

The fourth type of application is to demonstrate non co-located control. In this setting the objective is to control the absolute orientation of the mechanical beam tip (e.g. beam tip mirror), but without a tip-mounted actuator. Now it is the beam tip orientation that represents line-of-sight; the table top-mounted torque motor acts as a structural controller for an elastically-mounted telescope or laser beam expander; and the table rim control is what then serves as the pointing and tracking actuator. In this case it is no longer the small angles versus large angles dichotomy that distinguishes the two torques as before, but rather bandwidth separation, wherein only the table-top motor is to be high-bandwidth-capable, while the table-rim motors are to provide higher slew control authority in magnitude instead of frequency. (In fact, both torque sources can be profitably used interactively, as will be seen in a later section).

V. ANALYTICAL MODEL

In this section a mathematical model of the experimental test bed is developed. The roles of sensors and actuators required for use of this model are also described where needed.

A. Structural Beam Dynamics

Let q denote a vector of generalized coordinates describing the transversal deflection of the beam representing the beam expander metering (i.e., mirror connection) truss. (e.g., the sum of terms made up of each component q_i multiplied by a corresponding cantilever mode shape models the instantaneous lateral mechanical beam deflections). Let M and K denote the

corresponding modal mass and stiffness matrices, and d the coupling matrix between the elastic and angular motion of the beam. Moreover, let u denote a (vector of) beam-mounted transversal force(s) or moment(s), and let E be the corresponding coupling matrix of such forces or torques with the beam dynamics. Let also θ_1 denote the table top slew motor shaft (and therefore beam) orientation. Under the hypothesis of small deformations and small angular motion, the slew-coupled beam dynamics then takes the form of Equation (1).

$$M\ddot{q} + Kq + d\ddot{\theta}_1 = Eu \tag{1}$$

(In the presence of large angular rates a gyroscopic coupling term $K_1(\dot{\theta}_1)$ proportional to the square of the angular rate $\dot{\theta}_1$ is added to the stiffness matrix, as is shown in [1], for example, and can be incorporated into the model as needed).

B. Beam Slew Dynamics

Let now J_1 denote the sum of the axial moments of inertia of the undeformed beam, the beam mounting bracket, the dynamometer (if present), and the table top slew motor inertia. Let also K_{T1} denote the motor constant relating armature current I_1 and the torque T_1 applied by the table-mounted central torque motor (operating in the current-controlled mode recommended by the users of the proposed motor at Sandia and at Texas A&M). If there is significant friction induced by the relatively heavy load (representing the telescope or laser beam expander) this can be modeled by a torsional friction coefficient b_1. In this case, the angular motion of the top mounted body (e.g. the slewing mechanical beam representing the optical beam expander's metering truss) is coupled with the angular motion of the rotary table (e.g. the aft body emulator). The orientation of the latter is labeled here by the angle θ_o. Let also e^T denote the coupling coefficient (row matrix) of the slewing beam-mounted torque(s) u with the angular beam dynamics. One then has Equation (2):

$$J_1\ddot{\theta}_1[+ b_1(\dot{\theta}_1 - \dot{\theta}_o)] + d^T\ddot{q} = K_{T1}I_1 + e^Tu \tag{2}$$

Alternatively, let M denote the table top-mounted dynamometer torque reading along the vertical slew axis, and let J′ be the (smaller) axial moment of inertia given only by the sum of those of the table top motor and of the "external" (i.e., strapped down) portion of the dynamometer casing. Now all elastic quantities ($\ddot{q}_i$'s and u_i's) are absorbed into the single dynamometer reading M_z, so that Equation (2) is replaced by Equation(2′):

$$J'\ddot{\theta}_1[+ b_1(\dot{\theta}_1 - \dot{\theta}_o)] = K_{T1}I_1 - M_z \qquad (2')$$

C. Table Slew Dynamics

Let now J_o denote the sum of the axial moments of inertia of the table-top external motor armature and mounting on the rotary table, together with the internal parts of the table rim motors and their mounting brackets to the rotary table. Let V_o denote the voltage applied to the series-connected motor rim windings. Let also R_o denote the total resistance of the table rim motor windings, neglecting the inductance (a valid assumption in the low frequency range). If K_{TO} denotes the motor constant relating current to torque and if K_{VO} denotes the motor constant relating the back EMF to the table's angular rate, one then has Equation (3) for the rotary table dynamics:

$$J_o\ddot{\theta}_o + (K_{TO}K_{VO}/R_o)\dot{\theta}_o = (K_{TO}/R_o)V_o - K_{T1}I_1 \qquad (3)$$

The angular rate term $\dot{\theta}_o$ disappears from Equation (3) in current-controlled mode. In this case the voltage V_o to the table rim motors is replaced as a control variable by the current I_o applied to the rim motors, and Equation (3) is replaced by Equation (3′):

$$J_o\ddot{\theta}_o = K_{TO}I_o - K_{T1}I_1 \qquad (3')$$

The model given by Equation (3′) has the advantage over that given by Equation (3) of being equally valid in the high frequency range, but the present TACOS laboratory apparatus is configured for voltage control of the table rim motors.

In contrast the PMI motor herein proposed for the emulation of an optical beam expander/telescope gimbal torque actuator can operate in

current controlled mode at will. This motivates the current-controlled model for slew control given by Equations (2) or (2').

VI. PARAMETER ESTIMATION

The model constants can be experimentally obtained by the following sequence of measurements.

A. Rotary Table Parameters

The table rim motor resistance R_o is directly measured with an ohmmeter. The table rim torque constant K_{TO} can be found by externally locking the rotary table top, after removing the table top motor and mounting the dynamometer directly on the rotary table, then using a non-invasive flux meter to measure the table rim motor current I_o, whence one gets $K_{TO} = M_z/I_o$. The table rim back EMF constant K_{VO} can be obtained from the frequency response of the table angular position θ_o versus applied voltage V_o in absence of the table top motor (i.e. $I_1 = 0$), after ascertaining the table and dynamometer mounting inertia J_o (if necessary geometrically), as is seen from inspection of Equation (3): indeed, the transfer function (for low frequency) from the voltage V_o to the table orientation θ_o is seen to have a pole at $-K_{TO}K_{VO}/R_oJ_o$. The pole can be read as a break frequency on the frequency response magnitude, which then yields K_{VO}. A GENRAD frequency analyzer available in the TACOS laboratory has successfully been used to obtain the required frequency response curves, from applied random voltages and angular position measured from an LVDT (linear velocity and displacement transducer) mounted on the table, for DC bias readings, combined with a center bracket-mounted dynamic angular position sensor for AC readings.

B. Beam Slew Parameters

The table top PMI motor constant K_{T1} can be similarly obtained, but is also available from the experience of other investigators using it, or from the supplier. By now locking the rotary table so that $\theta_o = 0$ and subtracting the dynamometer reading M_z, it is also seen from Equation (2') that the mechanical beam (e.g. emulated optical laser beam expander or telescope metering truss) torsional friction coefficient b_1 can be likewise

obtained from the frequency response function relating the commanded table top current I_1 to the table top motor shaft orientation θ_1.

C. Beam Structural Parameters

Finally, the structural mass and stiffness matrices M and K, as well as the slew coupling coefficient matrix d and the structural actuator coupling coefficient matrices e and E in Equation (1) can be modeled from assumed mode shapes or by B-splines as in [1] and [2]. Alternatively, these constants (except for d) may also be obtainable from stationary modal test results performed earlier by TACOS laboratory personnel. The all-important slew-coupling coefficient matrix d can finally be obtained by removing structural control (i.e. setting u = 0) and rotating the beam with the table top motor, to generate the angular acceleration excitation $-d\ddot{\theta}_1$ of Equation (1). An accelerometer is available for mounting on the table top motor. Either modal analysis methods (from the mechanical frequency response of the beam under slew obtained from presently beam-mounted accelerometers, or else from strain gauges that could also be employed) or else by the technique based on time response records detailed in [3] can be used to infer $d^T = (d_1, d_2, \ldots)$.

VII. CONTROL

Three types of limitations that severely affect pointing and tracking control are to be addressed by such experimental apparatus: one is actuator bandwidth and dynamic range constraints; another is real time control throughout; and finally the modeling accuracy issue must be considered.

A. Control Issues

Even for an accurately timed analytical or computer model, it is usually necessary to purposely delete a large part of the model during the design of on-line estimation and control laws. Both of these are due to the inability of the actuators to respond to the higher frequency information contained in the model, and to the inability of operational signal processing to estimate high dimensional system states and compute high dimensional model-based control signals. This is particularly the case for agile target tracking, where target model and system model-based control is

essential. This is in sharp contrast to classical regulator design (step input reference) or velocity control (ramp reference), where at worst only an error signal is to be asymptotically attenuated. These two scenarios correspond to the difference between the problems of point-to-point transfer versus path following in robotics, and even worse if the reference trajectory is not designer-selected but is handed over to the controller by an autonomous target model generator.

B. Control Procedures

Two techniques presently used with success in the robotics field can be demonstrated on the TACOS test bed as configured according to our present recomendations. One of these, labeled here "optimal boundary layer sliding control", addresses precision pointing and tracking in the presence of poorly known vehicle and target dynamics. The other technique, here labeled "slew-induced deformation shaping on slow integral manifolds", addresses precision pointing and tracking in the presence of high bandwidth elastic dynamic response with low bandwidth slew torque generation limitations.

C. Sliding Control

The basic idea of sliding control in the setting of pointing and tracking consists of replacing the poorly known elastic dynamic coupling with the line-of-sight (or alignment, or aft body motion) dynamics by upper bound envelopes thereof. The control law obtained is then composed of two parts. One part is a nominal computed slew torque based on the reduced order pointing dynamics where the elastic coupling is regarded as a disturbance. To this baseline control, an event-driven correction is added or subtracted, as the error sign changes between the detected angular rate and the desired present angular rate computed from the presently detected angular orientation. Only the line-of-sight control problem is considered here, which is illustrative of the procedure.

Based on the line-of-sight dynamic model given by Equation (2'), let an estimate $b_1\dot{\phi}$ of the aft body coupling term $b_1\dot{\phi} = b_1(\dot{\theta}_1 - \dot{\theta}_o)$ be obtained from rate gyros or integrated angular accelerometer data as well as the previously (and possibly poorly) estimated friction coefficient. Let also M_z be the dynamometer torque measurement (reflecting the possibly inaccurate dynamometer response, especially for higher frequencies

contributed from the mechanical beam deflection dynamics $\ddot{q}$). Let a "sliding surface" $s = 0$ be defined by Equation (4).

$$s = \Delta\dot{\theta}_1 + \lambda\Delta\theta_1 \tag{4}$$

where $\Delta\theta_1 = \theta_1 - \theta_1(\text{reference})$
and λ is a designer-chosen time constant. The nominal part $\hat{I}_1$ of the control current I_1 is found by expressing the line-of-sight angular acceleration $\ddot{\theta}_1$ appearing in the time rate of change $\dot{s}$ of s. The correction ΔI_1 is then found by imposing the negative-definiteness of the time rate of change $\dot{s}J's$ of the positive definite Lyapunov function $\frac{1}{2}$ sJ's (the insertion of the inertia J' has the effect of removing the presence of the possibly uncertain value of its inverse as a coefficient of ΔI_1 in the computation of $\dot{s}J's$). This procedure has the effect of keeping s near zero by reversal of the sign of the correction ΔI_1. To avoid chattering, the Lyapunov condition is enforced only outside a (generally time-varying) boundary layer $|s/\sigma| < 1$. The choice of the boundary layer can be made in such a manner that the closed loop tracking error dynamics takes the form of the response of a critically damped ocillator driven by the model error B (the difference between M_x and its estimate $\hat{M}_x$ as well as between $b_1\dot{\phi}$ and its estimate $\widehat{b_1\dot{\phi}}$)

$$(d/dt + \lambda)^2\Delta\theta = B \tag{5}$$

(A factor $J'^{-1}\hat{J}'$ appears multiplying the cut-off frequency if the inertia is inaccurately known, which only marginally alters the tracking error bandwidth. As is shown in [4], [5], [6], [7], the required optimal boundary layer is itself generated by a "computable" version of Equation (5), as given by Equation (6) below, where the driving term $\bar{B}$ is an upper bound envelope for the model error:

$$(d/dt + \lambda)\sigma = \bar{B} \tag{6}$$

(It should be noted that B in general depends on the elastic dynamics, so that the closed loop stability of the coupled Equations (1) and (2') must be ascertained, with consequent limitations on the line-of-sight tracking error bandwidth λ, as is discussed in [6], [7]).

D. Slow Manifold Control

Still considering line-of-sight control, it is also possible to add to the standard "structural" vibration damping control $u_f = -A_1\dot{q} - A_0 q$, a correction determined by the angular motion, which has the effect described next.

The slew-excited elastic response can be made to separate into two terms: one is a "fast" transient q_f, which decays according to the time constant determined by the structural stiffness K together with vibration damping terms EA_1 and EA_0. The other is a "slow" persistent term q_s, which is expressible in terms of (higher derivatives of) the angular slew dynamics θ_1. The simplest case is when "independent modal space control" is available, i.e., if the structural control distribution matrix E in Equation (1) is invertible: indeed, in this case the "slow" part of the elastic response vanishes. The pointing control can then be generated from the "rigidified" slew dynamic model given by Equation (7):

$$\tilde{J}_1\ddot{\theta}_1 = T_1(-b_1\dot{\phi}) \tag{7}$$

where $\tilde{J}_1 = J_1 - e^T E^{-1} d$

while the required (slow part of the) "structural" control u (in addition to structural damping feedback) is found as follows: the closed loop line-of-sight pointing angle θ_1 is computed by inversion of Equation (7) in terms of the slew torque T_1 (and the aft body, i.e., rotary table, dynamic coupling rate term $\dot{\phi}$), and is then inserted into the rigidifying control law given by Equation (8):

$$u = E^{-1} d\ddot{\theta}_1 \tag{8}$$

Thus no higher derivatives of the slew angle θ_1 are needed in the generation of u from Equation (8), due to the smoothing effect of the transfer function from $T_1 - b_1\dot{\phi}$ to θ_1.

When there are insufficiently many structural actuators then E is not invertible. In this case it is still possible to force the elastic dynamics to evolve in a "slow manifold", where the high frequency disturbance $d\ddot{q}$ in Equation (1) is replaced by a (necessarily low frequency) expression in

terms of higher slew rates. In particular, with only one structural actuator (say, the recommended tip PMA or VCA or torque actuator of previous sections of this report) and two significantly excited vibratory modes, the following control procedure ensues: the slow part of the elastic dynamic response is found to be of the form given by Equation (9),

$$q_s = K^{-1}(Eu_o - d\ddot{\theta}_1) \tag{9}$$

where u_o is a "zero order" term in a two term expansion of the slow part of the structural control input, namely

$$u_s = u_o + \xi u_1 \tag{10}$$

Here ξ is an artificial singular perturbation parameter, which can be interpreted as shown below,

$$\xi = (w_1^2)^{-1} \tag{11}$$

where w_1 is the first (lowest) undamped structural modal frequncy (i.e., if $K = \text{diag}(w_1^2, w_2^2)$). Likewise the slew current is modeled as shown by Equation (12):

$$I_1 = I_{10} + \xi I_{11} \tag{12}$$

These two term singular perturbation expansions are inserted into the coupled Equations (1) and (2) of vibration and rotation, together with the corresponding representation for the elastic response given below,

$$q = q_s + q_f \tag{13}$$

(Since it can be shown that higher corrections ξq_1, etc. vanish in the case dim u = 1, dim q = 2.) The identification of equal powers of the singular perturbation parameters (after appropriate normalization of the stiffness matrix K) in this situation yields a fourth order transfer function from the vector (I_{10}, I_{11}), hence I_1, to θ_1, and another fourth order transfer function from the vector (u_o, u_1), hence u_s, also to θ_1.

From the former, one designs the current control I_1 to make the line-of-sight angle θ_1 track any jerk-rate-limited angular reference θ_1^*. The closed loop line-of-sight angle θ_1 is then computed in terms of the commanded motor current I_1. Finally, the required "shaping" control u_s is generated by insertion of θ_1, computed in terms of T_1, into the transfer function from θ_1 to u_s. (The "fast" term of u_f can be generated by feedback of $q - q_s$ and $\dot{q} - \dot{q}_s$, where q, and $\dot{q}$ require structural sensor feedback, while q_s is found from Equation (9) in terms of θ_1, I_1 and u_s). This procedure thus only requires low bandwidth capability from the slew actuator, with structural feedback and consequent high bandwidth torque required only of the structural actuator, and then only if there is insufficient passive structural damping already present! This technique is developed in detail in [8], [9], motivated by [10], and applied to an optical pointing apparatus available at the Aerospace Corporation as documented in [11].

VIII. CONCLUSIONS AND RECOMMENDATIONS

This report demonstrates the steps necessary to use the TACOS pointing and tracking apparatus at WL/ARCD for proof-of-concept demonstration of several new techniques of precision control with uncertain models or with low bandwidth slew actuators, for line-of-sight, mirror alignment and aft body station keeping during rapid retargeting and target tracking maneuvers.

The apparatus was shown to be functionally traceable to (single axis maneuvers of) either a space based laser or a space telescope. The control design procedures, previously developed and recorded elsewhere, were illustrated here only for line-of-sight control. It can be easily seen, however that alignment and aft body control can then be simultaneously executed, with feedforward cancellation of the line-of-sight control torque T_1 into their control loops. This is the counterpart of the feeding forward of structural effects (M_z) as well as of aft body effects ($b_1\dot{\phi}$) into the line-of-sight control loop.

Recommendations on desirable reconfiguration of the experimental apparatus, followed by proposed parameter estimation and control algorithms have been presented in their natural order in the body of the report. These can be traced by the chosen section and subsection titles, thereby requiring

no further review here. Thus all the objectives of the present study have been attained. Indeed, objective (1) corresponds to section III, (2) to section IV, (3) to sections V and VI, and (4) to section VIII.

POINTING AND TRACKING ON TACOS

BEAM EXPANDER ANALOGY

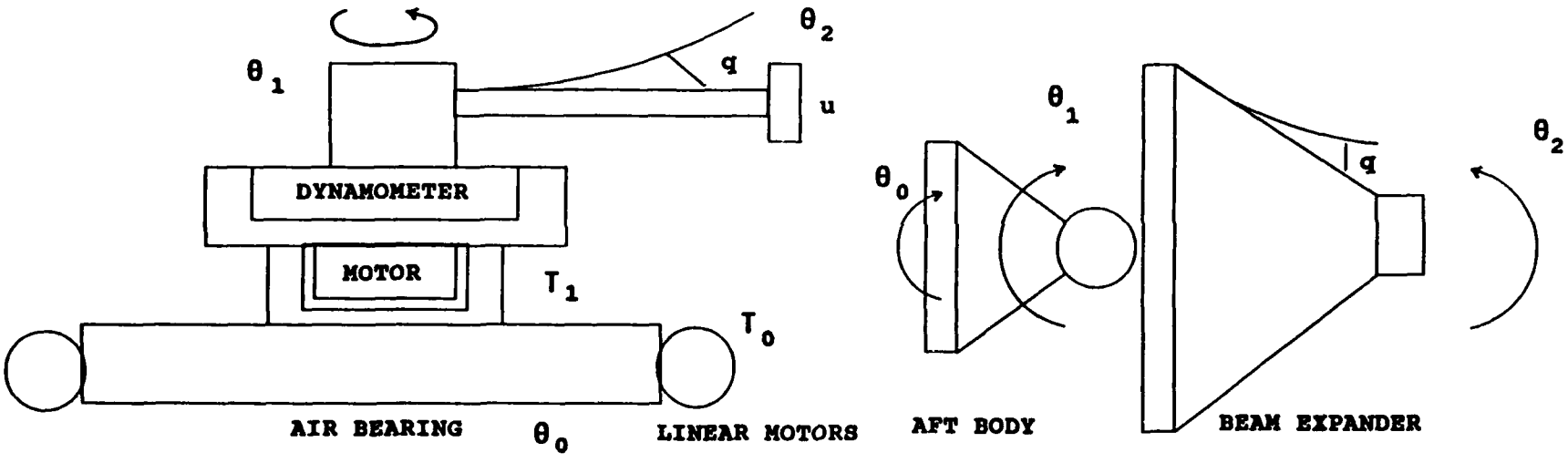

θ_0 : AFT BODY θ_1 : LINE-OF-SIGHT θ_2 : ALIGNMENT q : ELASTIC DEFORMATION

LOS CONTROL: θ_1 CORRUPTED BY q

ALIGNMENT CONTROL: $\theta_2 - \theta_1$ CORRUPTED BY q

TWO BODY CONTROL: θ_0 , $\theta_2 - \theta_1$ CORRUPTED BY q

REFERENCES

1. Junkins, J.L., and Turner, J.D., Optimal Spacecraft Rotational Maneuvers, Amsterdam, Elsevier Science Publishers, 1986.

2. Bennett, W.H., Kwatny, H.G., Blankenship, G.L. and Akhrif, O., "Nonlinear Dynamics and Control of Flexible Structures", Technical Report SEI-88-11-15-WB, Nov. 1988 (Annual Report, AFOSR contract F49620-87-C-0103).

3. Hendricks, S.L., Rajaram, S., Kanat, M.P. and Junkins, J.L., "Identification of Mass, Damping, and Stiffness Matrices for Large Linear Vibratory Systems", AIAA/AAS Astrodynamics Conference, San Diego, CA, Aug. 9-11, 1982, paper AIAA-82-1406.

4. Slotine, J.J.E., "Sliding Controller Design for Non-Linear Systems", International Journal of Control, 1984, v.40, pp. 421-434.

5. Dwyer, T.A.W.,III, "Optimal Coupled Beam Expander and Aft Body Repointing and Tracking", SEI Report, March 1988 (AFOSR Contract F49620-87-C-0103).

6. Dwyer, T.A.W.,III and Kim, J., "Bandwidth-Limited Robust Nonlinear Sliding Control of Pointing and Tracking Maneuvers", American Control Conference, Pittsburgh, PA, June 21-23, 1989.

7. Dwyer, T.A.W.,III, and Kim, J., "Bandwidth-Limited Robust Sliding Control of Multiaxial Spacecraft Pointing and Tracking Maneuvers", in the book Variable Structure Control for Robotics and Aerospace Applications, (K.K.D. Young, Editor), Amsterdam, Eleseveir Science Publishers, to appear.

8. Dwyer, T.A.W.,III, "Slew-Induced Deformation Shaping", 27th IEEE Conference on Decision and Control, Austin, TX, December 9-11, 1988.

9. Dwyer, T.A.W.,III, "Slew-Induced Deformation Shaping on Slow Integral Manifolds", in the book Control Theory and Multibody Dynamics, (J.Marsden and P.S. Krishnaprasad, Editors, American Mathematical Society, to appear.

10. Spong, M. W., Khorasani, K. and Kokotovic, P.V., "An Integral Manifold Approach to the Feedback Control of Flexible Joint Robots", IEEE J. of Robotics and Automation, Vol. RA-3, August 1987, pp. 291-300.

11. Dwyer, T.A.W.,III, and Hoyle, J.R., jr, "Elastically Coupled Precision Pointing by Slew-Induced Deformation Shaping", American Control Conference, Pittsburgh, PA, June 21-23, 1989.

1989 USAF-UES SUMMER FACULTY RESEARCH PROGRAM/

GRADUATE STUDENT RESEARCH PROGRAM

Sponsored by the

AIR FORCE OFFICE OF SCIENTIFIC RESEARCH

Conducted by the

Universal Energy Systems, Inc.

FINAL REPORT

LINKING THE TWODANT S_N CODE AND THE MCNP MONTE CARLO CODE

Prepared by:	William L. Filippone
Academic Rank:	Associate Professor
Department and University:	University of Arizona Department of Nuclear and Energy Engineering
Research Location:	Weapons Laboratory, Kirtland AFB, New Mexico Applied Technology Division Space Nuclear Power Systems
USAF Researcher:	Dr. Frank Jankowski
Date:	August 30, 1989
Contract No.:	F49620-88-C-0053

LINKING THE TWODANT S_N CODE AND THE MCNP MONTE CARLO CODE

by

William L. Filippone

ABSTRACT

A computer code SNMCSRC has been written to couple the TWODANT S_N code with the MCNP Monte Carlo code. The system of codes has been installed on the SUN computer at the weapons lab and is intended to be used to determine the radiation dose to sensitive areas of nuclear powered spacecraft. The code SNMCSRC reads the binary angular flux file produced by TWODANT and produces a surface source input deck for a subsequent MCNP calculation. The location of the source plane is selected by the user and forms an exterior surface for the MCNP run. Thus, TWODANT can be used to analyze the reactor and possibly the reactor shield, while MCNP can be used to track particles through the spacecraft.

ACKNOWLEDGEMENTS

I wish to thank Dr. Francis Jankowski and Colonel David Boyl for their help and encouragement during this project and for providing a pleasant work environment. I would also like to thank the Air Force Systems Command, Air Force Office of Scientific Research and the Space Nuclear Power Systems Group, Applied Technology Division, Weapons Laboratory, Kirtland AFB for supporting this research.

I. INTRODUCTION: While most of the radiation produced in a nuclear powered spacecraft would be stopped in the reactor shield, some radiation will reach sensitive areas of the spacecraft. It is essential to be able to predict the resultant radiation dose to space craft components so that optimal, relatively light weight shield configurations can be designed.

My research interest for several years has been numerical methods of charged and neutral particle transport theory. I have written and modified several computer codes that can be used for predicting the transport of radiation in nuclear powered spacecraft.

II. OBJECTIVES OF THE RESEARCH EFFORT: To assess the radiation dose to the sensitive areas of a nuclear powered spacecraft it is necessary to model the production of neutrons and gamma rays in the reactor core, the attenuation of these particles in the reactor shield, their passage through the spacecraft and their reactions in the spacecraft components. None of the currently available particle transport codes are well suited for solving the entire problem. Most transport calculations are carried out using the S_N or the Monte Carlo methods. However, the S_N technique would not be accurate in the spacecraft due to its complicated geometry and large void regions, while the Monte Carlo method would not be efficient for calculating criticality together with the particle penetrations through the reactor shield.

The object of this research effort has been to couple the S_N and Monte Carlo methods so that each technique could be used to solve those aspects of the problems where it performs most efficiently.

III.

A. A computer code SNMCSRC has been written to read RAFLXM, the binary angular flux file produced by TWODANT. From these angular fluxes SNMCSRC generates a source input deck to be used by MCNP in a sesequent Monte Carlo calculation. The source is planar,

perpendicular to the z axis, and at a location z_s selected by the user.

To use the code package, the entire spacecraft is modeled in r-z geometry using TWODANT. The value of z_s is then set equal to an edge value, $z_{j\pm\frac{1}{2}}$ of one of the z-mesh cells, with $z_b \le z_s \le z_t$, where z_t and z_b are the top and bottom extremities of the spacecraft. To run SNMCSRC an input file LINKDATA must be prepared that contains in free format

1. $J_1 \equiv j+\frac{1}{2}$, which defines $z_s = z_{j+\frac{1}{2}}$

   (x_0, y_0, z_0) = the MCNP coordinates (named pos by MCNP) of the S_N/Monte Carlo interface

   NSUR = The MCNP surface number for the S_N/Monte Carlo interface

   NGAM = The first gamma group for the TWODANT calculation

   ITP = [0,1], 0 => prepare a MCNP neutron source / 1=> prepare a MCNP gamma source

2. The N+1 limits of the N energy groups used in the TWODANT run (N is named NGROUP in TWODANT)

3. The I+1 limits of the I radial mesh cells (I is named NINTI in TWODANT)

The remaining information needed by SNMCSRC is obtained from RAFLXM.

The source deck produced by SNMCSRC is called MCSRC. Because TWODANT is run in r-z geometry and because MCNP cannot accept a totally general source, several approximations are required in the preparation of MCSRC:

1. The radial distribution at z_s is considered to be independent of energy.

2. The polar distribution at z_s can depend on energy but not radius.

3. The azimuthal angular distribution at z_s is taken to be isotropic.

Let ϕ_{ig}^{m} denote the angular flux determined by TWODANT at $z = z_s$, discrete direction m, radial mesh cell i and energy group g. The following relative probabilities are determined,

$$P_i = \sum_m \sum_g \phi_{ig}^{m} , \tag{1}$$

$$P^g = \sum_i \sum_m \phi_{ig}^{m} , \tag{2}$$

and

$$P_k^g = \sum_i \sum_{m \epsilon k} \phi_{ig}^{m} , \tag{3}$$

where

P_i = relative probability that a source particle appears in the i'th radial mesh cell

P^g = relative probability that a source particle appears in the g'th energy group

P_k^g = relative probability that a source particle appears in energy group g and polar angle bin k.

The second summation in Eq. (3) is over all discrete directions $\hat{\Omega}^m$ for which $\mu_{k-\frac{1}{2}} < \hat{\Omega}^m \cdot \hat{e}_z < \mu_{k+\frac{1}{2}}$, where the $\mu_{k\pm\frac{1}{2}}$ define the limits of the k'th polar angle bin.

Using these relative probabilities the source input deck MCSRC is generated. Then,

MCNP is run in the region $z_a \leq z \leq z_b$. The radial, energy and angle bins are sampled in accordance with P_i, P^g and P^g_k. The distributions within each bin are sampled randomly.

Notice that the region $z_a \leq z \leq z_b$, which we assume contains voids and complicated structures is modeled by both the S_N and Monte Carlo codes. While a highly accurate Monte Carlo calculation should be carried out, the S_N calculations need contain only enough detail to insure that the ϕ^m_{ig} are sufficiently accurate to generate the P_i, P^g and P^g_k.

B. To date the code package has been tested on only one simple problem. The transmitted current through an iron disk was obtained using TWODANT by itself and also using TWODANT coupled to MCNP. Although the agreement between the two calculations is excellent, further testing on more complicated problems should be carried out.

IV. RECOMMENDATIONS:

A. The code package is set up such that TWODANT is used for the reactor core, MCNP is used in the spacecraft and either TWODANT or MCNP is used in the shield. If the shield can be modeled in r-z geometry then it is preferable to use TWODANT since it is considerably faster than MCNP. For three-dimensional shield calculations MCNP would have to be used.

B. The three approximations listed in Section III can be avoided by writing our own source subroutine to replace the source subroutine of MCNP. This has the disadvantage that it requires modifying MCNP, however it can be done in such a way that the original source routine could still be selected by the user.

It may be true that the approximations of Section III introduce very little error in the dose calculations for the spacecraft, however it would be hard to verify this without first testing a more general source routine.

C. Dose calculations for nuclear powered spacecraft involve some of the most difficult transport calculations imaginable. There are void regions, complicated geometries, deep penetrations and criticality consideration all in the same problem. Most of the errors for the S_N method are due to numerical diffusion and ray effects.

The first of these results from the spatial discretization of the streaming term of the transport equation. The differencing approximations tend to "smear" the streaming particles into spatial regions that are, in reality physically unaccessible. The smearing can be quite severe near flux discontinuities.

Ray effects are anomalies that arise from the angular discretization of the streaming term of the transport equation, and are therefore most noticable in highly absorbing or low scattering media, such as shields. For such media, the streaming contributions to the angular flux will be over estimated at mesh cells that can be connected to the source by one of the discrete directions, and underestimated elsewhere. The effect is to produce non-physical distortions which appear as ripples in the scalar flux.

While the streaming term is the part of the transport equation that is most difficult to model numerically, it is also the part most amenable to analytic treatment. As a consequence, the efficiency of the S_N method can be greatly improved by using analytic or semi-analytic technique such as the analytic first collision source and integral transport methods.

An analytic first collision source is currently available in TWODANT, however at the moment all particles must originate from an isotropic point source at r=o, and there is no provision for the analytic treatment of multi-collided particles. Furthermore, TWODANT is unapplicable to three-dimensional shields.

Implimenting a semi-analytic n'th (n>1) collision source routine in a three-dimensional S_N code should produce a fast and accurate solver for spacecraft shielding problems.

D. The reactor shield should be optimized to minimize weight, while maintaining acceptable radiation dose rates in the spacecraft. Two methods are available, for determining the

dose rates. The straight forward method is to calculate the flux and to integrate the flux times a kerma factor over the volume of the target.

Alternatively, the ajoint flux could be found in the spacecraft and the doses obtained by integrating the adjoint flux times the source (from TWODANT). For shield optimization studies the adjoint approach has two advantages:

1. With forward (conventional) Monte Carlo, a new flux calculation would be required with each shield design. On the other hand a single adjoint flux calculation would suffice in the spacecraft, provided it remains unchanged as the shield is modified.

2. Forward Monte Carlo is not well suited for optimization studies since variation in calculated doses would be due to both variations in shield design and statistical fluxuation of the different flux calculations.

An adjoint capability should therefore be quite valuable to the laboratory.

1989 USAF-UES SUMMER FACULTY RESEARCH PROGRAM

GRADUATE STUDENT RESEARCH PROGRAM

Sponsored by the

AIR FORCE OFFICE OF SCIENTIFIC RESEARCH

Conducted by the

Universal Energy Systems, Inc.

FINAL REPORT

SIMULATION OF A SPRAY REACTOR FOR GENERATING EXCITED OXYGEN

Prepared by:	William M. Grissom
Academic Rank:	Assistant Professor
Department and University:	Physics Department Morehouse College
Research Location:	WL/ARDJ Kirtland AFB Albuquerque, N.M. 87108
USAF Researcher:	Lt. Craig Woolhiser
Date:	August, 1989
Contract No:	F49620-88-C-0053

SIMULATION OF A SPRAY REACTOR FOR GENERATING EXCITED OXYGEN

by
William M. Grissom

ABSTRACT

A one dimensional dynamic simulation was developed to model the droplet-gas reacting flow in a proposed spray reactor for generating excited oxygen. In this reactor uniform-sized droplets of hydrogen peroxide in a basic water solution are sprayed into a flow of gaseous chlorine. The reaction produces oxygen in an excited electronic state, termed the "singlet delta" state. This excited oxygen is used to collisionally excite iodine gas in a chemical laser.

The simulation follows the droplets as they flow down the generator. The relative motion between the droplets and gas determines the gas phase mass transfer coefficient. The liquid phase mass transfer is modelled as gas absorption by a flowing liquid film. The contact time between the gas and liquid is calculated by an internal circulation model in the droplet. The liquid becomes saturated with oxygen, so that the generated oxygen immediately comes out of solution, with negligible deactivation in the liquid. The excited oxygen is deactivated by collisions with other molecules, with droplet surfaces, and the walls. The purpose of the simulation is to guide selection of the operating parameters to optimize the excited oxygen yield and the chlorine utilization.

ACKNOWLEDGEMENTS

Appreciation is due to the Air Force Systems Command, Air Force Office of Scientific Research for sponsoring the Summer Research Program, to Universal Energy Systems for administering the program, and the Air Force Weapons Laboratory for providing the facilities to accomplish the effort.

Lt. Col. Eric Jumper and Lt. Col. LaRell Smith suggested the area of research. Captain Thomas G. Gates provided the working space in the Fluid Mechanics Group of WL/ARDJ, and Lt. Craig Woolhiser followed the details of the analysis.

I. INTRODUCTION

The existence of two low-lying, excited electronic states of the oxygen molecule, termed the singlet states, was predicted by quantum mechanics and verified by spectroscopy in the first half of this century, however, interest in reactions involving singlet oxygen was limited. The chemical applications of singlet oxygen began after Seliger (Reference 1) rediscovered that the reaction between sodium hypochlorite and a basic solution of hydrogen peroxide produced a red (634.3 nm) glow, which was later attributed to collisions between two excited oxygen molecules.

The reaction between chlorine and hydrogen peroxide in basic solution (HOO^-,H^+) produces singlet oxygen molecules. The pair of oxygen atoms remain bound throughout the reaction, as opposed to more common oxygen syntheses which join two separate oxygen atoms. This produces molecular oxygen with the π orbital electrons in a different orientation, with a higher energy, than the normally produced ground state oxygen (Ref. 2). This excited state is termed the singlet delta state, $^1\Delta$. Decay to the ground state by radiation is forbidden by the quantum mechanical selection rules, so that an isolated $O_2(^1\Delta)$ molecule can exist in this metastable state for a long time (45 min). However, rapid deactivation can occur from collisions with another molecule or with a surface.

It was recognized that the energy of the $^1\Delta$ state closely matched that needed to raise atomic iodine to an excited state, from which lasing had been demonstrated. A small number of excited oxygen molecules in the higher $^1\Sigma$ excited state are also needed to dissociate the molecular iodine, but these are continuously formed by collisions between $O_2(^1\Delta)$ molecules. This discovery that excited oxygen could be used as a chemical pumping source for an iodine laser led to the demonstration of the Chemical Oxygen Iodine Laser (COIL) (Ref. 3).

The operation of a COIL is strongly dependant upon the concentration of $O_2(^1\Delta)$ input to the laser. Significant effort has gone into studying different concepts for excited oxygen generators. Spargers, which bubble gaseous chlorine through a basic hydrogen peroxide solution (BHP) have been used with some success. However, the presence of a large volume of liquid, which strongly deactivates $O_2(^1\Delta)$, limits their

effectiveness. Another concept passes gaseous chlorine past walls wetted with BHP. This design has proven successful. However, neither system is easily adapted to zero gravity operation or to flight.

Another concept is to spray BHP droplets into a flow of chlorine gas. Such spray generators have been studied previously, but were not fully developed. The focus of the present research was to model a spray generator under development which generates uniform-sized BHP droplets, the idea being that greater control over the reaction is possible if all of the droplets behave identically.

I have a background in mechanical and aerospace engineering with experience in heat transfer, droplet sizing, combustion, and dynamic simulation, all of which contributed to my assignment to model the spray generator. However, the problem also involved mass transfer, kinetics, and phase equilibrium, areas in which I have limited knowledge. This required significant background study to approach the problem competently. A chemical engineer with experience in reaction modeling might have had an easier time.

II. OBJECTIVES OF THE RESEARCH EFFORT

The goal of the modeling effort was to develop a computer code which would model the flow and reactions of the droplet/gas flow as it passes through the spray reactor and to calculate the singlet oxygen yield and the chlorine utilization in the reactor.

The model was to complement a transient analysis of mass transfer for the case of a droplet surounded by a spherical volume of quiescent gas, developed by Lt. Craig Woolhiser of WL/ARDJ. Woolhiser's model is appropriate for small droplets, which would closely follow the flow of chlorine gas. The present convective model became necessary when it was determined that the contractor building the spray generator would use much larger 500 micron droplets, which might not closely follow the flow.

III. GAS/DROPLET FLOW DYNAMICS

A. Droplet Momentum

As a sign convention, it is assumed that the droplets are injected with a higher velocity than the gas flow. The downward force acting on a droplet is the difference between the weight and the buoyancy force, W-B. Opposing this is the drag force (F_d). Additionally, the droplet must accelerate the mass flow of chlorine (m_i) transferred to the droplet from the slower gas flow velocity (v) to the droplet velocity (v_d). Applying Newton's 2nd law, the acceleration (a) is found:

$$m_d\, a = (W-B) - F_d - m_i v_{rel}$$

$$a = (1-\rho/\rho_l)g - (F_d - m_i v_{rel})/m_d$$

where m_d is the droplet mass, ρ is the gas density, ρ_l is the liquid density, and $v_{rel} = v_d - v$.

The drag force on a droplet can be expressed in terms of a drag coefficient:

$$F_d = C_d\, A_c(\tfrac{1}{2}\rho v_{rel}^2)$$

For solid spheres the drag coefficient depends upon the Reynold's number as:

$$C_d = 24/Re(1+0.15Re^{0.687}) + 0.42/(1+425Re^{-1.16})$$

where $Re = \rho D v_{rel}/\mu$, D is the droplet diameter, $A_c = \pi D^2/4$, ρ is the gas density, and μ is the gas viscosity. A plot is given in Figure 6.3-1 of Reference 5. For creeping flow ($Re < 0.5$) this reduces to Stokes Law.

Internal circulation of the liquid in the droplet decreases the drag force in creeping flow ($Re < 0.5$) by a factor (Reference 6, p.601):

$$K_{circ} = (2\mu+3\mu_l)/(3\mu+3\mu_l)$$

where: μ_l = liquid viscosity

Since this correction is suffices for all Reynold's numbers.

The droplet velocity is found by numerically integrating the acceleration over time and the position is found by time integration of the velocity. For clarity in the program, simple Euler integration is used and proves satisfactory.

B. Gas Momentun · alance

A control volume for the gas momentum balance is shown in Figure 1 with the following nomenclature:

m = mass flow rate of gas
m_i = mass flow rate into each droplet
m_o = mass flow rate out of each droplet
n = no. density of droplets
= $m_l/(m_d v_d A)$
N = no. of droplets in volume = $nA\Delta x$
m_l = total liquid mass flow rate
A = chamber cross-sectional area

For steady flow:

$$\Delta(\text{momentum}) = \Sigma(\text{Forces})$$

$$(m+Nm_o)(v+\Delta v) - (mv+Nm_o v_d) = NF_d - A\Delta P$$

Collecting terms and substituting the expression for N above:

$$m\Delta v + nAm_o\Delta x\Delta v = nA\Delta x(F_d+m_o v_{rel}) - A\Delta P$$

Dividing by $A\Delta x$, taking the limit as $\Delta x \to 0$, noting that the second term drops out:

$$G\frac{dv}{dx} = n(F + m_o v_{rel}) - \frac{dP}{dx}$$

where: $G = \frac{m}{A} = \rho v$ (gas mass flux)

The pressure increase acts to compress the gas. In general, the relation between pressure and density can be expressed by a polytropic constant (b) as:

$$P = C\rho^b \quad , \quad \text{where: } C = P_0/\rho_0$$

where P_0 and ρ_0 are the initial pressure and density of the gas.

For a large gas viscosity, the compression approaches a reversible, adiabatic process for which $b=\gamma$ ($=Cp/Cv$). For low gas viscosity, the process approaches an isenthalpic throttling process, which for a perfect gas is isothermal ($b=1$) and is probably the best assumption. Then,

$$dP/dx = Cb\ \rho^{b-1}\ d\rho/dx$$

Conservation of mass in a constant area duct requires $\rho = G/v$. So,

$$\frac{dP}{dx} = -Cb\ \frac{G^b}{v^{b+1}}\ \frac{dv}{dx}$$

Substituting, the gas momentum equation becomes:

$$\frac{dv}{dx} = \frac{n}{G}(F + m_o v_{rel})\left[1 - Cb\ \frac{G^{b-1}}{v^{b+1}}\right]^{-1}$$

It is interesting that the droplet forces can cause the gas to either accelerate or decelerate, depending upon whether the gas velocity is above or below a critical value. For isentropic compression ($b=\gamma$) this critical velocity is the acoustic velocity,

sqrt(γRT), whereas for isenthalpic compression the critical velocity is sqrt(RT). In either case, the velocity in the spray reactor is normally below the critical value, so that the drop forces act to decrease the gas velocity.

This result sounds counter-intuitive, however consider that a positive pressure gradient is required to counter the force of the droplet spray. If the pressure downstream increases, the density must also increase. To satisfy continuity the velocity must decrease, since $v = G/\rho$. While the formulation of the gas momentum equation is of academic interest, in the actual spray generator the droplet densities are so small that the gas flow is hardly affected by the spray.

C. Group Effects:

The droplets occupy a fraction $\epsilon = nV_d$ of the chamber volume, where V_d is the volume of a droplet. To satisfy continuity, the effective gas mass flux through the void area between the droplets is larger than that based upon the chamber area by a factor $G_{eff} = G/(1-\epsilon)$.

For the special case of an incompressible flow, the effective fluid velocity past the droplets varies inversely with the void fraction. In creeping flow, the drag force is proportional to the velocity, so one would expect the coefficient of drag in a group of droplets, based upon the average flow velocity, to be higher than that for a single droplet by a factor:

$$\frac{C_d}{C_{d0}} = \frac{1}{1-\epsilon} \simeq 1+\epsilon \qquad (\text{for } \epsilon << 1,\ Re < 1)$$

Measurements in an incompressible creeping flow show that the drag increase for a low density of randomly packed particles is actually $(1+2.65\epsilon)$. The difference is attributable to the strong interaction between distant droplets when the flow is controlled by viscous forces. In fact, theory predicts a factor of $(1+4.55\epsilon)$ (Reference 7).

At higher Reynold's numbers the shear forces are confined to a thin boundary layer around each droplet, so that each droplet acts as if isolated in a flow at the effective fluid velocity, and the drag increase should approach the factor $(1+\epsilon)$. However, at the same time, the drag force begins to deviate from the strict proportionality with velocity of creeping flow. In fact, at very high Reynold's numbers the drag force varies as the square of the velocity, so the drag increase expected is:

$$\frac{C_d}{C_{d0}} = \frac{1}{(1-\epsilon)^2} \simeq 1+2\epsilon \quad (\text{for } \epsilon << 1,\ Re > 10{,}000)$$

Measurements at $Re = 500$ give a drag increase factor of $(1 + 1.78\epsilon)$, which is a reasonable average between the two extremes (Reference 7).

It is not obvious how to extend this analysis to a compressible flow without including a capacitave term. Since the effect is small, the incompressible result is used. Each droplet is assumed to act as isolated in a flow with an effective velocity a factor $(1-\epsilon)^{-1}$ higher than the mean velocity.

IV. TRANSPORT PROCESSES

A. Mass Transfer and Reaction

The convective mass transfer coefficient for chlorine to a solid sphere in laminar flow is (Reference 5, Equation 21.2-25):

$$k_{y_1} = Sh\ C\ D_{1m}/D$$

where: $Sh = 2 + 0.60\ Re^{\frac{1}{2}}\ Sc^{0.333}$ (Sherwood number)
C = molar density of gas
D_{1m} = diffusivity of chlorine in gas mixture
$Sc = \mu/(\rho D_{1m})$ = Schmidt number

The molar flow rate per area of chlorine to the droplet surface is then:

$$N_1 = k_{y_1}(y_1 - y_{1i}) \qquad \text{(Equation 4.1)}$$

where y_1 and y_{1i} are the mole fractions of chlorine in the free stream gas and at the liquid interface, respectively. Since the molar flux of oxygen out of the droplet equals the chlorine flux in, the bulk flow term which often complicates the mass transfer equation does not arise.

The liquid phase mass transfer is more difficult to treat. To simplify the problem several assumptions are used:

1. The chlorine does not penetrate far into the liquid, so that a transient penetration depth model can be used.
2. The concentration of chlorine in the gas phase at the interface is uniform over the droplet surface, and in equilibrium with the chlorine concentration in the liquid.
3. The singlet oxygen is not deactivated in the water solvent.

The first two assumptions are commonly made when modeling the absorption of a gas by a droplet or a liquid film. The last assumption is discussed further in Section V.

The droplet circulates, continually bringing unreacted liquid to the surface at the bottom of the droplet. This liquid flows along the surface, absorbing chlorine and reacting as it moves to the top of the droplet. Following Example 17.5-1 of Reference 5, for gas absorption from bubbles, the mass transfer at the droplet surface can be modeled as absorption into a liquid film flowing on a flat surface. For small penetration depths the spherical geometry is unimportant.

The liquid phase mass transfer coefficient for gas absorption into a flowing liquid film, with zero initial concentration of absorbed gas is:

$$k_X = 2C_\ell \, \mathrm{sqrt}[D_{6\ell} / (\pi T_{con})]$$

where C_ℓ is the molar density of the liquid, $D_{6\ell}$ is the diffusivity of Cl^- in BHP, and T_{con} is the contact time between the liquid and gas.

The second order reaction between Cl_2 and H_2O_2 in the liquid increases the mass transfer coefficient by a factor given in Figure 14-4 of Perry (Reference 15). The reaction actually consists of several steps, however, it will be taken as a single reaction:

$$Cl_2 + HO_2^- \rightarrow Cl^- + HCl + O_2(^1\Delta)$$

with a rate:

$$\frac{d[Cl_2]}{dt} = -k_2[Cl_2][HO_2^-] = -k_1[Cl_2]$$

where k_2 is the second order reaction rate constant, estimated to be between 10^7 and 10^8 $m^3/(kg\text{-}mole \cdot s)$ (Reference 11), and the terms in brackets are the molar concentrations of the reacting species.

If it is assumed that the H_2O_2 concentration remains fairly constant as the liquid flows along the interface, the reaction can be treated as first order with a constant $k_1 = k_2[HO_2^-]$, as shown above. The mass transfer coefficient in this case is given in Problem 17.L of Reference 5:

$$k_{X1} = \frac{C_\ell}{Tcon} \sqrt{\frac{D_{1\ell}}{k_1}} \left[\left(\tfrac{1}{2}+u\right) \mathrm{erf}\sqrt{u} + \mathrm{sqrt}(u/\pi) \exp(-u) \right]$$

where $u = k_1 T_{con}$. The error function is approximated within 1% by:

$$\mathrm{erf}(z) = (1+z^{-4.26066})^{-1/4.26066} + 0.70852 \exp(-7.75827\, z^2)$$

For $u > 10$ this reduces to $k_{X1} = C_\ell \, \mathrm{sqrt}(k_1 D_{6\ell})$, in which case the contact time is unimportant. This is normally the case.

The molar flow rate per area of chlorine into the liquid film is then:

$$N_1 = k_{X1} (x_{1i} - 0) \qquad \text{(Equation 4.2)}$$

where $x_{1\,i}$ is the mole fraction of Cl_2 at the interface.

The liquid and gas interface concentrations are not known, however they are assumed to be in phase equilibrium. For low concentrations they are linearly related:

$$y_{1\,i} = m_{xy}\ x_{1\,i}$$

Eliminating N_1 between Equations 4.1 and 4.2 and using the above relation:

$$y_{1\,i} = y_1\ [k_{x1}/(k_{y1}\ m_{xy}) + 1]^{-1}$$

Substituting into Equation 4.1, the total molar flow rate of Cl_2 into a droplet is:

$$W_1 = k_{xy}\, A\, y_1$$

where $k_{xy} = (m_{xy}/k_{x1} + 1/k_y)^{-1}$ is an overall mass transfer coefficient, and $A = \pi D^2$ is the droplet surface area.

Multiplting by the heat of reaction gives the heat generated in the droplet:

$$Q_{gen} = 1.73\ 10^8\ J/kg\text{-}mole\ W_1$$

B. Water Vapor

The water evaporation rate is calculated as in Example 21.2-1 of Reference 5:

$$W_3 = k_y\ A\ \frac{y_{3\,i} - y_3}{1 - y_{3\,i}}$$

where y_3 is the water vapor molar concentration in the free stream gas. The molar concentration at the interface in the gas phase ($y_{3\,i}$) is determined from the vapor pressure of water at the droplet temperature $y_{3\,i} = P_V/P$. Since the vapor pressure of water over BHP was not found, that for pure water is used.

The energy required to evaporate the water vapor is:

$$Q_{vap} = W_3\ \lambda$$

where λ is the latent heat of vaporization, in units of J/kg-mole.

C. Internal Circulation Model

1. Steady-State Circulation

The contact time between the liquid and gas, needed in the penetration depth model, is determined by the velocity of the liquid flowing along the interface. This is the time for the liquid to flow from the bottom of the droplet to the top, along the interface. The steady-state liquid interface velocity in creeping flow is calculated from the internal stream function given by Equation 29 of Lamb (Reference 6, p. 601).

$$\psi = \frac{v_{rel}}{4(1+\mu_1/\mu)} \left[1 - \left(\frac{r}{R}\right)^2\right] r^2 \sin^2\theta$$

then,

$$v_\theta = -\frac{1}{r\sin\theta}\frac{\partial \psi}{\partial r} = \frac{v_{rel}\sin\theta}{2(1+\mu_1/\mu)} \qquad (\text{at } r=R)$$

Although strictly applicable only to creeping flow, this result is used for all Reynold's numbers. The justification is that the increased drag above the Stoke's Law prediction at high Reynold's number is due mainly to form drag. The viscous drag remains closer to the creeping flow solution.

An average interface velocity is found by averaging over θ, giving:

$$v_i = \frac{1}{\pi}\frac{v_{rel}}{(1+\mu_1/\mu)}$$

The contact time (at steady-state) is then:

$$T_f = \frac{\pi D/2}{v_i} = 4.935\,\frac{D}{v_{rel}}(1+\mu_1/\mu)$$

Ideally the contact time would be calculated by integrating $Rd\theta/v_\theta$ over θ. However, this gives the unrealistic result of infinite contact time, because the liquid lingers too long at the ends of the droplet.

2. Angular acceleration of droplet

The time required for the internal circulation in the droplet to equilibrate with the gas shear stresses is not insignificant, so that a reasonable model of the angular acceleration of the circulating droplet is warranted.

The shear stress on the surface of a sphere in creeping flow is given by Equation 2.6-9 of Bird (Reference 5) as $(3\mu/2R)\,v_{rel}\sin\theta$.

The liquid in the droplet circulates in two hemispheres. The center of rotation of each hemisphere is taken as a point ½R from the base. The torque acting on a hemisphere about this center is found by integrating the product of the shear stress, differential area, $\pi R^2 \sin\theta\, d\theta$, and lever arm, $R(1-\frac{1}{2}\sin\theta)$, from $\theta = 0$ to π, giving a torque of $4.261\,\mu\, v_{rel} R^2$. The moment of inertia about the centroid of a solid hemisphere is $0.130\,MR^2$, where M is the mass of the entire sphere.

The initial angular acceleration of a droplet hemisphere is found by the ratio of the viscous torque and the moment of inertia:

$$\alpha_o = 32.8\,\mu\, v_{rel}/m_d$$

This simple analysis neglects a number of factors. The liquid does not rotate about a single axis. Due to internal slippage it does not rotate as a rigid body.

Creeping flow does not normally exist. Since the acceleration time is fairly short, these approximations are of little consequence.

The droplet velocity approaches the final angular velocity asymptotically. At the final velocity the internal viscous forces balance the external shear torques. Since the viscous forces are proportional to the velocity, the angular velocity should change as an exponential function of time, expressed in differential form:

$$\frac{d\omega}{dt} = \frac{\omega_f - \omega}{\tau}$$

But $d\omega/dt$ at $t=0$ is defined as α and $\omega(0)=0$ so, $\tau = \omega_f/\alpha$.

The final angular velocity is related to the final contact time as $\omega_f = \pi/T_f$. Thus,

$$\tau = \frac{0.0194\ m_d}{D(\mu+\mu_l)}$$

With $\omega(t)$ determined, the contact time is calculated as $T_{con} = \pi/|\omega(t)|$. The absolute value insures that the contact time is always positive, regardless of the direction in which the droplet rotates. The differential form allows the droplet circulation to dynamically adjust to changing free stream conditions.

In actual calculations the reaction rate is so large that the product $u = k_1 T_{con}$ is much greater than 10, so that the contact time is insignificant in determining the diffusion rate.

C. Convective Heat Transfer

The convective heat transfer coefficient for a laminar flow of gas around a solid sphere is given by Frossling's Correlation (Reference 5, Eq. 13.3-1), analogous to that for mass transfer:

$$Nu = 2 + 0.60\ Re^{1/2}\ Pr^{0.333}$$

$$h = Nu\ K_g/D$$

The heat convected from the droplet to the gas is then:

$$Q_{conv} = h\ A_d\ (T_d - T)$$

Thus,

$$Q_{tot} = Q_{gen} - Q_{conv} - Q_{vap}$$

The droplet is assumed uniform in temperature, giving a temperature increase:

$$\frac{dT_d}{dt} = \frac{Qtot}{m_d C_{pl}}$$

A similar energy balance on the gas flow gives:

$$\frac{dT}{dx} = \frac{n\ Qconv}{G\ C_p}$$

V. MASS CONSERVATION

A. Mass Balances

Due to mass transfer with the droplets, the gas mass flow increases at a rate:

$$\frac{dG}{dx} = n(m_o - m_i)$$

G is found by integrating this expression, starting at the inlet gas mass flow. Similarly, the droplet mass changes at a rate $dm_d/dt = m_i - m_o$.

B. Gas Species Balances

The molar flow rates per area are denoted by J_i, where the subscripts for each gas species are: 1-Cl_2, 2e-$O_2(^1\Delta)$, 2g-$O_2(^3\Sigma_g)$, 3-H_2O, 4-He. From Sections IV. A and B, W_1 and W_3 are the calculated total molar flow rates of Cl_2 into the droplet and H_2O out of a droplet, respectively. A molar balance on the Cl_2 flow in a length Δx of the reactor gives:

$$A\,\Delta J_1 = -(nA\Delta x)\,W_1$$
$$\frac{dJ_1}{dx} = -\,n\,W_1$$

The chlorine molar flow is found by integrating this expression from $x = 0$, at which $J_1 = y_1 J$, where J is the total molar flow rate of gas entering the reactor and y_1 is the initial mole fraction of Cl_2 in the gas. Since one mole of $O_2(^1\Delta)$ is generated for each mole of chlorine flowing into the droplet,

$$\frac{dJ_{2e}}{dx} = -\,n(W_1 - Wbhp) - N_{wall}*(4/D_h)$$

where W_{bhp} is the deactivation rate (per droplet) of $O_2(^1\Delta)$ on the BHP surface, N_{wall} is the molar deactivation rate per area of $O_2(^1\Delta)$ at the walls of the spray reactor, and D_h is the "hydraulic diameter" of the reactor, equal to $4*A_{cross}$/perimeter. All of the deactivated $O_2(^1\Delta)$ is accounted for as ground state O_2.

Similarly for H_2O, $dJ_3/dx = nW_3$, and the change in the total molar flow is $dJ/dx = nW_3$. The local mole fraction of each species is then $y_i = J_i/J$.

C. Liquid Species Balance

The liquid molar accounting is easiest done on a per droplet basis. The total number of moles of species i in a droplet are denoted by N_i , where the subscripts for each liquid species (consistent with Welch and Bateman for BHP property data) are: 1-KOH, 2-H_2O_2 , 3-H_2O , 4-OH^- , 5-K^+ , 6-Cl^- , 7-KCL . The overall stoichiometry of the reaction is:

$$Cl_2 + H_2O_2 + 2\,KOH \rightarrow 2\,KCl + O_2 + 2\,H_2O$$

The molar rate of change of moles of each species in a droplet is expressed in terms of the molar flows of Cl_2 into the droplet (W_1) and H_2O out of the droplet (W_3) as: dN1/dt=-2W1 , dN2/dt=-W1 , dN3/dt=2W1-W3 , dN7/dt=2W1 . The total molar change is the sum of these: $dN_{tot}/dt = W_1 - W_3$. The ions OH^-, K^+, and Cl^- only enter into the BHP density correlation of Welch and Bateman and are presently neglected.

D. Deactivation of $O_2(^1\Delta)$

The $O_2(^1\Delta)$ generated at the droplet can be deactivated by several mechanisms. The molar rate of deactivation at a droplet surface is

$$W_{bhp} = \gamma_{bhp}\, A_d\, (Vo/4)\, y_{2ei}\, C$$

where γ_{bhp} is the deactivation probability for an O_2 collision with the liquid surface, given as 0.002 by Blauer (Reference 16), Vo is the mean kinetic velocity of the O_2 molecules $= \mathrm{sqrt}(8RT/\pi M_{O_2})$, C is the total molar concentration of the gas, and y_{2ei} is the molar concentration of $O_2(^1\Delta)$ in the gas at the liquid interface. y_{2ei} is higher than the free stream concentration since the $O_2(^1\Delta)$ must diffuse away from the droplet. Indeed: $y_{2ei} = y_{2e} + (W_1 - W_{bhp})/(A_d\, k_{y2})$

where k_{y_2} is found as for Cl_2 in Section IV.A.

Similarly, the deactivation rate per area at the walls is

$$N_{wall} = \gamma_{wall}\, (Vo/4)\, y_{2ew}\, C$$

The molar concentration of $O_2(^1\Delta)$ at the wall (y_{2ew}) is lower than the free stream concentration by an amount N_{wall}/k_w , where $k_w = 0.332\ \mathrm{sqrt}(Rex)\ Sc^{0.333}$ is the mass transfer coefficient to the wall, for a laminar boundary layer.

Additional deactivation occurs from molecular collisions in the free stream gas. These are well characterized, but time has not permitted inclusion in the program.

VI. COMPARISON WITH PREVIOUS ANALYSES

Most previous models of excited oxygen generators have approached the gas side mass transfer in a similar manner, however, the liquid phase diffusion and reaction has been handled in different ways.

Most reports consider diffusion of chlorine into the BHP, a finite rate reaction, and diffusion of the generated excited oxygen back to the liquid surface. The difficulty recognized is that the $^1\Delta$ oxygen has a very short lifetime in the liquid (2 μsec). Since each $^1\Delta$ molecule has an equal probability of diffusing either towards or away from the liquid surface, and diffusion away from the surface leads to deactivation, such an analysis would predict a 50% yield of $O_2(^1\Delta)$ at best. However, yields approaching 100% have been measured (Reference 9).

To overcome this limitation all of the reports assume that the generated oxygen departs the liquid without deactivation (References 10-14). To justify this assumption various arguments have been used. Some authors imagine an innate desire of the $O_2(^1\Delta)$ to diffuse only towards the surface, neglecting the randomness which defines diffusion. Others give no justification.

Blauer (Reference 13) justifies the 100% yield assumption by a penetration depth analysis which calculates a high $O_2(^1\Delta)$ concentration in the initial flux out of the liquid surface. The difficulty with this conclusion is that his accounting system is valid only for steady-state diffusion and the penetration depth model is a transient case which only appears steady state as an ensemble average. He does not properly account for the $O_2(^1\Delta)$ which diffuses further into the droplet.

A more reasonable justification for the 100% yield of $O_2(^1\Delta)$ is that the liquid quickly becomes saturated with O_2, so that any additional O_2 produced immediately comes out of solution. It is assumed that the deactivation rate for $O_2(^1\Delta)$ gas as it leaves the liquid is much smaller than for dissolved $O_2(^1\Delta)$. It is not known whether this O_2 gas would form observable bubbles.

In a recent report Blauer (Reference 16) states that the generated $O_2(^1\Delta)$ "migrates" to the surface, which implies that it is not dissolved in the liquid. He uses the reduced form of the liquid phase mass transfer coefficient, with reaction, given in Section IV.A (with the mass transfer coefficient defined differently).

VII. PROPERTY VALUES

The property values are updated in the program at each write increment. The viscosity of each gas species is calculated with the Chapman-Enskog theory (Reid, Equation 9-3.9), and the mixture viscosity is calculated with the Herning and Zipperer simplification of Wilke's method (Reid, Equation 9-5.17). The thermal conductivity of the gas is calculated using the cubic polynomials given in Table 10.3 of Reid for each species, with the same mixture weightings as used for viscosity. The specific heat of each gas species is calculated using the cubic polynomials given in Appendix A of Reid. The equations for O_2 and He are used outside the stated range, but they compare favorably with values from another source. A molar weighting is used in calculating the mixture specific heat.

The diffusivity of Cl_2, O_2, and H_2O in the gas mixture is found using Blanc's Law for trace species (Reid, Equation 11-7.4). Since He accounts for about 70% of the gas molar composition, this is reasonable. Cl_2 is assumed to diffuse in a mixture of He and O_2, O_2 is assumed to diffuse in a mixture of He and Cl_2, and H_2O is assumed to diffuse in a mixture of He, Cl_2, and O_2. The binary diffusivities are calculated with Fuller's Equation (Reid, Equation 11-4.4).

The vapor pressure of water is calculated from Appendix A of Reid. The latent heat of vaporization of water from 273 to 300 K (Reference 14, Appendix A) was fit to a cubic polynomial. The other properties of liquid BHP are coded exactly as given in a summary of BHP property correlations compiled by Keith Truesdale of AFWL.

The slope of the equilibrium curve (m_{xy}), needed in Section IV.A, for Cl_2 dissolved in BHP was determined from the solubility given in Truesdale's compilation. The solubility in this reference is described by a Henry's Law constant (H^*), defined in as the ratio of partial pressure (P_i) in the gas to the molar concentration in the liquid. A more common definition of Henry's constant relates the partial pressure in the gas to the mole fraction in the liquid as $P_i = Hx_i$. The two definitions can be related by $H = H^* \rho_\ell / M_\ell$, where ρ_ℓ is the density of BHP and M_ℓ is the molecular weight. Since the mole fraction in the gas is $y_i = P_i/P$ (Dalton's Law), Henry's law can be written as: $y_i = m_{xy} x_i$, where $m_{xy} = H/P = H^* \rho_\ell / (P M_\ell)$. The plot of H^* versus T in the data summary was fit to a function:

$$H^* = \exp(23.923\text{-}2848.6/T) \ < > \ J/kg \bullet mole \ \text{for} \ T < > K$$

As a check on the definitions, the H^* value for O_2 in water, given in the same source, was converted to the normal Henry's Law constant (H), as above. This exactly matched the value given in Reference 17. Note that Reference 13 defines m_{xy} differently.

VIII. SIMULATIONS RESULTS

Time did not allow thorough testing of the computer program. One useful check was the simulation of the evaporation of a water droplet falling through air, given as Problem 21.E of Reference 5. This case checked the steady-state results of the droplet momentum, heat transfer, and water vapor mass transfer equations. The calculated terminal velocity of 3.36 m/s was 14% lower than stated, due to the using a different drag coefficient. The calculated steady-state droplet temperature of 285.9 K agreed with the stated answer.

Using the Spectra Technology's Baseline Design (Reference 11, Table 4-1) gave an $O_2(^1\Delta)$ yield of 62.3% and a Cl_2 utilization of 89.5% at a distance of 0.5 m, using the same $k_2 = 10^7$ m^3/kg-mole$\bullet$s as Spectra Technology. These are preliminary results, and do not include homogeneous deactivation, but they are in range of the values plotted in Reference 11.

VIII. RECOMMENDATIONS

A computer program which implements the analysis described here has been delivered to the Weapons Laboratory. It is recommended that a sensitivity analysis be performed to determine the importance of each variable in the spray reactor towards the excited oxygen yield and the chlorine utilization.

It is also recommended that an experimental program be initiated to determine the influence of droplet size and BHP composition on the excited oxygen yield. These experiments would utilize a single stream of uniform size BHP droplets in a flow of chlorine gas. The goal would be to determine the optimum droplet size and composition and to compare with the results of the computer program. This experiment is being proposed as a follow-on minigrant.

REFERENCES

1. Seliger, H.H. "A Photoelectric method for the measurement of Spectral Light Sources of Rapidly Varying Intensities", Analytical Biochemistry. no.1, p.60 (1960)

2. Kasha, M. and Brabham, D.E. in Wasserman, H.H. and Murray, R.W. ed. Singlet Oxygen, Academic Press, (1979).

3. Benard, D.J. et. al. "Efficient Operation of a 100 W Transverse Flow Oxygen-Iodine Chemical Laser," Applied Physics Letters. 34, p. 40 (1979).

4. Faeth, G.M. Prog. Energy Comb. Sci. no.3, p.191 (1977).

5. Bird,R.B., Stewart, W.E., and Lightfoot, E.N. Transport Phenomena. Wiley (1960)

6. Lamb, H. Hydrodynamics. 6th ed. Dover.

7. O'Rourke, P.J. "Collective Drop Effects on Vaporizing Liquid Sprays". Phd Thesis. Princeton University. Chapter 3 (1981).

8. Reid, R.C. et. al. The properties of Gases and Liquids 4th ed., McGraw-Hill (1986)

9. Conn, P.K. et al. "Engineering Development of a Singlet Delta Oxygen Generator", Final Report, WL-TR-80-144, (Bell Textron), May 1981

10. Crowell, P.G., WL-86-A/K-35-0.0323, (RDA Associates). August 8, 1986

11. "Uniform Droplet Oxygen ($^1\Delta$) Generator Development", Interim Report, WL-F29601-88-C-0019, (Spectra Technology), May 9, 1989

12. Harpole, G.M. et al "Oxygen-Iodine Supersonic Technology", Vol II, Final Report, WL-TR-85-43, (TRW). October 1985

13. Blauer, J., et al. "Oxygen-Iodine Supersonic Technology Program", Vol III, WL-TR-82-37, (Rockwell Rocketdyne). March 1985

14. Brodkey, R.S. and Hershey, H.C. Transport Phenomena - a unified approach. McGraw-Hill, 1988.

15. Perry, R.H. and Chilton, C.H. Chemical Engineer's Handbook. McGraw-Hill, 1973.

16. Blauer, J.A. et al. "Aerosol Generators for Singlet Oxygen Production", Journal of Applied Physics. 62, no.6 p. 2508 (September 15, 1987).

17. Hines, A.L. and Maddox, R.N. Mass Transfer - fundamentals and applications. Prentice-Hall, 1985. Table B.6

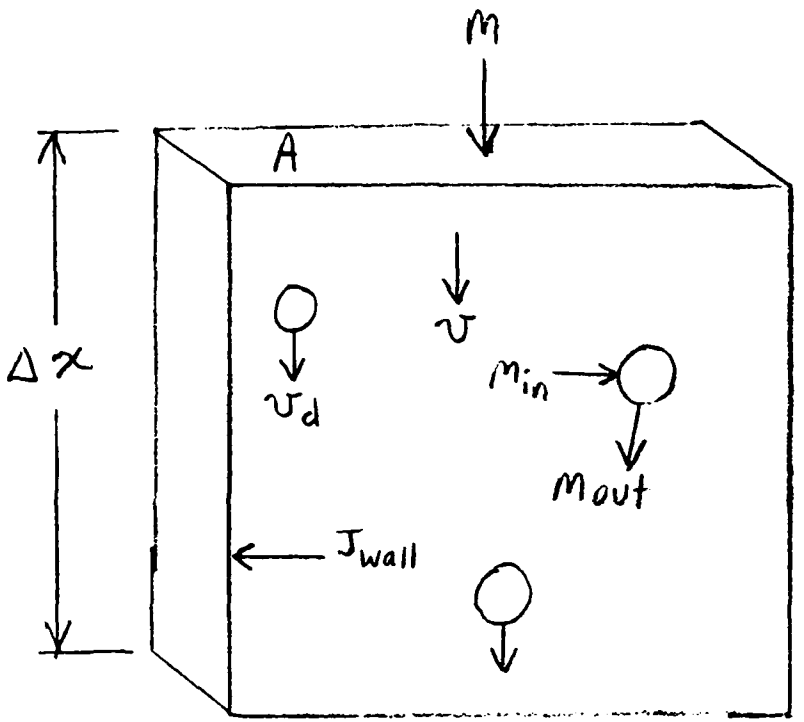

Figure 1. Momentum Control Volume

1989 USAF-UES SUMMER FACULTY RESEARCH PROGRAM

GRADUATE STUDENT RESEARCH PROGRAM

Sponsored by the

AIR FORCE OFFICE OF SCIENTIFIC RESEARCH

Conducted by

Universal Energy Systems, Inc.

FINAL REPORT

MODELING THE RESPONSE OF PRESSURIZED COMPOSITE CYLINDERS TO LASER DAMAGE

Prepared by:	Harry A. Hogan, Ph.D. Stuart J. Harbert, M.S.
Academic Rank:	Assistant Professor Graduate Assistant
Department and	Department of Mechanical Engineering
University:	Texas A & M University
Research Location:	WL/TALE Kirtland Air Force Base Albuquerque, NM 87117
USAF Researchers:	Mr. Jorge Beraun Dr. Pat Vail
Date:	26 July 1989
Contract No:	F49620-88-C-0053

MODELING THE RESPONSE OF PRESSURIZED COMPOSITE CYLINDERS TO LASER DAMAGE

by

Harry A. Hogan
and
Stuart J. Harbert

ABSTRACT

The response of pressurized composite cylinders to laser damage is a problem of interest to the Air Force and the Weapons Lab because of its application to the Strategic Defense Initiative. Current numerical models for this problem, however, are generally inadequate to allow predictions outside the range of parameters for which a large experimental database already exists. Thus, the advantages of modeling cannot be fully exploited. In an effort to develop an improved model that includes more basic mechanisms and first principles, several related tasks were undertaken. First, current models and experimental test results were evaluated and studied in order to gain as comprehensive an understanding of the problem as possible. In addition, the broader composite materials research literature was searched and reviewed in an effort to establish the current state of the art in areas closely related to the problem at hand. The two topics focussed upon were delamination at free edges and failure analysis and prediction for laminates with holes or notches. Finally, preliminary modeling activity was initiated at WL/TALE using in-house software and hardware. Short-term recommendations for improved modeling center on evaluating the effects of delamination on critical stress states near the damage site and implementing more advanced failure criteria for predicting laminate rupture.

ACKNOWLEDGEMENTS

We would like to thank the Air Force Systems Command, the Air Force Office of Scientific Research, Universal Energy Systems, and the Weapons Lab Office of the Chief Scientist for their respective roles in making the summer research programs possible. The experience has been tremendously challenging, refreshing, and enjoyable. A special word of thanks is due Mr. Jorge Beraun and Dr. Pat Vail for their guidance and assistance throughout the summer research period. We also appreciate the informative discussions with Lt. Dan Hodgkiss and other WL/TAL personnel and staff. Lt. Lee Turner's graciousness in sharing his office is also appreciated. Finally, we sincerely acknowledge the cordial hospitality extended to us by the characters of the WL Technology Assessment Office.

I. INTRODUCTION:

The response of composite material pressurized cylinders to laser damage is an area of considerable interest to the Air Force because of its relevance to Strategic Defense Initiative technologies. The Weapons Laboratory at Kirtland AFB plays a significant role in assessing various techniques and methodologies proposed for both defensive and offensive strategies. One area of particular interest to the Directed Energy Effects Branch of the Technology Assessment Office is the use of lasers to damage missile motorcases. In the case of solid-fueled missiles, motorcases typically consist of organic matrix continuous fiber reinforced composite materials. The problem therefore consists to a large extent of understanding the response of pressurized composite material cylinders, or bottles, to laser damage. Current analytical models are largely empirically based and lack sufficient generality to confidently predict results for a range of size scales of interest and for new material systems. Hence, a need exists for improved models that are derived from basic principles and include more fundamental mechanisms and effects.

The interests and abilities of both participants, H. A. Hogan (SFRP) and S. J. Harbert (GSRP), are particularly suitable and appropriate for researching this problem. Dr. Hogan has a strong interest in using finite element analysis to study composite material response and failure mechanisms, even down to the micromechanical level. Mr. Harbert has considerable background in solid mechanics, advanced finite element techniques, and materials science.

II. OBJECTIVES OF THE RESEARCH EFFORT:

The basic purpose of the research effort was to devise a strategy for developing improved analytical models for this problem. In order to accomplish this overall goal, the following specific objectives were identified:

(1) to study in detail current models and experimental test results;

(2) to identify and review current related research from the more general composite materials literature;
(3) to initiate preliminary modeling efforts at WL/TALE using in-house software and hardware.

The reasoning behind this approach is that as much as possible must be learned about all aspects of this problem before meaningful recommendations can be rendered. The first objective most directly addressed this concern, while the second sought to bring the latest knowledge and advances in understanding to bear on this particular problem. The purpose of the last objective was to explore and evaluate in-house modeling capabilities and, more importantly, to gain first-hand experience with problems similar to the specific problem of interest.

Detailed procedures for using PATRAN and NASTRAN for finite element modeling at WL/TALE are summarized in a report generated during the summer research period [1]. Subsequent analysis included a series of numerical experiments and test problems. This more complete awareness of the specific requirements, difficulties, and relevant issues associated with modeling the problem of interest provided practical insight and guidance for the recommendations developed during this work. The following two sections summarize the activities and findings involved with the first two objectives.

III. REVIEW OF CURRENT MODELS AND TESTS:

A variety of reports and documents was reviewed and studied as part of this activity. They ranged from classified to unclassified with unlimited distribution, but most were unclassified distribution limited. Thus, no direct reference to specific documents is made; information is simply summarized with an emphasis on basic features and findings.

NRL Model. The model developed at the Naval Research Laboratory treated an angled slew laser spot with thermal degradation of material properties directly below the laser spot. A portion of a round

circular cylinder was modeled with curved shell finite elements. The analysis code was ABAQUS and geometrically nonlinear behavior was included. Cyclic symmetry and similar arguments were invoked to reduce the model to a rectangular region containing half of the laser slew spot and the surrounding material. This rectangular region was oriented obliquely to the axis of the cylinder. A baseline graphite epoxy/composite material was modeled. The maximum stress failure criterion was used to predict the failure of plies in the composite laminate. Results are in the form of shaded contour plots showing the number of plies failed at successive load levels. This gives a picture of the shape and depth of damage near and around the laser spot.

MDAC Model. A round flat-bottom laser spot was modeled by workers at McDonnell Douglas Astronautics Company. A flat rectangular section was modeled with a quarter-hole partially through the thickness in one corner of the region. 3-D brick elements were used with NASTRAN to obtain solutions for biaxial applied stresses. Both S-glass/epoxy and graphite/epoxy composite systems were considered. Contour plots of stresses on the free surface of the inside of the hole are the major results. No attempt was made to predict failure or rupture of the composite. This model was also used to study delamination by inserting a small starter crack completely around the bottom of the hole. Crack growth was then simulated using a critical strain energy release rate approach with all three cracking modes combined to form an elliptic paraboloid failure envelope.

SwRI Model. A group at Southwest Research Institute considered only the cross-section of a circular cylinder. This 2-D model assumed a plane strain stress state in the cylinder wall and modeled the laser damage by a Gaussian shaped thinned region of the wall. Geometric non-linearities were included in the solutions obtained using the ADINA finite element code. The composites treated were S-glass/epoxy, Kevlar/epoxy, and graphite/epoxy. A maximum stress failure criterion was invoked to predict the Gaussian spot depth at which the first hoop ply would fail. It was then assumed that the entire laminate would

fail locally creating a perforation through the cylinder wall under the laser spot. Global failure was not addressed.

RDA Model. A round flat-bottom laser spot was also modeled by R & D Associates - Logicon. In this case a curved rectangular region of the cylinder was modeled with curved shell finite elements using NASTRAN. Geometric nonlinearities were included as well. Symmetry considerations again allowed modeling only a quarter of the hole. Laser ablation was modeled by simply removing individual plies or portions of plies from the shell elements in the laser spot region of the model. These elements also had their mid-planes offset by rigid bar elements in order to more accurately depict a partially through hole. Shaded contour plots of stresses in each ply of the laminate near and around the hole were produced as output. Critical stresses are shown to be in the outermost ply near the hole and in the center of the hole in the ply at the immediate bottom of the hole. These stresses are intended to be used with a maximum stress failure criterion to predict overall failure of the cylinder.

LMSC Model. The model used by Lockheed Missiles & Space Company is a lower order model than the others reviewed and basically consists of an extension, or adaptation, of an approach developed for hybrid tanks, which have both metal and composite layers. The so-called QDLAM approach focusses on three basic variables: a material response damage parameter (Q_d), a critical damage depth (X_d), and a critical damage spot size (D_d). A relationship between internal pressure and X_d has been derived theoretically using classical laminate theory, while the other two parameters are much more empirically based. The relationship between pressure and D_d is essentially a simple linear elastic fracture mechanics treatment but requires considerable experimental test data for determination of the correction factors employed. The model has been used to predict times to failure and mode of failure, i.e. vent or burst.

Comments on Models. Although not addressed in the preceding descriptions of each model, a comment regarding the accuracy of the models is warranted. Generally, very little experimental verification

of these models has been achieved. The NRL model has been compared with two tests but has not yet been used for predicting results for a range of parameters and materials. The LMSC model has been used most extensively for pre-test predictions and post-test analysis but is highly dependent on empirical test data for accurate results. The other models have not been compared directly to specific experimental results or used to provide pre-test predictions.

The brief model descriptions also serve to highlight several other issues. First, there seems to be a mix of opinions on whether modeling should include geometrically nonlinear deformation modes and whether shell or 3-D brick finite elements are best. The balance of evidence suggests that nonlinear effects should be included since significant solution differences have been reported in comparisons with simple linear analyses. There is not, however, a clear indication of a preferable approach in terms of shell vs. brick elements. Shells are much more computationally efficient, but they are also constrained kinematically to prescribed deformation patterns. For an extremely complicated deformation field, like may exist in the vicinity of a part-through hole in a curved laminate, shells may not model the stresses and strains with sufficient accuracy. Brick elements can model more complex stress variations but only at great computation expense. Balancing these issues and evaluating the relative trade-offs should continue to be examined.

With the lone exception of the NRL model, all of the other models neglect thermal degradation of the composite material in the vicinity of the laser spot hole. This is widely accepted as being justifiable for high laser irradiances because the ablation process proceeds so rapidly that significant heat transfer does not occur. Again with only one exception, the MDAC model in this case, delamination of the composite laminate plies has been neglected in the modeling efforts. The modelers do recognize the importance of delamination and almost universally comment to that effect in their reports, but as yet very little has been done to include this in the modeling. A final observation is that the maximum stress failure criterion is widely used

in current modeling efforts despite being the simplest and most basic composite material failure criterion [2].

Experimental Test Results. Numerous reports containing results and analyses from various experimental programs were reviewed and studied. These included hybrid metal/composite tanks or bottles in addition to composite only structures and rep-pulse lasers in addition to continuous wave lasers. The size scale also spanned a substantial range, from relatively small subscale test articles to fullscale targets. High speed films from some of the tests on composite bottles were also available for viewing. These proved particularly valuable in gaining insight into failure processes and mechanisms. Several of the tests showed a consistent pattern of failure beginning with delamination of the outer hoop layers followed by delamination of underlying layers and finally ending with rupture of the material remaining at the bottom of the laser hole. Frequent discussions with WL personnel and contractors were also beneficial in garnering a detailed understanding of this problem.

IV. CURRENT RELATED RESEARCH:

Current ongoing research in the more general composite materials research community was reviewed and studied with an emphasis on identifying topics and problems similar to or related to the problem of interest. The works reviewed typically fell into two main areas: delamination at free edges and failure of composites with holes or notches.

Delamination of Composite Laminates at Free Edges. The extensive delamination that has been observed in tests of pressurized composite bottles emphasizes the importance of understanding and modeling this phenomenon. Due to the orthotropic nature of each individual ply in a composite material, there exists a mismatch of material properties between these plies when they are combined to form a multilayered composite laminate. This mismatch gives rise to a 3-D stress state near the surface of a free edge that is without loading. This more complicated 3-D stress state only occurs in a relatively small

"boundary layer" near the free edge and is composed of both normal and shear "interlaminar stresses" in addition to the usual 2-D in-plane normal and shear stresses. The effect of the interlaminar stresses is to peel and or shear two adjacent plies apart. Delamination can be considered as an initiation and growth process, in which initiation does not necessarily imply final failure, but after stable growth may interact with other failure modes to cause final failure [3].

Delamination has been studied extensively by composite materials researchers since the early 1970's. Initially, delamination was primarily examined along the straight free edge of a laminate in order to understand the nature of interlaminar stresses. Anaylses utilized a variety of techniques including finite differences, boundary layer theory, series solutions, hybrid finite elements, displacement finite elements and classical elasticity [4]. From these different techniques, it was well established that interlaminar stresses become pointwise singular at the free edge and decrease away from the free edge. Finite elements have been the most popular method of evaluating interlaminar stresses, and are able to account for these singularities but they generally do not provide insight into the relation between interlaminar stresses and laminate stresses and applied tractions. To address this issue, Whitcomb [4] developed a superposition method to transform the edge stress problem. He essentially found that interlaminar stresses are related to the negative of the laminate stresses, when they are applied to the free edge of the laminate in the absence of other stresses and tractions. In addition, Conti and De Paulis [5] and Valisetty and Rehfield [6] both present simplified models that are applicable for first approximation evaluation of interlaminar stresses.

Research work has not only been concerned with understanding the nature of interlaminar stresses near a free edge, but also with the more difficult problem of predicting the initiation of delamination cracks. A simplified initiation criteria for delamination was derived by O'brien [7] that is characterized by using strain energy release rates. This criteria, which allows the stress singularity to be

bypassed, accurately predicted delamination onset in selected symmetric angle ply laminates. More recently, Brewer and Lagace [8] developed a quadratic delamination criteria that predicts delamination onset using averaged stress quantities near the free edge. Furthermore, this criteria is particularly useful since it is able to determine a relative propensity of a composite layup to delaminate.

Because of the lower order of complexity presented by the straight free edge geometry, it has been studied most extensively. However, recent work has been directed at more complex problems such as free edges associated with circular and elliptical holes in composite plates and/or shells. Zhang and Ueng [9] used an approximate analytical method to determine the interlaminar stresses around a circular hole in symmetric angle ply laminates and characterized the singular radial and normal stresses. Both Lucking et al. [10] and Ericson et al. [11] have used 3-D finite elements to analyze interlaminar stresses around a through hole in symmetric cross ply laminates. Lucking et al. [10] showed that the normal and radial stresses near the hole boundary increase with increasing radius/thickness ratio. Furthermore, for large ratios, the normal and radial stresses occur in the same region, which may adversely affect the laminate strength. Ericson et al. [11] give some insight as to where delamination may initiate around the hole in a symmetric cross ply laminate. They predicted delamination initiation to occur approximately 60 degrees from the loading axis.

Failure of Composite Laminates with Holes. The problem of predicting the failure of composite laminates with holes, notches, or cracks is an area of continuing research work and is similar in many respects to the failure of laser damaged composite cylinders. Even for completely through holes in flat laminates the problem is complicated by different failure modes and mechanisms for different material systems and for different lay-ups of the same material. Delamination, matrix cracking, and fiber pull-out and breakage are also present to varying degrees. The recent comprehensive review article by Awerbuch and Madhukar [12] provides an excellent starting point for evaluating the current state of the art in this area.

In this review, eleven similar "semi-empirical fracture models" for predicting the notched strength of composite laminates were critically evaluated and compared with available experimental results. Both round circular and straight crack "notches" have been treated, but always as completely through-the-thickness flaws. Loading modes were restricted to uni-axial tension only. In these models, classical isotropic linear elastic fracture mechanics concepts have been extended or modified for application to composite materials. Damaged material near the notches is assumed to be an "effective" crack that grows in a self-similar manner. The models are shown to predict essentially the same results and require one or two new experimentally determined material parameters. The accuracy of the predictions is dependent upon the quantity of experimental data used in determining the new parameters and the inherent scatter in the standard properties of the laminate. Results generally correlate well with experiment due to the empiricism the models.

Backlund and Aronsson [13,14] have recently developed a theoretically more general, and therefore less empirical, approach to this problem. Their damage zone model (DZM) was originally developed for fracture of concrete [15] and treats the damage zone near a notch as a crack with cohesive stresses on its surfaces. The model does not, however, require new material parameters; only the unnotched laminate tensile strength, laminate stiffness, and apparent fracture energy (G_c^*) are needed as input. The method has been incorporated into a finite element analysis and used to study a variety of materials, lay-ups, and notch shapes. Round holes, slots with both square and round ends, and straight sharp cracks have been considered. More recently Carlsson, Aronsson, and Backlund [16] have compared the notch sensitivity of thermoset and thermoplastic resin laminates using the DZM. Fiber dominated quasi-isotropic and matrix dominated angle-ply lay-ups were studied. The degree of correlation with experiment was found to be highly dependent upon the particular failure mechanisms. Only the quasi-isotropic lay-ups exhibited sufficiently linear deformation responses to fit the assumptions of the DZM, and even then

only the thermoset composite failed in a manner deemed consistent with the assumption of "collinear" equivalent crack growth.

Tan [17] has also proposed a set of models for predicting the notched and unnotched strengths of composite laminates. An approximate analytical solution for the normal stress distribution around an elliptical hole in an infinite orthotropic symmetric laminate forms the starting point for these models. Each of the three models employs a characteristic length to determine an "effective stress concentration", with the distinction between them being the particular method used calculate the characteristic length. The method is intended for multidirectional fiber dominated laminates with at least one ply parallel to the axis of loading. Graphite/epoxy laminates with "notch" shapes ranging from circular to elliptical to straight cracks were tested experimentally under uni-axial loading. Predictions generally fell within 20% of experimental results for the two notch sizes considered.

Two other recent works are particularly noteworthy since they dealt with more in-depth characterization of the detailed processes and mechanisms in the failure of laminates with holes. In the first, fully reversed cyclic loading has been used by Reifsnider et al. [18] to study the failure of orthotropic and quasi-isotropic graphic/epoxy laminates with a central circular hole. Penetrant-enhanced X-ray radiography was used to monitor matrix cracking and other microdamage, while surface coated photoelasticity was used to determine the redistribution of stresses around the hole during failure. Residual tensile and compressive strengths were also determined after various stages of damage accumulation.

Reddy, Wang, and Zhong [19] also used X-ray radiography to observe the sequence of matrix cracking in cross-ply graphite/epoxy laminates with a central through hole. A three-dimensional finite element analysis accompanied the experiments. A longitudinal surface crack in the matrix parallel to the fibers of the outer ply was built into the model to simulate experimental observations. Crack propagation was modeled via a combined mode critical strain energy release rate

approach. Delaminations emanating from the longitudinal cracks were also modeled. Model predictions correlated well only for very low load levels because the model did not include the transverse matrix cracking that was observed experimentally.

Comments on Current Research. It is apparent from this review of literature in these two topic areas that there exists current ongoing research that could be of potential benefit in developing improved models of laser damage to pressurized composite cylinders. Important differences remain, however, between the research cited and the particular details of the problem of interest. Modifications, adaptations, and extensions of the methods and techniques will likely be required in applying them to the pressurized cylinder configuration. Delamination and failure associated with a part-through hole in a curved cylinder under bi-axial loads is essentially an unsolved problem currently. Thus, advances made in the solution of the problem at hand will also be of benefit to the entire composite materials research community.

V. RECOMMENDATIONS:

The research conducted during the summer program indicates that promising areas for improving the modeling of pressurized composite cylinders with laser damage are to: (1) treat delamination more explicitly, and (2) implement more advanced composite failure criteria. Recent and continuing research activity in these areas not only provides reasonable encouragement that better models can be developed but also provides a source of fresh insight and new knowledge upon which to draw. A more fundamentally sound approach embodying basic failure mechanisms is critical to the ultimate development of a truly general, and therefore much more useful, model.

Given the considerable complexity and difficulty of accurately predicting delamination initiation and growth at the curved free edge of a part-through hole, a more practical short-term strategy is proposed. With further study of results from tests of pressurized composite bottles, a typical pattern of delamination will be

established. The similarity in delamination development observed in the films of several tests supports this approach. These cracks will then be directly built into a finite element model of the bottles, and their effects on critical stress states in the vicinity of the hole will be detailed. Sensitivity studies varying the size, location, shape, and sequence of delaminations will likely be required to some extent. This approach would not only determine whether delamination effects are significant or not, but it would also provide quantitative solutions for such effects. If delamination proves significant, then the more challenging problem of predicting delamination initiation and growth can be addressed in subsequent research. Otherwise, if delamination effects are deemed relatively insignificant, then further research can be directed elsewhere.

The need for more advanced failure criteria is rather compelling considering the rudimentary simplicity of the maximum stress failure criterion, its prevalence in current models, and the relative inaccuracy of these models not only in predicting failure from laser damage but also in predicting undamaged burst pressures. Another short-term priority will therefore be to critically evaluate such advanced criteria and approaches, beginning with those reviewed above. Applying such criteria to the problem at hand will not be a trivial task. As evident in the previous section, these criteria are currently being developed for the simpler problem of a completely through hole in a flat laminate under uni-axial loading; whereas, composite motorcases are curved laminates under bi-axial loading with the laser damage forming a part-through hole. In addition to the obvious test of how well these alternate theories predict experimental results, other evaluation factors will include finite element implementation considerations and additional experimental requirements for determining new material constants. Excessively burdensome demands in either of these areas would be considered inappropriate from a practical perspective.

An essential ingredient in successively pursuing these goals is the continuous collecting and studying of results from past and future

experimental tests and from current research work in related topic areas. Furthermore, longer term research should be directed at considering continuum damage mechanics as a means of modeling matrix microcracking, thermal degradation, and other damage processes. This would broaden the range of applicability to include tougher matrix composites and lower laser irradiation regimes.

REFERENCES

1. Harbert, S. J. and Hogan, H. A., "Finite Element Modeling at WL/TALE Using PATRAN and NASTRAN," report submitted to WL/TALE, July 1989.

2. Jones, R. M., Mechanics of Composite Materials, Washington, D.C., Scripta Book Co., 1975.

3. Halpin, J. C., Primer on Composite Materials: Analysis, 2nd ed., Lancaster, PA, Technomic Publishing, 1984.

4. Whitcomb, J. D. and Raju, I. S., "Superposition Method for Analysis of Free-Edge Stresses," J. Comp. Matl., v. 17, 1983, pp. 492-507.

5. Conti, P. and De Paulis, A., "A Simple Model to Simulate the Interlaminar Stresses Generated Near the Free Edge of a Composite Laminate," Delamination and Debonding of Materials, ASTM STP 876, W. S. Johnson, ed., 1985, pp. 35-51.

6. Valisetty, R. R. and Rehfield, L. W., "A New Ply Model for Interlaminar Stress Analysis," Delamination and Debonding of Materials, ASTM STP 876, W. S. Johnson, ed., 1985, pp. 52-68.

7. O'Brien, T. K., "Characterization of Delamination Onset and Growth in a Composite Laminate," Damage in Composite Materials, ASTM STP 775, K. L. Reifsnider, ed., 1982, pp. 140-167.

8. Brewer, J. C. and Lagace, P. A., "Quadratic Stress Criterion for Initiation of Delamination," J. Comp. Matl., v. 22, 1988, pp. 1141-1155.

9. Zhang, K. and Ueng, C. E. S., "A Simplified Approach for Interlaminar Stresses Around a Hole in $[\phi/-\phi]_s$ Laminates," proceedings of the 6th Int. Conf. on Composite Materials and the 2nd European Conf. on Composite Materials, July 20-24, 1987, London, UK, F. L. Matthews et al, eds., Elsevier, v. 5, pp. 5.241-5.251.

10. Lucking, W. M., Hoa, S. V., and Sankar, T. S., "The Effect of Geometry on Interlaminar Stresses of $[0/90]_s$ Composite Laminates with Circular Holes," J. Comp. Matl., v. 17, 1984, pp. 188-198.

11. Ericson, K., Persson, M., Carlsson, L., and Gustavsson, A., "On the Prediction of the Initiation of Delamination in a $[0/90]_s$ Laminate with a Circular Hole," J. Comp. Matl., v. 18, 1984, pp. 495-506.

12. Awerbuch, J. and Madhukar, M. S., "Notched Strength of Composite Laminates: Predictions and Experiments -- A Review," J. Reinf. Plastics and Comp., v. 4, 1985, pp. 3-159.

13. Backlund, J. and Aronsson, C.-G., "Tensile Fracture of Laminates with Holes," J. Comp. Matl., v. 20, 1986, pp. 259-286.

14. Aronsson, C.-G. and Backlund, J., "Tensile Fracture of Laminates with Cracks," J. Comp. Matl., v. 20, 1986, pp. 287-307.

15. Hillerborg, A., Modeer, M. and Petersson, P. E., "Analysis of Crack Formation and Crack Growth in Concrete by Means of Fracture Mechanics and Finite Elements," Cement and Concrete Res., v. 6, 1976, pp. 773-782.

16. Carlsson, L. A., Aronsson, C.-G., and Backlund, J., "Notch Sensitivity of Thermoset and Thermoplastic Laminates Loaded in Tension," J. Matl. Sci., v. 24, 1989, pp. 1670-1682.

17. Tan, S. C., "Effective Stress Fracture Models for Unnotched and Notched Multidirectional Laminates," J. Comp. Matl., v. 22, 1988, pp. 322-340.

18. Reifsnider, K. L., Stinchcomb, W. W., Bakis, C. R., and Yih, R. Y., "The Mechanics of Micro-Damage in Notched Composite Laminates," in Damage Mechanics in Composites, A. S. D. Wang and G. K. Haritos, eds., proceedings of the ASME Winter Annual Meeting, December 13-18, 1987, Boston, MA, AD-Vol. 12, pp. 65-72.

19. Reddy, E. S., Wang, A. S. D., and Zhong, Y., "Simulation of Matrix Cracks in Composite Laminates Containing a Small Hole," in Damage Mechanics in Composites, A. S. D. Wang and G. K. Haritos, eds., proceedings of the ASME Winter Annual Meeting, December 13-18, 1987, Boston, MA, AD-Vol. 12, pp. 83-91.

1989 USAF-UES SUMMER FACULTY RESEARCH PROGRAM

Sponsored by the

AIR FORCE OFFICE OF SCIENTIFIC RESEARCH

Conducted by the

Universal Energy Systems, Inc.

FINAL REPORT

Parallel and Vector Processing for Nonlinear Finite Element Analysis

Prepared by:	Duc T. Nguyen, Ph.D.
Academic Rank:	Assistant Professor
Department and	Civil Engineering
University:	Old Dominion University
Research Location:	Weapons Laboratory Parallel Computing Group Kirtland AFB, NM 87117
USAF Researcher:	Captain Edward A. Carmona

Date:	22 Aug 89
Contract No:	F49620-88-C-0053

To be published as a

Technical Memorandum

1989 USAF-UES SUMMER FACULTY RESEARCH PROGRAM

GRADUATE STUDENT RESEARCH PROGRAM

Sponsored by the

AIR FORCE OFFICE OF SCIENTIFIC RESEARCH

Universal Energy Systems, Inc.

FINAL REPORT

SCATTERING OF ELASTIC WAVES IN A RANDOM INHOMOGENEOUS SOIL MEDIA

Prepared by:	Duane R. Sanders, Ph.D Robert W. Bolton, M.S.
Academic Rank:	Assistant Professor Lecturer
Department and University:	Civil Engineering Department Texas A&M University
Research Location:	WL/NTESG Kirtland AFB Albuquerque, NM 87117-6008
USAF Researcher:	Dr. Robert Reinke

Date:	12 Aug 89
Contract No:	F49620-88-C-0053

SCATTERING OF ELASTIC WAVES IN A RANDOM INHOMOGENEOUS SOIL MEDIA

by

Duane R. Sanders

and

Robert W. Bolton

ABSTRACT

A literature survey of wave scattering models applicable to random homogeneous soil media was performed. From the literature review the Kramers-Kronig method for calculating the dispersion in a random inhomogeneous media was selected. The Kramers-Kronig method was implemented into a plane wave computer code and a parameter study was performed in which the scatterer size, scatterer concentration, and elastic constants for the scatterer and matrix were varied for a range of values typical of the McCormick Ranch, Albuquerque, NM. It was determined that the Kramers-Kronig method was able to model the variability in acceleration spectra recorded at the McCormick Ranch due to a buried detonation for different azimuthal directions by considering: different combinations of scatterer size, scatterer concentration, elastic constants of scatterer and matrix and Q that are typical of the variability of these parameters in different azimuthal directions at the McCormick Ranch. The results of the study indicate that the Kramers-Kronig method does have application in modeling the wave propagation characteristics in a random inhomogeneous media.

ACKNOWLEDGEMENTS

I wish to thank the Air Force Systems Command and the Air Force Office of Scientific Research for sponsorship of this research. I further want to thank Mr. Rodney Darrah, director of the Summer Faculty Research Program, and his associates at UES for their assistance in guiding me through this program.

I want to thank Dr. Robert Reinke and Capt. John Gill for conferring with me during my pre-summer visit so a prudent area of research for the summer could be selected. I also want to thank them for their guidance, encouragement and for taking the time to see that I received everything I needed to complete this project. Dr. Robert Reinke interest and experience in addressing some of the issues related to the elastic wave scattering problem was invaluable. The encouragement and assistance of Kent Anderson in many aspects of this research was also greatly appreciated. Finally, I want to thank Audrey Martinez, Al Leverette, Lt. Georke, Dave Fernald and Jennifer Bienn for making me feel like one of the crew.

I. INTRODUCTION

To relate a seismic source to a receiver in a random inhomogeneous elastic or viscoelastic soil/rock media it is necessary to consider the scattering of energy which takes place at the interface of the inhomogeneities. This scattering takes place by reflection and refraction at the interfaces of each inhomogeneity. For an elastic media the scattered energy is taken from the incident wave energy, therefore, it is not loss but is redistributed into the scattered waves. The scattered wave energy is incoherent (no constructive interference) due to the random distribution of the inhomogeneities. Because the amplitude of the incident wave is reduced as it propagates, the medium appears to be attenuative even though for elastic media no energy is lost. The spatial decay of the pulse depends on the ratio of the wave length to the typical size of the inhomogeneity, with the scattering approaching zero as the ratio becomes large. For viscoelastic media there is an additional attenuation of the incident wave due to losses of energy through dissipative mechanisms which converts some of the energy into heat. The dispersion characteristics of the soil media are related to the attenuation characteristics of the soil media. In fact, without attenuation either due to scattering, viscoelasticity, or both, a soil medium will exhibit no dispersion.

If one considers only a few scatterers, closed form solutions are available that precisely give the solution to an elastic boundary value problem in terms of scatterer locations, and material properties of the matrix and scatterer. In situations of interest in this research, however, the exact locations of the scatterers are not known. The best that can be expected is a statistical description of the inhomogeneous random media.

The Geological Response Section of the Civil Engineering Research Division is interested in relating measured geological response to the magnitude and characteristics of the source for several reasons. First, they develop and validate most if not all of their ground motion

prediction schemes by analysis and modeling of small scale high explosive test data. Second, for treaties that limit the size of underground nuclear explosions one of the verification methods is the measurement of ground motions. In both of the example given above the scattering of elastic waves in a random inhomogeneous media is a very important consideration. Therefore, means by which waves recorded in a random inhomogeneous media can be related to the attenuation and dispersion is of fundamental importance.

I have recently been working in the area of elastic-plastic wave propagation in soil media due to a sudden impact of a large seismic source. The eventual goal of this research is to better understand the nature of wave propagation in the weathering zone in order to better interpret the measured response for seismic exploration purposes. One aspect of this research is the treatment of the elastic-plastic wave propagation in a inhomogeneous random media. The thrust of this research meshes very well with the interest of the Geological Response Section of the Civil Engineering Research Division.

II. OBJECTIVES OF THE RESEARCH EFFORT

The objectives of this research effort are: 1) perform a literature review of scattering theories that would apply to a random inhomogeneous soil media, 2) determine which of these theories have the most application to interpreting the wave propagation response in a random inhomogeneous soil media, and 3) apply the most promising scattering model using field data and perform a limited parameter study.

III. LITERATURE REVIEW OF SCATTERING MODELS

The purpose of the literature review was to catalog various approaches to modeling wave scattering which may have have application to inhomogeneous soil media. In this literature review 125 papers were collected. These papers have been sorted into seven different categories: 1) Configurational Averaging, 2) Perturbation/Born Approximation, 3) Kramers-Kronig, 4) Quality Q, 5) O'Doherty-Anstey and

6) others. The papers and books contained in the literature review are not included in this report but can be obtained from Robert Reinke or Duane Sanders.

As a result of the literature review the Kramers-Kronig method for modeling attenuation and dispersion was selected for further investigation.

IV. KRAMERS-KRONIG METHOD

The Kramers-Kronig method is based on the Kramers-Kronig relationships which were derived in 1927 by Kramers to describe the dispersion of electromagnetic waves in dielectrics. These relationships have since found application in other types of wave propagation problems. For example, sound waves in acoustical media Horton (1974) and O'Donnell et.al.(1981), elastic waves in isotopic viscoelastic media O'Donnell, et.al. (1981) and elastic waves in viscoelastic random fibrous and particulate composites Beltzer and Brauner (1984). Of course, our interest is in the application of the Kramers-Kronig relations to viscoelastic random soil/rock media.

Consider a plane wave in a viscoelastic medium represented by

$$e^{(i(K(\omega)x-\omega t))} \tag{1}$$

where ω is the real circular frequency and K is the complex wave number given by

$$K(\omega) = K_r + iK_i = \frac{\omega}{c(\omega)} + i\alpha(\omega) \tag{2}$$

where $c(\omega)$ is the phase velocity and $\alpha(\omega)$ is the attenuation. The attenuation term is responsible for the amplitude decay as function of propagation distance, x. In general, the attenuation is considered to be composed of two additive components,

$$\alpha = \alpha_{in} + \alpha_{sc} \tag{3}$$

where α_{in} is the attenuation due to viscoelasticity and α_{sc} is the attenuation due to scattering.

For a causal, linear system it has been shown by Weaver and Pao (1981,eqs. 12 and 13) and Aki and Richards (1980) that $\alpha(\omega)$ and $C(\omega)$, appearing in eq.(2), are related as follows:

$$\frac{1}{C(\omega)} = \frac{1}{C\infty} + \frac{1}{\pi} \mathbb{P} \int_{-\infty}^{\infty} \frac{\alpha(\zeta)}{\zeta(\zeta-\omega)} d\zeta \tag{4}$$

$$\alpha(\omega) = \alpha(0) - \frac{1}{\pi} \mathbb{P} \int_{-\infty}^{\infty} \frac{1/C(\zeta) - 1/C_{\infty}}{\zeta - \omega} d\zeta \tag{5}$$

where $C_{\infty} = \text{limit}_{\omega \to \infty} C(\omega)$ and $\alpha(0) = \text{limit}_{\omega \to 0} \alpha(\omega)$. These two equations are referred to as the Kramers-Kronig (K-K) relationships. From the above equations it can be seen that $\alpha(\omega)$ and $C(\omega)$ are not independent quantities but are intimately related. Thus, if one can specify either the phase speed or attenuation the other function can be readily calculated using the K-K relationships. It should be noted that the K-K relationships place no restrictions on the nature of the phenomenon causing the attenuation and dispersion other than causality and linearity.

If $\alpha(\omega)$ is an even function ($\alpha(\omega)=\alpha(-\omega)$) then eqs. (4) and (5) can be written as

$$\frac{1}{C(\omega)} = \frac{1}{C\infty} + \frac{2\omega^2}{\pi} \mathbb{P} \int_{0}^{\infty} \frac{\alpha(\zeta)}{\zeta^2(\zeta^2-\omega^2)} d\zeta \tag{6}$$

$$\alpha(\omega) = \alpha(0) - \frac{2\omega^2}{\pi} \mathbb{P} \int_{0}^{\infty} \frac{1/C(\zeta) - 1/C_{\infty}}{\zeta^2-\omega^2} d\zeta \tag{7}$$

Note in the above equation the limits of integra· are from 0 to ∞.

To apply the Kramers-Kronig relationships it is usual practice to specify $\alpha(\omega)$ and then use either eq. (4) or eq. (6) to determine $C(\omega)$. Beltzer and coworkers have used this approach in applying the Kramers-Kronig relationships to a variety of problems in particulate and fiber reinforced composites. Beltzer, Wegner, Tittman and Haddow (1989) have also suggested the application of the Kramers-Kronig relations to describe the dispersion of seismic waves.

In applying the K-K relationships Beltzer et.al. (1989) used a particular model of a random media, given by Wu (1982) to describe the attenuation coefficients due to scattering. This model consists of homogeneous layers of heterogeneities. Wu neglected the mode conversion and applied the Born approximation to calculate the scattered field. Then, he considered only the energy scattered to the backspace as lost. After averaging, Wu arrived at an approximate expression for the attenuation due to scattering, which depends on the adopted correlation coefficient.

Wu's (1982) attenuation coefficient due to scattering for the exponential, $e^{-r/a}$, and Gaussian, $e^{-(r/a)^2}$, correlation functions are given by

$$\alpha_{sc} = \frac{2\gamma_0^2 q^4}{(1 + 6q^2 + 8q^4)a} \quad \text{(exponential)} \tag{8}$$

$$\alpha_{sc} = \frac{\sqrt{\pi}}{2a} \gamma_0^2 q^2 \left(e^{-q^2/2} - e^{-q^2}\right) \text{ (Gaussian)} \tag{9}$$

, respectively. The quantity $\gamma_0 = \frac{\delta C}{C}$ is called the fluctuation index, and $q = \frac{\omega a}{C_0}$ ia dimensionless parameter.

Equation (8)and (9) are then used in the K-K relationships, (eq. (6)), to obtain the following relationships for the phase velocity, $C(\omega)$,

$$\frac{C(\omega)}{C_0} = \left\{ 1 - 4\gamma_0^2 q^2 \left[\frac{1}{\sqrt{2}\,(4q^2 + 2)} - \frac{1}{2(1 + 4q^2)} \right] \right\}^{-1} \qquad (10)$$

$$\frac{C(\omega)}{C_0} = \left\{ 1 + \frac{\gamma_0^2 q^2}{\sqrt{\pi}} \left[F(\tfrac{1}{2}, \nu) e^{-q^2/2} - F(1,q) e^{-q^2} \right] \right\}^{-1} \qquad (11)$$

for the exponential and Gaussian correlation functions, respectively. Where

$$F(1,q) = -\sqrt{\pi} \int_0^1 e^{x^2 q^2} dx \qquad (12)$$

$$F(\tfrac{1}{2},q) = -\sqrt{\pi} \int_0^{\frac{1}{\sqrt{2}}} e^{x^2 q^2} dx \qquad (13)$$

For $q \to \infty$ both of the correlation functions give

$$\frac{C_\infty}{C_0} = \left[1 + \gamma_0^2 \,(1 - \sqrt{2}\,)/2 \right]^{-1} \qquad (14)$$

For the intrinsic attenuation, α_{in}, Beltzer et.al. (1989) adopted Azimi's model

$$\alpha_{in}(\omega) = \frac{\delta_1 \omega}{1 + \delta_2 \omega} \qquad (15)$$

where δ_1 and δ_2 are constants. The use of this equation in eq. (6) will give a singular value for $C(\omega)$ at $\omega \to 0$. To eliminate the singularity at 0 a cut-off frequency is introduced

$$\begin{aligned} \alpha_{in}(\omega) &= 0, && \omega < \varepsilon \\ \alpha_{in}(\omega) &= \frac{\delta_1 \omega}{1 + \delta_2 \omega}, && \omega > \varepsilon \end{aligned} \qquad (16)$$

The cutoff frequency ε is selected to be sufficiently small that dispersion can be neglected.

Equation (15) is now substituted into eq. (6) to obtain the following relationship for the velocity dispersion due to viscoelasticity alone as

$$C(\omega)/C_o = [1 - H(q - \nu)\delta_1 C_o f(q,b,\nu)/\pi]^{-1} \quad (17)$$

where

$$f(q,b,\nu)=\{(-bq-1)\ln(q+\nu) + (bq-1)\ln(q-\nu) + [2b^2\ln(b\nu+1) - 2b^2\ln \nu - 2b^2\ln b]q^2 + 2\ln \nu\}/(b^2q^2-1) \quad (18)$$

$H(\ )$ is the Heavyside step function, $\nu=\varepsilon a/c_o$ and $b=\delta_2 c_o/a$. The limiting dispersion velocity as $\omega \to \infty$ is given by

$$C_\infty/C_o=[1-H(q-\nu)\delta_1 C_o f_\infty(b,\nu)/\pi]^{-1} \quad (19)$$

where $f_\infty(b,\nu) = 2[\ln(b\nu+1)-\ln(\nu b)]$. Since $b\nu<<1$ this complies with the limit that $C_\infty > C_o$.

If one now considers both sources of attenuation to occur together then we get the following expression for the phase velocity, $C(\omega)$, for the exponential correlation function

$$\frac{C(\omega)}{C_0} = \left\{4\gamma_0^2 q^2 \left[\frac{1}{\sqrt{2}\,(4q^2 + 2)} - \frac{1}{2(1 + 4q^2)}\right]\right.$$

$$\left. 1 - H(q - \nu)\delta_1 C_o f(q,b,\nu)/\pi]\right\}^{-1} \quad (20)$$

In the next section a parameter study will be performed using the Kramers-Kronig method given above for the exponential correlation function.

V. PARAMETER STUDY

As part of the investigation of various scattering theories the theory

presented by Beltzer (1989) utilizing the Kramers-Kronig relationships was implemented in a FORTRAN computer code on a VAX 8600. Initial runs were made to duplicate the results presented by Beltzer in order to verify the accuracy of the computer code. Various coding errors were discovered and corrected. All presented results were duplicated with the exception of a power spectra for viscoelastic attenuation. No error in the code could be found to account for this discrepancy.

After validation of the code a parameter study was conducted to quantify and bound the effects of various scattering parameters on the attenuation of a displacement pulse for a plane wave in elastic and viscoelastic media similar to that found on the McCormick Ranch. Parameters varied in the study included: scatterer size, a, velocity fluctuation index, γ_o, inclusion concentration, ϕ, and the ratio of the inclusion to the matrix Lame constants, Ep.

Material properties were obtained from Bogaards (1988) report. A common mass density was used for both the matrix and inclusions. Lamé elastic constants, λ and μ, were derived from a mean p-wave speed of 700 m/s using the relationship between propagation speed and the constrained modulus, $\lambda + 2\mu$, and mass density. Table 1 lists the material properties used in the study. Elastic constants of the scatterers were computed using Ep and the matrix material properties. The effect of variation of Poisson's ratio was not studied since the constrained modulus, $\lambda + 2\mu$, is invariant with respect to Poisson's ratio.

The velocity fluctuation index for this study is calculated using the following equation:

$$\gamma_o = \frac{\Delta C}{C} = \left[\frac{(1-\phi)(C_1-C_o)^2 + \phi(C_2-C_o)^2}{C_o^2} \right]^{\frac{1}{2}} \qquad (21)$$

where

$$C_o^2=(\lambda_o+2\mu_o)[(1-\phi)\rho_1+\phi\rho_2] \qquad (22)$$

$$\lambda_o+2\mu_o=(\lambda_1+2\mu_1)\left\{1+3\phi\left[\frac{\lambda_1+2/3\mu_1-\lambda_2-2/3\mu_2}{3\lambda_2+2\mu_2+4\mu_1}\right.\right.$$

$$\left.\left.+\ 20/3\ \frac{\mu_1(\mu_1-\mu_2)}{\mu_2(16\mu_1+6\lambda_1)+\mu_1(14\mu_1+9\lambda_1)}\right]\right\}^{-1} \quad (23)$$

$$C_1^2=\frac{\lambda_1+2\mu_1}{\rho_1} \qquad C_2^2=\frac{\lambda_2+2\mu_2}{\rho_2} \quad (24)$$

C_1, C_2 and C_o are the matrix, inclusion and composite static phase velocities, respectively; ϕ is the scatterer concentration; ρ is the mass density and λ and μ are the Lamé constants, with a subscript 1 and 2 indicating the values of these constants for the matrix and scatterer, respectively. This equation is derived by calculating the variance of the velocity in each phase from the average value of the phase velocity of the composite media. As can be seen from the above equation, the velocity fluctuation index is a function of the ϕ, ρ_1, ρ_2, λ_1, λ_2, μ_1 and μ_2. *Figure 1. shows the velocity fluctuation index* as a function of ϕ and the ratio of the Lame constants of the scatterer to the matrix, $Ep=(\lambda_2+2\mu_2)(/\lambda_1+2\mu_1)$. Analysis of Figure 1 indicates a strong correlation between γ_o and elastic ratio, Ep, and inclusion concentration, ϕ. High velocity fluctuation indexes occur only with high elastic property ratios and high inclusion concentrations. Figure 1 was used as a guide in selecting various combinations of these variables for use in the parameter study. From Figure 1 one can also see that γ_o has an upper bound of 0.44 for the McCormick Ranch since an Ep of 5 and ϕ of 0.30 are upper bound on Ep and ϕ at this site.

A preliminary parameter matrix was run using the exponential scattering model (see eq. (8)) to evaluate the effects of various media parameters on the scattering attenuation constant α_{sc}. Selected results of these runs are shown in Figure 2. These results indicate that attenuation is most sensitive to changes in the velocity fluctuation index followed by the scatterer size and relatively insensitive to variations in inclusion concentrations. Note that some of the inclusion concentration -

velocity fluctuation index combinations violate equation (21) discussed previously. Comparison of trace (a) and (b) indicate a 960% increase in attenuation at 100 hertz for a change in velocity fluctuation index from 0.10 to 0.30. Comparison of traces (b) and (d) indicate an increase in attenuation of 92% at 100 hertz for a change in scatterer size from 0.5 to 1.5. Comparison of traces (b) and (c) indicate the inclusion concentration with constant velocity fluctuation index has little effect on attenuation. Also note the attenuation for all runs shown is insignificant below a frequency of 20 to 30 hertz and increased monotonically with frequency. These results were used as a guide to selection of subsequent ranges for the parameter study.

Results of the parameter study are presented in a number of formats two of which are described below. The first is an acceleration spectra which is calculated from the attenuated displacement spectra, $F(\omega)J(\omega)$, using the relation $Mod(A(\omega)) = \omega^2 Mod(F(\omega)J(\omega))$. Acceleration spectra were used for presentation of results so comparisons could be made with similar recorded spectra presented by Reinke and Stump (1988). Model results were scaled up by a factor of 100 (40 dB) to provide a dB scale similar to Reinke and Stump (1988). The second format for presentation of results is an attenuated displacement trace. This trace is obtained by taking the inverse Fourier transform of the attenuated displacement spectra, $F(\omega)J(\omega)$, using an inverse FFT routine. The displacement pulse propagated in the various run series is shown in Figure 3. This trace was derived from an integrated radial acceleration trace from Stump(1983), corrected for initial slope. The digitized trace was transformed into the frequency domain using an FFT routine to obtain $F(\omega)$ and then this quantity is multiplied by $J(\omega)$ to obtain the attenuated displacement spectra.

The exponential scattering model (see eq. (8)) was studied using the matrix of runs shown in Table 2. Selected results from these runs (see Figures 4-7) will be discussed below.

Table 1 Material Properties

Mass Density	1900 Kg/m^3
Lamé Constant λ	646 MPa*
Lamé Constant μ	142 MPa*

*Poisson's ratio = 0.43

Table 2 Run Matrix for Elastic-Exponential Scatterer Series

Run	a	γ_o	Ep
1	0.5	0.28	3.0
2	1.5	0.28	3.0
3	2.5	0.28	3.0
4	3.5	0.28	3.0
5	10.	0.28	3.0
6	1.5	0.04	1.2
7	1.5	0.17	2.0
8	1.5	0.44	5.0
9	1.5	0.50	5.0*

* Violates equation (21)

Figure 4 shows the effect of variation of scatterer size on the acceleration spectra. Deviations of the modulus become apparent at a frequency of 7 to 10 hertz and increases monotonically to maximum of -3 dB at 100 hertz for a scatterer size of 1.5. Deviations in scatterer size from 1.5 resulted in reduced attenuation. This was unexpected but further investigation of the exponential attenuation function explains the result. Figure 5 is a plot of attenuation for several values of scatterer size ranging from 0.5 to 10 meters for a γ_o = 0.28. The attenuation curves reach an asymptotic peak at lower frequencies as the scatterer size increases. However, the limiting value of these curves decreases significantly with scatterer size. For the frequency range of interest, 0 to 100 hertz, a scatterer size of 1.5 gives the largest attenuative effect. Scatterer sizes less than 1.5 will have larger maximum attenuation, but at frequencies above the range of interest. The scatterer size corresponding to maximum attenuation was not found.

Figure 6 shows the effect of variation of velocity fluctuation index on the acceleration spectra. Deviations in modulus for the heterogeneous cases become apparent at 15 hertz and significant at 30 hertz. The attenuation increases monotonically to a maximum of -7 dB at 100 hertz.

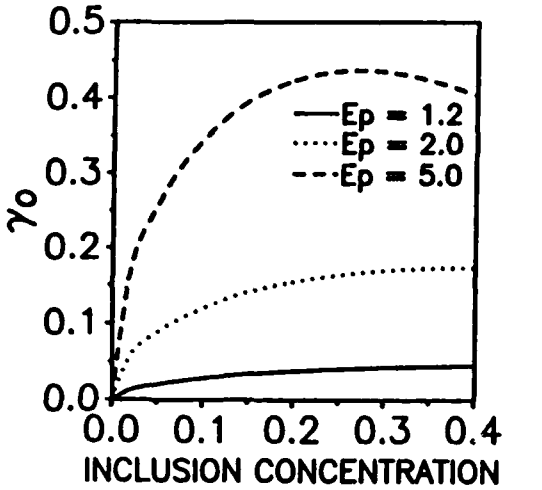

FIG. 1 γ_o VS ELASTIC PROPERTIES

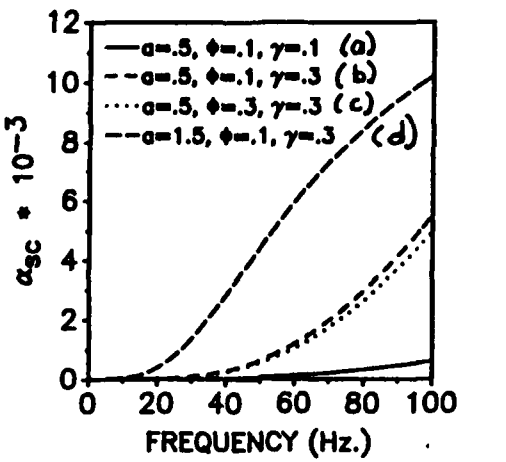

FIG. 2 α_{sc} VS MEDIA CONFIGURATION

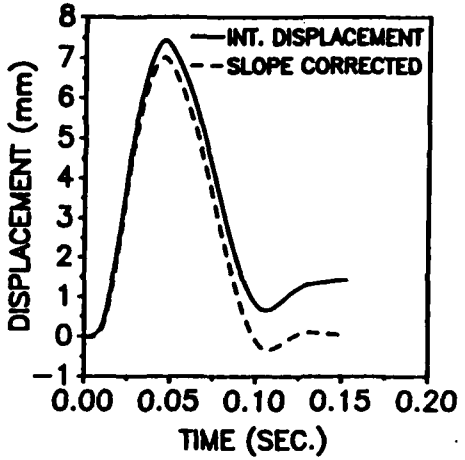

FIG. 3 DISPLACEMENT PULSE

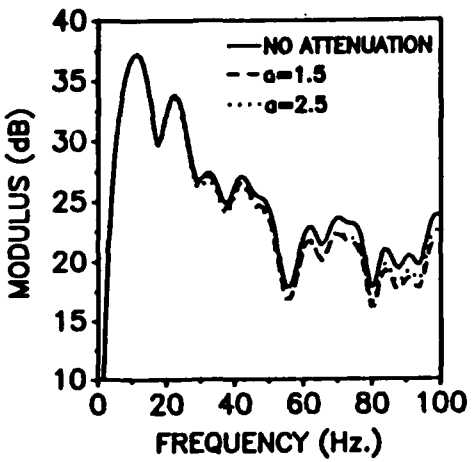

FIG. 4 EFFECT OF a ON ACCEL.SPECTRA

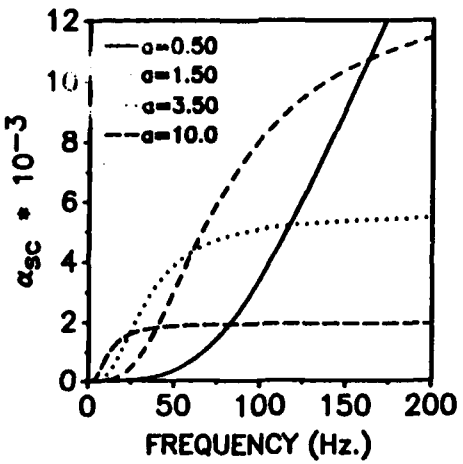

FIG. 5 α_{sc} VS SCATTERER SIZE

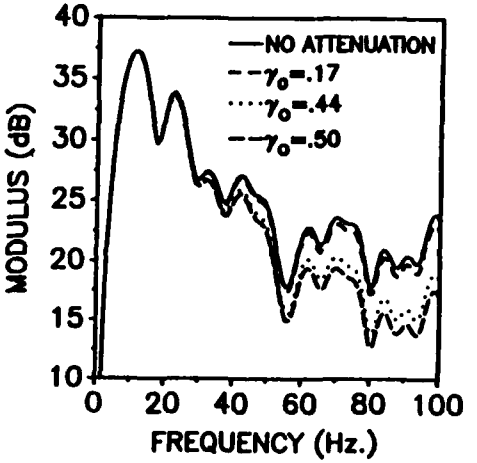

FIG. 6 EFFECT OF γ_o ON ACCEL. SPECTRA

Figure 7 shows the propagated displacement trace for selected heterogeneous cases (Table 3; runs 10, 11 and 12). The traces show little attenuation or dispersion but displays a shift in arrival time. This occurs because of slight changes in the static phase velocity C_o which is derived from the composite material properties which change with each run.

To include viscoelastic attenuation Beltzer (1989) used Azimi's model (see eq. (15)). This required the calibration of Azimi's model in terms of Q. To do this the first term in the model $\delta 1$ is related to the media Q factor by the equation $\delta 1 = 1/2CQ$, where C is the phase velocity. Q was initially taken as 8 with a phase velocity of 700 m/s. $\delta 2$ was calibrated to obtain an attenuation curve that was relatively linear over the 0 to 100 hertz frequency range. Figure 8 shows the result of the calibration relative to a linear model. Computer runs for this portion of the study are tabulated in Table 3

Table 3 Run Matrix for Viscoelastic-Exponential Attenuation Model

Run	a	γ_o	Ep	$\delta 1$	$\delta 2$	Q
10	1.5	0.17	2.0	8.9E-5	1.3E-4	8
11	1.5	0.28	3.0	8.9E-5	1.3E-4	8
12	1.5	0.44	5.0	8.9E-5	1.3E-4	8
13	--	--	--	8.9E-5	1.3E-4	8
14	--	--	--	4.4E-5	1.3E-4	16

Figures 9 and 11 show selected results for the runs 12, 13 and 14 listed in Table 3. Figure 9 shows the modulus of the acceleration spectra for various combinations of attenuative effects. From the figure it seems that viscoelastic attenuation effects are detectable starting at 5 hertz and becomes significant at 10 hertz while scattering attenuation effects start at a higher frequency range, 15 to 30 hertz. The deviation in modulus due to viscoelastic effects alone result in maxima of -13 dB and -7 dB for Q's of 8 and 16, respectively. The maximum deviation of the acceleration spectra for combined effect was for run 12 with an attenuation of -18 dB. As expected, the scattering attenuation is additive, the -5 dB increase in the combined effect is the same as

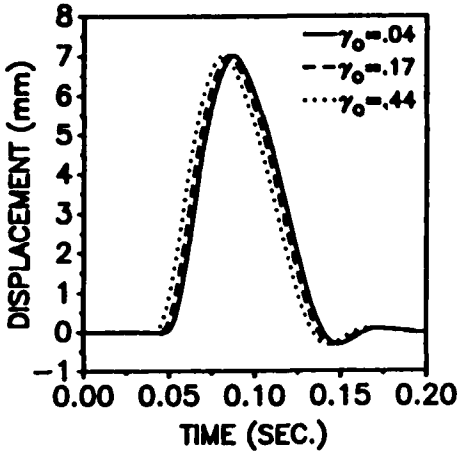

FIG. 7 EFFECT OF γ_0 ON DISPLACEMENT

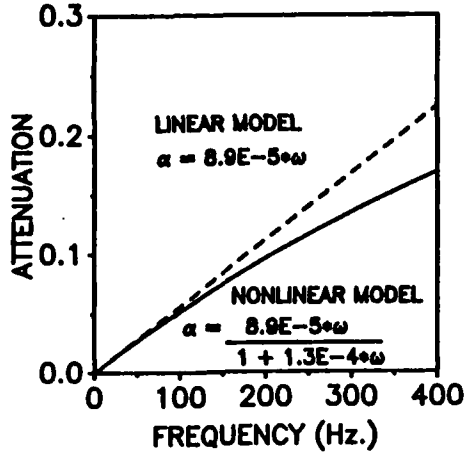

FIG. 8 INTRINSIC ATTENUATION MODEL

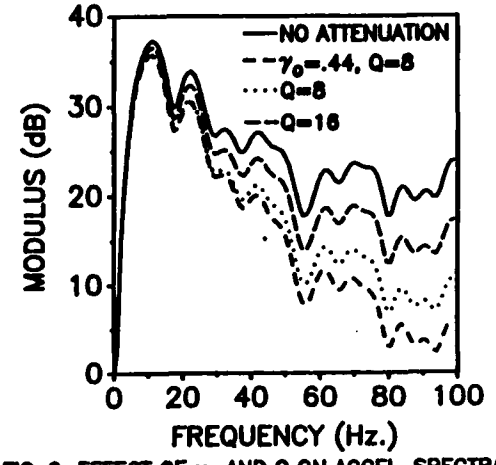

FIG. 9 EFFECT OF γ_0 AND Q ON ACCEL. SPECTRA

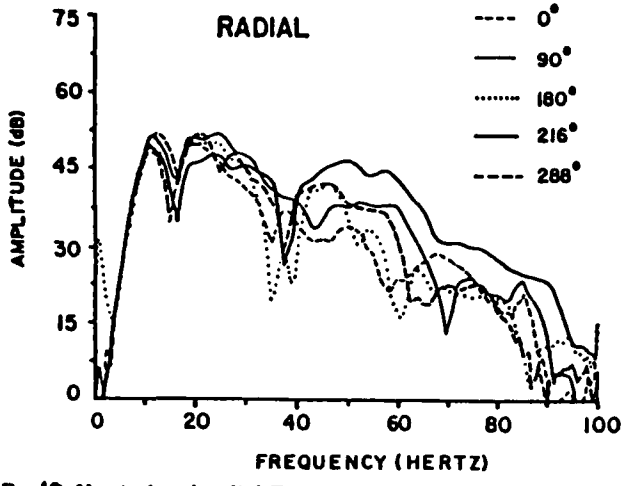

FIG. 10 Vertical and radial Fourier acceleration spectra for ART 2.

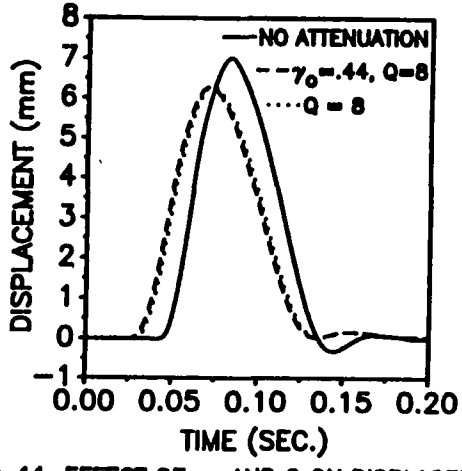

FIG. 11 EFFECT OF γ_0 AND Q ON DISPLACEMENT

shown previously for exponential scattering attenuation only. The most important result shown in Figure 9 is the effect of variations in media Q on attenuation of the spectra. Approximately 2/3 of the attenuation for the maximum attenuative case is the result of viscoelastic effects. Changing the media Q to 16 results in a reduction of attenuation from -18 dB to -11 dB. This change is similar in magnitude to the effect of scattering alone. The results indicate that variability in the intrinsic attenuation due to spatial variability in Q should be included in the total attenuation in order to account for the variability found in experimental results of Reinke and Stump (1988).

Figure 10 is a reproduction of radial acceleration spectra recorded by Reinke and Stump (1988). Comparison of these spectra with results presented in Figure 9 show a surprising degree of similarity. Both the recorded and modeled spectra show variability in amplitude starting at about 10 hertz and increasing with frequency. The variability in amplitude is somewhat higher in the experimental results than in our plane wave model. This is attributed to noise in the recorded spectra, variability in the spectra due to wave interference in the more complex recorded acceleration traces, differences in the amplitude scaling of the two spectra, and two and three dimensional effects. Comparison of the spectra indicate the combined effects of viscoelastic attenuation and scattering attenuation using the exponential correlation function can account for the majority of the variability of attenuation found in the recorded spectra. The modeled spectra (see Fig. 9) for a plane wave does not account for the variability due to lobbing that is present in the recorded spectra (see Fig. 10). This lobbing is attributable to the interference between multiple arriving waves.

Figure 11 shows the propagated displacement pulse for runs 12 and 13. Significant attenuation and some dispersion is apparent in the pulses for the two runs. All of the attenuation appears to be the result of viscoelastic effects. The slight shift in arrival time between the two runs is again attributable to variations in C_o.

IV. RECOMMENDATIONS

a. The results for the Kramers- Kronig method has shown (for a plane wave) that the method is capable of modeling most of the features of the acceleration spectra recorded for a buried detonation by Reinke and Stump (1988). However, one feature of the acceleration spectra which is not accounted for in the above plane wave results is the interference of direct, reflected and refracted waves which is present in the recorded data.. Therefore, it is recommended that the Kramers-Kronig method be applied to one, two and three dimensional wave propagation in which interference between direct, reflected and refracted waves is taken into account.

b. The Kramers-Kronig relations used in the above study applies only to low concentrations of scatterers. In fact, the maximum concentration of $\phi = 0.3$ used in the parameter study may be beyond the concentration for which the theory is strictly applicable. A variant of the K-K used in this study called the causal differential scheme is applicable up to higher inclusion concentrations. It is recommended that the K-K causal differential scheme be used to determine the limit of applicability of the K-K method used in this study. The K-K causal differential scheme adds a low concentration of scatters in a series of steps until the desired concentration of scatterers is reached. In applying causal different scheme one can insert a different size of scatterers in each step, thus, overcoming the restriction of the present theory which allows for only one size scatter at a low concentration.

c. To better understand scattering in inhomogeneous soil media it is recommended that scaled experiments be performed in a soil box in which one can construct various inhomogeneous soil/scatterer configurations. The experimental set up should have the capability of generating P and S waves of different frequency content into the scattering medium. Buried accelerometers would be used to determine phase velocities and dispersion.

REFERENCES

K. Aki and P. Richards, Quantitative Seismology, San Francisco,W. H. Freeman and Company, 1980.

A. I. Beltzer and N. Brauner, "Waves of an arbitrary frequency in random fibrous composites," Journal of the Acoustical Society of America, 1984, Vol. 76(3), pp. 962-963.

A. I. Beltzer and N. Brauner, "The Dynamic Response of Random Composites by a Causal Differential Method," Mechanics of Materials, 1987, Vol. 6, pp. 337-345.

A. I. Beltzer, J. Wegner, B. R. Tittman and J. B. Haddow, "Pulse Propagation in Random Media by a Causal Approach," Bulletin of the Seismological Society of America, 1989, Vol. 79(1), pp. 113-126.

M. A. Bogaards, "Characterization of Whole Wave Seismograms in the Shallow Weathered Zone," Masters Thesis, Southern Methodist University, Dallas, Texas, 1989.

C. W. Horton, "Dispersion relationships in sediments and sea water," Journal of the Acoustical Society of America, 1974, Vol. 55(3), pp. 547-549.

M. O'Donnell, E. T. Jaynes and J. G. Miller, "Kramers-Kronig relationship between ultrasonic attenuation and phase velocity," Journal of the Acoustical Society of America, 1981, Vol. 69(3), pp. 696-701.

R. Reinke and B. Stump, "Stochastic Geologic Effects on Near-Field Ground Motions in Alluvium," Bulletin of the Seismological Society of America, 1988, Vol. 78(3), pp. 1037-1058.

B. Stump, "Source Characterization of Bermed Surface Bursts, "Bulletin of the Seismological Society of America, 1983, Vol. 73(4), pp. 979-1003.

Wu Ru-Shan, "Attenuation of Short Period Seismic Waves due to Scattering," Geophysical Research Letters, 1982, Vol. 9(1), pp. 9-12.

1989 USAF-UES SUMMER FACULTY RESEARCH PROGRAM/

GRADUATE STUDENT RESEARCH PROGRAM

Sponsored by the

AIR FORCE OFFICE OF SCIENTIFIC RESEARCH

Conducted by the

Universal Energy Systems, Inc.

FINAL REPORT

A POSSIBLE NEW SOURCE OF NEGATIVE HYDROGEN IONS

Prepared by:	Hugh E. Siefken
Academic Rank:	Professor
Department and	Physics Department
University:	Greenville College, Greenville, IL 62246
Research Location:	WL/AWYW Kirtland AFB Albuquerque, NM 87117-6008
USAF Researcher:	Charles Stein
Date:	14 Aug 89
Contract No:	F49620-88-C-0053

A POSSIBLE NEW SOURCE OF NEGATIVE HYDROGEN IONS

by

Hugh E. Siefken

Abstract

By directly heating lithium hydride in a vacuum to evolve the large amount of stored hydrogen from the crystal lattice, experiments have been done which indicate this material and probably other alkali metal hydrides can produce a significant amount of negative hydrogen ions. The ion current appears to be emission limited and saturates with extraction voltage. The electrons accompanying the negative ions were removed by a magnetic trap. A Wien velocity filter was designed and built to provide definite mass analysis of the extracted ion species. The amount of ion current extracted and analyzed is closely related to the temperature of the sample and to the rate at which the temperature is changed.

Please regard the new ideas contained herein as proprietary to WL and to Charles Stein in particular.

Acknowledgements

The ten weeks of research passed very quickly as a result of the many persons at the Laboratory who provided a positive atmosphere in which to work. Charles Stein, whose idea launched this research, was always ready to discuss results and share insights. Dick Copeland helped in overcoming technical problems and shared his knowledge of developmental ion source work. I appreciate the help of Lt Didi Kuo and the support of Capt LeAnn Brasure who invited me to the Laboratory. Col Anderson was always interested in the latest results and provided comfortable office space which I appreciated.

The opportunity extended to me by the Air Force Office of Scientific Research to enegage in this work is particularly acknowledged. It has been a challenge to help open the door on this work. Hopefully it will be of some future benefit to scientific and technological communities.

I. INTRODUCTION

Since L. Alvarez[1] introduced the idea of using negative hydrogen ions (H^-) in particle accelerators back in 1951, atomic and nuclear science has seen this specie of ion used for many applications. Today, the production H^- ions are viewed as one of the critical components involved in the production of a neutral beam of hydrogen atoms which can be used to penetrate the strong magnetic fields of fusion machines or alternatively used as beams for space based weapons.

For several years at the Weapons Laboratory a group has been assessing developments in neutral particle beam technology. It is from this background that Charles Stein has proposed the innovative idea that the alkali metal hydrides might be a potential source of H^- ions. Such a source might operate without the complications inherent in present day H^- sources, it would in principle possess a very small transverse emittance and it should be a highly reliable source. This report will outline some of the early work which has been done in an attempt to begin to transfer the idea into reality.

My research interests were, for years, in the area of nuclear physics, principally gamma ray spectroscopy and neutron time of flight spectra. However in recent years, after constructing a low energy ion accelerator, I became interested in atomic physics, principally ion physics. During a sabbatical leave in 86-87 I served as the physicist for the McDonnell-Douglas injector group working on the neutral particle beam integrated experiment. I was responsible for the ion source and the ion optics calculations for the transport of the ions through the LEBT. My work on a volume source test stand and my interest in ion sources helped in my assignment to the present project. My original proposed research at KAFB was to set up a laser diagnostic which could be used on a various H^- ion source to measure the concentration of H_2 and H^- ions. Due to a reorganization within the Laboratory, the laser work was not pursued. I was fortunate to move into the innovative work with the alkali metal hydrides.

While at WL, as a secondary effort, I supervised the assembly of an H^- volume source and the design of the associated electronics. I was glad to assist in this way since I have had considerable experience with this particular type of source in a test stand environment.

II. OBJECTIVES OF THE RESEARCH EFFORT

The principal objective of this research is to be able to produce an H^- beam by a new, direct process. The two types of H^- ion sources presently considered for neutral particle beam applications each use a pulsed, high current, arc discharge.[2,3] The intent of the present work is to try to produce a non-pulsed beam by a more direct process.

A second objective is to investigate the dependence of H^- ion production on temperature. Since the normalized transverse emittance is directly proportional to the aperture size and the ion temperature in the source, the lower the temperature at the production site, the higher the quality of the H^- beam.

A third objective is to acquire enough data to begin to characterize this source (e.g., ion and electron currents, temperatures, voltages, geometrics, pressures, etc.). This is a multiparameter problem in which several quantities interact to produce the observable result.

An objective which was added involved the need to definitely determine the mass of ions leaving the sample. This mass analysis must be able to completely resolve those masses near that of hydrogen, M=1.

III. BACKGROUND

The idea of producing H^- ions from a compound by heating the sample appears to be unique. There is a paucity of information in the literature with no references cited in the western world.[4] In the case of the alkali metal hydrides, there are three important factors which converge to make these compounds feasible H^- sources.

First, they store a lot of hydrogen. The formation of the hydride occurs when the metal chemisorbs the hydrogen at a given temperature and reaches an equilibrium pressure. For LiH at 700°C the equilibrium pressure is 30 mm.[5]

Secondly, the bonding is quite ionic. As hydrogen is taken into the metal, the metal lattice spacing decreases due to the strong electrical attraction between the metal cation and the hydrogen anion. The density of the hydride is thus much larger than the metal. The relatively large crystal lattice energies, defined as $MH \rightarrow M^+ + H^-$ vary from 9.5 ev for LiH to 6.7 ev for CsH.[5] These strong forces provide a bond which is considerably ionic. Using Pauling's[6] electronegativity data to estimate the ionic character of a bond shows the LiH bond to be about

43% ionic and NaH to be about 47%. A quantum mechanical calculation by Lundquist[7] indicates the bonding for LiH to be about 35% ionic. Thus there is a reasonable probability of finding two electrons attached to the proton. Additional support is given to this moderately strong ionic bond model by the fact that when molten LiH is electrolyzed, hydrogen appears at the positive electrode.[5]

Several theoretical studies[8-11] have been done which model alkali metal hydride diatomic molecules. A result which appears in most of the studies is that the deeply bound X Σ potential well (ground state) is primarily due to the $Alk^+ + H^-$ ion pair attractive Coulomb interaction even though the dissociation is normally to neutral atoms. These studies are all concerned with the gaseous state so the results are only indirectly applicable to the alkali metal hydride lattice system.

IV. METHODS USED TO ADDRESS OBJECTIVES

In this work LiH has been used exclusively to try to understand the processes involved with the removal of H^-. As the temperature increases, the pressure of the vacuum systems increases. Starting at a base pressure of 3 X 10^{-6}mm, the pressure typically rises to 8 X 10^{-6}mm during the run. Knowing the pumping speed of the vacuum pump and the conductance of the system a gas load of approximately 4 X 10^{-2} torr l/s $\simeq$ 3 sccm is present. The hydrogen would like to establish the partial equilibrium pressure ($H+H \rightarrow H_2 + 4.5$ ev). However, since the heated hydride is connected to a power supply an excess of negative charge is available to neutralize the Li^+ as the H^- leaves the surface. Whether this is the precise mechanism must still be verified.

The experimental arrangement used to separate the electrons from the ions is shown in Figure 1. The electron trap has a magnetic rigidity $\int$ Bdl = 3000 gauss-cm and an average field of 600 gauss. The Faraday plate is made of carbon to minimize the production of secondary electrons. The small bias voltage on the plate made approximately a 15% effect on the H^- current.

To determine whether the mechanism for H^- production is a surface or a volume process, three different heater geometries were used. A flat pancake heater, a helical coil and a boat-shaped heater were each used to heat the sample. The results of heating a larger volume with a boat did produce more stable currents but did not produce larger currents than the other geometries. This seems to indicate that the H^- production involves a surface mechanism.

It became clear that not only is the temperature of the sample important but also the rate at which the temperature is changed. Figure 2 shows a typical result. The ion current response to a change in temperature is almost instantaneous. A static temperature usually produced an H^- current with a slow decay, most likely due to the depletion of the hydrogen. When the temperature change of the LiH was changed by 56°C in approximately 60 seconds, an increase in H^- current of 17 microamperes was measured. The ratio of currents I_{H^-}/I_e usually varied between 1/10 to 1/4 but occasionally would reach 1/100.

The results of placing an intermediate electrode between the sample and the anode (extractor) show that it strongly affects the electron ion currents. When a fine mesh was used on the electrode, a potential of approximately +4 volts seemed to maximize the H^- current. For an open aperture, approximately +9 volts was required. There were times, however, when the H^- current increased directly with the positive grid potential. When a negative potential with respect to the sample was placed on the grid, both the electron and H^- currents could be quenched. The variation of H^- current with extraction potential showed that the current saturated usually around 4 kV. For most of the work described here, a potential of 6 kV was used.

To conclusively determine the masses of the possible ion species coming off the hydride sample, a Wein filter was constructed following the ideas of Seliger.[12] Under the balanced condition, a specific ion velocity will pass straight through the analyzer with the electric field force counterbalancing the Lorentz force. Since all ions are extracted through the same potential difference, the velocity of a given ion will depend on its mass. Those ions with mass other than those selected for the balance condition will be deflected and not enter the Faraday cup.

The uniform magnetic field was provided by permanent magnets in a steel yoke with soft iron pole faces. The magnetic field was mapped on axis on four parallel axes within 1 cm of the principal axis. Fig 3 shows the strength and uniformity of the resulting field. At each end a copper plate with two sheets of mu-metal was used to terminate the E&B fields. It was found that the addition of a copper cylinder lined with mu-metal greatly reduced the B field at each end. The effective magnetic length of the mass filter is taken to be L_m = 12cm. Upon exiting the mass filter, the ions drifted 9 cm to the aperture of the Faraday cup. The overall resolution of the apparatus is calculated to be 10% ($\frac{\Delta m}{m} = .1$).

The optics used to form a beam prior to entering the mass analyzer were designed using a cylindrical Pierce geometry[13] for the electrodes. This design is intended to give the ions parallel flow between the cathode and anode. Following the anode, the optics produce a negative focal length of f = -3 cm. The lithium hydride sample of approximately .5 gram was heated in a container below the Pierce electrode. The anode surface was formed from copper with a radius of 2.5 cm. For an aperture of r_o = 2 mm the half angle divergence of the beam is 3.8°. The entire anode-cathode assembly is housed in a steel yoke so small NdFe magnets can be used to remove electrons generated in the emission process if desired. The mapping of the magnetic field in this region produced a value $\int$ Bdl = 450 gauss-cm. with an average value of B = 340 gauss which is sufficient to remove 6 kev electrons. When used, this electron trap produced a slight bend of 2° for the H^- ions at 6 keV. The entire assembly is shown in Figure 4.

An einzel lens was constructed to improve the focusing of the ions prior to entering the mass analyzer. This reduced the drift distance following the analyzer to 5 cm but did not significantly affect the resolution of the mass peaks.

A series of potential difference readings across the electric field plates in the analyzer were made for four accelerating voltages V_o. A typical voltage sweep is shown in Figure 5. The power supply providing the accelerating voltage was not regulated and tended to drift. This produced a slightly larger FWHM on the peak than expected. The nearest mass peak at M = 2 which would be found several hundred volts away from M = 1 was not observed. Electrons were removed from the beam promptly upon entering the crossed fields of the analyzer.

Using the condition for the balance of forces in the analyzer and conservation of energy gives

$$\Delta V^2 = 2B^2d^2 \frac{q}{m} V_o \qquad \text{-------- (1)}$$

where $2B^2d^2 = 9.99 \times 10^{-6}\ T^2.m^2$. A plot of ΔV^2 vs. V_o in Figure 6 shows the resulting slope is produced by ions with q/m corresponding to H^-.

V. RECOMMENDATIONS

To begin to understand the physical mechanisms taking place at or near the hydride-vacuum surface, there are some basic diagnostic experiments which can be done. There is also a set of interesting follow-on experiments that could possibly increase the amount of H^- current.

The diagnostic work needed at this stage of development of this source of H^- ions is to try to investigate the atomic, ionic and molecular states coming off the hydride surface. By using a laser spectroscopic technique rather than an electrostatic probe, information can be gathered with less uncertainty and without perturbing the productive region near the surface. The use of high power lasers to acquire such information has increased in the recent years and appears to be the next step for this ion source.

By using a laser diagnostic technique, the following investigations can be made:

I. Measure the H^- concentration profile in an axial direction from the hydride surface.

II. Determine the state(s) of molecular hydrogen.

III. Identify atomic species relevant to the production and attenuation of H^- ions.

To achieve I. the most straight-forward method involves a photodetachment technique.[14] $H^- + h\nu \rightarrow H(n) + e^-$. By using a laser pulse of photons, the increased number of electrons are collected and compared to the static value of electron current. The ratio is a direct measure of the H^- concentration. When the energy of the photon is less than 10.9 ev the H atom is left in the ground state. Such a study in an axial direction would answer a key question regarding the possibility of stripping the electron from the H^- due to collisions near the surface.

To achieve II., the same laser can be used to produce Raman spectra. Molecular hydrogen is infrared inactive but is Raman active.[15] The same Stokes or anti-Stokes shifts from the Rayleigh line occur regardless of frequency. However, the intensity of the spectral lines can be increased by increasing the frequency. By tuning the laser resonance Raman spectra may be achievable which is much more intense than ordinary Raman spectra.

The main reason for including III as part of the diagnostic effort is that the attenuation of H^- by atomic hydrogen is now well known by the reaction $H + H^- \rightarrow 2H + e$. The two approaches which have been used to measure atomic concentration are (a) laser induced fluorescence[16] and (b) UV absorption.[17]

The first approach requires a tunable dye to produce Balmer series emission. The laser power density must be able to saturate the atomic transition. This method requires less optical and vacuum equipment than the second approach.

The second approach involves the Lyman absorption of UV radiation by the H atom. The UV is produced by using an eximer laser to pump two dyes. The resulting combined beam is sent through mercury vapor which is excited and deexcites by emitting photons in the UV. This method has produced high quality absorption peaks in a small optical path length. These two approaches might be suitable to investigate other atomic species involved in the H^- production.

An interesting set of follow on experiments involves the possibility of increasing the output of H^- using the ideas of Manning[18] applied to the MH systems. By controlling the direction of the vacancies, one may be able to preferentially direct H^- to the surface. The driving force to move the vacancies can be created by an electric field externally produced across the sample. Such a field will lower the energy barrier seen by the vacancy when it tries to make a jump. This would be like an internal Schottkey effect.

I intend to apply for a minigrant which would keep this introductory work moving ahead. The development of ion sources, as evidenced again by this report, is a complex but exceedingly rich field of research which may require years of effort before a technological transfer occurs.

REFERENCES

1. L. W. Alvarez, Rev. Sci. Instrum. 22, 705 (1951).

2. K. N. Leung, C. A. Hauch, W. B. Kunkel and S. R. Walther, Rev. Sci. Instrum. 60, 531 (1989).

3. G. E. Derevyanki and V. G. Dudnikov, IYaF 86-20, Novosibirsk (1986).

4. A. P. Strokach, Report NIIEFA-P-K-0470, Lenningrad (1980).

5. W. M. Mueller, J. P. Blackledge and G. G. Libowitz, Metal Hydrides, Academic Press, New York, (1968).

6. L. Pauling, The Nature of the Chemical Bond, Cornell University Press, Ithica, NY, (1960).

7. S. O. Lundquist, Ark. Fys. 8, 177 (1954).

8. R. E. Olson and B. Liu, J. Chem. Phys. 73, 2817 (1980).

9. G. Doggett, F. N. Yousif and J. A. Matthew, Molecular Physics 57, 1297 (1986).

10. F. B. Orth, W. C. Stwalley, S. C. Yang and Y. K. Hsieh, J. Mol. Spectr. 79, 314 (1980).

11. R. S. Mulliken, Phys. Rev. 50, 1028 (1936).

12. R. L. Seliger, J. Appl Phys. 43, 2352 (1972).

13. A. T. Forrester, Large Ion Beams, John Wiley and Sons, New York, (1988).

14. M. Bacal, Proceedings of the Fourth International Symposium on the Production and Neutralization of Negative Ions and Beams, (Brookhaven National Lab, Upton, NY, 1986), p. 120

15. N. B. Colthup, L. H. Daly and S. E. Wiberley, Infrared and Raman Spectroscopy, Academic Press, (1964).

16. M. P. S. Nightingale, A. J. T. Holmes, M. J. Forrest and D. D. Burgess, J. Phys. D: Appl. Phys. 19, 1707 (1986).

17. G. C. Stutzin, A. T. Young, A. S. Schlacter, J. W. Stearns, K. N. Leung and W. B. Kunkel, G. T. Worth and R. R. Stevens Rev. Sci. Instrum. 59, 1363 (1988).

18. J. R. Manning, Diffusion Kinetics for Atoms in Crystals, Van Nostrand, 1968, p. 13.

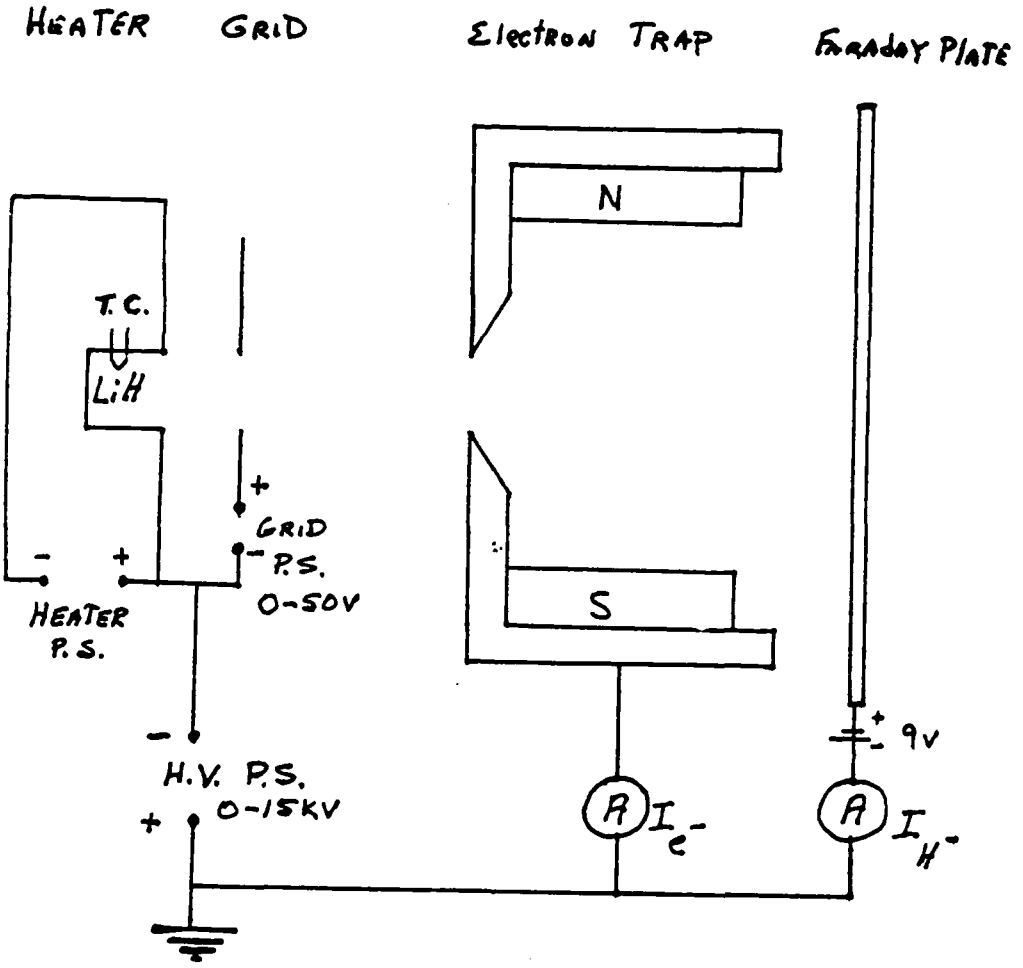

Figure 1. Experimental Setup used to measure electron and ion currents

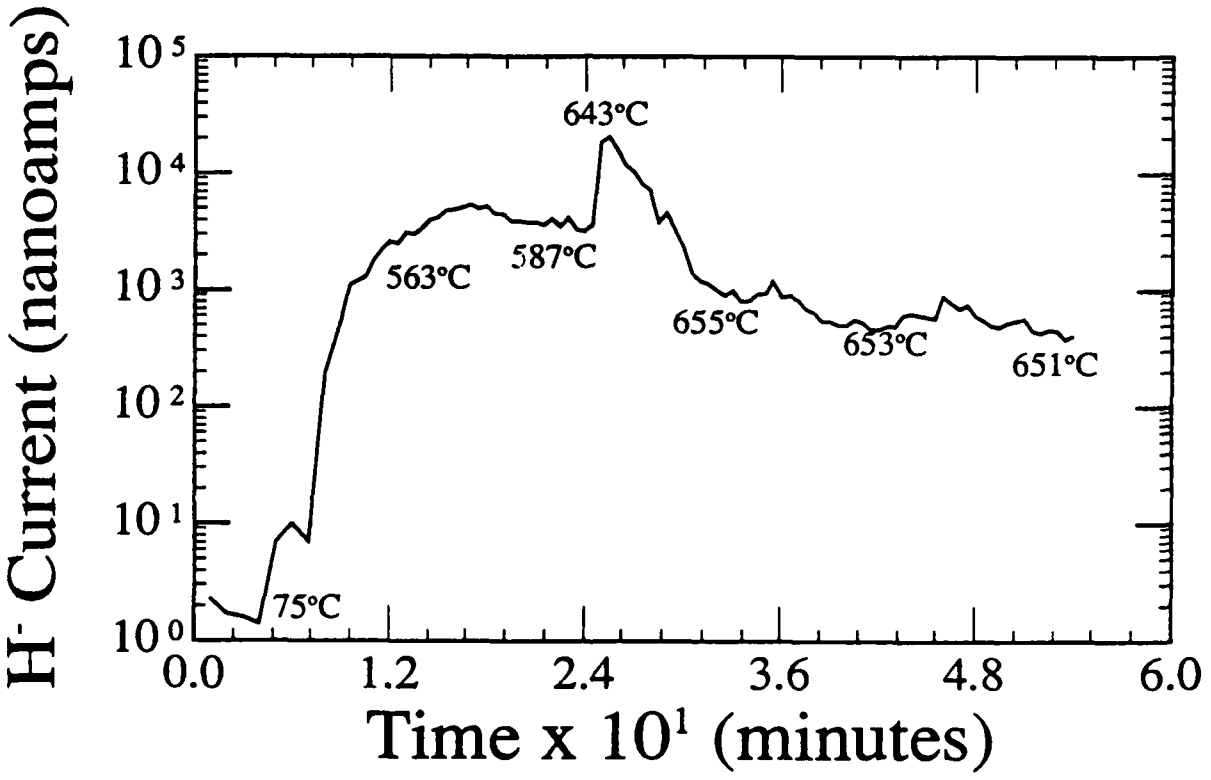

Figure 2. H^- current on Faraday plate versus time. Temperature of sample measured by thermocouple is shown.

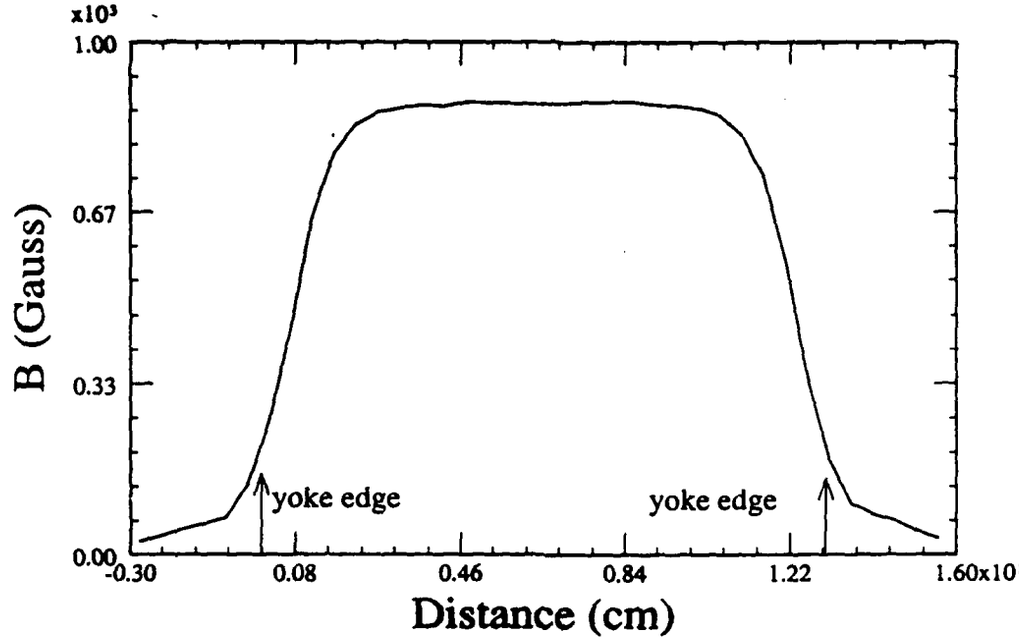

Figure 3. Mapping of Magnetic Field along ExB axis.

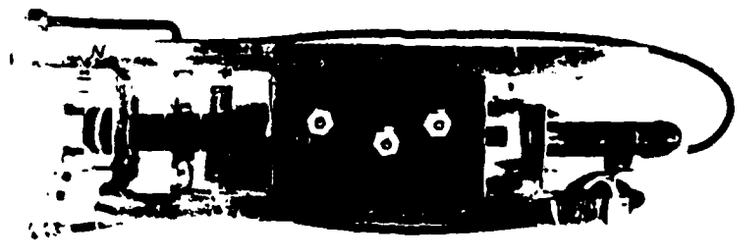

Figure 4. Assembly used to measure charge to mass ratio.
Left to right: Pierce electrodes, einzel lens, ExB analyzer, Faraday Cup

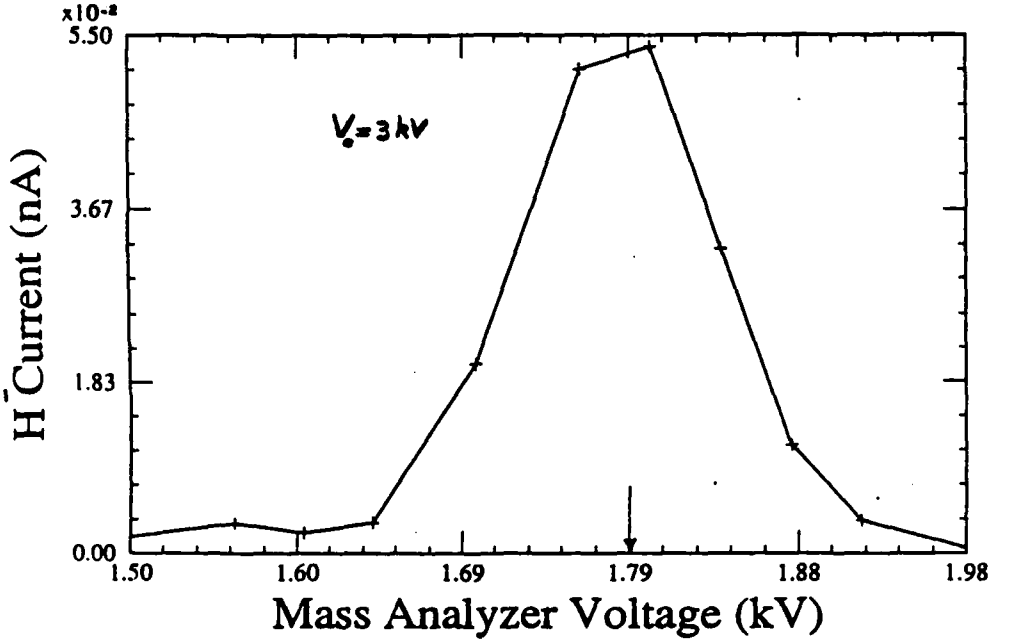

Figure 5. H^- current collected by Faraday cup as electric field is changed in E×B analyzer. Voltage uncertainties are ±50 v.

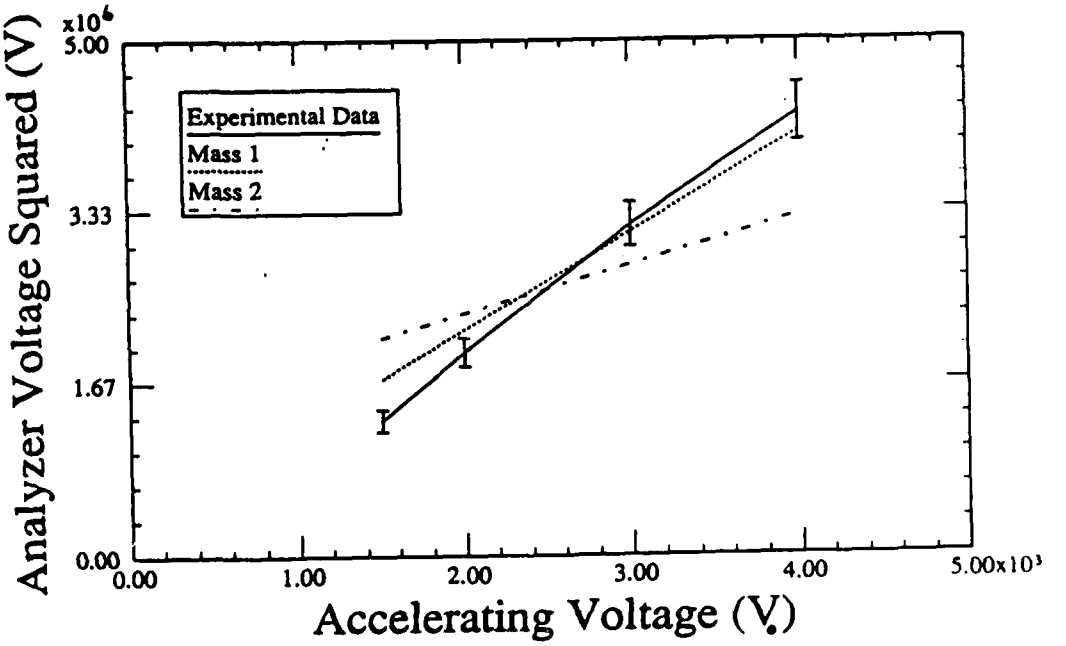

Figure 6. A plot using experimental data in equation (1). Accelerating voltage uncertainties are ± 75 v.

1989 USAF-UES SUMMER FACULTY RESEARCH PROGRAM/

GRADUATE STUDENT RESEARCH PROGRAM

Sponsored by the

AIR FORCE OFFICE OF SCIENTIFIC RESEARCH

Conducted by the

Universal Energy Systems, Inc.

FINAL REPORT

The Effect of a Maverick Missile on a Test Antenna at Spacings Less than $2D^2/\lambda$

Prepared by:	John W. Silvestro, Ph. D.
Academic Rank:	Asst. Professor
Department:	Electrical and Computer Engineering
University:	Clemson University
Research Location:	Weapons Lab
	Kirtland AFB, NM 87117
USAF Researcher:	William Lewis
Date:	September 20,1989
Contract Number:	F49620-88-C-0053

The Effect of a Maverick Missile on a Test Antenna at Spacings Less than $2D^2/\lambda$

by

John W. Silvestro

ABSTRACT

Testing of weapon system susceptibility to RF energy may require placing the system in the near zone of the transmitting antenna. Since scatterers that are not in the far zone of an antenna may influence the antenna, this poses a problem. A test of the Maverick missile later this summer, will require such placement. To estimate the effects this near placement has on the antenna, low power S and L band coupling tests of the complete experiment using Narda 644 and 646 horns and an instrumented Maverick missile nose cone were performed. In conjunction with these tests a simplified computer model of the scattering was also developed using the NEC-BSC scattering code. The computed results for predicting the change in the horn's voltage reflection coefficient agreed quite well with the measured results. These reflected field amplitudes, at the horn, were on the order of 24 dB down from the incident horn fields. As a test of the effect on the antenna's radiated power, the fields scattered back to the horn aperture by the nose cone were assumed to be totally re-reflected by the horn. The re-scattered fields at the missile were found to be almost 20 dB down from the original fields levels. The small values for both of these effects at the distances analyzed (as close as ~2λ) show that the missile-horn interactions should be small enough to be ignored in this situation.

ACKNOWLEDGEMENTS

I wish to thank the Air Force Systems Command Weapons Lab and the Air Force Office of Scientific Research for supporting this research. I would especially like to thank the Weapons Laboratory's Chief Scientist, Dr. Brendan Godrey, for supporting summer faculty research. Dr. William Baker of the Advanced Weapons Office also provided an outstanding research environment. Universal Energy Systems and Dr. Dick Keppler must also be mentioned for their administrative help.

My experience was very enriching because I was able to interface with researchers whose expertise was different from my own. The support of my two technical focal points Capt. Kyle Hendricks and Lt. Bill Lewis was greatly appreciated. The technical help from Dr. Robert Koslover, Dr. Don Voss and David Cremer was invaluable to this work. The concern and support of Maj. Schlicher was also greatly appreciated.

I also had many very enlightening conversations with Dr. A. Biggs and Dr. P. Vail.

I. INTRODUCTION

There has been much interest over the last several years in the generation of high power microwaves. Their possible use in such areas as electronic counter measures, communications and radar make this an important emerging technology.

The High Power Microwave Simulator Division at the Weapons Lab at Kirtland Air Force Base is particularly interested in this technology. While much of their work involves research into new and better microwave sources, they are also involved in the testing of high power microwave effects on military test assets. A major test to be performed later this summer will measure these effects on a Maverick missile. Connected with this test are all of the problems associated with the RF illumination of an asset. One concern at the moment is what effect moving the asset in closer then the far zone distance of the transmitting antenna will have on the antenna's characteristics, and the coupling of RF to the missile.

My research interests have been in the areas of antennas, scattering and numerical modelling of electromagnetic phenomenon. My experience in the solution of scattering problems using the Geometrical Theory of Diffraction (GTD) and in the characterization of aperture antennas was particularly useful in the work this summer.

II. OBJECTIVES OF THE RESEARCH EFFORT

Current testing of radar and antenna systems requires that the fields being considered are in the far zone of the antenna. This is to keep the field wavefront approximately planar and also to be far enough away from the source antenna so that the measuring or scattering device will not affect the antenna's characteristics. With present state-of-the art high power microwave sources it is necessary to move in closer to the source antenna to get the energy fluences needed for testing. This poses two problems. First, is the

effect the missile has on the antenna. This interaction may so change the antenna characteristics that the power density at the missile is affected. Second, for an operational scenario the missile should be in the far zone of the antenna. The coupling into it in those cases would be via an incident plane wave. Fields near antennas are usually not planar. This means that we have to be very careful to account for these variations in our test procedures.

My assignment as a participant in the 1989 Summer Faculty Research Program was to consider this problem with regard to the Maverick missile test to be performed later this summer and fall. I was to look at the effects on the horn antenna and its radiated fields due to this missile when it is in closer then the far zone distance of the antenna. Considering the time limit on this work (10 weeks), I was to work on an approximate solution to this problem.

III. SOLUTION AND RESULTS

The problem that needed to be solved was to quantify the effects on the test antenna of a Maverick missile that was moved in close. This was done by creating a simplified computer model of the test problem using the NEC-BSC scattering code [Marhefka, 1982]. The specific problem considered here involved a Narda 646 standard gain horn with a Maverick missile nose cone moved to within ~2λ of the aperture. Due to the time restrictions of the summer, several approximations were made in the course of this project. The worst case scenario was chosen every time when making an approximation so that the results overestimated the actual effects. A cold test of the above configuration was also run and comparisons against computed data showed a good agreement. The final results did show that these effects were small and that testing should be possible at these distances for this configuration.

The first task was to model the test antenna to be able to calculate the fields at distances closer to the antenna then those at which the far zone

patterns are calculated at. A computer model that does this was developed earlier by Dr. Robert Koslover of Voss Scientific for the High Power Microwave Simulator Division. This model was used as a test for the computer data generated here. The model used the Stratton-Chu approximation [Li, 1964] to solve for the fields that were in the near zone. The distance that the far zone starts at is $r>2D^2/\lambda$ (r is the distance from the antenna, D is the maximum dimension of the antenna and λ the free space wavelength). The part of the near zone closer than $k_0 r>>1$, also known as the reactive near zone [Dyson,1973], is a region where reactive components of the power density are large (k_0 is the free space wavenumber, $k_0=2\pi/\lambda$). Testing in this region would lead to capacitive coupling to the test asset and that would not be representative of coupling in an operational environment. Therefore no testing should be performed in this close. The region of interest then is all r such that $k_0 r>>1$ (or $r>>\lambda/2\pi$), the radiating near zone. To model the antenna in this region the source modelling part of the NEC-BSC scattering code was used. Fields for aperture antennas, such as the flared horns used here, can be calculated using the aperture electric field. The aperture fields are replaced by equivalent currents and these currents are treated as sources [Silver, 1948]. For this model, the aperture of the antenna was split into small patches. The patches were small enough so that the fields from each patch would be in the patch's far zone and also so that the currents over each patch were approximately constant. For the former to be true it is also necessary that $1/(k_0 r)<<1$,(this restriction is satisfied if $r\sim 1\text{-}2\lambda$) and for the latter the maximum patch dimension must be kept less then $\lambda/10$. The NEC-BSC allows the user to model an aperture antenna with constant current patches by solving for the far zone field of each patch and summing their contributions.

The assumptions made in determining the aperture field for the

horn shown in Figure 1 are:

(1) the field is that of the dominant mode of a rectangular waveguide (TE_{10})

(2) the phase error due to the flare in the horn is quadratic [Collin, 1968]:

$$e^{-\frac{jk_0}{2}\left(\frac{x^2}{\rho_x}+\frac{y^2}{\rho_y}\right)}$$

The coordinate system shown in Figure 1 will be used throughout this report.

These restrictions for the patch mean that this model should be valid in the near zone for r as small as 1 to 2λ. Using this model the fields could be easily calculated. Figure 2 shows a comparison between this model with 600 patches across the aperture and the earlier model developed by Dr. Koslover. As we can see there is an excellent agreement between the two models. Therefore, the horn will be modelled with 600 patches for all the calculations in this report. Some of the data in these figures is for fields at $r<2\lambda$. *Since both models assume* $k_0 r>>1$, *they agree* at those distances even though they may not be completely correct there.

Once the horn itself was accurately modeled the next step was to include in the model the missile and to calculate its scattering. The missile nose cone is shown in Figure 3. The front of the missile has a dielectric window. Inside the window is an infrared eye that is part of the missile guidance system. The zinc sulfide dielectric window was the most difficult part to model, but after conversations with the engineers at Hughes (the manufacturer of the Maverick missile) it was decided to treat it as if it were completely transparent. Hughes engineers had stated that in the past that is what they had always done. The scattering from the missile, with a transparent window, was calculated by modelling it as a circular cylinder with a 2" radius located at the eye's position, as shown in Figure 4. The radius was determined after comparisons with the measured data to be discussed later and is an effective scattering radius. Therefore the scattering from the missile

was treated as reflection from a 4" diameter circular plate (the cylinder end cap). The energy that couples to creeping waves on the outside of the missile's conducting skin was ignored since this tends to contribute very little to the backscattering for curved bodies. The coupling into and out of the missile cavity was too difficult to calculate quickly, but since it should be a second order effect on the external fields it was also ignored. Using this model then it is possible to approximate the amount of energy coupled back to the horn antenna.

This backscattered coupling can also be handled using the NEC-BSC. The code calculates the scattering from the missile model using the GTD. The scattered power density over the horn aperture then is used to calculate the coupling to the antenna's fields. This is done in the code using a coupling term derived from the Reaction Principle [Marhefka, 1982]. For cases such as these, especially with the scatterer close to the antenna, the results from these calculations are approximate. They are related to the scattered power density over the aperture taking into account the amplitude taper of the TE_{10} aperture field and so should be an adequate approximation. The 2" effective radius discussed above was chosen to be larger then the physical scatterer to take into account the fact that these calculations are approximate and to include some room for error. Therefore, using this model an approximation to the amount of reflected signal that couples back to the horn could be calculated. To test the validity of these approximations comparisons with the measured data were performed. An overview of the cold test is to follow.

The test was performed in the High Power Microwave Simulator Division's anechoic chamber in building 909. At one end of the chamber was placed the transmitting antenna, the Narda 646 horn, driven by a signal generator swept in frequency over the L band. An instrumented nose cone was placed at various distances from the horn and data was collected at all

frequencies. The nose cone was oriented as shown in Figure 4. Inside the missile were several field sensors. Readings from the sensors measured at far zone distances could then be compared with those made at the closer spacings, taking into account the higher energy fluences at the closer distances. These comparisons would tell if the coupling into the missile was being affected as the missile moved closer to the antenna. At the same time the reflection coefficient of the transmitting antenna was also measured. This tells the effect on just the antenna and is the quantity addressed in this report.

The test setup and the sources of reflected energy are shown in Figure 4. The actual reading of reflected power at the output port of the directional coupler has three components to it. They are: (1) the energy coupled from input power port of the direction coupler (shown as Γ_1 in the figure), (2) the energy reflected at the horn to free space interface (Γ_2) and (3) the energy scattered by the missile and coupled back to the horn (Γ_3). These 3 reflected signals beat with each other to give an oscillatory reflected power reading. To take these into account, the theory of small reflections [Collin, 1966] was used to calculate the total reflection coefficient from these three individual terms. This theory assumes that if the individual terms are small enough that any higher order interactions between them can be ignored. Thus:

$$\Gamma_T = \text{the total voltage reflection coefficient} \approx \Gamma_1 e^{-j2k_1 d_1} + \Gamma_2 e^{-j2k_2 d_2} + \Gamma_3 e^{-j2k_3 d_3}$$

where k_i and d_i are the propagation constant and distance from the reflection point to the reflected power output connector for the i^{th} term. The d's are easily determined and likewise the k's, but the complex value for Γ_1, Γ_2 and

the phase of Γ_3 were not known (the amplitude, $|\Gamma_3|$, is the only value the computer generates). Using the magnitude and phase form for the reflection terms to rewrite the equation:

$$\Gamma_T \approx |\Gamma_1| e^{j\alpha_1} e^{-j2k_1 d_1} + |\Gamma_2| e^{j\alpha_2} e^{-j2k_2 d_2} + |\Gamma_3| e^{j\alpha_2} e^{-j2k_3 d_3}$$

The unknowns are: $|\Gamma_1|$, $|\Gamma_2|$ and all the α_i's. Using the experimental data for this specific configuration these values were calculated. Even though so many of the terms were determined from the measured data the one important term, $|\Gamma_3|$, was calculated using the computer model. Using these terms the Γ_T was calculated and compared against measured, as shown in Figures 5 and 6. In these figures the comparison is shown for four different missile spacings. As we can see from these plots the computed data agrees reasonably well with the measured. In fact, when they don't agree the computed data tends to give the envelope of the measured data, often being too large (predicting too much reflected energy back). A source of error in these calculations, other than the ignored scattering terms, is the fact that the $|\Gamma_i|$'s and the α_i's are assumed to be constant with respect to frequency. This is not true. The computed values of $|\Gamma_3|$ at 1.3 GHz. for the 4 spacings are:

Distance (m)	$\|\Gamma_3\|$ (dB)
.41	-24
.58	-25
.82	-26.6
1.82	-31.7

From this we see that the coupling into the dominant mode of the horn for this configuration is small. Therefore we can say with some certainty that the horn

is not being affected significantly at these missile spacings.

The last step in the analysis is to determine how the antenna's radiated fields change due to this missile interaction. An upper and lower bound on this effect was computed. The complete scattered fields over the antenna aperture were calculated and then assumed to be totally reflected back to the missile. These re-reflected fields were then added or subtracted to the original fields (calculated with no missile) to determine a worst case upper and lower bound to the perturbed fields. This technique was first used by Winchell and Davis [Winchell, 1980] to determine the effect of a ship's masts on the radiation patterns of the ship's antennas. In essence what is being done is to assume that the entire missile scattered signal is reflected back to the missile by the transmitting horn. Since the phasing of this reflection can't be easily calculated, the field magnitudes are assumed to reflect from the horn as if they were incident on a flat conducting plate. This gives a worst-case estimate of the true fields re-radiated by the horn. In fact some of the energy couples into the antenna (as discussed above) and what is reflected goes through a complex process before being re-radiated (making the phasing hard to determine). Therefore, by choosing to use the complete magnitude, allowing all of it to reflect and then adding and subtracting the resulting fields to the original terms an estimate of the upper and lower bounds on the total fields near the missile can be determined. With the model so chosen and using this technique the re-radiated fields for the case of the missile at z=.5 m were calculated. Figure 7a shows the power density contours (in dB kW/cm^2) at the missile for a 5 MW source feeding a Narda 646 at 1.3 GHz. with no re-radiated fields present (no missile scattering in the computation). Figure 7b shows the re-radiated fields due to the missile, calculated at z=.5 m. Notice in 7b that the fields are ~20 dB down. Therefore any second order reflections would be ~40 dB down and so can be ignored. To get the upper and lower bounds then 7b is first added to and then subtracted from 7a. This was done in Figure 8 for the E and H plane cuts at .5 m., normalized to show the values

for a 1MW source. The error bars in Figure 8 are the bounds given by adding and subtracting the re-radiated fields. Looking at these worst case bounds we see that across the missile window, which is ~7" in diameter, the maximum deviation to the fields is less than $\pm$1.5 dB. Therefore there does not appear to be much change in the fields at the missile due to the missile interacting with the transmitting antenna. The assumption that the fields are approximately planar should be valid here.

From these two calculations we see that for this test the missile can be moved up to approximately .5 m (~2λ), which is a fraction of D^2/λ ($D^2/\lambda \approx 1.2$ m at 1.3 GHz.), without degrading the test parameters. In fact, the data from the sensors inside the missile showed this assumption to be true at even smaller distances. There was little change in the coupling to the sensors as the missile was moved up. This data will appear in an Air Force technical report of the Maverick missile test at a later date and the interested reader should refer to it for more details. In conclusion the worst-case calculations made with the computer model did predict little affect on the antenna and it's radiated fields, which agrees with other testing to appear later.

IV. RECOMMENDATIONS

Regarding the work performed this summer it must be realized that due to effects that could not be calculated in the time frame given, the data are very much dependent on the given test configuration. While the computer and test data showed that it was valid to do this test at ~2λ, that may not be true for other setups.

To completely look at the problem more time needs to be spent on it's solution. The affects on the horn could be handled in a similar manner ,but the method of moments should be used to determine the actual coupling into the horn and to calculate the re-radiated fields. For the non-planar effects the method of moments could be used again to determine the effects of phase and

amplitude tapers on the coupling into cavities such as are present in these types of problem. Both of these problems can be solved given sufficient time and if they are done for the various scattering shapes and cavity types a library of standard configurations could be created. This data could then be used in developing valid approaches to future testing.

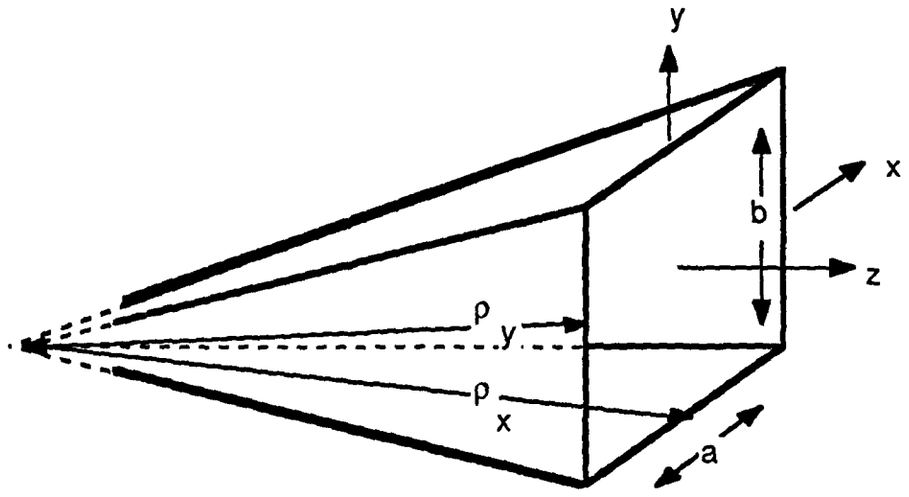

Figure 1 The parameters for a pyramidal horn.

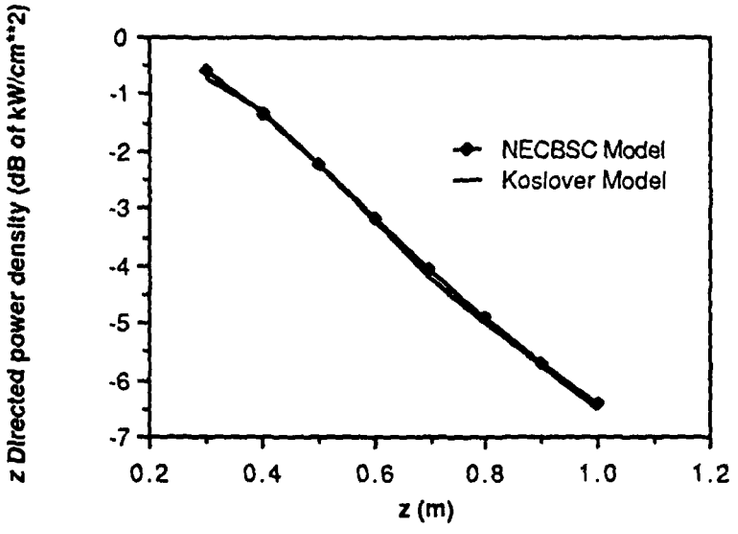

Figure 2 Model comparison of the z directed radiated power density for a Narda 646 horn at 1.3 GHz with a 1 MW source. Taken at x=y=0, where z=0 is at the face of the antenna.

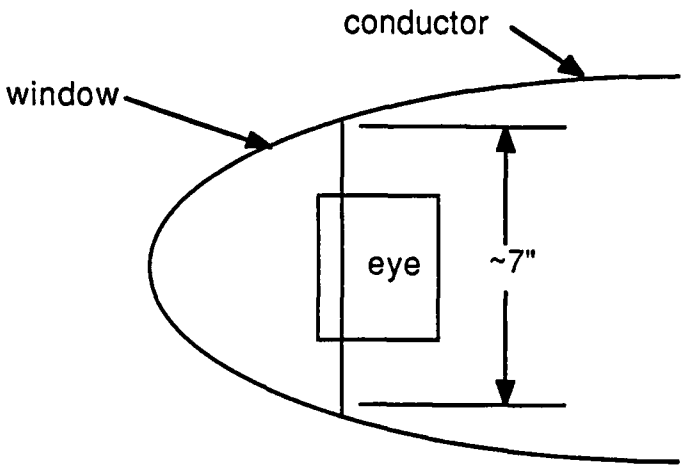

Figure 3 The missile nose cone.

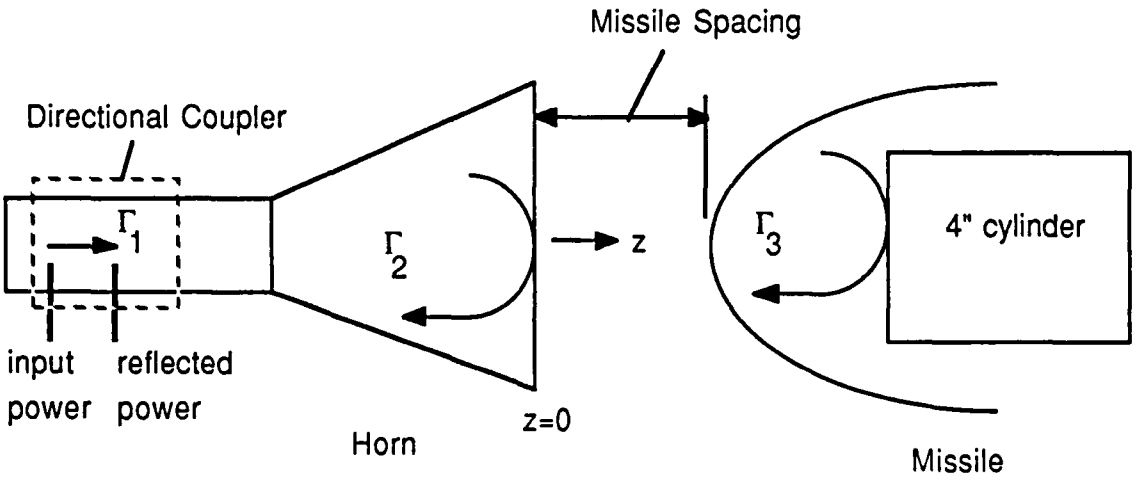

Figure 4 The cold test set-up. Horn and Missile are centered.

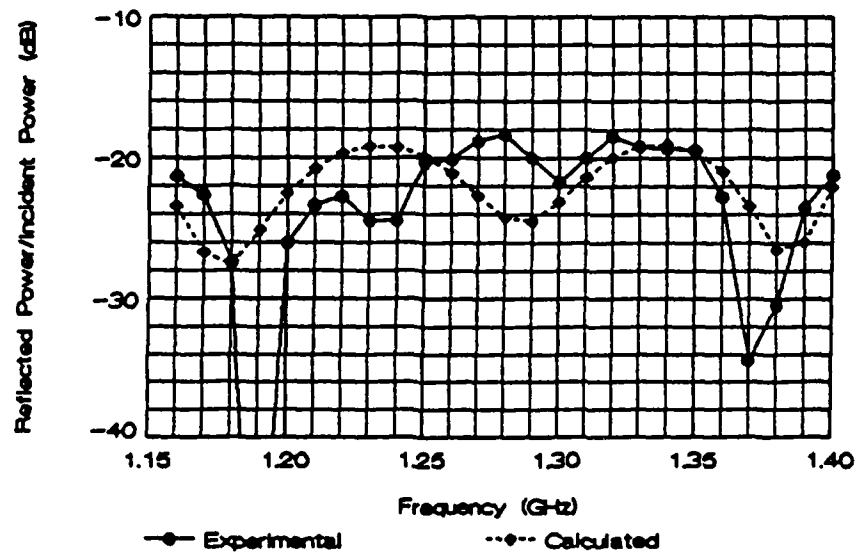

(a)

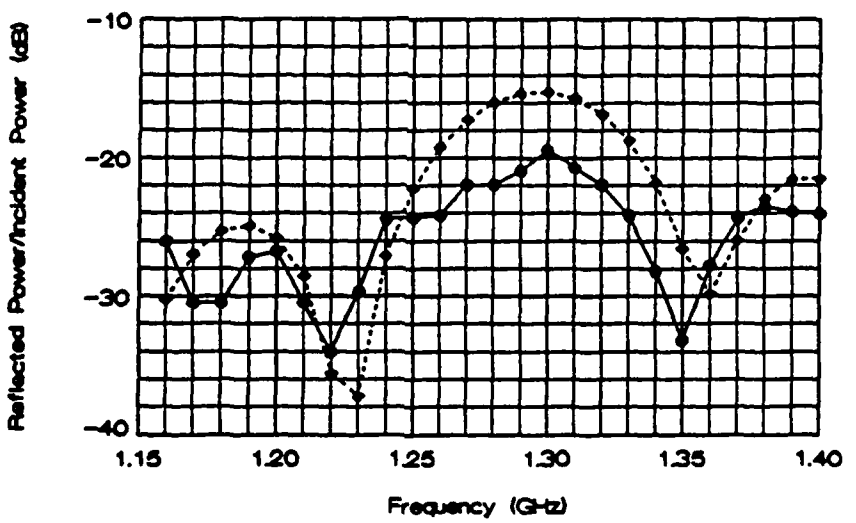

(b)

Figure 5 $|\Gamma_T|$ measured at the reflected power port due to a missile at: (a) 41 cm. and (b) 58 cm.

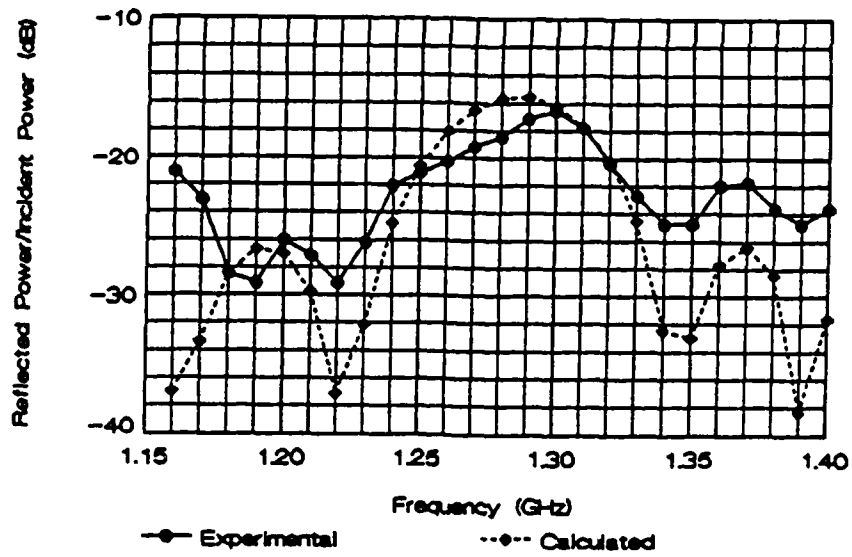

(a)

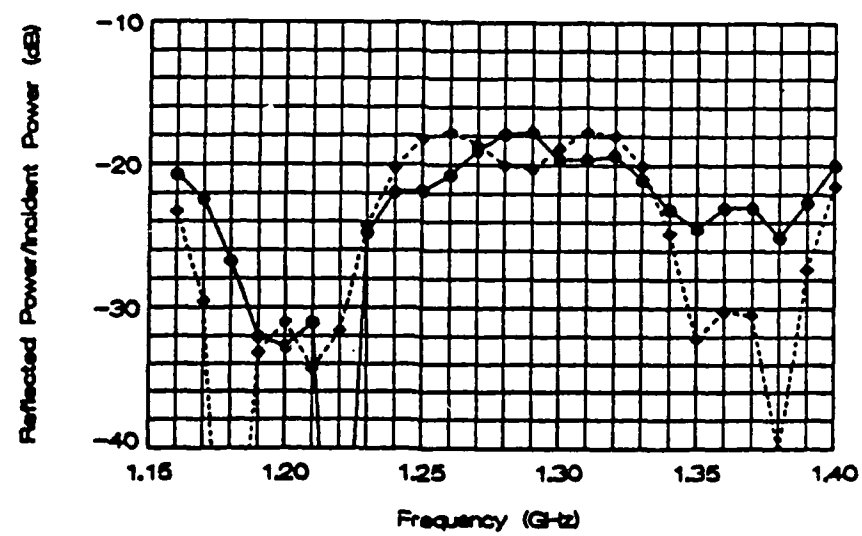

(b)

Figure 6 $|\Gamma_T|$ measured at the reflected power port due to a missile at: (a) 82 cm. and (b) 182 cm.

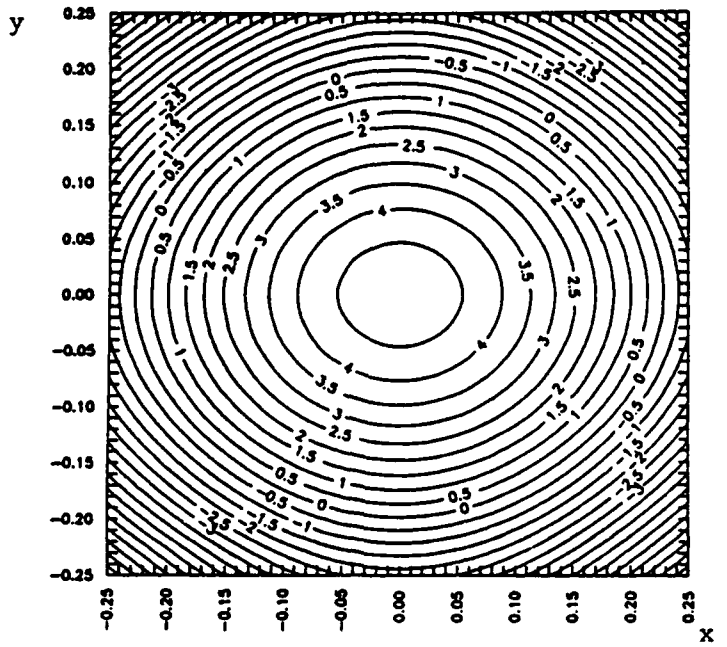

(a)

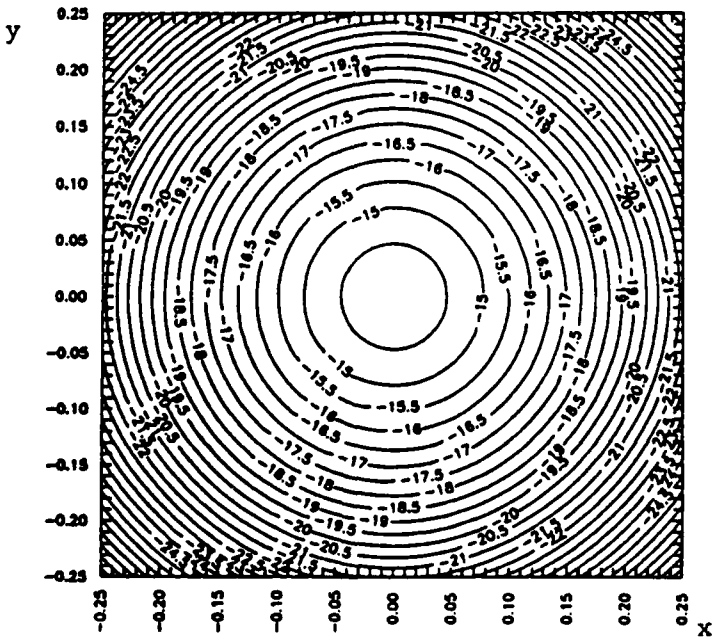

(b)

Figure 7 z directed power density contours at z=.5m in dB of kW/cm^2 for (a) 5 MW, 1.3 Ghz source, centered Narda 646 horn no missile (b) the re-radiated power density at z=.5 m. (distances are in meters)

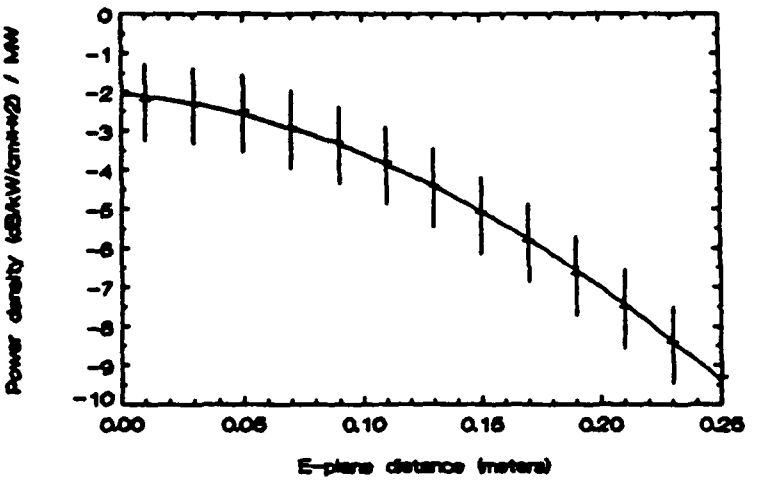

(a)

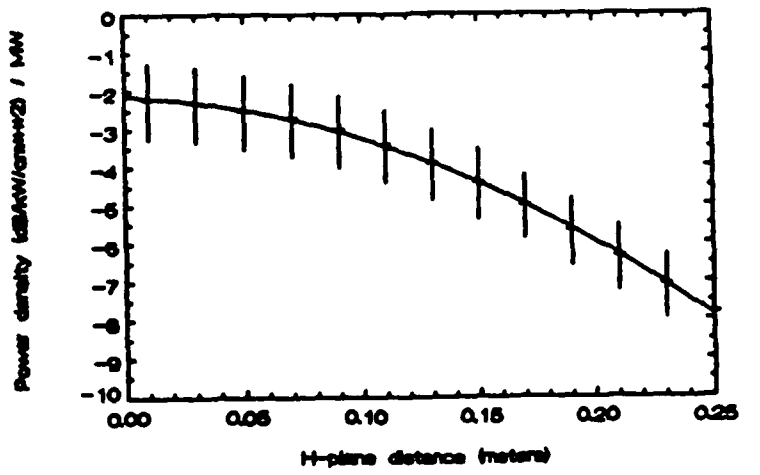

(b)

Figure 8 z directed power density in E and H plane at z=.5 m with error bars signifying worst case bounds on fields. (Same configuration as Figure 7, but with a 1 MW source)

V. REFERENCES

1. Marhefka, R. J. and W. D. Burnside, Numerical Electromagnetic Code- Basic Scattering Code, Part I, User's Manual, The Ohio State University, 1982

2. Li,T. and R. H. Turrin, "Near-zone Field of the Conical Horn", IEEE Trans. on Ant. and Propagat., November 1964, pp. 800-2

3. Dyson, J. D. , "Measurement of Near Field of Antennas and Scatterers", IEEE Trans. on Ant. and Propagat., July 1973, pp 446-60

4. Silver, S., Microwave Antenna Theory and Design, McGraw-Hill Company, New York, 1948

5. *Collin, R. E. and F. J. Zucker,* Antenna Theory, Part I, McGraw-Hill Company, New York, 1968

6. Collin, R. E., Foundations for Microwave Engineering, McGraw-Hill Company, New York, 1966

7. Winchell, S. G. and D. Davis, "Near-Field Blockage of an Ultralow Sidelobe Antenna", IEEE Trans. on Ant. and Propagat., July 1980, pp. 451-9